

Technische Universität Dresden

Investigation of physical and chemical interactions during etching of silicon in dual frequency capacitively coupled HBr/NF₃ gas discharges

Marco Reinicke

von der Fakultät Elektrotechnik und Informationstechnik der
Technischen Universität Dresden
zur Erlangung des akademischen Grades eines

Doktoringenieurs

(Dr.-Ing.)

genehmigte Dissertation

Vorsitzender: Prof. Dr.-Ing. habil. G. Gerlach

Tag der Einreichung: 27.02.2009

Gutachter: Prof. Dr. rer. nat. J.W. Bartha

Tag der Verteidigung: 21.07.2009

Prof. Dr. rer. nat. A. Kersch

Prof. Dr. rer. nat. E. Schultheiß

Bibliografische Information der Deutschen Nationalbibliothek
Die Deutsche Nationalbibliothek verzeichnet diese Publikation in der Deutschen
Nationalbibliografie; detaillierte bibliografische Daten sind im Internet über
<http://dnb.d-nb.de> abrufbar.

© 2009 Marco Reinicke
Herstellung und Verlag: Books on Demand GmbH, Norderstedt

Printed in Germany

ISBN 978-3-83913-844-1

Contents

Contents	i
Abbreviations	iii
Symbols	v
Abstract	ix
1 Introduction	1
1.1 Capacitive rf discharges	4
1.2 Plasma boundary sheath.	9
1.3 Sheath ion transport	17
1.4 Silicon etching with halogen chemistry	22
1.5 In situ plasma diagnostics.	29
1.5.1 Mass resolved ion energy analysis	29
1.5.2 Infrared absorption spectroscopy	35
1.6 HPSM simulations	36
2 Mass resolved ion energy analysis.	40
2.1 Analyzer ion optics.	41
2.2 Electrode voltage settings.	42
2.3 Determination of floating potential.	45
2.4 Comparison to HPSM simulations.	48
2.4.1 Extraction effects	49
2.4.2 Orifice transmission function.	51
2.4.3 Energy transmission function	52
2.4.4 Mass transmission function	54
2.4.5 Sheath behaviour in front of different dielectric surfaces	54
2.4.6 HPSM extensions and modifications	58
2.5 HPSM simulation studies.	63
2.5.1 Argon discharges.	63
2.5.2 Hydrogen bromide discharges.	72
2.5.3 Summary and discussion	79
3 Complementary diagnostic techniques	81
3.1 In situ plasma diagnostic techniques	81
3.1.1 Mass spectrometry for plasma flux analysis	81
3.1.2 Appearance potential mass spectrometry	83
3.1.3 Quantum cascade infrared laser absorption spectroscopy	85
3.1.4 RF probe measurements	90
3.2 Evaluation of etch results	91
3.2.1 Gravimetry (weight loss measurements)	91
3.2.2 Ellipsometry	93
4 Experimental investigations and results	95
4.1 Plasma reactor design and experimental setup	95
4.2 Argon discharges	104
4.2.1 Neutral mass spectra	104
4.2.2 Variation of power	105
4.2.3 Variation of pressure	111
4.2.4 Variation of gas flow rate	115
4.2.5 Variation of magnetic field	117
4.2.6 Summary	121
4.3 Hydrogenbromide discharges	124
4.3.1 Neutral mass spectra and degree of dissociation	124
4.3.2 Variation of power	126
4.3.3 Variation of pressure	133
4.3.4 Variation of gas flow rate	137
4.3.5 Variation of magnetic field	140
4.3.6 Summary	142

4.4 Nitrogen trifluoride discharges	144
4.4.1 Neutral mass spectra and degree of dissociation	145
4.4.2 Variation of power	147
4.4.3 Variation of pressure	154
4.4.4 Variation of gas flow rate	157
4.4.5 Variation of magnetic field	160
4.4.6 Summary	162
4.5 HBr/NF ₃ mixtures	164
4.5.1 Neutral mass spectra	164
4.5.2 Variation of power	166
4.5.3 Variation of pressure	173
4.5.4 Variation of gas flow rate	177
4.5.5 Variation of magnetic field	178
4.5.6 Etch mechanisms in HBr/NF ₃ discharges	179
4.5.7 Summary	185
4.6 Complex halogen mixtures	188
4.6.1 Neutral mass spectra	189
4.6.2 Further discharge analysis	194
4.6.3 Summary and discussion	196
5 Summary and conclusions	200
Appendix A: Heavy particle collision parameters for Ar	206
Appendix B: Heavy particle collision parameters for HBr	207
Appendix C: HPSM simulation results for Ar	208
Appendix D: HPSM simulation results for HBr	216
Appendix E: Experimental results for Ar	231
Appendix F: Experimental results for HBr	234
Appendix G: Experimental results for NF ₃	237
Appendix H: Experimental results for HBr/NF ₃	240
Appendix I: Experimental results for SiF ₄	242
Appendix J: Experimental results for SiCl ₄	245
References	247
Acknowledgement	265
Erklärung	267
Publications	269
Lebenslauf	271

Abbreviations

AAS	Atomic Absorption Spectroscopy
APMS	Appearance Potential Mass Spectrometry
ARDE	Aspect Ratio Dependent Etching
BS	beam splitter
CARS	Cavity Ring-Down Spectroscopy
CCP	Capacitively Coupled Plasma
CCRF	Capacitively Coupled Radio Frequency
CD	critical dimension
CEM	Channeltron Electron Multiplier
cf.	confer (compare)
CVD	Chemical Vapor Deposition
CX	charge exchange
dc	direct current
DRAM	Dynamic Random Access Memory
DT	Deep Trench
e.g.	exempli gratia (for example)
EEDF	Electron Energy Distribution Function
EQP	Electrostatic Quadrupole Probe
ES	elastic scattering
ESA	Electrostatic Sector Field Analyzer
ESC	electrostatic chuck
et al.	et alii (and others)
FD	fluid-dynamic
FEM	Finite Element Method
FOUP	Front Opening Unified Pod
FTIR	Fourier Transform Infrared
FWHM	full width at half maximum
GDP	gas distribution plate
GEC	Gaseous Electronics Conference
HAR	high aspect ratio
HART	High Aspect Ratio Trench
hf	high frequency
HITRAN	High Resolution Transmission Molecular Absorption Database
HMDSN	Hexamethyldisilazane (C ₆ H ₁₉ NSi ₂)
HMDSO	Hexamethyldisiloxane (C ₆ H ₁₈ OSi ₂)
HPBM	Hybrid Plasma Bulk Model

HPSM	Hybrid Plasma Sheath Model
IAD	Ion Angular Distribution
IADF	Ion Angular Distribution Function
IDF	Ion Distribution Function
i.e.	id est (that is)
IEAD	Ion Energy and Angular Distribution
IEDF	Ion Energy Distribution Function
IR	infrared
IVDF	Ion Velocity Distribution Function
LAS	Laser Absorption Spectroscopy
lf	low frequency
LIF	Laser-Induced Fluorescence
MBMS	Modulated Beam Mass Spectrometry
MC	Monte Carlo
MERIE	Magnetically Enhanced Reactive Ion Etcher
MIR	mid-infrared
OAP	off-axis paraboloid
PC	personal computer
PIC	Particle-In-Cell
QCL	quantum cascade laser
QCLAS	Quantum Cascade Laser Absorption Spectroscopy
Q-MACS	Quantum Cascade Laser Measurement and Control System
QMS	quadrupole mass spectrometer
rf	radio frequency
RGA	Residual Gas Analysis
RIE	Reactive Ion Etching
SEM	Secondary Electron Multiplier
SNR	signal-to-noise ratio
TCAD	Technology-oriented Computer Aided Design
TDLAS	Tunable Diode Laser Absorption Spectroscopy
TEOS	Tetraethylorthosilicate ($C_8H_{20}O_4Si$)
TIMS	Threshold Ionization Mass Spectrometry
TRIM	Transport of Ions in Matter
VMDSO	Divinyltetramethylsiloxane ($C_8H_{18}OSi_2$)

Symbols

<i>A</i>	area [m ²]; A_{el} , powered electrode area; A_{gr} , ground electrode area
<i>b</i>	impact parameter [m]
<i>B</i>	magnetic induction [T]
<i>C</i>	conductance [l/s]; effective parameter
<i>d</i>	thickness [m]
<i>D</i>	diffusion coefficient [m ² /s]; dissociation fraction; D_l , lower limit of the dissociation fraction; D_u , upper limit of the dissociation fraction
<i>e</i>	unsigned electron charge (1.602×10^{-19} C)
<i>E</i>	electric field [V/m]; energy [eV]; E_a , appearance energy; E_{aff} , electron affinity; E_b , bond energy; E_{el} , sheath electric field in front of the powered electrode; E_{gr} , sheath electric field in front of the ground electrode; E_i , ion or ionization energy; E_{kin} , kinetic energy; E_t , target surface binding energy; E_{thr} , threshold energy; E_{trans} , transmission energy
<i>f</i>	frequency [Hz]; distribution function [m ⁻⁶ s ³]; f_{ce} , electron cyclotron frequency; f_{ci} , ion cyclotron frequency; f_{pe} , electron plasma frequency; f_{pi} , ion plasma frequency
<i>F</i>	force [N]; F_L , Lorentz force
<i>I</i>	electrical current [A]; radiation intensity [Js ⁻¹ m ⁻²]; I_e , electron current; I_{el} , displacement current through the sheath in front of the powered electrode; I_{gr} , displacement current through the sheath in front of the ground electrode; I_{rf} , rf current
<i>j</i>	electrical current density [A/m ²]; ion flux; j_c , conduction current density; j_d , displacement current density
k_B	Boltzmann's constant (1.381×10^{-23} J/K)
K_L	Langevin constant
<i>L</i>	distance [m]
<i>m</i>	mass [g]; m_e , electron mass; m_i , ion mass; m_n , neutral mass
<i>M</i>	molar mass [g/mol]
<i>n</i>	number density of species [m ⁻³]; plasma density; n_e , electron density; n_g , neutral gas density; n_i , ion density; n_s , plasma density at sheath edge
<i>N</i>	quantity; N_A , Avogadro number ($N_A = 6.022 \times 10^{23}$ molecules/mol)
<i>p</i>	pressure [Pa]; scaling exponent; p_d , electric dipole moment [Cm]
<i>P</i>	probability; power [W]; P_{trans} , transmission probability
<i>q</i>	electric charge [C]; scaling exponent
<i>Q</i>	pumping speed [l/s]; gas flow rate [sccm] or [mol/s]

r	radial position [m]; r_p , reflectance of p polarized electromagnetic wave; r_s , reflectance of s polarized electromagnetic wave
R	radius [m]; etch rate [nm/min]; R_{bb} , beam-to-background signal ratio
s	sheath thickness [m]; s_{el} , sheath thickness in front of the powered electrode; s_{gr} , sheath thickness in front of the ground electrode
S	signal intensity [counts/s]; S_{rf} , signal intensity for plasma-on condition; S_0 , signal intensity for plasma-off condition
t	time [s]; transmission efficiency
T	temperature [K]; T_e , electron temperature; T_{el} , powered electrode temperature; T_g , neutral gas temperature; T_i , ion temperature; T_{lid} , reactor lid temperature; T_v , boiling temperature; T_{wall} , reactor wall temperature
v	velocity [m/s]; v_{Bohm} , Bohm velocity; v_e , electron velocity; v_i , ion velocity; v_s , ion velocity at sheath edge; V_{sc} , scattering potential
V	voltage or electric potential [V]; V_{dc} , dc bias voltage; V_e , electron energy equivalent potential; V_{eff} , delivered power; V_{el} , voltage drop across the sheath in front of the powered electrode; V_{gr} , voltage drop across the sheath in front of the ground electrode; V_{pp} , peak-to-peak voltage; V_{react} , reflected power; V_{rf} , rf voltage; V_s , sheath voltage; V_0 , electrode voltage; V_{mol} , molar volume ($V_{mol} = 22414 \text{ cm}^3 \text{ mol}^{-1}$)
w	aperture diameter [m]
x	rectangular coordinate [m]
Z	relative atomic mass; impedance [Ω]; Z_i , relative ion charge in units of e ; Z_t , relative atomic mass of the target atom
α	ratio of negative ion to electron density; low-voltage CCRF discharge mode
β	extraction efficiency of ions
γ	secondary electron emission coefficient; high-voltage CCRF discharge mode; γ_r , reaction probability; γ_{rec} , recombination/wall loss probability; γ_{sput} , sputtering coefficient
Γ	particle flux [$\text{m}^{-2}\text{s}^{-1}$]; Γ_e , electron flux; Γ_i , ion flux
Δ	denotes the change of a quantity; Stokes parameter; $\Delta W_{Doppler}$, Doppler broadening [m]
ε	dielectric constant [F/m]; ε_0 , vacuum permittivity ($8.854 \times 10^{-12} \text{ F/m}$)
θ	angle [rad]; spherical polar angle; detection coefficient
Θ	scattering angle in center of mass system [rad]
λ	mean free path [m]; λ_{CX} , mean free path between two charge exchange collisions; λ_D , electron Debye length; λ_i , ion mean free path
μ	mobility [m^2/Vs]; μ_0 , vacuum permeability ($4\pi \times 10^{-7} \text{ H/m}$)
π	3.1416
ρ	density [g/m^3]

σ	cross section [m^2]; σ_a , absorption cross section; σ_{CX} , charge exchange collision cross section; σ_{ES} , elastic scattering cross section; σ_{HS} , hard sphere cross section; σ_i , ionization cross section; σ_L , Langevin enhanced cross section; σ_m , elastic momentum transfer electron collision cross section
τ	mean free time [s]; τ_i , ion transit time; τ_m , time between two elastic momentum transfer collisions; τ_{rf} , rf period
ν	friction term; wavenumber [m^{-1}]; ν_e , electron friction term; ν_i , ion friction term; ν_m , electron collision rate for elastic momentum transfer [s^{-1}]
φ	angle [rad]
Φ	electric potential [V]; Φ_s , sheath potential
Ψ	Stokes parameter
ω	radian frequency [rad/s]; ω_c , cyclotron frequency; ω_i , ion transit frequency; ω_{pe} , electron plasma frequency; ω_{pi} , ion plasma frequency
Ω	solid angle [sr]
\wp	polarizability [m^3]

Abstract

In this study, physical and chemical interactions during plasma etching of silicon in capacitively coupled processing discharges were investigated in detail for different HBr and NF_3 mixed chemistries at medium pressures. As publications are very limited, this work contributes to expand the knowledge of etch fundamentals for high aspect ratio silicon etching in semiconductor fabrication. The influence of important discharge control parameters was investigated for both 60 MHz as well as 60+2 MHz dual frequency operation inside an industrial MERIE CCP reactor typically used for etching high aspect ratio features for DRAM applications. The final goal of this work was to investigate the utilization of the dual frequency concept as well as the impact on discharge properties and finally on etching at relevant substrate surfaces. The complex nature of multi frequency rf sheaths was both analyzed experimentally and from simulations. The low-voltage sheath dynamics in front of the grounded electrode was investigated by applying mass resolved ion energy analysis from a Hiden EQP 500 analyzer installed at the reactor wall. To support an interpretation of results from plasma diagnostic measurements, a Hybrid Plasma Sheath Model (HPSM) was used for calculation of ion energy distributions. Discharge composition and etch processes were investigated in detail by applying standard mass spectrometry, Appearance Potential Mass Spectrometry (APMS), Quantum Cascade Laser Absorption Spectroscopy (QCLAS), rf probe measurements, gravimetry and ellipsometry.

A careful analysis was performed for the different techniques to minimize measurement artefacts and to allow for a qualitative comparison to HPSM calculations. Calibration in the electrically floating environment could be achieved from IDF structures which enabled for comparison of different plasma conditions. Interpretation of interactions in HBr/ NF_3 mixed discharges was enabled from knowledge about interactions in pure HBr and NF_3 discharges. However, differences from a simple superposition indicated that more complex interactions can occur during etching on the substrate surface. From a simplified etch model, limitations of silicon etching in HBr/ NF_3 mixed discharges are explained by passivation properties of bromine and oxygen to achieve highly anisotropic etching. Whereas etching is influenced stronger by the high frequency for NF_3 dominated HBr/ NF_3 chemistries, the etch rate enhancement from the low frequency is more pronounced for HBr dominated mixtures. This is due to a more efficient contribution of ion flux and ion energy for bromine dominated HBr/ NF_3 chemistries, as compared to a more chemically driven etching for fluorine dominated mixtures. Hydrogen radicals from dissociated HBr can be an effective loss channel of fluorine radicals which shifts the equilibrium for the etch process. Empirical found process settings used for high aspect ratio silicon etching in complex HBr/ $\text{NF}_3/\text{O}_2/\text{SiCl}_4$ discharges appear already well optimized with regards to the process chemistry. From the knowledge obtained here, the potential for further improvements is expected to be low.

From this work, the concept of separate control of ion energy and ion flux by the two frequencies works generally well for the investigated reactor setup. The high frequency mainly determines ion flux and radical formation in the halogen discharges, whereas ion energies are strongly influenced by the low frequency. Deviations from an ideally separated control of ion flux and energy are caused by influences on discharge parameters and interactions between the two frequencies since the rf power sources are coupled to each other in the current setup.

1 Introduction

For the last decades, the interest in fundamentals and applications of low temperature discharges has been growing tremendously. In semiconductor device manufacturing, the use of plasma technologies for structuring nanoscale anisotropic features has mostly replaced traditional wet etch techniques. In fact, plasma etching, or more specifically reactive ion etching (RIE), is understood as the only commercial technology to achieve highly anisotropic etch profiles. With the combined chemical and physical reactions in reactive ion etching, disadvantages of purely chemical and physical processes can be overcome. Chemical etching for example causes isotropic etch profiles resulting in an undercut below the mask layer. Underetching results in widening of critical dimensions (CDs) that becomes more severe for decreasing feature dimensions in sub 100 nm technologies. Purely physical sputtering reveals reduced selectivities and can further support unwanted crystal damage, as well as deposition of nonvolatile sputter products. For a long time, Dynamic Random Access Memories (DRAMs) have been the technology drivers for innovative processing to realize required structures in highly integrated circuits. During the development of 4 MBit DRAMs in the late 1980s, the cell size became for the first time smaller than the electrode area of a planar storage capacitor. This resulted in the introduction of a three-dimensional storage capacitor [1-3]. During development of the 4 MBit DRAM (Dynamic Random Access Memory) storage capacitor, the DT (deep trench) capacitor cell concept was followed by the majority of DRAM producers. Therefore, DRAM fabrication has driven trench technology requiring appropriate dry etch processes for etching trenches into single crystalline silicon. Today, deep trench etching development still remains as one of the biggest challenges in semiconductor fabrication, driven by the demands of high etch rate, anisotropy profile control, selectivity and process uniformity that become tighter with further decreasing feature sizes. These demands strongly require well understood and characterized process fundamentals. Due to the high complexity, such knowledge is usually poor and empirical process methodologies are typically applied. By investigating more closely general chemical and physical interactions during etching silicon in single as well as dual frequency HBr and NF₃ based discharges, this work shall contribute to expand the knowledge of etch fundamentals to enable a more efficient process development. The final goal of this work was to investigate in particular the utilization of the dual frequency concept. The work presented here was conducted at *Qimonda Dresden GmbH & Co. OHG* and the former *Infineon Technologies Dresden GmbH & Co. OHG*.

Plasma based processes mainly depend on energetic ions that are accelerated before they hit the substrate. During plasma processing, substrates are in direct contact with the discharge and are set to a negative potential which accelerates positive ions to the surface. Ion acceleration is achieved in the comparably small plasma sheath region where the electric field is much higher than inside the plasma bulk. Thus, control and optimization of plasma processes requires a detailed knowledge of this plasma sheath area. Sheath properties and ion energy distribution functions (IEDFs) are determined by the discharge type, where in principle dc and rf discharges are common. Depending on the nature of coupling the electric field, rf discharges can be further divided into capacitive and inductive discharges. Capacitive discharges are suitable to provide high sheath voltages which makes

them favorable for situations where high ion energies are required. Therefore, only capacitive discharges will be discussed in more detail here. Besides providing high ion energies, another essential advantage relies on a mostly vertical impact angle of the projectile ions which allows to achieve highly anisotropic features with high aspect ratios (i.e., trench depth to trench width ratio). Close control of the ion energy enables to adjust etch rates as well as optimize removal of passivation layers at the bottom of even very deep features. Besides ion energy, the ion flux is an important parameter in etch processes. The rf power controls both ion energy and the ion flux to the substrate. Manipulation of the ion transport in the sheath and hence the ion energy distribution function (IEDF) is highly desirable to optimize material processing.

Whereas a temporally constant electric field exists in dc discharges, the field is oscillating in rf discharges. Since a considerable extent of the discharge current in the sheath region is due to displacement current, the oscillating nature is of advantage for discharge operation with electrodes covered by insulating and semiconducting materials or substrates. Moreover, this relegates the need of substantial electron emission from the electrodes to sustain the discharge, as required in case of dc discharges. However, secondary electron emission may significantly influence the discharge behavior and could cause a discharge transition from the low-voltage (or α) to the high-voltage (or γ) mode with increasing discharge current density [4-6]. While at low rf discharge voltages the ionization is maintained by the bulk plasma electrons, the ionization at high voltages is provided by secondary electron emission from the electrodes due to ion bombardment. Both transitions involve changes in the electron distribution function (EEDF) and the mean electron energy. For reasons of processing insulating or semiconducting materials, most plasma technology applications use rf discharges. However, this is in strong contrast to the current status of knowledge about the sheath and ion energy distributions. Whereas distributions in dc discharges are well understood today, knowledge about the sheath dynamics in rf discharges can only be classified as qualitative. This is basically due the highly complex nature of ion distributions in rf discharges [7,8]. The inhomogeneous and time dependent behavior of the sheath structure as well as the influence of collisions on the ion dynamics in the sheath region highly complicate investigations of IEDFs. Since ion bombardment is essential in anisotropic etching of semiconductor materials in rf plasmas [9] and etch anisotropy and rates are subject to variations in ion flux and ion kinetic energies [10], knowledge about IEDFs appears crucial for application of plasma technologies. A close examination of ion distribution functions for different discharge parameters and chemistries is therefore one of the main subjects in this work. Sheath properties have been extensively studied in literature in the limit of collisionless particle dynamics and almost exclusively in laboratory systems typically comprising noble gases or basic molecular discharges [11-15]. However, there is still a lack of experimental studies for typical processing discharges with electronegative gases involved and medium pressures applied (i.e., hundreds of millitorrs) where the sheaths are collisional. The ion flux to the substrate is determined by the ion density which for electronegative discharges can considerably deviate from the electron density in the plasma bulk. The experiments performed here concentrate upon relevant electronegative discharge chemistries at medium process pressures typically used in DRAM processing.

Besides contribution of ion energy and ion flux, surface processes in plasmas are importantly influenced by the flux of energetic neutrals and reactive particles (radicals). Energetic neutrals result from charge exchange collisions between energetic ions and

initially thermal (parent) neutrals in the sheath. Ion-neutral collisions in the sheath are very likely to occur for typical process pressures of several ten or hundred millitorrs. Radical formation is mainly determined by the plasma chemistry and influenced by the EEDF. The EEDF itself is determined by the discharge design and can be influenced by the dissipated power (e.g., power modulation, power pulsing). Dissociation, ionization and excitation mechanisms, and further elastic scattering, charge transfer, generation and destruction of negative ions, and gas-phase and surface chemical reactions have to be considered since they are critical to most processing applications. The complexity of potentially significant gas phase reactions in molecular discharges can be overwhelming. Modeling molecular discharges is mostly limited by the fact that most cross sections have neither been measured nor calculated. This expresses the general need to apply in situ diagnostic techniques as well as computational effort to overcome these limitations.

In this work, rf sheath dynamics at the low-voltage boundary sheath of asymmetric Capacitively Coupled Radio Frequency (CCRF) discharges are investigated for different HBr and NF_3 mixed chemistries. Experiments are conducted for both single as well as dual frequency discharge operation inside a prototype commercial Applied Materials HART (High Aspect Ratio Trench) CCP (Capacitively Coupled Plasma) reactor [16] at medium pressures typically used for etching high aspect ratio features for DRAM applications. A mass resolved ion energy analyzer (Hiden EQP 500) is installed at the grounded reactor wall to enable measurements of ion distributions after passing the low-voltage boundary sheath, as well as the discharge composition (feed gas dissociation and etch products, by-products, etc.). To support an interpretation of results from plasma diagnostic measurements, a Hybrid Plasma Sheath Model (HPSM) [17,18] is used for the calculation of angle-resolved ion energy distributions. To enable a comparison between measured ion velocity distributions and calculated ion energy distribution functions at the low-voltage boundary sheath, special emphasis is placed on a determination of relevant transmission functions. The discharge composition is investigated as well by applying standard mass spectrometry, Appearance Potential Mass Spectrometry (APMS), Quantum Cascade Laser Absorption Spectroscopy (QCLAS), and rf probe measurements. Based on QCLAS, a new diagnostic arrangement - the Q-MACS Etch system - is designed and tested during different experiments performed in this work. Here, the Q-MACS Etch system is applied for in situ monitoring of NF_3 feed gas as well as SiF_4 etch product molecules in the HART plasma reactor. Additional standard techniques are used to characterize etch processes at different relevant substrates.

This chapter will start with an overview about the current understanding of CCRF discharges. Concepts of plasma boundary sheaths and aspects of the sheath ion transport are discussed in more detail to provide a basis for the discharge characterization performed in this work. A first insight is given into the two main techniques applied in this work, i.e., mass resolved ion energy analysis and infrared absorption spectroscopy based on narrow-bandwidth quantum cascade diode lasers. Principles of the HPSM simulator are introduced as well. In chapter 2, details of the mass resolved ion energy analysis technique will be discussed further where special emphasis is placed on enabling a comparison of measured ion velocity distributions and calculated ion energy distribution functions. This requires to determine relevant transmission functions for the EQP probe which can then be used for processing of angle-resolved IEDFs from HPSM simulations. In chapter 3, additional plasma diagnostic methods and measurement techniques used during this work are described briefly. After a short introduction of the HART CCP reactor design and specifics of the

experimental setup at the plasma reactor, chapter 4 finally deals with a successive development of knowledge for complex molecular halogen mixed discharges which are typically used for high aspect ratio silicon etching. Initial basic studies in this work comprise electropositive argon as well as electronegative HBr and NF_3 discharges. Generally, only the most relevant process parameters (e.g., applied power, discharge pressure, gas flow rates, magnetic fields) are investigated for 60 MHz single frequency as well as 60+2 MHz dual frequency discharges. To get a more detailed insight into the complex plasma chemistry and sheath behavior for processing discharges at typical operating conditions, further analysis is performed for different HBr/ NF_3 mixed chemistries, and finally for complex HBr/ $\text{NF}_3/\text{O}_2/\text{SiCl}_4$ discharges. A summary of the results obtained during this work will be conducted in chapter 5.

1.1 Capacitive rf discharges

CCPs, or more specifically CCRF discharges, are the most widely used low-pressure discharges for processing applications [4,19,20]. These discharges are sustained by rf currents and voltages applied to an electrode immersed in the plasma which leads to formation of a high-voltage capacitive sheath between the electrode and the plasma bulk. Low-temperature plasmas investigated here are characterized by charged particles and neutrals which are not in thermodynamic equilibrium. The electron mean temperature T_e is typically in the range of a few electron volts ($\approx 1\text{--}4$ eV), whereas the ion and neutral gas temperatures T_i and T_g are close to room temperature (≈ 0.025 eV). This property arises from a rather inefficient energy transfer from electrons to heavy particles as a result of the strongly different mass ratio of the colliding species. The non-equilibrium property of low-temperature rf discharges is in general attractive to be used in processing applications for treatment of insulating, semiconducting and conducting materials.

Most commonly, a parallel plate reactor arrangement with one electrode grounded and the other one powered is used (cf., Fig. 1.1-a). The powered electrode is typically driven with a high frequency (sinusoidal) voltage. The operating frequency $\omega = 2\pi f$ is typically above the ion plasma frequency ω_{pi} but well below the electron plasma frequency ω_{pe} ($\omega_{pi} < \omega \ll \omega_{pe}$). Assigned by international telecommunication laws, 13.56 MHz and harmonics thereof are most commonly used for industrial applications. At this frequency, electrons readily follow the oscillations of the rf electric field while the heavier ions can only respond to the time-averaged field. For example, a typical argon discharge with a plasma density of 10^{10} cm^{-3} yields $f_{pAr^+} = \omega_{pAr^+}/2\pi = 3.3$ MHz and $f_{pe} = \omega_{pe}/2\pi = 897.8$ MHz. As indicated in the schematic, the ground electrode area usually exceeds that for the powered electrode in industry relevant reactors. Due to the blocking capacitor, the dc current must be zero. Thus, under steady state conditions the electron flux must balance the ion flux during one rf period at both electrodes. Due to their higher mobility, the electrons will reach the surface surrounding the plasma much faster than the heavier ions. To ensure a balanced charge carrier flux, a negative potential V_{dc} develops for the stationary case. This negative potential suppresses the electron current during the main part of an rf period. For minimum dc bias and rf total voltage, a high electron current pulse flows to the electrode to balance for a constant low ion current incident on the electrode surface. This eventually leads to the buildup of a positive space charge region (sheath) between plasma and electrodes which breaks quasi-neutrality in front of the electrodes.

The corresponding sheath electric field accelerates ions to the electrodes and repels electrons. Positive ions leaving the plasma bulk and moving towards the electrodes gain energy through acceleration by the sheath electric field, corresponding to the potential difference between plasma bulk and electrode surface. In contrast to the stationary case of a dc discharge, the sheath is modulated by the rf voltage of the rf power drive. The sheath region extends to a maximum and retracts to a minimum value. During typical application of high rf peak voltages, the sheath region s exceeds the electron Debye length λ_D , which is the minimum scale length in the discharge. Generally,

$$s = \lambda_D f\left(\frac{V}{V_e}\right) \quad (1.1)$$

where

$$V_e = \frac{k_B T_e}{e} \quad (1.2)$$

and

$$\lambda_D = \sqrt{\frac{\epsilon_0 k_B T_e}{e^2 n}} \quad (1.3)$$

where n is the plasma density in an undisturbed plasma bulk. More specifically, the sheath thickness will be discussed for the Child law high voltage sheath model in section 1.2. The electron Debye length is the characteristic scale over which mobile charge carriers screen out electric fields in quasi neutral plasmas. For the example of an argon discharge with a plasma density of 10^{10} cm^{-3} , the electron Debye length is about $100 \mu\text{m}$.

As discussed above, most capacitive discharges are asymmetric since usually more electrode surface area is naturally grounded than driven. This applies also to the reactor used in this study. As a result, a larger rf voltage drop occurs across the sheath in front of the smaller (powered) electrode which hence yields higher ion bombardment energies at the powered electrode. For a qualitative investigation of capacitive discharges, a simplified equivalent circuit can be used as shown in Fig. 1.1-b. The sheath regions in front of powered and ground electrode are each represented by a capacitor, a resistor and a diode connected in parallel. Each capacitor represents the displacement current, the resistor represents the ion current and the diode represents the electron current in the respective sheath. The plasma bulk is described by a resistor which represents the electron current. Due to the high electron mobility, the plasma bulk resistance is typically very low. The electron inertia can be accounted for by an inductor. Since the inductive impedance of the plasma bulk is rather small compared to the capacitive impedance of the sheaths, the inductor is neglected here. The electrode potential in rf discharges can be expressed by

$$V(t) = V_{dc} + V_{rf}(t) \quad (1.4)$$

where in case of a purely sinusoidal rf voltage one obtains $V_{dc} \approx -V_{rf}$ [15]. The electrode voltages for the asymmetric case discussed here can be roughly estimated from the equivalent circuit in Fig. 1.1-b, by assuming the displacement current dominates the conduction current. This is valid for operating frequencies exceeding the ion plasma frequency, from the capacitive voltage divider one obtains

$$\frac{\bar{V}_{el}}{\bar{V}_{gr}} = \left(\frac{A_{gr}}{A_{el}}\right)^4 \quad (1.5)$$

for the collisionless Child-Langmuir law [20]. This scaling with the fourth power of the electrode area ratio could not be verified experimentally. Instead a much weaker scaling is usually observed according to

$$\frac{\bar{V}_{el}}{\bar{V}_{gr}} = \left(\frac{A_{gr}}{A_{el}} \right)^q \quad (1.6)$$

with the exponent $q \leq 2.5$. Here, $q=2.5$ corresponds to the limit of a collisional sheath [20]. From this discussion, limitations of the simplified equivalent circuit become obvious. This is mainly a result of not accounting for losses by the simple sheath model.

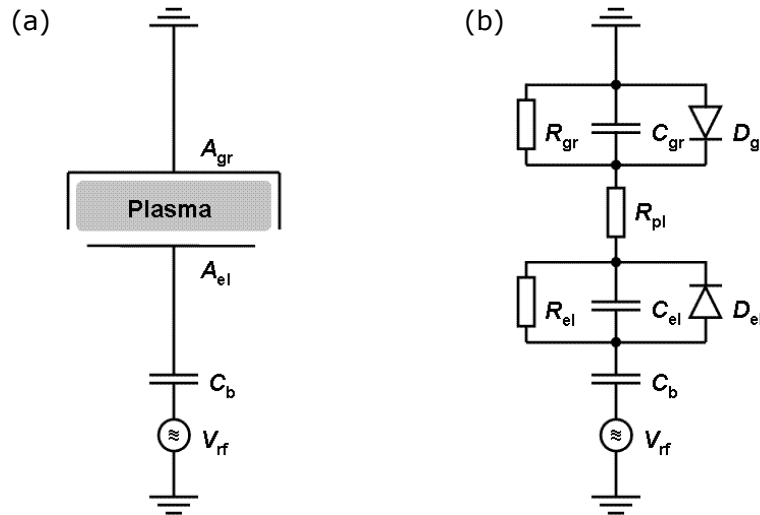


Figure 1.1: Asymmetric CCRF discharge: (a) schematic, (b) simplified equivalent circuit.

One primary limitation of CCRF sources is that the ion flux to the substrate can not be varied independently of the ion bombardment energy. High power levels must be employed to obtain high ion densities required for processing applications. This however yields an increased voltage drop across the sheaths and simultaneously raises the ion impact energy at the surface, causing damage to the substrate. Recently, limitations of conventional single frequency driven discharges have been overcome by application of multi-frequency power sources [21-29]. Combinations typically include a high- and low-frequency drive enabling for (fairly) independent control of plasma density (and hence ion flux as well as radical density) and ion energy by controlling the sheath voltage. Frequencies are chosen both below and above the characteristic ion plasma frequency, such that ions can still follow the low frequency oscillations but not the the high frequency component. The HART reactor used in this work applies a 60+2 MHz frequency combination. The 60 MHz frequency rf power source is used to sustain the plasma and control the plasma density, whereas the 2 MHz frequency drive allows to control the ion energy.

The energy of a positive ion depends on the frequency applied to the plasma. For 60 MHz, high frequencies where the ion transit frequency (cf., equation 1.62) exceeds the rf frequency, the ion dynamic is determined by the time-averaged field since the ions are not able to follow the oscillations due to their inertia. In this case, the potential difference between plasma bulk and substrate determines the ion energy incident on the electrode. For 2 MHz excitation where the rf frequency is below the ion transit frequency, ions cross the sheath in a fraction of an rf period and hence experience a nearly stationary electric field. In this case, the ion energy is typically characterized by the delivered rf peak voltage.

Higher frequencies produce a reduced ion bombardment energy and thinner sheaths for a given ion flux to the substrate and permit the addition of a second low-frequency driving voltage. For a wide separation of the frequencies for the high and low frequency drives, independent control of the ion flux and energy can be achieved [20]. At low pressures ($p < 50$ mTorr), the ion flux Γ_i onto the substrate can be expressed as

$$\Gamma_i = n_0 v_{\text{Bohm}} \quad (1.7)$$

where n_0 is the plasma density at the plasma sheath boundary, and v_{Bohm} is the Bohm velocity [20]. The impact energy of ion projectiles striking the electrode surface depends on the sheath potential influencing the ions while traversing the sheath. The energy gained by ions traversing the sheath is orders of magnitude higher compared to the initial thermal energy at the plasma sheath boundary. For sufficiently low pressures ($p \leq 50$ mTorr), the energy gain approximately corresponds to the energy equivalent potential drop

$$E_i = eV_s \quad (1.8)$$

with the time-averaged sheath potential V_s . Therefore, if plasma density and sheath voltage can be controlled separately, the ion flux and the ion impact energy onto the substrate can be controlled independently. For higher pressures, the energy is reduced due to collisions in the sheath. Also, it should be noted that electromagnetic effects like standing waves and skin effects can become severe at high frequencies which can not be described with conventional electrostatic analysis [30].

To further improve the performance of capacitive discharges by achieving lower sheath voltages and higher ion densities (and independent control of both parameters), capacitive discharges can be modified by implementing a magnetically enhanced reactive ion etcher (MERIE) or rf magnetron [20]. In these discharges, a relatively weak (50-200 G) dc magnetic field is imposed parallel to the surface of the rf powered electrode. A number of effects are introduced by the magnetic field, yielding higher densities and reduced sheath voltages at fixed absorbed powers. The magnetic field yields strong nonuniformities of the plasma for both radial and azimuthal directions which is attributed to $\vec{E} \times \vec{B}$ drifts, where \vec{E} and \vec{B} are the local dc electric and magnetic fields, respectively. The Lorentz force

$$\vec{F}_L = q \cdot \vec{v} \times \vec{B} \quad (1.9)$$

provokes electrons to circularly move along the magnetic field lines. For an electric field which is superposed by a magnetic field, the electrons do not move any longer parallel to the electric field lines. This results in a reduced effective loss area of the discharge and hence in an increased electron (and ion) density. Hence, the plasma can be sustained at quite low pressures during application of a magnetic field. Besides a reduced power loss, the electron effective path is increased by the gyrating motion which leads to an enhanced probability of collisions with the neutral background gas, and finally to an increased ion density. Electrons injected ideally 90 degrees with respect to the magnetic field will move circularly, all other electrons will rotate along the field lines. Hence the plasma is distorted towards the field lines which affects to process uniformity. These inhomogeneities are avoided by rotating the magnetic field at low frequencies (typically about 0.5 Hz) such that the time-averaged plasma density is equally distributed with respect to the substrate surface.

Although models and discussions are almost exclusively based on electropositive discharges, principles also apply to electronegative discharges which are typically applied for various plasma technologies, and further constitute the majority of discharges investigated in this work. A good review on electronegative plasmas has been recently given by Franklin [31]. Electronegative plasmas are generally defined as plasmas formed in electron attaching gases and having a significant density of negative ions that they must be taken into account. Quasi-neutrality and ambipolarity still hold in electronegative plasmas, i.e.,

$$n_{i+} = n_e + n_{i-} \quad (1.10)$$

and

$$\Gamma_{i+} = \Gamma_e + \Gamma_{i-}, \quad (1.11)$$

where

$$\Gamma_{i+} = n_{i+} v_{i+}, \quad (1.12)$$

$$\Gamma_e = n_e v_e \quad (1.13)$$

and

$$\Gamma_{i-} = n_{i-} v_{i-}. \quad (1.14)$$

The negative ion temperature is comparable to that of the neutral gas, and hence about

$$T_{i-} \sim 0.01 T_e. \quad (1.15)$$

The fact that $T_{i-} \ll T_e$ is described as the main feature differentiating active electronegative plasmas from electropositive ones. It results in electrostatic fields that slow down the electrons and speed up the positive ions which in turn effectively reduces the negative ion wall flux to zero. Negative ions are born and die in the plasma volume, resulting in a structured plasma with an ion-ion core and an outer electron-positive-ion plasma. The size of the core increases with electronegativity and further as the rate coefficient for ionization approaches the attachment rate coefficient [31]. As well, the ion-ion core structure is expected to change with pressure. The low-mobility, low-temperature negative ions typically constitute most of the negative charge and hence essentially influence the discharge dynamics. This is in contrast to the properties of conventional electropositive plasmas that are characterized by the large mass difference between the positive and negative charge carriers. The proportion of negative ions to be significant is described for an electronegativity $\alpha > 3$ at low pressures and $\alpha > 300$ at higher pressures [31], where the electronegativity α is defined as the ratio of the negative ion density n_n and the electron density n_e

$$\alpha \equiv n_{i-} / n_e. \quad (1.16)$$

For the range of gases used in microelectronics processing, the electronegativity can typically range from 1 to about 1000. From experimental investigations and simulations, the electronegativity in the ion-ion core can rise to 30 in oxygen [32-35], 200 in chlorine [36] and can exceed 1000 in SF₆ [37].

For modeling of low-pressure electropositive discharges, volume electron-ion recombination processes are usually neglected. For investigation of electronegative discharges it is however not straightforward to neglect negative-positive ion recombination due to its large rate constant. General consideration on electronegative plasmas include

moderate to high electronegativities where calculation are most often performed for oxygen and chlorine [20,31]. In electronegative plasmas with $n_e \ll n_i$, the voltage drops across the bulk resistors can be comparable to or even exceed the voltage drops across the sheath capacitors, and the discharge can enter a resistive regime [20].

1.2 Plasma boundary sheath

As a consequence of the different mobilities of the plasma species, a boundary sheath is formed between the plasma and a wall in contact with the plasma. Sheath properties have been extensively investigated using theoretical models [38-43]. In contrast to the plasma bulk, strong electric fields are generated in the sheath region accelerating positively charged particles and repelling negatively charged species. Positive ions created in the plasma bulk enter the sheath region, gain energy through the sheath electric field acceleration and can loose energy through collisions. Hence, the boundary sheath determines important aspects of plasma-surface interactions. The ion impact energy onto the electrode surfaces depends on sheath characteristics, like sheath potential, sheath thickness, ion-neutral mean free path, transit time through the sheath [44,45].

For a collisionless sheath, the behavior of ions and electrons in the sheath can be described by simple models [20]. Variation of the sheath potential Φ_s is described by Poisson's equation

$$\frac{d^2 \Phi_s}{dx^2} = \frac{e}{\epsilon_0} [n_e(\Phi_s) - n_i(\Phi_s)] \quad (1.17)$$

with the electron and ion densities $n_e(\Phi_s)$ and $n_i(\Phi_s)$, and ϵ_0 the permittivity of free space. A complete solution of this nonlinear equation can only be found numerically, details are discussed for example in [20] and shall not be further investigated here. At this point it should be emphasized that the following assumption must be met to obtain physically meaningful solutions:

$$v_s \geq v_{\text{Bohm}} = \sqrt{\frac{k_B T_e}{m_i}} \quad (1.18)$$

which is known as the Bohm sheath criterion for the formation of a sheath. The ion velocity at the sheath edge v_s must exceed the critical value of the Bohm velocity v_{Bohm} . In order to accelerate the ions to the Bohm velocity, a small electric field must be present between the bulk plasma and the sheath [39], which happens in an essentially neutral presheath region. A small potential difference has a quite significant influence on the thermal ions with

$$v_i = \sqrt{\frac{k_B T_i}{m_i}} \quad (1.19)$$

whereas the already hot electrons are virtually not affected. At the sheath-presheath boundary there is a transition from subsonic ($v_i < v_{\text{Bohm}}$) to supersonic ($v_i > v_{\text{Bohm}}$) ion flow which leads to a breakdown of charge neutrality. The transition can arise from geometric contraction of the plasma, from friction forces in the presheath or from ionization in the bulk plasma [39]. For the limit $\omega_{pi} \ll \omega$ where the ions experience an average sheath potential it can be shown that the Bohm criterion is still valid in high frequency rf discharges [46].

Sheath potential at a floating wall

By equating the electron and ion flux at an electrically floating wall, the dc potential difference between the plasma and the wall can be determined. Both fluxes should balance each other in the sheath

$$\Gamma_i = \Gamma_e. \quad (1.20)$$

From flux conservation in the sheath the flux of ions at the floating wall equals the ion flux at the sheath edge

$$\Gamma_i = n_s v_{\text{Bohm}} \quad (1.21)$$

where n_s is the plasma density at the sheath edge. The electron flux at the wall is given by

$$\Gamma_e = \frac{1}{4} n_s \exp\left(\frac{e\Phi_s}{k_B T_e}\right) \bar{v}_e \quad (1.22)$$

where T_e is the electron temperature and \bar{v}_e is the electron mean velocity for an assumed Maxwellian distribution

$$\bar{v}_e = \sqrt{\frac{8k_B T_e}{\pi m_e}}. \quad (1.23)$$

The dc sheath potential can now be calculated to

$$\Phi_s = -\frac{k_B T_e}{2e} \ln\left(\frac{m_i}{2\pi m_e}\right) \quad (1.24)$$

which yields a proportional scaling to the ion-to-electron mass ratio m_i/m_e , and the electron temperature T_e . According to (1.24), the floating potential becomes more negative at higher electron temperature and ion mass, which is illustrated for various ion species in Fig. 1.2. The energy different ions can gain in the presheath and sheath are found to be $E_i(\text{H}_2^+) \cong 3.7k_B T_e$, $E_i(\text{F}^+) \cong 4.8k_B T_e$, $E_i(\text{Ar}^+) \cong 5.2k_B T_e$, $E_i(\text{Br}^+) \cong 5.5k_B T_e$, $E_i(\text{Br}_2^+) \cong 5.9k_B T_e$.

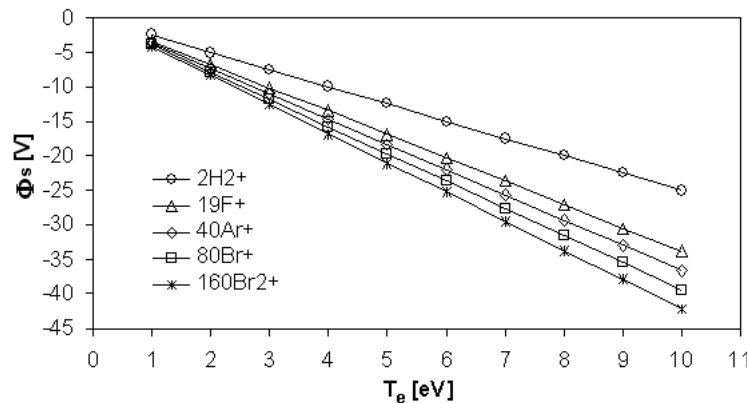


Figure 1.2: DC sheath potentials for 2H_2^+ , 19F^+ , 40Ar^+ , 80HBr^+ , 160Br_2^+ ionic sheaths in front of a floating electrode plotted as a function of the electron temperature according to (1.24).

High voltage sheath

Application of external high potentials to the powered electrode changes the sheath potential. A simple model describing the high voltage sheath is the *Matrix* sheath model. Unlike the zero net current requirement of the floating wall sheath, the potential difference

between plasma and electrode sets the sheath conditions here. The model is not completely accurate by assuming the ions to be fixed in a uniform matrix, i.e., homogeneously distributed throughout the sheath ($n_i = \text{constant}$). The electron density is assumed to be zero in the sheath since electrons are confined in the plasma bulk which is due to the large potential barrier between plasma and biased electrode. The sheath potential can be calculated by

$$\Phi_s = -\frac{en_s x^2}{2\epsilon_0} \quad (1.25)$$

with x ranging from zero at the plasma/sheath boundary to s at the electrode surface. The matrix sheath model can be used as a good approximation at higher pressures for a mobility limited ion motion in the sheath.

A more accurate model is the *Child* (or *Child-Langmuir*) sheath model [47] which accounts for the effect of a reduced ion density due to ion acceleration towards the electrode. The potential within the sheath as a function of position is given by [20]

$$\Phi_s = -V_0 \left(\frac{x}{s}\right)^{4/3} \quad (1.26)$$

where V_0 is the applied electrode voltage and x ranging again from zero at the plasma-sheath boundary to the sheath width s at the electrode surfaces. The sheath width can be calculated

$$s = \frac{2}{3} \left(\frac{2e\epsilon_0^2}{m_i} \cdot \frac{V_0^3}{J_0^2} \right)^{1/4} \quad (1.27)$$

which for $J_0 = en_s v_{\text{Bohm}}$ yields

$$s = \frac{\sqrt{2}}{3} \lambda_D \left(\frac{2eV_0}{k_B T_e} \right)^{3/4} \gg \lambda_D = \sqrt{\frac{\epsilon_0 k_B T_e}{e^2 n}} \quad (1.28)$$

with the electron Debye length λ_D at the sheath edge and the density

$$n = \frac{4}{9} \cdot \frac{\epsilon_0}{e} \cdot \frac{V_0}{s^2} \cdot \left(\frac{x}{s}\right)^{-2/3}. \quad (1.29)$$

Equation (1.29) yields $n = \infty$ at the sheath edge $x = 0$. This is consequence of neglecting the initial ion energy in the ion energy conservation equation. The decreasing ion density within the sheath between the plasma-sheath edge and the collecting boundary yields an increased sheath width compared to the matrix sheath width. It further leads to an increase of the sheath velocity in the regions of decreasing ion density (following from continuous rf current and decreasing electron density to preserve charge neutrality) - the result is a substantial increase in the stochastic sheath heating [20]. For typical processing discharge conditions, the Child law sheath thickness can exceed the Debye length by a factor of about 100 (~ 1 cm). For rf modulated discharges, the Child law for the self-consistent ion sheath yields the mean sheath thickness

$$s = \left(\frac{200}{243}\right)^{1/2} \left(\frac{2e\epsilon_0^2}{m_i} \cdot \frac{V_0^3}{J_0^2} \right)^{1/4}. \quad (1.30)$$

Due to the space charge reduction within the sheath as a result of a nonzero time-average electron density, the self-consistent ion sheath thickness (1.30) is by a factor of $(50/27)^{1/2}$ larger than the Child law sheath thickness for the dc case (1.27).

Collisional sheaths

As the pressure increases, ions experience collisions with the background neutral gas while traversing the sheath. Collision dominated sheaths are assumed for pressures exceeding 50 mTorr. Therefore this situation is of most interest for the typical discharge conditions investigated in this work. The energy lost during collisions results in a reduced mean ion impact energy at the electrode. For a highly collisional sheath, ions will not gain the full potential difference across the sheath. The energy of ions will depend on the collisions while travelling through the sheath. For an ion mean free path $\lambda_i < s$, the assumption of energy conservation is no longer fulfilled. This yields modified dynamics in the high potential sheath region as well as a different ion velocity at the sheath edge. Assuming particles are neither destroyed nor generated by ionisation, recombination, dissociation or other reactions, the flux is still conserved. For an intermediate pressure regime (100-600 mTorr) investigated in this work, a constant mean free path can be assumed for ions crossing the sheath. The sheath potential can be determined by [20]

$$\Phi_s = -V_0 \left(1 - \frac{x}{s}\right)^{5/3}. \quad (1.31)$$

Analog to (1.30), the sheath thickness for a collision-dominated sheath in rf modulated discharges is given by the Warren law [48]

$$s = \left(1.68^2 \cdot \frac{e\lambda_{CX}\epsilon_0^2}{\pi m_i} \cdot \frac{\bar{V}^3}{J_i^2}\right)^{1/5} \quad (1.32)$$

with the mean free path between two charge exchange collisions

$$\lambda_{CX} = \frac{1}{n_g \sigma_{CX}}. \quad (1.33)$$

The main difference between Child-Langmuir law and Warren law is the weaker scaling of the rf potential for collisional sheaths.

Single frequency rf sheaths

Applying an rf potential to the powered electrode results in an oscillating sheath with a temporarily varying sheath thickness. Considering a symmetric discharge with ground and powered electrode sheaths s_{gr} and s_{el} , and further assuming a uniform and time-constant ion density throughout the discharge and neglecting electrons in the sheath region [20], the sheath electric field within the electrode sheath is obtained upon integration of Poisson's equation

$$E_{el}(x, t) = \frac{en}{\epsilon_0} [x - s_{el}(t)], \quad (1.34)$$

where $s_{el}(t)$ is the position of the instantaneous sheath edge

$$s_{el}(t) = s[1 - \sin(\omega t)] \quad (1.35)$$

with the time averaged sheath width s . The displacement current through the electrode sheath is

$$I_{el}(t) = \varepsilon_0 A \frac{\partial E_{el}}{\partial t} \quad (1.36)$$

where A is the electrode area. For simplification, a harmonic cosine rf discharge current is typically specified to obtain the sheath voltage [38,49]. From current continuity

$$I_{el}(t) = I_{rf}(t) = \hat{I}_{rf} \cos(\omega t) \quad (1.37)$$

which results in

$$I_{rf}(t) = -enA \frac{d}{dt} s_{el}(t) \quad (1.38)$$

with the relationship

$$s = \frac{\hat{I}_{rf}}{en\omega A}. \quad (1.39)$$

The voltage across the electrode sheath is given by

$$V_{el}(t) = \int_0^{s_{el}(t)} E_{el}(x, t) dx = -\frac{en}{2\varepsilon_0} (s_{el}(t))^2 = -\frac{ens^2}{2\varepsilon_0} [1 - \sin(\omega t)]^2. \quad (1.40)$$

Similarly, the sheath voltage across the ground sheath is given by

$$V_{gr}(t) = -\frac{ens^2}{2\varepsilon_0} [1 + \sin(\omega t)]^2. \quad (1.41)$$

Neglecting the voltage drop across the plasma bulk, the total discharge voltage is obtained

$$V_{rf}(t) = V_{el}(t) - V_{gr}(t) = \frac{2ens^2}{\varepsilon_0} \sin(\omega t). \quad (1.42)$$

Where for the individual sheath voltages there is a second harmonic generation, the total voltage drop across the discharge is free of harmonic generation. This is shown in Fig. 1.3-a, where the waveforms of the individual sheath voltages and the total applied rf voltage are plotted. For an applied rf voltage

$$V_{rf}(t) = \hat{V}_{rf} \sin(\omega t), \quad (1.43)$$

the sheath voltage for the powered and ground electrode sheath are described by

$$V_{el}(t) = -\frac{\hat{V}_{rf}}{4} [1 - \sin(\omega t)]^2 \quad (1.44)$$

and

$$V_{gr}(t) = -\frac{\hat{V}_{rf}}{4} [1 + \sin(\omega t)]^2. \quad (1.45)$$

The sheath width can then be expressed by

$$s = \sqrt{\frac{\varepsilon_0 V_{rf}}{2en}}. \quad (1.46)$$

It should be noted that the assumption of an harmonic cosine rf current in (1.37) is hardly met in reality where rather strongly nonharmonic currents are observed. A more reasonable description of the discharge current is enabled by the HPSM simulator by using a sufficient number of Fourier components (cf., sections 1.6 and 2.5).

For an asymmetric discharge where the sheath voltage ratio can be expressed by equation (1.6), (1.42) becomes more complicated

$$V_{rf}(t) = V_{el}(t) - V_{gr}(t) = -\left(\frac{A_{gr}}{A_{el}}\right)^q \frac{ens^2}{2\epsilon_0} [1 - \sin(\omega t)]^2 + \frac{ens^2}{2\epsilon_0} [1 + \sin(\omega t)]^2. \quad (1.47)$$

In Fig. 1.3-b, the waveforms of the individual sheath voltages and the total applied rf voltage are plotted for an asymmetric discharge configuration ($q = 2.5$). Compared to the symmetric case, the total voltage drop is not free of second harmonic generation anymore, and from contribution of the dc bias voltage it can become significantly negative.

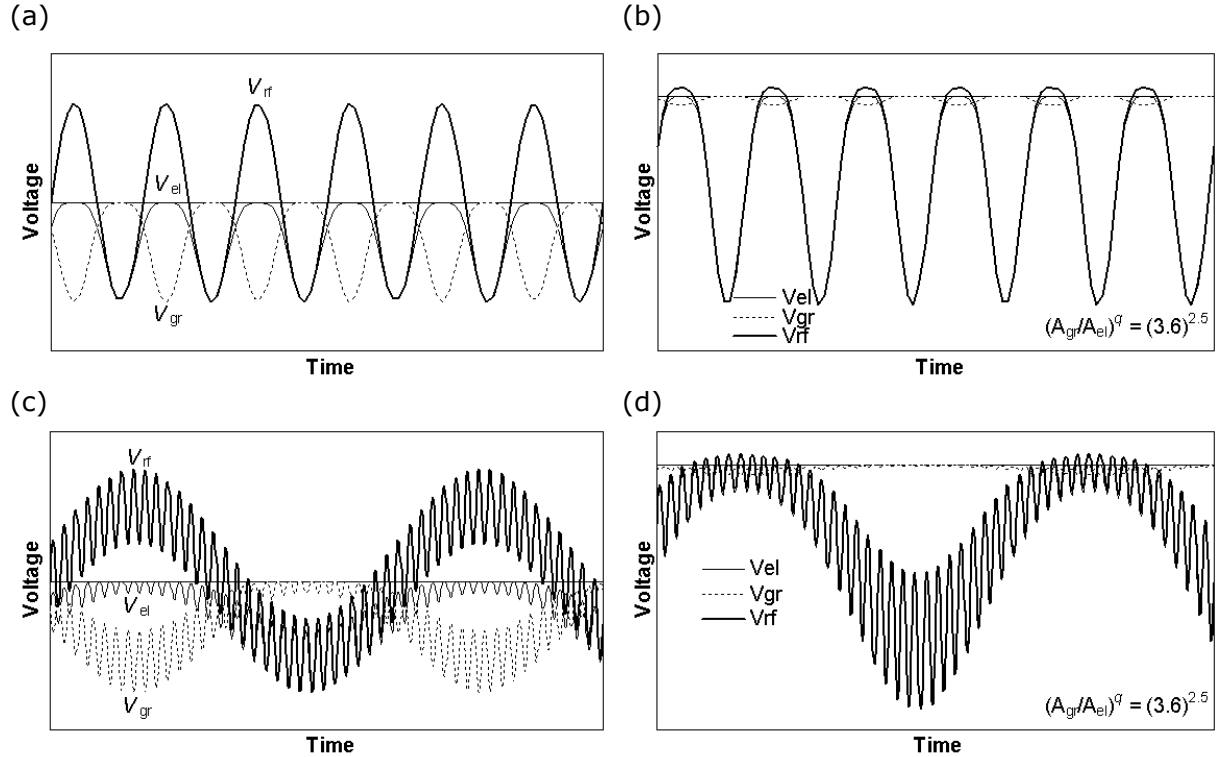


Figure 1.3: Sheath voltages as a function of time for different CCRF discharge configurations: (a) single frequency symmetric case, (b) single frequency asymmetric case, (c) dual frequency symmetric case, (d) dual frequency asymmetric case.

Dual frequency rf sheaths

Again, a symmetric discharge with sheaths s_{el} and s_{gr} is considered with the assumptions of constant ion density throughout the discharge and no electrons in the sheath region.

The dual frequency rf current $I_{rf}(t)$ is given by

$$I_{rf}(t) = I_1 \cos(\omega_1 t) + I_2 \cos(\omega_2 t + \varphi). \quad (1.48)$$

Upon current continuity and integration of Poisson's equation the sheath width for the electrode sheath is obtained

$$\frac{d}{dt} s_{el}(t) = -\frac{I_{rf}(t)}{enA}. \quad (1.49)$$

Integration yields

$$s_{el}(t) = s - s_1 \sin(\omega_1 t) - s_2 \sin(\omega_2 t + \varphi), \quad (1.50)$$

where

$$s = s_1 + s_2 \quad (1.51)$$

and

$$s_{1/2} = \frac{I_{1/2}}{enA\omega_{1/2}}. \quad (1.52)$$

The voltage across the powered electrode sheath is given by

$$V_{el}(t) = -\frac{en}{2\varepsilon_0} s_{el}^2(t) = -\frac{en}{2\varepsilon_0} [s - s_1 \sin(\omega_1 t) - s_2 \sin(\omega_2 t + \varphi)]^2. \quad (1.53)$$

Correspondingly, the ground electrode sheath voltage is calculated to be

$$V_{gr}(t) = -\frac{en}{2\varepsilon_0} [s + s_1 \sin(\omega_1 t) + s_2 \sin(\omega_2 t + \varphi)]^2. \quad (1.54)$$

Neglecting the voltage drop across the plasma bulk, the total discharge voltage is obtained by combining the sheath voltages V_{el} and V_{gr}

$$V_{rf}(t) = V_{el}(t) - V_{gr}(t) = \frac{2ens}{\varepsilon_0} [s_1 \sin(\omega_1 t) + s_2 \sin(\omega_2 t + \varphi)]. \quad (1.55)$$

Similar to the single frequency case, the total voltage drop across the discharge is free of harmonic generation, whereas for the individual sheath voltages there is a second harmonic generation.

For an applied rf voltage

$$V_{rf}(t) = V_1 \sin(\omega_1 t) + V_2 \sin(\omega_2 t + \varphi), \quad (1.56)$$

the sheath voltages are given by

$$V_{el}(t) = -\frac{V_1 + V_2}{4} \left[1 - \frac{V_1}{V_1 + V_2} \sin(\omega_1 t) - \frac{V_2}{V_1 + V_2} \sin(\omega_2 t + \varphi) \right]^2, \quad (1.57)$$

$$V_{gr}(t) = -\frac{V_1 + V_2}{4} \left[1 + \frac{V_1}{V_1 + V_2} \sin(\omega_1 t) + \frac{V_2}{V_1 + V_2} \sin(\omega_2 t + \varphi) \right]^2. \quad (1.58)$$

The voltage waveforms are plotted in Fig. 1.3-c (for a superposition of a high and low frequency component) illustrating the nonlinearity of the single sheath voltages and the linear nature of the combined sheath voltage. Compared to Fig. 1.3-a, a longer timescale is used to demonstrate the impact of both the high and low frequency contribution. The time averaged sheath width resulting from the applied voltage is given by

$$s = \sqrt{\frac{\varepsilon_0}{2en}(V_1 + V_2)}. \quad (1.59)$$

Using the simple model is just meant to show basic phenomena, the full complexity of dual frequency sheath dynamics is not accounted for. More complex models have been published recently [25,41,42].

For an asymmetric discharge where the sheath voltage ratio can be expressed by equation (1.6), (1.55) becomes more complicated

$$\begin{aligned} V_{rf}(t) = V_{el}(t) - V_{gr}(t) = & -\left(\frac{A_{gr}}{A_{el}}\right)^q \frac{en}{2\varepsilon_0} [s - s_1 \sin(\omega_1 t) - s_2 \sin(\omega_2 t + \varphi)]^2 \\ & + \frac{en}{2\varepsilon_0} [s + s_1 \sin(\omega_1 t) + s_2 \sin(\omega_2 t + \varphi)]^2. \end{aligned} \quad (1.60)$$

In Fig. 1.3-d, the waveforms of the individual sheath voltages and the total applied rf voltage are plotted for an asymmetric discharge configuration ($A_{gr}/A_{el} = 3.6$, $q = 2.5$). Again, the total voltage drop is not free of second harmonic generation any longer, and the electrode/total sheath voltage drop can become quite negative.

Multiple positive ion species

Using processing gas feedstocks usually yields more than one positive ion species in the plasma. For this case, analysis of the sheath region becomes much more difficult. Up to now, no model has been developed which is similar to the Bohm criterion based descriptions for a single positive ion species. From examination of the fluid equations for a plasma containing more than one species of positive ion, a multispecies Bohm criterion approach was described in [50,51]. From the assumption of spatially constant ionization frequencies during electron impact ionization, the various ion spatial distributions and transverse ion speed distributions were found to be geometrically similar. Only from that very specific situation it was thus concluded that each species arrives at the sheath with its own Bohm speed. A different approach considering multiple ion species is implemented in the HPSM code which is used in this work [52,53]. Approximate algebraic expressions derived for the field being valid both in the sheath and in the bulk serve as a basis of the self-consistent model of the plasma boundary sheath. The approximations were obtained from careful investigation of the transition from quasineutrality to electron depletion in the plasma boundary sheath by extending the electron step function model known in literature [20,38,54,55]. The model covers the range of collisionless and collisional pressure regimes and can be used to analyze rf modulated sheaths having multiple species [53].

Electronegative plasmas

The Bohm criterion (1.18) and the corresponding ion speed play an important role in electropositive plasmas. The question if there is an equivalent in electronegative plasmas is discussed in [31]. At low ion-to-electron density ratios, the negative ion density is reduced to zero before the plasma edge and the normal Bohm criterion applies. At higher ratios, the plasma edge can become multi-valued [56–58] which are terminated by a conventional positive-ion–electron sheath, or the sheath can finally contain also negative ions where it becomes comparably thin.

Density and temperature of the negative ions trapped in the glow determine the Bohm velocity of the positive ions entering the sheath, but they have no further influence on the dynamics of the positive ions in the sheath. The Bohm velocity in electronegative gases is smaller than in a plasma without negative ions. The consequence of this is that the positive ion density decreases more rapidly toward the electrode than in a plasma without negative ions. Subsequently the sheath thickness is larger than in a plasma without negative ions [59]. Up to now little is known about sheath dynamics in electronegative discharges from literature, but there appears to be a general agreement that significantly different sheath structures develop in electronegative discharges. Basic relationships in electronegative plasmas with a multiplicity of negative and positive ion species have been theoretically examined in [60].

From investigations performed in this work, it appears that medium-pressure electronegative halogen CCP discharges are not subject of fundamental changes, and discrepancies to the comparably simple picture of electropositive discharges with the applicability of the Bohm criterion appear to be generally rather small.

1.3 Sheath ion transport

For CCRF discharges discussed here, both the potentials of the plasma bulk and the plasma boundary sheaths are spatially and temporally rf modulated [61]. Ions traversing the rf sheaths reach the electrode surface with a characteristic distribution of energies [62]. The energy distribution reflects the acceleration of ions by the sheath electric field and is determined by the potential difference the ion experiences during travelling through the plasma sheath. The ion energy distribution function is mainly influenced by the transit time an ion takes to cross the sheath and by collisions the ions experience in the sheath region. Numerous experimental studies have been published about IEDs for ions incident at the electrodes of rf discharges [14,59,61,63-81]. The cases investigated in this work comprise the high (60 MHz) and intermediate frequency (2 MHz) regime, with ion transit times below or comparable to the rf period, respectively [66]. In the latter case the IEDF depends on the external voltage phase in which the ions enter the sheath which defines the potential difference they can cross [7,8]. Most ions enter the sheath at the maximum and minimum sheath potential since these values are experienced longer than intermediate sheath potentials. As a result, the IEDF of ions incident on the electrode surface will be characterized by the well-known saddle-shaped structure [61,82] comprising the two peaks of the energy equivalent of the maximum and minimum sheath potentials, respectively (cf., Fig. 1.4). In the following, the two cases of collisionless and collision-dominated rf sheaths are investigated in more detail. Due to high operating pressures (up to a few hundred mTorr) and large sheath voltage drops (up to kilovolts), the sheaths in commercial RIE reactors are typically collisional.

Both the ion angular and velocity distribution are anisotropic at the presheath-sheath boundary and at the electrode surface. An ion traversing the presheath and sheath region is accelerated by the electric field normal to the electrode surface and hence only influencing the ion velocity component normal to the surface. Dictated by the Bohm criterion and for $T_e \gg T_i$ in a typical electropositive discharge consisting of a single ion species, acceleration in the presheath occurs from a low thermal velocity in the bulk (1.19) to the Bohm velocity (1.18). Due to acceleration normal to the surface, faster ions should show narrower impact angles than slower, less energetic ions.

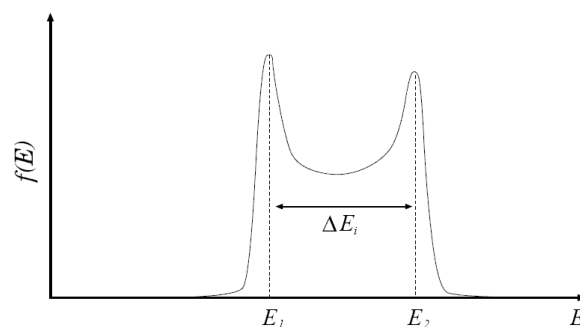


Figure 1.4: Bimodal structured ion energy distribution.

Collisionless sheaths

At low pressures, ions do not undergo collisions while travelling through the sheath. Hence, the ion energy is determined by the potential of the sheath edge with respect to the

electrode potential. For a collisionless sheath, the shape of the IEDF is determined by the ratio of the ion transit time τ_i to the rf period τ_{rf} [62]

$$\frac{\tau_i}{\tau_{rf}} = \frac{3\bar{s}\omega}{2\pi} \sqrt{\frac{m_i}{2e\bar{V}_s}} \quad (1.61)$$

where \bar{s} is the time-averaged sheath thickness, m_i is the ion mass, \bar{V}_s is the mean (dc) sheath voltage, $\tau_{rf} = 2\pi/\omega$ is the rf period of the rf frequency ω , and $\tau_i = 2\pi/\omega_i$ is the time an ion takes to traverse the sheath when the sheath voltage drop is at its dc value. The corresponding ion transit frequency

$$\omega_i = \frac{2\pi}{3\bar{s}} \sqrt{\frac{2e\bar{V}_s}{m_i}} \quad (1.62)$$

should not be used interchangeably by the ion plasma frequency of the plasma bulk

$$\omega_{pi} = \sqrt{\frac{n_0 e^2}{\epsilon_0 m_i}}, \quad (1.63)$$

as it is often observed in literature. Both frequencies will only be close in value for a typical presheath voltage drop of about 1 V and a dc sheath voltage of about 100 V [62].

For the low-frequency regime where $\tau_i/\tau_{rf} \ll 1$, the ions traverse the sheath in a short fraction of an rf cycle and respond to the instantaneous sheath potential. In this case the ion energy is determined by the phase of the rf cycle in which the ion enters the sheath. For example, low-energy ions entering the sheath near a minimum voltage see a shorter sheath width than the high-energy ions entering the sheath near a maximum voltage. Due to their shorter path, low-energy ions can traverse the sheath without seeing a significant voltage spread while, due to their greater acceleration, high-energy ions can also cross the sheath without seeing a significant voltage spread. The ion response to the time-varying sheath electric field leads to an rf modulated ion energy distribution showing a broad double peak structure. The lower energy peak corresponds to the influence of the minimum sheath voltage, whereas the higher energy peak is caused by the maximum sheath voltage. An analytical calculation for a voltage-driven low-frequency symmetric rf reactor is given in [62]. The analysis predicts non-sinusoidal voltage drops across the sheaths due to the nonlinear properties of the sheath capacitances and the conduction currents, and further the sheath voltage being for a longer fraction of the rf cycle at a minimum than at the maximum value. This results in IEDs with dominant low-energy peaks, and further distributions are found to be broad and independent of the ion mass, since ions of different masses can respond to the full range of the slowly varying sheath potential $V_s(t)$.

For the high-frequency regime where $\tau_i/\tau_{rf} \gg 1$, the ions experience many rf cycles while crossing the sheath and are no longer able to correspond to the instantaneous sheath potential. As a result of an increasing τ_i/τ_{rf} ratio, the peak separation will be reduced, the peaks will approach each other until eventually they can no longer be resolved. The ions will then only respond to an averaged sheath potential and the phase of the rf cycle in which they enter the sheath region becomes unimportant.

First systematic studies regarding ion energy distributions were conducted in laboratory systems under approximately collisionless sheath conditions [67-69,83]. As expected, a maximum in the distributions was found at the equivalent mean sheath voltage. This maximum peak was furthermore observed to split into a saddle shaped double peak structure for lower mass ions of the same gas discharge. From several attempts to find a

theoretical model that explains the observed phenomena, Benoit-Cattin and Bernard [84] first calculated an analytical expression for the energy separation of the ion energy distribution in this high frequency regime by assuming a constant sheath width, a Child–Langmuir space-charge sheath electric field in a collisionless rf sheath, a sinusoidal sheath voltage $V_s(t) = \bar{V}_s + \tilde{V}_s \sin(\omega t)$ and zero initial ion velocity at the plasma–sheath boundary:

$$\Delta E_i = \frac{8e\tilde{V}_s}{3\bar{V}_s\omega} \sqrt{\frac{2e\bar{V}_s}{m_i}} = \frac{4e\tilde{V}_s}{\pi} \left(\frac{\tau_{rf}}{\tau_i} \right). \quad (1.64)$$

As a result, for each ion species in an rf discharge there will be two IEDF peaks centered at eV_s where the peak separation was found to be inversely proportional to the frequency $\Delta E_i \sim 1/f$ and the square root of the ion mass $\Delta E_i \sim 1/\sqrt{m_i}$, and further proportional to the applied rf voltage $\Delta E_i \sim \tilde{V}_s$. This confirmed very well the experimental results. As τ_i/τ_{rf} increases, the ion energy distribution will finally change to a narrow structure where the two peaks are no longer resolved and appear as a single peak which is centered at the time-averaged sheath potential. Further work strongly adapted the model from Benoit-Cattin and Bernard [70,85] without major improvements regarding the initial assumption of the oscillating field just being a minor disturbance of a quasistatic field. A more promising attempt was published in [86] where the long ion flight time is decoupled from the comparably short rf period.

The intermediate frequency regime where $\tau_i/\tau_{rf} \sim 1$ is not well understood [85]. Ions take only a few cycles to cross the sheath moving with a velocity slightly below that of the sheath boundary. Ions will thus spend some time in the low sheath electric field close to the sheath edge, and part of their time in the high sheath electric field towards the electrode surface. On their way to the electrode, the ions experience a varying acceleration and the ion trajectory depends on the number of times the oscillating plasma–sheath boundary crosses the ion’s path. The resulting energy distribution depends on both the phase of the rf cycle in which the ions enter the sheath and also the number of rf cycles it takes to cross the sheath. The two peaks can be observed to be close together with varying peak heights. Sometimes the asymmetry favours the high-energy peak. Whether or not one of the two IED peaks will dominate generally depends on whether or not the sheath voltage $V_s(t)$ is mostly at a maximum or minimum during an rf cycle. The sheath voltage waveform strongly depends on the nature of the sheath, i.e. whether the sheath is resistive ($j_c \gg j_d$, where j_c is the conduction and j_d the displacement current density) or capacitive ($j_c \ll j_d$). For the low frequency regime where $\tau_i/\tau_{rf} \ll 1$, the sheath tends to be resistive, whereas for the high frequency regime where $\tau_i/\tau_{rf} \gg 1$, the sheath tends to be capacitive. Hence, as the ratio τ_i/τ_{rf} increases, a transition from a low-frequency ($\tau_i/\tau_{rf} \ll 1$), resistive ($j_c/j_d \gg 1$) sheath with a broad bimodal ion energy distribution and a dominant low-energy peak to a high-frequency ($\tau_i/\tau_{rf} \gg 1$), capacitive ($j_c/j_d \ll 1$) sheath with a narrow bimodal IED and peaks of more or less equal height is observed [62].

Collisional sheaths

The assumption for a collisionless sheath are not longer valid if the ion mean free path becomes equal or shorter than the sheath thickness. This is caused by a change of the field and potential distribution from the influence of ion–neutral collisions, and furthermore a scattering of ions towards lower energies. Compared to the collisionless case discussed above, the shape of the ion energy distribution can significantly change and the IEDF structure will eventually become broadened and move to lower energies. Whereas for dc

discharges the low energy part of the distributions is typically observed to be flat [87,88], pronounced peak structures were found at the low energy IEDF region for collisional rf discharges [7,8]. This was confirmed by several further measurements [44,72,89]. The final IEDF structure is not only determined by the probability of collisions, but also by its type. Thus, the impact of elastic collisions and charge exchange collisions on the IEDF shape will be discussed in more detail.

Elastic collisions between ions and neutrals will result in a loss of ion kinetic energy and a change of directionality of perpendicular incidence on the electrode. For an ion traversing the sheath, its velocity component normal to the surface is accelerated. In case the ion does not experience collisions it arrives at the electrode surface with a large perpendicular component and a small parallel component. If the ion experiences collisions with neutrals in the sheath it will lose energy and become scattered anisotropically. Due to the accelerating field, the ion arrives at the electrode with an incident angle that is typically smaller than the scattering angle. Elastic scattering will generally yield a broader angular distribution of the ion velocity and further a low energy tail in the ion energy distribution. Large angle scattering will result in significantly modified angular distributions, where lighter ions are scattered over larger angles than heavier ions [62].

Charge exchange collisions are most pronounced between ions and their parent neutrals (symmetric charge exchange) yielding additional peaks at distinct energies. During charge exchange, the charge is transferred from a fast ion to a slow thermal neutral. The incident ion will then continue travelling as a fast neutral, whereas the former neutral has turned into a slow thermal ion and will be accelerated by the field towards the electrode. The IED show typically a quite large spread caused by multiple secondary peaks which appear at lower energies than the two primary IED peaks [7,8]. The secondary peaks are caused at lower energies than the two primary IED peaks because the slow ions formed inside the sheath do not experience the full potential difference of the ions which enter at the sheath edge. A simple ad-hoc model was used by Wild and Koidl [7,8] to explain the secondary peak structures. The model included harmonic potential distribution and symmetric charge exchange collisions between fast ions and cold neutrals which lead to slow ions. Model results were adapted to experimental measurements by adapting free model parameters. The origin of the peak structure was explained by the combination of charge exchange collisions and modulation of ions in the oscillating rf field. Two conditions have to be fulfilled in order to cause discrete secondary peaks:

(1) For a fixed position s_0 inside the sheath at a time t_0 , a secondary peak is obtained when secondary ions are created at phase angles ωt_0 such that $dE/d(\omega t_0) = 0$. This is explained by the following situation for an ion traversing the sheath. Periodically moving back and forth from the electrode, the modulated electron density front passes by s_0 on its way to the electrode. The local electric field at s_0 will be zero during the time interval it takes the electron front to reach the electrode, bounce back and pass by s_0 again. Thus any secondary ions created at s_0 during this time interval will be virtually at rest and accumulate at s_0 . However, when the receding electron front passes by s_0 again, the electric field at s_0 reappears and accelerates the bunched ions towards the electrode. The bunched ions reach the electrode surface with the same impact energy E , causing a secondary peak in the ion energy distribution.

(2) The secondary ions must further be created at positions s_0 within the sheath such that $dE/ds_0 = 0$. Otherwise, secondary ions can be created at every point s_0 within the sheath, so that IED peaks caused by bunched ions that were created at different s_0 will wash each other out. Creating ions such that $dE/ds_0 = 0$ occurs only at discrete s_0 , resulting in discrete secondary IED peaks. While an ion traverses the sheath, the electron front will be moving back and forth from the electrode intersecting the ion path for a maximum as often as is determined by the ratio τ_i/τ_{rf} . This explains qualitatively why the number of secondary peaks in the energy distribution is then characteristic for the average number of rf cycles it takes an ion to cross the sheath. From the analysis, secondary IED peaks can furthermore only be observed for $\tau_i/\tau_{rf} > 1$.

Since charge exchange collisions produce fast neutrals that bombard the target electrode in parallel to the positive ions, this necessitates in principle to consider neutral energy and angular distributions as well when calculating sputter and etch yields under collisional sheath conditions [90,91].

In summary, both collision mechanisms have similar effects: Ions are scattered into the low energy part of the distribution. During an elastic collision, ions transfer energy according to the laws of momentum conservation and energy conservation on their collision partner. Ions created by charge exchange within the sheath start with an initial thermal velocity. In both cases, the ions do not experience the total potential drop on their remaining way and can not gain the maximum energy. Collisional ion energy distributions will typically consist of both a broad continuous time-averaged background which is skewed toward lower energies [88], as well as secondary peak structures resulting from rf modulation and charge exchange collisions [7,8]. The effect of sheath collisions is to reduce the ion bombarding energy but to proportionally increase the total energetic particle flux (ions and fast neutrals) to the electrode [20].

Ion angular distributions (IADs)

For the low-frequency regime ($\tau_i/\tau_{rf} \ll 1$), the IED is broad and bimodal with a dominant low-energy peak at the dc potential V_{dc} , and a high-energy peak at the maximum sheath voltage drop $V_{s,max}$. Due to $V_{dc} \gg k_B T_i/e$ and $V_{dc} \ll V_{s,max}$, many ions hit the electrode surface with lower energies and wider impact angles, resulting in a wider IAD.

For the high-frequency ($\tau_i/\tau_{rf} \gg 1$) regime, the IED is narrow and centred about the energy equivalent of the dc sheath voltage drop $e\bar{V}_s$. Since typically $e\bar{V}_s \gg k_B T_i$, most of the ions will hit the electrode surface with high energies and narrow impact angles resulting in a narrow IAD.

In the collisionless case, the ion angular distribution can be in principle deduced from the IED [62]. For collisional sheaths as experienced in typical RIE reactors, the collisions affect the ion velocity component parallel to the surface of the electrode. As for the IED, the IAD is affected by the influence of elastic and charge exchange collisions. Elastic scattering can cause an ion velocity component parallel to the electrode surface and hence broaden the IADs of incident ions. Due to the anisotropy of the collisional scattering, the parallel component after a single collisional event is however only a fraction of the perpendicular component. Slow ions created from charge exchange collisions will typically not experience a significant change of the velocity parallel component. When these ions are accelerated by the sheath electric field, the normal velocity component will dominate. Since the ratio of the velocity component normal to the electrode surface is decreased over the

parallel velocity component when charge exchange collisions occur, the IAD however appears still broadened compared to the case when collisions are absent.

Modeling approaches

Monte Carlo simulations allow for a systematic investigation of the peak structure [82,89,90,92,93]. The influence of collisions and discharge parameters like pressure, ion mass and frequency on the ion energy and angular distributions (IEADs) can be investigated in detail by following the trajectory of particles. All results confirm the experimental investigations as well as the theoretical explanation of Wild and Koidl [7,8]. The charge exchange model from Wild and Koidl, the Monte Carlo simulations as well as collisionless models have in common that the electrical field in the rf discharge is described by intuitive ad-hoc assumptions to gain insight into the origin of IEDFs and for interpretation of measurement results. So far, all these models lack to provide a self-consistent description of the sheath problem. This problem is addressed by application of hybrid models [17,18,94]. Here, the field distribution and particle dynamics are self-consistently calculated from Poisson's equation and the hydrodynamic equations. The rf field is used to determine the distributions by applying a Monte Carlo model. Such a hybrid model is also used in this work and described in more detail in section 1.6. Besides the hybrid models, the PIC (Particle-In-Cell) method is used as a further approach [11,12,27,62,95-98]. Here, plasma particles are simulated by a significantly smaller number of super particles. From their distribution, charge carrier densities and electric field distributions are calculated. As for the hybrid models, ion distribution functions are calculated again by the Monte Carlo method. The biggest diadvantages of all self-consistent simulations is the considerable numerical effort, and further they are not useful to derive simple scaling laws and analytical expressions to enable simple estimations or to describe simple correlations between physical parameters. From these reasons, consistent semi-analytical rf sheath models are required which focus on the essential core of the problems. Such models can be classified by the operating frequency. Low operating frequencies ($\omega \ll \omega_{pi}$) allow for a quasi-stationary description [99-101] since the ions cross the sheath in a fraction of rf period and hence experience a nearly stationary electric field. For high frequencies ($\omega \gg \omega_{pi}$), the ion dynamic is determined by the time-averaged field since they are not able to follow the oscillations due to their inertia. In both cases, electrons can readily follow the electric field oscillation since $\omega \ll \omega_{pe}$. Typically, the electron step function model was successfully applied to obtain an approximate potential profile. The frequency region around $\omega \sim \omega_{pi}$ is difficult to describe with analytic models, attempts to describe this regime were published in [40,102-105].

1.4 Silicon etching with halogen chemistry

Selective, anisotropic etching of silicon and removing of patterned silicon films by using halogen etch species is considered to be one of the most important plasma etching applications in semiconductor fabrication. In principle, four basic low-pressure plasma processes are known to remove material from surfaces:

Sputtering In this process, atoms are released from surfaces through energetic ion bombardment. The ions are generated inside the plasma bulk and accelerated to the target (i.e., the substrate) where they can gain energies of a few hundred volts. From the ion energy that is deposited, atoms are sputtered off the target surface. The momentum that

is transferred to the target atoms leads to a cascade of collision inside the lattice. After several collisions, some atoms possess a momentum directing away from the center of the crystal. Atoms being close enough to the surface and carrying a sufficient amount of energy are able to leave the target. The amount of sputtered target atoms per incident ion projectile is described by the sputter yield and is a function of energy and mass of the ion projectiles, as well as the binding energy of surface atoms of the substrate lattice and the target atom mass. A reasonable estimate of the sputtering yield can be obtained from the semi-empirical formula [106]

$$\gamma_{\text{sput}} \approx \frac{0.06}{E_t} \sqrt{Z_t} (\sqrt{E_i} - \sqrt{E_{\text{thr}}}) \quad (1.65)$$

for $0.2 \leq Z_t/Z_i \leq 5$ with $Z_t, Z_i \gg 1$ where

$$\bar{Z}_t = \frac{2Z_t}{\left(\frac{Z_i}{Z_t}\right)^{\frac{2}{3}} - \left(\frac{Z_t}{Z_i}\right)^{\frac{2}{3}}} \quad (1.66)$$

Here, Z_t and Z_i are the atomic numbers of the target atom and the incident ion, E_t is the surface binding energy, and E_{thr} is the threshold energy. For mass ratios $m_i/m_t \geq 0.3$, the threshold energy can be estimated by [107,108]

$$E_{\text{thr}} \approx 8E_t \left(\frac{m_i}{m_t}\right)^{\frac{2}{5}} \quad (1.67)$$

Sputtering yields obtained for typical ions incident on a silicon substrate are calculated using equations (1.65) to (1.67) and plotted in Fig. 1.5. Besides the energy dependence, the sputter yield also depends on the incidence angle of the ion projectile. The sputter yield can reach unity (one sputtered target atom per incident ion) for typical ion energies of a few hundred electron volts. Both sputter yield and ion flux determine the sputter rate which describes the target surface erosion. Whereas the dependency between sputter rate and ion energy is described by a power function, there is a linear dependency between sputter rate and ion flux. A sputter rate is observed for ion energies exceeding a threshold which corresponds to the binding energy in the lattice of the target atoms. Projectile energies exceeding the binding energy initially yield a strongly increased sputter rate where the incline decreases with ion energy.

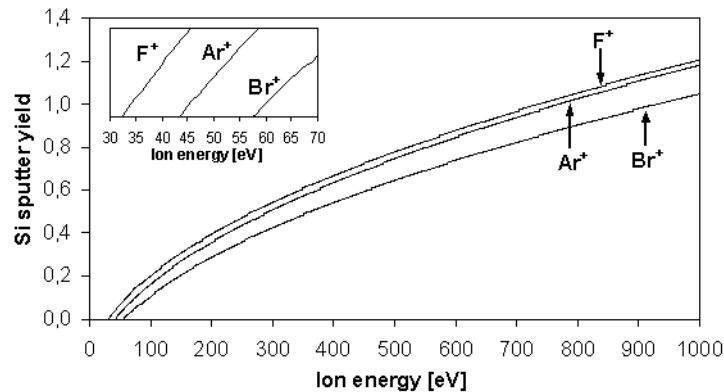


Figure 1.5: Silicon sputter yield for F^+ , Ar^+ , and Br^+ ions, calculated thresholds are 32.3 eV for F^+ , 43.5 eV for Ar^+ , 57.4 eV for Br^+ [106-108].

Whereas the ion energy dominates at lower sputter rates (above the threshold), the ion flux dominates the sputter rate at higher values. Strictly, this relation is only valid for sufficiently low pressures where the ion mean free path exceeds the sheath thickness (i.e., the ion energy is not reduced by collisions inside the sheath). At higher pressures, the sputter rate will be reduced by these collisional effects. Due to a typically low sputter yield $\gamma_{\text{sput}} \leq 1$ and comparably small ion fluxes incident on the substrates, pure sputter rates usually range from angstroms to a few ten nanometers per minute. Sputtering is an unselective but very anisotropic process, since it strongly depends on the angle of incidence of the ion. Although for ions with normal incidence on the substrate there is essentially no sidewall removal of material, sputtering causes facetting of structures which is due to the sputter yield peaking at an angle of incidence which is greater than zero. Sputtering is the only etch process that is able to remove involatile products from a surface. However, such products can easily be redeposited on different locations at the substrate (and reactor surfaces) where they inhibit the etch reaction and have to be removed again by sputtering in order to continue etching. For high ion energies there is also an increasing chance of ion implantation into the substrate. Strictly speaking, purely physical sputtering applies only for the argon discharges investigated in this work.

Chemical etching Gas-phase etchant atoms and molecules delivered from the discharge react with the surface and form volatile gas-phase etch products. The selectivity can be very high, but a purely chemical etch process is inherently very isotropic (nevertheless, etch rate dependencies upon the crystal orientation might appear) since gas phase etch species reach the surface with a near uniform angular distribution. High etch rates can be achieved from the high fluxes of etch species and etch rates are less affected by the rate of arrival at the surface, but rather by the complex set of surface reactions leading to formation of the etch product. A well-known example is spontaneous chemical etching of silicon with fluorine chemistry.

Ion-assisted etching During this process both reactive neutrals and energetic ions are supplied from the discharge. This case applies for the different halogen discharges investigated in this work. Flowing an etch gas into the reactor will soon cause a monolayer to be build on the substrate (as well as the reactor surfaces). Ions incident on the substrate may react with the substrate material and/or induce a reaction between the adsorbed etch gas molecules and the substrate if the reaction does not occur spontaneously. To initiate a chemical reaction requires energies of only a few electronvolts which are easily acquired for typical operating conditions. Combination of etch species and ions can yield larger amounts of etch products than those observed for purely physical sputtering or purely chemical etching. From different experiments it is suggested that the etching is chemical in nature but reaction rates are determined by energetic ion bombardment [109,110]. Above a certain threshold the etch rate will generally increase for increasing ion energies. As in the case of purely chemical etching, the etch product must be volatile. Highly anisotropic etching can be achieved due to angular distributions of ions striking the surface which are usually highly directional. Selectivity can be very poor for ion energy driven etching. Hence knowledge of the trade-off between anisotropy and selectivity is an important factor in designing etch processes. Detailed mechanisms for plasma etch processes are not well understood and simple empirical models created from key observations are often used to gain some insight into the use of various processes. In some etch models, gas-phase etch species are first physisorbed and subsequently react with the surface to form an etch product. Rate-limiting steps are chemisorption of physisorbed

species and desorption of the etch product. For other etch models, physisorbed or gas-phase etch species directly react with the surface to form the etch product which is desorbed immediately. The latter model may suffice to describe purely chemical F-atom etching of fluorinated silicon films (SiF_x with $x \approx 3$) [110].

Ion-enhanced inhibitor etching This process involves an inhibitor species in parallel to etch species and energetic ions. The inhibitor molecules (like CF_2 , CF_3 , CCl_2 , CCl_3) deposit on the substrate to form a protective layer or polymer (fluoro-, chloro-carbon) film. Alternatively, oxygen is added to the feed gas mixture to support creating a protective (SiO_x) sidewall layer which constantly builds during etching and more efficiently resists the attack of etch species (radicals) as compared to the silicon etch front at the trench bottom. Etch species are chosen to have high etch rates for cases where no ion bombardment and inhibitors are involved. The role of the ion flux is to locally remove the inhibitor layer exposing the surface to the chemical etchant. Highly anisotropic etching can be achieved, typical processes involve anisotropic etching of the SiO_2 hard mask layer for the trench structures investigated in this work, where sidewalls are protected by deposited polymer films. Compared to ion-assisted etching, this process yields similar features. However, contamination of the substrate and final inhibitor film removal can cause serious issues.

Having been studied for about 20 years now, etching of silicon with fluorine atoms is experimentally the most well-characterized surface etch process but is still not thoroughly understood [20,110]. Fluorine atoms are known to spontaneously etch silicon and silicon dioxide even in the absence of ion bombardment. Etch rates were measured to roughly exhibit an Arrhenius form over a wide range of temperatures, and a linear dependency upon the F atom gas phase density was observed up to very high densities. Published reaction rates can differ considerably [111,112] which is attributed to surface contamination, residual ion bombardment from the F-atom plasma source, and unknown distributions of etch products. In steady state, a weakly bound, unsaturated, fluorinated silicon SiF_x (fluorosilyl) layer [113] of several monolayers thickness forms at the surface, where x is about 3 (SiF_3) at the top of the layer falling smoothly to zero at the SiF_x -Si interface. The thickness of the SiF_x layer is influenced by the etch conditions, e.g. for an high etch rate the SiF_x layer thickness is observed to be rather thin, and vice versa. The process is assumed to be balanced by diffusion of fluorine atoms into the surface and surface erosion during etching. From molecular dynamics simulations, the porosity of the the SiF_x layer is observed to increase with increasing fluorine content which is believed to be important for chemical sputtering (i.e., chemically enhanced physical sputtering) [113]. At room temperature, this layer is found to be stable, whereas a decomposition is measured for temperatures exceeding 300-400°C. Products of the decomposition comprise $\text{SiF}_2(\text{g})$ and $\text{SiF}_4(\text{g})$. Whereas $\text{SiF}_4(\text{g})$ is the main etch product during etching, larger molecules like $\text{Si}_2\text{F}_6(\text{g})$ or $\text{Si}_3\text{F}_8(\text{g})$ have also been observed [110]. Etch product distributions and decomposition properties of the SiF_x layer vary greatly at different temperatures leading to the assumption that the etch mechanisms differ also. The electron affinity of an F atom in free space is $E_{\text{aff}} \approx 3.45$ eV. This value is further increased near the surface, e.g. an F-atom at about 1 Å distance from the SiF_x surface has an affinity of about $E_{\text{aff}} \approx 7.05$ eV [20]. Therefore, negative ion formation at the surface is favored. Such negative ions experience a strong image force directed into the surface which promotes lattice penetration and subsequent attack of Si-Si bonds after F-atom neutralization.

Etch rates at constant F-atom fluxes can be increased by up to one order of magnitude for sufficiently high ion fluxes and ion energies bombarding the surface. Etch product distributions are observed to change during additional ion bombardment due to an efficient reduction of the fluorine content in the SiF_x surface layer. The enhanced etch rate due to ion-assisted F-atom etching of silicon can result from (1) formation of damaged regions being more reactive to subsequently arriving fluorine - however this is probably not important for F-atom etching of silicon [20]; (2) increase of the temperature due to etch reactions or ion bombardment - however the temperature rise is not high enough [20]; (3) chemically enhanced physically sputtering - however this is not believed to mainly contribute to ion-enhanced etching for typical neutral-ion flux ratios [113,114]; (4) chemical reaction and desorption due to ion bombardment - this is likely to be important for ion-energy assisted F-atom etching of silicon [113,114]; (5) enhanced chemical etching - this mechanism is also believed to contribute to an etch rate enhancement [20].

Compared to silicon, the purely chemical etch rate of F-atoms on silicon dioxide is small and no more than a monolayer of fluorine is adsorbed on an SiO_2 surface. Higher SiO_2 etch rates are ion energy-driven where a comparably high degree of anisotropy can be obtained. However, fluorine is in general no suitable candidate for processes where highly anisotropic etching is required, and other (chlorine and bromine based) halogen chemistries are generally used to fulfill such requirements.

Compared to chemical etching of silicon with fluorine atoms, etching with chlorine shows pronounced crystallographic effects (i.e., different densities of atoms in the silicon lattice) and also large doping effects. Moreover, lower etch yields are observed for Cl^+ ions as compared to F^+ ions incident on silicon which is explained by a lower halogen sputtering coefficient and higher ion reflection for Cl^+ [114]. Similar to fluorine, Cl^- ions formed at the surface appear to play a critical role in Cl-atom etching. Exposure of a silicon surface to Cl atoms yields formation of a chlorosilyl (SiCl_x) layer with a coverage of a few monolayers. However, this chlorosilyl layer is observed to be thinner than a SiF_x layer formed when F atoms are present. SiCl_4 and possibly Si_2Cl_6 and SiCl_2 are identified as typical etch products. Ion assisted etch yields from etching silicon with a Cl_2 chemistry were found to up to one order of magnitude lower than for a F_2 chemistry. Both Cl atoms and Cl_2 molecules can be important etch species for ion-energy driven etching. Penetration depths are observed to range few angstroms up to few nanometers deep in the silicon lattice [114].

Whereas chlorine chemistry is commonly used in the technology of Si-etching, utilization of bromine-containing plasma chemistries was stimulated by the demand of a higher Si-to- SiO_2 selectivity. Bromine plasma chemistries in MERIE systems were found to provide both high selectivity and anisotropy [115]. Bromine atoms are even less reactive than Cl atoms and room-temperature chemical etching does not occur spontaneously. Hence, etching of silicon with bromine has to be stimulated by ion bombardment, and hence requires a combined physical-chemical process [116]. The ion bombardment enhances the formation of volatile etch products by providing the activation energy for the rate-limiting step of the surface processes (i.e., adsorption of etch species, reaction and desorption of etch products). Thus, bombardment with energetic ions enhances etch rates and can significantly influence anisotropy.

Etching yields for silicon (number of silicon atoms removed per incident ion) in F_2 , Cl_2 , Br_2 , and HBr plasmas published by Vitale et al. [117] were measured to approximately increase with the square root of ion energy. It was pointed out that spontaneous etching influences the silicon etching yield which for fluorine is much more severe than for chlorine and bromine that exhibit only very low spontaneous etching. Depending on the neutral-to-ion flux ratio, spontaneous etching might be independent of ion flux and surface coverage. However, the authors subtracted the saturation halogenation spontaneous etching rate in the absence of ion bombardment from the total etching rate with ion bombardment to determine the saturation halogenation fraction ion enhanced etching yield. The saturated ion enhanced etching yield for fluorine was found to increase approximately with the square root of energy with a threshold energy of about zero. This appears reasonable since etching occurs spontaneously (i.e., a zero energy F^+ ion still contributes to the etching). For chlorine, the etching yield increased again with the square root of energy. The threshold energy was determined in the range of about 7-25 eV, depending upon the composition of the ion beam that can consist of Cl^+ and/or Cl_2^+ ions. For bromine, the silicon etching yield also increased with the square root of energy. Etching yields were observed to be considerably higher in HBr plasmas compared to Br_2 plasmas. This is likely due to the hydrogen atoms being present from dissociation of HBr in the discharge that can cause an enhanced etching in the presence of ion bombardment. From different studies [118-123], hydrogen atoms were reported to etch silicon spontaneously. However, chemical etching without ion bombardment appears negligible which might be due to the surface coverage by bromine atoms preventing hydrogen to penetrate into the silicon lattice. Under additional ion bombardment, the small hydrogen atoms can easily bond to silicon to occupy sites that are sterically hindered to bromine due to its large atomic radius, and further hydrogen can penetrate into the silicon lattice and break silicon backbonds which are difficult to be reached by Br atoms. This might explain the differences for the threshold energy which is about 10 eV for HBr and around 44 eV for Br_2 . In the latter case, the threshold for silicon etching is already close to that for physically sputtering (about 57 eV, see above). It also shows that a considerably higher energy is required to disrupt the silicon surface, and enable large bromine atoms to penetrate into the silicon lattice and to react with the silicon backbonds. Moreover, etching of silicon with HBr might result in SiH_xBr_y reaction products that are more volatile than $SiBr_4$ products formed from etching with Br_2 . In case of product desorption being rate limiting, this might further contribute to differences in etching yields.

From further studies, the etching yield for HBr plasmas was found to decrease with temperature which is attributed to a reduced surface coverage of adsorbed Br and H atoms. This is promoted from determination of corresponding sticking coefficients [124,125]. With regards to etch profile control, bromine is known to produce more anisotropic feature profiles than chlorine [126-130] and to provide a higher selectivity during etching [115]. Nevertheless, chlorine is sometimes added to increase the etch rate. In commercial systems, the silicon etch rate with pure HBr can be lower than in pure Cl_2 discharges [117,126,131]. Since etching yields are quite comparable for both halogen chemistries, differences in the etch rate might result from differences in the ion flux (the etch rate is a product of etching yield and ion flux).

Ion scattering at feature sidewalls can result in etch profile distortions, like undercutting, tapered or bowed sidewalls, and microtrenching at the sidewall bottom of the feature. In contrast to the angular dependence of a pure physical silicon sputtering yield (which shows a maximum around 50° for argon), the ion enhanced chemical etching yield for silicon in

halogen reactive gases is fairly flat and tends to decrease monotonically with angle [117,132] in the surface saturation coverage regime. Compared to bromine chemistries that typically exhibit a good profile control with vertical sidewalls in the silicon substrate/layer, chlorine tends to produce significant sidewall bowing and microtrenching at the feature bottom [129,131,133]. Possible explanations range from the influence of mask selectivity and faceting, differences in the composition of sidewall passivation layers, a higher tendency of ion reflection instead of etching at the sidewall in case of chlorine, a different etch yield dependency upon ion bombardment angle, and/or feature charging effects. In the latter case, a localized buildup of charges on insulating surfaces might possibly yield deflection and subsequent scattering of incoming ions within the trenches. This could explain microtrenching as is sometimes found at the bottom of the feature. From continuous debates about ion deflection by the electric field of substrate surface potential, some researchers hold the view that the mask surface potential necessary to efficiently deflect ions can hardly be obtained because it would require the mask potential to be higher than the plasma potential which in turn would destroy stable plasma conditions [134]. Another mechanism is cavernous undercutting on the upper part of a narrow deep Si trench that could occur due to ion scattering from the mask opening [134]. The evolution of undercut may be detrimental to a subsequent refill process involved in trench capacitor formation. In general, the etch process comprises complex mechanisms which change dynamically. Mechanisms yielding the final etch profile are quite complex and often can not be separated easily when investigating the obtained etch result. An equilibrium state is obtained only in very limited situations. The stability of an etch process is sometimes found to be quite high, sometimes even very small changes of the discharge parameters or the etch process on the substrate surface can yield drastic changes in the obtained etch result.

In the neutral flux limited regime and for the usual case that the reaction probability is large compared to the recombination probability, a reduction in the etch rate can occur which is called loading effect [109,135]. Whereas for F atoms it is generally the case that the reaction probability exceeds by far the recombination probability $\gamma_r \gg \gamma_{rec}$ and considerable loading is observed, γ_{rec} for other etch species like Cl, Br, O can be of the order of or even exceed γ_r and only weak or even negative loading is observed [20]. Besides the loading effect that describes differences for the etching of structures with different open areas, further influences on the etch rate are known. For increasing trench depth or decreasing trench width, the silicon etch rate was observed to decrease [135-137] - an effect that is also known as RIE lag. RIE lag is an expression of Aspect Ratio Dependent Etching (ARDE) which describes the dependence of the silicon etch rate on the aspect ratio of relevant features. Different possible mechanisms for aspect ratio dependent etching [138] have been published to explain how feature dimensions influence the etch rate. Most commonly, Knudsen transport of neutrals [139], ion shadowing [140], neutral shadowing [141], differential charging of insulating microstructures [142,143] are considered.

1.5 In situ plasma diagnostics

1.5.1 Mass resolved ion energy analysis

A mass resolved ion energy analyzer or so-called plasma monitor is a versatile plasma diagnostic technique which allows for analysis of neutrals and radicals [144,145], and positive [12,59,63-65,146,147] as well as negative ions [63,148] formed in the plasma. In the following, principles of operation of the commercially available Hiden EQP 500 high energy system applied for standard mass spectrometry, APMS and IVDF (Ion Velocity Distribution Function) measurements are described.

The Hiden EQP plasma probe consists of four main sections: the ion optics, an electrostatic 45° sector field energy analyzer (ESA), a quadrupole mass spectrometer (QMS), and a secondary electron multiplier (SEM) for ion detection (cf., Fig. 1.6).

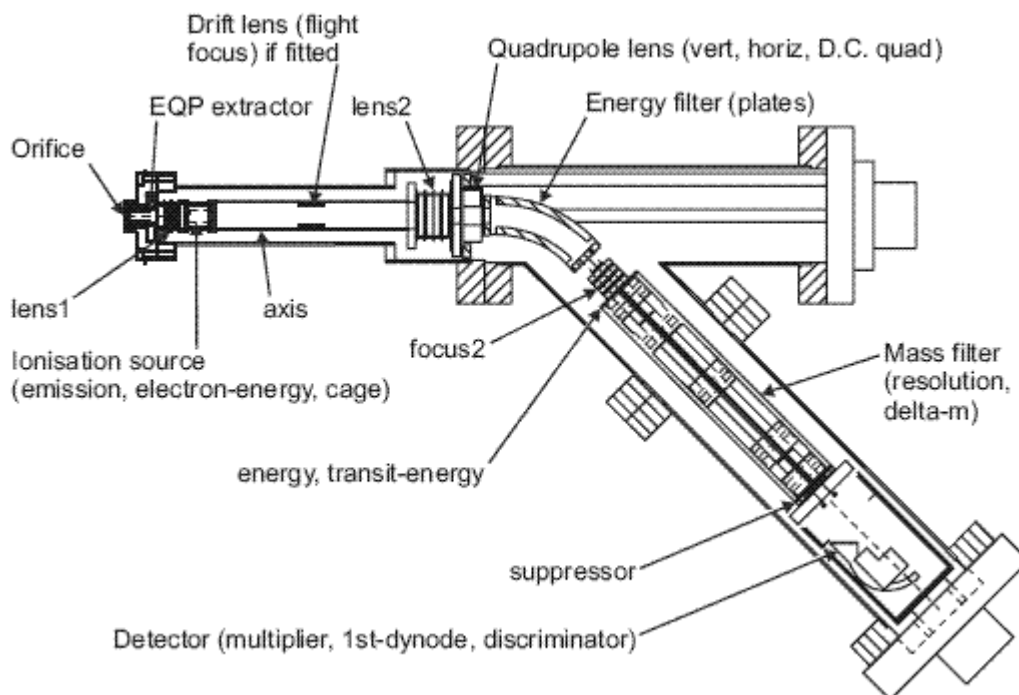


Figure 1.6: Hiden EQP system.

Signal optimization and finally ion energy scans are performed at a particular mass-to-charge ratio during sweeping the various electrode voltages. The EQP probe is mounted at the plasma reactor wall via the side window access port. The analyzer system is differentially pumped by its own 230l/s turbo pump to maintain a base pressure of $p_{\text{EQP}} \leq 5 \times 10^{-6}$ Torr inside the EQP. Maintaining the base pressure is important for providing a collision free environment for sampled species, as well as protect the SEM detector and avoid enhanced degradation.

Sampling orifice

Neutral and charged particles can be extracted from the plasma. Whereas neutrals simply drift into the analyzer, positive and negative ions require specific arrangements. Positively charged ions leave the plasma bulk and are accelerated toward the ground electrode by the sheath electric field. A small fraction of these ions can pass the 50 μm sampling aperture and enter the EQP. Due to their lower mobility compared to electrons, negatively charged

ions are usually efficiently trapped inside the discharge and can not reach the ground or powered electrodes of the plasma reactor. However, highly energetic electrons can reach the walls during the collapse of the sheath potential during one rf cycle. To avoid interferences by negatively charged particles entering the EQP, these particles are repelled by applying a negative voltage via the *extractor* electrode right behind the entrance orifice. Further, the *extractor* is also part of the ion optics and helps to accelerate and focus positive ions into the instrument. Detection of negative ions can be enabled by plasma modulation, forcing the sheath potential to collapse and enabling these ions to reach the surface [149].

Compared to typically used metal orifice plates connected to a well defined potential (e.g. ground), the main difference of the particular orifice plate used in this work is made of ceramic MACOR [150] material. This modification was found to be a necessary and a major requirement for installation at the HART process development and production reactor used for the investigations in this work.

Ionization Source

The dual-filament electron-impact ionization source is used for analysis of neutrals or radicals when performing standard mass spectrometry or APMS. Neutrals can not be detected directly since both energy and mass filter exploit electric fields for particle analysis. Hence, uncharged particles must be first converted into positive or negative ions to allow for their detection. The ionization source filament can both be energized to emit electrons. The electron energy is controlled for a defined bombardment of the neutrals sampled from the plasma. For standard mass spectrometry, usually 70 eV electron energy are applied to create positive ions. For analysis of radicals, the electron energy can be varied between zero and 150 eV maximum energy. Negative ions can be created by electron attachment [151], a process that can occur for low electron energies (in the range of a few eV). Sometimes the latter process is chosen in cases where bombardment at high electron energies leads to very complex mass spectra due to various fragmentation products. Low electron energy bombardment will usually cause the main product or very few additional products to be created. Ions created inside the instrument are analyzed by the energy and mass filter in the same way as ions directly created in the plasma. The ionization source is switched off for detection of plasma ions.

Extraction

After passing the orifice ions are focused onto the ion source exit aperture by the three electrodes *extractor*, *lens1* and *axis* forming the first electrostatic lens. In this lens the entire ion distribution function (IDF) is accelerated or decelerated. Since these are the first electrodes incident ions encounter, voltage settings are quite critical for determination of the IDF. The particular EQP model used in this work has an extended extractor region to fit the EQP probe front end into the HART plasma reactor via the side access port.

Drift tube

From the ion source ions are transmitted through the drift region and focused into the energy analyzer. Corresponding to the drift space potential, ions are accelerated or decelerated to reach the pass energy to transit the energy filter (ESA). The pass energy is defined by the *axis* potential. The *lens2* electrode is used to create a parallel beam at the ESA entrance and efficiently focus the ions into the ESA.

Energy analyzer

The energy analyzer used here is a 45° electrostatic sector field energy analyzer consisting of two concentric cylinders. According to [152], an electrostatic sector field deflects relativistically slow particles (for which $v_{ion} \ll c$, as considered here) with different mass-to-charge ratios equally as long as their energy-to-charge ratios are the same. Ions entering the sector field are deflected according to their kinetic energy. Only those ions with an energy equal to the analyzer pass energy can transit the 45° bend. This pass energy is a fixed value which is needed to pass the 45° electrostatic energy analyzer. The pass energy depends on *plates* which is the potential setting between the two analyzer plates. The pass energy was set at a fixed value of -40 eV during all positive ion measurements performed in this work, as recommended by the manufacturer [153]. As described above, ions with selected energies are accelerated or decelerated to the ESA pass energy set by *axis* in the drift tube before entering the energy filter. There are additional voltages *vert*, *horiz*, and *D.C. quad* which are used to adjust the ion beam alignment.

The energy resolution of the sector field ESA is given by [153]

$$\Delta E = \frac{w \cdot E_{\text{trans}}}{R(1 - \cos \varphi) + L \sin \varphi}, \quad (1.68)$$

where w is the aperture diameter, E_{trans} is the transmission energy, R is the sector mean radius, φ is the sector angle, and L is the distance to the exit aperture (cf., Fig. 1.7). In the EQP, the following values are used: $w = 3$ mm, $E_{\text{trans}} = 40$ eV (energy equivalent of axis potential), $R = 75$ mm, $\varphi = 45^\circ$, and $L = 35.4$ mm. From these values, an energy resolution of 2.55 eV is obtained. Compared to the half-width of typical distribution functions measured in this work, this value is comparably small.

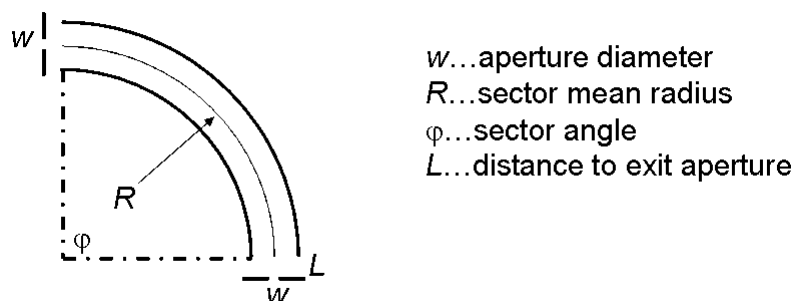


Figure 1.7: Schematic of the 45° sector field energy analyzer.

Mass filter

When leaving the energy filter, all ions have the same energy but may have different masses due to ion trajectories in constant electrostatic fields being independent of ion mass [152]. A quadrupole mass filter is used to differentiate between ions according to their mass-to-charge ratio (Fig. 1.8-a and Fig. 1.8-b). Mass discrimination in transmission occurs as a result of using constant transmission energy, as the transmission efficiency depends on the ion velocity [154]. The quadrupole consists of two pairs of parallel and equidistant metal rods forming nearly ideal hyperbolically shaped electrodes. Two opposite rods are connected electrically with a positive potential applied while the other pair is at a negative potential of the same value. Applied potentials are a superposition of fixed dc and alternating rf components creating time-varying electric fields. These oscillating electric

fields affect the trajectories of ions transiting the mass filter according to their mass-to-charge ratio m/q [154]. A mass scan is performed by increasing the amplitudes of the dc and rf voltage (starting from small values) for a constant dc-to-rf voltage ratio.

When entering the quadrupole, ions will be deflected from their original trajectory to an extent related to their mass-to-charge ratio. Ions with a prescribed m/q can describe stable paths allowing these ions to pass and exit the mass filter. Other ions are excluded due their unstable paths. Unstable trajectories are characterized by exponentially increasing amplitudes of oscillations performed in the quadrupole field. These ions will strike the rods, be neutralized and exhausted off the system. To achieve a sufficient mass resolution, ions must have a sufficiently long residence time inside the quadrupole. Consequently the entrance energy should be low in the order of a few meV. The ion kinetic energy is therefore reduced by the decelerating lens *focus2* and the beam further focused before injection into the quadrupole filter. Mass resolution can be adjusted by *delta-m* and *resolution* voltage settings.

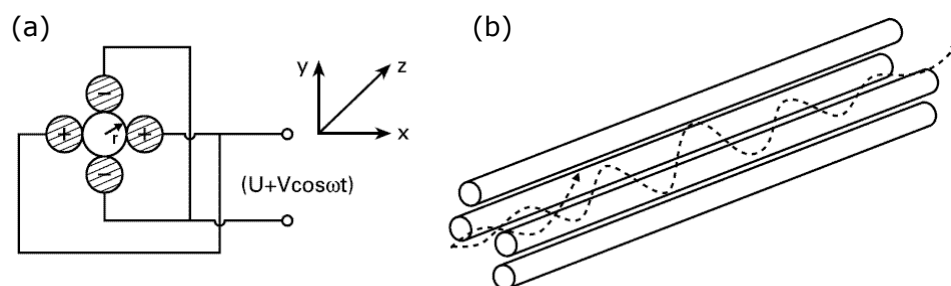


Figure 1.8: Quadrupole mass filter (a) field generating potentials, (b) ion trajectory.

The EQP triple quadrupole mass filter comprises an rf+dc driven main filter, with a rf only driven pre- and post-filter. Pre- and post-filter are used to reduce the influence of the (rf+dc) quadrupole dc fringing fields and act as an ion guide for ions within a broad mass range. In the present configuration, molybdenum rods of 6 mm diameter and 127 mm length are used for the main filter, and 25 mm length for the pre- and postfilter, to allow for mass detection up to 512 amu. The mass resolution becomes better for increasing ion masses, where in general it is more difficult to achieve a good mass separation for low masses such as hydrogen. Since manufacturing precision of the rod surface is limited to the micrometer range, the rod diameter in the millimeter range determines the accuracy of the electric field at the quadrupole axis. Mass separation can be increased by increasing the diameter of the quadrupole rods, and also by extending the quadrupole rods. Detection of ions in the low mass region (such as H^+) would require at least 9 mm rod diameter [11]. Therefore the mass-to-charge ratio for the present EQP model is limited to a minimum of 2 amu, which corresponds to H_2^+ .

Ion detection

Ions of selected energy and mass finally reach the detector. The EQP systems comprises two different options to detect ions: a *channeltron SEM*, and a *Faraday cup*.

The *Secondary Electron Multiplier (SEM)* is an off-axis mounted continuous dynode channeltron detector [153,155] operating in pulse counting mode and preceded by a conversion dynode (*1st-dynode*). Ions striking the surface of the first dynode result in

secondary electron emission of typically a few electrons. The electrons strike the channel walls, producing additional electrons (and so on, forming an avalanche) until, at the output end a pulse of up to 10^7 to 10^8 electrons emerges. Emission of secondary electrons generally depends on the velocity of the incident ion. Accordingly, detection of ions with higher masses but the same amount of kinetic energy becomes less sensitive and detection efficiency decreases nearly exponentially with increasing mass. The cascade is controlled by the voltages *1st-dynode* and *multiplier* which are applied at the first surface on the front of the detector, and on all other surfaces across the detector, respectively. For positive ions, the input is generally at a negative potential of 1200 to 3000 volts and the CEM (Channeltron Electron Multiplier) output end is at ground. For detection of negative ions, the input is generally at ground or some positive potential and the output is at a high positive voltage. The resulting ion current is measured by a sensitive amplifier. A *suppressor* operating at a negative voltage (for positive ions) precedes the detector to prevent electrons triggering it.

Channeltron CEMs are constructed from a specially formulated lead silicate glass to form a curved tube. The stable glass surfaces can withstand repeated cycling between vacuum and atmosphere without a significant degradation in performance common to traditional CuBe discrete dynode multipliers. The reduction of lead oxide on the glass surface by a high purity hydrogen treatment at high temperature produces the conductivity and secondary emissive characteristics critical to CEM performance. Secondary emission takes place within the first 200 Å of the surface. Underneath this emissive layer there is a conductive layer several hundred to several thousand angstroms thick. The conductive coating is interrupted at one point on the outer surface to produce a single series conduction path down the interior of the multiplier.

Pulse-counting enables detection of even extremely small amounts of sampled species and provides for highest sensitivity among available SEMs. The operating point for a CEM in the pulse counting mode is usually determined by the point at which a plateau is reached in the count rate versus voltage characteristic. The plateau occurs when all the signal is being collected at the input of the CEM. As the multiplier ages, the knee moves to the right and the voltage must be increased.

The conversion dynode arrangement simplifies the pulse detection electronics as only one particle polarity needs to be detected, the detector circuit for a combined positive and negative ion detection is shown in Fig. 1.9. For positive ion detection, the *1st-dynode* is operated at a net negative potential, and for negative ions it is set to a positive potential. The voltage between the conversion dynode and the SEM (MULTHT) remains at a constant positive potential to attract the electrons to the SEM. The conversion dynode further serves to optimize the lifetime of the SEM input surface. The impact of high molecular weight ions at high energies can result in chemical changes in the glass surface and even physical sputtering which can reduce the effective sensitivity of the device. The conversion dynode arrangement configured to detect secondary electrons prevents ions from striking the CEM directly. The CEM surface is much less affected by electrons than by much more massive and chemically active ions.

Due to high electron densities existing within the CEM channel near the output end, gasses adsorbed on the surface of the walls are desorbed and ionized, forming positive ions. These ions can travel back toward the input of the device and strike the walls near the input producing secondary electrons which are subsequently amplified and detected at the output end as a noise pulse (i.e. not due to an incident particle, but generated within

the CEM itself). This phenomenon is known as ion feedback. Curving the channel effectively minimizes this problem by preventing desorbed ions from traveling far enough to gain sufficient energy to produce secondary electrons.

Detection efficiency is the probability of a charged particle (or photon) incident on the CEM input producing an output pulse. This parameter is strongly dependent upon the energy, mass and velocity of the incident particle as well as the number of charges on the particle and the angle of incidence. For mass spectrometry applications, the most important particles of interest are positive and negative ions. Electron detection efficiency is important in some instances, such as when a conversion dynode is used and the CEM is detecting secondary electrons emitted from the dynode surface. Photon detection can also be important in a negative sense in that it is often a source of unwanted noise. The case of ions is unique; the detection efficiency is a function of both ion energy or, more properly, ion velocity at the point of impact on the secondary emitting surface and ion mass-to-charge ratio m/q .

Mounting the SEM detector input aperture out of the line-of-sight of the quadrupole mass filter exit aperture is conducted to avoid noise by effectively eliminating neutrals and photons coming from the plasma or EQP ionizer filaments or being due to the decay of metastables within the analyzer or detector chamber.

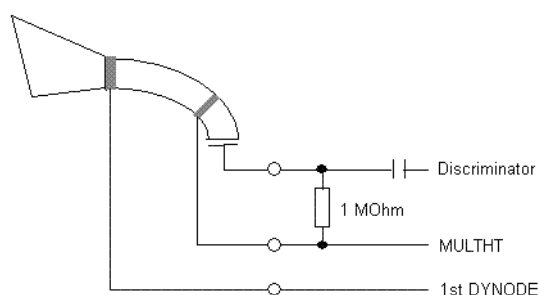


Figure 1.9: Positive/negative ion SEM detector [153].

A *Faraday Cup* is fitted in addition to the SEM detector. It comprises a closed end cylindrical conducting surface with a suppressor electrode to avoid false measurement. Ions striking the surface produce a shower of secondary electrons causing a current which is amplified by a pre-amplifier in the rf head. Using a cup rather than a plate prevents ions to escape after entering the cup, and also an enhanced sensitivity through a higher collection efficiency of emitted electrons. Unlike the SEM detector, sensitivity for detection of ions does not depend on the ion velocity. However, the sensitivity of a Faraday detector is by far lower than that of a SEM detector. The Faraday detector is intended for use in situations when pressure or count rate are too high for the SEM detector.

Compared to the Faraday detector, the SEM is far more sensitive (and hence suitable to measure even very small amounts of species), and is therefore used during all measurements performed in this work. However, extra care has to be taken when using the SEM since the surface can change quite quickly in time causing the gain to deteriorate. The detector lifetime is especially limited during investigations in aggressive environments. Halogen gases are chemically very active and will attack the SEM active coating. Changing the surface coating will change the workfunction, and hence the efficiency of secondary

electron emission. The lifetime of a SEM detector is further determined by the total ion charge it measures. High count rates at relatively long timescales will lead to an enhanced decrease of the detector performance. The high density electron cloud at the output end of the SEM results in physical and chemical changes to the surface which can reduce the secondary emission coefficient of the glass, and in turn cause a reduction in gain. Therefore, the SEM detector performance was controlled regularly and calibrated when necessary during all experiments. Further, the SEM was not operated above a base pressure of 5×10^{-6} Torr inside the EQP to avoid detector damage and ensure correct and uniform performance.

1.5.2 Infrared absorption spectroscopy

Tunable IR lasers draw an increasing attention as sensitive and selective probes for species relevant in plasma processing. Besides difference-frequency lasers, color-center lasers, and Raman-shifted dye lasers, diode laser sources are most commonly employed for a continuous tuning and detection of stable molecules, free radicals, and ions [156].

Absorption spectroscopy can yield absolute concentrations provided the absorption cross section is known. Sensitivity is determined by Lambert-Beer's law

$$\frac{I}{I_0} = e^{-\sigma_a n L} \quad (1.69)$$

with the incident light intensity I_0 , the light intensity I transmitted through the path length L of species with an absorption cross section σ_a and number density n .

Broad band infrared spectroscopy, in particular Fourier Transform Infrared (FTIR) spectroscopy has been used as an approach for investigations of plasma etching and CVD processes. Recently, Graehlert and co-workers analysed the composition of exhaust gases with the help of a FTIR arrangement in a special designed measuring cell [157]. These measurements were performed in the exhaust of the process reactor outside of the clean room area. For appropriate sensitivity of the absorption measurements, a liquid nitrogen cooled detector was used. Although the measuring frequency and spectral resolution were rather low, 0.14 Hz and 1 cm^{-1} , respectively, information about several stable components of the exhaust gas could be achieved.

In the past few attempts of using laser absorption and interferometer techniques were made for on-line monitoring in plasma etch reactors. A laser interferometer using linearly polarized radiation of a He-Ne laser at 632.8 nm has been demonstrated by Sternheim et al. [158] for monitoring etching rates in plasma and controlling the etched depth of isolation areas in silicon for oxide isolated bipolar devices. Similar work has been done by Heason et al. [159] using tuneable near infrared lasers. An endpoint detection system for plasma etching based on Tunable Diode Laser Absorption Spectroscopy (TDLAS) in the infrared spectral range with lead salt lasers was described by Sun et al. [160]. Lead salt lasers are narrow band laser sources with the advantage of high spectral intensity, narrow bandwidth, and continuous tuneability over the absorption profile. Using TDLAS, Sun et al. monitored the concentration of SiF_4 by measuring its absorption at 1023 cm^{-1} .

The main disadvantage of TDLAS systems (based upon lead salt diode lasers) is the necessary cryogenic cooling of the lasers (and also of the detectors), because they operate at temperatures below 100 K. Systems based upon lead salt diode lasers are typically large in size and require closed cycle refrigerators and/or cryogenics, like liquid nitrogen. The

recent development and commercial availability of pulsed quantum cascade lasers (QCLs) offers an attractive new option for infrared absorption spectroscopy [161-164].

Pulsed QCLs are able to emit mid-IR radiation near to room temperature. Compared to lead salt lasers, QCLs allow the realization of very compact mid-infrared sources characterized by narrow line width combining single-frequency operation and considerably higher power values, i.e. of tens of mW. The output power is sufficient to combine them with thermoelectrically cooled infrared detectors, which permits a decrease of the apparatus size and gives a unique opportunity to design compact liquid nitrogen-free mid-IR spectroscopic systems. These positive features of QCLAS are found to open up new fields of application in research and industry, including in situ control of industrial plasma processes. More details of the QCLAS technique applied during several investigations in this work [165-167] are summarized in section 3.1.3. A summary of important parameters for broad and narrow band infrared absorption techniques is given in Table 1.1.

Table 1.1: Comparison of infrared absorption techniques.

	FTIR	IR-TDLAS	IR-QCLAS
sensitivity $(I_0 - I)/I_0$	$10^{-2} \dots 10^{-3}$	$10^{-4} \dots 10^{-5}$	$10^{-4} \dots 10^{-5}$
selectivity $\Delta\nu$	0.1 cm^{-1}	10^{-4} cm^{-1}	10^{-3} cm^{-1}
temporal resolution	minutes	ms... μ s	ms... μ s
tunability	whole MIR	$10 \dots 100 \text{ cm}^{-1}$	$1 \dots 10 \text{ cm}^{-1}$
calibration	yes	no	no
operation	room temperature	$10 \dots 130 \text{ K}$	room temperature
detection	liquid nitrogen	liquid nitrogen	TE detectors

1.6 HPSM simulations

Combinations of experiments and simulation can have synergetic effects for exploring new phenomena and validating current models in plasma science. Also, simulations can provide results which can be difficult to obtain experimentally. Various modeling approaches do exist, for example, analytical models [168], fluid models [169-174], Boltzmann models [175,176], Monte Carlo (MC) simulations [177-179], electrical circuit models [180,181], kinetic models (e.g., Particle-In-Cell) [97,182-184], hybrid or global models [13,185-191], and further complex feature scale models [192].

In rf discharges, electrons, ions and reactive species are generated mainly in the plasma bulk. However, the energy distribution and the angular distribution of the particles impinging at the surface are determined by the characteristics of the plasma sheath. These properties affect important manufacturing goals, e.g., etch rate or deposition rate, etch anisotropy, conformality, radiation damage, etc. A detailed understanding of the sheath kinetics is therefore helpful to more efficiently optimize plasma based process steps.

In this study, the Hybrid Plasma Sheath Model is used for calculation of angle-resolved ion energy distributions which will be compared to measured ion velocity distribution functions. The HPSM simulator is part of the discharge model used which also comprises a Hybrid Plasma Bulk Model (HPBM) as outlined in Fig. 1.10. Here, only the HPSM parts will

be described in more detail since main emphasis is placed on ion distribution functions on the electrodes of the CCRF discharge. It should just be noted that the HPBM is kept very simple by processing discharge relevant parameters like electron temperature, ion densities and Bohm velocity.

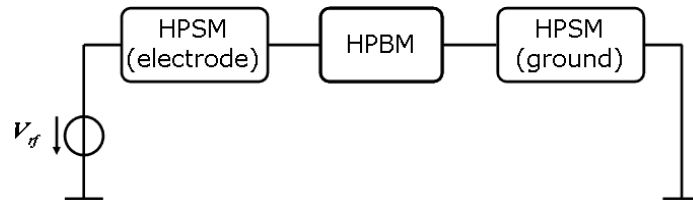


Figure 1.10: Structure of the discharge model used comprising the HPSM (Hybrid Plasma Sheath Model) and HPBM (Hybrid Plasma Bulk Model) parts.

The HPSM simulator comprises a hybrid fluid-dynamic/kinetic model describing the sheath and presheath regions of dc or rf driven gas discharges in a realistic and self-consistent way, detailed descriptions can be found in [17,18,52,53]. The model assumes an infinitely extended sheath parallel to the electrode, allowing a one-dimensional spatial description. Most of the published models for the study of ions impinging a surface behind an rf sheath are either based on computationally intensive first-principle calculations, or limited to qualitative descriptions due to simplifying assumptions [17]. In contrast to these models, HPSM covers the requirements of a technology-oriented computer aided design (TCAD)-suited simulator:

- description of realistic process conditions like nonharmonic modulation of the periodic boundary sheath, multiple positive ion species, interaction with the background gas, etc., and
- computational efficiency and numerical stability of the model.

The input required by the model consists of the fluxes of the incoming ions, the modulating voltage, and of the pressure, the composition, and the temperature of the background gas. On output, the model provides the values of the electric field and of the particle densities within the sheath and the presheath, the total voltage drop across the sheath, and also the energy and angular distributions of the positive ions and the energetic neutrals which impinge at the material substrate.

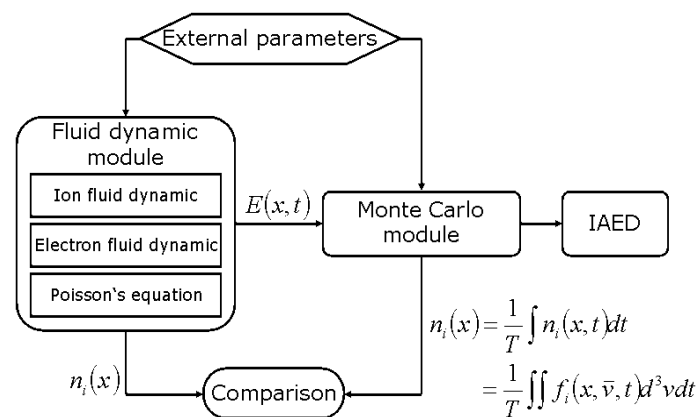


Figure 1.11: Structure of the hybrid plasma sheath model [17]. The time modulated electric field within the boundary sheath is calculated self-consistently by the fluid-dynamic part. It serves as an input to the Monte Carlo module where the motion of a sufficient large number of particles subjected to the field is followed.

The hybrid model consists of a fluid-dynamic (FD) part for the computation of the time-modulated potential within the boundary sheath, and a one-particle Monte Carlo (MC) part which treats the particle dynamics of a sufficiently large number of energetic neutrals and positive ions subjected to the electrical field. The structure of the model is illustrated schematically in Fig. 1.11.

Fluid-dynamic model

The fluid-dynamical approximation takes into account the first two moments of the Boltzmann equations for electrons and ion species. The HPSM considers (Langevin enhanced) elastic scattering (ES) and resonant charge exchange (CX) with the neutral background gas. The model solely treats the sheath and presheath region of the plasma, so ionization, attachment, and other chemical reactions are neglected. Coulomb interactions between charged particles are neglected as well because of the small degree of ionization for low temperature discharges considered here. The governing fluid-dynamical equations are the continuity (or particle conservation) equation and the momentum conservation equation for the electrons

$$\frac{\partial n_e}{\partial t} + \frac{\partial}{\partial x}(n_e v_e) = 0, \quad (1.70)$$

$$\frac{\partial v_e}{\partial t} + v_e \frac{\partial v_e}{\partial x} = -\frac{e}{m_e} E - \frac{T_e}{m_e n_e} \frac{\partial n_e}{\partial x} - \nu_e v_e, \quad (1.71)$$

and for all ion species

$$\frac{\partial n_i}{\partial t} + \frac{\partial}{\partial x}(n_i v_i) = 0, \quad (1.72)$$

$$\frac{\partial v_i}{\partial t} + v_i \frac{\partial v_i}{\partial x} = \frac{q_i}{m_i} E - \frac{T_i}{m_i n_i} \frac{\partial n_i}{\partial x} - \nu_i v_i, \quad (1.73)$$

with index "e" for electrons, index "i" for the particular ion species ranging from 1 to N , electron and ion velocities v_e and v_i , particle masses m_e and m_i , electron temperature T_e , constant bulk temperature of the ions T_i , electron and ion density n_e and n_i , electrical field E , electron and ion charges e and q_i , and electron and ion friction terms ν_e and ν_i . The friction terms depend on the cross section for elastic scattering σ_{ES} , the Langevin enhanced constant K_L , and the charge exchange cross section σ_{CX} .

The set of fluid-dynamical equations is completed by the Poisson's equation

$$\epsilon_0 \frac{\partial E}{\partial x} = \sum_i q_i n_i - e n_e \quad (1.74)$$

to obtain a self-consistent electric field distribution. Equations (1.70)–(1.74) form a set of coupled partial differential equations which are solved using an asymptotic time and length scale expansion. Further assumptions include periodic (not necessarily harmonic) external fields with frequency ω_{rf} , and an intermediate frequency regime $\omega_{pi} \leq \omega_{rf} \ll \omega_{pe}$, with plasma frequencies of ions ω_{pi} and electrons ω_{pe} (resulting in ions being influenced by the mean electric field only). Furthermore, a small Debye length with respect to the sheath thickness $\lambda_D \ll s$ is assumed.

Monte Carlo model

In the Monte Carlo part the trajectories of a sufficiently large number of particles are followed. The ions move in the electric field according to the Newton-Lorentz equation

$$m_i \frac{d^2 x}{dt^2} = q_i E(x, t), \quad (1.75)$$

with the electric field $E(x, t)$ as calculated by the FD module. Elastic and charge exchange collisions with a spatially uniform background gas are accounted for. The initial hard sphere collision model assumed isotropic scattering in the center-of-mass frame. To obtain more accurate results for the calculated IEADs, the collision model was changed during this work by implementation of anisotropic deflection functions and energy-dependent cross sections as described in section 2.4.6. For the elastic-type collisions the scattering angle ($0 \leq \theta \leq 180^\circ$) is now calculated from previously determined impact parameters. The energy transfer of the impinging particles is calculated by accounting for the laws of momentum conservation and energy conservation. In the simulation each particle is monitored until it hits the surface. Ions that escape to the plasma bulk due to backscattering are restarted in order to keep the ion flux ratio constant. Ion trajectories are calculated using a time-of-flight analysis. Particle collisions are treated by applying a null collision method. Above a user-specified energy threshold, energetic neutrals generated by scattering processes of ions with the background gas can be tracked in addition to the ions.

Particles hitting the surface contribute to the calculation of the energy and angular distributions of ions and energetic neutrals which are monitored separately for every species. An energy discrimination in the angular distribution of the neutrals separates thermalized particles from energetic particles. Since details of the angular distribution were found to not only depend on the field structure of the sheath itself but also on that of the presheath, the influence of the presheath is included in the simulator. Results of the HPSM model are described to be more reliable than those of previous models which restricted themselves to the sheath region [17].

2 Mass resolved ion energy analysis

A system to measure ion distribution functions was first described by Coburn in 1970 [193]. Today, different systems are available to perform IDF measurements, comprising time of flight spectrometers [194,195], retarding field analyzers [44,87,196,197], and combined energy and mass analyzer systems [193,59,63-65,146,147]. Retarding field analysis is performed by measuring an ion current as a function of a retarding potential. The derivative of this current with respect to the potential yields the distribution function. The biggest disadvantage of the retarding field technique is that there is no mass discrimination. This shortcoming is avoided by using a combined energy and mass analyzer probe, which sometimes is also called plasma monitor. The mass resolved energy analyzer used in this work is a Hiden EQP 500 probe. Such a system consists of a transverse electric field energy analyzer and a quadrupole mass spectrometer. The EQP probe measures an ion current which represents an ion distribution function when it is displayed versus energy. Principles of operation have been discussed in section 1.5.

Proper operation of the EQP system can be quite challenging [198,11]. The angle of incidence at the electrode determines whether an ion can reach the detector. Limiting factors like orifice geometry and voltage settings on the EQP electrostatic lenses are discussed in this chapter. Measured IDFs can considerably be affected by the selected ion optics settings which influence and determine the ion transmission of the probe. From careful investigation of such limiting factors, determination of specific transmission functions relevant for the diagnostic instrument can be achieved. This knowledge can enable to gain access about undistorted ion distribution functions for ions incident on the extraction region. Due to the fact the EQP orifice plate is made of an insulating material and thus forms a floating electrode in the investigated discharge, the approach of enabling comparison of different discharge conditions and chemistries becomes quite challenging. An important but complicated task is therefore the exact determination of the floating potential. It will be discussed how the IDF analysis is affected by the floating potential of the different dielectric surfaces inside the plasma reactor. To support an interpretation of plasma diagnostic measurement results and gain further insight into discharge behavior at even difficult or impossible experimental conditions, various calculations were performed using the Hybrid Plasma Sheath Model (described in section 1.6). For calculation of IDFs, the hybrid-fluid simulator was additionally modified by implementation of differential cross sections resulting from ab-initio calculations for relevant ion-atom collisions in the sheath regions. This effort appeared necessary to achieve an accurate modeling of the scattering angle as a function of impact parameter and energy for the wide range of relevant scattering energies occurring in the sheaths of typical medium pressure CCP discharges. The HPSM model initially suited to calculate single species Ar discharges was additionally extended to enable simulations of HBr discharges consisting of multiple ion species. Finally, parameter studies were performed for both the modified Ar and the HBr model, including variations of the rf peak voltage, neutral gas pressure, neutral gas temperature, electron density, electron temperature, magnetic field, and the rf frequency mix. Results of these investigations will be discussed in section 2.5.

2.1 Analyzer ion optics

The Hiden EQP analyzer comprises several electrostatic lenses which focus the sampled ions into the energy and mass filter. A detailed description of the analyzer sections was given in section 1.5.1. The ion optics consist of a number of electrostatic lenses which can be tuned by applying different potential settings as shown in Fig. 2.1. During scanning the velocity distribution function of ions entering the EQP system from the plasma for example, the electrode voltage *energy* is varied for a specified range. Before scanning distribution functions for different ions it is necessary to optimize the signal-to-noise ratio. This is achieved by either manually or automatically tuning the EQP electrodes. As can be seen from Fig. 2.1, there is a big degree of freedom for choosing and varying values of the electrode voltages. Improper voltage settings on the electrostatic lenses can change the energy discrimination of the system and hence cause distortions of the measured distribution functions. Therefore, a detailed understanding of the electrode potential operation is essential for a proper operation of the EQP analyzer and to acquire correct information about the ion energy distribution.

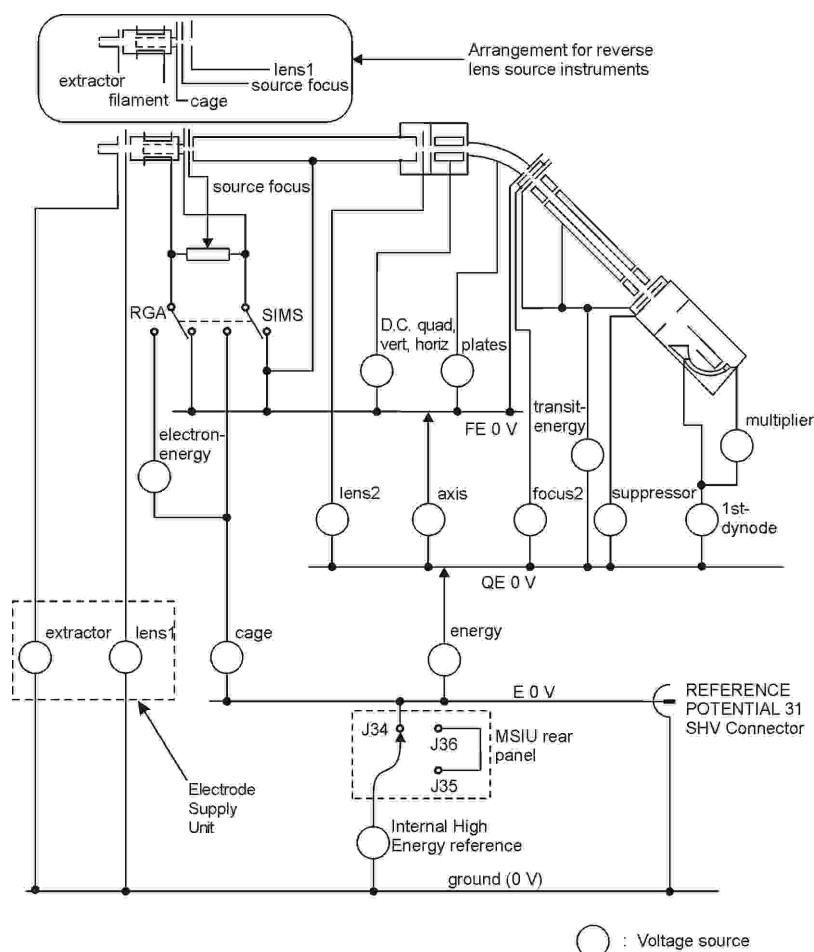


Figure 2.1: Power supply references, high energy EQP system [153].

Aberrations known for optical lenses also apply for electrostatic lenses [152]. For the EQP system, the effect of chromatic aberration can be problematic and should be therefore known [198]. Chromatic aberration is a characteristic of all lenses and describes the dependence of the focal length of a lens on the ion energy. Usually, ions sampled from the plasma can exhibit a wide range of energies. The effect of chromatic aberration will cause

ions with different energies to be focussed at different positions. Problems can arise where this effect results in superior acceptance at certain ion energies. For the IVDF measurements performed during this work, voltage settings for the electrostatic lenses were obtained from tuning procedures recommended by the manufacturer [153]. To ensure chromatic aberration is kept to a minimum for the obtained settings, the energy discrimination is investigated in more detail as discussed in the next section.

2.2 Electrode voltage settings

A computer simulation package called SIMION [199] is usually used to simulate ion trajectories through ion optics arrangements. During this work, the open source freeFEM++ [200] development environment was alternatively chosen to calculate ion trajectories inside the EQP. In a first step, the FEM-based model calculates the electrostatic fields and forces exerted by the electrodes. Once the fields have been obtained, trajectories of charged particles can be calculated. FreeFEM++ was used to investigate aberration effects for voltage settings on the lenses obtained after performing tuning routines for an optimized signal-to-noise ratio.

The cylindrical EQP sampling tube is treated as a 3D axisymmetric problem, the ion optics section simulated in freeFEM++ is shown in Fig. 2.2, comprising all electrodes of importance to the energy dependent transmission. Ions from the plasma enter the analyzer tube via the sampling aperture in the orifice plate. Since this orifice plate is made of a ceramic material, the surface around the aperture is likely to get charged when the discharge is turned on. A floating potential will develop which affects the ion trajectories and causes a shifted energy scale, as will be discussed later.

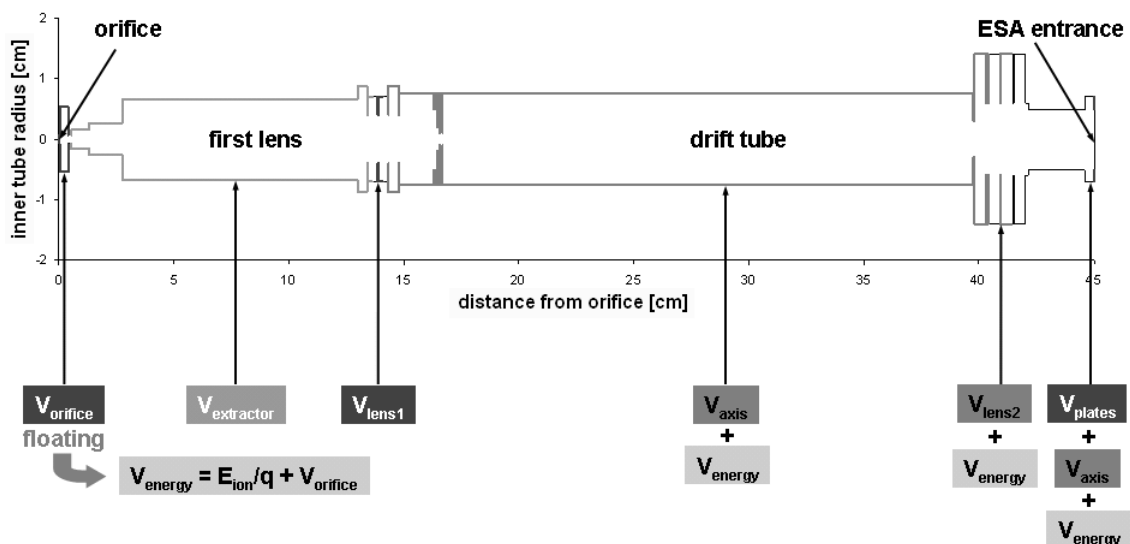


Figure 2.2: Ion optics section simulated in freeFEM++.

The first lens, which is formed by the three electrodes *extractor*, *lens1* and *axis*, is used to shape the ion beam and accelerate or decelerate the ions to acquire the pass energy of the energy analyzer. The incoming ions are focussed into the drift tube which is at the fixed potential *axis*. Tuning routines include a variation of the potentials *extractor* and *lens1*, causing a variation of the electric field strength which acts on the incoming ions and hence

determines the extent to which ions are deflected and collected. The voltage settings on the described electrodes will hence strongly influence the acceptance angle of the EQP system. As discussed previously, care must be taken to avoid or minimize effects of chromatic aberration which can result from an ion energy dependent focal length. After entering the drift tube, all ions that are able to pass the energy filter will have the same energy and hence, no chromatic aberration effects will be present behind the drift tube.

Using the freeFEM++ automatic mesh generator, a mesh is adapted to the boundaries according to the local dimensions of the ion optics. Processing includes a mesh refinement according to the field gradient for the given electrode potentials. The electric field is obtained by numerically solving the Laplace partial differential equation for the specified potentials at different electrodes. Once the electric field is determined, trajectories of charged particles can be finally calculated. This task is performed by solving the equations of charged particle movement under the influence of electric fields. A step width control is used which is again adapted to the field gradient. Input parameters for calculation of trajectories comprise the ion start location in the plane of the orifice, the ion incident angle, the ion mass, and the initial ion energy. For illustration, ion trajectories simulated for 10 eV and 100 eV ion energies are plotted in Fig. 2.3-a and Fig. 2.3-b. Trajectories start from the center of the orifice region, voltage settings are $extractor = -18\text{ V}$, $lens1 = -98\text{ V}$, $axis = -40\text{ V}$, $plates = 7.27\text{ V}$, $lens2 = -127\text{ V}$. The graphs include a variation of the starting angle of the ions in the plane of the orifice which was varied here between 0 and 1 degree. As can be seen, the 10 eV energy ions are focussed into the entrance of the drift tube while the 100 eV high energy ions remain unfocused after the first lens. Ions with 10 eV ion energy will pass the ion optics and enter the energy filter for all angles within the considered interval of incidence angles, whereas only few ions with energies of 100 eV are able to traverse the ion optics without being lost at the surface of the drift tube. As will be discussed later, the acceptance for ions with initially high energies is significantly smaller and those ions with greater incident angles will be lost after hitting the surface inside the drift tube. The example was chosen to illustrate the effect of chromatic aberration where the focal length of the first lens depends on the ion energy. Additionally, corresponding ion energies are plotted in Fig. 2.3-c and Fig. 2.3-d, demonstrating acceleration and deceleration of the 10 eV and 100 eV ions in order to acquire the pass energy ($axis$) to transit the energy analyzer.

One additional parameter which had to be considered was the influence of a floating potential at the orifice plate. This floating potential contributes to the electric field of the first lens inside the orifice region and can somewhat change the acceptance angle. For the calculations performed here, the influence of a floating orifice plate was generally accounted for by introducing an additional electrode V_{orifice} (cf., Fig. 2.2). The systematic investigation of ion trajectories included a variation of the floating potential between -100 V and +25 V.

In Fig. 2.4, a plot of the EQP acceptance angle is given as a function of ion energy and different floating potentials, using the same settings obtained from tuning as specified above. From calculations, deviations from the smooth function for the acceptance angle at zero floating potential (thick continuous line) start to exceed a 10-20% range for floating potentials below -20 V (dashed line) and above +15 V (dotted line). However, this is already outside the range of typical floating potentials identified from most experimental conditions (see chapter 4). Within the range of about -20 V to +15 V, small deviations from a smooth curve are subject to numerical noise which occurs during data compiling. This

was confirmed by investigations about the influence of marginally changed initial conditions. The acceptance angle is generally observed to be quite small, where there is a large acceptance of low-energy ions with a maximum of 3.5 degrees (61 mrad) for 1 eV ions (for zero floating potential). This reflects the fact, that it is more easy to deflect and focus low-energy ions in the presence of an electric field. For ions with ion energies above 20 eV, the acceptance angle is observed to be below 0.5 degrees (9 mrad). A constant transmission is calculated for ions with ion energies above 60 eV. The acceptance angle is generally found to be smaller than those calculated for a standard EQP probe [153]. This can be explained by modifications made to the used EQP analyzer which comprises an extended first lens section to adapt to the reactor access port, and to ensure a smooth fitting to the reactor wall surface being in contact with the plasma. From the calculated acceptance angles in Fig. 2.4, no chromatic aberration is apparent.

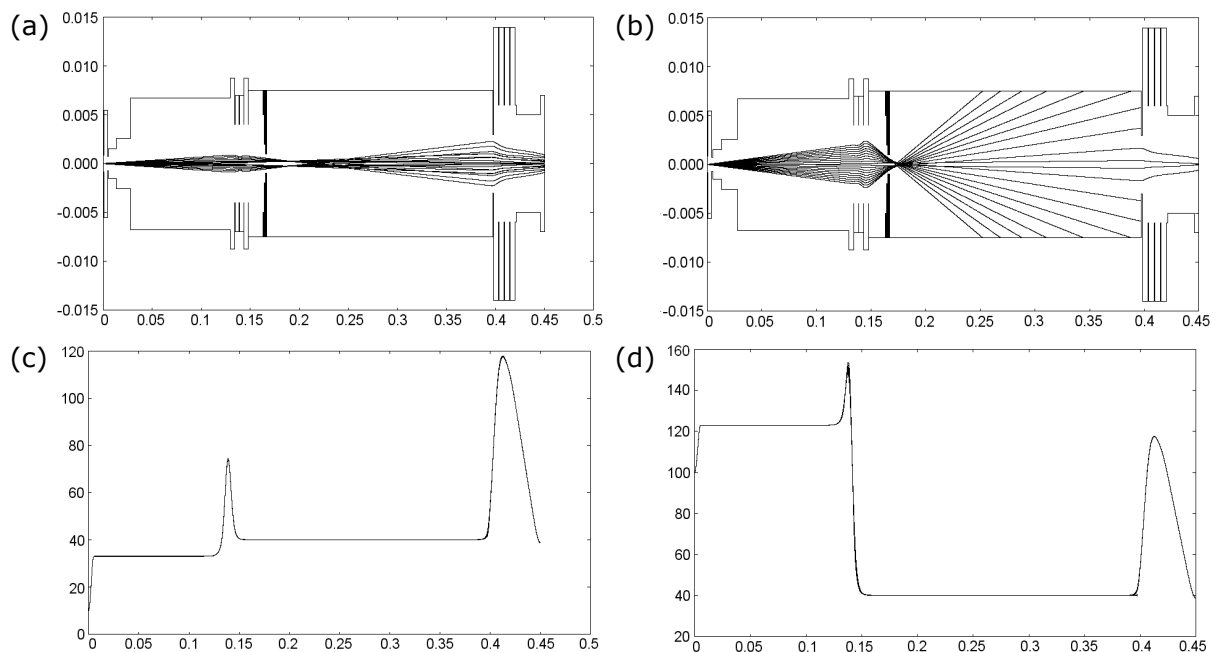


Figure 2.3: Calculated ion trajectories for (a) 10 eV ions and (b) 100 eV ions; corresponding ion energies inside the ion optics section of the energy analyzer for (c) 10 eV ions and (d) 100 eV ions.

To ensure reliability of the method employing freeFEM++ simulations and minimizing chromatic aberration, ion distribution functions were measured after all electrodes (*extractor*, *lens1*, *lens2*) were set to the pass energy of the energy analyzer (*axis* = -40V). For this case, no focusing effects exist and the distribution function should hence not be distorted. The advantage is that a true representation of the forward part of the distribution function can be obtained. However, this method is only applicable to conditions with initially sufficient signal intensity, since only a small fraction of ions entering the analyzer will be detected. In Fig. 2.5 two measured distributions of Br^+ ions are compared for the different EQP electrode settings discussed above. The full black line shows the IVDF recorded with the settings obtained from tuning, the dotted grey line shows the IVDF recorded after setting all electrode voltages to -40 V. Measured intensities have been normalized to allow for comparison of the curves. The shapes of the distributions show reasonable agreement giving confidence in the applied technique.

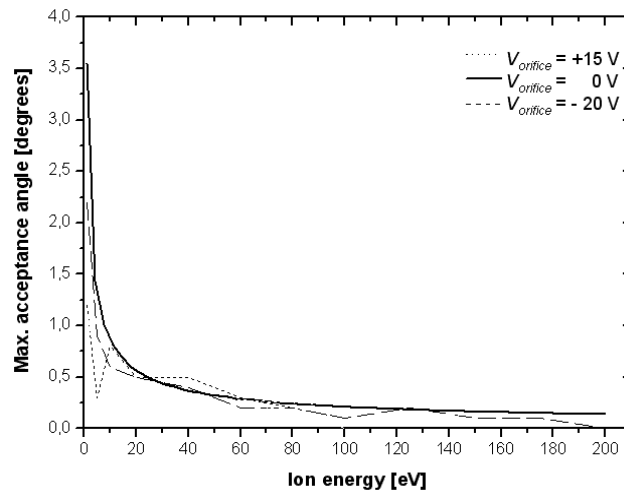


Figure 2.4: Acceptance angle as a function of incident ion energy and floating potential at the orifice plate.

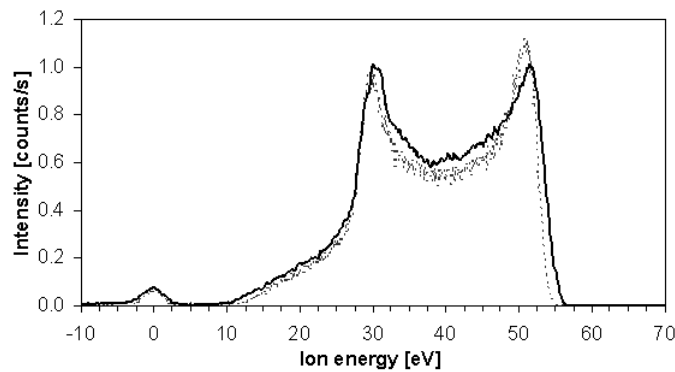


Figure 2.5: Comparison of Br^+ distribution functions recorded with (full black line) and without (dotted grey line) focusing effects.

2.3 Determination of floating potential

A distinct difference between a typical experimental CCP reactor setup and the reactor type used here is the complete hard anodization or concealing of all inner surfaces of the HART reactor by dielectric components. This leaves no bare metallic surfaces exposed to the plasma, as is typically the case for experimental setups. Here, coating of metal surfaces is required to avoid degradation and consequent formation of particles in an aggressive halogen process chemistry, as is used in the HART process reactor. Particles (like AlF_3) could cause partial masking of the wafer surface to be etched, inhibit sufficient chucking when reaching the surface of the electrostatic chuck, or lead to drifting process results due to changed thermal coupling between the electrostatic chuck and the substrate. Additionally, an enhanced growth of surface layers could influence process results to uncontrollable degrees, leading to a higher portion of required clean cycles and enhanced consumption of reactor parts. Further, the risk of arcing would considerably increase if conducting surfaces are exposed to the plasma and further during uncontrolled formation of surface layers with different thicknesses (especially for high input powers typically

applied in the CCP reactor). Arcing could again yield formation of particles, damage of product wafers or at least plasma inhomogeneities influencing the etch result.

Consequently, floating potentials will develop at the insulating surfaces during plasma operation. From a plasma analysis point of view, this difference places a big challenge when applying plasma diagnostics which rely on calibration to a reference potential. Utilization of a typical grounded metal orifice plate for plasma diagnostic investigations fails due to the reasons that typical discharge conditions would be changed to at least some extent, and further due to sharing plasma analysis experiments with ongoing hardware and process development. From these considerations, the EQP orifice plate was hence designed using a MACOR ceramic plate with a 50 μm laser drilled orifice. During discharge operation the orifice plate will be floating as well and the EQP reference potential will change accordingly. To obtain reproducible results during baseline experiments and calibration, and to further allow for comparison of different discharge conditions, determination of the floating potential is mandatory.

A first attempt to estimate typical floating potentials could be based on calculations for the sheath potential at a floating wall, as given in section 1.2. Strictly speaking, this approach applies for dc discharges only since very basic assumptions for a stationary case are made, and an oscillating plasma potential (as is experienced in the rf discharges investigated here) is neglected. Furthermore, the contribution of a displacement current through the insulating material is not examined either. Now, assuming electron temperatures of about 2.5 eV and 6 eV for typical Ar and HBr discharge conditions (see also section 2.5), dc sheath potentials of about -9 V for Ar and -24 V for HBr can be calculated from equation (1.24). These values appear to be somehow realistic, and also this is not too far off the values determined for different discharge conditions, as given in chapter 4.

In a second approach, FreeFEM++ was used to perform calculations for an assumed quasistatic floating potential distribution. For an adiabatic solution without considering the effect of surface charging, the potential in the plane of the orifice is found to be close to the plasma potential (Fig. 2.6-a). From further calculations, the situation changes significantly when the orifice plate is locally set to zero volts. Following the simulation, the potential in the orifice plane is shifted to virtually zero values (cf., Fig. 2.6-b). In reality, this situation should apply if a conducting layer is deposited onto the surface of the low-pressure side of the insulating orifice plate (i.e., the area not exposed to the plasma), and if connection to ground is ensured. Grounding can be achieved easily by connection to the ground shield plate which is located in front of the EQP extractor (this ground plate is however not visible for ions entering through the orifice - they just see the extractor). From these considerations, a second MACOR orifice plate was sputter-coated with a 200 nm thick aluminum layer on the low-pressure side to investigate the influence predicted by the simulations. It was ensured that the sputter-coated low-pressure side was then tightly connected to the stainless steel extractor ground plate to achieve zero volt potential at the aperture. From various IVDF measurements conducted with the modified orifice plate, an expected shift of the energy axis for measured distribution functions could however not be observed. IVDFs were instead found to be reproducible to those measured without modifications on the sampling arrangement. The contrary observations emphasize the limitations of the simple model used here.

In literature few hints can be found about investigations comprising floating arrangements. A model developed for expanding sheaths at insulating dielectric surfaces in front of a metal electrode, for example, is described in [201] for plasma source ion

implantation using pulsed plasmas. Due to the low conductivity of a dielectric material, charge accumulation on the surface of the dielectric is considered to result from ion implantation in the several 10 keV range. However, the model is based on assumptions that are only valid for supersonic sheaths as observed for pulsed plasmas, and the model is not able to describe the situation of a stationary sheath (neglecting an hf modulation of the oscillating sheath for the investigations at the HART reactor here). Furthermore, typical ion energies inside the CCRF reactor investigated here will remain below 1-2 keV [202].

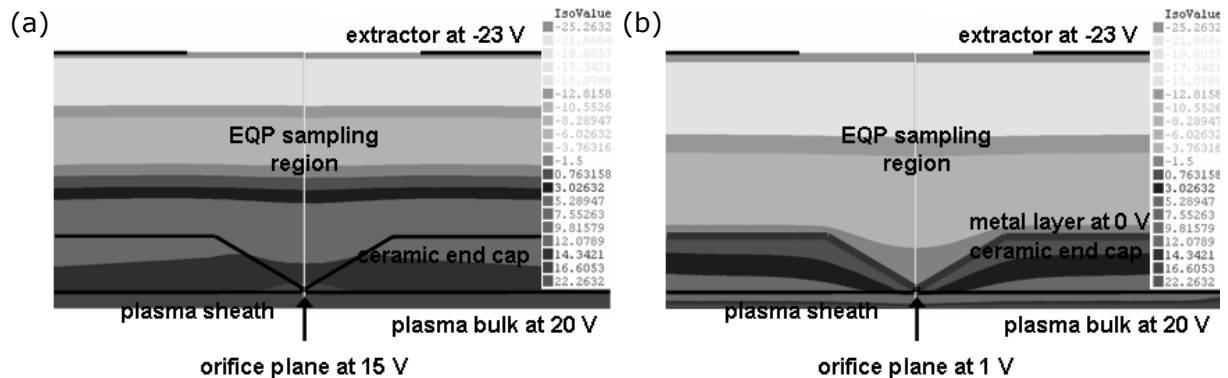


Figure 2.6: FreeFEM++ potential distributions in the vicinity of the MACOR sampling aperture for (a) the initial MACOR orifice plate; (b) MACOR orifice plate modified by introduction of a conducting layer (on the low pressure side of the aperture) being connected to ground.

The very basic assumptions made above yield some hints of negative floating potentials up to around -25 V. A more precise picture of the floating potential for different discharge conditions and chemistries was obtained after noticing the following phenomenon: For sufficiently high intensities, a distinct low-energy peak appears in the measured ion distribution functions. This is demonstrated in Fig. 2.7, where the inset shows enlarged details at the low energy tail of measured IVDFs. This distinct low-energy peak in the respective distribution function is attributed to resonant charge exchange collisions occurring in the sheath in the proximity of the extraction aperture of the ion energy analyzer [7,8,203,204]. In literature, these low-energy peaks were reported to coincide with 0 eV when the extraction hood was connected to a grounded aluminum electrode inside a GEC cell [203]. During the experiments conducted in this work, positions of the low-energy peak are finally used for determination of the floating potential at the sampling aperture and calibration of the energy axis. As will be discussed in chapter 4, this allows for explanation of negative recorded energies and for comparison of different plasma conditions. Floating potentials determined in this work were not found to exceed -25 V, which is in good agreement with the estimations from the very basic calculations discussed above.

From a more detailed analysis, slight shifts in the floating potential were observed. The variations are attributed to slightly varying surface charge densities at the sampling plate (e.g., due to build-up of contamination layers, rf phase modulation). This can be seen from the discussed low-energy peak which exhibits a more or less smeared feature (cf., inset in Fig. 2.7). Varying reference potentials (or energy shifts in the scale of measured distribution functions) were also reported for experimental setups comprising metal reactors with virtually defined potentials [14]. The variation was attributed to surface charging due to formation of thin oxide or contamination layers around the orifice region.

Under stationary conditions, surface charge densities may vary periodically with the rf phase, which in [14,205] was discussed to imply that the energy shift need not necessarily be the same for all energies recorded. For completeness, one should mention that charging can also occur on the inner surface of the sampling plate (i.e., in the EQP low-pressure region) hence causing acceleration of ions from the orifice into the ESA [64].

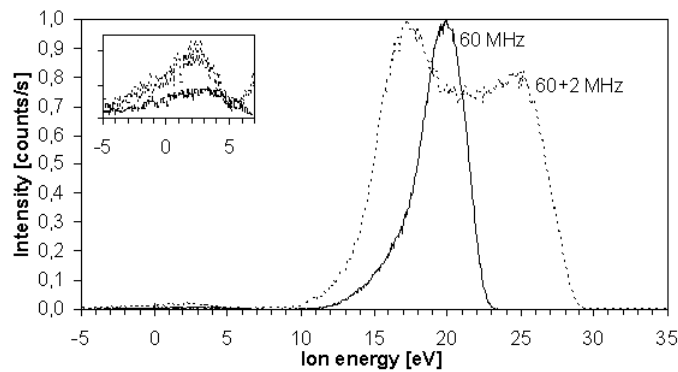


Figure 2.7: Comparison of ion distribution functions for $^{36}\text{Ar}^+$ isotope measured for 60 MHz (continuous line) and 60+2 MHz Ar plasma at 150 mTorr (broken line). The insert shows the low-energy peaks which are caused by charge exchange collisions near the sampling aperture, and which are used to calibrate the energy axis.

Besides the influence of surface charges, negative recorded energies are also possible to be observed if a significant fraction of the ions is created in the acceleration region of the analyzer [14,74]. However, no evidence to support this possibility is found from dependencies of ion species, discharge pressure, different extractor potentials, and further IDF profiles were not found to be significantly modified comparing different measurements.

2.4 Comparison to HPSM simulations

For well-characterized discharges, measured ion distribution functions can be compared to angle-resolved IEDFs calculated from HPSM simulations. An approach to enable experimental processing of simulation data will be described in the following. To support an interpretation of results from plasma diagnostic measurements by sheath calculations, two major requirements have to be met: knowing the specific transmission functions relevant for the diagnostic instrument, and simulating realistic distribution functions.

The first requirement comprises investigations about the influence of the EQP probe setup and internal arrangement on ion distribution functions. Difficulties in measuring IVDFs are minimized by simulation of ion trajectories and a careful determination of the relevant transmission functions specific for the plasma monitor used. According to [206-208], the forward part of the ion velocity distribution function is measured by the EQP. Thus, a transformation of IEDFs calculated from the HPSM is performed in order to allow for an appropriate comparison. This transformation requires knowledge about the specific transmission functions of the EQP diagnostic arrangement. Several effects involved in ion sampling have to be accounted for and investigated in detail. First, collisions of ions passing the sampling orifice are discussed in section 2.4.1. Further, it is essential to gain knowledge about the acceptance angle of the sampling aperture, and more importantly, about the instrument ion optics. Not all ions arriving at the orifice plate can pass the EQP system and

finally reach the detector. Limitations due to the geometry of the sampling aperture and further by the voltage settings of the electrostatic lenses forming the EQP ion optics are discussed in sections 2.4.2 and 2.4.3, respectively. These limitations yield specific transmission functions which will result in only a very narrow angular distribution being measured by the EQP. It should be noted that from the measured distribution functions it is in general difficult to draw conclusions about the true IEAD for ions incident at the reactor wall.

Simulation of realistic distribution functions requires detailed knowledge about various discharge parameters. Besides very few published studies (e.g., in [13]), this requirement is hardly met in reality. Extensive measurements comprising all known plasma diagnostic techniques on specially designed laboratory systems would have to be performed, which is usually a topic for many research groups. Such studies are usually limited to noble or very simple molecular gases, where basic knowledge is available from literature. Furthermore, results only apply to a specific reactor type. For the work here, an extensive baseline characterization for relevant discharge does not exist up to now and knowledge is either very limited or restricted by the respective manufacturers. From these reasons, calculations were performed for a wide range of plasma parameters as an initial start point which is described in section 2.5.

From this overview, this work will give a first attempt towards enabling a comparison of experimental and simulation results. The study of various discharge parameters will give valuable support for the interpretation of results from an analysis of different discharge chemistries. It is demonstrated, how typical ion distributions can be obtained from simulations and compared to measured IVDFs by applying transmission functions and transformation of calculated energy distribution functions to measured velocity distribution function.

2.4.1 Extraction effects

When travelling through the sampling orifice, ions can collide with either the static background neutral gas inside the ion analyzer or the expanding gas from the plasma reactor. As a result, ion bombardment measurements can be potentially corrupted. Ideally, the gas density should change stepwise at the orifice plane. However, there is a transition region from the higher density region of the plasma reactor (viscous flow) to the very low density in the EQP chamber (molecular flow) causing a significant density of neutral molecules to exist a few pinhole radii from the orifice on the low pressure side. According to Coburn and Kay [209], the attenuation of the ion beam downstream of the orifice can be calculated for both effects. Due to maintaining a base pressure below 5×10^{-6} Torr inside the EQP, the mean free path is in the order of several meters (molecular flow regime). Hence, the static background pressure is sufficiently low and scattering of ions with background neutrals is negligible. The ion current attenuation due to the influence of the static pressure can be calculated using the expression

$$\frac{I(x)}{I_0} = \exp[-\sigma_{CX}n x] = \exp\left[-\frac{\sigma_{CX}n_0 C x}{C+Q}\right] \quad (2.1)$$

where $I(x)$ is the ion current at distance x from the orifice, I_0 is the ion current at the orifice, σ_{CX} is the charge exchange collision cross section, n_0 is the neutral density at the high pressure side of the orifice, n is the neutral density in the low pressure region of the

orifice, C is the orifice conductance, and Q is the pumping speed in the low pressure region. The conductance C of the aperture is given by [144]

$$C = 11.7\pi R^2 \sqrt{\left(\frac{28}{Z}\right)\left(\frac{T}{298}\right)} \quad (2.2)$$

with the orifice radius R , the relative atomic mass Z , and the temperature of species inside the plasma reactor T . For $R = 25 \mu\text{m}$, $M = 40$, $T = 343 \text{ K}$, $x = 5 \text{ cm}$, $\sigma_{\text{CX}} = 4 \times 10^{-19} \text{ m}^2$ (Ar resonant charge exchange [210,211]), less than 0.1% of the ions undergo collisions with neutrals effusing through the orifice even at high plasma reactor pressures of 600 mTorr.

The expanding gas forms a localized high gas density downstream the orifice which significantly varies with pressure inside the plasma reactor and the orifice diameter. The influence of the expanding gas can be described by

$$\frac{I(x)}{I_0} = \exp\left[-\frac{\sigma n_0 R}{2} \arctan\left(\frac{x}{R}\right)\right] \quad (2.3)$$

which for $x \rightarrow \infty$ yields [212]

$$\frac{I(x)}{I_0} = \exp\left[-\frac{\sigma n_0 R \pi}{4}\right]. \quad (2.4)$$

As can be seen from equation (2.4), the beam pressure effect is independent of the pumping speed in the low-pressure region. For a reactor pressure as high as 600 mTorr, up to 12.4% of all ions suffer collisions after passing through the 50 μm diameter orifice (cf., Fig. 2.8). These collisions can yield a reduced ion energy and hence contribute to an artificial distortion of the actual IDF at the electrode surface.

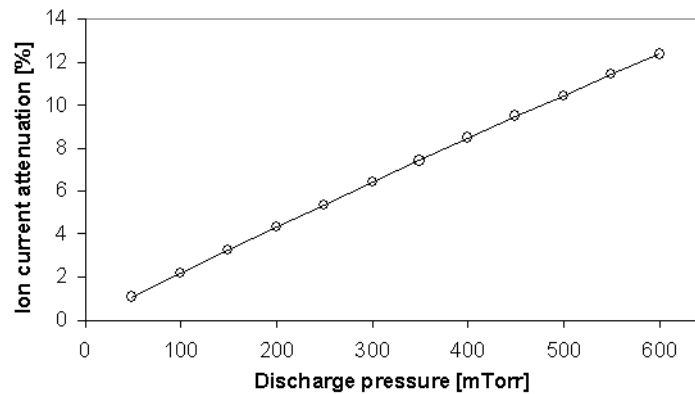


Figure 2.8: Attenuation of the ion current due to collisions with neutral species effusing through the sampling orifice.

Thompson et al. [212] pointed out the pressure on the plasma side of the orifice in general being less than the plasma pressure well away from the orifice. The assumed lower pressure will result in fewer collisions as compared to the situations at an undisturbed electrode surface. Assuming an approximately symmetric effect of the orifice on the neutral gas density, about the same percentage of ions should be affected by a decreased density at the high pressure side, as are affected by a significant density at the low pressure side of the orifice. Further, an increased average ion energy above the orifice resulting from fewer collisions should somewhat compensate an collision induced ion energy loss behind the orifice.

From the above considerations for various pressure effects it is assumed that measured energy distributions are only negligibly influenced and no relevant transmission function is identified.

2.4.2 Orifice transmission function

The finite thickness of the sampling orifice requires further correction of the actually measured IVDF since not all impacting ions will reach the opposite side of the aperture and be sampled by the EQP ion optics. As an approximation of the orifice shape, an ideal cylindrical aperture of radius R and length L is considered. The probability of passing through the aperture depends on particle arrival position and angle. Considering a flux of particles evenly distributed over the pinhole entrance, the fraction of particles passing through the cylindrical aperture without colliding with the cylinder walls is calculated. The arrival position of a particle is defined by the radial coordinate r , the angle between the particle trajectory and the orifice surface normal is defined as θ .

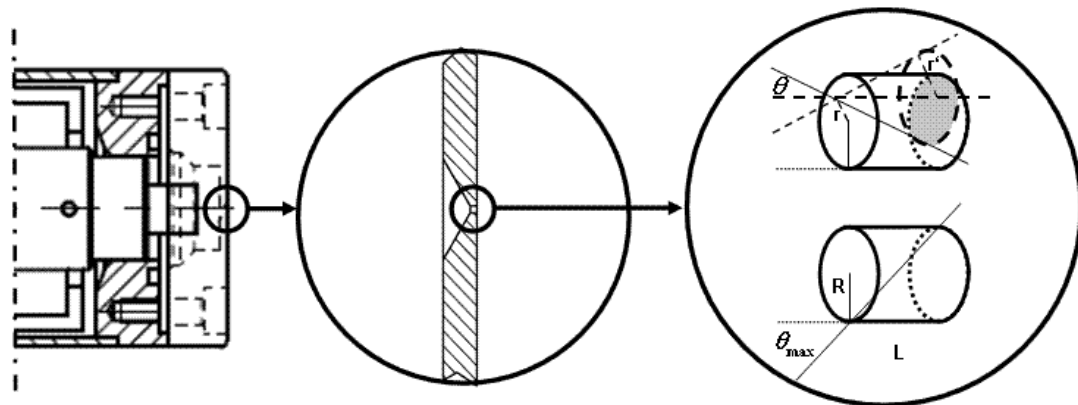


Figure 2.9: Sampling orifice geometry.

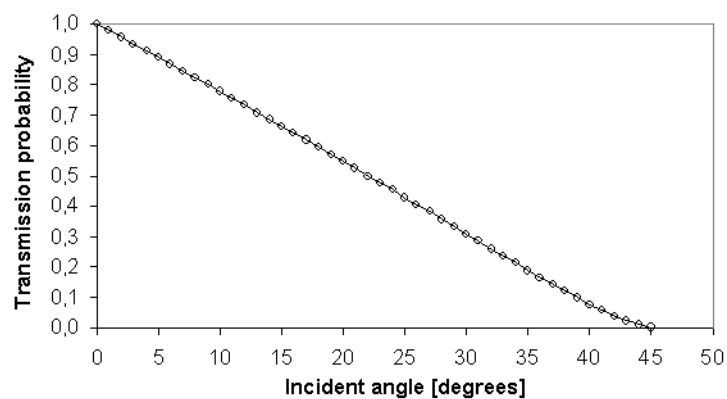


Figure 2.10: Orifice transmission probability as a function of the ion incident angle.

The maximum angle for transmission is given by

$$\tan(\theta_{max}) = \frac{2R}{L}. \quad (2.5)$$

The particle trajectory will be part of the surface of a cone with radius $r' = L \tan \theta$ at the exit aperture. The fraction of incoming particles traversing the orifice will be the fraction of the circumference of the cone lying within the exit aperture of the sampling orifice in Fig.

2.9. Calculating the effective collection area enables the flux of ions at various IAD incident angles to be normalized to the same collection. According to [89], the transmission probability is calculated from the effective collection area finally yielding

$$P_{\text{trans}}(\theta) = 1 - \frac{\frac{L}{R} \tan(\theta) \sqrt{4 - \left(\frac{L}{R}\right)^2 \tan^2(\theta)} - 2 \arcsin(\tan(\theta)) - \sin(2 \arcsin(\tan(\theta)))}{\pi}. \quad (2.6)$$

The derived orifice transmission function which is used to alter the calculated IEAD from the MC part of the HPSM simulation is plotted in Fig. 2.10.

2.4.3 Energy transmission function

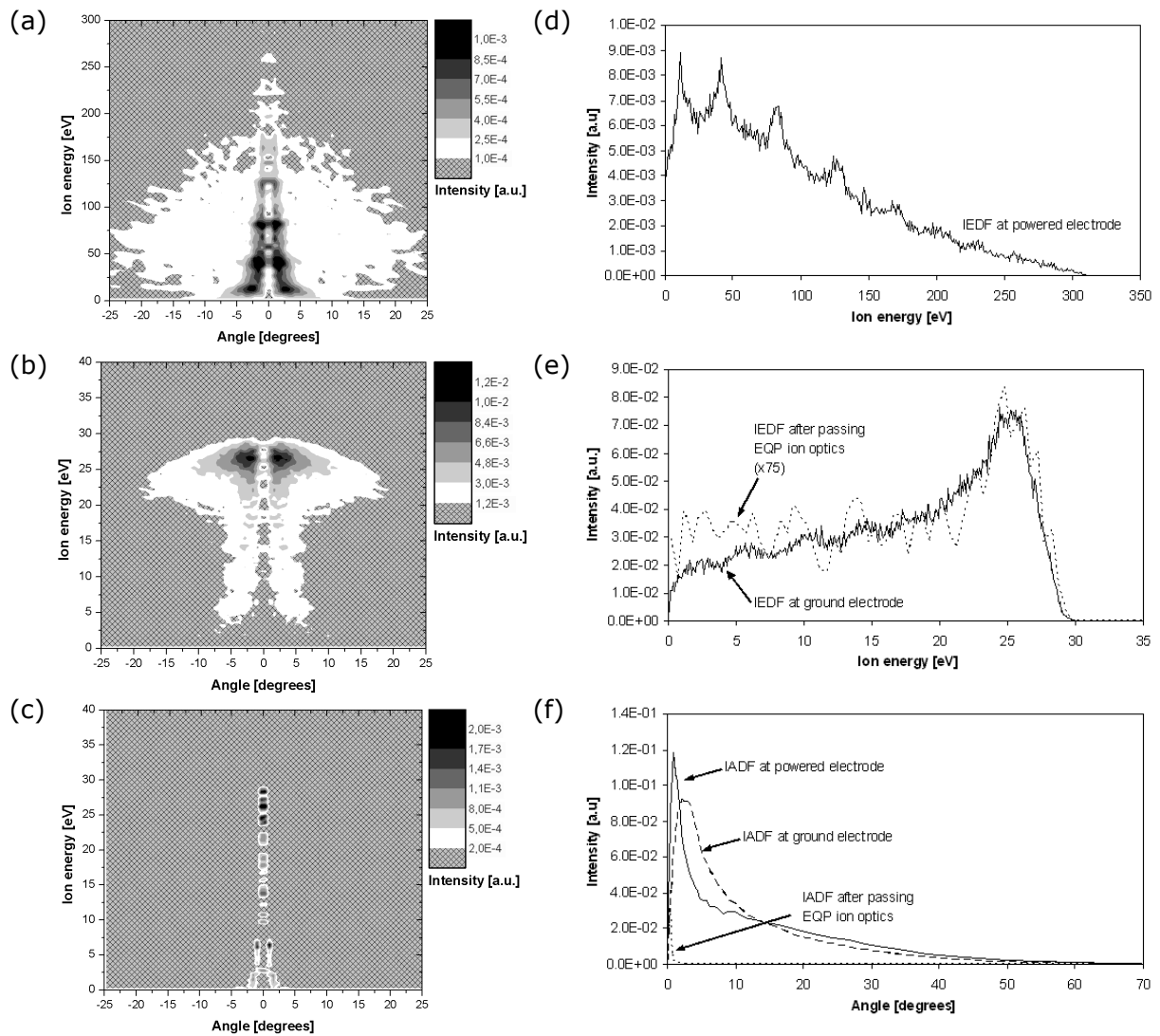


Figure 2.11: Results of HPSM simulations for a typical 60 MHz frequency argon discharge: (a) IEAD for Ar⁺ ions at the powered electrode; (b) IEAD for Ar⁺ ions at the ground electrode; (c) IEAD for Ar⁺ ions after passing a 50 μm sampling orifice at the powered electrode and further the EQP ion optics section before entering the energy analyzer; (d) IEDF for Ar⁺ ions at the powered electrode as obtained after integration over all angles; (e) IEDF for Ar⁺ ions at the ground electrode as obtained after integration over all angles; (f) IADF for Ar⁺ ions corresponding to cases (a)-(c) as obtained after integration over all energies. HPSM input parameters used were 300 V rf peak voltage, 150 mTorr background neutral gas pressure, 500 K neutral gas temperature, 2.58 eV electron temperature, $1 \times 10^{10} \text{ cm}^{-3}$ plasma density, and no magnetic field was applied.

As discussed in section 2.2, an energy-dependent transmission is caused by the EQP ion optics. Settings of the EQP electrostatic lenses determine the electric field strength, and thus the acceptance angle for incoming charged particles. The acceptance angle serves as a good approximation of the energy dependence of the measurement system.

The maximum acceptance angle was calculated using freeFEM++ with settings of the electrostatic lenses obtained from tuning for SNR optimized ion optic settings for all cases when achieving the passing energy required to transit the 45° sector field energy filter. From Fig. 2.4 it is obvious, that only the forward part of the ion distribution function is measured which is due to the very narrow acceptance angle of the instrument. The acceptance angle is found to decrease from a maximum of 2.2° (38 mrad) at 1 eV ion energy to less than 0.5° (9 mrad) for an ion energy above approximately 20 eV. This proves the fact of low-energy ions to easier be deflected and focussed. The acceptance angle and hence the energy dependence results in an artificial distortion of the IDF in particular in the low-energy region. From a best fit to the data, the energy dependent transmission function is calculated to be

$$P_{\text{trans}}(E_i) = 2.20 \left(\frac{E_i}{\text{eV}} \right)^{-0.55} \quad (2.7)$$

with the ion energy E_i . Besides the orifice transmission function, the energy transmission is also applied to results of the HPSM simulation for comparison to the experimental data.

For further illustration, typical IEADs obtained from HPSM simulations for a 60 MHz argon discharge at 150 mTorr are plotted in Fig. 2.11. From the IEAD for Ar⁺ ions at the powered electrode (cf., Fig. 2.11-a) it can be seen that most ions are forward-directed within an interval of ±5 degrees. Compared to the range of ion energies calculated, those ions are however found at lower energies resulting from resonant charge exchange collisions. A significant amount of ions is further found to hit the electrode with also considerable off-normal incidence in the ±25 degree range. The IEAD for Ar⁺ ions at the ground electrode are shown in Fig. 2.11-b. Here, the probability for resonant charge exchange is less if being compared to that for the high voltage sheath. Also, less pronounced scattering is observed as compared to the former case when comparing for the same range of the relative ion flux plotted here. Fig. 2.11-c shows the IEAD for Ar⁺ ions after passing a 50 μm sampling orifice at the powered electrode and further the EQP ion optics section before entering the energy analyzer. This result is obtained from application of the orifice and energy transmission functions to the true IEAD plotted in Fig. 2.11-b. The strongly modified result demonstrates again the limited interval that can be measured from the true IEAD for ions incident at the relevant electrode. This example leads to the conclusion that situations can arise where information about the measured ion distribution function can considerable deviate from the true IEDF. This can happen if for example (at high pressures) a high amount of ions is scattered in the sheath region to arrive at the electrode at marked off-normal incidence. However for asymmetric discharge geometries as the one considered here, more pronounced scattering and charge exchange collisions can occur in the typically thicker high voltage sheath in front of the powered electrode. Hence, performing IEDF measurements at the powered electrode would cause results to deviate even more from reality. IEDFs obtained from measurements at the ground electrode will yield a good agreement to the true IEDF at low to intermediate pressures. Plots depicted in Fig. 2.11-d and Fig. 2.11-e show the corresponding IEDFs for Ar⁺ ions at the powered and ground electrode which are obtained after integration of the IEAD over all angles. Despite the higher noise for the

calculated IEDF for ions that have successfully passed the EQP ion optics (dotted line) - which is due to low statistics-, the agreement to the true IEDF (solid line) is quite good (Fig. 2.11-e, note that the measured IEDF has been multiplied by a factor of 75). Finally, in Fig. 2.11-f, the IADFs for Ar^+ ions corresponding to cases (a)-(c) are plotted as obtained after integration of the respective IEADs over all energies.

2.4.4 Mass transmission function

Both the quadrupole mass filter and the SEM pulse-counting detector contribute to a mass transmission function. The mass discrimination is attributed to the presence of a quadrupole pre-and postfilter reducing the influence of the quadrupole dc fringing fields, and further to the detection coefficient of the SEM caused by a mass-dependent emission of secondary electrons. According to [145,213], both the transmission efficiency of the quadrupole mass filter $t(m/q)$ as well as detection coefficient of the channeltron detector $\theta(m/q)$ scale with the inverse square root of the ion mass. Hence when plotted as a function of the ion mass, the measured signal will approximately scale with the inverse of the ion mass, which for singly charged ions is expressed by

$$t(m)\theta(m) \sim m^{-1}. \quad (2.8)$$

Equation (2.8) implies that high mass species are suppressed in a mass scan. In Fig. 2.12 this correlation is supported quite well by mass discrimination data provided from the manufacturer [153].

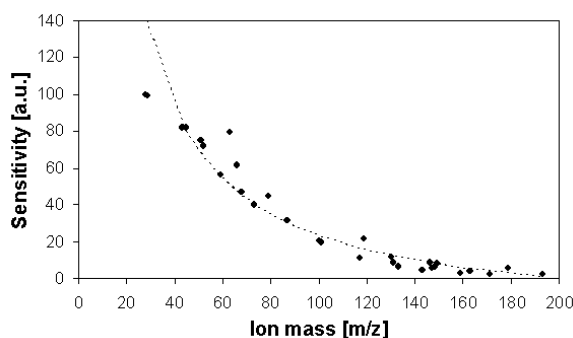


Figure 2.12: Mass discrimination of the EQP probe obtained from spectral data for investigation of the complex substances (TEOS, HMDSO, VMDSO, HMDSN) applying 70 eV electron energy in RGA mode [153]. Spectral intensities measured (points) are fitted well by the inverse ion mass function from equation (2.8).

2.4.5 Sheath behaviour in front of different dielectric surfaces

In this section it will be discussed how the presence of the different dielectric materials MACOR and Y_2O_3 influences the ion distribution functions. This evaluation effort is done to examine if measured IVDFs are representative for distribution functions of ions incident on the Y_2O_3 coated reactor walls (forming the dominating electrode area in the plasma).

Estimation of the difference in the sheath voltage drops in front of different dielectrics requires knowledge of currents from the plasma bulk to the MACOR and Y_2O_3 surfaces, as well as floating potentials of the different surfaces. Since these parameters remain inaccessible, it is only possible to determine the relationship for the two limiting cases assuming a (1) homogeneous potential distribution, and (2) homogeneous current density. In Fig. 2.13, a model is given for the rf voltage drops across the sheaths that develop in

front of different dielectrics while connecting the plasma potential to ground. The model will be used to investigate the differences caused by the presence of the different dielectrics.

(1) Homogeneous potential distribution

Assuming that equal potentials develop at the surfaces of the different dielectrics

$$V_{\text{MACOR}} = V_{\text{Y2O3}} \quad (2.9)$$

which requires

$$\frac{I_{\text{MACOR}}}{I_{\text{Y2O3}}} = \frac{\epsilon_{\text{MACOR}}}{\epsilon_{\text{Y2O3}}} \left(\frac{A_{1\text{MACOR}}}{d_{1\text{MACOR}}} + \frac{A_{2\text{MACOR}}}{d_{2\text{MACOR}}} \right) \frac{d_{\text{Y2O3}}}{A_{\text{Y2O3}}} = 9.41 \times 10^{-5} \quad (2.10)$$

with the dielectric constants $\epsilon_{\text{MACOR}} = 6$ (remaining nearly unchanged for a wide range of frequencies and temperatures [150]) and $\epsilon_{\text{Y2O3}} = 11.5$, the MACOR orifice plate physical dimensions $A_{1\text{MACOR}} = 0.95 \text{ cm}^2$, $d_{1\text{MACOR}} = 1 \text{ mm}$, $A_{2\text{MACOR}} = 9.23 \text{ cm}^2$, $d_{2\text{MACOR}} = 7.5 \text{ mm}$, and the yttria coated ground electrode surface area $A_{\text{Y2O3}} = 2419.15 \text{ cm}^2$ with an average thickness of $d_{\text{Y2O3}} = 200 \text{ }\mu\text{m}$. From its geometry, the MACOR plate is approximated by 2 parallel capacitors $C_{1\text{MACOR}}$ and $C_{2\text{MACOR}}$ representing the inner and outer section (cf., Fig. 2.9). From

$$V_{\text{sheath1}} + V_{\text{MACOR}} = V_{\text{sheath2}} + V_{\text{Y2O3}} \quad (2.11)$$

in Fig. 2.13 it is obvious that

$$V_{\text{sheath1}} = V_{\text{sheath2}} \quad (2.12)$$

must be satisfied here, which is fulfilled for

$$\frac{j_{\text{MACOR}}}{j_{\text{Y2O3}}} = \frac{I_{\text{MACOR}}}{I_{\text{Y2O3}}} \frac{A_{\text{Y2O3}}}{A_{\text{MACOR}}} = 2.24 \times 10^{-2}. \quad (2.13)$$

In this limit, the IVDFs measured at the MACOR orifice plate correspond to the IVDFs of ions incident on the yttria ground electrode.

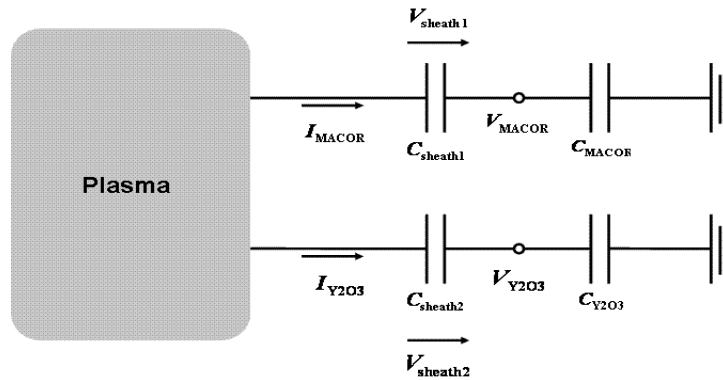


Figure 2.13: Capacitive voltage divider model for the presence of different dielectric surfaces in the plasma.

(2) Homogeneous current density

Assuming current densities at the different dielectric surfaces are equal,

$$j_{\text{MACOR}} = j_{\text{Y2O3}} \quad (2.14)$$

which requires

$$\frac{I_{\text{MACOR}}}{I_{\text{Y2O3}}} = \frac{A_{\text{MACOR}}}{A_{\text{Y2O3}}} = 4.21 \times 10^{-3}. \quad (2.15)$$

The surface potential distribution in this limit will be different from the case considered above and yield the following ratio

$$\frac{V_{\text{MACOR}}}{V_{\text{Y2O3}}} = \frac{I_{\text{MACOR}}}{I_{\text{Y2O3}}} \frac{C_{\text{Y2O3}}}{C_{\text{MACOR}}} = \frac{A_{\text{MACOR}}}{d_{\text{Y2O3}}} \frac{\epsilon_{\text{Y2O3}}}{\epsilon_{\text{MACOR}}} \left(\frac{A_{1\text{MACOR}}}{d_{1\text{MACOR}}} + \frac{A_{2\text{MACOR}}}{d_{2\text{MACOR}}} \right)^{-1} = 35.13. \quad (2.16)$$

From

$$V_{\text{sheath1}} + V_{\text{MACOR}} = V_{\text{sheath2}} + V_{\text{Y2O3}} \quad (2.17)$$

in Fig. 2.13 it follows that

$$V_{\text{sheath1}} + 34.13 V_{\text{Y2O3}} = V_{\text{sheath2}}. \quad (2.18)$$

From that, two limiting cases can be determined

$$(2a) \quad V_{\text{Y2O3}} \approx 0 \Rightarrow V_{\text{sheath1}} \approx V_{\text{sheath2}}, \quad (2.19)$$

$$(2b) \quad V_{\text{Y2O3}} \gg 0 \Rightarrow V_{\text{sheath1}} < V_{\text{sheath2}}. \quad (2.20)$$

If the floating potential at the dielectric surface is zero, the voltage drops of the sheaths in front of MACOR and yttria are equal as well, which is also a special case of the above assumption for a homogeneous potential distribution. However, if the floating potential can not be neglected (which is usually observed to be the case for the vast majority of measurements conducted in this work), the sheath voltage drop in front of the MACOR orifice plate can be considerably smaller compared to the sheath voltage drop in front of the yttria coated ground electrode. From Fig. 2.13, the floating potential at the yttria coating can be expressed by

$$V_{\text{Y2O3}} = \frac{d_{\text{Y2O3}}}{2\pi f \epsilon_{\text{Y2O3}} \epsilon_0} j_{\text{Y2O3}}. \quad (2.21)$$

For the two frequency drives used in this work, the following relations can be calculated

$$f = 60 \text{ MHz} \Rightarrow V_{\text{Y2O3}}[\text{V}] = 0.0052 j_{\text{Y2O3}}[\text{Am}^{-2}], \quad (2.22)$$

$$f = 2 \text{ MHz} \Rightarrow V_{\text{Y2O3}}[\text{V}] = 0.1563 j_{\text{Y2O3}}[\text{Am}^{-2}]. \quad (2.23)$$

The current density can be derived from

$$j = en_i v_{\text{Bohm}} = en_i \sqrt{\frac{k_B T_e}{m_i}} \quad (2.24)$$

and is plotted in Fig. 2.14 for Ar^+ ions in Ar plasmas (full lines) and Br^+ ions in HBr discharges (dotted lines) as a function of electron temperature and electron density. Strictly speaking, the calculation is valid only for electropositive discharges with a single ion species, as is usually the case for argon. Application to Br^+ ions in slightly electronegative HBr discharges is only a very crude approximation for the limit of Br^+ ions dominating over all further ions present in HBr discharges. Further, the sheath structure may not be comparable to those observed for electropositive discharges. For argon discharges in the range of about 2-4 eV mean electron temperature and common electron densities of 10^{10} - 10^{11} cm^{-3} [214,215], typical Ar^+ ion current densities exhibit about 3-44 A/m^2 . Inserting these values into equations (2.22) and (2.23) and further into (2.18) yields

$$f = 60 \text{ MHz} \Rightarrow V_{\text{sheath1}} + (0.53 \dots 7.82)V = V_{\text{sheath2}}, \quad (2.25)$$

$$f = 2 \text{ MHz} \Rightarrow V_{\text{sheath1}} + (16.00 \dots 234.74)V = V_{\text{sheath2}}. \quad (2.26)$$

This demonstrates that pure 60 MHz discharges yield essentially no dramatic differences between the ion energies at the yttria ground electrode as well as at the MACOR orifice plate. However, for a certain contribution of the 2 MHz frequency, ion energies can be considerably lower at the MACOR surface compared to those at the Y_2O_3 coated ground electrode.

Electronegative HBr discharges will exhibit lower electron densities due to efficient electron attachment in the plasma bulk. This is however not indicative of the ion densities which in electronegative discharges can be up to about three orders of magnitude higher compared to electron densities [31]. For HBr discharges in the range of about 4-7 eV mean electron temperature and common electron densities of 10^9 - 10^{10} cm^{-3} [214,215] similar ion densities as those observed in Ar discharges are expected, which would correspond to an estimated electronegativity of about ten. The higher mass and electron temperature in (2.24) will then almost cancel out, and typical Br^+ ion current densities exhibit about 3-41 A/m^2 . Inserting these values into equations (2.22) and (2.23) and further into (2.18) yields

$$f = 60 \text{ MHz} \Rightarrow V_{\text{sheath1}} + (0.53 \dots 7.29)V = V_{\text{sheath2}}, \quad (2.27)$$

$$f = 2 \text{ MHz} \Rightarrow V_{\text{sheath1}} + (16.00 \dots 218.73)V = V_{\text{sheath2}}. \quad (2.28)$$

Calculated differences for the developing sheaths are comparable to argon, and measured ion energies can again be considerably lower than those at the Y_2O_3 coated ground electrode in case there is certain contribution of 2 MHz power to the 60 MHz power.

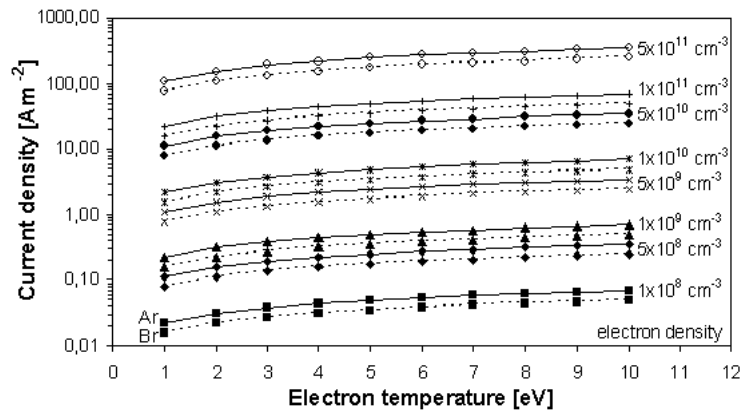


Figure 2.14: Current density calculated from (2.24) for Ar (full lines) and Br (dotted lines) as a function of electron temperature and electron density.

In summary, we can expect that IVDFs measured at the MACOR orifice plate will be identical to IVDFs of ions incident on the Y_2O_3 coated ground electrode in the limit of a homogeneous potential distribution (at the MACOR and Y_2O_3 dielectric surfaces), and further when assuming an ideally zero floating potential of the dielectric surfaces in the limit of homogeneous current densities. Considerable deviations can however occur for non-negligible floating potentials in the limit of homogeneous current densities. Floating potentials observed for the different discharges discussed in chapter 4 were found to deviate from a zero potential. This clearly demonstrates that the theoretical limit of an ideally zero floating potential is not fulfilled in reality. In these cases, the IVDFs measured

at the MACOR plate would appear at lower energies than those obtained for ions incident on the yttria coated ground electrode. From the halogen chemistries typically used in the reactor it is known, that surface contamination layers can develop during plasma operation through adsorption and deposition of plasma species/products at the reactor surfaces. These surface layers will remain to a certain extent even after standard plasma cleans (as a consequence, all chamber parts have to be replaced and wet-cleaned regularly). Neglecting differences in the sticking coefficient of product species for the different coatings discussed here, it can be assumed that surface charging becomes dominated by a uniform build-up of surface contamination layers. This would support the assumption that the case of a homogeneous potential distribution most likely applies here.

Influence of orifice geometry on sheath potential lines

The orifice diameter of the used extraction hood is 50 μm which is smaller than the sheath thickness and also does not exceed $2\lambda_D$. For a plasma with assumed $T_e = 4 \text{ eV}$ and $n_e = 1 \times 10^{10} \text{ cm}^{-3}$ the Debye length [20] is calculated to be about 149 μm . For this case the sheath will remain undisturbed [208].

2.4.6 HPSM extensions and modifications

The initial model applied in this work is sufficient to study CCRF argon discharges. In the HPSM code, initially constant hard sphere and charge exchange collision cross sections $\sigma_{\text{HS}} = 2.5 \times 10^{-19} \text{ m}^2$ and $\sigma_{\text{CX}} = 4.0 \times 10^{-19} \text{ m}^2$ were used for argon [17,18] as determined from experimental data [210,211]. To enable a more precise comparison of calculated and measured IVDF structures, the existing model which assumed isotropic scattering in the center-of-mass frame was modified by application of anisotropic deflection functions (as calculated from previously determined impact parameters). The initially constant hard sphere and charge exchange cross sections were further substituted by energy dependent cross sections determined from ab initio calculations. This effort appeared necessary to achieve an accurate modeling of the scattering angle as a function of impact parameter and energy for the wide range of relevant scattering energies (about zero eV to keV range) occurring in the sheaths of typical medium pressure CCP discharges. Additionally, the model was extended to allow for simulation of CCRF hydrogen bromide discharges consisting of multiple species.

To describe ion-neutral scattering for a given impact parameter, the differential scattering cross section is used [20]

$$\frac{d\sigma}{d\Omega} = \frac{b}{\sin\Theta} \cdot \frac{db}{d\Theta} \quad (2.29)$$

The impact parameter b denotes the distance of closest approach between the two colliding particle centers without any particle interaction. The scattering angle Θ changes characteristically with the impact parameter b (Θ becomes larger for decreasing b). Determination of the differential scattering cross section requires knowledge about the dependency $\Theta(b)$ which is determined from the scattering potential $V_{\text{sc}}(r)$. The interaction potential $V_{\text{sc}}(r)$ is determined as a function of the impact parameter b from ab initio calculations (i.e., solving the Schrodinger equation). The deflection angle $\Theta(b)$ of the scattering process is then calculated for various impact energies (1...1000 eV) by applying the Kepler formula. This approximation has shown to yield reasonable results for the high energy range being of main interest here, solving the time-dependent Schrodinger equation for the complete scattering process is not relevant at this point. To account for

the projectile energy, the deflection angle has now become a function of both impact parameter and ion energy $\Theta(b, E)$. For a specific ion energy, the cross section for elastic scattering can then be determined for the point where the scattering angle becomes negligibly small by using

$$\sigma_{\text{ES}}(E) = \pi b_{\text{ES},\text{max}}^2(E) = \pi [b_{\text{ES},\text{max}}(1\text{eV})E^{-p}]^2. \quad (2.30)$$

To further account for the possible capture of an ion by a neutral at small impact parameters, the Langevin enhanced cross section can be calculated from

$$\sigma_{\text{L}} = \pi b^2 = \frac{1}{v_{\text{R}} \sqrt{\frac{m_{\text{n}} + m_{\text{i}}}{m_{\text{n}} m_{\text{i}}} \cdot \frac{\pi q_{\text{i}}^2 \wp_{\text{n}}}{\epsilon_0}}} = \frac{K_{\text{L}}}{v_{\text{R}}} \quad (2.31)$$

with the relative velocity before the collision v_{R} , the masses of neutral and ion species m_{n} and m_{i} , charge of the ion q_{i} , the polarizability of the neutral species \wp_{n} , and the Langevin constant K_{L} . Now, equation (2.29) can be finally written

$$\left. \frac{d\sigma}{d\Omega} \right|_{\text{ES}} = \frac{d\sigma_{\text{ES}}}{d\Omega} + \frac{\sigma_{\text{L}}}{4\pi}. \quad (2.32)$$

Whereas the elastic scattering cross section σ_{ES} dominates at higher energies, the Langevin enhanced cross section σ_{L} contributes at low energies.

Resonant charge exchange between an ion and its parent neutral is treated with the same energy dependence as determined for elastic collisions. The probability for resonant charge exchange is a rapidly oscillating function of the collision parameters. This oscillating function is represented well by its mean value of 50% [216]. Cross sections for charge exchange were deduced from literature [217]. Similar to the energy dependence of elastic collisions, the energy dependence for charge exchange collisions can be accounted for by using

$$\sigma_{\text{CX}}(E) = 2\pi b_{\text{CX},\text{max}}^2(E) = 2\pi [b_{\text{CX},\text{max}}(1\text{eV})E^{-p}]^2 \quad (2.33)$$

where the factor of two accounts for the 50% charge exchange probability, and $b_{\text{CX},\text{max}}$ is deduced from [217].

As an example, the collision parameters for $\text{Ar}^+ + \text{Ar}$ interactions with Ar^+ projectile energies for 1 eV and 1000 eV are illustrated in Fig. 2.15. In general, the interaction comprises short range forces at low impact parameters resulting from repulsion of the electron clouds, and further long range forces at higher impact parameters which result from (induced) dipole and van-der-Waals interactions. For a time-efficient treatment in the Monte Carlo part of the HPSM, three distinct regions can be identified and used for a fit model of the final energy dependent cross sections (cf., Fig. 2.15-b): (1) At low impact parameters momentum and charge transfer are significant leading to large deflections of the projectile. Starting from $\Theta = 180^\circ$, the fit function is used up to a defined minimum deflection angle where deflections have become infinitesimally small. (2) At higher impact parameters where deflections are practically zero due to negligible momentum transfer, the probability for charge transfer still remains at 50%. Hence, elastic scattering processes are neglected and charge transfer is the only process that is considered here. A maximum impact parameter $b = b_{\text{ES},\text{max}}$ for elastic scattering can be defined which divides regions (1) and (2), for 1 eV argon ions it is calculated to be 4.52 Å. (3) For impact parameters exceeding a certain value, no collision process will occur anymore. Regions (2) and (3) are divided by a maximum impact parameter $b = b_{\text{CX},\text{max}}$ for resonant charge exchange

processes which for 1 eV argon ions is 6.18 \AA . This value is calculated from published charge exchange cross sections [217] by using (2.33).

In summary, the fit model for the energy dependent cross sections comprises the following parameters: (1) maximum elastic impact parameter $b_{ES,max}$ at a relative kinetic energy $E_{kin} = 1 \text{ eV}$ for a projectile as defined by a minimum deflection angle of interest, (2) maximum impact parameter b_{max} at $E_{kin} = 1 \text{ eV}$ as defined by the charge exchange cross section taken from literature [217], (3) exponent p for the energy dependence as obtained from a fit to the deflection function giving a maximum impact parameters which is $\sim (E_{kin})^{-p}$, (4) constant charge exchange probability of 50% is applied for resonant processes [216].

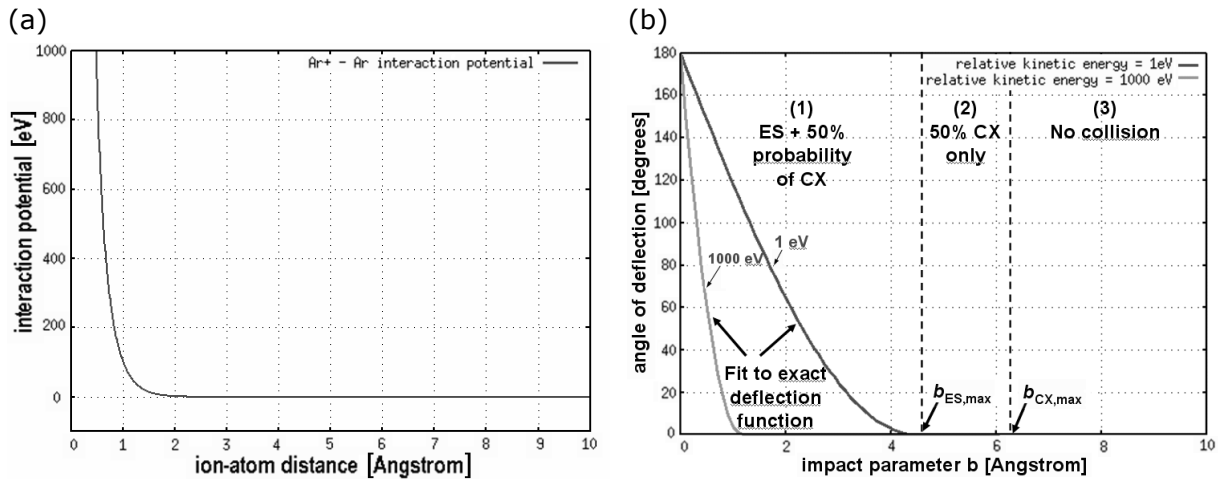


Figure 2.15: Model of ion-atom collisions for argon: (a) collision dynamics $V_{sc}(r)$, (b) angle of deflection $\theta(b, E)$.

Heavy particle collision parameters for ion-atom and atom-atom collisions in argon calculated in this work are listed in Table A.1 in appendix A. As described above, the energy-dependent interaction parameters were obtained from fitting the results of the calculated deflection functions and relative kinetic energies of the argon ion projectile. Cross sections for elastic collisions and charge exchange were calculated according to (2.30) and (2.33) by using the maximum impact parameter for elastic scattering and charge exchange, respectively. The Langevin constant K_L for argon ion-atom interactions was calculated by using (2.31) with the polarizability taken from [218].

Further extensions were made by implementation of multiple species observed in typical CCRF hydrogen bromide discharges. First, mole fractions of relevant neutral and ion species are required as input for the HPSM simulator. Neutral species mole fractions were determined by applying mass spectrometry for a typical HBr discharge (medium pressure, 60 MHz frequency) at the HART plasma reactor. For these experiments, the electrostatic chuck was covered by an Y_2O_3 wafer to minimize chemical reactions with surfaces exposed to the plasma and avoid distinct modification of the discharge chemistry by additional etch (by)products. The Hiden EQP was applied in RGA mode with 70 eV electron energy. The mass spectrum contains typically major peaks for the following species: H_2^+ , H_2O^+ , Br^+ , HBr^+ , and Br_2^+ (cf., Fig. 2.16). hydrogen bromide is partly dissociated into atomic hydrogen and bromine, where H_2^+ and Br_2^+ result from recombination of these atoms at the reactor walls surrounding the discharge. Unfortunately, the mass spectrometer used is not able to reliably measure the $m/q = 1 \text{ u}$ peak in the mass spectrum, so H^+ is not

reported here but is believed to be present as well. Water is detected due to the significant amount of humidity contained in the hydrogen bromide feedstock gas. From the analysis, peaks for H_2^+ , Br^+ , HBr^+ , and Br_2^+ were used to calculate the neutral mole fractions. From application of APMS it was concluded that all species considered here result from direct ionization in the mass spectrometer ionizer region (with Br being an exception). Threshold energies were determined as follows:

- 15.66 eV for H_2^+ which is only slightly above the reported value of 15.43 eV for direct ionization of hydrogen molecules [219].
- (1) about 12.5 eV and (2) 17.3 eV for Br^+ resulting from (1) direct ionization of bromine neutrals $\text{Br} + e \rightarrow \text{Br}^+ + 2e$, and (2) from dissociative ionization of either hydrogen bromide $\text{HBr} + e \rightarrow \text{Br}^+ + x$ or molecular bromine $\text{Br}_2 + e \rightarrow \text{Br}^+ + x$ or both type of species. The value measured for (1) is slightly above the first ionization potential of 11.81 eV [219], whereas for (2) values were only found to be reported for Br^+ formed during dissociative ionization of molecular bromine $\text{Br}_2 + e \rightarrow \text{Br}^+ + x$ in the range of 10.31-10.48 eV [218,219]. Hence, it is concluded that the second threshold of about 17.3 eV for Br^+ observed here must be due to dissociative ionization of molecular hydrogen bromide according to $\text{HBr} + e \rightarrow \text{Br}^+ + x$. This is also supported by further investigations when applying APMS in HBr discharges, as described in section 3.1.2.
- 11.86 eV for HBr^+ which is close to 11.68 eV for direct ionization of HBr molecules reported in [219].
- 10.66 eV for Br_2^+ which is comparable to the reported value of 10.52 eV for direct ionization of bromine molecules [219].

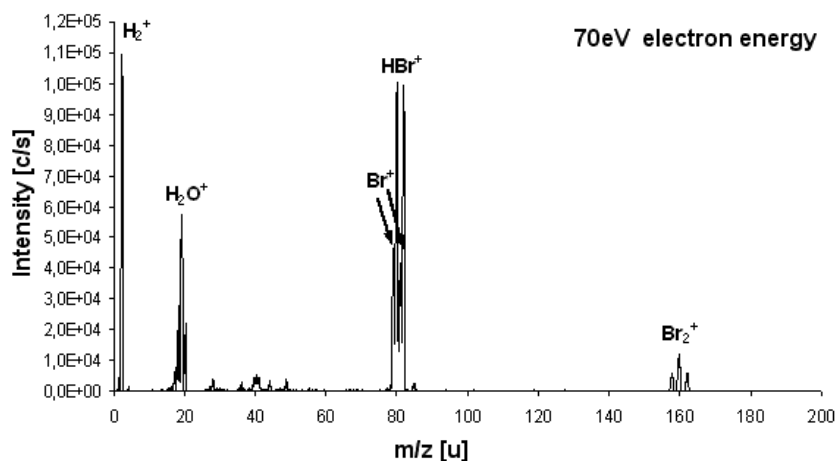


Figure 2.16: Neutral species mole fractions determined for a pure HBr plasma using Y_2O_3 wafer with Hiden EQP 500 applied in RGA mode with 70 eV electron energy (mass spec data compensated by application of mass transmission function $\sim m^{-1}$), parameters: 300 sccm HBr, 150 mTorr process pressure, 1500 W (60 MHz), 0 W (2 MHz), 0G, 15 Torr helium backside cooling pressure.

Mole fractions for the described neutral species were obtained by integrating the measured peaks, compensating data by application of the mass transmission function from equation (2.8), taking into account the different isotopes for each species, accounting for the sources of Br^+ as determined after direct and dissociative ionization inside the EQP ionization source, and calculating the ratio of the integrated intensity for each species and the total integrated intensity for all species regarded here. It should be noted that these

conclusions can only be considered as a rough estimation since several side effects (like an unknown contribution of pyrolysis effects at the filaments of the EQP ionizer, and more importantly due to a high recombination coefficient of bromine atoms on stainless steel surfaces [125] inside the EQP tube) remain unknown. Furthermore, a correct determination of mole fractions for ion species inside the plasma is more complex than the method explained above since tuning of the EQP ion optics is different for each ion species extracted from the plasma and ions exhibit different distribution functions. At this point, mole fractions of the corresponding ion species were implemented into the HPSM with the same values that were determined for the neutral species. From the assumptions made above it is expected that results from HPSM simulations can deviate from the behaviour of real HBr discharges investigated here. Deviating mole fractions will lead to a deviating effective ion mass which further affects the sheath calculations. However, this might be of minor importance since the HPBM part of the discharge model (cf., Fig. 1.10) is kept relatively simple and hence results are in either case subject to deviations. As described in the following, deviations from reality can also occur due to a lack of information about cross sections for relevant particle interactions in hydrogen bromide molecular discharges.

Assuming the mole fractions for the relevant neutral and ion species are known, all important interactions for the species considered here can now be implemented. Compared to the quite simple interactions in argon (cf., Table A.1), more complex interactions have to be considered in hydrogen bromide molecular discharges (cf., Table B.1 in appendix B). Elastic collision parameters for atom-atom interactions were determined from ab initio calculation as described above. Due to the lack of published data for the molecular species observed in HBr discharges, simplifications for the elastic collision cross sections had to be adapted. Cross sections for interactions between atomic bromine and molecular hydrogen bromide were adapted from those calculated for bromine atom-atom elastic scattering. Elastic scattering cross sections for interactions including molecular hydrogen and molecular bromine were taken from ab initio calculations for hydrogen-bromine and bromine-bromine atom-atom collision pairs and multiplied by a factor of two in each case.

Compared to symmetric (or resonant) charge exchange between identical species



cross sections for asymmetric (non-resonant) charge exchange between two nonidentical species



are significantly lower (up to orders of magnitude), especially at lower impact energies [220,221]. Hence, non-resonant charge exchange processes are neglected in the current version of the HBr model and the probability for charge exchange is set to zero in Table B.1 (while values for each charge exchange cross section and exponent are adapted from the calculated parameters for elastic scattering). However, asymmetric charge transfer becomes important to be considered when there is close resonance between the energy levels of the positive ion species and the ionic energy level of the atoms to be ionized.

As was already described above, the Langevin rate constant is relevant for the cases of impact with low energy projectiles involved. For molecular ion-neutral interactions with a molecular ion carrying a permanent dipole moment p_d involved, (2.31) has to be modified to [222]

$$K_{L\alpha} = \sqrt{\frac{m_n + m_i}{m_n m_i}} \cdot \frac{\pi q_i^2}{\epsilon_0} \cdot \left[\sqrt{\phi_n} + C p_d \sqrt{\frac{2}{\pi k_B T}} \right] \quad (2.36)$$

where the first term in square brackets gives the Langevin rate constant and the second term gives the increase due to the permanent dipole moment. The parameter $C \in [0, 1]$ describes the effectiveness of charge "locking" in the dipole and is a function of T and $\sqrt{p_d/\phi_s}$. Since only the hydrogen bromide molecule carries a permanent dipole momentum [223], equation (2.36) was used for interactions with hydrogen bromide molecules involved, with the parameter C determined from [222]. Langevin rate constants involving the other species considered here were calculated according to (2.31) for all ion-neutral interactions by using polarizabilities for the neutral target particles published in [218,223].

2.5 HPSM simulation studies

Using the hybrid sheath model, simulations were performed for a wide range of parameters. This is mainly due to two major reasons. First, simulations aim to gain a detailed knowledge about the plasma sheath properties and ion distributions at the different electrodes. Second, due to the lack of precise knowledge about plasma parameters for the different investigated discharges, it is ensured that typical process conditions are included in the study. Here, the effect of variations in the rf peak voltage, pressure of the neutral background gas, neutral gas temperature, electron density, electron temperature, as well as magnetic field for both 60 MHz and 2 MHz, and selected 60+2 MHz dual frequency mixes will be discussed. Information about the reactor geometry, investigated process parameters, species mole fractions, and model parameters is summarized in Table 2.1. Plots of the respective discharge sheath characteristics can be found in appendix C and appendix D, as will be indicated in the following discussion.

2.5.1 Argon discharges

From HPSM simulations of argon discharges, the following calculated parameters will be discussed:

- sheath thickness in front of powered and ground electrode;
- elastic scattering (ES) and charge exchange (CX) collisions for Ar^+ ions in the sheath regions;
- Langevin collisions for Ar^+ ions in the sheath regions;
- dc bias voltage;
- scaling exponent q to characterize the discharge asymmetry according to (1.6);
- Ar^+ IEDFs at ground and powered electrode;
- Ar^+ mean energies at ground and powered electrode.

Variation of rf peak voltage and electron density

Results of a variation of rf peak voltage and electron density can be found in Fig. C.1 in appendix C, where other input parameters were held constant at 150 mTorr background neutral gas pressure, 500 K neutral gas temperature, 2.58 eV electron temperature, and no magnetic field was applied. Independent of the applied frequency, the mean sheath thickness is found to increase with rf peak voltage and exponentially decrease at higher

plasma densities (cf., Fig. C.1-a). The rf peak voltages will influence the amplitudes of the sheath oscillations, whereas increasing the plasma density will reduce the sheath width. The minimum sheath thickness for typical plasma densities ranging between $5 \times 10^9 \text{ cm}^{-3}$ and $1 \times 10^{11} \text{ cm}^{-3}$ is found for 100 V rf peak voltage and $1 \times 10^{11} \text{ cm}^{-3}$ plasma density yielding 133 μm in front of the ground and 415 μm in front of the powered electrode, whereas a maximum sheath thickness is observed for 900 V rf peak voltage and $5 \times 10^9 \text{ cm}^{-3}$ plasma density resulting in 827 μm at ground and 5.3 mm at powered electrode.

Table 2.1: HPSM input parameters.

Reactor geometry	Ar discharges	HBr discharges
Height	3.2 cm	3.2 cm
Radius	25.5 cm	25.5 cm
Electrode area A_{el}	706.9 cm^2	706.9 cm^2
Ground area A_{gr}	2547.2 cm^2	2547.2 cm^2
$A_{\text{gr}}/A_{\text{el}}$	3.6	3.6
Process parameters		
rf frequency	60, 2, 60+2 MHz	60, 2, 60+2 MHz
rf peak voltage	100...900 V	100...900 V
Gas pressure	50...600 mTorr (7...80 Pa)	50...600 mTorr (7...80 Pa)
Gas temperature	300...1500 K	300...1500 K
Electron temperature	1...10 eV	1...10 eV
Electron density	$5 \times 10^9 \dots 5 \times 10^{11} \text{ cm}^{-3}$	$1 \times 10^8 \dots 1 \times 10^{11} \text{ cm}^{-3}$
Magnetic field	0...150 G	0...150 G
Species mole fractions		
Ar, Ar^+	1.0000	-
H_2 , H_2^+	-	0.0055
Br, Br^+	-	0.2648
HBr, HBr^+	-	0.5927
Br_2 , Br_2^+	-	0.1371
Model parameters		
Number of particles	100 000	100 000
Start position	3 cm	3 cm

A comparison of HPSM calculation results with a sheath thickness scaling described by the Child-Langmuir law (1.30) for a collision-free sheath and the Warren law (1.32) for the other limit of a collision-dominated sheath is given in Fig. 2.17. The neutral gas density n_g

in (1.33) can be approximated by the ideal gas law, and the charge exchange cross section σ_{CX} can be taken from literature [217]. Here, the energy dependence of the cross section is accounted for by using (2.33) with mean ion energies as plotted in Fig. C.1-j and Fig. C.1-k. The ion current density is calculated from the wall flux according to $j_i = e\Gamma_i = en_0v_{Bohm}$. Whereas from the Child-Langmuir law (1.30) a stronger scaling (up to +9%) of the sheath thickness dependence on both the electron density and rf peak voltage is noticed, scaling of the sheath thickness from the Warren law (1.32) shows very good agreement to HPSM calculations (deviations below 1-2%). Quantitatively, HPSM calculations deviate -24%...-63% (-49%...+10%) for the electrode (ground) average sheath thickness in the limit of a collision-free sheath. A smaller offset of -28%...-39% (-21%...-32%) for the electrode (ground) average sheath thickness is noted in the other limit of a collisional sheath. From the qualitative scaling, this comparison emphasizes that assumptions for a collision-dominated sheath are applicable here. Despite the (small) absolute offset between the different results, this gives also confidence in the HPSM calculations.

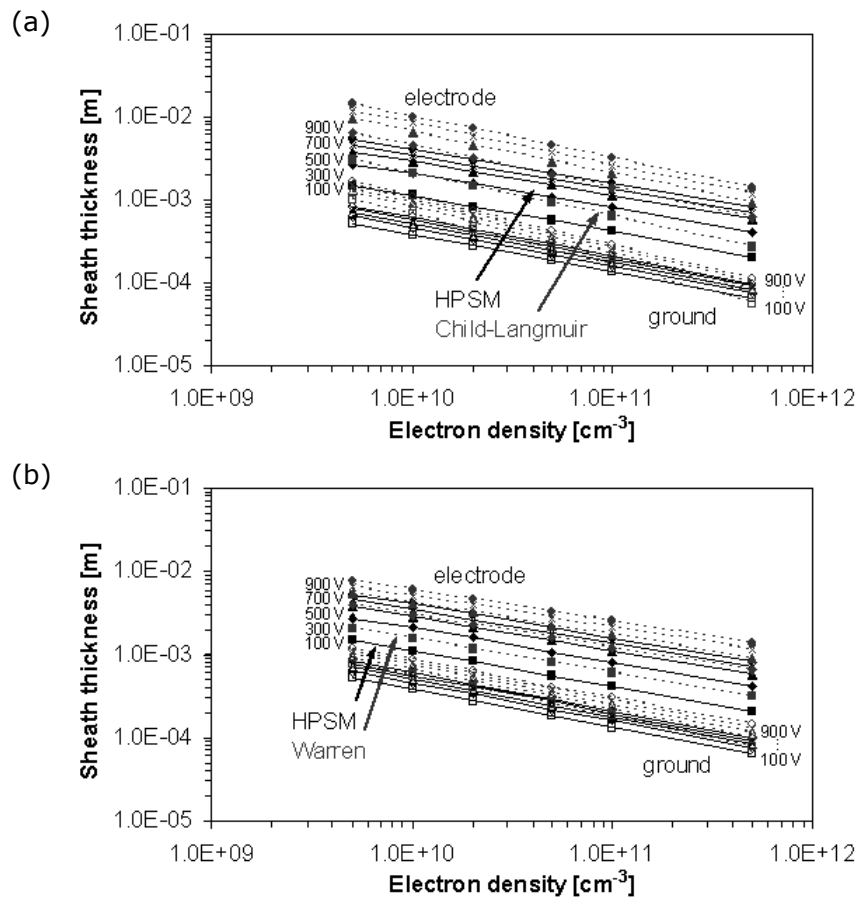


Figure 2.17: Comparison of the sheath thickness in front of powered (solid symbols) and ground electrode (open symbols, values have been multiplied by a factor of five) for a variation of electron density and rf peak voltage in Ar discharges (a) from HPSM simulations (continuous dark-colored lines) and calculated from Child-Langmuir law (dotted light-colored lines); (b) from HPSM simulations (continuous dark-colored lines) and calculated from Warren law (dotted light-colored lines). Constant input parameters were used: 150 mTorr background neutral gas pressure, 2.58 eV electron temperature, 500 K neutral gas temperature, no magnetic field.

While from Fig. C.1-b the number of ES and CX collisions for Ar^+ ions is hardly exceeding 1 in the ground electrode sheath region, multiple collisions can occur in the sheath at the powered electrode. As expected, the number of Langevin collisions is less than that observed for ES and CX collision processes (cf., Fig. C.1-c). Scaling of sheath collisions is proportional to the calculated development of the sheath thickness since the ion transit time across the sheath will become short for a reduced sheath thickness, thus decreasing the probability of collisions in the sheath.

The dc bias voltage in Fig. C.1-d is found to change for different rf peak voltages but remains virtually unchanged for different plasma densities. The dc bias voltage corresponds to about 80...90% of the rf peak voltage. Compared to 60 MHz, slightly lower values are calculated for 2 MHz. This reflects the fact that the average sheath electric field of the oscillating sheath differs slightly for the 60 MHz and the 2 MHz case. Whereas in reality the ions will be also influenced by the rf phase to some extent (especially for 2 MHz excitation), Ar^+ ions in the model only respond to the mean sheath electric field. This frequency dependent average sheath voltage is further expected to explain the slightly different scalings for both frequencies in Fig. C.1-e. The scaling exponent $1.1 \leq q \leq 2.6$ for (1.6) is found to agree very well with typical values for most experimental observations yielding $q \leq 2,5$ [20]. The discharge becomes more symmetric at lower rf peak voltages (up to 50% lower values for q) and further at lower plasma densities (up to 30% lower values for q).

IEDFs for Ar^+ ions are plotted in Fig. C.1-f to Fig. C.1-i for 300 V rf peak voltage and different plasma densities, as indicated by the labeling. From Fig. C.1-f, the IEDFs for 60 MHz frequency cover similar ion energies as those measured for 60 MHz frequency argon discharges in chapter 4. The double peak remains unresolved up to about $5 \times 10^{10} \text{ cm}^{-3}$. For higher densities a shoulder becomes visible until at $5 \times 10^{11} \text{ cm}^{-3}$ a broad double peak distribution is observed. The low-energy peak of the saddle is favored over the higher energy peak which can be attributed to the non-sinusoidal nature of the oscillating rf sheath. Another explanation could be attributed to enhanced collisions: a maximum energy can be obtained when the sheath has expand to its maximum, at this point the ions traversing the sheath will experience a longer path with also a higher probability of collisions. From Fig. C.1-b the collisionality is however quite low for 300 V rf peak voltage and high densities in the ground electrode sheath region. Despite the low collisionality of the ground electrode sheath, the influence of more pronounced elastic scattering and charge exchange collisions at low densities can still be observed in the low-energy part of the Ar^+ IEDFs below $1 \times 10^{11} \text{ cm}^{-3}$. For the corresponding Ar^+ IEDFs at the powered electrode (cf., Fig. C.1-g), scattering is more severe at low densities where a maximum sheath thickness is found which leads to multiple collisions being visible in the low-energy part of the distributions. For decreasing densities, the mean ion energy will shift to lower values and high energy structures are efficiently damped. For 2 MHz frequency argon discharges, the double peaked IEDF structure is maintained in principle (Fig. C.1-h). At higher densities, the low-energy peak of the saddle becomes more pronounced due to less scattering and fewer collisions in the sheath region. In contrast to 60 MHz, the peak separation barely changes for 2 MHz. A similar behaviour is observed for the IEDFs for ions incident at the powered electrode, ions are again scattered into the low-energy part of the IEDF for decreasing plasma densities (Fig. C.1-i). As can be seen from the mean ion energies drawn in Fig. C.1-j and Fig. C.1-k, ion energies at the powered electrode where found to increase at higher rf peak voltages according to the calculated dc bias, energies of ions incident on the ground electrode where found to increase slightly. In contrast to

results for pure 60 MHz discharges, a non-monotonic scaling is observed for a variation of the plasma density in 2 MHz discharges.

Variation of neutral background gas pressure

Variation of the neutral gas background pressure is illustrated in Fig. C.2 in appendix C for constant input parameters of 500 V rf peak voltage, 500 K neutral gas temperature, 2.58 eV electron temperature, $1 \times 10^{10} \text{ cm}^{-3}$ plasma density, and no magnetic field. The mean sheath thickness is found to decrease at higher pressures according to a power law (cf., Fig. C.2-a). The effect of a decreasing sheath thickness is more pronounced at the powered electrode indicating that the discharge becomes more symmetric at high pressures. Note that the thickness for the ground electrode sheath has been multiplied by a factor of five for a better illustration. Similarly to the comparison in the previous section, a comparison of HPSM sheath thickness scalings and those obtained for a collision-free (1.30) and collisional (1.32) sheath is given in Fig. 2.18-a and Fig. 2.18-b, respectively. From the Child-Langmuir approximation, the sheath thickness is found to drop less pronounced (and more linearly) for the electrode sheath, and the ground sheath thickness is found to even increase with pressure (stating a decreasing discharge asymmetry). Quantitatively, HPSM results are found to deviate as much as -47%...-67% (-34%...-55%) for the electrode (ground) sheath thickness from those obtained for the Child-Langmuir approximation. The deviation becomes higher with pressure emphasizing the increasing offset from assumptions for a collision-free sheath. From the Warren approximation, the sheath thickness is found to drop according to a power law for both sheaths. In both cases, the scaling of Warren law and HPSM calculations show good agreement. Quantitatively, HPSM results at 50 mTorr pressure are found to deviate -35% (-36%) for the electrode (ground) sheath thickness from those obtained from the Warren approximation. The difference decreases to -26% (-22%) for electrode (ground) at 600 mTorr pressure, indicating that the Warren law gives more accurate results at higher pressures.

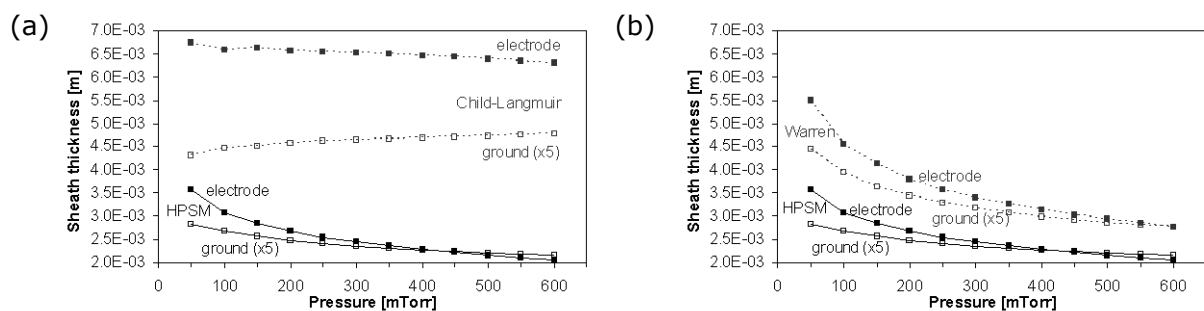


Figure 2.18: Comparison of the sheath thickness in front of powered (solid symbols) and ground electrode (open symbols, values have been multiplied by a factor of five) for a variation of pressure in Ar discharges (a) from HPSM simulations (continuous dark-colored lines) and calculated from Child-Langmuir law (dotted light-colored lines); (b) from HPSM simulations (continuous dark-colored lines) and calculated from Warren law (dotted light-colored lines). Constant input parameters were used: 500 V rf peak voltage, 2.58 eV electron temperature, $1 \times 10^{10} \text{ cm}^{-3}$ electron density, 500 K neutral gas temperature, no magnetic field.

From Fig. C.2-b, the number of ES and CX collisions for Ar^+ ions will exceed 3 and 14 at high pressures in the ground and powered electrode sheath region, respectively. As the pressure increases, the number of Langevin enhanced collisions becomes dominant as well (cf., Fig. C.2-c). Compared to Langevin collisions, the number of ES and CX sheath

collisions is somehow reduced due to the decreasing sheath thickness at higher pressures. Differences in the scaling can be explained by a slightly weaker scaling of the ES cross section with energy ($\sigma_{ES} \sim E^{-p} = E^{-0.195}$) as compared to the Langevin cross section ($\sigma_L \sim E^{-0.5}$). The observation of a more symmetric discharge at higher pressures is supported by the decreasing scaling coefficient (cf., Fig. C.2-e) and also the decreasing dc bias voltage (Fig. C.2-d). The scaling coefficient however decreases by only a maximum of 10% at high pressures for 60 MHz frequency, and even less for 2 MHz frequency. The dc bias voltage is found to be more efficiently reduced at 60 MHz. The origin of the erratic behaviour observed for 60 MHz at low pressures is not understood so far, but is believed to be an artefact from the HPSM calculations.

IEDFs for Ar^+ ions are plotted in Fig. C.2-f to Fig. C.2-i for chosen pressures. Generally, the distributions will become shifted towards lower energies at higher pressures until the high energy peak has disappeared at 300 mTorr. The low energy background increases due to more efficient elastic scattering at higher pressures. Additionally, multiple secondary peaks appear for 60 MHz discharges at low energies which is attributed to resonant charge exchange collisions in the sheath. When rising the pressure, mean ion energies are found to decrease at the powered electrode according to a power law (cf., Fig. C.2-k), and almost linearly at the ground electrode (Fig. C.2-j).

Variation of neutral gas temperature

Variations of the neutral gas temperature are expected to yield similar effects observed for a variation of the pressure, since the neutral gas density is the key parameter here. According to the approximation of an ideal gas, the neutral gas density scales inversely when changing the neutral gas temperature while maintaining a constant pressure in the discharge reactor. Thus, the sheath collisionality is again dictated by the changing neutral density. In principle, the velocity of the thermal particles in the MC calculation change as well - which however can be neglected here. For different reactor pressures, the actual neutral density will always result from a superposition of the impact of gas heating and variation of reactor pressure which complicates a determination of the different discharge parameters discussed here. Results of the influence of the neutral gas temperature are plotted in Fig. C.3 (appendix C) for constant input parameters of 500 V rf peak voltage, 150 mTorr, 2.58 eV electron temperature, $1 \times 10^{10} \text{ cm}^{-3}$ plasma density, and no magnetic field. The mean sheath thickness in Fig. C.3-a shows a square root like dependency on the gas temperature, demonstrating that the discharge becomes more symmetric at lower gas temperatures. As observed for the pressure variation, the sheath thickness facing the powered electrode is more affected than that in front of the ground electrode. The non-monotononic behavior at high gas temperature observed for 60 MHz hints similar inconsistencies for the calculations that were already observed for variation of the neutral gas pressure. Note that the thickness for the ground electrode sheath has been again multiplied by a factor of five. As expected, the number of ES and CX collisions for Ar^+ ions decreases when rising the gas temperature due to the decreased gas density (Fig. C.3-b). Compared to ES and CX collisions, Langevin enhanced collisions are damped more efficiently for higher gas temperatures (cf., Fig. C.3-c), which is again due to the different energy dependence of the collision cross sections. Further, Langevin collisions are observed to yield a higher contribution for the ground electrode sheath region. The dc bias voltage in Fig. C.3-d should develop similarly to the sheath thickness which is confirmed for 2 MHz. The development for neutral gas temperatures exceeding 1000 K for 60 MHz frequency

argon discharges appears to be again an artefact from the HPSM calculations. From the scaling coefficient plotted in Fig. C.3-e, the discharge becomes a bit more symmetric at lower gas temperatures (about 5 % for 60 MHz, even less changes are observed for 2 MHz frequency) which supports the above considerations.

IEDFs for Ar^+ ions plotted in Fig. C.3-f to Fig. C.3-i for different gas temperatures resemble to the distributions observed for a variation of the background gas pressure. From the reduced background gas density at high temperatures, the ions are less scattered and the IEDFs show a distinct high energy tail. At lower gas temperatures the gas density will increase causing the distributions to shift to lower energies, until the high energy peak has disappeared at room temperature. The low energy background increases due to more efficient elastic scattering at higher gas densities. The secondary peak structures at low energies observed for 60 MHz discharges can be explained by resonant charge exchange collisions in the sheath. The mean energies for Ar^+ ions are found to almost linearly increase after traversing the powered electrode sheath when the background gas temperature rises, whereas for ions traversing the low-voltage sheath a more square root like dependency is observed (cf., Fig. C.3-j and Fig. C.3-k). For neutral gas temperatures around 1000°C the mean ion energy for ions incident on the powered electrode has more than doubled compared to initial values close to room temperature. For ions incident on the ground electrode this gain remains below 50%.

Variation of electron temperature

The influence of the electron temperature is illustrated in Fig. C.4 (appendix C) for constant input parameters of 500 V rf peak voltage, 150 mTorr, 500 K neutral gas temperature, $1 \times 10^{10} \text{cm}^{-3}$ plasma density, no magnetic field. When rising the electron temperature, the mean sheath thickness is found to decrease for the powered electrode sheath according to a power law, but to monotonically increase for the ground electrode sheath (Fig. C.4-a). Note that the thickness for the ground electrode sheath has been multiplied by a factor of five for a better illustration. Scalings of the sheath thickness indicate that the discharge becomes more symmetric at high electron temperatures, which is supported by a decreasing dc bias voltage (Fig. C.4-d) and also a decreasing scaling coefficient (Fig. C.4-e). From Fig. C.4-b, the number of ES and CX collisions for Ar^+ ions change slightly according to the different changes observed for the thickness of the respective sheath regions. Langevin enhanced collisions plotted in Fig. C.4-c are found to slightly decrease for both sheaths. From the scaling coefficient in Fig. C.4-e, the discharge becomes efficiently more symmetric at high electron energies and up to 47% decreased values for q are noted. 2 MHz frequency argon discharges are found to only negligibly deviate from 60 MHz argon discharges at high electron temperatures.

The influence of electron temperature on the IEDFs for Ar^+ ions are plotted in Fig. C.4-f to Fig. C.4-i. Ion energies incident on the ground electrode drastically increase while increasing the electron temperature (cf., Fig. C.4-f and Fig. C.4-h), as is expected from the discussed increase of the ground electrode sheath thickness. The high energy peak becomes suppressed and finally vanishes at high electron temperatures which is observed for both 60 and 2 MHz frequency. Secondary peak structures observed at low energies are again attributed to sheath collisions for the relatively high pressure investigated here. In contrast to the IEDF structures at the ground electrode, IEDFs for Ar^+ ions incident on the powered electrode yield only marginal changes. This is also reflected in the calculated mean ion energies which are plotted in Fig. C.4-j and Fig. C.4-k. The mean ion energy increases

almost linearly at the ground electrode when rising the electron temperature, whereas a more square root like increase is observed for the ion energies at the powered electrode. Slight changes in the development of the mean energies are seen when comparing results for 60 MHz and 2 MHz for ions incident at the powered electrode.

Variation of magnetic field

A magnetic field parallel to the surface of the powered electrode can have several impacts on the discharge characteristics. The magnetic field causes a reduced sheath voltage and an increased plasma density, and typically the plasma becomes strongly nonuniform both radially and azimuthally. The nonuniformities are due to $\vec{E} \times \vec{B}$ drifts, where \vec{E} and \vec{B} are the local dc electric and magnetic fields, respectively. Beyond that, a significant fraction of the total rf discharge voltage can be dropped across the plasma bulk at high magnetic fields.

When considering diffusion in the presence of magnetic and electric field gradients, the electron mobility can be strongly reduced across the electric field yielding a nonambipolar flux in cross-field directions [20]. The magnetic field can further confine the electrons to a small volume near the electrode, which leads to an increased ion flux to the powered electrode. The electrons which are forced to gyrating motions will collide with the sheath edge and gain energy during the coherent motions. The coherent energy gain is terminated upon collisions with gas neutrals. From collisions, the electron changes its directions, and hence also the center of gyration. Deriving the perpendicular mobility and diffusion coefficients gives [20]

$$\mu_{\perp} = \frac{\mu_{\parallel}}{1 + (\omega_c \tau_m)^2} = \frac{\mu_{\parallel}}{1 + \left(\frac{|q|B_0}{m v_m}\right)^2} \quad (2.37)$$

and

$$D_{\perp} = \frac{D_{\parallel}}{1 + (\omega_c \tau_m)^2} = \frac{D_{\parallel}}{1 + \left(\frac{|q|B_0}{m v_m}\right)^2} \quad (2.38)$$

with the cyclotron frequency ω_c , and the electron collision rate for momentum transfer $v_m = \sigma_m n_g v$. For argon, the elastic momentum transfer cross section σ_m can be adopted from the elastic momentum transfer electron collision cross section set published in [224]. The factor $\omega_c \tau_m$ is an important measure in magnetic confinement, where $\omega_c \tau_m \gg 1$ indicates a significant reduction of the electron mobility (or a strong retardation of diffusion). From HPSM calculations performed here, this factor is calculated to range between 1.79 and 26.85. As can be seen from the plot in Fig. 2.19-a, the resulting ratio between perpendicular and parallel mobility (or diffusion) is found to drop significantly. The ratio for cyclotron frequency and collision frequency is plotted in Fig. 2.19-b, where the cyclotron frequency is given by

$$f_{ce,i} = \frac{qB}{2\pi m_{e,i}} \quad (2.39)$$

and the collision frequency can be calculated from

$$v = n_g \sigma_m \sqrt{\frac{2E}{m}}. \quad (2.40)$$

Clearly, electrons are well confined perpendicular to the magnetic field for already low magnetic flux densities, whereas ions are not well confined in the weakly magnetic discharges investigated here.

As discussed above, an increased magnetic field parallel to the surface of the powered electrode is expected to yield a decreased dc bias voltage due to a sheath thickness reduction at higher densities. The influence of the magnetic field is illustrated in Fig. C.5 in appendix C for constant input parameters of 500 V rf peak voltage, 150 mTorr, 500 K neutral gas temperature, 2.58 eV electron temperature, and $1 \times 10^{10} \text{ cm}^{-3}$ plasma density. The mean sheath thickness in Fig. C.5-a is observed to strongly decrease in pure 60 MHz frequency argon discharges for both powered and ground electrode sheaths. Only slight changes are observed for pure 2 MHz discharges, the powered electrode sheath is found to decrease whereas the ground electrode sheath is even (marginally) increasing. From these observations, 60 MHz discharges will become highly symmetric at higher magnetic fields. This is indeed observed from the calculated dc bias voltage (Fig. C.5-d) as well as the scaling factor (Fig. C.5-e). According to these results, the 60 MHz discharges become almost completely symmetric at high magnetic fields (up to 92% decreased values for q). In contrast, the asymmetry of pure 2 MHz discharges is only negligibly changing within the investigated parameter space (up to 6% decreased values for q). Compared to the discussed sheath thicknesses, the number of ES, CX and Langevin collisions in Fig. C.5-b and Fig. C.5-c is found to develop similarly. Applying magnetic fields to 60 MHz argon discharges, the number of ES and CX collisions in the sheath is efficiently reduced from above 4 without magnetic field to about 1 for magnetic fields exceeding 100 G. These findings also explain the Ar^+ IEDFs observed at the different electrodes. At higher magnetic fields the ion energies are efficiently reduced at both electrodes for pure 60 MHz, from the low-energy part of the distributions secondary structures which are due to collisions and elastic scattering in the sheath will disappear at high magnetic fields (cf., Fig. C.5-f and Fig. C.5-g). Basically, no changes in the distributions are observed for a variation of the magnetic field in 2 MHz discharges (cf., Fig. C.5-h and Fig. C.5-i). According to the described influence of the magnetic field, mean ion energies for Ar^+ ions exhibit a drastic decrease at even quite low magnetic fields for 60 MHz discharges, whereas for 2 MHz discharges ion energies remain virtually unaffected at both electrodes (cf., Fig. C.5-j and Fig. C.5-k).

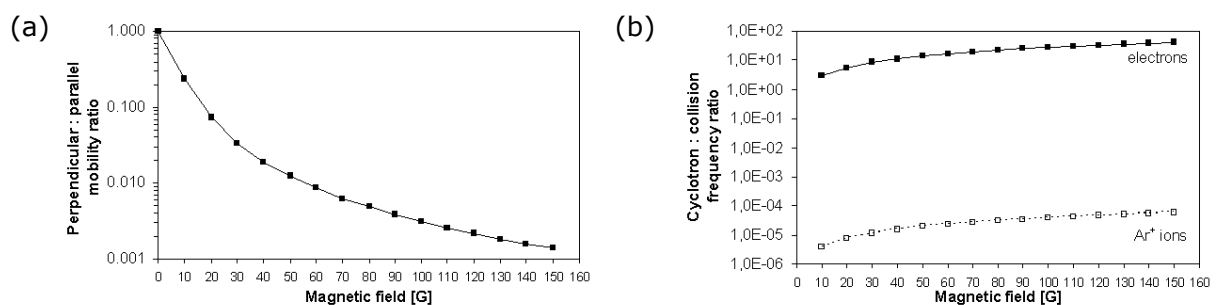


Figure 2.19: (a) Ratio between perpendicular and parallel electron mobility according to equation (2.37); (b) ratio between cyclotron and collision frequency according to equations (2.39) and (2.40) for electrons (continuous line with solid symbols) and Ar^+ ions (dotted line with open symbols). Constant HPSM input parameters were used: 500 V rf peak voltage, 2.58 eV electron temperature, $1 \times 10^{10} \text{ cm}^{-3}$ electron density, 500 K neutral gas temperature, no magnetic field.

Influence of frequency mix

For the 60+2 MHz dual frequency discharges investigated in this work it is also important to gain understanding of different mixed frequency discharges. Up to now, only very limited data about the influence of mixed frequency discharges is reported in literature. Numerical investigations of conventional 13.56 MHz single frequency and 27+2 MHz dual frequency Ar/CF₄/N₂ discharges (0.8/0.1/0.1 ratio) using an one-dimensional PIC/MC model were reported in [24,98]. As a result, a notably wider ion bombardment energy range was calculated for the hf+lf dual frequency scheme. Furthermore, the IEDFs in the hf discharges were found to only slightly depend upon the phase of the rf cycle, whereas the IEDF was severely modulated during the lf cycle in hf+lf dual frequency discharges.

For the calculations performed here, a power split factor is defined such that the 60 MHz frequency source is driven with the power split factor times the overall power calculated from the input parameters. A power split factor of "0" thus would correspond to a pure 2 MHz discharge, whereas "1" would correspond to a pure 60 MHz discharge. Different 60+2 MHz mixed discharges were investigated for constant input parameters of 500 V rf peak voltage, 150 mTorr, 500 K neutral gas temperature, 2.58 eV electron temperature, $1 \times 10^{10} \text{ cm}^{-3}$ plasma density, no magnetic field. The mean sheath thickness in Fig. C.6-a (appendix C) shows a hat-shaped development for the electrode sheath, and further a concave-like dependency for the ground electrode sheath (multiplied by a factor of six). The sheath thicknesses as a function of the frequency mix appear to be approximately symmetric about a power split factor of 0.5. The thickness of the ground electrode sheath remains constant for different 60+2 MHz mixes, a higher sheath thickness is obtained for pure 2 and 60 MHz discharges. ES, CX and Langevin enhanced collisions in the sheath are not found to change much while scaling according to the discussed sheath thicknesses (cf., Fig. C.6-b and Fig. C.6-c). The dc bias in Fig. C.6-d is found to exhibit a hat shaped structure as discussed above, with remarkably increased values for all frequency mixes, the maximum is found for a power split factor of 50%. The scaling exponent q as a function of different mixes is found to be a crooked function (Fig. C.6-e), the highest and lowest asymmetry is found at 40-50% 60 MHz and 100% 2/60 MHz, respectively (up to 12% changes for the values of q). From the Ar⁺ IEDFs at the ground electrode (Fig. C.6-f) it is noticed that a splitting of the bimodal structure can be resolved for even small contributions of the 2 MHz frequency. Increasing the contribution of 2 MHz yields a broadening of the IEDF and the low-energy peak of the saddle becomes suppressed as a result of the increased high energy tail. Due to the relatively high pressure of 150 mTorr, the IEDFs at the powered electrode are not observed to differ considerably (Fig. C.6-g). This can be also seen from the calculated mean ion energies where changes for different frequency mixes remain within an approximately 10% range (Fig. C.6-h and Fig. C.6-i).

2.5.2 Hydrogen bromide discharges

From HPSM simulations of HBr discharges, the following calculated parameters will be discussed:

- sheath thickness in front of powered and ground electrode;
- averaged number of elastic scattering (ES) processes for ions in the sheath regions;
- averaged number of charge exchange (CX) collisions for ions in the sheath regions;
- averaged number of Langevin collisions for ions in the sheath regions;
- dc bias voltage;

- averaged scaling exponent q to characterize the discharge asymmetry from (1.6);
- Br^+ , HBr^+ , H_2^+ , Br_2^+ IEDFs at ground and powered electrode;
- Br^+ , HBr^+ , H_2^+ , Br_2^+ mean energies at ground and powered electrode.

Variation of rf peak voltage and electron density

Results of a variation of rf peak voltage and electron density can be found in Fig. D.1 in appendix D, other input parameters were held constant at 150 mTorr background neutral gas pressure, 500 K neutral gas temperature, 6.32 eV electron temperature, and no magnetic field was applied. Unlike for argon discharges where the electron density equals the ion density $n_e = n_{i+}$ and the approximation of a single ion discharge (consisting of Ar^+ ions) is valid, molecular electronegative HBr discharges consist of multiple positive and negative ion species yielding $n_{i-} + n_e = n_{i+}$. The correct degree of electronegativity for the HBr discharges investigated here remains unknown and would require a combined application of reliable optical methods, like AAS (Atomic Absorption Spectroscopy, e.g., LAS - Laser Absorption Spectroscopy, or CARS - Cavity Ring-Down Spectroscopy) and LIF (Laser-Induced Fluorescence) spectroscopy [13]. From [31], an electronegativity on the order of 10 is assumed to be reasonable for electronegative HBr. Electron densities in HBr discharges are found to be about one order of magnitude lower as compared to typical values for argon discharges [214]. Combining these findings with reasonable estimations of the electronegativity in HBr gives ion densities that are about equal to those for argon. The HPSM does not consider changes due to electronegativities deviating from one, hence the electron density used as an input for the sheath model must be about one order of magnitude higher than typically observed for HBr discharges, i.e. on the order of about $1 \times 10^{10} \text{cm}^{-3}$. Nevertheless, the electron (ion) density was varied from very low values of $1 \times 10^8 \text{cm}^{-3}$ to include discharge conditions of very low (ion) densities as well.

As observed for modeling argon discharges, the mean sheath thickness is found to increase with rf peak voltage and exponentially decrease at higher plasma (ion) densities in HBr discharges (cf., Fig. D.1-a). Differences between the two applied frequencies were not observed to be significant, hence results are shown only for 60 MHz frequency HBr discharges for the powered (solid symbols with solid lines) and the ground electrode sheath (open symbols with dotted lines). Compared to typical sheath thicknesses obtained for argon discharges, sheath thicknesses are observed to be up to 20% higher/lower for the ground/power electrode sheath in HBr discharges with (ion) densities of $1 \times 10^{10} \text{cm}^{-3}$. For a plasma (ion) density ranging between $5 \times 10^9 \text{cm}^{-3}$ and $1 \times 10^{11} \text{cm}^{-3}$ (comparable to argon, see above), a minimum sheath thickness is found for 100 V rf peak voltage and $1 \times 10^{11} \text{cm}^{-3}$ plasma density yielding about 157 μm in front of the ground and 321 μm in front of the powered electrode, whereas a maximum sheath thickness is observed for 900 V rf peak voltage and $5 \times 10^9 \text{cm}^{-3}$ plasma density resulting in 883 μm at ground and 4.19 mm at the powered electrode. At very low plasma (ion) densities, quite high sheath thicknesses on the order of cm can be obtained, which imply that the gap between the electrodes can be predominantly covered by the respective sheaths, while the plasma bulk is strongly confined within a very small area between both electrodes. At (ion) densities of $1 \times 10^{10} \text{cm}^{-3}$, slightly less sheath collisions are experienced in HBr discharges as compared to argon. Considerably high sheath thicknesses at low (ion) densities will give rise to the number of ES, CX and Langevin enhanced collisions in the sheath. Several ES collisions are already observed in the ground electrode sheath (Fig. D.1-b), the number of ES events can even exceed 20 at low densities in the powered electrode sheath. CX collisions are found

to be considerably lower if compared to ES collisions (Fig. D.1-c), and found to be even similar to the number of Langevin collisions (Fig. D.1-d). This can be easily explained by a rather incomplete implementation of CX cross sections for interactions of the relevant molecules (cf., Table B.1). The incomplete implementation of relevant cross sections is due to a lack of data for HBr relevant molecules from the literature, limitations of the ab initio calculations to determine scattering parameters for molecules, and also neglecting non-resonant collisions (due to their relatively low importance in general). The dc bias voltage in Fig. D.1-e is found to change for different rf peak voltages but remains rather unchanged for different plasma densities at 2 MHz frequency. Nonlinear deviations are observed for 60 MHz frequency, where the average sheath electric field of the oscillating sheath is somewhat different from the 2 MHz case. Compared to argon, the dc bias voltage is slightly lower and corresponds to about 65-85% of the rf peak voltage (for 2 MHz). From the higher ground electrode sheath thickness and lower powered electrode sheath thickness, HBr discharges are observed to be more symmetric than argon discharges (cf., Fig. D.1-f). The discharge becomes more symmetric at low rf peak voltages and further at low plasma densities. Again, strong nonlinearities are observed for 60 MHz frequency.

IEDFs for different ion species in HBr discharges are plotted in Fig. D.1-g1 to Fig. D.1-j4 for 100 V rf peak voltage and different plasma densities, as well as different frequencies for both ground and powered electrode sheaths. From Fig. D.1-g1, the double peak remains unresolved for Br^+ IEDFs at 60 MHz frequency as a result of the ion high mass. For very low densities, ions are efficiently scattered into the low-energy part of the IEDF due to the high sheath thicknesses obtained under these conditions, which result in a high degree of scattering and charge exchange collisions. For HBr^+ IEDFs plotted Fig. D.1-g2, the high energy peak becomes efficiently damped at low densities with a higher background contribution at low energies which is due to scattering. Unlike for Br^+ ion, an exponentially decreasing function at high ion energies is not obtained here. This reflects the fact that charge exchange collision cross sections for HBr^+ molecules in the sheath are not considered in the current model as they remain unknown. A broad splitting of the two peaks of the bimodal structure is observed for H_2^+ ions at 60 MHz and for typical densities (cf., Fig. D.1-g3), since light hydrogen molecules can correspond the sheath oscillations even at comparably high frequencies. Contribution of elastic scattering and collisions are very low which again appears to be due to an insufficient description of the collisional processes for H_2^+ molecules in the sheath. Br_2^+ IEDFs for 60 MHz frequency at different densities in Fig. D.1-g4 exhibit similar shapes as observed for HBr^+ . Ion energy distributions at the powered electrode for 60 MHz frequency are found to follow similar tendencies for a variation of the plasma (ion) density as those explained for the ground electrode (Fig. D.1-h1 to Fig. D.1-h4). At high densities, bimodal structures are observed for the different ions incident on the powered electrode. H_2^+ ion energies appear evenly distributed over a broad range which reflects the fact that control over the energies of light ions in molecular discharges can not be achieved to a comparably high extent observed for heavy ion species. IEDFs at 2 MHz frequency are observed to yield the expected double peak structures (Fig. D.1-i1 to Fig. D.1-j4) since all ions are able to respond to the slowly oscillating sheath electric field for 2 MHz frequency. The saddle is washed out at lower densities due to a high contribution of elastic scattering and ion-neutral collisions. H_2^+ IEDFs remain about unchanged for different densities at 60 MHz as well as 2 MHz frequency. The peak separation of the bimodal IEDF structure is generally observed to be broadened further in the powered electrode sheath at 2 MHz. As can be seen from the mean

ion energies drawn in Fig. D.1-k1 to Fig. D.1-l4, ion energies at the powered electrode were found to increase at higher rf peak voltages according to the calculated dc bias. Energies of ions incident on the ground electrode were found to increase slightly. These findings are in agreement with the observations for Ar discharges described in the previous section. Again, different scalings are observed to result for pure 60 MHz and 2 MHz discharges. From Fig. D.1-k2 to Fig. D.1-k4, ion energies for HBr^+ , H_2^+ , Br_2^+ ions hitting the ground electrode are found to be only negligibly influenced by the plasma density. This is in contrast to the strong scaling of the mean Br^+ ion energy with the plasma density plotted in Fig. D.1-k1. As explained above, these findings support the rather unsatisfactory current implementation of collision parameters for the different species. Similar scalings of the mean ion energy as a function of the plasma (ion) density are however found for the three most important species in HBr discharges (Br^+ , HBr^+ , Br_2^+) at the powered electrode (cf., Fig. D.1-l1 to Fig. D.1-l4). H_2^+ ions are only negligibly influenced due to their comparably low occurrence and hence low probability of collisions.

Variation of neutral background gas pressure

Results for a variation of the neutral gas background pressure are plotted in Fig. D.2 (in appendix D) for constant input parameters of 500 V rf peak voltage, 500 K neutral gas temperature, 6.32 eV electron temperature, $1 \times 10^{10} \text{ cm}^{-3}$ plasma density, and no magnetic field. Similar to the observations for argon discharges, the mean sheath thickness is found to decrease at higher pressures according to a power law (cf., Fig. D.2-a). Note that the thickness for the ground electrode sheath has been multiplied by a factor of four for better illustration. From Fig. D.2-b, the number of ES for relevant ions will exceed 2 and 8 at high pressures in the ground and powered electrode sheath region, respectively. From Fig. D.2-c, only few CX collisions are recorded, reasons were given above. As the pressure increases, the number of Langevin enhanced collisions increases as well (cf., Fig. D.2-d). Compared to Langevin collisions, the number of ES and CX sheath collisions is observed to less efficiently increase by the decreasing sheath thickness at higher pressures. This is qualitatively in agreement with results obtained for argon, and differences in the scaling can be explained again by a slightly weaker scaling of the ES cross section with energy ($\sigma_{\text{ES}} \sim E^{-p} = E^{-0.177}$) as compared to the Langevin cross section ($\sigma_{\text{L}} \sim E^{-0.5}$), cf., Table B.1. A slightly more symmetric discharge is found at higher pressures, as indicated by the decreasing scaling coefficient (Fig. D.2-f) and also the decreasing dc bias voltage (Fig. D.2-e) for 2 MHz frequency. The scaling coefficient changes by a maximum of 10% at high pressures for 2 MHz frequency. The clear trend observed for 2 MHz is not reproduced for 60 MHz frequency, where the symmetry develops non-monotonically but hardly changes quantitatively. This hints inconsistencies of the current version of the HPSM simulator (presumably in the FD part), which however could not be identified during this work. Qualitatively the same observations are made for the dc bias voltage (Fig. D.2-e).

IEDFs for the various ion species are plotted in Fig. D.2-g1 to Fig. D.2-j4 for different pressures. The ion energy distributions become shifted towards lower energies by increasing the pressure until the high energy peak has disappeared at 300 mTorr for Br^+ (Fig. D.2-g1). Other ion species are found to exhibit also more pronounced elastic scattering in the sheath at higher pressures, however this occurs to a considerably fewer extent than is observed for Br^+ . The maximum energy is found to slightly increase for ions incident on the ground electrode, whereas this is not the case at the powered electrode. Interestingly, the fine structure of the saddle at high energies is resolved for ions incident

on the powered electrode (cf., Fig. D.2-h1 to Fig. D.2-h4). The distinct peaks are efficiently damped and broadened at high pressures, as can be observed in detail for H_2^+ IEDFs for 60 MHz frequency in Fig. D.2-h3. The low-energy peak of the bimodal structure obtained for 2 MHz at the ground electrode appears preferred over the high energy peak (Fig. D.2-i1 to Fig. D.2-i4). This can be explained by a higher probability of scattering and collisions when ions enter and traverse the sheath at its maximum extent. The Br^+ ion mean energy (Fig. D.2-i1) is efficiently reduced at high pressures due to multiple collisions and a high probability of elastic scattering. A higher influence of scattering is also noticed in the low energy part of the HBr^+ and Br_2^+ IEDFs (Fig. D.2-i2 and Fig. D.2-i4), whereas the low energy part of the H_2^+ IEDFs remains unchanged (Fig. D.2-i3). The low-energy peak of the saddle shaped IEDF structure must not necessarily be favored over the high energy peak, as can be seen from IEDFs obtained after traversing the sheath in front of the powered electrode (Fig. D.2-j2 and Fig. D.2-j4). This could be an effect of the non-sinusoidal nature of the oscillating rf sheath. From the mean ion energies plotted in Fig. D.2-k and Fig. D.2-l, Br^+ , HBr^+ and Br_2^+ ion energies are found to decrease when rising the pressure as is expected according to the enhanced collisionality in both sheaths. Again, Br^+ energies are most efficiently reduced at high pressures which is according to the more complete implementation of cross sections for scattering and charge exchange. Energies for H_2^+ ions are hardly influenced by the variation of pressure and exhibit even a slight increase in the intermediate pressure regime.

Variation of neutral gas temperature

Variations of the neutral gas temperature at a fixed pressure will change the neutral gas density, and hence influence the sheath collisionality. Results of the influence of the neutral gas temperature are plotted in Fig. D.3 (in appendix D) for constant input parameters of 500 V rf peak voltage, 150 mTorr, 6.32 eV electron temperature, $1 \times 10^{10} \text{ cm}^{-3}$ plasma density, and no magnetic field. The mean sheath thickness in Fig. D.3-a shows a square root like dependency on the gas temperature, demonstrating that the discharge becomes more symmetric at lower gas temperatures. As observed for the pressure variation, the sheath thickness facing the powered electrode is more affected than that in front of the ground electrode (please note the thickness for the ground electrode sheath has been again multiplied by a factor of four). The non-monotononic development at high gas temperatures observed for 60 MHz hints similar inconsistencies for the calculations in the FD part of the HPSM simulator that were already observed for variation of the neutral gas pressure. As expected, the number of ES, CX and Langevin collisions for ions in the sheaths of HBr discharges decreases when rising the gas temperature due to the decreased gas density (cf., Fig. D.3-b to Fig. D.3-d). The dc bias voltage in Fig. D.3-e should develop according to the changing sheath thickness, which is only confirmed for 2 MHz frequency discharges. Strong deviations of the expected behavior are observed for calculations during applying 60 MHz. From the scaling coefficient plotted in Fig. D.3-f, the discharge appears to become slightly more symmetric at lower gas temperatures, effects however remain low (about 3 % for 2 MHz).

IEDFs for the different ions plotted in Fig. D.3-g1 to Fig. D.3-j4 for different gas temperatures are found to follow similar tendencies described for the distributions at different background gas pressures. From the decreased gas density at high temperatures, the ions are less scattered and the IEDFs show a distinct high energy tail. At lower gas temperatures the gas density will increase causing the distributions to shift to lower

energies and the high energy peak structure is efficiently damped. The low energy background increases due to more efficient elastic scattering at higher gas densities. From the mean ion energies plotted in Fig. D.3-k and Fig. D.3-l, energies of Br^+ ions are efficiently reduced by decreasing the gas temperature over the whole temperature range investigated, whereas ion energies of the further investigated species are only affected at low temperatures (300-600 K), which corresponds to higher neutral gas densities.

Variation of electron temperature

The influence of the electron temperature is illustrated in Fig. D.4 (in appendix D) for constant input parameters of 500 V rf peak voltage, 150 mTorr, 500 K neutral gas temperature, $1 \times 10^{10} \text{ cm}^{-3}$ plasma density, no magnetic field. Comparable to argon, the mean sheath thickness is found to decrease for the powered electrode sheath (according to a power law), and to monotonically increase for the ground electrode sheath when rising the electron temperature (cf., Fig. D.4-a). Note that the thickness for the ground electrode sheath has been multiplied by a factor of six for a better illustration. Scalings of the sheath thickness indicate that the discharge becomes more symmetric at high electron temperatures, which is indeed supported by a decreasing dc bias voltage (Fig. D.4-e) and the decreasing scaling coefficient q from Fig. D.4-f. The number of ES and CX collisions change slightly according to the different changes observed for the thickness of the respective sheath regions (Fig. D.4-b and Fig. D.4-c). Langevin enhanced collisions plotted in Fig. D.4-d are found to slightly decrease for both sheaths. From the scaling coefficients in Fig. D.4-f, 60 MHz and 2 MHz frequency HBr discharges are found to change similarly, becoming more symmetric at high electron temperatures (up to about 50% decreased values for q).

The influence of electron temperature on the IEDFs of the different ions are plotted in Fig. D.4-g1 to Fig. D.4-j4. As already observed for argon, ion energies incident on the ground electrode drastically increase while increasing the electron temperature (cf., Fig. D.4-g1 to Fig. D.4-g4, and Fig. D.4-i1 to Fig. D.4-i4), as is expected from the discussed increase of the ground electrode sheath thickness. The high energy peak is efficiently suppressed and finally disappears at high electron temperatures which is observed for both 60 and 2 MHz frequency. Increased background contributions at low energies are attributed to elastic scattering and sheath collisions for the relatively high pressure investigated here. In contrast to the IEDF structures at the ground electrode, IEDFs for Br^+ , HBr^+ , H_2^+ and Br_2^+ ions incident on the powered electrode yield negligible changes (cf., Fig. D.4-h1 to Fig. D.4-h4, and Fig. D.4-j1 to Fig. D.4-j4). This can be seen from the calculated mean ion energies plotted in Fig. D.4-k and Fig. D.4-l. Ion energies at the ground electrode increase almost linearly when rising the electron temperature. In contrast, considerably less changes with a slight (square root like) increase are noted for the ion energies at the powered electrode. Different frequencies further reveal slight differences for the calculated mean ion energies as a result of the differences in the average sheath electric fields.

Variation of magnetic field

Results of a variation of the magnetic field in HBr discharges are illustrated in Fig. D.5 (in appendix D) for constant input parameters of 500 V rf peak voltage, 150 mTorr, 500 K neutral gas temperature, 6.32 eV electron temperature, and $1 \times 10^{10} \text{ cm}^{-3}$ plasma density. The mean sheath thickness in Fig. D.5-a is found to strongly decrease in 60 MHz frequency discharges for both powered and ground electrode sheaths, until a minimum is reached

above 50 G. For 2 MHz frequency, the sheath thickness is found to decrease monotonically for the powered electrode sheath, above 70 G also for the ground electrode sheath. From these results, 60 MHz discharges will become symmetric at even low magnetic fields. This is supported by the sharp drop in the dc bias voltage which becomes negligible above 50 G (Fig. D.5-e), as well as by the scaling factor which approaches zero corresponding to an ideally symmetric discharge (Fig. D.5-f). For the same set of parameters, 2 MHz discharges strongly become more symmetric by increasing the magnetic field (the scaling coefficient q changes up to 60%). Compared to the discussed sheath thicknesses, the number of ES, CX and Langevin collisions in Fig. D.5-b to Fig. D.5-d is found to develop similarly. The strong scaling of sheath parameters for HBr is in contrast to argon discharges (cf., Fig. C.5) where less pronounced changes were observed (especially in case of 2 MHz frequency). The differences result from different electron collision mechanisms used as input for modeling of both gases. Compared to argon, slightly lower electron-neutral collision cross sections are assumed and less electron-neutral collisions are effectively modeled for HBr which is simply due to the current lack of detailed knowledge for a more appropriate collision model. From a lower collisionality, the electrons will be much stronger confined when applying magnetic fields. As an example, the electron mobility is reduced more effectively from initially higher mobilities in case of HBr as compared to Ar discharges (e.g., $\mu_{\text{Ar}}(0 \text{ G}) = 1.81 \times 10^3 \text{ m}^2/\text{Vs}$, $\mu_{\text{HBr}}(0 \text{ G}) = 2.16 \times 10^4 \text{ m}^2/\text{Vs}$, $\mu_{\text{Ar}}(40 \text{ G}) = 34.0 \text{ m}^2/\text{Vs}$, $\mu_{\text{HBr}}(40 \text{ G}) = 2.9 \text{ m}^2/\text{Vs}$).

Applying magnetic fields to 60 MHz HBr discharges reduces the number of collisions in the sheath which is due to an effective reduction of the sheath thickness. At higher magnetic fields, the ion energies are drastically reduced at both electrodes for both 60 MHz and 2 MHz frequency, as can be seen from the IEDFs plotted in Fig. D.5-g1 to Fig. D.5-j4. Since positions of the low-energy peak of the bimodal structures remain about the same for the different conditions investigated, the reduced energy yields a marked reduction of the peak splitting. According to the described influence of the magnetic field, mean ion energies for all ion species exhibit a drastic decrease at very low magnetic fields (10-30 G) for 60 MHz discharges, whereas for 2 MHz discharges ion energies are reduced more noticeably at high magnetic fields above 60 G (cf., Fig. D.5-k and Fig. D.5-l).

Influence of frequency mix

Variation of different 60+2 MHz mixed dual frequency discharges were investigated for constant input parameters of 500 V rf peak voltage, 150 mTorr, 500 K neutral gas temperature, 6.32 eV electron temperature, $1 \times 10^{10} \text{ cm}^{-3}$ plasma density, no magnetic field. The mean sheath thickness is plotted in Fig. D.6-a (in appendix D) showing a convex scaling for the electrode sheath and a concave scaling for the ground electrode sheath (multiplied by a factor of four) as a function of the power split factor. The sheath thicknesses as a function of the frequency mix appear to be approximately symmetric about a power split factor of 0.4-0.5. The thickness of the ground electrode sheath remains constant for different 60+2 MHz mixes, a higher sheath thickness is obtained for pure 2 and 60 MHz discharges, whereas these points yield the lowest sheath thicknesses in front of the powered electrode. ES, CX and Langevin enhanced collisions in the sheath are not found to change much while scaling according to the discussed sheath thicknesses (cf., Fig. D.6-b to Fig. D.6-d). The dc bias in Fig. D.6-e shows significantly increased values for all frequency mixes, the maximum is found for a power split factor of 40-50%. The scaling exponent q as a function of different mixes in Fig. D.6-f is found to agree with above

observations, the highest and lowest asymmetry is found at 40-50% 60 MHz and 100% 2/60 MHz, respectively (up to 15% changes for the values of q).

From the IEDFs for different ions incident on the ground electrode (Fig. D.6-g1 to Fig. D.6-h4) it is noticed that a splitting of the bimodal structure can be resolved for the heavy ions Br^+ , HBr^+ and Br_2^+ for even small contributions of the 2 MHz frequency. Increasing the contribution of 2 MHz yields a broadening of the IEDF and the low energy peak of the saddle becomes suppressed as a result of the increased high energy tail (cf., Fig. D.6-g3). Br^+ IEDFs at the powered electrode (Fig. D.6-h1) are not observed to differ considerably, as was already observed for Ar^+ in 60+2 MHz argon discharges. In contrast, IEDFs for HBr^+ , H_2^+ and Br_2^+ exhibit reductions in the maximum ion energy and the peak splitting by increasing the contribution of 60 MHz frequency (cf., Fig. D.6-h2 to Fig. D.6-h4). Calculated mean ion energies (Fig. D.6-i and Fig. D.6-j) are observed to scale according to the sheath thickness and number of collisions for the respective sheath as a function of different frequency mixes, for Br^+ remaining within an approximately 10% range as was also observed for Ar^+ in dual frequency argon discharges. In contrast, mean ion energies for HBr^+ , H_2^+ and Br_2^+ are subject to major changes of up to 20-30% for different frequency mixes.

2.5.3 Summary and discussion

Ion densities in both electropositive argon and electronegative hydrogen bromide discharges are comparable assuming an electronegativity of about 10 for HBr. Compared to an ionized Ar noble gas, a higher sheath thickness can be obtained in molecular HBr discharges. This yields a higher number of sheath collisions for HBr and further to a more pronounced scattering of ions in the sheath region.

Besides differences in the collision cross sections, the abundance of the respective molecular species determines the probability of collisions in the sheath region. Additionally, non-resonant collisions will contribute further to scattering processes in HBr molecular discharges, whereas in pure argon discharges only resonant collisions can occur. Compared to argon, the dc bias voltage is observed to be (slightly) lower in HBr discharges. Furthermore, HBr discharges typically appear to be more symmetric than argon discharges. For both types of discharges, ion energies at the electrodes were found to generally increase with rf peak voltage according to the differences in the calculated dc bias, and further with plasma density. Also, a reduction of the discharge pressure is suitable to efficiently increase the mean ion energy. Decreasing the pressure reduces the number of collisions (ES, CX) and off-axis scattering in both sheath regions. The pressure reduction gives also rise to an increased sheath width. As a result, the angular distribution becomes more anisotropic in forward direction, and ions can gain more energy on their way through the sheath region. Since the discharge asymmetry increases as well for high plasma densities, high rf peak voltages, and somewhat also for reduced pressures, the net energy gain becomes higher for ions incident at the substrate. Ion energies of species with a low mass (e.g., hydrogen molecules) usually appear evenly distributed over a broad range. This reflects the fact that control over the energy of light ions in molecular discharges can not be achieved to a comparably high extent observed for heavy ion species. In practice, these light ions may however only play a minor role during etching. For the discussed case of HBr, the higher sheath thickness observed at high rf peak voltage and/or electron densities and/or low pressures could potentially lead to a collapsing discharge for small

electrode-electrode distances, as for the small gap used in the experimental setup of the present work.

From comparison of HPSM results for argon with those obtained from the two limits of a collisionless and a collision-dominated sheath, the qualitative scaling agrees very well with simplified assumptions for a collision-dominated sheath. Quantitatively, differences between HPSM calculations and results obtained from the Warren law were found to remain within 20-40%, where deviations become smaller at higher pressures.

Increasing the mean electron temperature was found to yield a reduced sheath width in front of the powered electrode and hence reduced ion energies at this electrode. In real discharges, the mean electron temperature might change due changes in the EEDF caused by variations of pressure and rf voltage (or applied power level), for example. Discharge operation will lead to increasing neutral gas temperatures, which in turn affects the neutral gas density. The increased gas temperature will result in an enhanced ion energy at the powered electrode by a factor of about 2, whereas the gain in ion energy at the ground electrode remains below 50% compared to initial values close to room temperature.

Application of (weak) magnetic fields was shown to decrease both sheath thickness and dc bias voltage. This in turn influences the IEDF structure and reduces the mean ion energy. Furthermore, the magnetic field tends to strongly reduce the discharge asymmetry. In particular, this was observed for 2 MHz HBr discharges which became markedly more symmetric when increasing the magnetic field. In contrast, the asymmetry changed less dramatically for argon (especially for 2 MHz excitation). Different scaling of sheath parameters was found to originate from different electron collision mechanisms used as input when modeling of both gases. As a result, less electron-neutral collisions were effectively modeled for HBr. Compared to argon, this yields a more pronounced electron confinement during application of magnetic fields. Whereas for 60 MHz discharges mean ion energies for all ion species generally exhibit a strong decrease for even low magnetic fields, for 2 MHz discharges ion energies become reduced more noticeably at higher magnetic flux densities. Reduction of the electron mobility by a magnetic field was demonstrated from calculations. Whereas electrons are well confined (perpendicular to the magnetic field) for already low magnetic flux densities, ions are not well confined in the weakly magnetic discharges investigated here.

The influence of different 60+2 MHz frequency mixes reveals a distinct splitting of the bimodal structure of the different ion species for even small contributions of the 2 MHz frequency. Increasing the contribution of 2 MHz yields a broadening of the IEDF and the low energy peak of the saddle becomes suppressed as a result of the increased high energy tail.

Both qualitative differences in the IEDF structure as well as quantitative differences in the scaling of the investigated parameters appear for the different ion species in HBr. Those deviations can be explained by a currently insufficient description of the collisional processes for the different molecular species in HBr discharges. The incomplete implementation of relevant cross sections is due to a lack of data for HBr relevant molecules from the literature, limitations of the ab initio calculations to determine scattering parameters for molecules, and neglecting non-resonant collisions.

3 Complementary diagnostic techniques

3.1 In situ plasma diagnostic techniques

3.1.1 Mass spectrometry for plasma flux analysis

Mass spectrometry is a well-known technique for characterization and control of vacuum-based processes, such as dry etching and sputtering. If the process pressure exceeds about 10^{-5} Torr, differential pumping must be implemented between the reactor volume and the quadrupole mass spectrometer. In that case, the mass spectrometer is placed in a separate enclosure with its own vacuum pump, where connection to the reactor volume is provided by an aperture of appropriate size, or a leak valve. Since the EQP mass spectrometer is installed at the reactor that the ionizer is placed on a line-of-sight with the plasma, the setup allows for detection of condensable and reactive species traversing the aperture without colliding with any surfaces. The flux analysis technique samples only reaction products that result from interactions in the vicinity of the extraction orifice [225].

As was reported in [144], there can be a significant contribution of the background gas pressure which is superimposed on the beam (i.e., the line-of-sight) component. The mass spectrometer accepts only a small solid angle of the species sampled from the aperture between discharge reactor and mass spectrometer chamber, which constitutes the beam component of the species entering the ionizer. For the EQP setup discussed here, this solid angle is about 3 degrees. Any species sampled from the plasma that are not within this solid beam angle, enter the mass spectrometer ionizer region after several collisions with the walls of the housing and result in the background component of the signal. Here, only species with a low sticking coefficient on the stainless steel surfaces of the mass spectrometer housing will contribute to the background signal. For the halogen chemistries investigated in this work, this is primarily the case for F radicals. Due to the high recombination coefficient for O, Cl, and Br radicals on most surfaces, these species will rapidly react at the stainless steel walls inside the mass spectrometer chamber, or condense upon them (on stainless steel, the recombination coefficient is close to 1.0 [124,125,226,227]). Contribution of these species to the background signal is however still possible which is primarily due to thermal pyrolysis (thermal dissociation) of neutral molecular species on the (about 1800 K) hot electron emitting filaments in the EQP ionizer. As a result, radicals are created that can subsequently be ionized and detected. The different sources of background contribution can be significant and dominate the beam number density, especially in case of non-condensable and non-reactive species. Therefore, several stages of differential pumping are usually required to obtain high beam to background ratios. Furthermore, beam modulation techniques are appropriate to separate beam and background components of the measured signal [110,144,145]. Here, a mechanical chopper is applied between aperture and mass spectrometer ionizer, and the technique is known as modulated beam mass spectrometry (MBMS).

For the experimental setup discussed in this work, a 230 l/s Pfeiffer turbo molecular pump is used for pumping the mass spectrometer chamber. When using a 50 μm aperture, the operating pressure in the mass spectrometer chamber remains below 5×10^{-6} Torr (typically $2 \dots 8 \times 10^{-7}$ Torr) for process pressures up to 600 mTorr inside the plasma reactor. The low pressure in the mass spectrometer chamber assures single electron collision in the

ionizer. The ionizer of the mass spectrometer is located at a distance of 150 mm on a line-of-sight from the sampling aperture. The signal intensity of the mass spectrometer can be expressed by [145]

$$S = \beta t(m/e) \theta(m/e) L_{\text{cage}} I_e \sigma_i n_{\text{ionizer}} \quad (3.1)$$

with the measured signal S in counts/second, the extraction efficiency of ions from the ionizer β , transmission efficiency of the quadrupole mass filter $t(m/e)$, detection coefficient of the channeltron SEM detector $\theta(m/e)$, the length of the ionizer cage L_{cage} , the electron current in the ionizer I_e , the ionization cross section σ_i , and the species number density in the ionizer n_{ionizer} . The number density of species in the ionizer is the sum of beam and background contribution

$$n_{\text{ionizer}} = n_{\text{beam}} + n_{\text{background}}, \quad (3.2)$$

where only the beam component of the number density of species in the ionizer is proportional to the number density of species in the plasma. The incoming neutral flux depends upon the gas temperature as expressed by the mean species velocity

$$\Gamma = \frac{1}{4} n v. \quad (3.3)$$

However, the residence time of species is proportional to the inverse velocity of the species and hence, the temperature influence on the beam component cancels out. Apart from the dependency of radicals upon the wall loss coefficient, the background signal is further influenced by the flux of species and the effective pumping speed of species in the mass spectrometer system.

The beam-to-background ratio for the single stage of differential pumping employed in this work is given by [144]

$$R_{\text{bb}} = \frac{n_{\text{beam}}(x)}{n_{\text{background}}} = \frac{R^2}{x^2} \cdot \frac{Q}{C}, \quad (3.4)$$

where the beam number density is described for a distance x from the orifice with radius R ($R \ll x$). Q is the effective pumping speed of the species due to the vacuum pump, and C is the aperture conductance according to (2.2). Due to conductance limitations, the effective pumping speed of a species in the vacuum system is usually lower than the rated speed of the vacuum pump. It can be calculated from the slope of the curve that is obtained when plotting the pressure inside the mass spectrometer chamber as a function of the pressure of the species in the plasma reactor. Here, the pumping speed was determined for different feed gases (O_2 , Ar, NF_3 , SiF_4 , SiCl_4) inside the plasma reactor when the respective discharge was turned off and at a constant reactor wall temperature of 70°C . The pumping speed plotted in Fig. 3.1 is found to scale with the inverse of the molecular mass. The approximated pumping speed of about 170 l/s for nitrogen is also lower than the rated speed of 230 l/s which can be explained by conductance limitations of the current setup. From equation (3.4), the beam-to-background signals are then calculated as $R_{\text{bb}}(\text{O}_2) = 0.0185$, $R_{\text{bb}}(\text{Ar}) = 0.0130$, $R_{\text{bb}}(\text{NF}_3) = 0.0109$, $R_{\text{bb}}(\text{SiF}_4) = 0.0078$, and $R_{\text{bb}}(\text{SiCl}_4) = 0.0061$. These results indicate that slightly different beam-to-background ratios might be obtained for different feed-gas mixtures. The calculated values are much smaller than 1.0, which would be a desirable ratio for a good sensitivity to the beam component. Hence, no conclusion can be drawn here about radicals sampled from the discharge that have a high sticking coefficient on stainless steel (e.g., O, Br, Cl). Detection

of such radicals is only possible from thermal pyrolysis of neutral molecular species on the filaments in the EQP ionizer. A beam-to-background ratio close to 1 for a single stage setup employed in this work could only be obtained for a very short distance (about 2 cm) between the ionizer and the aperture [144]. For the single stage setup discussed here, this requirement can not be met due to system constraints caused by sealing flanges and clearance for bolts to adapt the EQP tube to the reactor. However, the plasma-induced background in axial orientation is generally reduced due to having the EQP quadrupole and detector mounted 45 degrees off-axis from a line-of-sight. This prevents contribution of plasma photons and metastables to the background signal [110].

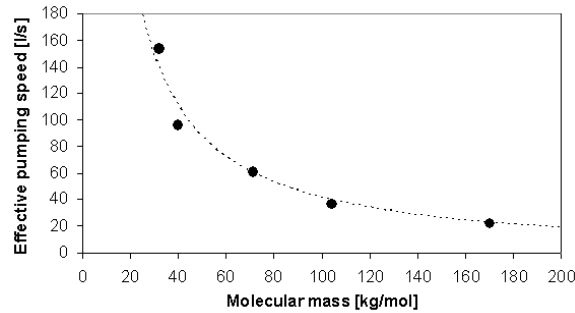


Figure 3.1: Effective pumping speed for the Hiden EQP system. The data can be fitted by a function that is proportional to $1/m_i$.

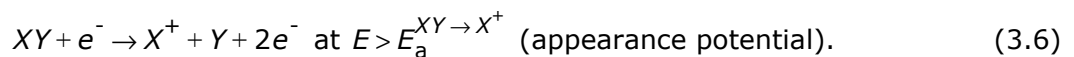
Ions will not contribute to the neutral mass spectra since the degree of ionization yields typically values in the range of 0.001%–0.01% for the discharges investigated here [13]. Beyond that, tuning for ions obtained from ionization of neutrals in the EQP ionizer yields significantly lower energy settings than typical ion energies obtained while traversing the sheath. Hence plasma ions will not be detected in RGA mode.

3.1.2 Appearance potential mass spectrometry

APMS (also called Threshold Ionization Mass Spectrometry - TIMS) is a well-known technique to detect and quantitatively measure neutral species from discharges [144,145,228-232]. APMS is based on selective ionization of radicals and utilizes the ionization threshold difference between direct ionization of a radical X



and dissociative ionization of its parent XY



Here, $E_a > E_i$ since $E_a \approx E_i + E_b(X-Y)$, where $E_b(X-Y)$ is the $X-Y$ bond energy. Typically, the difference between direct and dissociative ionization is greater than 2 eV. For electron energies $E_i^{X \rightarrow X^+} < E < E_a^{XY \rightarrow X^+}$, the measured signal is only due to a direct ionization of the radical and hence the radical number density can be estimated. For $E_a^{XY \rightarrow X^+} < E$, radicals formed through dissociative ionization of the parent will contribute to the number of radicals formed through direct ionization. Provided the electron energy dependent ionization cross section is known, it is possible to estimate the number density of radicals. This can be achieved since the ionization cross section is well approximated by a linear expression near the ionization threshold [233-236]. It is known from the cross-section

literature [237-242] that the extraction efficiency for ions formed through direct ionization of the radical in the ionizer of the mass spectrometer is typically higher than that for fragment ions formed through dissociative ionization of the parent molecule. In [145], the extraction efficiency for products formed through dissociative ionization was found to be up to 1.5 orders of magnitude smaller than the extraction efficiency for products from direct ionization. This was explained to result from dissociative ionization products carrying an excess kinetic energy due to the Franck-Condon effect. Ions with an excess kinetic energy (typically a few eV) exhibit a lower extraction and collimation efficiency as already discussed in section 2.4.3. Fractions of ions with high kinetic energy increase with electron energy [239] which will yield a further reduced collection efficiency for these species.

For investigations comprising different gases in this work, the electron energy was typically scanned from 0 to 50 eV in 0.1 eV increments. The filament electron emission current (which determines the electron flux incident onto the radical beam inside the ionizer) was set at 10 μA in order to protect the filaments from damage due to excessive current demands, and further to ensure the ionizer is not operated in the space-charge regime [243,244]. The electron energy scale was calibrated using argon with the well known ionization energy of 15.8 eV. For the different studies in this work, an energy scale offset of 2.0-2.4 eV was found for the appearance potential. The energy spread of the electron beam in the ionizer is specified by 0.3 eV (FWHM) [153] which enables sufficient determination of the neutral species from the measured threshold (provided the threshold energy is known from the literature). The electron energy discussed in this work is the corrected electron energy obtained after proper calibration. Measured ionization and appearance potentials for radicals and molecules from relevant gases used in this work were compared to available publications for HBr [218,219,245-248], NF_3 [218,219], O_2 [75,218,219], SiF_4 [218,219,249], SiCl_4 [218,219,245,246,250], SiBr_4 [218,219,251], and SiBrF_3 [252]. For illustration, a typical APMS scan performed for $m/q = 79$ u (Br^+) in an HBr discharge is shown in Fig. 3.2. The different curves plotted in Fig. 3.2 correspond to different situations in the plasma reactor. The residual signal (open triangles) is measured during base pressure conditions when there is no HBr gas flow or plasma and results from a unknown contaminant in the mass spectrometer system. The signal during discharge-off condition (open circles) results primarily from dissociative ionization of the HBr feed gas molecules. The residual signal and pyrolysis of the HBr feed gas on the ionizer filaments will further contribute to the measured signal. The discharge-on signal (full circles) includes both contributions from a background signal and the beam signal. The background signal is determined by Br^+ formed through dissociative ionization of the HBr feed gas, the residual signal, and pyrolysis of feed gas molecules as well as other bromine-containing products. The beam signal is due to Br radicals formed in the discharge that were sampled without collisions on their way to the ionizer. From the discharge-off curve, the threshold of Br^+ formation from dissociative ionization of HBr is measured around 17.3 eV. The low intensity measured below 17.3 eV indicates that there is either a negligible contribution of Br created through pyrolysis of HBr on the filaments and subsequent direct ionization, or dissociative ionization of recombined bromine. The latter is supported by a high recombination coefficient for Br which is close to 1.0 on stainless steel surfaces [125]. From the discharge-on signal, the threshold for direct ionization of Br is observed above 12.5 eV, which is slightly above the literature value of 11.8 eV [218]. This deviation is likely due to the low number density of radicals being detected which yields signals below the detection limit of the mass spectrometer near the threshold. The slope discontinuity

around 17.3 eV indicates an additional contribution of Br formed through dissociative ionization of the HBr feed gas, as it matches the threshold determined from the discharge-off curve. For electron energies above this second threshold, both radicals and parent molecules are ionized in parallel. From the stronger rise of the Br^+ signal in the logarithmic scale plot, in fact more Br^+ ions appear created through dissociative ionization of HBr (and other Br-containing) molecules than are created through direct ionization of the monitored Br neutral flux. Since the number of parent molecule species typically exceeds the number of radicals by about 3-6 orders of magnitude [13], most ions are formed through dissociative ionization of the parent molecule. Finally, at high electron energies $E > E_a$, the depletion of Br for the discharge-on condition explains the decrease of intensity with respect to the situation where the discharge is turned off. For the typical RGA operation mode where the electron energy is usually fixed at 70eV, this hints a comparably low detection sensitivity for neutral radicals in general. The detection sensitivity of the radical/precursor ratio is limited to about 10^{-4} for the current measurement setup, taking into account limitations by protection of the SEM detector from excessive count rates, the minimum signal required and energy spread of the electron beam.

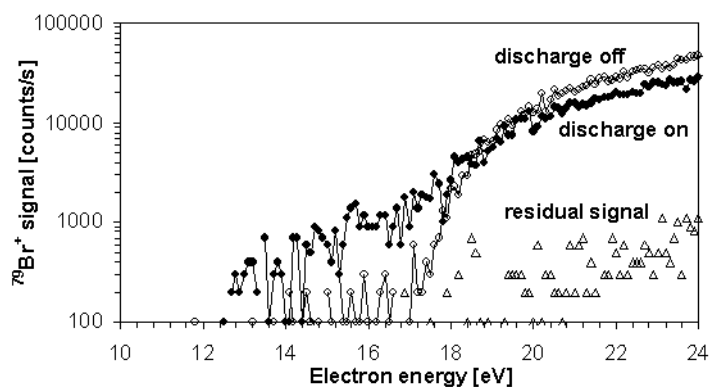


Figure 3.2: APMS scan at $m/q = 79$ u (Br^+) in the EQP differential pumping system. Open circles represent the signal measured when the discharge is off, full circles are the signal with the discharge turned on. The residual signal is the signal detected at base pressure conditions due to an unknown contaminant. From the discharge-on signal, the threshold for direct ionization of Br is observed at above 12.5 eV which is slightly above the literature value of 11.8 eV [218]. No evidence of thermal cracking of HBr is seen when the discharge is off since the discharge-off signal is observed to overlap the residual signal up to about 17.3 eV. Formation of Br from dissociative ionization of HBr occurs around 17.3 eV as can be seen from the rising discharge-off signal.

3.1.3 Quantum cascade infrared laser absorption spectroscopy

Recently, a compact quantum cascade laser measurement and control system (Q-MACS) was developed enabling for time-resolved plasma diagnostic absorption spectroscopy, process control and trace gas monitoring [253,254]. Based on Q-MACS, a new diagnostic arrangement, the Q-MACS Etch system, was designed and constructed during the time of the present work. Application of the Q-MACS Etch system as infrared absorption and interferometer tool for on-line in situ monitoring of molecular species and etch rates in the HART plasma etch reactor are described in detail in [165]. For the first time, concentrations of the precursor gas NF_3 and of the etch product SiF_4 were measured on-line and in situ under clean room conditions. In addition, the etch rates of SiO_2 layers and of the silicon wafer were monitored including plasma etching endpoint detection. In the following, the Q-

MACS Etch system is described in more detail. Furthermore, general spectroscopic issues, determination of the absorption cross sections, and finally SiF_4 concentrations are discussed briefly. Specifics of the experimental setup at the plasma reactor are described in section 4.1.

The quantum cascade laser system Q-MACS Etch consists of a pulsed infrared QCL source with the laser wavelength tuneable in the range $1027\text{--}1032\text{ cm}^{-1}$, optical components, detectors and data acquisition cards controlled by a PC. Details of the Q-MACS Etch optical arrangement are shown in Fig. 3.3. The laser driver used was a Q-MACS Basic [253,254]. The Q-MACS Basic provides a laser pulse width tuneable between 10 and 255 ns and a repetition frequency between 100 Hz and 1 MHz. Depending on the experimental requirements, the system can operate in the intra-pulse or inter-pulse mode [253]. Intra-pulse mode means that the laser frequency is tuned over the absorption spectrum during one relatively long single pulse, i.e. using a 50-200 ns laser pulse width. In the present experiments, the inter-pulse mode was used. The QCL was driven with a pulse width of 12 ns and a repetition rate of 500 kHz. The central frequency of the QCL is chosen by changing the working temperature between -30°C and $+30^\circ\text{C}$ and the feed current of the laser in the range of 0.5 to 15 A (peak current). In order to tune over a spectral range, an additional voltage ramp is applied to the laser with a frequency of 1 kHz. This allows scanning of the spectral range with a width of up to one wavenumber. Each millisecond a complete spectral region is scanned. Under each scan 500 single laser pulses are generated. As a result, the measured spectrum with a time resolution of 1 s is an average of a thousand spectra. One second time resolution is sufficient for most plasma etch processes which require a time scale typically in the range of seconds up to minutes.

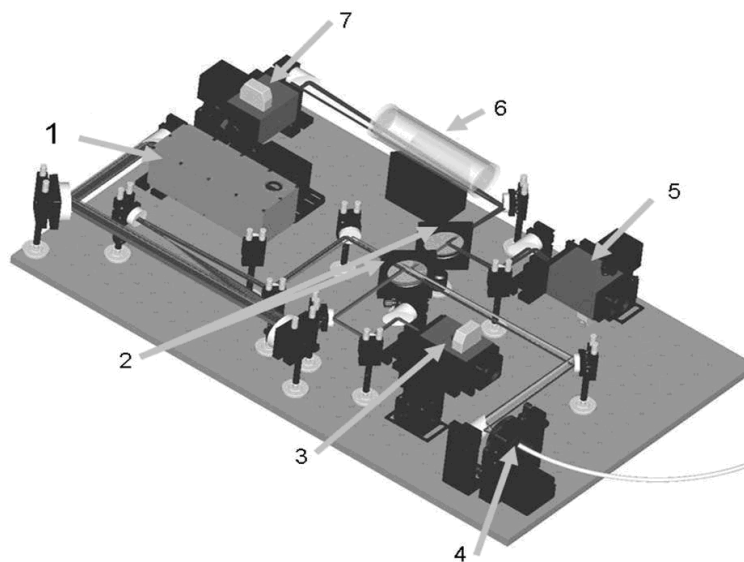


Figure 3.3: Optical arrangement of the Q-MACS Etch system (1: laser head, 2: beam splitters, 3,5,7: detectors, 6: reference gas cell, 4: IR optical fibre).

As depicted in Fig. 3.3 and Fig. 4.4, the IR beam is split into three channels using two IR transparent ZnSe beam splitters (BS). The main part of the beam is coupled into an IR fibre using an off-axis paraboloid (OAP) mirror, and then collimated into the plasma reactor using either lenses or OAPs. The second channel, operating as pulse normalisation channel, is used to reduce the fluctuation intensities of the QCL from pulse to pulse. In order to

calibrate the spectral region and to correct for drifts of the laser frequency due to temperature instabilities of the laser chip, a reference spectrum of C_2H_4 is measured through a reference gas cell as a third channel. For spectral calibration, a germanium etalon with the free spectral range of 0.012 cm^{-1} was used. A fringe spectrum was recorded and used to correct the nonlinearity of the spectral laser tuning. Together with the known spectra of the C_2H_4 [255], an absolute spectral calibration could be performed.

Fig. 3.4 shows a reference spectrum of C_2H_4 as recorded with Q-MACS Etch for an absorption length of 15 cm, at 2.25 Torr pressure and room temperature. The reference and the germanium etalon spectra were used for the wavelength calibration of the QCL spectrometer. The line profiles have a Doppler contribution, for which the full width at half maximum is given by

$$\Delta W_{\text{Doppler}} = 7.16 \times 10^{-7} v_0 \sqrt{\frac{T}{M}}, \quad (3.7)$$

where v_0 is the wavenumber of the central line, T is the temperature, M is the molar mass of the molecule. For the lines shown in Fig. 3.4, Doppler broadening contributes to about $2.4 \times 10^{-3}\text{ cm}^{-1}$. Another broadening effect contributing to the profile is due to the influence of different pressures. From the HITRAN (high resolution transmission molecular absorption) database [255], pressure broadening of these lines contributes to about $3 \times 10^{-4}\text{ cm}^{-1}$. Finally, the instrumental contribution to the laser lines can be obtained after deconvolution of the absorbance profiles. The measured absorption lines show an instrumental broadening (FWHM) of about $8 \times 10^{-3}\text{ cm}^{-1}$.

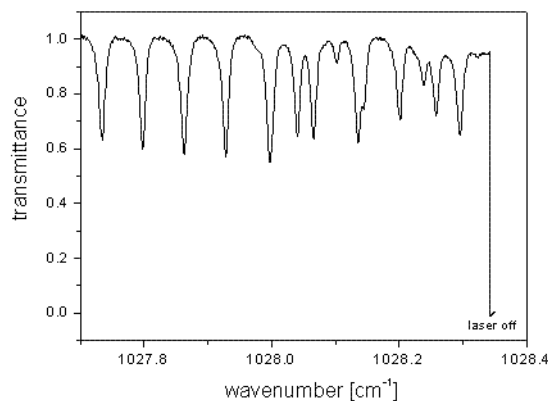


Figure 3.4: QCLAS spectrum of C_2H_4 at room temperature, 2.25 Torr pressure, absorption length of 15 cm and instrumental broadening of 0.008 cm^{-1} .

In Fig. 3.5, two FTIR spectra are shown as recorded with a Bruker IFS 66 v/s spectrometer. The spectra were recorded at room temperature in a gas cell of 15 cm length. The pressure inside the cell was adjusted to 375 mTorr for SiF_4 , and 750 mTorr for NF_3 , respectively. The approach for this work was to measure the etch product species SiF_4 , with NF_3 being the precursor molecule. From Fig. 3.5, the spectra of these two species show some overlapping. Thus in order to reliably measure the etch product SiF_4 , minimum overlapping has to be considered. The spectral region of $1028 \pm 0.3\text{ cm}^{-1}$ was finally chosen for the measurement of SiF_4 due to a maximum difference between the absorption cross sections of SiF_4 and NF_3 . Compared to NF_3 , the absorption cross section of SiF_4 is about 90 times larger. Other IR active vibrational modes of SiF_4 can be found at larger wavelength

values [256] where no QCLs are available. Hence, the choice was limited further to the detection of the ν_3 fundamental band.

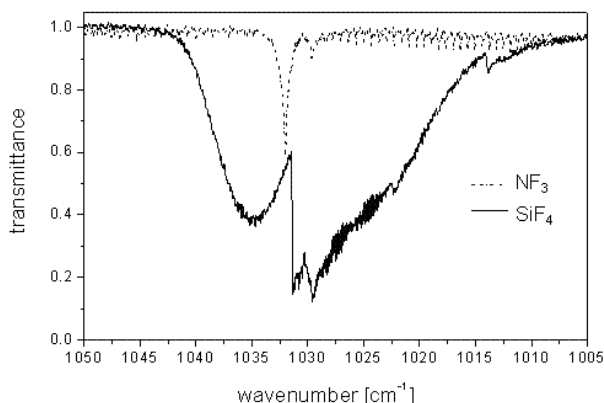


Figure 3.5: FTIR spectra of SiF_4 at 375 mTorr pressure and of NF_3 at 750 mTorr pressure. The spectra were recorded at room temperature, at a total absorption length of 15 cm and spectral resolution of 0.11 cm^{-1} .

The complex spectrum of SiF_4 is shown in the Fig. 3.6-a. It was recorded using Q-MACS Etch at a gas temperature of 70°C in a gas mixture with 90% Ar content. The total pressure was 250 mTorr. The measurement was done in the MERIE plasma reactor, where an absorption length of 108 cm was achieved in two passes. The same spectral region was recorded using NF_3 in gas phase at 600 mTorr, the corresponding spectrum is plotted in Fig. 3.6-b. The NF_3 pattern is different to that of SiF_4 , however showing also an unresolved structure.

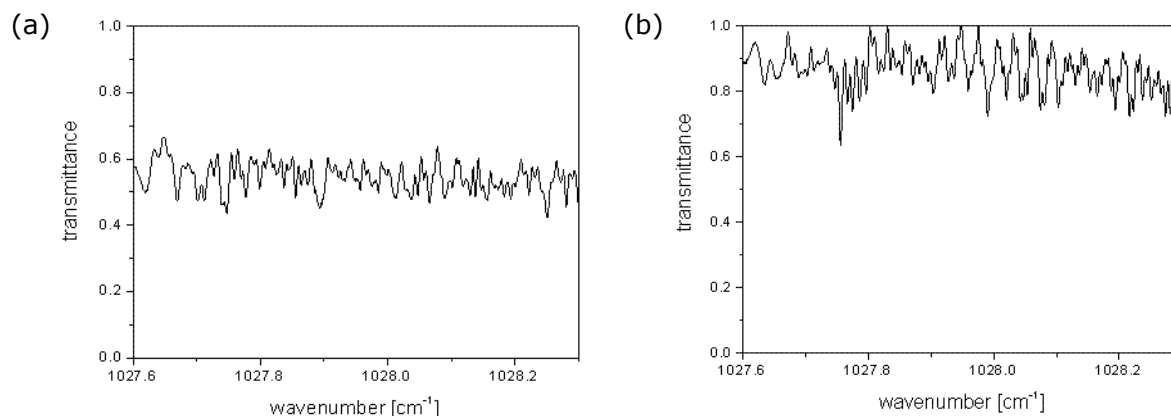


Figure 3.6: (a) QCLAS spectrum of 10% SiF_4 in mixture with Ar, measured at 70°C , 250 mTorr total pressure, absorption length of 108 cm and instrumental broadening of 0.008 cm^{-1} . (b) QCLAS spectrum of NF_3 measured at 70°C , 600 mTorr pressure, absorption length of 108 cm and instrumental broadening of 0.008 cm^{-1} .

In general, the accuracy of concentration measurements of molecules in plasmas depends primarily on the precision of available molecular data. For this purpose, the absorption cross sections of SiF_4 and NF_3 have been determined for the spectral range $1028 \pm 0.3 \text{ cm}^{-1}$. Furthermore, the absorption cross section of SiF_4 was characterized as a function of temperature and pressure. In Fig. 3.7, the SiF_4 absorbance function of the concentration is plotted. The gas temperature was varied between 60°C and 110°C by electrically heating the reactor walls. Variation of the neutral gas density was furthermore

achieved by changing the pressure from 50 to 500 mTorr. The absorption length was 6 cm. If the absorbance

$$\ln\left(\frac{I_0}{I}\right) = \sigma_a n L \quad (3.8)$$

is represented as function of the concentration, then the proportionality factor is the product $\sigma_a L$. From Fig. 3.7 it can be seen, that the data points can be linearly fitted. This shows that the absorption cross section is constant over the range of temperature and pressure used in the experiment. Because relatively low pressures are relevant for all investigations of interest here, pressure broadening effects are negligible. The main contribution to the absorption profiles is the instrumental broadening which is about 6 times larger than Doppler broadening, $\Delta W_{\text{Doppler}} = 1.24 \times 10^{-3} \text{ cm}^{-1}$ for SiF_4 at room temperature. Although the absorption cross section does not change for the range of temperatures investigated here, no conclusion can be drawn for the influence of (several hundred centigrades) high neutral gas temperatures during discharge operation discussed in chapter 4. Absorption spectroscopy at such high gas temperatures is not an easy attempt and could not be realized during this work. However since the integrated absorption coefficient is evaluated over a large number of absorption lines of the complex spectra (cf., Fig. 3.6), the total partition function is generally expected to be less sensitive to changes in temperature as in case of a single line.

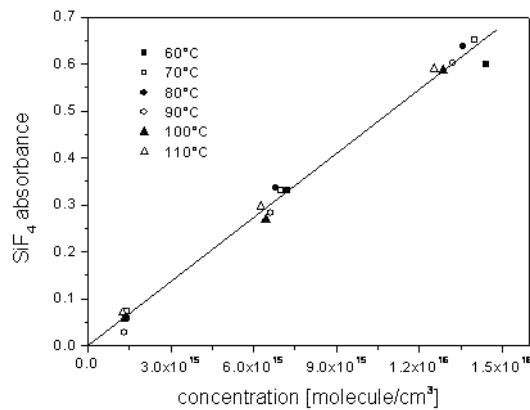


Figure 3.7: SiF_4 average absorbance as function of the concentration. The spectral region measured was $1027.6 - 1028.3 \text{ cm}^{-1}$, and the absorption length was about 6 cm.

The values of absorption cross sections have been obtained from both FTIR and QCLAS spectra. The average absorption cross sections at $1028 \pm 0.3 \text{ cm}^{-1}$ were measured $\sigma_a(\text{SiF}_4) = 7.7(\pm 0.7) \times 10^{-18} \text{ cm}^2 \text{ molecule}^{-1}$ and $\sigma_a(\text{NF}_3) = 8.7(\pm 0.8) \times 10^{-20} \text{ cm}^2 \text{ molecule}^{-1}$ for SiF_4 and NF_3 , respectively. Uncertainties are due to errors in the measurement of pressure and further of the I_0 reference. With the knowledge of the IR absorption cross sections for SiF_4 , absolute SiF_4 molecule number densities can be finally derived by applying Lambert-Beer's law

$$n_{\text{SiF}_4} = \frac{\ln\left(\frac{I_0}{I}\right)}{\sigma_a(\text{SiF}_4)L} \quad (3.9)$$

3.1.4 RF probe measurements

The rf probe installed in the matching network (cf., Fig. 3.8) can be tuned to measure rf characteristics of the load at the individual source frequencies used, i.e. determination of voltage, current, phase shift, and the load impedance from these values. Generally, the load impedance is dominated by the impedance of the reactor geometry, whereas the plasma impedance is expected to have only minor contribution. For determination of the rf characteristics at 2 MHz, the phase shift is measured negative which corresponds to a capacitive load (as one would expect for capacitive coupling). In contrast, rf characteristics at 60 MHz are measured with positive phase shifts during all experiments which corresponds to an inductive load. This is attributed to the excitation frequency of 60 MHz being above the resonance frequency of the reactor geometry (including feedthrough, electrostatic chuck, etc.) which is about 33 MHz for the reactor investigated here [257]. At frequencies around the reactor resonance frequency, the phase shift turns from positive to negative, and remains negative for excitation frequencies below the reactor resonance frequency. The resonance frequency is mainly influenced by the rf feedthrough, the remaining reactor geometry has only negligible impact [258,259]. Consequently at 60 MHz excitation frequency, the total impedance is determined by the dominating inductance of the feedthrough. This suggests a higher fraction of the delivered power is being lost through the coaxial feedthrough at 60 MHz.

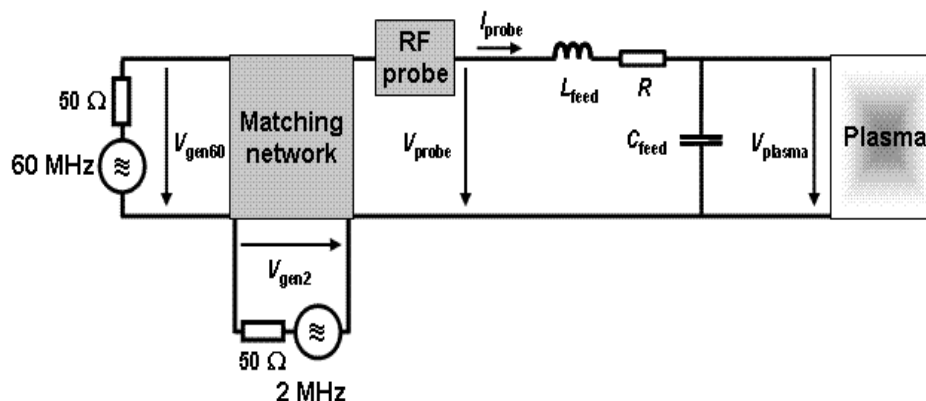


Figure 3.8: Schematic of the rf voltage, current and phase measurement performed by a V,I probe at the output of the matching unit.

The rf probe is mainly used to obtain the dc bias voltage from the voltage measured for the 2 MHz frequency source by using a simple model as described below. During the processing routine, the calculated dc bias voltage is used for compensation of a specified constant voltage to chuck the wafer when the plasma is turned on. Therefore, rf probe measurements used for discussion of various discharges in chapter 4 are based on the 2 MHz source. For 60 MHz single frequency discharges, no characteristics can be determined with the given configuration. Nevertheless, data for 60 MHz rf characteristics was collected for a few experiments as well after introducing some modifications to the initial setup. This included tuning of the rf probe for 60 MHz, and deactivation of the chucking voltage compensation.

For asymmetric discharges where more electrode surface area is naturally grounded than driven, a *dc bias voltage* V_{dc} will develop on the driven electrode (with respect to ground). The dc bias voltage occurs from the fact that the dc voltage between the plasma and the

driven electrode is larger than the dc voltage between the plasma and the grounded electrode [20]. This very important parameter depends on the discharge properties and is influenced by parameters like plasma chemistry, delivered power, pressure, magnetic field, etc. For the HART plasma etch reactor, the V_{dc} is used to compensate the chucking voltage. Due to the insulating reactor surfaces, the V_{dc} can not be measured directly. Instead, it is calculated from a fit model for a correlation to the 2 MHz peak-to-peak voltage V_{pp} [214], as described in the following:

- (1) An impedance scan of the powered electrode/reactor is performed.
- (2) A circuit analysis is done to calculate the impedance at 2 MHz.
- (3) Using the impedance from (2) together with the 2 MHz voltage and current measured by an rf probe at the output of the matching network, the V_{pp} seen on the wafer is calculated using a transform model.
- (4) Wafer contact HV probe measurements are performed allowing to determine the 2 MHz waveforms for different 60+2 MHz power levels, process pressure and magnetic field conditions. From a best fit to the plot of this data, a correlation between V_{pp} and V_{dc} is achieved.

The dc bias voltages recorded by the plasma etch hardware is based on a V_{dc} model for a complex HBr/NF₃/O₂ plasma chemistry in the 200-400 mTorr range yielding the following correlation:

$$V_{dc} = -\frac{V_{pp}}{3.2} + 220. \quad (3.10)$$

Calculation of the V_{dc} from the 2 MHz V_{pp} measurements are described to be accurate within 15% for the conditions described above. Larger discrepancies will occur at lower pressures and for different plasma chemistries (like pure Ar, HBr, etc.) [214].

Since fundamental investigations performed in this work are covering a wide range of different plasma chemistries, pressures, delivered powers and hence significantly varying discharge properties, the dc bias voltage can not simply be calculated using equation (3.10). Instead, wafer contact probe measurements must be performed for every single experiment. Since these measurements could not be made available during the period of this work, rf probe data measured at 2 MHz comprising voltage V , current I , and the phase shift φ are discussed instead in chapter 4. From these data, delivered power P_{eff} , reflected power P_{refl} , peak-to-peak voltage V_{pp} , and impedance Z can be calculated by

$$P_{eff} = V \cdot I \cdot \cos \varphi, \quad (3.11)$$

$$P_{refl} = V \cdot I \cdot \sin \varphi, \quad (3.12)$$

$$V_{pp} = 2\sqrt{2} \cdot V, \quad (3.13)$$

$$Z = \frac{V}{I}. \quad (3.14)$$

3.2 Evaluation of etch results

3.2.1 Gravimetry (weight loss measurements)

A fully automated Metryx Mentor scale [260] with integrated mini-environment is used to measure the weight of the 300 mm wafers. A pre and post measurement conducted

immediately before and after the etch process are combined to measure the weight difference and determine the weight loss obtained during etching.

The scale utilizes ambient sensors that continuously monitor ambient temperature, pressure and relative humidity. It uses these parameters to calculate instantaneous air density and applies this to the weight measurement to correct for changes in atmospheric buoyancy of the substrate. The balance load cell (cf., Fig. 3.9) is an highly accurate force meter that measures the gravitational force acting on a wafer that has been placed on the balance pan. The principle of operation is based on a moving electromagnet acting on a permanent magnet. The force exerted by the weight of a wafer is resisted by the current flowing in an electromagnet. When a wafer is placed on the pan, the weighing pan sags slightly under the additional force. The movement is amplified by a lever arrangement. It is detected by a position sensor and the current in the coil is increased in order to restore the pan to its original position. Once the transient has settled, the pan has been levitated back to its original position and the extra current flowing through the coil is recorded. This can be converted into a measure of the weight of the wafer.

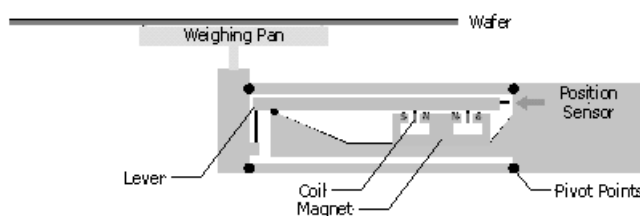


Figure 3.9: Schematic of the Metryx Mentor scale load cell.

Wafers are placed on the thermal plate before being measured on the balance in order to stabilize the temperature of the wafer to the equilibrium temperature of the measuring enclosure and to dissipate surface static charges present on the wafer. Wafers that arrive directly from processing tools at an elevated temperature will require additional time to stabilize. Also, wafers enclosed on a complete layer of an electrical isolator (e.g. silicon dioxide) may include trapped charges behind the insulator that may be difficult or impossible to discharge. Placing these types of wafers on the thermal plate may introduce additional charge into the wafer by an electrophoresis effect.

From the weight difference, a mean etch rate can be calculated by applying a simple cylinder model for an ideally uniformly etched surface by

$$R = \frac{\Delta d}{t} = \frac{\Delta m}{A \rho t} \quad (3.15)$$

with Δd the total change in thickness resulting from etching during the time t , the measured weight difference Δm , the surface area A of the 300 mm wafer substrate, and the density ρ of the material etched. For calculation of the etch rates densities of $\rho_{\text{Si}} = 2.33 \text{ g/cm}^3$ and $\rho_{\text{SiO}_2} = 2.27 \text{ g/cm}^3$ were used for bare silicon substrates and silicon substrates covered by a CVD SiO_2 hard mask layer. The advantage of the applied weight loss measurements is a direct measurement of the silicon etch rate using bare silicon wafers. No additional polysilicon layer has to be deposited in order to determine silicon etch rates, as required for example when applying ellipsometry. Since the results represent a mean value obtained from integration of the total wafer area, an assessment concerning the uniformity of etched layers can not be made by simply applying this technique. Therefore, 49 point ellipsometry measurements were performed additionally on

substrates with SiO₂ hard mask. A comparison between etch rate results from both techniques is presented in chapter 4.

The weight of the used silicon substrates with and without additionally structured or unstructured mask layers lies within the specified measurement range of 110 – 135 g. Unfortunately, determination of sputter erosion rates for Y₂O₃ wafers that were used for some of the experiments was not possible due to the weight of 350 g resulting from the specified density of $\rho_{Y_2O_3} = 4.90 \text{ g/cm}^3$ for the yttria plates. The static, dynamic, and long-term precision (1 sigma) is described to be below 80 µg (corresponding to a deviation expressed by a mean etch rate of 0.5nm/min for a 300 mm silicon wafer). Internal tool stability checks are performed by periodically measuring a "golden wafer" located inside the tool.

3.2.2 Ellipsometry

Ellipsometry is used as an additional technique to determine etch rates for silicon substrates containing additional layers and also to investigate etch rate nonuniformities caused during etching. Ellipsometry is a very sensitive optical measurement technique commonly used for thin film metrology. In general, this technique is applied to characterize the film thickness for single layers or complex multilayer stacks ranging from less than a nanometer to several micrometers with high accuracy, and to investigate dielectric properties (complex refractive index or dielectric function) of thin films [261-263]. Ellipsometry is an extension of a reflection technique in which the change of polarization upon reflection or transmission rather than just its intensity is measured. The nature of the polarization change is determined by sample properties, like thickness, complex refractive index or the dielectric function tensor. This gives access to probe fundamental physical parameters and sample properties, including morphology, crystal quality, chemical composition, or electrical conductivity. Although optical techniques are inherently diffraction limited, ellipsometry exploits phase information and the polarization state of light, and can achieve angstrom resolution. The sample must be composed of a small number of discrete, well-defined layers that are optically homogeneous, isotropic, and non-absorbing. More advanced variants of the technique have to be applied in cases where these assumptions are violated and the standard ellipsometric modeling procedure is invalidated.

For the investigation here, ellipsometry is performed in reflection mode using a KLA Tencor ASET-F5x [264]. Ranges of operation comprise the continuous wavelength spectrum from 190 nm to 800 nm. From the schematic of the ellipsometry setup plotted in Fig. 3.10, electromagnetic radiation is emitted by a light source (xenon lamp) and linearly polarized by a polarizer, it can pass an optional compensator (retarder, quarter wave plate), and falls onto the sample. After reflection, the radiation passes a compensator (optional) and a second polarizer (called analyzer) and falls into the detector. Instead of the compensators, some ellipsometers use a phase-modulator in the path of the incident light beam. The incident and the reflected beam span the plane of incidence, where the angle of incidence equals the angle of reflection. Electromagnetic waves which are polarized parallel or perpendicular to the plane of incidence, are called *p* or *s* polarized, respectively.

For standard ellipsometry, two of the four Stokes parameters are measured - conventionally denoted by Ψ and Δ . The polarization state of the light incident upon the sample may be decomposed into an *s* and a *p* component (the *s* component is oscillating

perpendicular to the plane of incidence and parallel to the sample surface, and the p component is oscillating parallel to the plane of incidence). The amplitudes of the s and p components, after reflection and normalized to their initial value, are denoted by r_s and r_p , respectively. Ellipsometry measures the complex reflectance ratio of r_s and r_p , which is described by the fundamental equation of ellipsometry:

$$\frac{r_p}{r_s} = \tan(\Psi)e^{i\Delta}, \quad (3.16)$$

where $\tan(\Psi)$ denotes the amplitude ratio upon reflection, and $\Delta = \Delta_p - \Delta_s$ the phase shift (difference) of Δ_p and Δ_s , which are the total phase changes on reflection of the parallel and perpendicular components, respectively. Measuring the ratio (or difference) of two values rather than absolute values makes this technique robust (to fluctuations), accurate and reproducible. Further, no standard sample or reference beam are required.

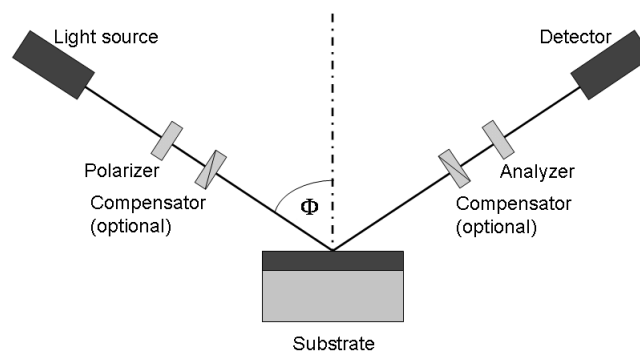


Figure 3.10: Schematic of the ellipsometry setup.

Ellipsometry is an indirect method, i.e. in general the measured Ψ and Δ can not be converted directly into the optical constants of the sample. Normally, a model analysis must be performed. Direct inversion of Ψ and Δ is only possible in very simple cases of isotropic, homogeneous and infinitely thick films. In all other cases a layer model must be established, which considers the optical constants (refractive index or dielectric function tensor) and thickness parameters of all individual layers of the sample including the correct layer sequence. Using an iterative procedure (least-squares minimization) unknown optical constants and/or thickness parameters are varied, and Ψ and Δ values are calculated using the Fresnel equations. The calculated Ψ and Δ values which best match the experimental data will finally provide the optical constants and thickness parameters of the sample.

4 Experimental investigations and results

In the first section, a detailed description of the HART plasma reactor used for this work is given which includes the two different designed experimental setups for conducting the plasma analysis in a production environment. The HART system is typically used in DRAM production for deep trench silicon etching to form capacitor structures. In subsequent sections, effects of applied power, pressure, gas flow rate and magnetic field are investigated for single and dual frequency discharges in Ar, HBr, NF_3 , HBr/ NF_3 , and further complex halogen chemistries. Analysis of interactions in the different discharges comprises an extensive set of measurements, including

- neutral mass spectra (etch species, byproducts),
- precursor gas dissociation,
- appearance potential mass spectrometry,
- silicon and silicon dioxide etch rates (selectivity, uniformity, anisotropy),
- IVDF analysis,
- SiF_4 etch product concentration measurements,
- rf probe data.

Simple Ar discharges were used for a baseline characterization to enable a comparison to literature data, modeling calibration, to separate the pure sputter component for the more complex reactive ion etch mechanisms, and to ensure stable conditions and reproducibility for the various conducted measurements. Pure HBr and NF_3 discharges were investigated to develop step by step a better and more detailed insight into the complex HBr/ NF_3 based process chemistries. Finally, interactions for mixed HBr/ NF_3 chemistries were characterized with additions of further precursors for sidewall passivation and selective mask deposition.

4.1 Plasma reactor design and experimental setup

Centura HART system

The Applied Materials Centura HART reactor used for the experimental investigations in this work is a MERIE reactor designed for the requirements of deep trench etching for DRAM capacitors on 300 mm wafers. The complete Centura setup comprises a factory interface, the loadlock system, a transfer chamber mainframe, up to four installed process reactors, and a gas panel (Fig. 4.1). The Centura HART system is controlled via an Windows NT-based graphical user interface.

The process wafers are contained in so-called FOUPs (Front Opening Unified Pod) and supplied to the etch reactor via load ports at the factory interface. Each FOUP has a twenty-five-wafer capacity and is used as a keyed base to keep and carry the wafers in a sealed level M1 environment. The factory interface is the interface between the Centura and the factory itself. After the FOUPs are docked to the system and unsealed, an atmospheric robot inside the factory interface picks up the wafers after a wafer mapping. After orientation for the wafer nodge position, the wafers are transferred to one of the two load locks which are located between the factory interface and the Centura mainframe. Each load lock has a dedicated rough pump to perform fast vent and pump times. The 300 mm Centura mainframe supports the installation of a total of 4 docking process reactors. The mainframe robot delivers the selected wafer from a load lock to the etch reactor chamber

via the transfer chamber slit valve and the reactor chamber liner door. Slit valve and liner door isolate the reactor chamber unit from the transfer chamber when processing a wafer. A ceramic electrostatic chuck (ESC) receives and holds the wafer in the reactor environment during its exposure to the process (Fig. 4.2). The dual zone ESC controls wafer temperature during processing. A thermal-transfer fluid loop controls the temperature of the driven electrode base on which the ESC is mounted. A second thermal-transfer fluid loop regulates the temperature of the reactor liner and the reactor lid to limit the deposition of process byproducts. The turbo pump, roughed and backed by a dry pump, maintains the processing vacuum in the reactor. A system controller regulates the gas panel to supply the gases required by the recipe via a showerhead in the grounded electrode (GDP - gas distribution plate). RF generators inject rf energy through the ESC into the reactor to produce a gas plasma through capacitive coupling.

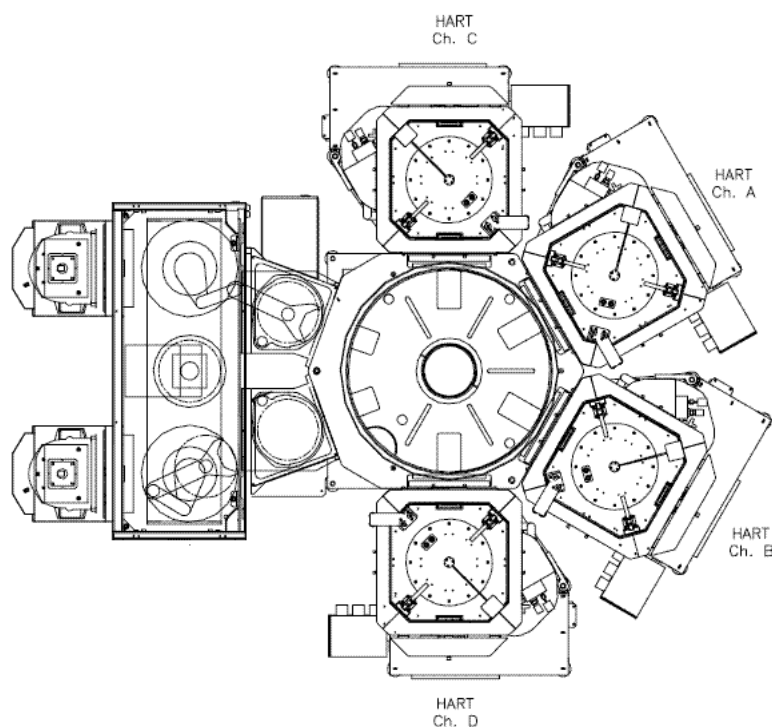


Figure 4.1: Centura with four HART 300 mm reactors installed (view from above) [16].

The capacitively coupled plasma is produced between a passive (ground) and an rf driven electrode in the process reactor. The ground electrode is formed by the cylindrical liner insert (protecting the reactor body from the process) which at the top is closed by the GDP integrated into the reactor lid assembly. The rf driven electrode (sometimes still called cathode) of 300 mm diameter is arranged opposite of the GDP. As part of the process kit, a quartz shadow ring is mounted to the ESC pedestal at the powered electrode to isolate the ESC pedestal from the chemical process and to extend the wafer surface to avoid nonuniformities in the electric field at the wafer edge. If not stated otherwise, GDP and rf driven electrode are separated by a gap of 1.25" (31.75 mm). The plasma is thus confined to the volume formed by the described gap and the 54 cm diameter of the liner insert surface. From the described geometry, the investigated discharge is asymmetric with the ratio of ground electrode surface to powered electrode surface

$$\frac{A_{gr}}{A_{el}} = 3.6 . \quad (4.1)$$

All inner reactor part surfaces which are in close vicinity or direct contact to the discharge are covered by an yttria hard anodization coating of 200 μm average thickness. The hard anodization coating is necessary to avoid enhanced degradation and particle formation due to using an aggressive halogen process chemistry with quite high ion bombardment energies. For typical process parameters, ion energies can even exceed 150 eV at the reactor walls (ground electrode area).

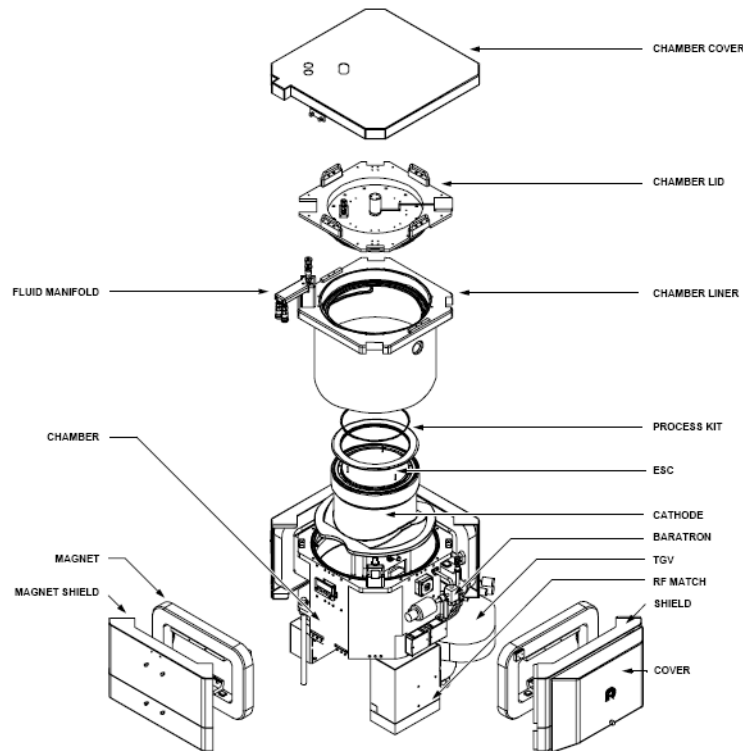


Figure 4.2: Silicon etch HART 300 mm process reactor (exploded view) [16].

Two separate single frequency rf generators for 60 MHz and 2 MHz are interfaced to the powered electrode using matching networks. A 60 MHz source power generator is used to sustain the plasma and control the plasma density, allowing to apply power levels up to 3.5 kW. A 2 MHz bias power generator allows to apply up to 3 kW and is used to control the ion energy. With the combination of a high- and low-frequency drive, nearly independent control of plasma density (and hence ion flux) and ion energy shall be obtained, being a main advantage in regards to conventional (13.56 MHz) RIE systems. An rf probe is installed between the matching network and the powered electrode allowing for measurements of voltage, current and phase. The rf match allows the complex impedance of the rf driven electrode-ESC-plasma circuit to be tuned to the output impedance of the rf generator (50 Ω resistive), providing maximum power transfer. The L-type matching units each comprise of a fixed coil, and two motor driven series tuning and load capacitors. The 60 MHz matching unit allows for 60 MHz power transmission to the plasma and rejection of 2 MHz signals, the 2 MHz matching network is designed to reject 60 MHz signals and transmit 2 MHz signals to the discharge. The 60 and 2 MHz signals are summed after both matching networks prior to connection to the driven electrode via a transmission line. For

illustration, voltage waveforms are plotted in Fig. 1.3-c and Fig. 1.3-d, showing a superposition of 60 MHz and 2 MHz voltages.

The ceramic electrostatic chuck clamps the wafer on the powered electrode during processing. The ESC consists of a pedestal, an aluminum plate with an integrated network of water cooling channels, and a ceramic (aluminum nitride) puck bonded to the surface of the plate. Chucking is achieved by applying a high dc voltage to the mesh through the high voltage contact located on the pedestal. The ceramic puck achieves chucking force for clamping the wafer by employing a coulombic chucking force [265]. The chucking force results from the high opposing electric fields formed across the gaps where the ceramic does not touch the wafer. A constant potential difference between the electrode and the wafer is maintained by varying the dc voltage to the ESC electrode potential using a high-voltage module. A reference voltage (V_{rf}) is input into the ESC controller from the rf matching network. From this V_{rf} signal the appropriate ESC voltage (V_{chuck}) is calculated by using a transfer function as described in section 3.1.4. The V_{chuck} typically varies from -300 V to -1500 V. The electronics adds the calculated negative V_{chuck} to the setpoint and outputs the appropriate voltage to the electrode during chucking. Because the electrode must conduct the rf energy used to form the gas plasma, the ceramic ESC also acts as an electrode for application of this energy. An rf choke isolates the rf from the dc chucking voltage. The powered electrode contains two sets of helium channels (inner zone and outer zone) for distribution of helium cooling to the ESC and the back of the wafer. Helium is used as a cooling gas here to enhance the thermal contact and improve the heat transfer between the wafer and the chuck. This is due to the temperature being a process parameter which must be controlled properly, meaning heat must be removed from or added to the wafer during processing. The cooling gas is furthermore necessary due to heat transfer in a low pressure or vacuum environment such as that used for plasma processing being generally poor. The cooling gas is introduced through holes in the chuck surface from a gas passage behind the chuck surface. The two independently adjustable helium flows for inner and outer ESC zone efficiently transfer heat from the wafer to the pedestal by conduction. The powered electrode assembly further comprises water channels that circulate heat-exchanger fluid to maintain the process temperature. The wafer temperature is controlled by regulation of the fluid temperature (pedestal temperature), and by adjusting the backside helium cooling pressure in the two zones. The required gas pressure is a function of the heat load imposed by the discharge, the desired wafer temperature, the temperature at which the chuck can be maintained, and heat transfer coefficients. Typically, a He backside pressure between 5 and 30 Torr is applied. From appropriate settings and control of fluid temperature and helium pressure, a good temperature control can be achieved. This is necessary for example to achieve a high CD uniformity when etching structures into a substrate.

In the pressure and temperature controlled environment of the HART process reactor, the gas plasma produces reactive species from the used etch gas chemistry: HBr, NF_3 , O_2 , SiCl_4 , Ar. The feedstock gas selection is given by the etch process requirements with respect to the materials to be etched, etch rate, anisotropy and selectivity. Etch gases are supplied from the gas panel and introduced into the reactor through the GDP in the grounded electrode. The gas flow of the feedstock gases (typically 1-1000 sccm, depending on feedstock gas) is controlled by standard mass flow controllers. Gas line and mass flow controllers for SiCl_4 are temperature-controlled to eliminate condensation and, as a consequence, erosion of the gas line assembly. A throttle gate valve between reactor

volume and turbo pump provides a variable conductance, regulating the process pressure in the reactor. The 1600 liter per second turbo pump maintains process vacuum in the reactor. A Baratron pressure gauge is installed next to a reactor side access port and used to determine the process pressure. The reactor is pumped to 1 mTorr before etch gases are admitted. The process pressure can be varied in a wide window of typically about 50 to 600 mTorr (7 to 80 Pa). The effective reactor volume was determined to be 42 liters.

Four independently driven, water-cooled, electromagnet coils surround the reactor for generation of a dc magnetic field which is imposed parallel to the surface of the rf-powered electrode. The character of the magnetic field produced by these magnetic coils is a function of the driving voltage waveform which can be chosen to be square or sinusoidal. The magnet drivers supply a slowly modulated dc current to the magnets producing a rotating magnetic field inside the reactor. Magnet shields surround each magnetic coil to contain the static magnetic field. Independent control of the current to each coil delivers the required phased current (typically 90 degrees phase shifted 0.25 Hz sinusoidal voltage) to the four coils, generating a rotating magnetic field. Each of the two magnet drivers controls two of the four electromagnetic coils, producing a magnetic field that varies in strength according to a sinusoidal or square wave relationship. The modulated magnetic field of typically 0 to 150 Gauss can increase the plasma density and reduce the sheath voltage at a fixed absorbed power [20]. As a result, a higher flux of ions with lower energy can be obtained.

Mass resolved energy analyzer experimental setup

The experimental setup designed to facilitate measurements of ion distribution functions and analysis of plasma species is described in the following. The Hiden EQP 500 mass and energy analyzer is mounted in a cross beam mode at the HART reactor side access port which is normally used as endpoint window (Fig. 4.3). The EQP sampling tube is moved through the reactor body access port and the liner opening into the plasma reactor by a manually driven z-shift. At the farthest point of movement, the EQP front end with the MACOR sampling orifice plate sits flush with the inner surface of the yttria coated liner insert which restricts the plasma. Hence, the near ideal cylinder geometry is maintained without perturbing the plasma by insertion of the ion sampling tube. To ensure a frictionless movement, about 1 mm are left in space between the MACOR orifice plate and the reactor liner opening. Consequently, the MACOR ceramic orifice plate forms a third electrode inside the liner wall ground electrode which is floating during plasma operation (see section 2.4.5). A 50 μm aperture at the center of the MACOR orifice plate allows for sampling of neutrals and a mass resolved ion energy analysis of plasma species impinging on the surface.

The mass spectrometer is differentially pumped by a 230 l/s (Pfeiffer) turbo molecular pump and a base pressure of about 1×10^{-8} Torr is achieved in the mass spectrometer chamber. Using a 50 μm orifice aperture plate during the experimental investigations, the operating pressure in the mass spectrometer chamber remains below 5×10^{-6} Torr for process reactor pressures up to 600 mTorr. Plasma species are sampled from the aperture which is located 27 cm from the radial center of the plasma and about 15 mm below the surface of the GDP. The mass spectrometer ionization source is located on a line-of-sight about 15 cm from the sampling aperture.

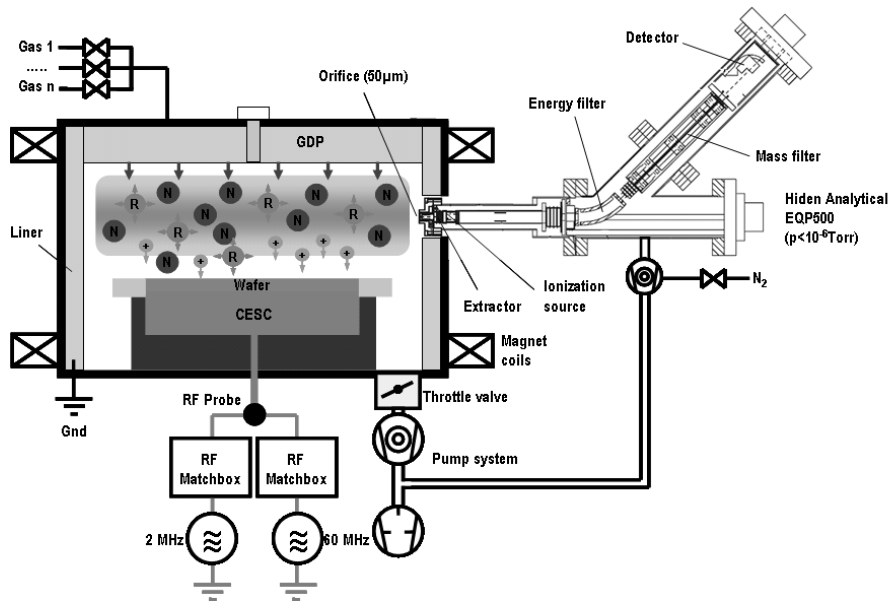


Figure 4.3: CCRF discharge experimental setup with Hidden EQP.

Infrared QCLAS experimental setup

A different experimental setup was designed to facilitate measurements of SiF_4 etch product concentrations and in situ wafer interferometry using infrared Quantum Cascade Laser Absorption Spectroscopy. Details about the Q-MACS optical arrangement can be found in section 3.1.3. For infrared beam coupling into the plasma reactor, two important requirements had to be met: (1) no open optical path, and (2) the availability of just one optical port access. The presented solution used for the different experiments is based on the use of mid-infrared (MIR) fibres, and internal reflections in the reactor chamber [266,267]. Two types of experimental setups have been utilized. Fig. 4.4-a shows a side access configuration used for SiF_4 concentration measurements, whereas Fig. 4.4-b sketches the top down access arrangement used for interferometer measurements. In both cases the IR laser beam is guided through a 1 m long IR fibre. The fibre ends have obtained an anti-reflection treatment for the specific laser wavelength used. The IR fibres are made of AgCl : AgBr materials. The laser has been collimated into the plasma reactor using an OAP for the side access and a ZnSe lens for the top down access. In case (a), the beam is reflected back using a retro-reflector which is installed at the plasma reactor wall. For the top down arrangement in case (b), the wafer and ESC surface is used for reflection. The reflected beam is coupled into the same path and reaches the detector using the second beam splitter (BS) in reflection mode. Several IR transparent SrF_2 windows were used to define the optical path of the beam through the reactor.

Description of used substrates

Different 300 mm substrates were used to cover the powered electrode (ESC) during the various experiments: (1) bare silicon wafers, (2) silicon wafers covered by an unpatterned silicon dioxide hardmask layer, (3) DT patterned process wafers, and (4) yttria wafers. For substrates (1)-(3), single crystalline $\langle 100 \rangle$ p-type silicon with resistivities of 14-22 Ωcm was used with a typical thickness of about 0.8 mm. In case of (2), an unpatterned 2 μm thick CVD SiO_2 hard mask layer was deposited onto the Si substrate. Few investigations were conducted using wafers with 512 MBit DRAM trench capacitor structures. These

process wafers were patterned by a similar SiO_2 hard mask for the deep trench silicon etch process. Furthermore, 300 mm yttria wafers were used for certain investigations. These Y_2O_3 substrates were specified with a thickness of about 1 mm and a surface roughness of about $0.8 \mu\text{m}$.

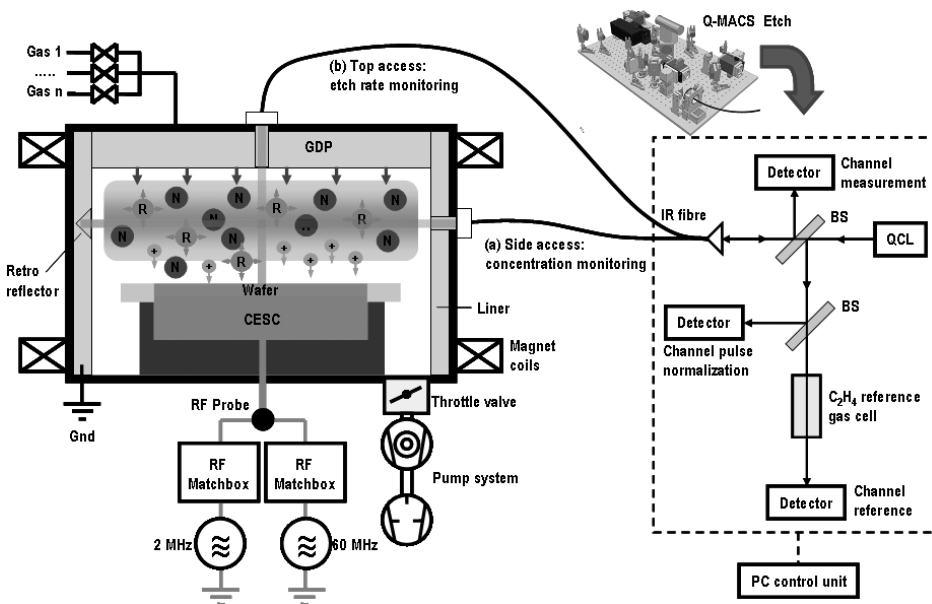


Figure 4.4: CCRF discharge experimental setup with the Q-MACS Etch system for (a) monitoring of SiF_4 concentrations in side access mode; (b) laser interferometry in top access mode.

Conduction of experiments

For the experiments, clean wafers were used in general. For investigations with SiO_2 masked substrates, a sufficient thickness before and after the experiment was ensured by applying ellipsometry. A standard NF_3 dryclean was employed to ensure comparable reactor conditioning prior every experiment. Contamination layers that can build up at the electrode surfaces will be efficiently removed by the chemical and physical attack during the NF_3 clean. Etch products adsorbed at the surface of the reactor walls were found to contribute to the measured plasma species to some extent during subsequent sequences of plasma processes. Without the clean plasma, particles resulting from contamination layers can be created in particular. Since particles can deposit on the wafer surface, this can lead to micromasking. If particles reach the ESC surface, an efficient wafer chucking will be impeded and the process aborted. In general, all reactor inner parts (liner, process kit quartz rings) were periodically cleaned from deposited process byproducts and replaced in case of advanced erosion.

Duration of the plasma process was fixed to 60 seconds for investigation of sputter and etch rates, otherwise the process time was appropriately chosen to satisfy limitations set by the sampling rate of the different plasma analysis techniques (e.g., IDF analysis, mass spectrometry, IR absorption spectroscopy). Ranges for the individual parameters varied during the experiments are given in Table 4.1. For some experimental configurations, the matching network could not find a stable position, e.g. high 2 MHz (bias) power vs. low 60 MHz (source) power. In most of these cases the plasma was turned off resulting from a high reflected power as is indicated in the discussions of the following sections. The different parameters investigated in this work do not include a variation of the substrate

temperature. The substrate temperature can not be controlled directly, but is influenced by the temperature of the powered electrode and the helium gas backside pressure. The helium backside cooling works such that an efficient temperature coupling is achieved by adjusting the backside pressure of helium gas streaming through small holes in the electrostatic chuck to the backside of the wafer.

Table 4.1: Ranges for the individual process parameters that were varied during this work.

Parameter variation	$P_{60\text{MHz}}$ [W]	$P_{2\text{MHz}}$ [W]	p [mTorr]	Q [sccm]	B [G]	$T_{\text{el}} / T_{\text{lid}} / T_{\text{wall}}$ [°C]
60 MHz power	250...3500	0	150	300 (Ar, HBr, NF ₃) 190 (SiF ₄)	0	90/70/70
60 + 2 MHz power	500...2500	500...2500	150	300 (Ar, HBr, NF ₃) 190 (SiF ₄)	0	90/70/70
Pressure	1500	0, 1500	50...600	300 (Ar, HBr, NF ₃) 190 (SiF ₄)	0	90/70/70
Ar gas flow rate	1500	0, 1500	150	100...800 (Ar)	0	90/70/70
HBr gas flow rate	1500	0, 1500	150	100...800 (HBr)	0	90/70/70
NF ₃ gas flow rate	1500	0, 1500	150	100...390 (NF ₃)	0	90/70/70
Magnetic field	1500	0, 1500	150, 300	300 (Ar, HBr, NF ₃) 190 (SiF ₄)	0...120	90/70/70

For investigation of plasma species by application of standard mass spectrometry, background measurements were performed prior every experiment to ensure sufficiently low background levels caused by adsorbed byproducts and stable etch species inside the EQP. However, this method is not sufficient to allow for a separation of the beam and background signals as determined from MBMS [144]. Mass spectra of neutral species were obtained by ionizing the gas effusing through the orifice into the EQP ionizer region with a 70.0 ± 0.3 eV electron beam prior to energy and mass selection. Differences in the mass spectra obtained with and without discharge operation were used to estimate the degree of the feed gas decomposition in the discharge following an approach presented in [80].

IDF analysis for particular plasma ions was conducted without changing the analyzer settings and scan rates, in order to allow for a comparison of all signal intensities for the same ion under different plasma conditions. Conversion dynode settings and scan rates were adjusted for each ion in order to provide adequate ion intensities without saturating the SEM. In the following sections, relative trends for the measured ion fluxes will hence be discussed for each single ion species.

Depending on the situation, measured ion distribution functions are plotted with as well as without corrections for shifts by the floating potential which is due to surface charging around the aperture at the dielectric orifice plate. As discussed in section 2.3, low-energy peaks are observed being attributed to charge exchange collisions in the proximity of the extraction hood (cf., Fig. 2.7). Peak positions are hence used for determination of the floating potential at the sampling aperture and calibration of the energy axis, which allows for comparison of different plasma conditions. During investigation of the different types of discharges, slight shifts in the floating potential were observed that are attributed to changing conditions of the sampling plate surface during operation of the discharge. This

can also be seen from the discussed low-energy peak which exhibits a more or less smeared feature (cf., inset of Fig. 2.7).

Once the IVDFs have been calibrated for the offset in the energy axis, a transformation to the corresponding IEDFs is performed to allow for a comparison with the calculated IEDFs. A straightforward evaluation of the ion energy distribution function that reflects the true distribution is not possible, except for cases where the angular variation of the distribution function is measured by a tiltable analyzer [72,73]. It should be noted here that computation of the IEDF from the IVDF strictly applies only for the assumption of an isotropic velocity distribution function, where the relation

$$f_E(\vec{r}, E_{\text{kin}}) = 4\pi \sqrt{\frac{2E_{\text{kin}}}{m^3}} f_v\left(\vec{r}, \sqrt{\frac{2E_{\text{kin}}}{m}}\right) \quad (4.2)$$

applies [206]. Here, f_E is the energy distribution, f_v the velocity distribution, and \vec{r} represents the location of each ion. As an example in Fig. 4.5, a comparison of a measured IVDF for Ar^+ ions and the calculated IEDF is given by assuming an isotropic velocity distribution function. As can be seen from this example, differences remain small if the measured IVDF does not involve a pronounced low energy part. Since most investigations are done at intermediate to relatively high pressures, contributions from elastic scattering and charge exchange collisions can be severe. This can finally result in lower mean energies obtained from the measured IVDFs, as compared to those obtained from the true IEDFs.

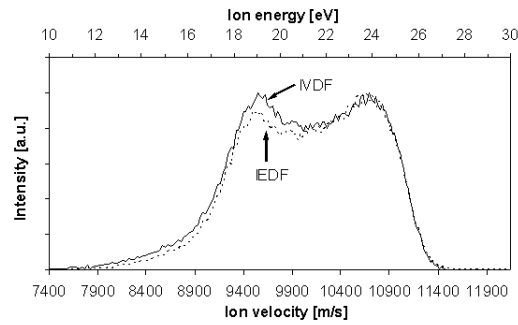


Figure 4.5: Comparison of a measured Ar^+ IVDF and the corresponding Ar^+ IEDF. Calculation of the Ar^+ IEDF from the measured forward part of the Ar^+ IVDF was performed according to [206] by assuming an isotropic velocity distribution function.

After calibration of the IVDFS and calculation of the corresponding IEDFs (with the assumption of an isotropic distribution), the mean ion energy can now be calculated to allow for comparison between the different types of investigated discharges and literature data. Furthermore, the mean ion energy remains as the parameter of choice to describe changes in the IDF since threshold energies to initiate etching with reactive ions are usually unknown. Such knowledge would be required to enable for a quantitative assessment on etch rate data. The mean ion energy was determined from the calculated IEDFs (that correspond to the measured IVDFs) by

$$\langle E_i \rangle = \frac{\int_0^{\infty} E_i \cdot f_E(E_i) dE_i}{\int_0^{\infty} f_E(E_i) dE_i} \quad (4.3)$$

As described in [206], calculation of the mean energy from a measured IVDF can sometimes yield considerable differences compared to the mean energy that is obtained from a corresponding IEDF. This is especially true when comparing low energies, as is the case for ions incident at the passive electrode of the asymmetric discharges investigated here. Mean ion energies determined with the described approach are influenced by the slightly shifting floating potential (few eV at most), and further by the uncertainty in the energy scale which is estimated to be ± 2.55 eV [153]. These values are however smaller than the width of typical IVDF structures observed in this work, hence allowing for a precise comparison of different IVDFs and determination of a nearly correct mean ion energy.

Theoretical analysis of aperture size effects on ion sampling indicates that an orifice of comparable size to that used here may affect the trajectories, and hence collection efficiencies, of ions with kinetic energies smaller than 5 eV [89,212]. Therefore, the relative ion signal intensities can be expected to exhibit more uncertainty and become increasingly less representative of the true energy distribution as the ion energy decreases below about 5 eV. Since most of the interesting structure in the distributions occurs above 5 eV, the low-energy discrimination effects at the orifice are not relevant to the interpretations of results presented here. Above 5 eV, the observed profiles of the kinetic-energy distributions exhibit a high degree of reproducibility.

4.2 Argon discharges

Applying mass resolved ion energy analysis, the $^{36}\text{Ar}^+$ ion was chosen to be monitored for studying the plasma and sheath behavior for all argon discharges investigated in this work. This second most frequent argon isotope was chosen because the main isotope $^{40}\text{Ar}^+$ causes excessive signal intensities, forcing the protection trip to abort the measurement in order to protect the EQP detector. The high signal intensities prohibit to achieve proper tuning of the ion optics section of the analyzer for minimized chromatic aberration effects and optimized signal-to-noise ratio. From the literature it is known, that further ions like Ar_2^+ , Ar^{++} , and ArH^+ (formed from residual water vapor in the reactor) can provide important information about ion formation, plasma-sheath characteristics, and the behavior of ions within the sheath [61,64-66,71,77,78,205]. However these ion species are characterized by densities typically several orders of magnitude lower than Ar^+ [13] and it is beyond the scope of this work to study argon discharges in more detail. Argon discharge characteristics at a comparable 300 mm CCP reactor have been recently reported in [268,269].

4.2.1 Neutral mass spectra

Mass spectra of neutral species in argon were obtained by ionizing the gas effusing through the orifice in the extraction hood with a 70 eV electron beam prior to energy and mass selection. In Fig. 4.6, a typical mass spectrum is plotted for a 60 MHz argon plasma at 150 mTorr. Besides the known isotopes $^{36}\text{Ar}^+$ and $^{40}\text{Ar}^+$ ($^{38}\text{Ar}^+$ is not shown due to its very low abundance), $^{40}\text{Ar}^{++}$ at $m/q = 20$ u is found as well. The threshold for double ionization is 27.6 eV which is well below the 70 eV delivered for ionization in the analyzer. Additional peaks appearing at $m/q = 18$ u and $m/q = 19$ u are attributed to H_2O^+ and F^+ , respectively. Fluorine is believed to result from dissociative ionization of ^{20}HF rather than from $^{38}\text{F}_2$, which is not detected. HF is a stable molecule that was formed during

previous plasma processes involving fluorine. ^{20}HF is believed to contribute to the $^{40}\text{Ar}^{++}$ peak at $m/q = 20$ u as well. The mass spectrum recorded for argon gas when the discharge was off is not plotted here since it reveals identical peak intensities.

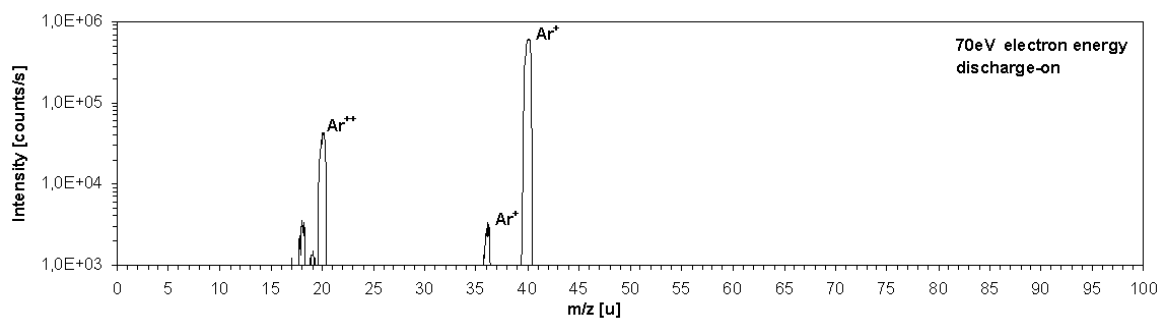


Figure 4.6: Mass spectrum of neutral species ionized by 70 eV electrons for Ar gas sampled from the reactor with rf discharge (150 mTorr, 1500 W 60 MHz power, 300 sccm Ar gas flow, silicon substrate). The spectrum for Ar gas without discharge was observed to be identical.

4.2.2 Variation of power

60 MHz single frequency discharges

For 60 MHz single frequency discharge operation, an increasing 60 MHz source power leads to a linear increase of the rf voltage up to 1500 W (Fig. E.1-a in appendix E), the slope starts to decrease slightly at higher power levels. The ion energy impacting on the substrate will increase proportionally caused by the increasing self-bias of the 60 MHz source. This is confirmed by $^{36}\text{Ar}^+$ IVDFs which shift towards higher energies (Fig. 4.7-a).

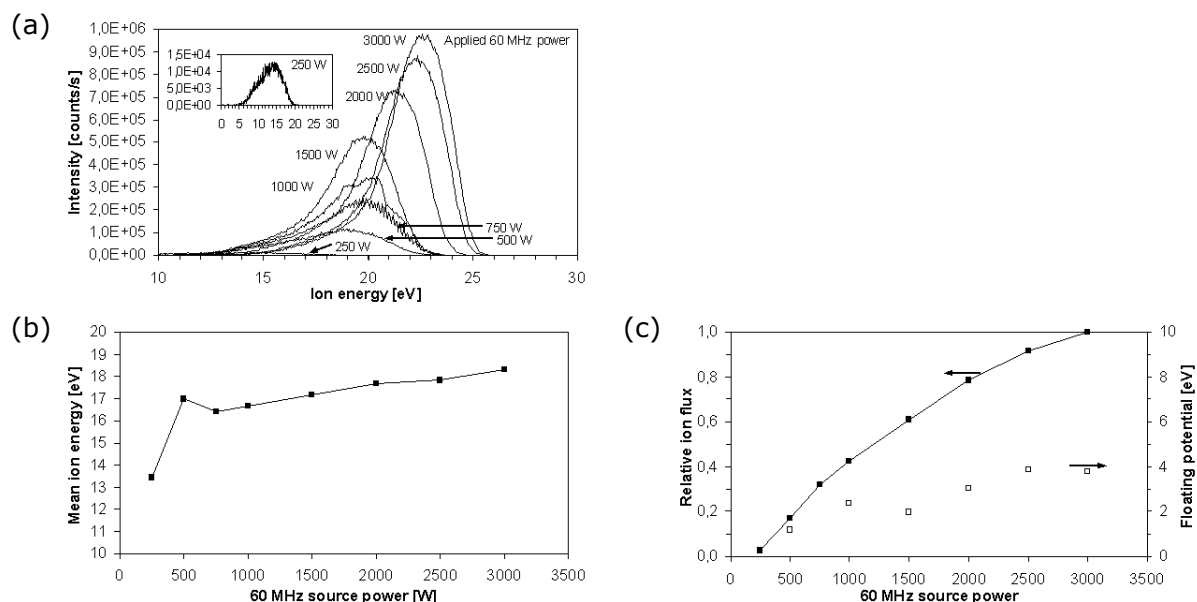


Figure 4.7: (a) $^{36}\text{Ar}^+$ IVDFs for power variation in 60 MHz argon discharges (150 mTorr, 300 sccm Ar gas flow rate, no magnetic field, silicon substrate); (b) corresponding mean ion energies; (c) relative ion flux (solid squares) and floating potentials at the extraction aperture (open squares) as determined from the position of the lowest energy peak. The IVDFs are plotted without applying corrections for the offset in the energy scale.

The IVDFs are plotted without applying corrections for the offset in the energy scale which is caused by a floating potential at the insulating orifice plate. The floating potential

will change for different plasma conditions. The mean ion energies calculated after applying corrections for the offset in the energy scale of the IVDF and further transforming the corrected IVDF into the corresponding IEDF (assuming an isotropic distribution function) are plotted in Fig. 4.7-b. Mean ion energies are found to increase slightly by rising the 60 MHz power as a result of the increasing self-bias of the 60 MHz frequency. As indicated by the measured rf current (cf., Fig. E.1-b), the electron density will increase when increasing the 60 MHz plasma excitation which causes the ion density to equally increase [214]. This is again supported by an increasing ion flux which is obtained from integration of the ion distribution functions, as shown in Fig. 4.7-c. For applied 60 MHz powers slightly above 1500 W, the ions impacting on the substrate appear to gain sufficient energy to overcome the threshold of the silicon binding energy which is about 44 eV, estimated from equations (1.65-1.67). This can be seen from the silicon sputter rate that starts to rise (Fig. 4.8-a).

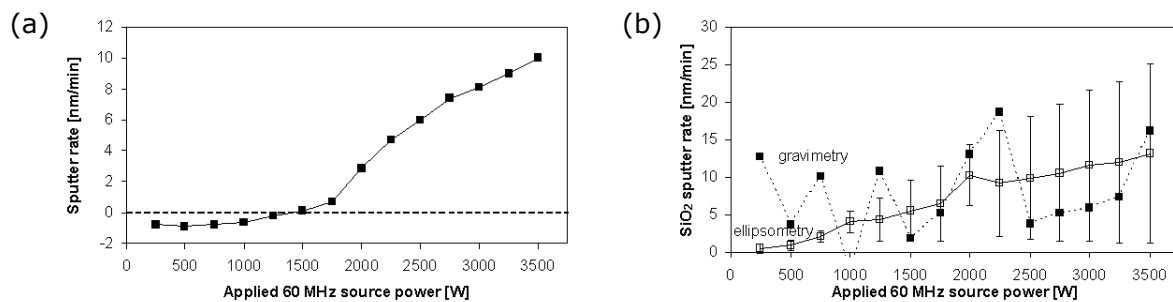


Figure 4.8: Sputter rates for 60 MHz power variation (150 mTorr, 300 sccm Ar gas flow rate, no magnetic field) for (a) silicon from gravimetry and (b) SiO₂ from gravimetry (full squares) and 49 point ellipsometry measurements (open squares).

Once sputtering is initiated, the effect of increasing ion flux and ion energy on the sputter rate can not strictly be separated anymore. As indicated by rf probe measurements from Fig. E.1-a and Fig. E.1-b and examination of the distribution functions, both ion energy and ion flux are rising less steeply for higher power levels which also explains the decreasing slope of the silicon sputter rate. That could indicate for example that the actual power dissipation in the plasma proceeds less linear compared to the applied power level, e.g., resulting from a decreasing power coupling efficiency at high power levels [258]. Other explanations could be the influence of argon incorporation and/or enhanced native oxide growth at a partially amorphous silicon substrate after exposing the substrate to atmosphere again, as discussed further below. Using a silicon substrate completely covered by an unpatterned SiO₂ hard mask layer yields slightly different results regarding the progression of the silicon dioxide sputter rate (Fig. 4.8-b). Neglecting the hump at 2000 W, a linear increase is observed from the mean values of the 49 point ellipsometry measurements (open squares) and the sputter rate already starts to rise from 250 W. The standard deviation increases as well reflecting the fact of an observed sputtering nonuniformity across the wafer where sputtering occurs predominantly at the wafer edge area. This can be explained by the skin effect becoming significant at 60 MHz high frequency plasma excitation which influences the local power dissipation in the plasma volume. Furthermore, edge effects in the gap region between wafer edge and focus ring can yield nonuniform distributions that can strongly deviate from the homogeneous electric field between powered (ESC) and opposite grounded electrode (GDP) area with peaks in the field strength at this region. Also, the plasma could penetrate into the gap [270,271].

As well, the temperature gradient between the wafer and the focus ring could be of some importance. From reactor simulations, spatial variations of the discharge pressure in the reactor remain negligible, and hence do not constitute to the observed sputter rate nonuniformity. The SiO₂ sputter rate as calculated from the integral weight loss measurements is plotted as well in Fig. 4.8-b (full squares). It shows large fluctuations which are attributed to an inefficient discharging of the SiO₂ layer corresponding to an experimental artefact of the gravimetry technique, as described in section 3.2.1.

From experimental data, the threshold for physical sputtering SiO₂ by Ar⁺ ions is calculated to about 49 eV, which is also supported by the literature [9,272-274] (cf., Fig. 4.9). This threshold is further found to be very close to the 44 eV sputtering threshold calculated for silicon. According to these values, silicon is sputtered at slightly lower energies than those needed to initiate sputtering of silicon dioxide. As can be seen from Fig. 4.7-b, at 250 W applied power the mean ion energy is already about 13.5 eV at the reactor wall. From typical values for the scaling exponent $1.1 \leq q \leq 2.6$ that describes the discharge anisotropy according to equation (1.6), ions accelerated in the sheath in front of the powered electrode can gain sufficient energy to exceed the threshold for sputtering at even very low power applied to the plasma. From comparison with results obtained for HPSM simulations of Ar discharges, mean ion energies calculated from the measured IDF would for example correspond well to an effective rf peak voltage between 100 V and 300 V for plasma densities in the $5 \times 10^9 \dots 1 \times 10^{10} \text{ cm}^{-3}$ range (cf., Fig. C.1-j in appendix C), provided the other plasma parameters used as input for the HPSM simulator apply as well. Then, the mean energy for ions at the powered electrode would be around 50 eV, which is slightly above the 44 eV threshold calculated for silicon physical sputtering. The observed differences between the sputter rates discussed above are attributed to an incorporation of argon projectiles into the silicon lattice, leading to negative values for the weight loss measurements [275]. At low power levels, the energy of these projectiles (Ar⁺ ions and fast neutrals) is not high enough to cause significant damage at the surface of the crystalline lattice, i.e. amorphization is negligible. Thus, the projectiles can travel a considerable distance below the surface by pronounced channeling. Also, the energy at this point may not be high enough to release silicon atoms through cascading in a certain depth, or a higher extent of Ar projectiles is incorporated into the substrate than silicon atoms are released. For a certain amount of energy, amorphization of the surface will become significant, inhibiting channeling effects. Also, incident projectiles will deposit a higher amount of energy at higher power levels. The sputter yield is increasing as a result of both an increasing Ar⁺ ion energy and Ar⁺ ion flux with rising 60 MHz power. Studies comprising interactions of Ar⁺ ions with silicon surfaces using molecular dynamics simulations [276] suggests a dynamic balance between ion-induced damage and recrystallization. According to that work, a near-surface amorphous layer created through Ar⁺ ion bombardment was calculated, ranging from about 1 Å at 10 eV to 15 Å at 200 eV. Besides the discussed incorporation of Ar into the substrate, amorphization and recrystallization effects, and the increasing sputter yield, native oxide growth is expected to further influence Ar sputter rates on silicon substrates to a certain extent [275]. Native oxide growth can occur when substrates are removed from the reactor and exposed to ambient atmosphere after a sputtering process. Oxide growth will be more efficient in cases of high surface amorphization after high plasma induced damage. In contrast to the silicon sputter rate, silicon dioxide is obviously sputtered at even very low power applied to the plasma. Unlike silicon, the silicon dioxide layer is initially amorphous and hence no channeling will occur.

The energy of Ar projectiles is deposited efficiently to sputter off substrate atoms even at the lowest 60 MHz power applied. To compensate for the observed differences between initial sputter rates for silicon and SiO₂, the required amount of argon deposited into the substrate surface would even exceed 1000 monolayers. This indicates that oxide growth of a few nanometers on the silicon surface appears to be the dominant mechanism to explain the observed differences.

Energy Dependence of Ar⁺ Sputter Yield

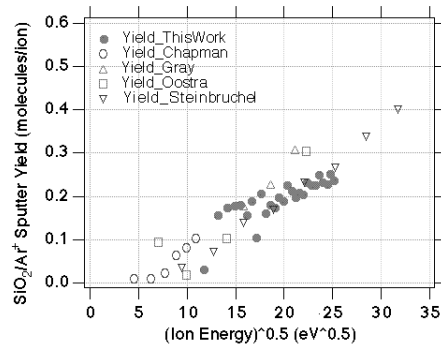


Figure 4.9: Ar sputter yield on SiO₂ from literature [9,272-274] and data obtained in this work.

Even at a quite high pressure of 150 mTorr, contribution due to collisions is observed to be minimal for the IDFs for ³⁶Ar⁺ plasma ions in Fig. 4.7-a. By increasing the 60 MHz power, the rf voltage is observed to rise as well (Fig. E.1-a in appendix E) further leading to higher sheath voltages. However, a separation of the IDF double peak structure predicted from equation (1.64) is not observed and the double peak structure remains unresolved, forming a single peak structure. This is due to the ion inertia for the relatively high mass ions investigated here. For the 60 MHz high frequency, the sheath is oscillating very fast making it impossible for the ions to follow. Hence, Ar⁺ ions respond only to the average of the time-varying sheath potential. As discussed in section 2.5, this interpretation of the measured IDFs differs slightly from HPSM calculation where IDFs are influenced by an average sheath electric field of the oscillating sheath only, and an influence by the rf phase is neglected. From Fig. 4.7-a, an increased contribution due to collisions to the IDF structure is not observed by rising the power. This can be explained by an increasing plasma density when rising the 60 MHz power (cf., Fig. 4.7-c), inducing the sheath width to decrease. The ion transit time across the sheath is very short and the probability of collisions in the sheath decreases. The low probability of sheath collisions also explains the very low intensity of the low-energy peak (not shown here) which is attributed to charge exchange collisions in the sheath in the vicinity of the extraction aperture. The peak can additionally appear smeared due to a varying floating potential of the dielectric orifice plate. The position of the discussed charge exchange peak is observed to increase slightly between +1 and +4 eV which can be explained by positive charge accumulation from Ar⁺ ions bombardment of the orifice plate surface.

60+2 MHz dual frequency discharges

For 60+2 MHz dual frequency discharge operation, the rf mean voltage measured for the 60 MHz source power component is hardly affected by a superposition of the 2 MHz bias power component (Fig. E.1-a). However, the 2 MHz rf voltage is observed to be significantly influenced by the 60 MHz component (Fig. E.2-a). Increasing the applied 60 MHz source

power yields drastically reduced rf voltages measured for 2 MHz, disproving an initial assumption of a simple superposition of the 60 MHz and the 2 MHz self bias here. This observed behaviour is transferred to the ion energy being mainly controlled by the 2 MHz bias power. In Fig. 4.10-a to Fig. 4.10-c, measured IVDFs for $^{36}\text{Ar}^+$ ions sampled from the discharges are shown for a variation of 60 MHz power at fixed 2 MHz power of 500 W (Fig. 4.10-a), 1500 W (Fig. 4.10-b), and 2500 W (Fig. 4.10-c). The wide peak separation caused by the low frequency sheath modulation is clearly visible, as is predicted from the inverse scaling of the peak separation with frequency according to (1.64). At low 60 MHz plasma excitation, the 2 MHz frequency determines the sheath modulation and the peak separation becomes very broad and maximum ion energies are observed. This is caused by a high sheath voltage from the dominating contribution of the 2 MHz frequency. The highest mean ion energies in Fig. 4.10-d are observed for lowest 60 MHz power, provided the 2 MHz power exceeds the 60 MHz power. For intermediate to high 60 MHz power applied to the discharges, only small differences are observed despite applying very different 2 MHz power levels. A lower mean ion energy at the ground electrode was observed from the HPSM simulations of 60+2 MHz mixed argon discharges (cf., Fig. C.6-h), whereas the energy for ions incident at the powered electrode was found to increase at the same time (Fig. C.6-i). The reduced ion energy at the ground electrode described here could yield a reduction in the ion energy gain, as would be expected when increasing the delivered power. As the 60 MHz power is increased, the density increases as well (Fig. 4.10-e) which causes the sheath width to become drastically thinner as can be seen from the reduced ion energies. Measured rf voltages appear sloped as described for 60 MHz single frequency operation. The slope is by far more decreasing for the 2 MHz rf voltages, also indicating a saturation for high 2 MHz bias power values. Increasing the 2 MHz bias power further from intermediate or high values will accordingly yield only a small further gain in the ion energy, meaning the 50 eV maximum ion energy observed in Fig. 4.10-c will not continue to increase as steeply by applying 2 MHz power levels higher than 2.5 kW. The increase observed for the 60 MHz rf mean current (Fig. E.1-b) agrees quite well with the increasing ion flux in Fig. 4.10-e. Again, the electron density will increase for increasing 60 MHz plasma excitation and cause the ion density to equally increase [214].

The lower energy peak of the bimodal structure appears to be preferred which can be attributed to the non-sinusoidal nature of the sheath voltage. The minimum of the sheath potential will be slower varying than the maximum, allowing more ions to enter the sheath during this phase which will contribute to the low-energy peak of the saddle-shaped structure [7,8]. As in the single frequency case, contributions due to collisions are almost negligible for the IDFs in dual frequency discharges operated at 150 mTorr. An increased contribution due to collisions to the IDF structure is not observed for the sheath in front of the passive electrode, even at maximum sheath widths for high 2 MHz powers applied. The sheath width will decrease when rising the 60 MHz power and the probability of collisions will decrease further. From Fig. 4.10-e, the low-energy peak for charge exchange in the sheath near the orifice appears to be affected little by both frequencies and is found to vary between +1 and +4 eV which is comparable to the results from single frequency argon discharges.

Addition of 500 W of 2 MHz bias power will yield a silicon sputter rate for even very low 60 MHz plasma excitation which is easily explained by supplying sufficient ion energy by the 2 MHz frequency drive to initiate efficient sputtering. A threshold for 2 MHz, similar to the investigations done for 60 MHz single frequency operation, was not studied in detail here.

All experiments including 2 MHz bias power were observed to yield sufficiently high ion energies to induce sputtering of both silicon and SiO₂. The silicon sputter rates are observed to increase for increasing 2 MHz bias power applied with near linear slopes (Fig. 4.11-a). For dual frequency plasma operation, the increasing silicon sputter rate caused by an increasing 60 MHz power is attributed to an increasing ion flux. The decreasing slope found for the measured ion flux is also observed in the sputter rate when increasing the 60 MHz power at fixed 2 MHz power. As explained above, the ion energy will drop slightly with increasing 60 MHz power, but still remains well above the threshold for silicon sputtering here. The increase of the silicon sputter rate due to an increasing 2 MHz bias power is affected by both an increasing ion flux and ion energy. When the applied 2 MHz power finally exceeds the 60 MHz power, the ion density is efficiently reduced by further increasing the 2 MHz power. The continuously rising sputter rate is then determined by a higher ion energy which in turn also starts to compensate for the decreasing ion flux. Unlike the decreasing slopes seen for the ion energy from Fig. 4.10-d, the silicon sputter rate does not tend to saturate. However, mean values of the SiO₂ sputter rate determined from 49 point ellipsometry (Fig. 4.11-b) indeed appear to saturate according to the above discussion.

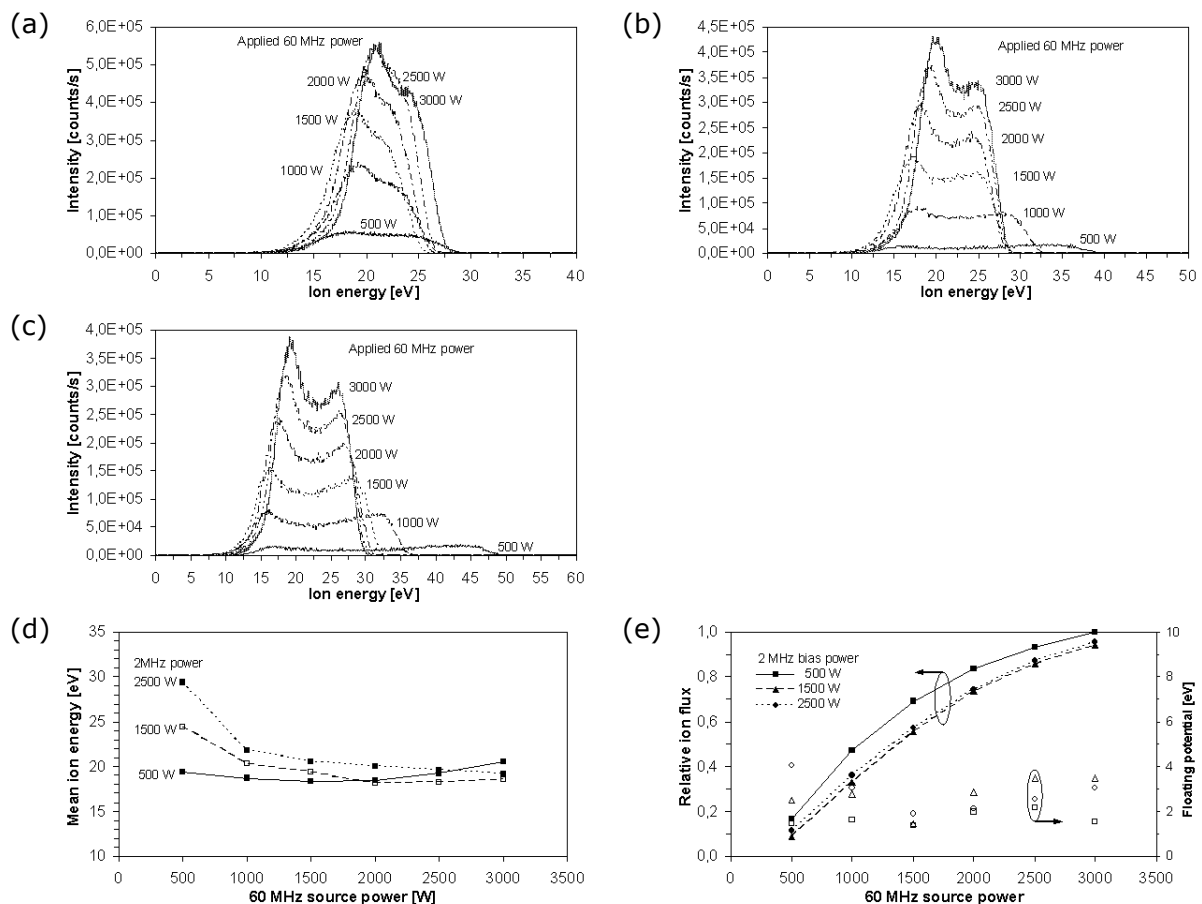


Figure 4.10: $^{36}\text{Ar}^+$ IVDFs for 60 MHz power variation in 60+2 MHz dual frequency argon discharges shown for fixed 2 MHz power of (a) 500 W, (b) 1500 W, (c) 2500 W (150 mTorr, 300 sccm Ar gas flow rate, no magnetic field, silicon substrate); (d) corresponding mean ion energies; (e) relative ion flux (solid squares) and floating potentials at the extraction aperture (open squares) as determined from the position of the lowest energy peak. The IVDFs are plotted without applying corrections for the offset in the energy scale.

Compared to the experiments using silicon substrates, rf probe voltages measured at 2 MHz for SiO₂ have a slope which is less steep (Fig. E.2-d), and are about 10-20 % lower at 2.5 kW applied 2 MHz power. This indicates a reduced ion energy compared to experiments using silicon substrates. For the measured current, the situation appears to be mirrored. Starting at comparable values at low 2 MHz power, the current is measured to be about 10-20 % higher at maximum 2 MHz bias power (Fig. E.2-e) for SiO₂. The difference can be explained by either an increased plasma density due to a higher ion-impact secondary electron emission coefficient [277] for Ar⁺ ions impacting at SiO₂, differences in the power coupling for different substrate materials, and/or a slightly different plasma chemistry (e.g., caused by released oxygen) leading to a different plasma impedance. The lower ion energy observed for SiO₂ in the intermediate and high dual frequency power regime seems to be responsible for the lower SiO₂ sputter rate, as observed from Fig. 4.11-b. The higher ion flux concluded from a higher current can only partly compensate the sputter rate loss due to a reduced ion energy. The standard deviation resulting from the 49 point ellipsometry thickness measurements are indicated only for the lowest and highest 60 MHz source power investigated here, reflecting the minimum and maximum nonuniformities measured for the different discharge conditions. As for the single frequency case, increasing the 60 MHz source power yields a sputtering nonuniformity across the wafer with a high argon sputter rate at the wafer edge area. This is again attributed to a pronounced skin effect at high 60 MHz source power levels, spatial distortions of the electric field distribution between the wafer edge and focus ring, plasma penetration into the gap between wafer and focus ring, and/or a temperature gradient between wafer and quartz focus ring. SiO₂ sputter rates extracted from gravimetry were not plotted here since these results were comparable to ellipsometry data shown in Fig. 4.11-b.

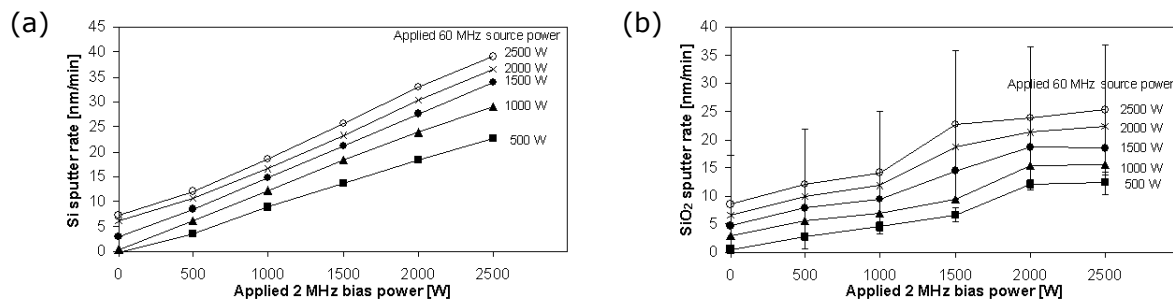


Figure 4.11: Sputter rates for 60+2 MHz power variation (150 mTorr, 300 sccm Ar gas flow rate, no magnetic field) for (a) silicon from gravimetry and (b) SiO₂ from 49 point ellipsometry measurements.

4.2.3 Variation of pressure

60 MHz single frequency discharges

In Fig. 4.12-a, IDFs for ³⁶Ar⁺ plasma ions are plotted for a variation of the discharge pressure from 50 mTorr to 600 mTorr where the 60 MHz power is held constant. The IVDF structures remain singly peaked at the time-averaged sheath potential due to the ions at 60 MHz being able to respond only to the time-averaged sheath electric field. At 50 mTorr, sheath collisions will be almost negligible [20]. Ions enter the sheath directly from the bulk plasma and become accelerated through the entire sheath potential. A transition from 50 mTorr to 100 mTorr is observed resulting in significantly reduced ion energies at higher pressures. This transition is most likely due to changes in the plasma confinement and an

expansion of the plasma volume from 50 to 100 mTorr, causing the average sheath thickness to become thinner (cf., Fig. C.2-a in appendix C). Since the effective electrode area ratio changes only slightly (about 3% reduction of the scaling coefficient q from Fig. C.2-e), the average energy of ions incident on the powered electrode should be effected similarly. The approximately 25% decrease for the measured mean ion energy is however higher than the 10% reduction obtained from HPSM calculations (for the corresponding 50 mTorr to 100 mTorr transition), assuming parameters like electron energy, electron temperature, electron density, rf peak voltage, neutral gas temperature, etc. remain constant. In reality, the discharge presumably stabilizes at a new operating point where those parameters have changed to a certain extent, leading to the observed stronger decrease of the mean ion energy. This might in particular be caused by changes in the EEDF and the mean electron energy that accompany a discharge transition. Two different types of discharge transitions involving such changes have been reported. When increasing the gas discharge pressure, a transition from collisionless (or non-Ohmic) to collisional (or Ohmic) electron heating can occur [278]. The collisionless heating mechanism in low pressure discharges is understood as stochastic heating. The other type of transition is known to occur from the low-voltage (or α) to the high-voltage (or γ) mode with increasing discharge current density [4,5]. While at low rf discharge voltages the ionization is maintained by the bulk plasma electrons, the ionization at high voltages is provided by secondary electron emission from the electrodes due to ion bombardment.

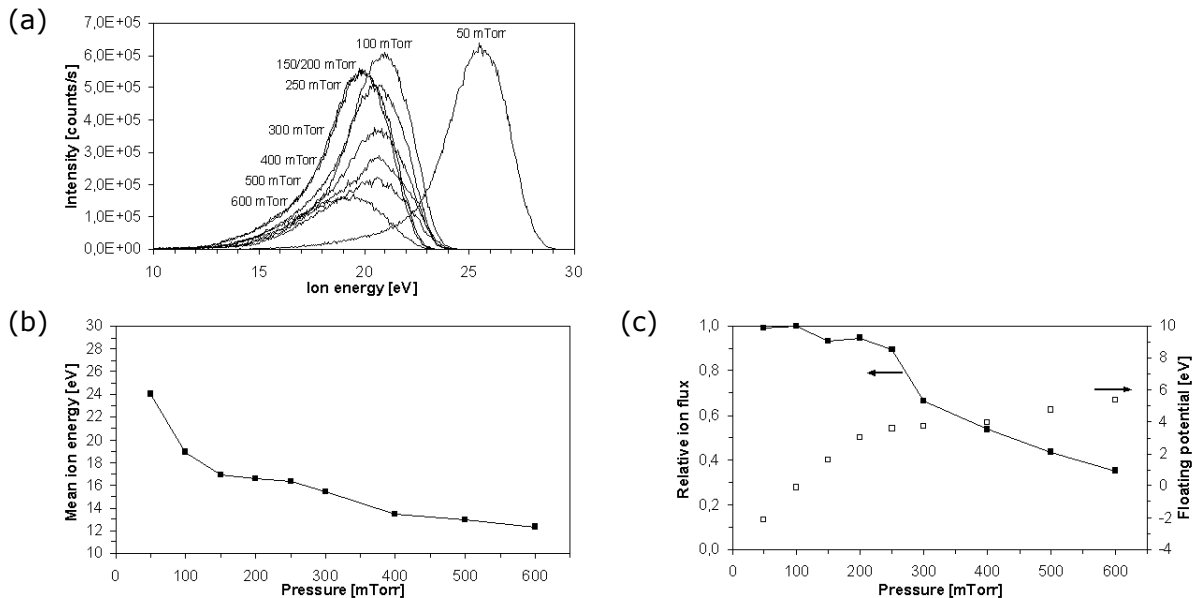


Figure 4.12: (a) $^{36}\text{Ar}^+$ IVDFs for pressure variation in 60 MHz argon discharges (1500 W, 300 sccm Ar gas flow rate, no magnetic field, silicon substrate); (b) corresponding mean ion energies; (c) relative ion flux (solid squares) and floating potentials at the extraction aperture (open squares) as determined from the position of the lowest energy peak. The IVDFs are plotted without applying corrections for the offset in the energy scale.

At higher pressures, the sheath becomes more collisional and ions traversing the sheath will experience more collisions with mainly the background neutral gas. This results in both momentum and energy transfer leading to a distribution broadening and moving the IDFs towards lower energies. The structure of the measured distribution functions remains comparable up to quite high pressures of 250 mTorr, and contributions due to sheath

collisions appear to remain quite small. At higher pressures, the mean ion energy is moving to lower values which is attributed to the influence of an increasing collisionality. Ions will be created in the sheath through enhanced resonant charge exchange collisions not experiencing the entire sheath potential anymore. The decreasing mean ion energy for an increasing pressure can be seen from Fig. 4.12-b. There is reasonable agreement to the mean ion energy at the ground electrode from HPSM simulations performed for a pressure variation of the same 50-600 mTorr range in 60 MHz argon discharges (cf., Fig. C.2-j). Parameters like rf voltage, electron temperature, electron density, gas temperature can however change during the experiment which could explain the deviations between experiment and simulation (where these parameters were held constant for the HPSM calculations). However, comparing mean energies at 50 mTorr minimum pressure and 600 mTorr maximum pressure yields about 24 eV and 11-12 eV, respectively, for both cases.

The floating potential determined from the position of the lowest energy is found to increase from about -2 eV to +6 eV (Fig. 4.12-c). At low pressures, the number of species is reduced and a decreased ion density is expected. However, the Ar^+ ion flux (cf., Fig. 4.12-c) surprisingly decreases continuously when rising the pressure. This could indicate either an increased charge carrier loss, e.g., through enhanced ion-electron neutralization collisions, or a less efficient ionization in the plasma at higher pressures. Further investigations comprising etch rate and rf probe measurements have not been performed here, but will be discussed for 60+2 MHz discharges below.

60+2 MHz dual frequency discharges

Results of rf probe measurements for a pressure variation in dual frequency Ar discharges (where both 60 MHz and 2 MHz power were held constant) are plotted in Fig. E.3 (in appendix E). For decreasing as well as increasing process pressures, the rf probe voltage is observed to increase exponentially showing a distinct minimum at 250 mTorr for silicon and 150 mTorr for SiO_2 (cf., Fig. E.3-a). At low pressures, the number of species is reduced and a decreased ion density is expected. This assumption is confirmed by the measured current which constantly decreases when the pressure is reduced (Fig. E.3-b). At low pressures, the sheath thickness will increase according to a power law (cf., Fig. C.2-a), and from the increased ion mean free path less collisions are expected.

In Fig. 4.13-a, $^{36}\text{Ar}^+$ IDFs are plotted for a variation of the discharge pressure. As seen for the single and dual frequency power variation in section 4.2.2, the Ar^+ ions will almost perfectly respond to the 2 MHz frequency, whereas at 60 MHz they will only respond to the time-averaged sheath voltage. For the dual frequency discharges investigated at different pressures, a generally broad bimodal IDF structure is observed. The preferred lower energy peak is possibly caused by a slower varying minimum sheath potential. As observed for single frequency argon discharges, the IDF shift to lower energies when rising the pressure above 50 mTorr as can be seen from Fig. 4.13-b. The reduction in ion energy is again attributed to an increased number of sheath collisions at higher pressures. Again, there is reasonable agreement between experiments and 2 MHz argon discharge simulations (cf., Fig. C.2-j). Slightly lower energies were found from experiments. This could be attributed to the influence of 60 MHz power superimposed on the 2 MHz power, which was found to yield reduced ion energies from both experiments (e.g., Fig. 4.10-d) and simulations (Fig. C.6-h). Deviations can further be caused by a varying electron temperature, rf voltage, electron density and gas temperature during the experiments, as discussed above for 60 MHz single frequency operation. Again, the EEDF might change considerably as a result of

stochastic-Ohmic heating [278] and/or α - γ mode discharge transitions [5,6]. Surprisingly, the mean ion energy is found to increase for pressures above 400 mTorr. This is caused by the considerable broadening of the IDFs to higher energies at 500 and 600 mTorr, which could be reproduced through several measurements. The higher energy values might be unexpected at first sight, following the expectation that at higher pressures the ions are subject to more collisions, hence resulting in lower energies. However, the higher pressure gives rise to a smaller sheath thickness (cf., Fig. C.2-a) which reduces the total number of collisions in the sheath and yields higher ion energies. Furthermore, the modified IDFs might result from a change of the different discharge parameters for a new stable operating point of the discharge. The floating potential plotted in Fig. 4.13-c is found to develop quite similar to the pressure variation in 60 MHz Ar discharges. The $^{36}\text{Ar}^+$ ion flux (cf., Fig. 4.13-c) is found to increase between 50 mTorr and 200 mTorr due to more ions created from the increased number of argon neutral gas in the plasma bulk. For pressures exceeding 200 mTorr, the ion flux now decreases, similarly to what was observed for the complete pressure variation from single frequency Ar discharges. These findings are however not supported by measurements of the current with the rf probe plotted in Fig. E.3-b. The current being proportional to the electron and hence ion density continuously rises, e.g., as one would expect for the case where the ionization is limited by the total number of neutral species in the discharge.

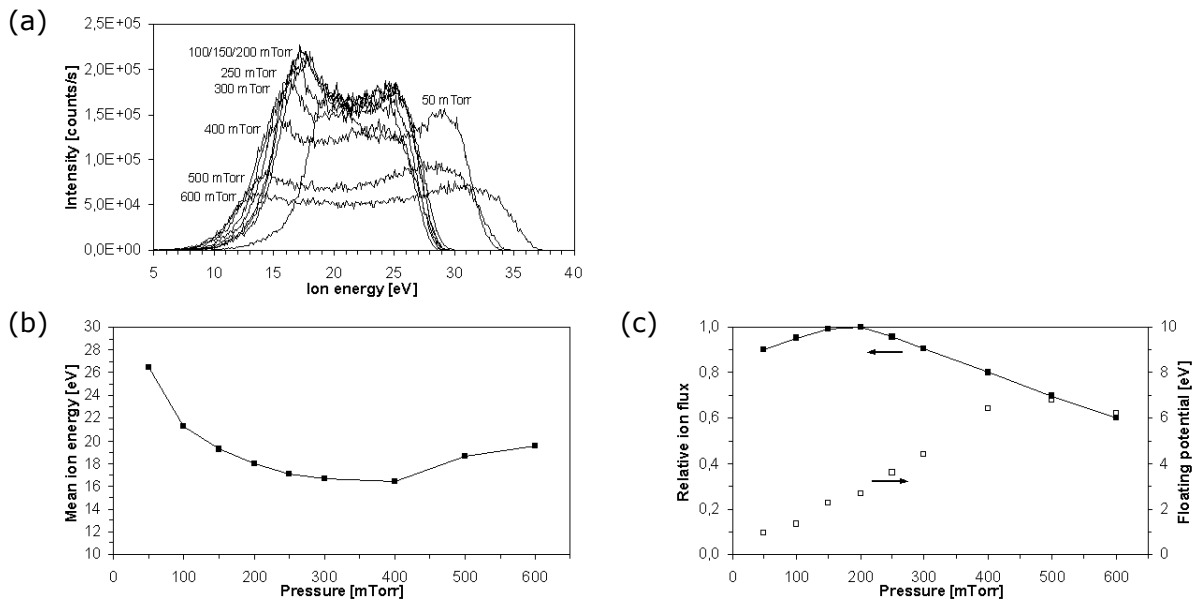


Figure 4.13: (a) $^{36}\text{Ar}^+$ IVDFs for pressure variation in 60+2 MHz argon discharges (1500+1500 W 60+2 MHz power, 300 sccm Ar gas flow rate, no magnetic field, silicon substrate); (b) corresponding mean ion energies; (c) relative ion flux (solid squares) and floating potentials at the extraction aperture (open squares) as determined from the position of the lowest energy peak. The IVDFs are plotted without applying corrections for the offset in the energy scale.

An increasing ion energy at decreasing pressure seems to mainly determine the progress observed for the silicon and SiO_2 sputter rates (Fig. 4.14-a and Fig. 4.14-b). For an increasing pressure, the sheath thickness decreases and ion energies will decrease as well due to an enhanced probability of sheath collisions. From HPSM calculations, the effect of a decreasing sheath thickness is more pronounced at the powered electrode indicating that the discharge becomes more symmetric at high pressures (Fig. C.2). These findings

strongly support results of the sputter rates on substrates at the powered electrode. According to rf probe measurements, the ion energy is furthermore observed to be the main factor dictating the pressure dependent sputter rate. An apparently increasing ion flux at intermediate pressures can obviously not compensate for the energy loss. From Fig. 4.14-b, the SiO₂ sputter rate shows large nonuniformities where the highest sputter rate is measured at the wafer edge area. This can again be attributed to a combination of skin effect, and edge effects in the gap region between wafer edge and focus ring due to potential and/or temperature gradients, as described in the sections before. The differences between integral weight loss measurements and mean values of the optical thickness measurements are attributed to measurement artefacts of the gravimetry technique, where charging of the SiO₂ layer is believed to inhibit correct balancing of the substrates after the sputter processes.

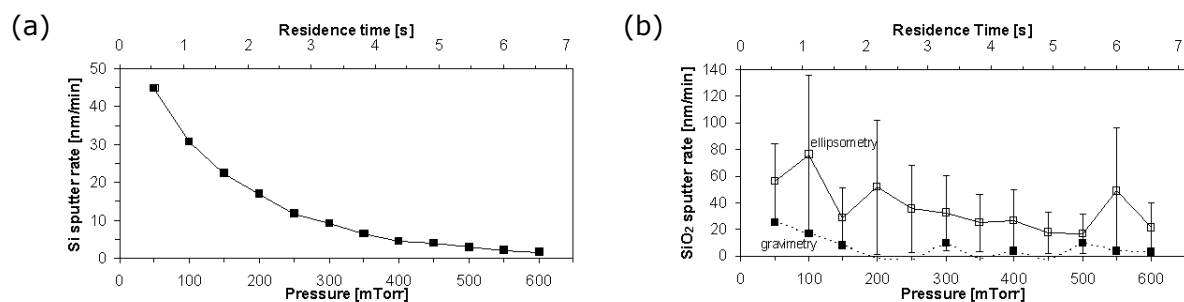


Figure 4.14: Sputter rates for pressure variation (1500+1500 W 60+2 MHz, 300 sccm Ar gas flow rate, no magnetic field) for (a) silicon and (b) SiO₂ from gravimetry (full squares) and 49 point ellipsometry measurements (open squares).

4.2.4 Variation of gas flow rate

60 MHz single frequency discharges

In Fig. 4.15-a, IDFs for ³⁶Ar⁺ plasma ions are plotted for a variation of the argon gas flow rate from 100 sccm to 900 sccm where the 60 MHz power and pressure were held constant. Generally, a high flow rate is expected to reduce the residence time of plasma species only. Surprisingly, the mean ion energy appears to slightly increase by 1.4 eV when increasing the argon gas flow rate (Fig. 4.15-b), and further the Ar⁺ flux is observed to dramatically increase for reduced residence times (Fig. 4.15-c). Both phenomena could be caused by strong changes of the background gas temperature. The Ar gas is assumed to be thermal and uniformly distributed, and for discharge-off conditions the gas temperature should finally equilibrate to the temperature of the surrounding reactor walls. As will be shown from calibration of SiF₄ concentrations later, the gas temperature in the plasma can however rise to fairly high values (several hundred kelvin above room temperature), and also be influenced by the temperature of the powered electrode surface [13]. In the case of considerably high gas flows as investigated here, the background gas is not uniformly distributed anymore. Nonuniform distributions can yield locally varying gas densities which will also affect collisions in the sheath region. The effect of different gas temperatures was investigated in detail from HPSM simulations (cf., section 2.5.1 and Fig. C.3 in appendix C). Variation of the neutral gas temperature results in changes of the neutral gas density since the reactor pressure is hold constant. The increasing ion flux at high gas flow rates might be due to an increasing plasma density for reduced gas temperatures which is supported by discharge simulations. From the slight changes of the mean ion energy for the argon

gas flow rate ranging from 100 sccm to 900 sccm it could be concluded, that the gas temperature changes by roughly 100-200 K (cf., Fig. C.3-j), which in detail depends upon the exact mean neutral gas temperature. However, the mean Ar⁺ ion energy increases slightly which would require the neutral gas temperature to increase with Ar flow. Since this does not appear consistent, changes of further discharge parameters must overcompensate a decreasing mean Ar⁺ ion energy from reduced gas temperatures in reality.

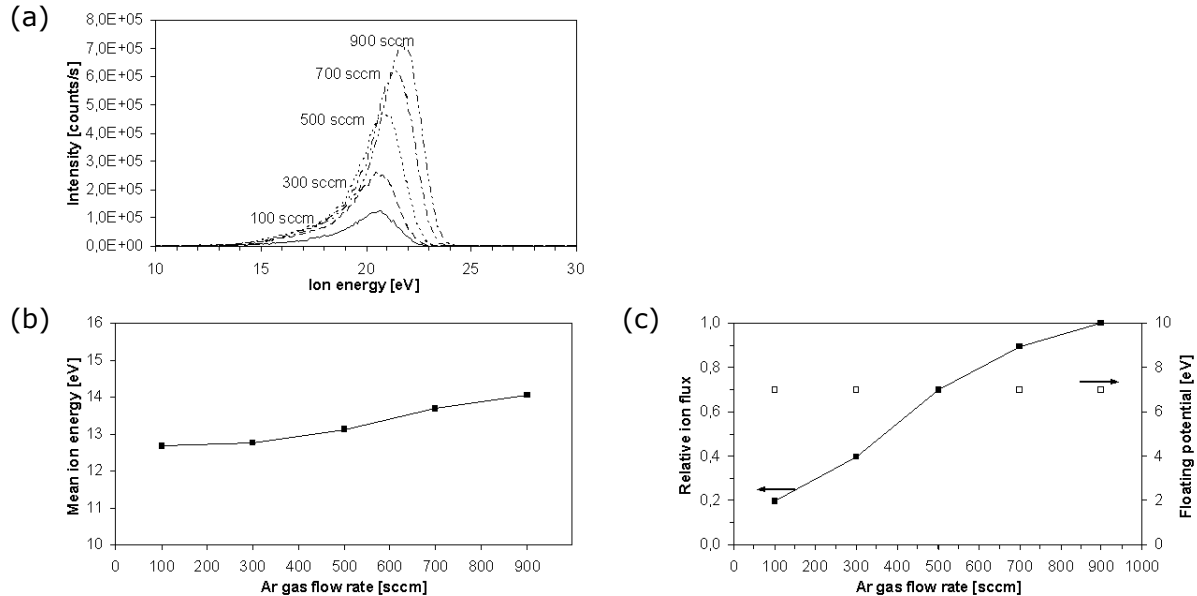


Figure 4.15: (a) $^{36}\text{Ar}^+$ IVDFs for variation of the argon gas flow rate in 60 MHz argon discharges (1500 W, 150 mTorr, no magnetic field, silicon substrate); (b) corresponding mean ion energies; (c) relative ion flux (solid squares) and floating potentials at the extraction aperture (open squares) as determined from the position of the lowest energy peak. The IVDFs are plotted without applying corrections for the offset in the energy scale.

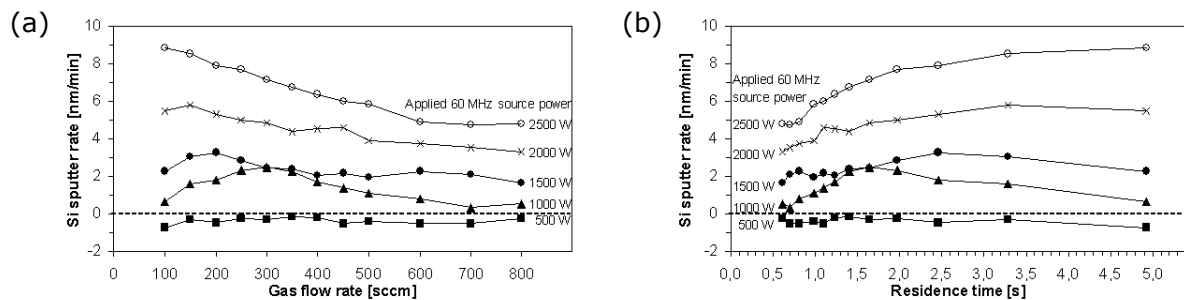


Figure 4.16: Silicon sputter rates (as determined from gravimetry) for variation of the Ar gas flow rate and different 60 MHz powers (150 mTorr, no magnetic field) displayed as a function of (a) gas flow rate and (b) corresponding residence time.

Variation of the gas flow is not expected to have a major effect on the sputter rate since no chemical reaction is involved. Surprisingly for 60 MHz single frequency discharge conditions, the silicon sputter rate is however observed to show a quite pronounced dependency on the gas flow rate (Fig. 4.16-a and Fig. 4.16-b). Highest sputter rates are measured at low flow rates, or high residence times, respectively. The Ar gas seems to be ionized more efficiently for longer residence times as a result of a predominantly indirect

ionization of argon atoms via metastables, yielding a larger ion flux that increases the etch rate up to a certain extent. These findings are however in contrast to the findings from the IDF measurements. One explanation could be explained by a change of the Ar^+ ion uniformity distribution where the maximum in the Ar^+ ion flux could shift from the reactor/wafer center towards the reactor walls (where ion fluxes are measured) when increasing the Ar gas flow. A clear picture of the mechanisms remains however unknown at this point and should be subject to further investigations. Aside, sputter rates on SiO_2 were not investigated here, and hence no uniformity data is available that could support the idea of a change in the Ar^+ ion flux distribution. From reactor simulations, spatial variations of the discharge pressure in the reactor are observed to be negligible (below 0.1%) and do not constitute to the observed changes in the IDF and sputter rates.

60+2 MHz dual frequency discharges

Increasing the argon gas flow rate in dual frequency argon discharges at constant power level and pressure yields similar effects as observed for 60 MHz single frequency discharges. Again, mean ion energies are found to slightly increase (Fig. 4.17-b), $^{36}\text{Ar}^+$ IDFs plotted in Fig. 4.17-a however do not exhibit the drastic changes in intensity (cf., Fig. 4.17-c) as measured for the single frequency cases (cf., Fig. 4.15-c).

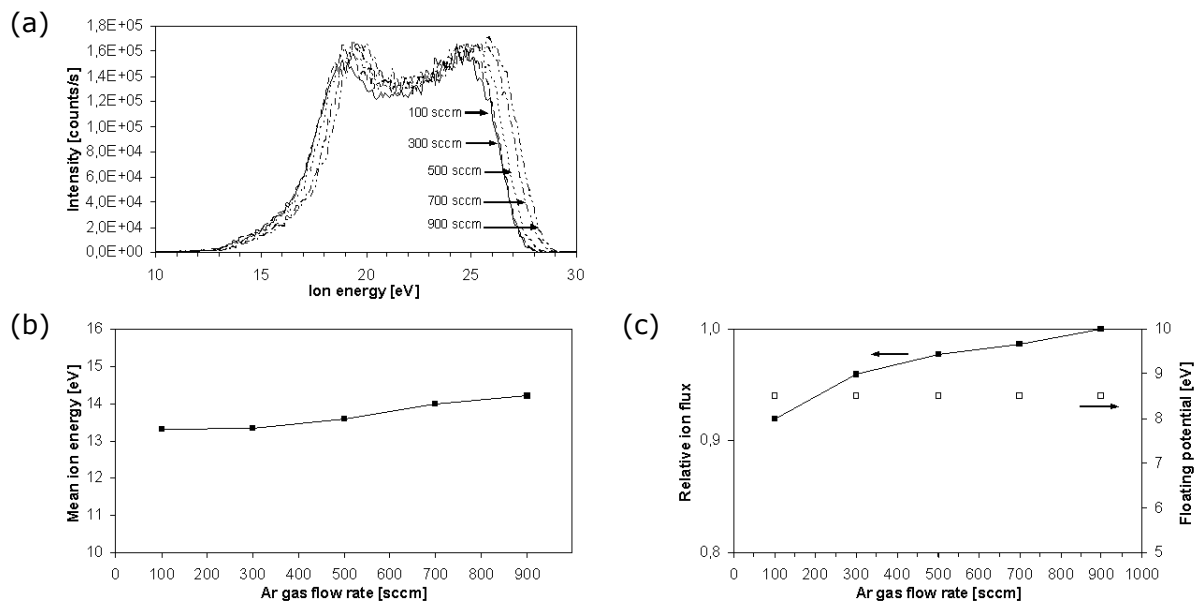


Figure 4.17: (a) $^{36}\text{Ar}^+$ IVDFs for variation of the argon gas flow rate in 60+2 MHz argon discharges (1500+1500 W 60+2 MHz power, 150 mTorr, no magnetic field, silicon substrate); (b) corresponding mean ion energies; (c) relative ion flux (solid squares) and floating potentials at the extraction aperture (open squares) as determined from the position of the lowest energy peak. The IVDFs are plotted without applying corrections for the offset in the energy scale.

4.2.5 Variation of magnetic field

60 MHz single frequency discharges

According to Lieberman [20], the sheath heating dynamics can considerably change during application of magnetic fields. For weak magnetic fields, the sheath motion is not assumed to be considerably influenced, but particle interactions are modified due to multiple correlated collisions of electrons with the moving sheath. The magnetic field is described to have two major effects on the discharge equilibrium: At low pressures,

stochastic heating can increase when the magnetic field is increased, and further a significant fraction of the total rf discharge voltage can be dropped across the plasma bulk at high magnetic fields. By increasing the magnetic field, the ion energy is expected to drop due to the reduced sheath voltages. The ion flux should increase through an enhanced ionization rate as a result from forcing the electrons to helical trajectories between collisions and reducing the effective loss area of the discharge. In Fig. 4.18-a and further in Fig. E.4-a to Fig. E.4-d in appendix E, ion distribution functions for $^{36}\text{Ar}^+$ ions sampled from the discharge are plotted for different magnetic fields of 0, 20, 50, 80, 110, and 140 G for constant 60 MHz power (1500 W) and discharge pressure (150 mTorr). To eliminate fluctuations in the recorded intensities from the influence of the rotating magnetic fields and enable an analysis of additional magnetic fields, the magnetic field was hold stationary during the time of the measurements. Ion distributions were recorded for each of the four different configurations (I)-(IV), as indicated by the schematic contained in Fig. 4.18-a. Here, each configuration corresponds to an operation mode of the pairwise driven electromagnet coils. From simulations of the magnetic field distribution inside the reactor [214], magnetic field densities close to the powered coils can typically be up to a factor of 3 higher compared to the wafer center. Close to the idle coil positions, magnetic fields reach about 50-70% of the value in the wafer center. For operating modes (II) and (III), one of the two driven coils is surrounding the EQP tube. This means that for those two operating modes the plasma density should peak towards the EQP orifice region, whereas for modes (I) and (IV) the region of higher plasma density should be opposite of the EQP mounting region. So far it remains unclear to what extent ion trajectories inside the EQP might be affected by the presence of magnetic fields. Parts of the IDF might become damped or even suppressed as a result of a magnetic deflection of sampled ions. This in turn would lead to distortions of the measured ion flux.

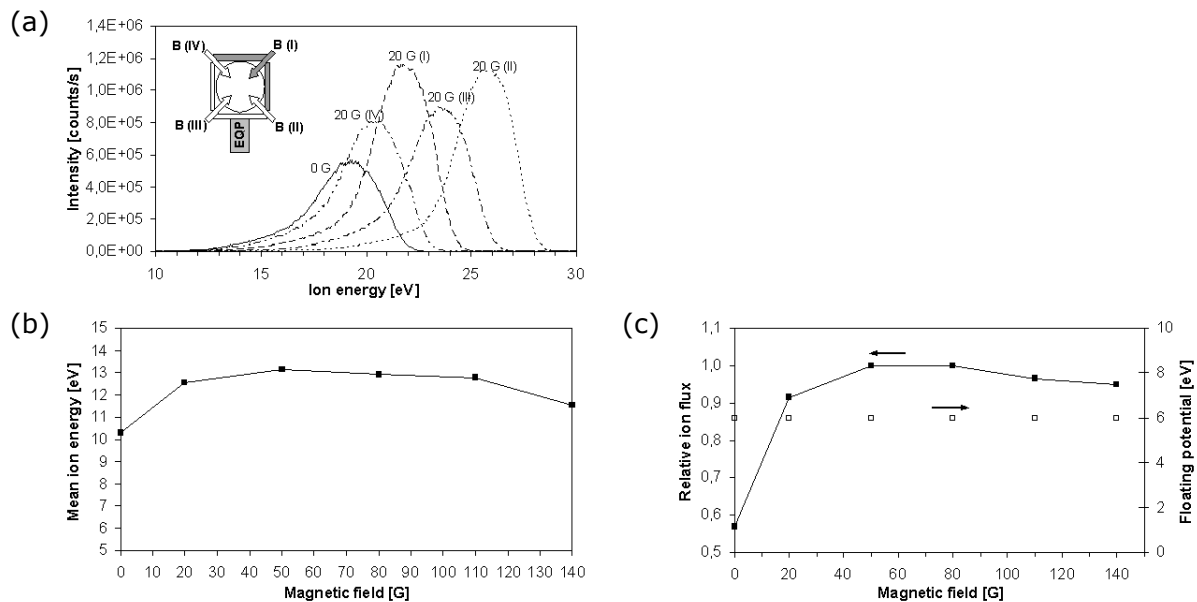


Figure 4.18: $^{36}\text{Ar}^+$ IVDFs for variation of the magnetic field in 60 MHz single frequency argon discharges shown for different configurations of the stationary magnetic field from the four-coil configuration as indicated in (a) for 20 G with the reference curve measured without magnetic field as indicated by 0 G (1500 W, 150 mTorr, 300 sccm Ar gas flow rate, silicon substrate); (b) corresponding mean ion energies; (c) relative ion flux (solid squares) and floating potentials at the extraction aperture (open squares) as determined from the position of the lowest energy peak. The

IVDFs are plotted without applying corrections for the offset in the energy scale, IVDFs measured for 50 G, 80 G, 110 G and 140 G can be found Fig. E.4 in appendix E.

The Ar^+ ion mean energy and flux plotted in Fig. 4.18-b and Fig. 4.18-c are obtained after averaging over the four distributions obtained for the respective magnetic field applied. What can be readily seen is that the ion flux is significantly increased in the presence of a magnetic field, as is predicted by the theory. A maximum in the ion flux is observed in the 50 to 80 G range. When comparing IDFs with applied magnetic fields to the reference curve at zero Gauss, mean ion energies are found to increase when a magnetic field is applied (cf., Fig. 4.18-b). From expectations, increasing the magnetic field should result in a reduction of the sheath thickness as a result of an increased density. From the reduced sheath thickness, the IDFs should shift to lower energies, as was also confirmed by HSPM simulations (cf., section 2.5, Fig. C.5-j in appendix C). A possible explanation for this discrepancy could result from the stationary magnetic field apparently yielding a locally strongly inhomogeneous plasma and sheath distribution. Field distortions could result in higher ion energies measured at the reactor wall. A strongly inhomogeneous sheath distribution might deviate from rotating magnetic fields usually applied during processing. From uniformity measurements, the sputter rate nonuniformity for argon on the wafer did not change for additional magnetic fields. However, this sensitively depends also on other discharge parameters and the chemistry. In case of pure HBr for example, etch rate distributions became more uniform when applying high magnetic fields. Further considerable deviations are expected in both magnitude and geometry from the homogeneous magnetic field applied for the HPSM calculations. Ion trajectories of sampled ions might be affected to some extent, which can also cause distortions of the measured IDFs.

60+2 MHz dual frequency discharges

In Fig. 4.19-a and further in Fig. E.5-a to Fig. E.5-d in appendix E, ion distribution functions for $^{36}\text{Ar}^+$ plasma ions are plotted for different magnetic fields of 0, 20, 50, 80, 110, and 140 G for constant 60 and 2 MHz power (1500 W each) as well as constant discharge pressure (150 mTorr). The four different magnet coil pair operation modes (I)-(IV) that were used to create the stationary magnetic fields are indicated by the schematic in Fig. 4.19-a. The corresponding Ar^+ ion mean energy and flux are plotted in Fig. 4.19-b and Fig. 4.19-c, after averaging again over the four distributions that were obtained for the respective magnetic field setting. As in the 60 MHz single frequency discharges, the ion flux is again significantly increased in the presence of the magnetic fields. A maximum ion flux is recorded at 110 G. Besides a varying plasma density, the stationary magnetic field seems to yield locally varying and strongly inhomogeneous sheath thickness distributions which are attributed to the observed peak broadening when increasing the magnetic field. The broadening above 80 G occurs with the high energy peak of the saddle structure being shifted to higher energies, which yields the pronounced increase in the mean ion energy shown in Fig. 4.19-b. From corresponding HPSM simulations, the ion energy is slightly increasing by about 1 eV from 0 G to 150 G in pure 2 MHz argon discharges (Fig. C.5-j in appendix C). In contrast, for pure 60 MHz a distinct drop in the ion energy was observed and sheath properties appear considerably more influenced for 60 MHz. As stated for 60 MHz argon discharges, inhomogeneities in plasma density and sheath thickness from the influence of the stationary magnetic fields could occur also for the dual frequency

discharges, thus potentially causing the discrepancy in the scaling of the ion energy at the reactor wall. At this point it is just noted, the complex sheath dynamics for the 60+2 MHz dual frequency discharges in the presence of a magnetic field prohibit to draw simple conclusions of the plasma and sheath behaviour. Furthermore, the experiments do not appear to be suited for comparison to the HPSM simulation performed, nor to draw conclusion about the influence of a rotating magnetic field that is applied during processing.

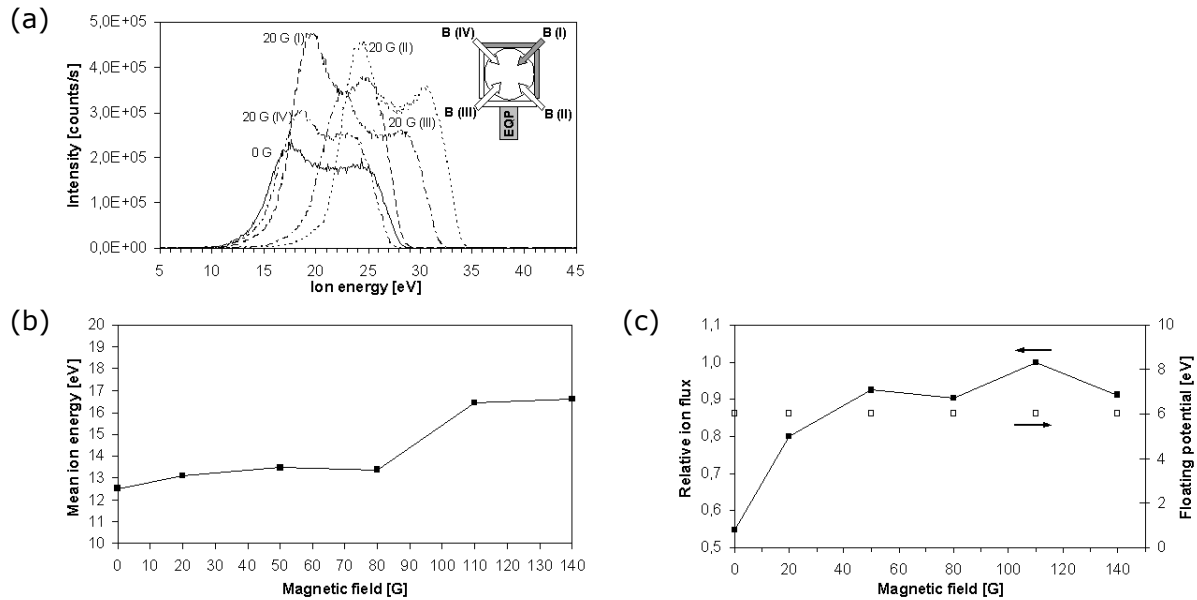


Figure 4.19: $^{36}\text{Ar}^+$ IVDFs for variation of the magnetic field in 60+2 MHz dual frequency argon discharges shown for different configurations of the stationary magnetic field from the four-coil configuration as indicated in (a) for 20 G (1500+1500 W 60+2 MHz power, 150 mTorr, 300 sccm Ar gas flow rate, silicon substrate); (b) corresponding mean ion energies; (c) relative ion flux (solid squares) and floating potentials at the extraction aperture (open squares) as determined from the position of the lowest energy peak. The IVDFs are plotted without applying corrections for the offset in the energy scale, IVDFs measured for 50 G, 80 G, 110 G and 140 G can be found Fig. E.5 in appendix E.

Whereas IDF were measured for stationary magnetic fields, rf probe and sputter rate measurements were conducted for rotating magnetic fields by applying a 0.25 Hz sinusoidal voltage to the magnet coils. From these experiments, the rf probe voltage measured with silicon substrates at the powered electrode decreases slightly to a minimum at 50 Gauss (Fig. E.6-a) and rises again for higher magnetic fields. For SiO_2 the voltage is observed to strongly increase above 20 G, saturating at high magnetic flux densities (>90 G). This scaling does not reflect that observed for sheath parameters from HPSM calculations of corresponding argon discharges (cf., Fig. C.5). The discrepancy might be due to the fact that measured rf voltages should not easily be attributed to sheath voltages since a significant fraction of the total rf discharge voltage can be dropped across the plasma bulk at higher magnetic fields [20]. From ion flux measurements, the ion density was observed to increase when increasing the magnetic field. This is supported by current measurements with the rf probe where the current is found to drastically increase with magnetic field (Fig. E.6-b). For substrates with SiO_2 hardmask, the current increase is found to be similar to changes in the ion flux determined from IDF measurements. For silicon substrates, the current increase is less than for the ion flux. From Fig. 4.20-a and Fig. 4.20-b, silicon and silicon dioxide sputter rates are observed to slightly increase at high

magnetic fields. This is attributed to the observed increase in ion density, and hence ion flux to the substrates. The SiO_2 sputter rate determined from ellipsometry (plotted with open squares in Fig. 4.20-b) shows known nonuniformities for the chosen combination of parameters (pressure, power), where a higher sputter rate is measured at the wafer edge area. Fluctuations observed from weight loss measurements for SiO_2 (plotted with full squares in Fig. 4.20-b) are attributed again to artefacts caused by an insufficient discharging of the oxide layer.

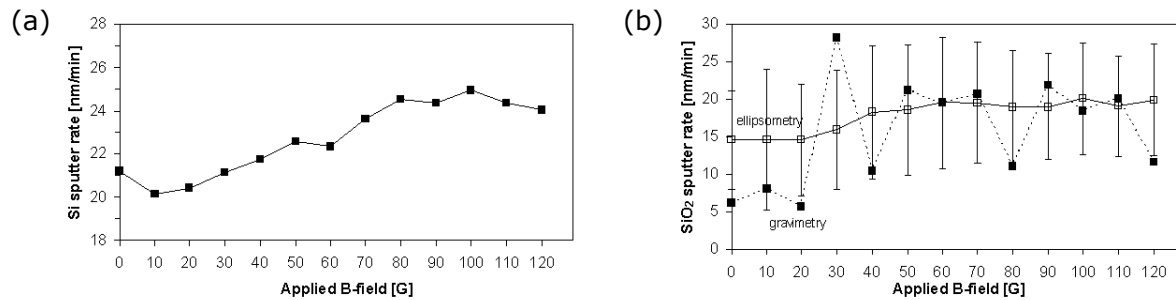


Figure 4.20: Sputter rates for variation of the magnetic field (1500+1500 W 60+2 MHz, 300 sccm Ar gas flow rate, 150 mTorr) for (a) silicon from gravimetry, (b) SiO_2 from gravimetry (full squares) and 49 point ellipsometry measurements (open squares).

4.2.6 Summary

Ar discharges were investigated for an initial baseline characterization, to enable a comparison to literature data and allow for HPSM modeling calibrations. Experiments with ionized argon noble gas were also intended to obtain results for purely physical sputtering since the physical etch component can initiate and enhance reactive ion etching in molecular halogen discharges.

From investigations of 60 MHz single and 60+2 MHz dual frequency discharge operation, the concept of separate control of ion energy and ion flux by the two frequencies appears to work well. The 60 MHz high frequency component mainly determines the ion flux, whereas ion energies are strongly influenced by the 2 MHz low frequency component. The ion flux is subject to minor changes from the influence of 2 MHz addition. The Ar^+ IDF structure is very different for the hf and lf component where the shape of the distributions transforms from an unresolved double-peak structure in 60 MHz discharges to a saddle-shaped structure with a wide peak separation when adding the 2 MHz frequency. Maximum Ar^+ ion energies become considerably higher for an additional 2 MHz excitation. Despite the fact that ion energies are mainly determined by the low frequency component, comparably low ion energies are obtained in the ground electrode sheath (where the IDF measurements are conducted) which is due to the asymmetric discharge geometry. This yields the 60 MHz high frequency component non-negligibly impacting ion energies as well where ion energies in 60 MHz single frequency discharges appear to be sufficient to exceed the thresholds for sputtering silicon and SiO_2 at even very low 60 MHz power levels. This is believed to result from effective gas heating (as will be demonstrated later from more detailed investigations in NF_3) which influences the neutral gas density and hence changes plasma density and sheath thickness. Compared to 60 MHz discharges, mean ion energies appear somewhat higher in 60+2 MHz discharges which is attributed to slight asymmetries in the double peak structures, as well as varying peak intensities as a result of non-sinusoidal sheath voltages. Similar to the ion flux being slightly affected by the 2 MHz

frequency, ion energies are subject to small variations for different 60 MHz power levels. Deviations from an ideally separated control of ion flux and energy are caused by interactions between the two frequencies since the rf power sources are coupled to each other in the current setup.

An optimized high ion flux as well as high ion energies are generally favoured to maintain high etch rates during etching high aspect ratio features. Since sputtering is a rather unselective process that comparably affects mask erosion, it appears natural that the physical sputter component should hence be optimized. High 60+2 MHz power levels are required to obtain high plasma densities and high rf peak voltages in the driven electrode sheath, hence resulting in high ion fluxes to the substrate (from contribution of 60 MHz) comprising highly energetic ions (from contribution of 2 MHz). According to argon sputter rates for Si and SiO₂, an initially higher contribution appeared from ion energy, as compared to the ion flux. However, contribution of the ion flux increased slightly with ion energy (for silicon), indicating a limitation of the sputter rate by both ion flux and ion energy. Linear correlations between applied power levels and ion flux/energy were not assumed since the efficiency of power coupling and dissipation in the plasma was found to decrease for intermediate to high power levels [258]. Factors like rf matching limits and temperature drift effects were assumed as root cause. From a quite high linearity of the sputter rates, the argon sputter yield does not appear to saturate but rather increases further within the range of discharge settings investigated in this work. Besides efficiently increasing sputter rates with 60 MHz and 2 MHz power, a further distinct gain could be achieved through reducing the discharge pressure below 250 mTorr - and more importantly below 100 mTorr. This is likely due to changes in the EEDF and mean electron energy that accompany a discharge transition from stochastic (collisionless) to ohmic (collisional) electron heating and/or from the low-voltage (or α) to the high-voltage (or γ) mode through an increasing discharge current density. Decreasing the discharge pressure reduced the number of collisions (ES, CX) and off-axis scattering in the sheath. The pressure reduction gives also rise to an increased sheath width. As a result, the ion angular distribution becomes more anisotropic in forward direction, and ions will gain more energy on their way through the sheath region. This will finally result in a higher fraction of ion projectiles that experience less collisions with the sidewalls in high aspect ratio structures. In order to keep the fraction of low-energy ions small, reduction of the pressure down to a certain minimum should further be an attractive option. At higher pressures, both Ar⁺ ion energies and Ar⁺ ion flux were found to decrease. A decreasing flux could either result from an increased charge carrier loss, e.g., through enhanced ion-electron neutralization collisions and/or less efficient ionization in the plasma. It should be noted that mask erosion can considerably increase as well when rising power levels and reducing discharge pressure.

Some minor gains in sputter rate can be obtained from application of (weak) magnetic fields (through an enhanced ion flux), and less importantly, also for reduced gas flow rates (i.e., longer residence time) through changes of the neutral gas temperature and hence the neutral gas density, which in turn will affect discharge properties (like plasma density, Ar⁺ ion energy and uniformity) to some extent. The impact of an increasing ion flux with magnetic field appears to dominate generally decreasing ion energies from a decrease of sheath thickness and dc bias voltage here. Strong changes of the argon feed gas flow appear to change the background gas temperature and hence the neutral gas density, which in turn will affect discharge properties (like plasma density, Ar⁺ ion uniformity) to

some extent. In contrast to Si, sputter rates for SiO₂ appeared to be somewhat lower and slightly less influenced by 2 MHz power and magnetic fields. This indicates an Si-to-SiO₂ etch selectivity between 1:1 and 2:1 can be reached. This result is somehow surprising for purely physical sputtering. The differences from a selectivity of 1 for physical sputtering could be explained by either an increased plasma density (and hence ion flux) due to a higher ion-impact secondary electron emission coefficient [277] for Ar⁺ ions impacting at silicon surfaces, differences in the power coupling for the different substrates, and/or a slightly different plasma chemistry (e.g., caused by released oxygen) leading to a different plasma impedance. Furthermore, low sputter rates can be influenced by an argon incorporation into the substrate, and more importantly by native oxide growth at amorphous (through the impact of ion bombardment) silicon surfaces when the wafers are exposed to atmosphere again. From ellipsometry, a markedly higher sputter rate was generally observed close to the wafer edge. This could be explained by skin effects at high 60 MHz source power levels influencing the local power dissipation in the plasma volume, spatial distortions of the electric field distribution between the wafer edge and focus ring, plasma penetration into the gap between wafer and focus ring [270,271], and/or temperature gradients between wafer and quartz focus ring. From reactor simulations, spatial variations of the discharge pressure in the reactor are observed to be negligible and do not constitute to the observed sputter rate nonuniformity.

From experimental data, the threshold for physical sputtering of SiO₂ by Ar⁺ ions was calculated to about 49 eV, which confirms values obtained from different publications [9,272-274]. From the 44 eV sputtering threshold calculated for silicon, silicon is sputtered at slightly lower energies than those needed to initiate sputtering of silicon dioxide. From different experiments, the energy of Ar projectiles appeared to be efficiently deposited to exceed the threshold for sputtering and sputter off substrate atoms even at the lowest (250 W) 60 MHz power applied. Besides a general sputter yield dependency, silicon sputter rates can become influenced significantly by amorphization and recrystallization effects as well as native oxide growth at the substrate surface when being exposed to atmosphere again [275], and less importantly also by an incorporation of argon projectiles into the silicon lattice (where effective sputter rates can appear even negative). In particular, these influences would explain the low silicon sputter rates measured at low (60+2 MHz) power levels which are in contrast to higher sputter rates measured for SiO₂. Despite slight differences discussed above, the range of sputter rates for Si and SiO₂ from all experiments conducted here is found to be comparable (cf., Fig. 4.21).

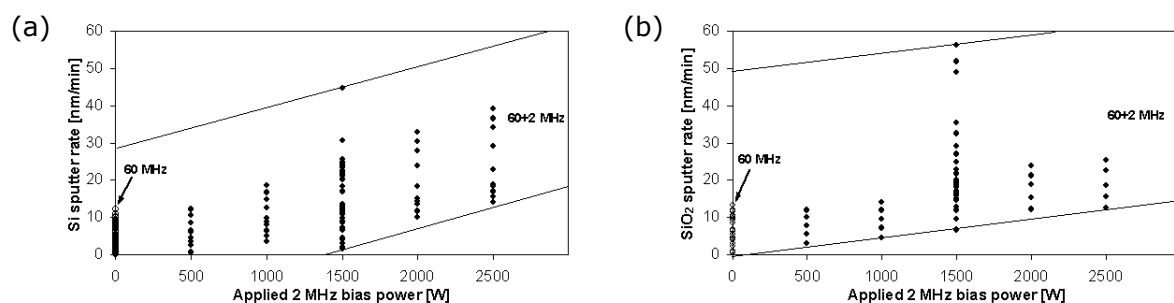


Figure 4.21: Sputter rates collected from all argon discharge experiments discussed in this chapter and plotted as a function of 2 MHz bias power for (a) silicon, and (b) silicon dioxide.

4.3 Hydrogen bromide discharges

For application of mass resolved ion energy analysis, $^{79}\text{Br}^+$ as well as $^2\text{H}_2^+$ and $^{160}\text{Br}_2^+$ plasma ions were chosen to be monitored for studying the plasma and sheath behavior for the different HBr discharge conditions examined in this work. Bromine ions are believed to play a major role in the reactive ion etching of silicon deep trench structures where a high degree of anisotropy is required. Molecular hydrogen and bromine ions were chosen due to their high abundance resulting from an efficient fragmentation decomposition of the hydrogen bromide feed gas. Due to their very different mass numbers they are expected to allow for a more detailed analysis of the sheath behavior. As can be seen from neutral mass spectra, a wide spectrum of different species covering a wide mass range can be expected for silicon etching in HBr discharges. The relatively high complexity complicates a more detailed study significantly.

4.3.1 Neutral mass spectra and degree of dissociation

In Fig. 4.22-a, a typical mass spectrum is shown for neutral species ionized by 70 eV electrons from HBr when the discharge is off. The spectrum agrees (to within the known uncertainties) with a "standard" HBr mass spectrum obtained at an electron-impact energy of 70 eV [219]. The two peaks identified with HBr^+ ions arise from the natural abundance of bromine isotopes ($^{79}\text{Br} = 50.7\%$ and $^{81}\text{Br} = 49.3\%$) and contribute the highest intensities, along with Br^+ which is created through dissociative ionization of HBr. The triplet structure identified with Br_2^+ is attributed to traces of molecular bromine that results from recombination of bromine radicals, created through wall collisions in the reactor and/or in the ionizer region. Indications of molecular hydrogen H_2^+ which could be created similarly from recombined hydrogen atoms are not found here. Atomic hydrogen can not be detected either since the used mass spectrometer is not able to reliably measure the $m/q = 1$ u peak in the mass spectrum. The absence of molecular hydrogen can be explained by an detection of quite large amounts of HF^+ . Together with further observed SiF_3^+ peaks, HF^+ is attributed to fluorine contamination inside the ionizing region of the measurement system as a result of a preceding NF_3 reactor clean plasma. The hydrogen released from HBr through dissociative ionization will be very reactive and readily bond to reactive fluorine radicals. Further, the HBr feed gas contains quite significant amounts of water. The Ar^+ peak results from small additions of argon feed gas to HBr.

The mass spectrum corresponding to the situation when the discharge is turned on is shown in Fig. 4.22-b. The spectrum applies to a 60 MHz single frequency discharge at 1500 W applied power and 150 mTorr. HBr^+ and Br^+ peaks are still observed, and significant amounts of molecular hydrogen H_2^+ and bromine Br_2^+ have appeared now. Again, these species can be either created through dissociative ionization of the parent molecule HBr, or through direct ionization of the respective molecule inside the EQP. Molecular bromine and hydrogen are observed for all HBr discharges investigated and may result from dissociation of HBr



and formation of molecules from neutral radical dissociation fragments or recombination of ionic dissociation fragments at the reactor walls. Fluorine containing molecules (HF^+ and SiF_3^+) are still observed and can be associated with discharge-generated decomposition and product species (HF , SiF_4) that are sputtered off the plasma reactor walls. Further observed SiBr_x^+ molecules are attributed to etch products formed through chemically

etching the silicon substrate. As discussed in the following sections, the self-bias for the 60 MHz plasma applied here is already sufficiently high to yield ion-induced chemical etching of silicon.

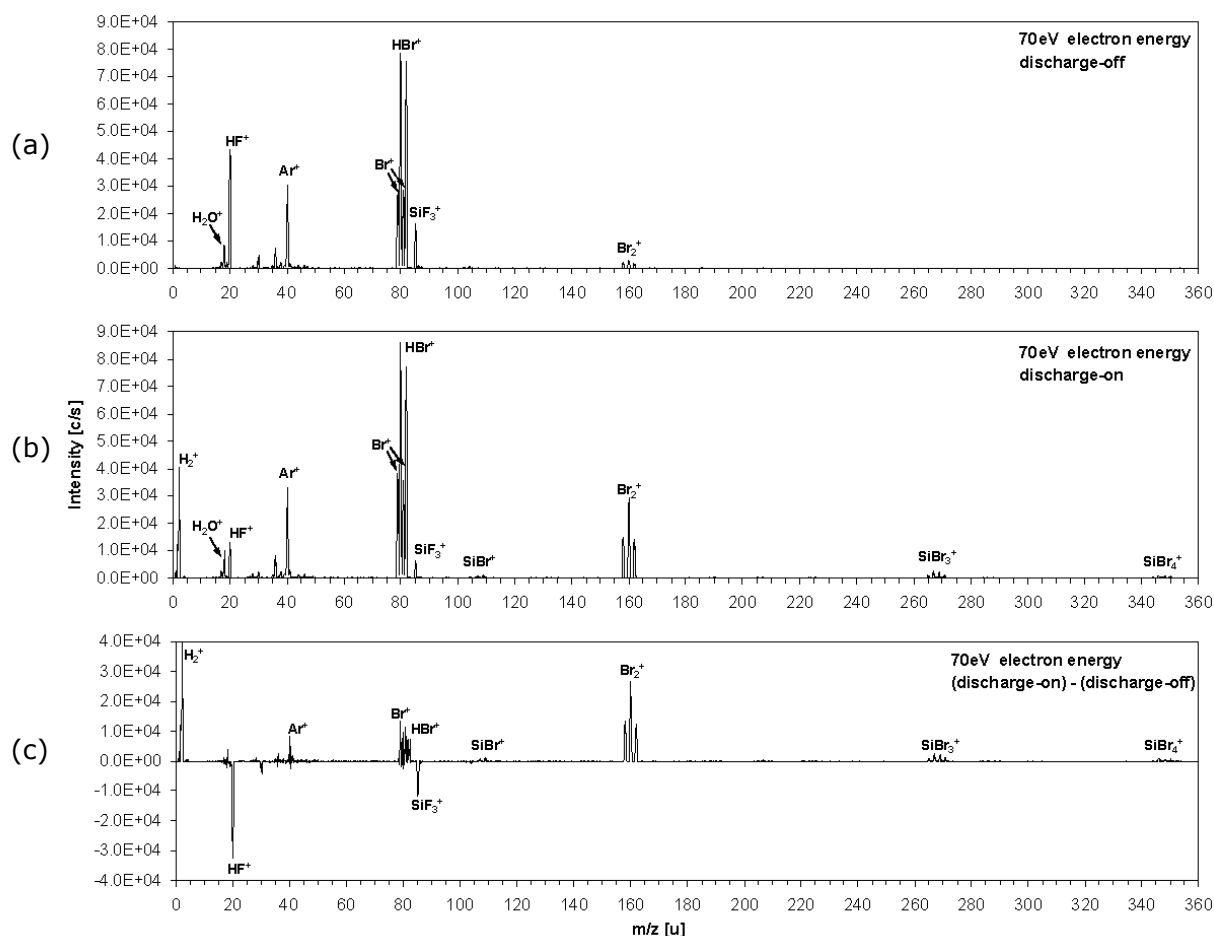


Figure 4.22: Mass spectrum of neutral species ionized by 70 eV electrons for (a) HBr (+Ar) gas sampled from the reactor without discharge; (b) HBr (+Ar) gas sampled from the reactor with rf discharge (150 mTorr, 1500 W 60 MHz power, 300 sccm HBr + 16 sccm Ar gas flow rate, silicon substrate); (c) difference of mass spectra b-a (negative values indicate a loss when the discharge is on).

In Fig. 4.22-c, the difference mass spectrum is plotted as is obtained by subtracting the mass spectrum recorded for plasma-on condition on from the mass spectrum recorded when the plasma was turned off (for the same mass-spectrometer settings). Negative values indicate a loss when the plasma is on. According to the difference spectrum, the fluorine containing species HF and SiF_4 are efficiently removed from the reactor after ignition of the HBr discharge.

Due to a high recombination coefficient close to 1.0 for Br radicals on stainless steel surfaces [125], bromine will rapidly react at the walls inside the mass spectrometer chamber, or condense upon them. Hence, no conclusion can be drawn here about Br radicals sampled from the discharge. For that reason, it was not possible to reliably estimate the degree of an HBr decomposition in the discharge (from differences in the mass spectra obtained with and without discharge operation). The recorded Br^+ intensity appeared to change only slightly (by a few percent) for a wide range of 60 MHz power levels applied. The bromine recorded in the mass spectra will be created primarily through

thermal pyrolysis of neutral molecular species (HBr, Br₂, SiBr₄) on the hot filaments in the EQP ionizer. From recent publication [279], HBr dissociation fractions were measured in a 300 mm LAM ICP etch reactor (13.56 MHz) with in situ diode laser absorption spectroscopy. HBr dissociation fractions were mainly influenced by the applied ICP power and HBr gas flow rates, ranging from 25%–60% for the investigated range of parameters. Furthermore, different surface conditions of the quartz focus ring were found to have a great influence on the measured feed gas dissociation.

4.3.2 Variation of power

60 MHz single frequency discharges

Increasing 60 MHz source power leads to a monotonic increase of the rf probe voltage, where the slope decreases slightly at higher power levels (Fig. F.1-a in appendix F). The ion energy for ions impacting on the substrate will increase proportionally due to (slightly) rising sheath voltages caused by the increasing self-bias of the 60 MHz source. This is confirmed by IDFs for ⁷⁹Br⁺, ²H₂⁺ as well as ¹⁶⁰Br₂⁺ plasma ions that are observed to shift to higher energies (Fig. 4.23-a to Fig. 4.23-c). Measured distributions are observed to start at negative energies which is attributed to a negative floating potential that develops from negative surface charging around the aperture at the MACOR dielectric orifice plate (cf., Fig. 4.23-e). Generally, the EQP probe changes its reference potential according to the floating potential at the sampling aperture. Correcting for the offset and transformation to the corresponding IEDFs (as described in section 4.1) will yield the mean ion energies plotted in Fig. 4.23-d. Compared to ³⁶Ar⁺ ion energies measured in corresponding argon discharges, the different ions in HBr discharges exhibit up to 30% higher energies at high 60 MHz power levels. This is less than differences between calculated ion energies for Ar and HBr at the ground electrode, as obtained from HPSM simulations. For equal model input parameters but different electron temperatures (2.58 eV for Ar and 6.32 eV for HBr, as obtained from a best fit model [215]), almost doubled ion energies were found for HBr (cf., Fig. D.1-k1 to Fig. D.1-k4 in appendix D) compared to typical ion energies calculated for argon (Fig. C.1-j in appendix C). Differences in the HPSM calculations for HBr will be less pronounced at lower electron temperatures (cf., Fig. D.4-k). A 30% difference observed for the measurements would require the electron temperature in HBr discharges to be lower than 6 eV, and/or a lower rf peak voltage for HBr, and furthermore the influence of a lower neutral gas temperature in HBr discharges could play a non-negligible role when comparing calculated and measured Ar⁺ and Br⁺ mean energies. Despite the obvious quantitative deviations, higher ion energies in HBr discharges are certainly caused by a higher sheath thickness in HBr discharges, as discussed in section 2.5. Due to an assumed higher electron temperature, HBr discharges are found to be slightly more symmetric than argon discharges which can result in slightly lower mean ion energies at the powered electrode (and hence, the substrate) for HBr compared to argon (cf., Fig. D.1-l1 to Fig. D.1-l4 and Fig. C.1-k).

From the measured rf probe current in Fig. F.1-b (as for electropositive argon discharges, the conduction current in weakly electronegative HBr discharges is carried mainly by electrons), the electron density is expected to rise for increasing 60 MHz plasma excitation which should cause the ion density to increase as well. This assumption is only partly supported by the measured ion flux as obtained from integration of the ion distribution functions (Fig. 4.23-e). Reasons for the differences might be explained by a changing

negative floating potential which could influence sampling of plasma ions. Furthermore, results of the rf probe measurement may not be useful to draw conclusions about ion densities in electronegative discharges. For electropositive argon discharges, the situation is rather simple since electrons contribute the only negative charge carriers, and from the plasma charge neutrality condition an equal amount of positive Ar^+ ions will be present in the plasma bulk. In contrast, for electronegative gases like HBr negative ions like Br^- or HBr^- will be formed through electron attachment processes. For the investigated type of discharges, negative ions are typically confined to the core of the plasma bulk. From the equilibrium that holds in the bulk plasma

$$n_+ = n_- + n_e. \quad (4.5)$$

Thus, electron densities observed for electronegative gases are generally lower than positive ion densities. For strongly electronegative gases (like NF_3) it was reported that ion densities can be up to 2-3 orders of magnitude higher than the electron density [36,37]. In general, for increasing electronegativities the electron density is expected to decrease. This is supported by the measured rf probe current that is found to decrease when comparing results of argon, hydrogen bromide and nitrogentrifluorine discharges. From the above considerations, the discrepancy between a constantly rising rf current and, e.g., a saturating Br^+ ion flux remains. This could indicate either a (slightly) changing negative to positive ion ratio as a function of 60 MHz power, and/or limitations of the IDF measurements which are in general closely related to the vicinity of the sampling aperture. The decrease observed for the Br_2^+ ion flux might result from severe surface conditioning effects during discharge operation. From changes of reactor surfaces by the HBr chemistry, the probability of bromine radical recombination might decrease. Unknown sources for the ion flux dependency should be subject to more detailed further investigations.

Compared to argon, contributions due to collisions at 150 mTorr are observed to be more significant for HBr related ion distributions in Fig. 4.23-a to Fig. 4.23-c. This is attributed to a usually wider sheath thickness for hydrogen bromide, as compared to the sheath thickness in typical argon discharges. Whereas from the unresolved double peak the heavy atomic and molecular bromine can only respond to the average of the time-varying sheath potential, the IDFs measured for the light hydrogen ions reveal a clear separation of the double peak structure. However, the peaks rapidly disappear by increasing the 60 MHz power and a separation is not observed to scale according to equation (1.64). This could be explained by a decreasing sheath width due to higher densities at higher power levels, as observed from HPSM simulations for HBr (discussed in section 2.5.2). However, the sheath thickness is not believed to change much since no significant changes are observed for the low energy part of the distribution functions where sheath collisions influence the IDF structure. An explanation for the apparent discrepancy could be that the double peak structure for hydrogen ions is very sensitive to even very small changes in the sheath thickness, which from the low energy part of the measured IDFs for $^2\text{H}_2^+$ can however not be resolved anymore. This appears plausible from a comparably low probability of sheath collisions as concluded from the low-energy part of IDFs for $^2\text{H}_2^+$ ions, in contrast to those for $^{79}\text{Br}^+$ and $^{160}\text{Br}_2^+$. The low probability of sheath collisions also explains the very low intensity of the low-energy peak from charge exchange collisions near the orifice which could not be detected for all cases. As discussed above, the peak position is observed at negative energies due to the negative floating potential which builds up at the orifice plate.

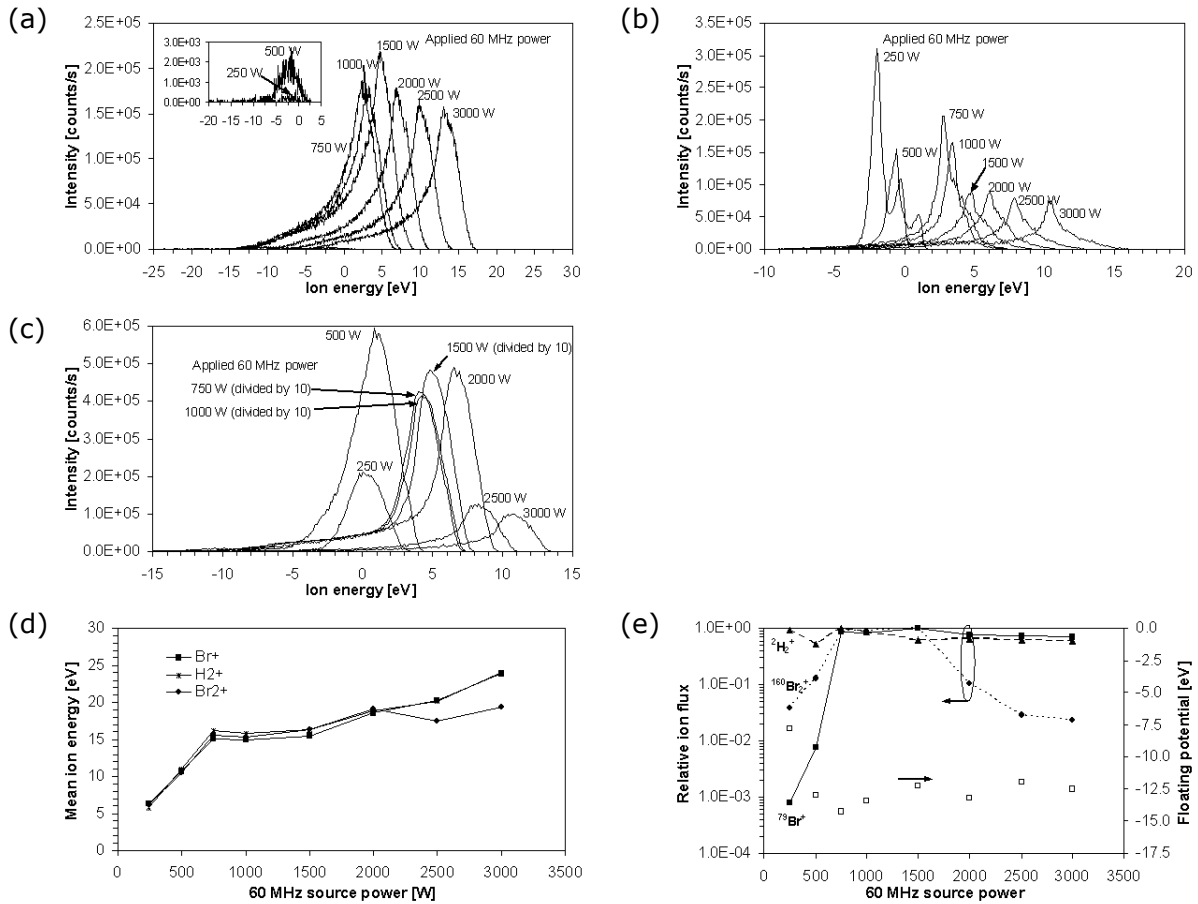


Figure 4.23: (a) $^{79}\text{Br}^+$, (b) $^2\text{H}_2^+$, (c) $^{160}\text{Br}_2^+$ ion distribution functions for power variation in 60 MHz HBr discharges (150 mTorr, 300 sccm HBr gas flow rate, no magnetic field, silicon substrate); (d) corresponding mean ion energies; (e) relative ion flux (solid squares, logarithmic scale) and floating potentials at the extraction aperture (open squares) as determined from the position of the lowest energy peak. The IVDFs are plotted without applying corrections for the offset in the energy scale.

For etching silicon in HBr discharges, the role of ions is to physically induce and support chemical reactions at the substrate surface which can finally yield volatile etch products (like SiBr_4). A chemical reaction will involve also reactive bromine atoms created from dissociation of the HBr feed gas molecules. The degree of HBr dissociation will depend upon the power dissipated in the plasma. For applied 60 MHz power levels exceeding 500 W, ions impacting the substrate gain sufficient energy to initiate chemical etching, as can be observed for the etch rate in Fig. 4.24-a that starts to rise above zero. At the lowest power applied (250 W), the weight loss measurement yields a negative value of about -1 nm/min. This is similar to the phenomenon observed for silicon sputter rates in argon discharges when using comparable discharge parameters. At such low power processes, bromine may to some extent be incorporated into the silicon surface leading to formation of a halogenated surface layer which can grow to a few monolayer thickness [116]. As discussed for argon discharges, native oxide growth under atmospheric pressure after removal from the etch reactor could also influence silicon sputter rates. Once ion-assisted etching is initiated, the complex interactions in the plasma and at the surface of the substrate prohibit to assign clear contributions to changes in the etch rate for the separate components like ion flux, ion energy, dissociation of HBr and formation of reactive bromine

atoms, etc. Recorded intensities of molecular species attributed to SiBr_4 were generally found to correlate very well to the silicon etch rate.

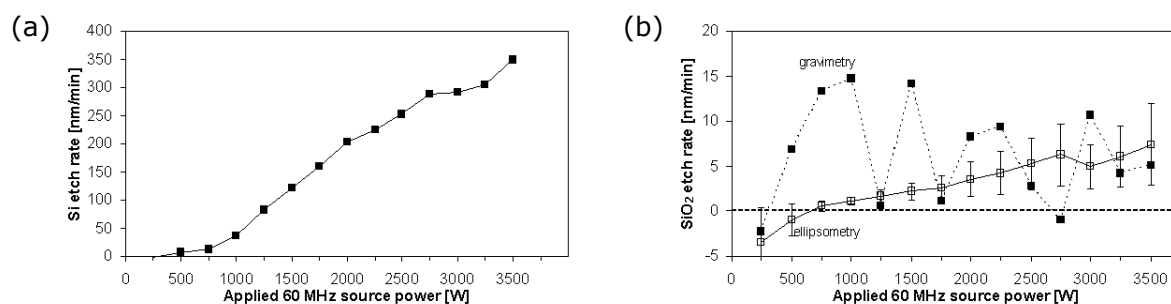


Figure 4.24: Etch rates for 60 MHz power variation (150 mTorr, 300 sccm HBr gas flow rate, no magnetic field) for (a) silicon from gravimetry, and (b) SiO_2 from gravimetry (full squares) and 49 point ellipsometry measurements (open squares).

From Fig. 4.24-b, the mean oxide etch rate determined from ellipsometry is increasing almost linearly for 60 MHz power, but remains below 10 nm/min for a power level of 3500 W (compared to 350 nm/min for silicon). A threshold of 750 W indicates that the ion energy may equal the binding energy of the amorphous SiO_2 layer to either start sputtering off target atoms, or initiate a chemical reaction and assist a formation of etch products. Negative etch rates observed at low 60 MHz source power indicate a significant incorporation of etch species into the amorphous silicon dioxide layer which can also result in formation of a halogenated surface layer, as described above for silicon substrates. The selectivity remains very high for purely 60 MHz discharges, even at very high power levels (at 3500 W, the selectivity is close to 50). A high standard deviation of the oxide etch rate determined from 49 point ellipsometry measurements is attributed to a pronounced etch nonuniformity across the wafer, where the highest etch rates were measured close to the wafer edge region. The SiO_2 sputter rate as calculated from the integral weight loss measurements shows large fluctuations which are attributed to experimental artefacts (as discussed in section 3.2.1).

60+2 MHz dual frequency discharges

For 60+2 MHz dual frequency discharge operation, the rf mean voltage measured for 60 MHz frequency is hardly affected by superposition of the 2 MHz frequency (Fig. F.1-a). Compared to experiments with bare silicon substrates (Fig. F.2-a), the 2 MHz rf voltage is more affected by the 60 MHz frequency for substrates with an SiO_2 hard mask layer (Fig. F.2-d). For argon, rf voltages were influenced stronger by 60 MHz power when silicon substrates were involved. This could indicate differences in the dynamic range of the rf matching unit for both types of discharges (since the load impedance will be influenced when using different substrates). Increasing the 60 MHz power level yields reduced rf voltages measured for fixed 2 MHz power, where for SiO_2 a more pronounced scaling is observed compared to silicon. This behaviour is attributed to the ion energy being mainly controlled by the 2 MHz power. In Fig. 4.25-a to Fig. 4.25-c, IDFs measured for $^{79}\text{Br}^+$ plasma ions are shown for a variation of 60 MHz power at fixed 2 MHz power levels of 500 W, 1500 W, and 2500 W, respectively. The wide peak separation caused by the low frequency sheath modulation is considerably more pronounced compared to IDFs measured in dual frequency argon discharges. This may be explained by a higher sheath thickness as a result of an (assumed) higher electron temperature, as observed from HPSM

simulations of HBr discharges (see section 2.5.2). At low 60 MHz plasma excitation, the 2 MHz frequency determines the sheath modulation yielding a very broad peak separation and maximum ion energies. This is again a result of the high sheath voltage caused by the dominating contribution of the 2 MHz frequency. Increasing the 60 MHz power yields an increased ion flux (Fig. 4.25-e) which causes the sheath width to become clearly thinner, as is supported also by the reduced mean ion energies (Fig. 4.25-d). The difference between mean ion energies for different 2 MHz power levels becomes smaller in the high 60 MHz power regime, but remains non-negligible as compared to argon. Comparable to argon, a lower mean ion energy at the ground electrode was observed from the HPSM simulations of 60+2 MHz mixed HBr discharges (cf., Fig. D.6-i), whereas the energy for ions incident at the powered electrode was found to increase slightly (Fig. D.6-j). From the lowest energy charge exchange peak, the floating potential at the extraction aperture is observed to develop non-monotonically between -5 eV and +7 eV (cf., Fig. 4.25-f), with a dip observed at medium 60 MHz power. The current measured for 60 and 2 MHz frequencies (Fig. F.1-b, Fig. F.2-b and Fig. F.2-e in appendix F) is observed to increase for rising 60 MHz power levels. However as already discussed for single frequency operation, this must not necessarily agree with changes in the ion density.

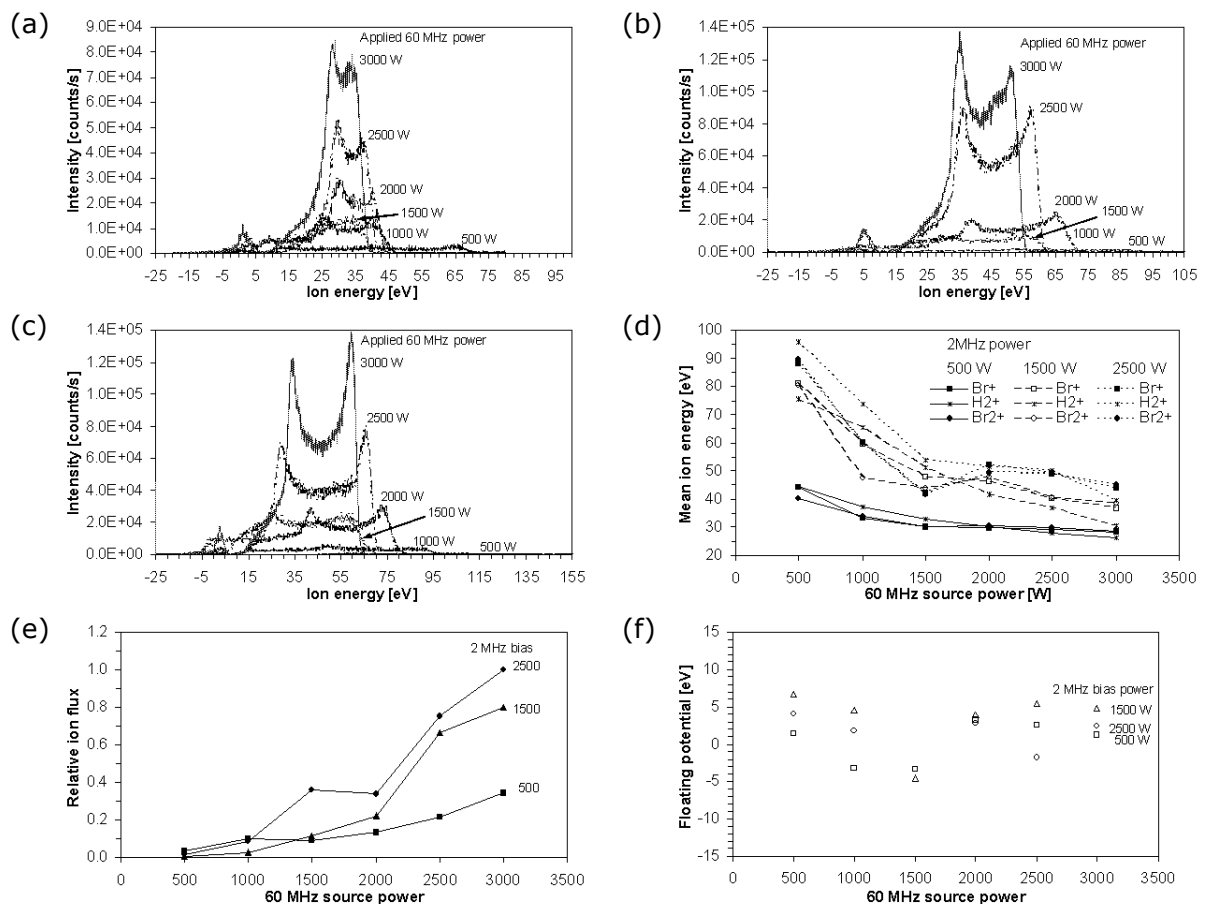


Figure 4.25: $^{79}\text{Br}^+$ IVDFs for 60 MHz power variation in 60+2 MHz dual frequency HBr discharges shown for fixed 2 MHz power of (a) 500 W, (b) 1500 W, (c) 2500 W (150 mTorr, 300 sccm HBr gas flow rate, no magnetic field, silicon substrate); (d) corresponding mean Br^+ ion energies (including mean ion energies for H_2^+ and Br_2^+); (e) relative Br^+ ion flux; (f) floating potentials at the extraction aperture (open squares) as determined from the position of the lowest energy peak. The IVDFs are plotted without applying corrections for the offset in the energy scale.

Whereas from Fig. 4.27-a to Fig. 4.27-c the IDFs measured for $^{160}\text{Br}_2^+$ are very similar to those for $^{79}\text{Br}^+$, distributions measured for $^2\text{H}_2^+$ (Fig. 4.26-a to Fig. 4.26-c) yield very complex structures. Compared to the initially saddle-shaped structure measured for 60 MHz frequency discharges, the peak separation has become quite broad due to the influence of the 2 MHz frequency. Also, a low-energy and a high-energy shoulder become visible. As the 2 MHz power is increased further, ions respond to the time varying oscillations of both 2 MHz and 60 MHz. The two main peaks in the bimodal structure of the IDF begin to split and up to four well-defined maxima can be distinguished in the distributions. The first of the main peaks at the lowest energy is caused by ions entering the sheath at the minimum sheath potential. The next peak is possibly due to a maximum of the 60 MHz voltage around the 2 MHz voltage minimum. The two high energy peaks correspond to ions entering the sheath at extrema of the 60 MHz voltage around the 2 MHz voltage maximum. From literature, similar findings were obtained for hydrogen molecules in 1.94+27.12 MHz dual frequency hydrogen CCRF discharges [11,12]. By increasing the 60 MHz power, the distribution shifts to lower energies which is attributed to a decreased sheath voltage at higher plasma densities. Increasing the 2 MHz power causes the separation of the center of the low and high energy peaks to increase as well, since this separation is determined by the 2 MHz voltage. The two inner peaks of the IDF structure are eventually found to be more pronounced which is due to more ions being able to enter the sheath at these potentials.

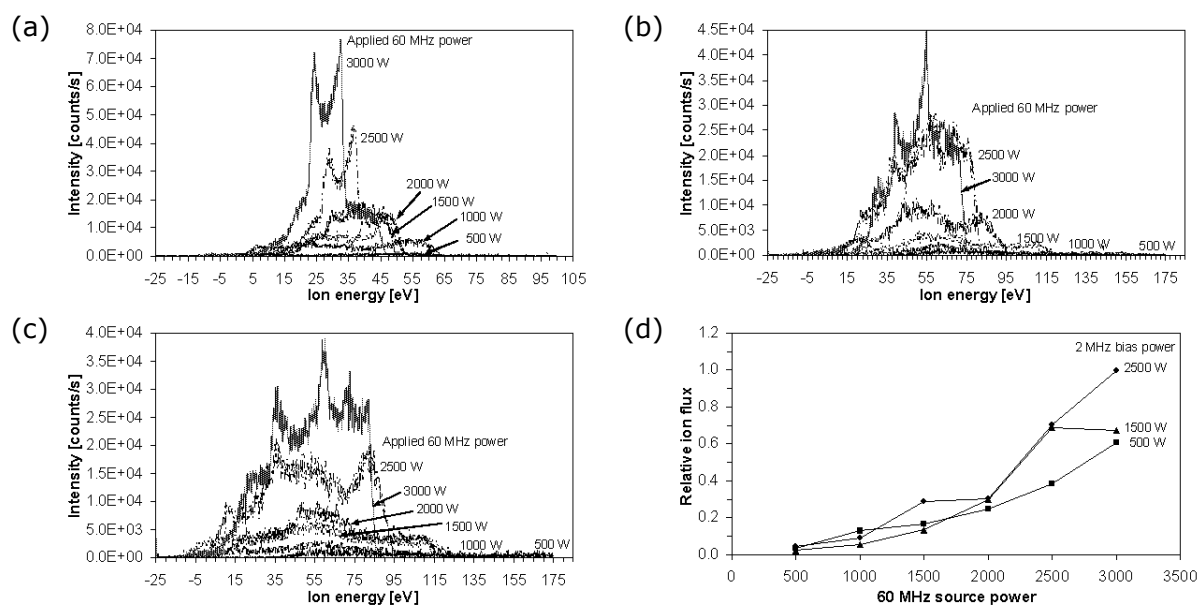


Figure 4.26: $^2\text{H}_2^+$ IVDFs for 60 MHz power variation in 60+2 MHz dual frequency HBr discharges shown for fixed 2 MHz power of (a) 500 W, (b) 1500 W, (c) 2500 W (150 mTorr, 300 sccm HBr gas flow rate, no magnetic field, silicon substrate); (d) corresponding relative H_2^+ ion flux. The IVDFs are plotted without applying corrections for the offset in the energy scale, corresponding floating potentials are plotted in Fig. 4.25-f.

When increasing the 60 MHz power, ion fluxes plotted in Fig. 4.25-e, Fig. 4.26-d and Fig. 4.27-d are observed to increase by a power law for additional high 2 MHz power. This might indicate that the 2 MHz frequency has significant influence on generation and recombination of ions here. The low-energy peak in the IDFs which corresponds to charge exchange collisions in the sheath near the sampling orifice yields comparable results for the

different ion species. This proves again that determination of the floating potential at the sampling aperture from the low energy peak is a valid approach. Minor variations of the peak position were observed when repeating experiments. This can be explained by changing surface conditioning effects from slight differences in the effectiveness of plasma surface cleaning between the experiments, causing in turn the observed variations of the floating potential at the orifice plate.

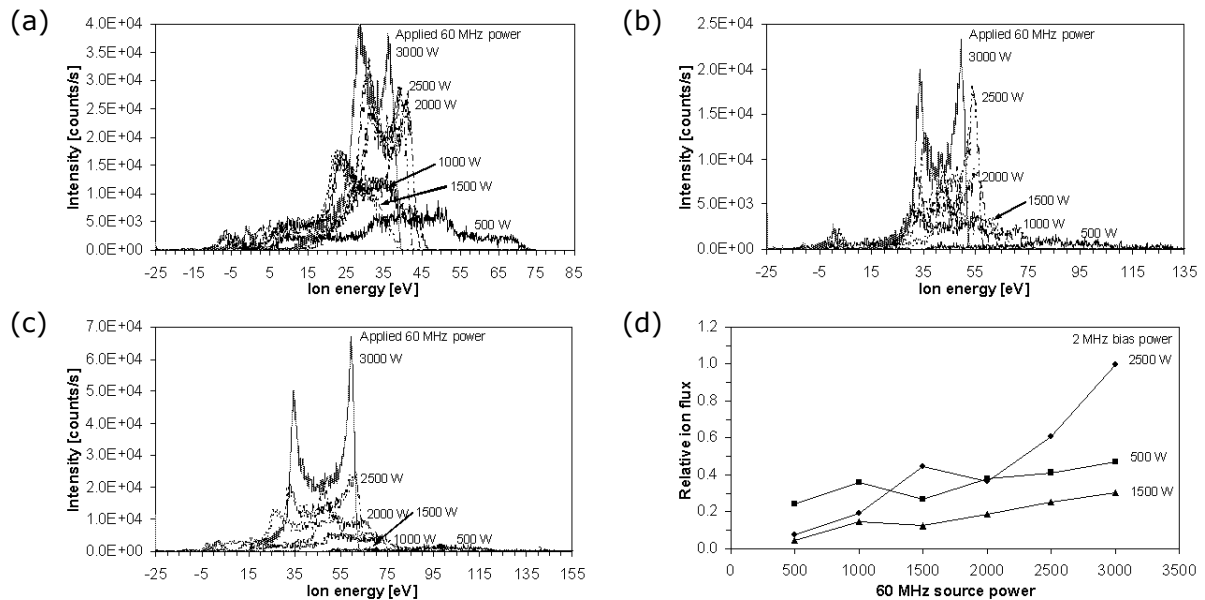


Figure 4.27: $^{160}\text{Br}_2^+$ IVDFs for 60 MHz power variation in 60+2 MHz dual frequency HBr discharges shown for fixed 2 MHz power of (a) 500 W, (b) 1500 W, (c) 2500 W (150 mTorr, 300 sccm HBr gas flow rate, no magnetic field, silicon substrate); (d) corresponding relative Br_2^+ ion flux. The IVDFs are plotted without applying corrections for the offset in the energy scale, corresponding floating potentials are plotted in Fig. 4.25-f.

The silicon etch rate for dual frequency HBr discharges is shown in Fig. 4.28-a. The etch rate increases continuously by increasing the 2 MHz power. The highest gain is achieved from addition of 500 W bias power (compared to pure 60 MHz frequency discharges), which is the lowest 2 MHz power level applied here. The low energy range of the 2 MHz power was not investigated in detail in this work. At high 2 MHz power levels, the etch rate starts to saturate, and the gain in etch rate decreases. Raising the 60 MHz power level is also suitable to increase the etch rate. This yields a near linear dependency that has already been observed for variation of the power for 60 MHz single frequency operation. At constant 60 MHz power, the etch rate clearly indicates a limitation by either the ion flux and/or formation of radical species from dissociation of the feed gas molecules. The ion energy which is predominantly determined by the 2 MHz frequency can not compensate the chemical component of the etch process. From investigations of argon discharges, purely physical sputtering was observed to yield solely very low rates. The excess energy from the ions will cause a significant heating of the substrate, which in turn might affect the neutral gas density resulting in a lower neutral densities at high temperatures (the pressure is held constant). Also, at higher power values, the degree of coupling the power to the plasma is likely to be decreasing due to increasing power losses in the feedthrough [258]. From the discussion it has become obvious, that (once initiated by a sufficient amount of ion energy) the silicon etch rate is chemically driven. The oxide etch rate examined from Fig. 4.28-b

appears to increase with a near linear slope as a function of 2 MHz power, whereas an influence of 60 MHz power is hardly visible. These findings strongly support a pronounced physical sputtering component for etching of silicon dioxide. From comparison of the slopes of the etch rates it can be seen that the Si-to-SiO₂ selectivity disproportionately decreases when rising the 2 MHz power. In Fig. 4.28-b, a typical standard deviation of the SiO₂ etch rate as obtained from applying 49 point ellipsometry is demonstrated for medium 60 MHz power (1500 W). Deviations are caused by an etch pattern nonuniformity across the wafer where a higher etch rate is observed at the wafer edge region. SiO₂ etch rate data as calculated from the integral weight loss measurements are not shown since they yield comparable results.

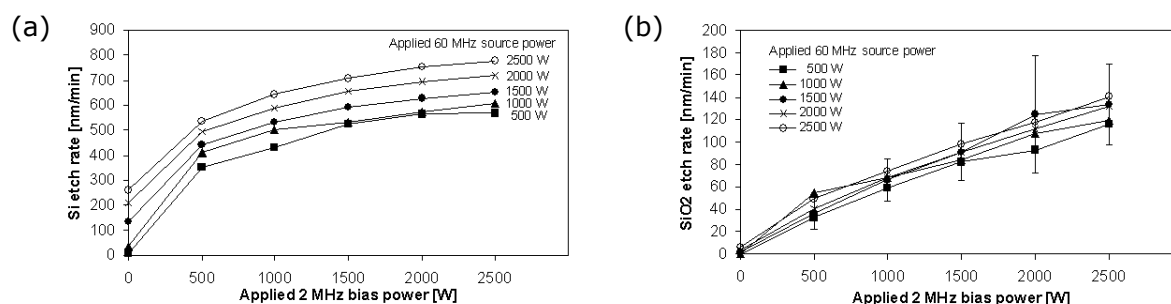


Figure 4.28: Etch rates for 60+2 MHz power variation (150 mTorr, 300 sccm HBr gas flow rate, no magnetic field) for (a) silicon and (b) SiO₂, as determined from gravimetry.

4.3.3 Variation of pressure

60 MHz single frequency discharges

In Fig. 4.29-a, ⁷⁹Br⁺ ion distributions are plotted for a variation of the discharge pressure from 50 mTorr to 600 mTorr where the 60 MHz power was held constant. The structures remain singly peaked at the time-averaged sheath potential. Unlike observed for argon, the sheath is already collisional at 50 mTorr as can be seen from the pronounced low energy part of the distribution (notice that all intensities have been divided by a factor of four for 50 mTorr). Most ions that enter the sheath become accelerated through the entire sheath potential. Similar to argon, a transition from 50 mTorr to 100 mTorr is observed resulting in significantly reduced ion energies at higher pressures (cf., Fig. 4.29-d). As discussed for a variation of the pressure in argon, this might indicate a stochastic-Ohmic heating [278] and/or an α - γ mode discharge transition [5]. At higher pressures, the sheath becomes more collisional and ions traversing the sheath region will experience a further enhanced probability of collisions with mainly the background neutral gas. This results in both momentum and energy transfer leading to peak-broadening and moving the IDFs towards lower energies. The low energy part of the IDFs appears to become more pronounced at higher pressures which is due to enhanced sheath collisions. From results of sheath simulations for HBr discharges, these findings are confirmed in general (see section 2.5.2). However, there is rather poor agreement between measured ion energies and those obtained from HPSM simulations (cf., Fig. D.2-k). This is attributed to deviations between the chosen constant input parameters (like rf voltage, electron temperature, electron density, gas temperature) and reality. Further, the mentioned insufficient collisional parameters in the HPSM code for the implemented molecular species HBr⁺, H₂⁺ and Br₂⁺ lead to ion energies at the ground electrode which are not as severely affected by the neutral gas pressure as observed for Br⁺ ions (cf., Fig. D.2-k). At pressures exceeding 300

mTorr, measured IDFs eventually become completely suppressed. This can be seen from the sharp drop (by several orders of magnitude) in the calculated ion flux in Fig. 4.29-e. The comparably high sheath thickness observed in HBr discharges will lead to an enhanced loss of ions through inelastic collisions at high pressures, until finally at very high pressures almost no ion is able to transit the sheath without experiencing inelastic collisions anymore. The IDFs for ${}^2\text{H}_2^+$ and ${}^{160}\text{Br}_2^+$ ions plotted in Fig. 4.29-b and Fig. 4.29-c support these findings, all ion species investigated are found to be suppressed below the detection limit at high pressures. Note that IDF intensities for ${}^2\text{H}_2^+$ and ${}^{160}\text{Br}_2^+$ have also been divided by a factor of four at 50 mTorr pressure. The bimodal peak structure observed for ${}^2\text{H}_2^+$ ions (which is due to the light ions being able to follow the 60 MHz frequency) finally becomes suppressed at high pressures. The low-energy peak indicating charge exchange near the sampling aperture is not influenced by the discharge pressure.

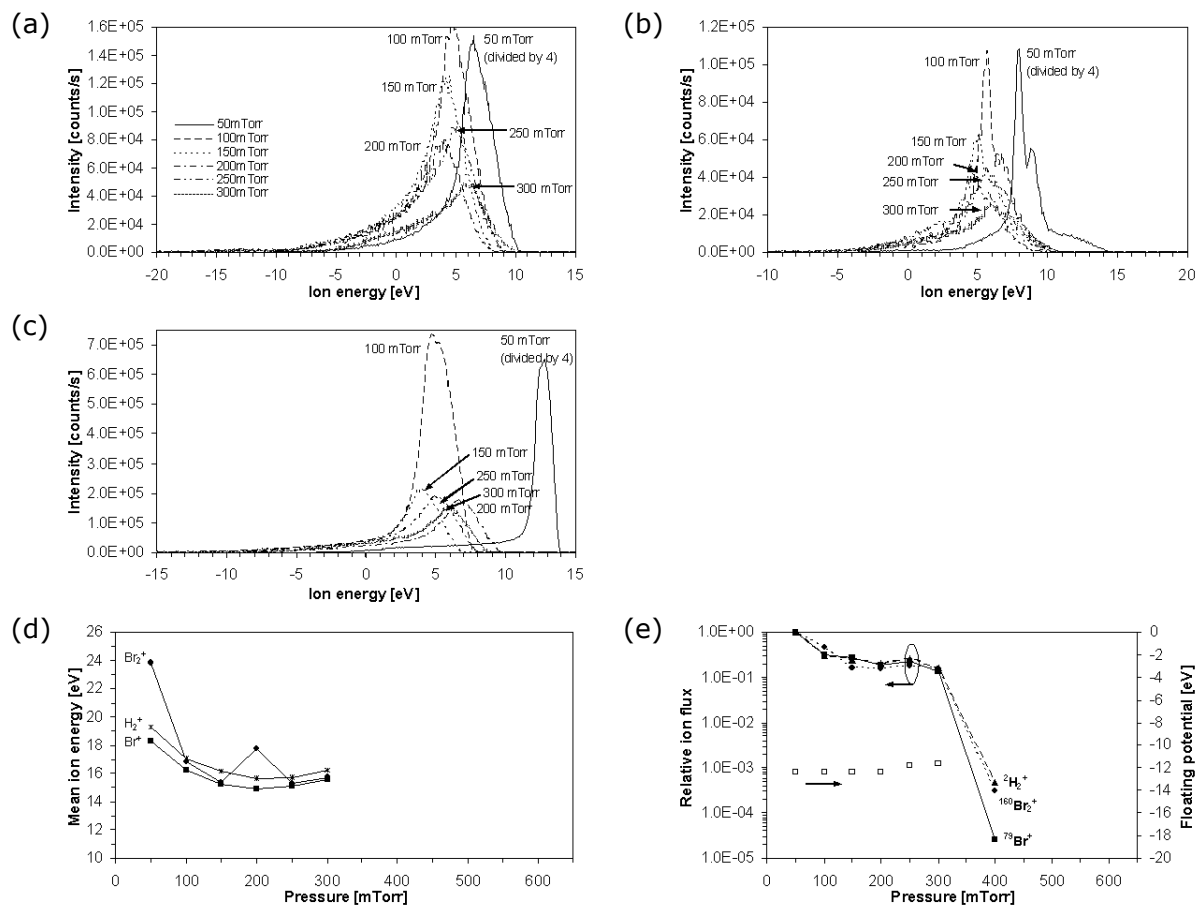


Figure 4.29: (a) ${}^{79}\text{Br}^+$, (b) ${}^2\text{H}_2^+$, (c) ${}^{160}\text{Br}_2^+$ ion distribution functions for pressure variation in 60 MHz HBr discharges (1500 W, 300 sccm HBr gas flow rate, no magnetic field, silicon substrate); (d) corresponding mean ion energies; (e) relative ion fluxes (solid squares, logarithmic scale) and floating potentials at the extraction aperture (open squares) as determined from the position of the lowest energy peak. The IVDFs are plotted without applying corrections for the offset in the energy scale.

60+2 MHz dual frequency discharges

In Fig. F.3-a the 2 MHz rf probe voltage is plotted for a variation of the discharge pressure from 50 mTorr to 600 mTorr and different substrates, where both 60 MHz and 2 MHz power were hold constant during the experiments. When decreasing the process pressure, the rf probe voltage is observed to increase by a power law during dual frequency operation.

From these findings the ion energy is expected to increase as well at lower pressures. However, from the IDFs for $^{79}\text{Br}^+$ plasma ions plotted in Fig. 4.30-a, these conclusions are not supported after applying corrections for the floating potential that builds up at the orifice plate (Fig. 4.30-e). Mean ion energies are observed to increase slightly for Br^+ and more strongly for H_2^+ while increasing the pressure. This behavior does not agree with sheath simulations for a pressure variation in HBr discharges (see section 2.5.2 and Fig. D.2-k in appendix D). Differences are believed to be due to deviations from the assumed electron temperature, rf voltage, electron density and gas temperature during the experiments, which are sensitive parameters influencing the complex sheath dynamics for the 60+2 MHz dual frequency discharges. The increasing mean ion energies observed when rising the pressure are further in contrast to results obtained from comparable argon discharges (cf., Fig. 4.13-b). The low energy shoulder occurring at 100 mTorr is attributed to a decreased ion mean free path due to an enhanced probability of collisions in the sheath (cf., Fig. 4.30-a). As the pressure increases further, the high energy contribution in the IDF is reduced and the low energy contribution in the IDF becomes more prominent. At higher pressures, elastic scattering starts to dominate over charge exchange collisions and washes out the IED peaks.

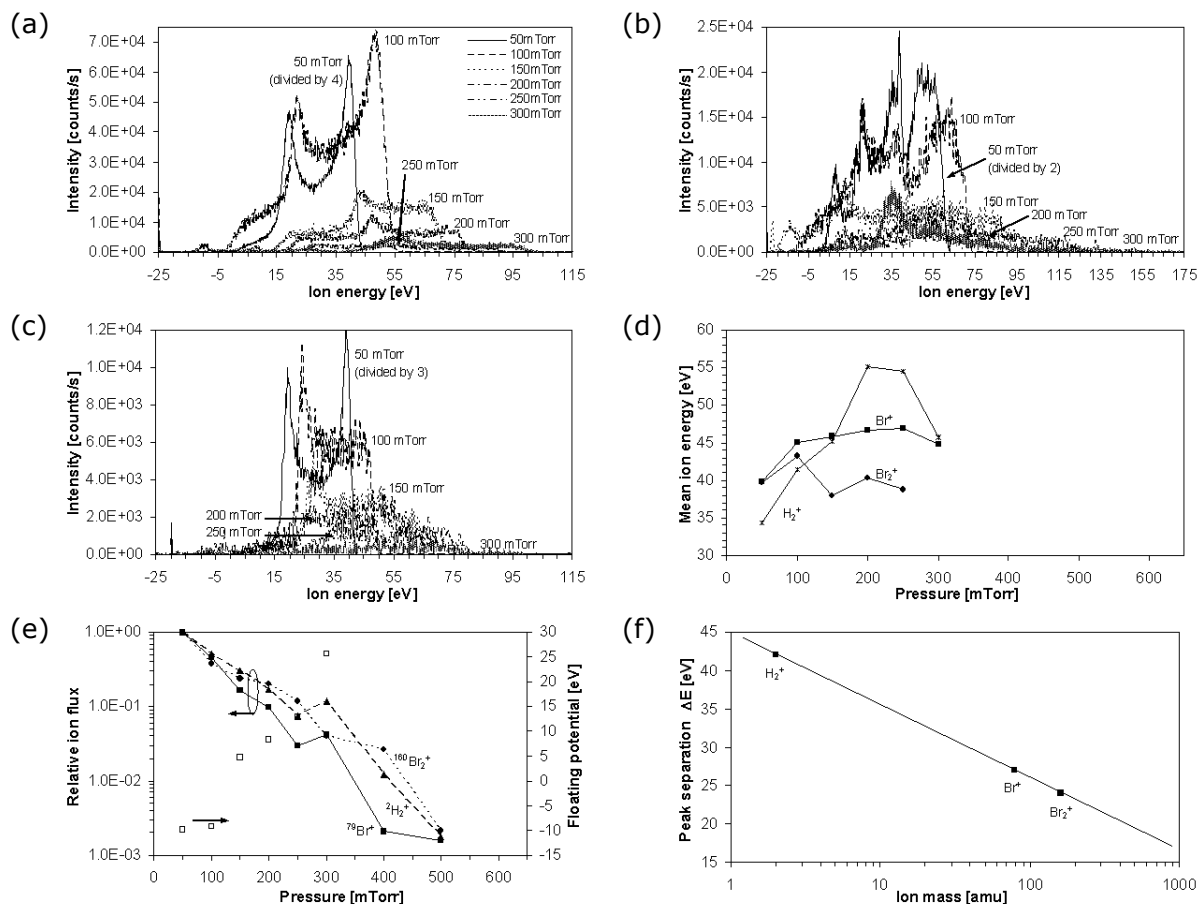


Figure 4.30: (a) $^{79}\text{Br}^+$, (b) $^2\text{H}_2^+$, (c) $^{160}\text{Br}_2^+$ ion distribution functions for pressure variation in 60+2 MHz dual frequency HBr discharges (1500+1500 W 60+2 MHz power, 300 sccm HBr gas flow rate, no magnetic field, silicon substrate); (d) corresponding mean ion energies; (e) relative ion fluxes (solid squares, logarithmic scale) and floating potentials at the extraction aperture (open squares) as determined from the position of the lowest energy peak; (f) scaling of double peak separation with ion mass. The IVDFs are plotted without applying corrections for the offset in the energy scale.

These findings are in agreement with the development of the $^{160}\text{Br}_2^+$ IDF structures from Fig. 4.30-c. The IDFs obtained for $^2\text{H}_2^+$ are observed to exhibit the characteristic four peak structures at low pressures which is attributed to the ions responding to both the 60 and the 2 MHz frequency. By increasing the pressure this structure is efficiently damped, and further the low energy contribution in the IDF becomes more prominent. Note that for reasons of better illustration ion distributions obtained for 50 mTorr have been scaled down accordingly (cf., Fig. 4.30-a to Fig. 4.30-c). In Fig. 4.30-f, the peak separation of the characteristic double peak is demonstrated to scale with the inverse square root of the ion mass, according to (1.64). Results for 100 mTorr pressure were chosen for this demonstration since secondary peak structures from the dual frequency sheath modulation as well as charge exchange collisions in the sheath start to dominate the saddle structure at higher pressures, and therefore do not allow for a precise determination of the peak separation of the bimodal structure.

From Fig. F.3-b (in appendix F), the current is observed to increase when increasing the pressure. This supports the idea of an increased number of collisions in the plasma, resulting in a higher electron density. When rising the discharge pressure, the current is found to increase strongly for SiO_2 , whereas only slight changes are observed for bare silicon substrates. Ion fluxes at the reactor wall plotted in Fig. 4.30-e are found to exhibit a rapid decrease when increasing the pressure. These findings are attributed to a significant loss of these ions due to an increasing number of collisions in the sheath, or enhanced recombination effects in the plasma bulk.

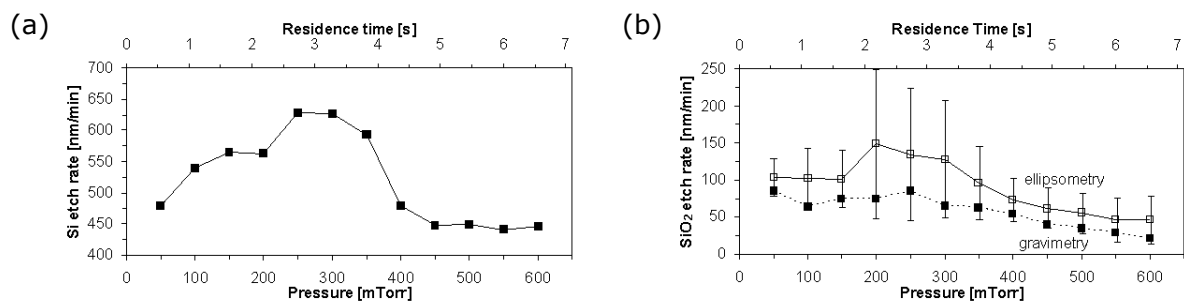


Figure 4.31: Etch rates for variation of the pressure in 60+2 MHz HBr discharges (1500+1500 W 60+2 MHz, 300 sccm HBr gas flow rate, no magnetic field) for (a) silicon from gravimetry, and (b) SiO_2 from gravimetry (full squares) and 49 point ellipsometry measurements (open squares).

The ion-assisted chemical etch rates for silicon as a function of the applied discharge pressure for constant 60+2 MHz power levels (1500 W each) are plotted in Fig. 4.31-a. A significant gain in the etch rate is observed while increasing the pressure, until at intermediate pressures of 250-300 mTorr the highest etch rate of about 650 nm/min is measured. Increasing the pressure further yields a sharp drop in the etch rate, until a saturation occurs above 450 mTorr. From the investigations above, the etch process might be enhanced by the higher ion energies measured at higher pressures. Additionally, at high pressure a higher number of HBr molecules is provided which can be dissociated into hydrogen and bromine atoms. These species subsequently form etch products (like SiBr_4) during chemical reactions at the silicon surface. The ion flux which strongly supports the etch process, was found to decrease strongly at higher pressure. This behavior could explain the silicon etch rate which is found to drop at pressures exceeding 300 mTorr. Additional limitations by a decreasing mean ion energy (due to enhanced collisions in the

sheath) are not supported by IDF measurements. SiO₂ etch rates plotted as a function of process pressure develop quite similar to those measured for silicon (cf., Fig. 4.31-b). Again, a reduced ion flux at high pressures is believed to mainly limit the etch rate at higher pressures. From comparison of Si and SiO₂ etch rates, the selectivity will increase slightly at higher pressures which is attributed to the continuously dropping SiO₂ etch rate while the silicon etch rate finally saturates at high pressures. The high standard deviation of the oxide etch rate in the intermediate pressure regime determined from ellipsometry (open squares) is attributed to a markedly higher etch rate at the wafer edge region, resulting in a considerably nonuniform etch rate distribution across the wafer. From comparison in Fig. 4.31-b, this can cause stronger deviations from an integral gravimetry technique (full squares).

4.3.4 Variation of gas flow rate

60 MHz single frequency discharges

For the experiments conducted here, a variation of the HBr gas flow rate was performed in the range of 100 sccm to 900 sccm, 60 MHz power and reactor pressure were held constant at 1500 W and 150 mTorr, respectively. The following discussion of gas flow effects is based on an IDF analysis for ⁷⁹Br⁺ only, and silicon etch rates. A high flow rate will generally result in a lower residence time for plasma species inside the reactor, but is initially not assumed to affect ion energies. However, the gas flow dependency of the IDFs for ⁷⁹Br⁺ plotted in Fig. 4.32-a reveals a distinct influence on the ion energy. After corrections applied to the offset IDF scale, mean ion energies are found to decrease from 21.7 eV for the lowest gas flow rate (100 sccm) to 14.6 eV for 900 sccm. The decrease of the mean ion energy appears comparable with the decrease observed when rising the pressure above 50 mTorr (cf., Fig. 4.29-d) and therefore hints a correlation to the gas density. As discussed for argon, spatial variations of the discharge pressure from reactor simulations however remain negligible and can not explain the observed changes. Here, the decreasing ion energies are further in contrast to the slightly increased ion energies observed for comparable gas flow experiments in 60 MHz argon discharges (cf., section 4.2.4). Floating potentials determined as a reference to correct for the energy scale offset (Fig. 4.32-c) are not found to deviate much besides a slightly lower value detected for 100 sccm gas flow rate. Deviating floating potentials however can not correct for the large differences of the shifted IDFs at different HBr gas flow rates. The ion flux plotted in Fig. 4.32-c exhibits a maximum at 500 sccm HBr gas flow rate. As discussed for argon discharges, the observed phenomena could be caused by changes in the neutral gas temperature of the nonuniformly distributed background gas (and/or changes in the Br⁺ ion uniformity distribution), which in turn can be due to distinct turbulences at high gas flow rates and heating induced by surface processes at the powered electrode [13]. As observed from HPSM simulations for a variation of the neutral gas temperature in HBr discharges, a decreased mean ion energy could result from a decreasing gas temperature at high gas flow rates (cf., Fig. D.3-k). However, an impact of the gas temperature alone would require changes of several hundred centigrades, to cause a shift of about 7 eV. It is more likely that other discharge parameters like electron temperature, plasma density, etc. change as well, yielding the observed changes of the ion energies. Since the plasma density depends on the electronegativity of the discharge chemistry, this might also be a reason for the observed differences between the different types of discharges investigated in this

work. The question whether the Br^+ ion uniformity distribution differs from that of an Ar^+ distribution in argon discharges (due to differences in the ratio of dissociative/direct Br^+ ionization and an indirect Ar^+ ionization and the respective residence time inside the reactor) can not be answered at this point and should be subject of further analysis.

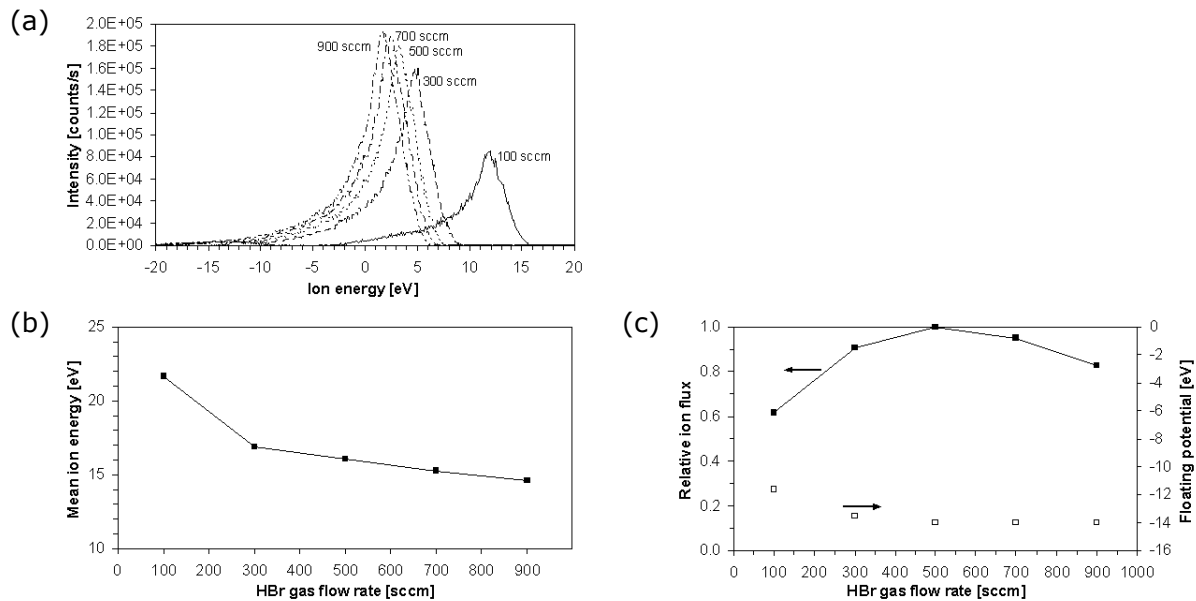


Figure 4.32: (a) $^{79}\text{Br}^+$ ion distribution functions for variation of the HBr gas flow rate in 60 MHz frequency HBr discharges (1500 W, 150 mTorr, no magnetic field, silicon substrate); (b) corresponding mean ion energies; (c) relative ion flux (solid squares) and floating potentials at the extraction aperture (open squares) as determined from the position of the lowest energy peak. The IVDFs are plotted without applying corrections for the offset in the energy scale.

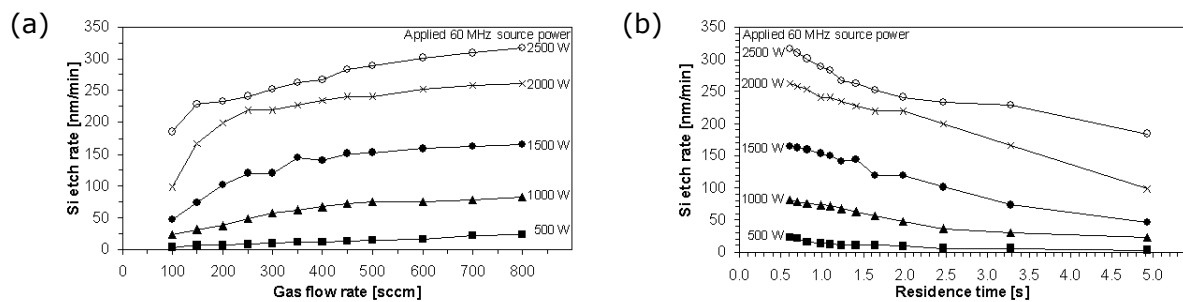


Figure 4.33: Silicon etch rates (as determined from gravimetry) for variation of the HBr gas flow rate and different 60 MHz powers displayed as a function of (a) gas flow rate and (b) corresponding residence time (150 mTorr, no magnetic field).

Besides influencing ion energy distributions, changing the gas flow is expected to affect etch rates since chemical reactions are involved. For 60 MHz single frequency discharges, the silicon etch rate is found to considerably increase when increasing the gas flow rate, or decreasing the residence time, respectively (Fig. 4.33-a and Fig. 4.33-b). The enhancement in the silicon etch rate will additionally depend on the 60 MHz power level. These findings support both a chemical as well as a physical etch component that determine the silicon etching process in HBr discharges. Increasing the 60 MHz power yields an enhanced HBr dissociation, and hence creation of more bromine radicals. A high HBr flow will probably result in a lower degree of dissociated HBr, but also reduce the

concentration of reaction products in the gas phase. A more efficient desorption and removal of etch products on the silicon surface can occur from a decreased residence time. In addition, increasing 60 MHz power also yields somewhat higher ion energies due to the increasing self-bias. Moreover, increasing the 60 MHz power will also give rise to the ion flux, as discussed earlier. The different mechanisms will all contribute to the observed etch rate dependency. From comparison to 60 MHz power and NF_3 gas flow rate variations in NF_3 discharges discussed in section 4.4.4, the offset at the lowest gas flow rate for HBr indicates a more pronounced physical etch component.

60+2 MHz dual frequency discharges

Increasing the HBr gas flow rate for constant 60+2 MHz power (1500+1500 W) and pressure (150 mTorr) in dual frequency HBr discharges yields even more severe changes to the structure and energies of measured ion distributions, compared to those obtained from single frequency discharges. Here, investigations of gas flow effects in dual frequency HBr discharges are limited to the discussion of an IDF analysis for $^{79}\text{Br}^+$ only.

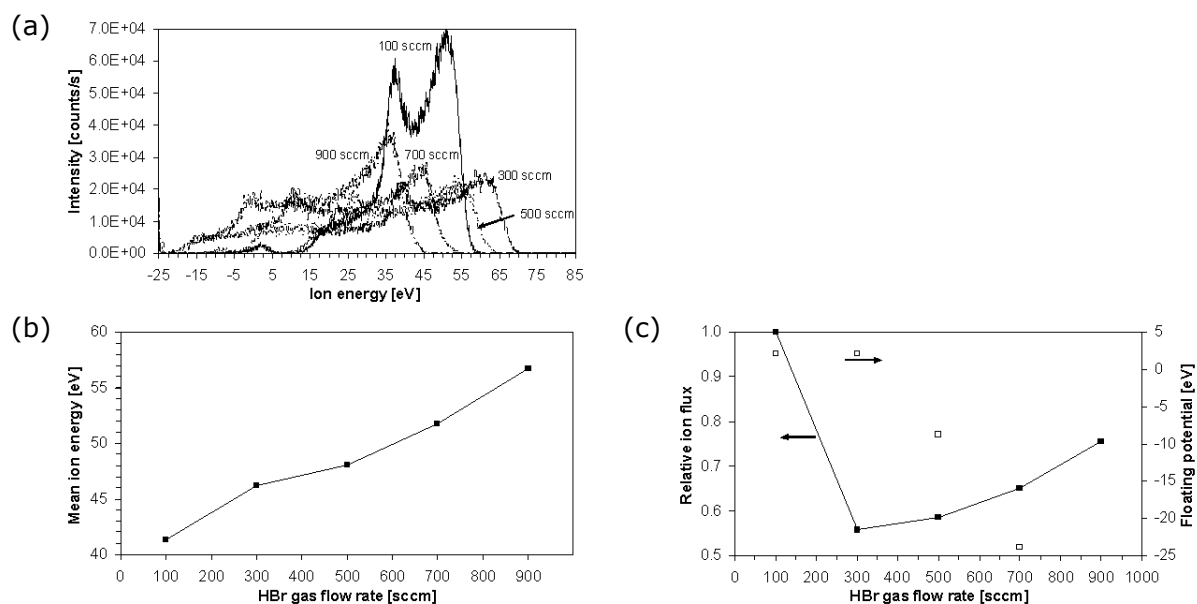


Figure 4.34: (a) $^{79}\text{Br}^+$ ion distribution functions for variation of the HBr gas flow rate in 60+2 MHz dual frequency HBr discharges (1500+1500 W 60+2 MHz power, 150 mTorr, no magnetic field, silicon substrate); (b) corresponding mean ion energies; (c) relative ion flux (solid squares) and floating potentials at the extraction aperture (open squares) as determined from the position of the lowest energy peak. The IVDFs are plotted without applying corrections for the offset in the energy scale.

The peak splitting of the double peak structures is determined by the 2 MHz frequency (cf., Fig. 4.34-a). Contributions of the 60 MHz are not visible which is due to the heavy bromine ions being unable to respond to the 60 MHz frequency sheath modulation. The peak splitting becomes broader when increasing the gas flow rate. Interestingly, the lower energy peak of the saddle-shaped structure remains at about 35 eV after applying corrections to the shifted distributions by using the low-energy peak position from Fig. 4.34-c. Due to the broadening, the maximum energies observed are 58/69/74/79/82 eV for corresponding gas flow rates of 100/300/500/700/900 sccm, corresponding mean energies plotted in Fig. 4.34-b are found to increase from about 41 eV at 100 sccm to 57 eV at 900 sccm HBr gas flow rate. Interestingly, the increase of the mean ion energy appears comparable with that observed from Fig. 4.30-d when rising the discharge

pressure (although the pressure is hold constant for the gas flow rate variation) which indicates again a correlation to the neutral gas density. The floating potential at the non-conducting sampling orifice plate is decreasing considerably, as can be seen from Fig. 4.34-c. Further, the ion flux will exhibit a drastic decrease by increasing the gas flow rate from 100 to 300 sccm, further increasing the gas flow rate yields an ion flux that starts to rise again.

From comparison to 60 MHz HBr discharges, both $^{79}\text{Br}^+$ ion flux and energies appear to scale inversely here. Also, ion energies exhibit a stronger incline in HBr dual frequency discharges (Fig. 4.34-b) compared to the decline observed for HBr single frequency discharge operation (Fig. 4.32-b). The increase of ion energies at the reactor wall is generally comparable to argon discharges, despite the distinct higher absolute changes for $^{79}\text{Br}^+$ ion energies. Variations of the neutral gas temperature alone can not explain the strong scaling for $^{79}\text{Br}^+$ ion energies, nor the non-monotonical development of the measured ion flux here. It appears to be more likely that the discharge operation point is subject to strong deviations when changing the gas flow rate (from changes of the different plasma parameters discussed before). More satisfying explanations can not be given here and should be subject to further investigations.

4.3.5 Variation of magnetic field

60 MHz single frequency discharges

From an IDF analysis for $^{79}\text{Br}^+$ plasma ions for different stationary magnetic fields in the 0-140 G range at constant 60 MHz power (1500 W) and discharge pressure (150 mTorr), ion flux and mean ion energy were obtained again after averaging over the four distributions corresponding to the operating modes (I)-(IV) of the pairwise driven electromagnetic coils (cf., Fig. F.5-a to Fig. F.5-g in appendix F). The ion flux in Fig. F.5-g increases considerably in the presence of a magnetic field, following the predictions from a higher degree of ionization through increased electron collision rates. Unexpectedly, ion energies measured at the reactor wall increase with magnetic flux density (Fig. F.5-f). Comparing experimental results with HPSM calculations in Fig. D.5-k (appendix D) does not confirm the strong changes observed from simulations. This is again believed to be due to strongly inhomogeneous sheath distribution that can considerably deviate in both magnitude and geometry from the homogeneous magnetic field applied for the HPSM calculations. As discussed for argon, the experimental setup may not be representative for a time-averaged sheath thickness occurring during a constant rotation of the magnetic field.

60+2 MHz dual frequency discharges

In Fig. F.6-a to Fig. F.6-e (appendix F), ion distribution functions for $^{79}\text{Br}^+$ are plotted for different magnetic fields up to 140 G during 60+2 MHz frequency discharge operation for constant pressure and power. The characteristic bimodal IDF structure can become considerably distorted as a result of a highly nonuniform plasma which in turn influences the sheath dynamics, as discussed earlier. Sheath distortions from the stationary magnetic field might explain the higher ion energies observed for ions incident at the reactor wall, as compared to discharges without the presence of a magnetic field (cf., Fig. F.6-f). The averaged Br^+ ion flux is plotted as a function of the magnetic field in Fig. F.6-g. Again, the ion flux is found to increase when a magnetic field is present. A maximum ion flux is recorded at 110 G which also yielded the highest ion flux in 60+2 MHz argon discharges.

From examination of the measured IDFs, the complex sheath dynamics for the dual frequency discharges now additionally influenced by the presence of a magnetic field complicate a more precise description of the detailed processes that occur. Generally, IDF measurements performed during application of a stationary magnetic field appear not suited to simulate typical MERIE discharge conditions, and a gain in knowledge about discharge behavior and interactions influencing etch results remains limited.

In contrast to the IDF measurements, rf probe and etch rates measurements were conducted while simulating a rotating magnetic field from application of a 0.25 Hz sinusoidal voltage to the magnet coils. From these experiments, the rf probe voltage is found to strongly decrease for both silicon and SiO₂/Si substrates (cf., Fig. F.4-a in appendix F). This supports a sheath voltage that decreases (as a result of higher plasma densities) to a higher extent than a somehow increased voltage across the plasma bulk. The change in the measured voltage is however smaller than that observed for the power variation. Scaling of the rf voltage was found to agree to some extent to the scaling of sheath thickness and dc bias voltage from HPSM calculations for 60 MHz Ar discharges (cf., Fig. C.5-a and Fig. C.5-d in appendix C) and 60 MHz HBr discharges (cf., Fig. D.5-a and Fig. D.5-e in appendix D). From rf voltage measurements, an onset of saturation is indicated for high magnetic fields when using bare silicon substrates, and around 70 G when silicon substrates with an about 2 μm thick SiO₂ top layer were used. In principle, scaling of the sheath thickness appears to be predominantly determined by the 60 MHz frequency for the dual frequency discharges investigated here. As described above, measured ion energies are not found to decrease according to the decline of measured rf voltages. Nevertheless, mean ion energies calculated from measured IDFs appear to be roughly comparable to results from HPSM simulations for HBr (Fig. D.5-k) with regards to absolute values. Scaling of ion energies might change when applying rotating magnetic fields, and ion energies are expected to decrease according to the decline observed for the measured rf voltage. The rf current plotted in Fig. F.4-b increases which implies an increased electron density from enhanced collisions in the plasma bulk.

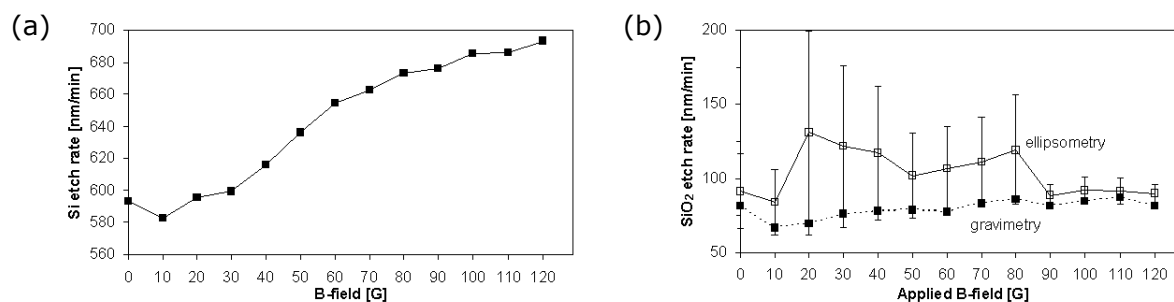


Figure 4.35: Etch rates for variation of the magnetic field (1500+1500 W 60+2 MHz, 150 mTorr, 300 sccm HBr gas flow rate) for (a) silicon from gravimetry, and (b) SiO₂ from gravimetry (full squares) and 49 point ellipsometry measurements (open squares).

From Fig. 4.35-a, the silicon etch rate is observed to continuously increase by about 20% from 10 G to the maximum of 120 G applied here. The enhanced silicon etch rate is expected to be mainly due to a higher density of bromine atoms. This can occur from enhanced collisions of electrons with the neutral gas in the plasma bulk which will yield an enhanced dissociation of HBr. Furthermore, an increased ion flux supporting a chemical reaction at the silicon surface will contribute as well, whereas purely physical sputtering is

believed to play only a minor role here. The influence of the weak magnetic field on the silicon dioxide etch rate in Fig. 4.35-b reveals a different picture. The higher mean etch rate calculated from 49 point ellipsometry measurements (plotted with open squares) for magnetic fields in the range of 20 to 80 G is caused by a more nonuniform etch rate pattern with strongly pronounced etching at the wafer edge area. Results from weight loss measurements (plotted with full squares) are comparable to ellipsometry results from the wafer center, where the etch rate remains constant up to the wafer edge region. From results of weight loss measurements, the Si-to-SiO₂ selectivity appears to remain essentially constant with respect to the magnetic field.

4.3.6 Summary

Similar to argon, separate control of ion energy and ion flux by the dual frequency operation can be achieved as well in HBr discharges. In contrast to argon discharges, the 60 MHz frequency determines both ion flux and radical formation from dissociation of the HBr molecular feed gas. Bromine plasma ions were usually monitored since they are most relevant determining the etch process. To allow for more detailed investigations of the sheath dynamics, light molecular hydrogen ions as well as heavy molecular bromine ions were monitored additionally from HBr discharges. As expected, the IDF peak splitting increases with rf voltage and decreased with rf frequency and ion mass. Light hydrogen ions respond best to the time dependence of the sheath potential and measured IDFs reveal a clear separation of the double peak structure even for 60 MHz frequency operation. Ion energies of low mass hydrogen molecules usually appear evenly distributed over a broad range which is due to the light ions being able to respond to temporal variations of the sheath potential caused by the low and high frequency component. At high 60 MHz power levels, effects from the high frequency dynamics become obvious where the saddle shaped structure splitted into four peaks. For the heavy atomic and molecular bromine ions species, high frequency oscillations could not be resolved. Consequently, IDFs are mainly controlled by the dynamics of the low frequency component. This reflects the fact that control over the energy of light ions in molecular discharges can not be achieved to a comparably high extent observed for heavy ion species. In practice, these light molecular ions may however only play a minor role during etching.

Interactions between the two frequencies are observed as well. By increasing the 60 MHz power, the distribution shifts to lower energies which is attributed to a decreased sheath voltage at higher plasma densities. In contrast to argon, contribution of sheath collisions to the low energy part of ion distributions is generally higher in HBr compared to Ar discharges. Unlike observed for argon, the sheath in HBr discharges appears already more collisional at 50 mTorr. This supports the idea of a generally higher sheath thickness for hydrogen bromide as compared to typical argon discharges, which is very likely due to a higher mean electron temperature in HBr discharges [215]. These findings are further supported from considerably wider peak separations of (mainly 2 MHz frequency) modulated Br⁺, Br₂⁺ and H₂⁺ IDFs in dual frequency HBr discharges (Fig. 4.25), compared to Ar⁺ IDFs measured in dual frequency argon discharges (Fig. 4.10). Due to pronounced sheath collisions for the relatively high pressures applied, mean ion energies will be typically lower than the time averaged sheath potential. Compared to argon, the higher collisionality for HBr is also due to formation of radicals from HBr dissociation caused by the 60 MHz rf source. The high frequency thus allows to control the ion flux but also

influences the mean ion energy more notably by formation of radicals that yield more pronounced scattering in the sheath than in the argon case.

Investigations of HBr discharges strongly indicate that silicon is chemically etched and etch reactions are induced and strongly supported by ion energy, whereas SiO₂ appears to be predominantly physically sputtered. Comparing mass spectra for HBr discharges with SiO₂ and bare silicon substrates supports these findings. SiBr_x species (SiBr⁺, SiBr₂⁺, SiBr₃⁺, SiBr₄⁺) indicate the main etch products of the chemical reaction involved in the etch process. From application of APMS, SiBr_x⁺ (x=1...3) products result from dissociative ionization of SiBr₄ molecules inside the ionizer of the EQP. The etch process can hence be characterized by the reaction



forming volatile SiBr₄ which is required to leave the surface in order to proceed etching. SiBr₄ etch products were only detected when exposing silicon surfaces to the plasma. The absence of SiBr₄ products in case of etching SiO₂ supports the major role of physical sputtering by bromine ions. However, SiBr₄ etch products may also be efficiently dissociated in the plasma and partially redeposited after formation of SiBr_xO_y if oxygen is present in the discharge. Remaining low SiBr₄ concentrations in the plasma may prohibit detection by the mass spectrometer.

Etch rates were observed to rise almost linearly with 60 MHz power. Significantly enhanced contribution is found from increasing the 2 MHz power level. At high 2 MHz power levels, the etch rate finally starts to saturate. Once initiated by a sufficient amount of ion energy, silicon etch rates are chemically driven whereas pronounced physical sputtering is effective for etching silicon dioxide with HBr. Maximum silicon etch rates were found at intermediate pressures, where a balance of high ion energies, ion fluxes and radical densities determine the etch process. A reduced ion flux at high pressures is believed to mainly limit etch rates at high pressures. From studies of the influence of HBr gas flow rates it was found that rising gas flows can yield higher silicon etch rates. High HBr gas flows might result in a lower degree of dissociated HBr (due to a lower residence time of species in the reactor), but more importantly reduce the concentration of reaction products in the gas phase through a more efficient desorption and removal of etch products on the silicon surface. The presence of magnetic fields can further enhance silicon etch rates. This is expected to be mainly caused by a higher density of bromine atoms as a result of enhanced electrons-neutral collisions in the plasma bulk enabling an enhanced dissociation of HBr. Furthermore, an increased ion flux (which supports chemical reactions at the silicon surface) will contribute as well, whereas purely physical sputtering is believed to play only a minor role here.

Besides significant contribution from ion flux and ion energy, maximum etch rates appear limited by radicals densities and an efficient removal of etch products from the substrate surface. This indicates requirements for a certain discharge pressure, feed gas flow rates and application of additional magnetic fields. At medium discharge pressures, ion distribution functions will predominantly consist of low and medium ion energies where the high pressure tail is suppressed due to sheath collisions. Also, off-axis scattering in the sheath becomes more severe which expresses the need of an appropriate sidewall protection when etching high aspect ratio features.

Due to a strong physical enhancement of the silicon etch process with HBr and an almost purely physical sputtering of SiO₂, changes in the Si-to-SiO₂ selectivity are primarily

caused by changes of the chemical etch component during silicon etching (cf., Fig. 4.36-a and Fig. 4.36-b). The selectivity was found to remain above 5:1, where from investigated discharge parameter settings minimum selectivities occurred at low discharge pressures. The chemical etch component must be fairly low but still play a non-negligible role, when comparing results from HBr discharges to purely physical sputtering in argon discharges (where selectivities generally ranged between 1:1 and 2:1). The etch selectivity increases with pressure and magnetic field which indicates enhanced chemical etching on bare silicon substrates. Besides pressure and magnetic field, the chemical etch component can be influenced by 60 MHz power which determines dissociation of the feed gas molecules and hence radical formation. It should be noted here, that 60 MHz power will also yield a certain physical etch contribution through influencing the plasma density (yielding a higher ion flux to the substrate) and ion energy (due to self-bias effects and assumed higher neutral gas temperatures during discharge operation).

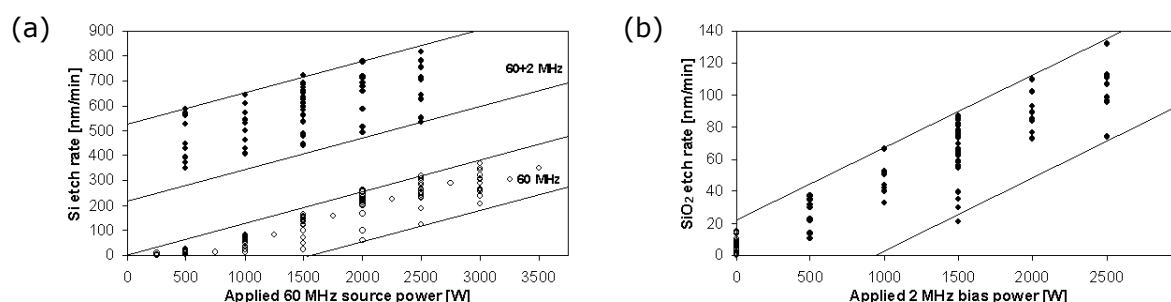


Figure 4.36: Etch rates collected from all hydrogen bromide discharge experiments discussed in this chapter and plotted as a function of (a) 60 MHz source power for silicon; (b) 2 MHz bias power for silicon dioxide.

Halogen molecules like SiBr_xF_y ($x=0\dots3$, $y=4-x$) indicate sputtering and chemical etching of adsorbed layers or byproducts from former NF_3 plasma clean processes. However from etch rate studies, this was not found to noticeably influence etch processes at the substrate surface. The reactor walls can contain significant amounts of fluorine being incorporated during NF_3 plasma clean processes. The fluorine is efficiently removed during HBr discharge operation which is likely to occur through plasma activation and formation of HF [258].

4.4 Nitrogen trifluoride discharges

For application of mass resolved ion energy analysis, $^{19}\text{F}^+$ ions were chosen to be monitored to study the plasma and sheath behavior for different NF_3 discharge conditions examined in this work. Fluorine is known to play a major role in chemically etching silicon and SiO_2 [110], and hence should strongly contribute to the etch rate during RIE of silicon high aspect ratio structures. Impact of the fluorine chemistry on the Si-to- SiO_2 selectivity is of major importance, since for example a high degree of anisotropy has to be ensured to allow for proper profile control during HAR (High Aspect Ratio) etching, the top CD of HAR structures has to be maintained to ensure maximum supply of reactants with minimum ion scattering, and consumption of the SiO_2 hard mask must be minimized to achieve the required etch depth.

4.4.1 Neutral mass spectra and degree of dissociation

In Fig. 4.37-a, a typical mass spectrum is shown for NF_3 from the reactor when the discharge is off. The spectrum is also found to agree (to within the known uncertainties) with a "standard" NF_3 mass spectrum that is obtained at 70 eV nominal electron-impact energy [219]. Traces of HBr and relatively large amounts of humidity are found as well resulting from contamination of the EQP system due to monitoring hydrogen bromide discharges. The peak identified with HF^+ is believed to result from either dissociative ionization of HBr and/or H_2O and fluorine containing molecules inside the EQP ionizer, or direct ionization of stable HF formed inside the plasma reactor during preceding plasma processes. The Ar^+ peak results from small additions of argon feed gas to NF_3 .

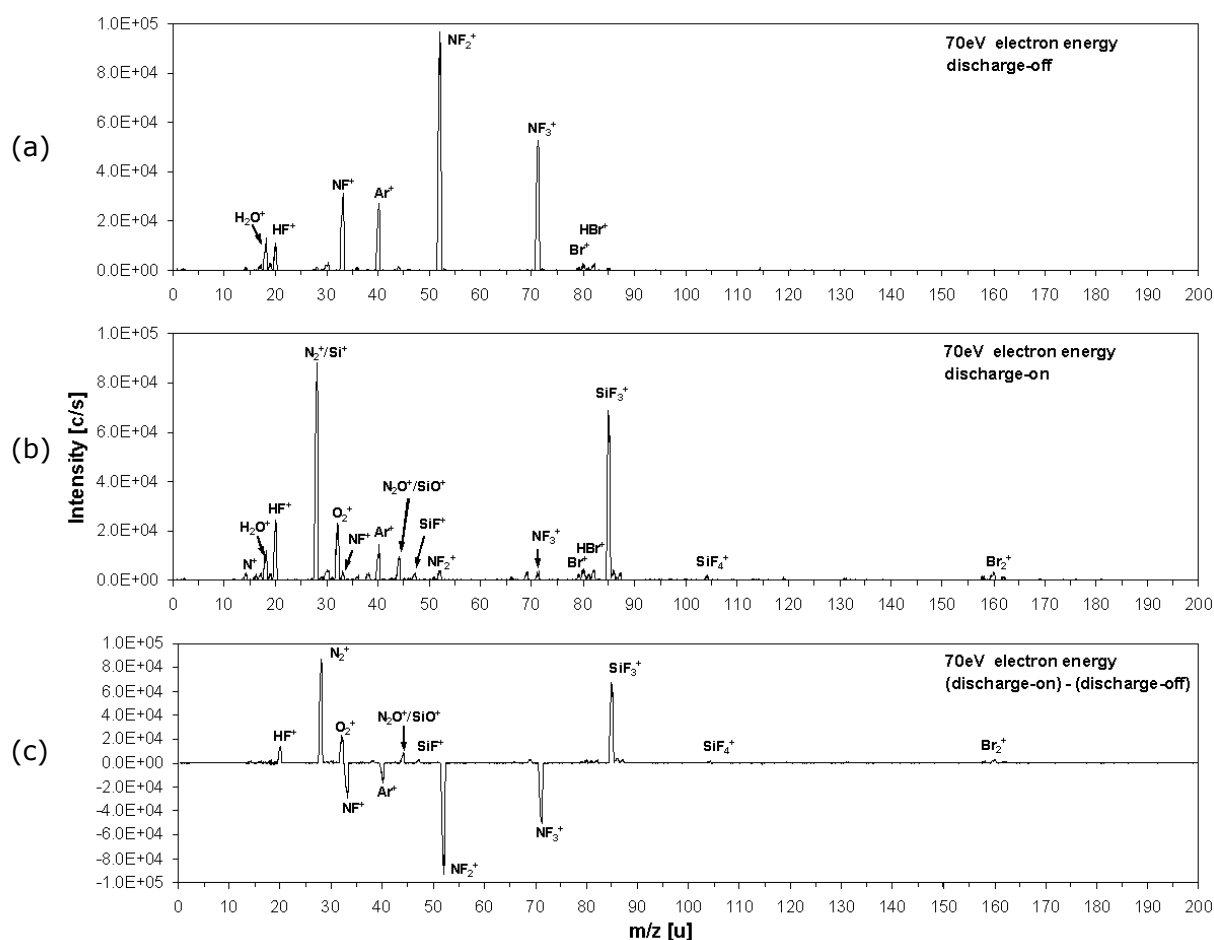


Figure 4.37: Mass spectrum of neutral species ionized by 70 eV electrons for (a) NF_3 (+Ar) gas sampled from the reactor without discharge; (b) NF_3 (+Ar) gas sampled from the reactor with rf discharge (150 mTorr, 1500 W 60 MHz power, 300 sccm NF_3 + 16 sccm Ar gas flow rate, silicon substrate); (c) difference of mass spectra b-a (negative values indicate a loss when the discharge is on).

The mass spectrum for the discharge-on case is shown in Fig. 4.37-b. The recorded spectrum exhibits a reduction in the relative intensities of ions derived from NF_3 , such as NF_3^+ , NF_2^+ and NF^+ , and the appearance of ions such as HF^+ , N_2^+ , O_2^+ , $\text{N}_2\text{O}^+/\text{SiO}^+$, SiF^+ , SiF_3^+ and SiF_4^+ that are associated with discharge-generated decomposition and reaction products like HF , N_2 , O_2 , and SiF_4 . SiF_4 molecules are mainly formed from chemical etch processes at the surface of the silicon substrate. Etch products from erosion of the quartz ring that is mounted to the electrostatic chuck and from silicon deposits inside

the reactor will contribute to the total amount of SiF_4 as well. The mass peak at $m/q = 44$ u is attributed to both N_2O^+ and SiO^+ . These ions result from N_2O (or N_xO_y) and SiO [280,281] which are both volatile products that can effuse into the EQP (formation of SiO^+ from SiO_2 is excluded here since SiO_2 is not a volatile product). The ratios of the $m/q = 85$ u mass peak to the further observed mass peaks at $m/q = 86$ u and $m/q = 87$ u are consistent with the known relative abundance for the isotopes of SiF_3 (which is mainly influenced by the relative abundance for the isotopes of silicon).

Fig. 4.37-c shows the difference mass spectrum which is obtained after subtracting the mass spectrum recorded when the discharge was on from the mass spectrum recorded for the same mass-spectrometer settings when the discharge was off. Notice the decrease of the Ar^+ peak which indicates dilution effects due to creation of large amounts of SiF_4 etch products, reducing the partial pressure of the feed gas components (gas flow rates of both feed gases as well as the discharge pressure remain constant during the process). The difference mass spectrum enables to estimate upper and lower limits for the dissociation of NF_3 in the discharge. Estimates described in the following are based on a methodology described in [80] and applied here to the recorded intensities of NF_3^+ for plasma-on $S_{\text{rf}}(\text{NF}_3^+)$ and plasma-off $S_0(\text{NF}_3^+)$ conditions. The NF_3^+ ion was chosen because it results from direct electron impact ionization of the parent NF_3 molecule. As confirmed by APMS, further ions such as NF_2^+ and NF^+ are predominantly created through dissociative ionization of NF_3 feed gas molecules.

Unknown effects caused by elevated gas pressure and temperature due to feed gas dissociation and discharge heating only allow to estimate limits of the dissociation fraction. The pumping system maintains both a constant input gas flow rate and pressure, regardless of whether the discharge is on or off (i.e., independent of the degree of dissociation that occurs during operation of the discharge). For an increasing number density of molecular species or fragments caused by dissociation, the turbo pump throttle valve opens to maintain a constant pressure. In the extreme case where it is assumed that the total gas number density does not increase with dissociation, an upper limit on the dissociation fraction can be obtained

$$D_u = \frac{S_0(\text{NF}_3^+) - S_{\text{rf}}(\text{NF}_3^+)}{S_0(\text{NF}_3^+)}. \quad (4.7)$$

In contrast, for the assumptions that two products are formed through dissociation of every NF_3 molecule and that a resulting pressure increase is compensated by the throttling action, a lower limit for the dissociation fraction can be calculated

$$D_l = \frac{S_0(\text{NF}_3^+) - S_{\text{rf}}(\text{NF}_3^+)}{S_0(\text{NF}_3^+) + S_{\text{rf}}(\text{NF}_3^+)}. \quad (4.8)$$

As some of the dissociation products might recombine through processes such as



the true value for the dissociation fraction can be expected between the limits D_u and D_l . The degree of an NF_3 dissociation calculated from equations (4.7) and (4.8) as a function of 60 MHz power and gas pressure is shown in Fig. 4.38-a and Fig. 4.38-b, respectively. D_u and D_l are found to increase when rising the 60 MHz power, finally approaching 100% for power levels exceeding 2500 W. From these results it becomes obvious that undissociated NF_3 molecules comprise less than half of the gas in the plasma reactor.

Different substrates were used to study the 60 MHz power dependency of the NF_3 dissociation. Compared to standard silicon substrates, yttria wafers were found to yield a slightly higher dissociation of the NF_3 feed gas. This observation could be explained by either more efficient power coupling for the yttria substrates (yielding slightly higher power densities in the plasma with a slightly modified EEDF), and/or a higher secondary electron emission (leading to an increased dissociation through a higher electron density). From investigation of a pressure dependency (Fig. 4.38-b) for fixed 1500 W 60 MHz power, the NF_3 dissociation was found to remain constant within the investigated range of 50-500 mTorr. All results shown in Fig. 4.38 were obtained at a constant gas flow rate of 300 sccm (2.23×10^{-4} mol/s). It is anticipated that the dissociation fraction will also increase with decreasing flow rates.

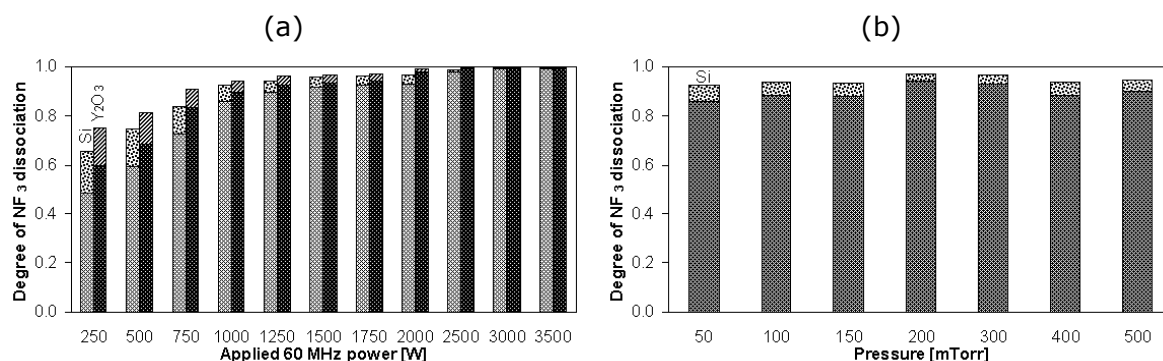


Figure 4.38: Fractional degree of NF_3 dissociation (dotted or striped area) with lower and upper limits determined from equations (4.7) and (4.8) applied to the mass spectral data for (a) NF_3 discharges at 150 mTorr with different 60 MHz power levels applied for silicon (dotted area) and yttria substrates (striped area) covering the electrostatic chuck surface; (b) NF_3 discharges with 1500 W 60 MHz power applied at different pressures using a silicon substrate to cover the surface of the electrostatic chuck. For all discharge conditions, a constant NF_3 gas flow rate of 300 sccm (2.23×10^{-4} mol/s) was used.

4.4.2 Variation of power

60 MHz single frequency discharges

Ion distribution functions measured for $^{19}\text{F}^+$ plasma ions sampled from 60 MHz frequency NF_3 discharges at constant pressure and gas flow rate are shown in Fig. 4.39-a for a variation of 60 MHz power. Similar to investigations in HBr discharges, IDFs start to evolve from negative energies which indicates that the orifice plate is floating at negative potentials. When comparing mean ion energies for different 60 MHz power levels (Fig. 4.39-b) after applying corrections for the energy scale offset caused by the floating potential (plotted in Fig. 4.39-c), F^+ ions are found to exhibit the highest energies compared to corresponding 60 MHz discharges for argon (Fig. 4.7-b) and HBr (Fig. 4.23-d). This might be due to a different sheath structure occurring in highly electronegative NF_3 discharges. The strongly increasing F^+ ion flux from Fig. 4.39-c is apparently due to a pronounced generation of fluorine ions from a highly efficient dissociation of the NF_3 feed gas, as described in the previous section. Reasons for the sharp drop at power levels exceeding 2000 W are currently unclear and should be subject of further investigations.

From Fig. 4.40, both silicon and SiO_2 etch rates are found to substantially increase when rising the 60 MHz power. For power levels between 1000 W and 1500 W, etch rates remain constant which is believed to be due to a constant NF_3 dissociation in that range. At higher

input power, a deeper NF_3 dissociation can occur creating higher concentrations of free fluorine. An efficient NF_3 dissociation yielding values between 60% and 100% for silicon substrates will lead to a formation of fluorine radicals which through chemical reactions at the substrate surface finally form SiF_4 etch products. The final SiF_4 etch product is observed to be very stable and will not contribute much to the etch rate after its formation. From comparison to etch rates in SiF_4 discharges (cf., Fig. I.3 in appendix I), contribution from SiF_4 will not exceed 5% for silicon substrates, and remain less than 15% for SiO_2 substrates. From ellipsometry measurements, the etch rate uniformity is observed to decrease for higher 60 MHz power levels, where a higher etch rate is again measured at the wafer edge region.

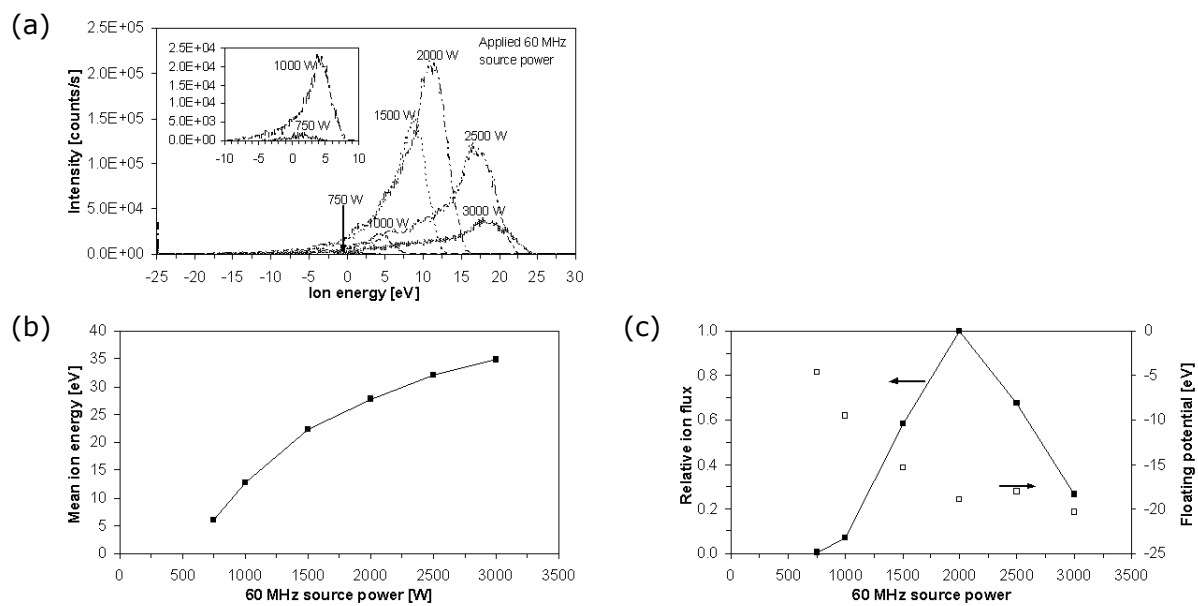


Figure 4.39: (a) $^{19}\text{F}^+$ IVDF for power variation in 60 MHz NF_3 discharges (150 mTorr, 200 sccm NF_3 gas flow rate, no magnetic field, silicon substrate); (b) corresponding mean ion energies; (c) relative ion flux (solid squares) and floating potentials at the extraction aperture (open squares) as determined from the position of the lowest energy peak. The IVDFs are plotted without applying corrections for the offset in the energy scale.

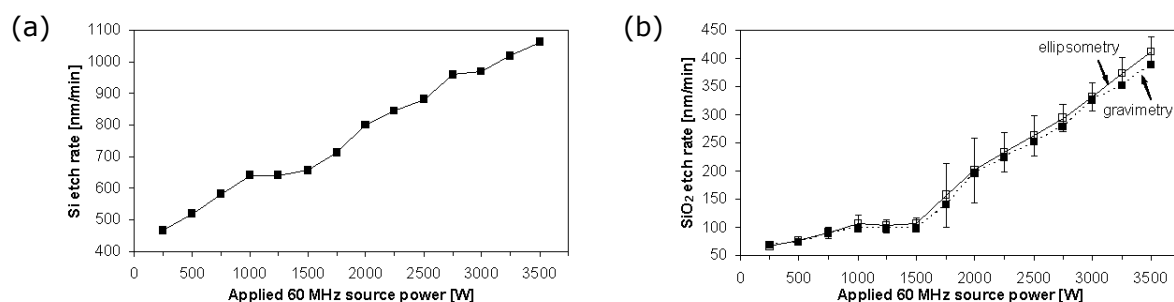


Figure 4.40: Etch rates for 60 MHz power variation (150 mTorr, 300 sccm NF_3 gas flow rate, no magnetic field) for (a) silicon from gravimetry, and (b) SiO_2 from gravimetry (full squares) and 49 point ellipsometry measurements (open squares).

60 MHz frequency NF_3 discharges were chosen also for a quantitative assessment of SiF_4 etch product concentrations, in order to allow for a calibration of the QCLAS technique. For this purpose, results of the different diagnostics as well as weight loss measurements were

combined as described in the following. Experiments conducted for this approach were carefully performed in order to minimize secondary effects, like influences of background contribution and detector degradation while performing mass spectrometry, and further degradation of the SrF₂ optical windows from deposition of thin surface layers which can cause shifts of the measured intensity for the infrared laser beam of the QCLAS system.

When applying mass spectrometry, background spectra were monitored before each measurement for correction of measured spectra for the cases when the discharge is turned on. Additionally, the detector voltage was scanned routinely to avoid influences of an enhanced degradation on measured intensities. To receive more stable results for peaks with even very low intensities, integration was performed for the peaks at m/q ratios of interest.

After performing mass spectrometry analysis, all isotopes relevant for detected SiF_x⁺ species (associated with SiF₄ etch products) were added after applying corrections for the mass ratio dependent decrease of the intensity caused by the EQP analyzer (see section 2.4.4). In detail, this can be expressed by

$$\sum_{x=47}^{49} {}^x\text{SiF}^+ = (47 \text{ u}) \int_{46.5 \text{ u}}^{47.5 \text{ u}} Sd\left(\frac{m}{q}\right) + (48 \text{ u}) \int_{47.5 \text{ u}}^{48.5 \text{ u}} Sd\left(\frac{m}{q}\right) + (49 \text{ u}) \int_{48.5 \text{ u}}^{49.5 \text{ u}} Sd\left(\frac{m}{q}\right), \quad (4.10)$$

$$\sum_{x=66}^{68} {}^x\text{SiF}_2^+ = (66 \text{ u}) \int_{65.5 \text{ u}}^{66.5 \text{ u}} Sd\left(\frac{m}{q}\right) + (67 \text{ u}) \int_{66.5 \text{ u}}^{67.5 \text{ u}} Sd\left(\frac{m}{q}\right) + (68 \text{ u}) \int_{67.5 \text{ u}}^{68.5 \text{ u}} Sd\left(\frac{m}{q}\right), \quad (4.11)$$

$$\sum_{x=85}^{87} {}^x\text{SiF}_3^+ = (85 \text{ u}) \int_{84.5 \text{ u}}^{85.5 \text{ u}} Sd\left(\frac{m}{q}\right) + (86 \text{ u}) \int_{85.5 \text{ u}}^{86.5 \text{ u}} Sd\left(\frac{m}{q}\right) + (87 \text{ u}) \int_{86.5 \text{ u}}^{87.5 \text{ u}} Sd\left(\frac{m}{q}\right), \quad (4.12)$$

$$\begin{aligned} \sum_{x=104}^{106} {}^x\text{SiF}_4^+ &= (104 \text{ u}) \int_{103.5 \text{ u}}^{104.5 \text{ u}} Sd\left(\frac{m}{q}\right) + (105 \text{ u}) \int_{104.5 \text{ u}}^{105.5 \text{ u}} Sd\left(\frac{m}{q}\right) \\ &+ (106 \text{ u}) \int_{105.5 \text{ u}}^{106.5 \text{ u}} Sd\left(\frac{m}{q}\right) \end{aligned} \quad (4.13)$$

where S is the intensity measured by the mass spectrometer in [counts/s], and m/q is the mass-to-charge ratio in atomic mass units [u]. The SiF₄ partial pressure could then be obtained from the ratio of the integrated SiF₄ intensity and the total integrated intensity of the complete mass spectrum

$$p_{\text{SiF}_4} = \frac{\sum_{x=47}^{49} {}^x\text{SiF}^+ + \sum_{x=66}^{68} {}^x\text{SiF}_2^+ + \sum_{x=85}^{87} {}^x\text{SiF}_3^+ + \sum_{x=104}^{106} {}^x\text{SiF}_4^+}{\int_{0 \text{ u}}^{512 \text{ u}} Sd\left(\frac{m}{q}\right)} p \quad (4.14)$$

where p is the process pressure in the plasma reactor.

Alternatively, calculation of the SiF₄ partial pressure from weight loss measurements was performed by the following procedure: First, the molar number of silicon etch species per time was calculated from

$$\frac{N_{\text{Si}}}{t} = \frac{\Delta m_{\text{Si}}}{t \cdot M_{\text{Si}}} \quad (4.15)$$

with the weight difference of the silicon substrate Δm_{Si} determined before and after etching, the silicon molar mass $M_{\text{Si}} = 28.09 \text{ g/mol}$, and the time for etching t . This

approach assumes negligible contribution of incorporated or deposited materials or layers at the substrate. Further, an average SiF_4 flow in [particle per time] can be estimated by applying the relation

$$Q_{\text{SiX}} = \frac{N_{\text{Si}}}{t} \cdot N_{\text{A}} \quad (4.16)$$

which strictly applies for the behavior of an ideal gas. From (4.16), the gas flow rate Q is calculated in [sccm] from the molar volume $V_{\text{mol}} = 22414 \text{ cm}^3 \text{ mol}^{-1}$ and the Avogadro constant $N_{\text{A}} = 6.022 \times 10^{23} \text{ mol}^{-1}$. The partial pressure for the etch products can then be determined from

$$p_{\text{SiX}} = \frac{Q_{\text{SiX}}}{Q_{\text{feed}} + Q_{\text{SiX}}} p \quad (4.17)$$

which assumes all of the silicon etched has been oxidized into stable SiX etch products containing one silicon atom, further neglecting subsequent dissociation of SiX and contribution of dissociated products to the etch process.

Now, calculation of SiF_4 concentrations measured by QCLAS was performed after applying corrections for intensity losses caused by a degradation of the SrF_2 optical windows. Concentrations were calculated by using equation (3.9), and initially assuming gas temperatures of 343 K corresponding to the wall and lid temperature that were hold constant throughout the experiments. Further corrections include accounting for a loss of SiF_4 due to dissociation in the discharge. For the NF_3 discharges investigated here, an average SiF_4 dissociation of 6% - as determined for pure 60 MHz frequency SiF_4 discharges (cf., Fig. I.2 in appendix I) - was assumed to apply also for the situation here.

Results for the SiF_4 partial pressures calculated from weight loss measurements (solid triangles) and mass spectrometry (solid circles) are plotted in Fig. 4.41-a. Taking into account uncertainties of the applied methods yields an acceptable correlation for comparison of the partial pressures. SiF_4 concentrations measured with QCLAS are included in Fig. 4.41-a as well, where a comparison of data is shown after applying corrections for an SiF_4 dissociation (solid squares) as well as uncompensated data (open squares) as a reference. The SiF_4 concentrations are found to decrease. This is mainly attributed to the initial assumption of a constant neutral gas temperature of 343 K which is obviously not fulfilled for the discharges investigated here, and strictly applies only for cases when the discharge is off. From these results a knowledge of neutral gas temperatures for different discharge conditions appears necessary to allow for calculation of SiF_4 concentrations from intensities measured with QCLAS. Through a combined application of the different diagnostic techniques, temperatures of the SiF_4 neutral gas can be roughly estimated by application of the ideal gas law

$$T_{\text{SiF}_4} = \frac{p_{\text{SiF}_4}}{n_{\text{SiF}_4} k_{\text{B}}} \quad (4.18)$$

with the SiF_4 partial pressure p_{SiF_4} as determined from weight loss measurements or mass spectrometry, the SiF_4 concentration n_{SiF_4} as measured by QCLAS, and k_{B} the Boltzmann constant, and further assuming a uniform density profile (which however is only valid if no significant gas heating occurs). Calculated temperatures can be used as a rough estimation of the real mean neutral gas temperature for the investigated 60 MHz NF_3 discharges. Neutral gas temperatures calculated from combined application of weight loss measurements and QCLAS (solid triangles) as well as mass spectrometry and QCLAS (solid

circles) are plotted in Fig. 4.41-b. SiF_4 neutral gas temperatures are found to rise from about 350°C for a 60 MHz power level of 500 W to above 1000°C for 3500 W. These values are slightly higher than those obtained from applying a similar procedure for 60 MHz SiF_4 discharges, where SiF_4 neutral gas temperatures were calculated to about 230°C at 500 W and 850°C at 3500 W (cf., Fig. I.4 in appendix I).

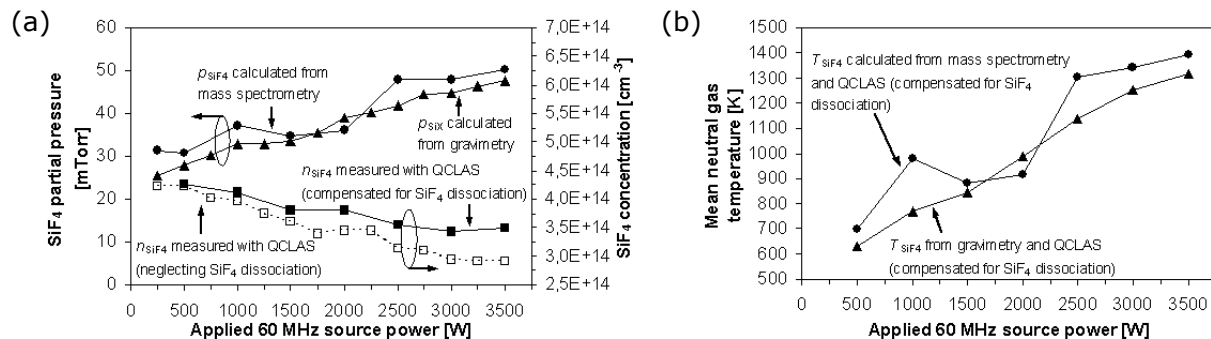


Figure 4.41: Combined application of mass spectrometry, gravimetry and QCLAS for 60 MHz power variation in NF_3 discharges (150 mTorr, 300 sccm NF_3 gas flow rate, no magnetic field): (a) SiF_4 partial pressure calculated from weight loss measurements (solid triangles) and mass spectrometry (solid circles), SiF_4 etch product concentrations measured with QCLAS uncompensated for variations of the neutral gas temperature (open squares: data obtained when neglecting an SiF_4 dissociation, solid squares: data after applying corrections for an SiF_4 dissociation); (b) SiF_4 neutral gas temperatures calculated from combined application of weight loss measurements and QCLAS (solid triangles) as well as mass spectrometry and QCLAS (solid circles).

For the same plasma reactor used in this work, neutral gas temperatures have been calculated from Doppler broadening of H_α and H_β emission lines by application of high resolution OES in HBr and N_2/H_2 discharges [282]. During these experiments, the pressure remained constant at 250 mTorr. Whereas neutral gas temperatures for N_2/H_2 discharges have been measured to increase from 1200 K to 1600 K, the temperature in HBr discharges dropped from 1700 K to 1400 K when increasing the 60 MHz power level from 1000 W to 4000 W. Compared to these results, SiF_4 neutral gas temperatures calculated in this work are not too far away. From results of forming gas discharges, also the trend of a rising temperature while increasing the 60 MHz power level is confirmed. For the decrease in case of HBr it has been speculated that discharge conditions as well as interactions between reaction products and feed gas species might change when rising the 60 MHz power. However, this was not observed in this work from mass-resolved ion energy analysis for the main species constituting the HBr plasma. Although it could not be detected with the current EQP setup, atomic hydrogen is not believed to be a significant species in HBr discharges since it will easily recombine to H_2 , or form HF with the fluorine released from the reactor walls. Since hydrogen is much lighter than the major species in HBr discharges (e.g., Br , HBr , Br_2 , SiBr_4), the temperature extracted in [282] may also not represent the mean neutral gas temperature in such discharges. Comparable high neutral gas temperatures were furthermore observed in Cl_2/BCl_3 CCP discharges [283], where temperatures were also found to rise with power and pressure.

60+2 MHz dual frequency discharges

In Fig. 4.42-a to Fig. 4.42-c, IDFs for $^{19}\text{F}^+$ are shown for a variation of 60 MHz power at fixed 2 MHz power of 500 W, 1500 W, and 2500 W, respectively. Compared to IDFs measured for argon and HBr discharges for similar conditions, the broadest peak separation

caused by the low frequency sheath modulation at 2 MHz is found for F^+ ions investigated here. For NF_3 , the sheath thickness is expected to be somehow comparable to that for HBr (from HPSM simulation, section 2.5.2). The comparably light fluorine ions will easily respond to the 2 MHz frequency, and gain high kinetic energies from acceleration in the sheath. The fluorine mass is however still too high to respond to the 60 MHz frequency modulation, as was observed for molecular hydrogen ions in 60+2 MHz dual frequency HBr discharges. For low 60 MHz plasma excitation, the 2 MHz frequency determines the sheath modulation where from the high sheath voltage the broadest peak separation and maximum ion energies are measured. An increasing 60 MHz power leads to the known reduction of peak broadening which is attributed to thinner sheaths at higher densities. The lower energy peak of the bimodal structure appears to be preferred which can be attributed to the non-sinusoidal nature of the sheath voltage. Again, this can cause the minimum of the sheath potential to be slower varying than the maximum which allows more ions to enter the sheath during this phase, and hence contributing to the low-energy peak of the saddle-shaped structure. The floating potential at the orifice aperture determined from the lowest energy peak is observed to become more negative when increasing the 60 MHz power level for fixed 2 MHz power (cf., Fig. 4.42-e). These findings agree with those observed for 60 MHz NF_3 discharges.

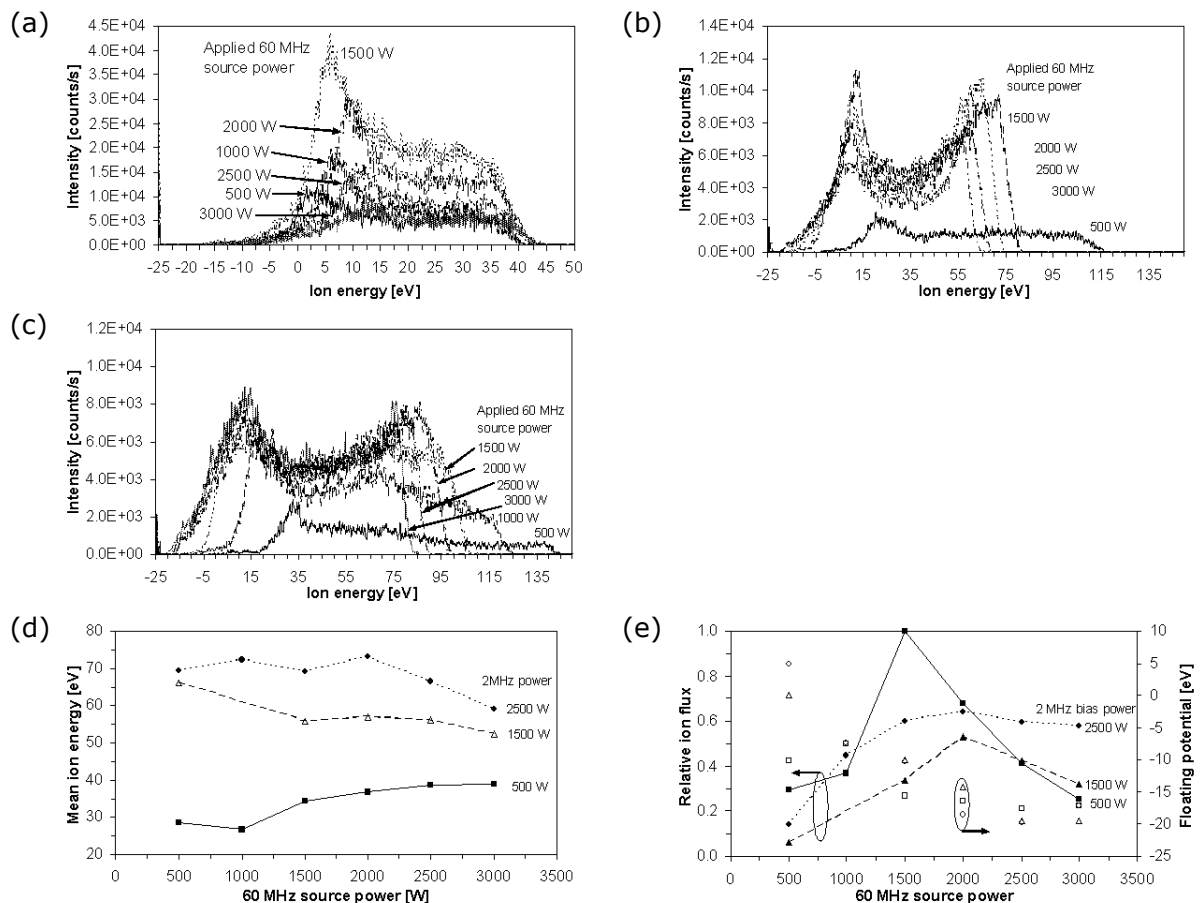


Figure 4.42: $^{19}F^+$ IVDFs for 60 MHz power variation in 60+2 MHz dual frequency NF_3 discharges shown for fixed 2 MHz power of (a) 500 W, (b) 1500 W, (c) 2500 W (150 mTorr, 200 sccm NF_3 gas flow rate, no magnetic field, silicon substrate); (d) corresponding mean ion energies; (e) relative ion flux (solid squares) and floating potentials at the extraction aperture (open squares) as determined from the position of the lowest energy peak. The IVDFs are plotted without applying corrections for the offset in the energy scale.

As illustrated in Fig. 4.43-a, the silicon etch rate increases monotonically when rising the 2 MHz power where the decreasing slope indicates saturation at high power levels. The influence of 60 MHz source power yields a significant contribution to increase etch rates further through enhanced dissociation of NF_3 and an increasing (fluorine) ion density. This is a clear demonstration of the well-known mechanism of spontaneous chemical etching of silicon and SiO_2 in fluorine chemistry [110], where etch rates can be markedly enhanced through the impact of ion bombardment energy and ion flux. According to equations (3.15), (4.15) and (4.16), a maximum possible etch rate of 1715 nm/min could be achieved assuming a complete conversion of 300 sccm NF_3 to SiF_4 product molecules as well as N_2 byproducts. Etch rates saturate below 85% conversion of NF_3 feed gas to SiF_4 products (and N_2 byproducts) which indicates a quite efficient conversion of the feed gas. A limitation by surface reactions could contribute as well to the observed saturation. From rf probe measurements it is observed that an increase of the 60 MHz power level yields reduced voltages (Fig. G.1-a in appendix G), and hence lower ion energies which for medium and high 2 MHz power levels agrees with the $^{19}\text{F}^+$ mean ion energies plotted in Fig. 4.42-d. Rising currents (cf., Fig. G.1-b) may indicate higher electron densities in the plasma. Since NF_3 is the most negative of the discharges investigated, negative ions in the plasma bulk will contribute the major part of negative species. At this point, the degree of electronegativity (negative ion density to electron density ratio) is estimated to exhibit about two orders of magnitude, according to [36,37]. This indicates that the ion density may scale very differently to the electron density. The $^{19}\text{F}^+$ ion flux sampled at the reactor wall is affected by the 60 MHz power by several ten percent, yielding a maximum around 2000 W (Fig. 4.42-e). Variations observed from different 2 MHz power levels may be caused by different loss mechanisms in the sheath since the sheath thickness is mainly controlled by the 2 MHz frequency. Etch rates appear limited by the 60 MHz power which emphasizes the importance of both chemical etch component and ion flux. For high 60 MHz power levels, NF_3 feed gas molecules are efficiently dissociated where formation of free radicals is further enhanced through an increasing dissociation of NF_3 related fragment molecules. The chemical etch component is strongly supported by the sputter component which for 60 MHz is mainly determined by the ion flux (as long as the ion energy remains sufficiently high), and for 2 MHz is due to a considerable gain in ion energy. The ion flux denotes an energy supply that enables and/or supports the chemical reactions taking place. As observed from the F^+ mean ion energies in Fig. 4.42-d, increasing the 60 MHz power can result in decreased ion energies (from a decreasing sheath thickness) which would imply a lower physical etch component provided for initiating/supporting the etch process.

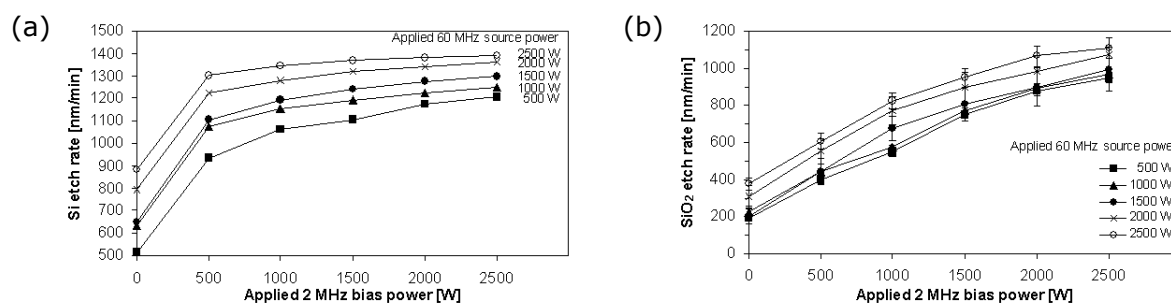


Figure 4.43: Etch rates for 60+2 MHz power variation (150 mTorr, 300 sccm NF_3 gas flow rate, no magnetic field) for (a) silicon from gravimetry, and (b) SiO_2 from ellipsometry.

From comparison of the slopes of the silicon and silicon dioxide etch rates (Fig. 4.43), the Si-to-SiO₂ selectivity is found to decrease for both a rising 60 MHz source power as well as 2 MHz bias power. This emphasizes again, that the etch process is chemically driven for both silicon as well as SiO₂ surfaces, and a strong enhancement is achieved from physical ion energy impact. The standard deviation of ellipsometry measurements for determination of the oxide etch rate increases slightly from initially very uniform etch rates when increasing the 60 MHz power level, causing again higher etch rates at the wafer edge region. In contrast, a higher etch rate is observed in the wafer center for 2 MHz dominated plasmas. This could indicate that skin effects dominate over additional effects here, like electric field distribution between wafer edge and focus ring, plasma penetration into the gap between wafer and focus ring, and temperature gradients between wafer and quartz focus ring. SiO₂ etch rates calculated from weight loss measurements are not shown here since they were comparable to the plotted ellipsometry data.

4.4.3 Variation of pressure

60 MHz single frequency discharges

During this series of experiments, the pressure was varied between 100 and 600 mTorr for constant 60 MHz power (1500 W) and gas flow rate (300 sccm NF₃). For 50 mTorr pressure, the plasma could not be stabilized within the range controlled by the matching unit. Ion distribution functions for ¹⁹F⁺ plasma ions measured through the insulating extraction hood fitted to the reactor side wall are plotted in Fig. 4.44-a to Fig. 4.44-c. IDFs are offset by a floating potential that was examined from the low-energy charge exchange peak, as given in Fig. 4.44c. The IDF structure is found to exhibit an unresolved double peak resulting from the inertia of fluorine ions to respond to the oscillations of the 60 MHz dictated sheath potential. Instead, the ions will experience an average sheath potential which is described by the position of the unresolved peak. Increasing the pressure yields a continuous shift of the IDFs to lower energies where mean ion energies are remarkably reduced (cf., Fig. 4.44-b). The strongly pronounced low energy shoulder indicates a distinct number of ions experiencing collisions in the sheath. This appears to be due to a high sheath thickness similar to that calculated for typical HBr discharges. Secondary peak structures are observed at medium pressures which result from charge exchange collisions in the sheath. Due to a low probability of elastic collisions, charge exchange collisions should generally be visible most likely for 60 MHz frequency operation and low pressures. The reason why charge exchange collisions from the IDFs in Ar and HBr were hardly or not visible at all could be explained by a high argon gas temperature resulting in a generally lower neutral density, or the presence of too many different species that suppress the fraction of resonant collisions in case of HBr. From the extensive dissociation observed for NF₃, a high amount of fluorine radicals is created which apparently yields to situations where resonant collisions dominate over non-resonant collisions.

While increasing the pressure, the number of collisions with the background gas will increase as well and elastic scattering starts dominating over charge exchange collisions. From the measured IDFs for ¹⁹F⁺ this transition is indicated at around 200 mTorr. From the multiple peaks at low energies, distributions for 100 and 150 mTorr pressure are clearly influenced by symmetric charge exchange collisions. Fast fluorine ions collide with the background gas producing slow F⁺ ions and fast neutrals. The new F⁺ thermal ions are accelerated towards the electrode by the sheath electric field. Since these ions do not

experience the full potential drop of the sheath, they appear as structures in the IDF low energy tail below the time-averaged potential. The energies of the secondary peaks depend on the sheath position at which the slow ions are formed [7,8]. The number of peaks in the distribution corresponds to the number of rf cycles it takes the ions to cross the sheath. For IDFs measured for 100 and 150 mTorr pressure, about 6 secondary peaks are observed where the peak at the lowest energy (from charge exchange in the proximity of the orifice) is included. At high pressure, secondary peaks are diminished due to the dominating contribution of elastic scattering. From the number of charge exchange collisions, a mean sheath thickness at the ground electrode can be estimated according to equation (1.61) that describes the collisionless sheath case. The mean sheath voltage at ground can be extracted from the mean ion energy in Fig. 4.44-b which finally results in a mean sheath thickness at ground of about 600 μm for fluorine at 60 MHz frequency. Since this estimation is valid only for collisionless sheaths, the real mean sheath thickness must exceed 600 μm for the collisional case investigated here. Nevertheless, the calculated thickness for the ground electrode appears to be reasonable.

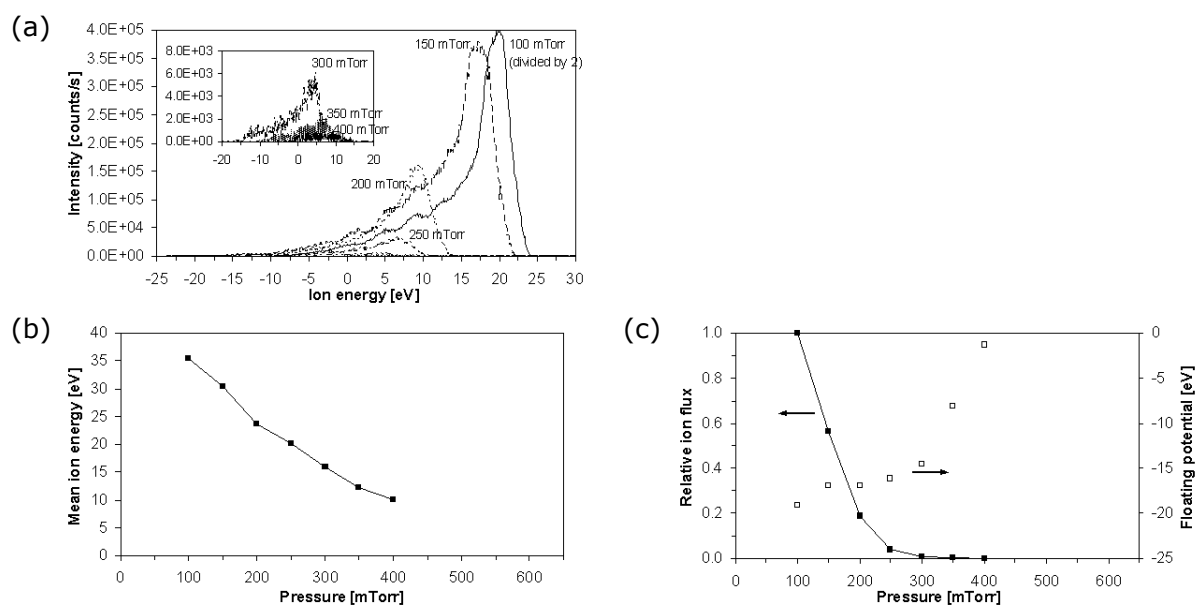


Figure 4.44: (a) $^{19}\text{F}^+$ ion distribution functions for pressure variation in 60 MHz NF_3 discharges (1500 W, 200 sccm NF_3 gas flow rate, no magnetic field, silicon substrate); (b) corresponding mean ion energies; (c) relative ion flux (solid squares, logarithmic scale) and floating potentials at the extraction aperture (open squares) as determined from the position of the lowest energy peak. The IDVDs are plotted without applying corrections for the offset in the energy scale.

From Fig. 4.44-c it can be seen that the F^+ ion flux at the reactor wall drops sharply, until at high pressures exceeding 400 mTorr ions from the plasma can not be detected anymore. This is believed to result from an enhanced negative-positive ion recombination (having a large rate constant in electronegative discharges [20]) at high pressures, and/or a decreasing ion generation at high pressures. Besides IDF analysis for F^+ ions, no further investigations were performed here but will be subject for dual frequency NF_3 discharges discussed next.

60+2 MHz dual frequency discharges

During these investigations, the discharge pressure was changed from 50 mTorr to 600 mTorr. Both 60 MHz and 2 MHz power were held constant during the experiments, as was

the NF_3 gas flow rate. Ion distribution for F^+ were obtained at different pressures as shown in Fig. 4.45-a, without applying corrections for the offset in the energy scale yet. After correcting for the energy scale offset (cf., Fig. 4.45-c), increasing the pressure from 50 mTorr to 100 mTorr is found to cause a broadening of the pronounced double peak structure. Further increasing the pressure does not affect the peak separation anymore. Similar to results from rising the pressure in 60 MHz NF_3 discharges, the F^+ mean ion energy at the passive electrode is found to drop (cf., Fig. 4.45-b). The ion flux incident at the reactor wall decreases exponentially (cf., Fig. 4.45-c), until finally for pressures exceeding 350-400 mTorr no ions can be detected anymore.

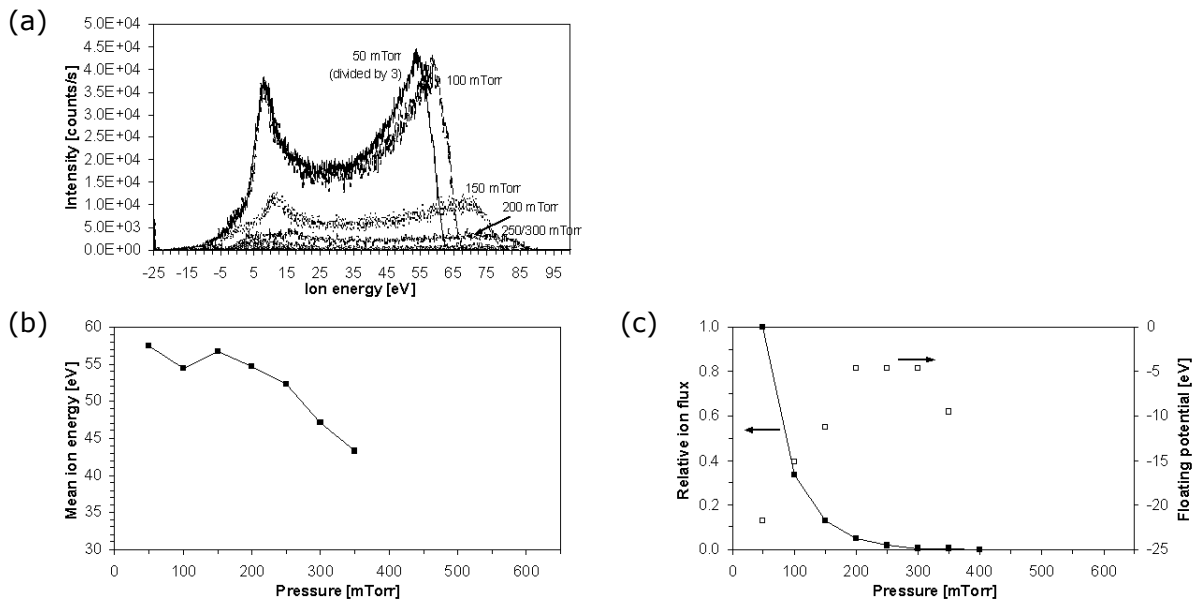


Figure 4.45: (a) $^{19}\text{F}^+$ ion distribution functions for pressure variation in 60+2 MHz dual frequency NF_3 discharges (1500+1500 W 60+2 MHz power, 200 sccm NF_3 gas flow rate, no magnetic field, silicon substrate); (b) corresponding mean ion energies; (c) relative ion flux (solid squares, logarithmic scale) and floating potentials at the extraction aperture (open squares) as determined from the position of the lowest energy peak. The IVDFs are plotted without applying corrections for the offset in the energy scale.

From rf probe measurements, the voltage increases strongly when decreasing the process pressure (Fig. G.2-a in appendix G). Conclusion on the ion energy would lead to the assumption, that ion energies should increase similarly. However, from the measured IDFs this was not found to be the case for ions incident on the reactor wall. At this point it is assumed that a nonlinear scaling can occur for the thickness and voltages of both sheaths that develop in front of the passive and active electrodes. From HPSM simulations for a pressure variation in HBr discharges, the scaling exponent that characterizes the discharge asymmetry (by relating the sheath voltage ratio to the ratio of the electrode areas) was found to decrease only slightly. Since both the sheath thickness at the ground as well as the powered electrode were found to decrease by increasing the pressure (when all other parameters are held constant) it is concluded that other discharge parameters will likely change simultaneously, until a new working point for discharge operation is reached.

When reducing the discharge pressures, the number of feed gas molecules decreases and therefore a reduction of the radical density is expected. Although both a higher ion energy (due to a higher sheath thickness at low pressures) and a reduced number of atoms

required for chemical etching can yield a compensation, the ion-assisted chemical etch rate for both silicon and SiO_2 is observed to decrease when reducing the process pressure (cf., Fig. 4.46). This is indicative for a limitation by a reduced radical density which confirms that the etch rate is chemically driven for NF_3 . The etch rates for both silicon and SiO_2 are observed to saturate in the high pressure regime which can be explained by surface reaction limitations. From the point of saturation, the etch rate could be increased further by increasing the gas flow rate, as will be shown in the next section. Tuning the two parameters pressure and gas flow can yield a maximum etch rate for a given power level. This is achieved by increasing the number of provided fluorine radicals for a chemical reaction and reducing the residence time of etch species locally hindering the etch rate to be enhanced.

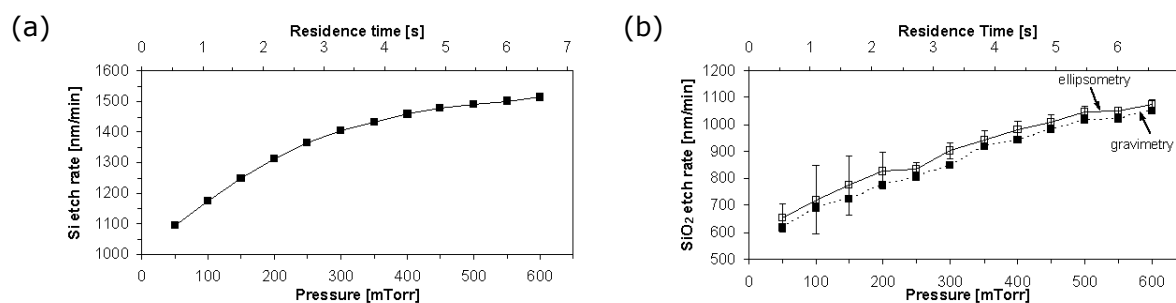


Figure 4.46: Etch rates for variation of the pressure (1500+1500 W 60+2 MHz, 300 sccm NF_3 gas flow rate, no magnetic field) for (a) silicon from gravimetry, and (b) SiO_2 from gravimetry (full squares) and 49 point ellipsometry measurements (open squares).

From 49 point ellipsometry measurements (open squares in Fig. 4.46-b), the etch rate distribution is observed to flip from a center fast etch at low pressures to an edge fast etch process at high pressures. The highest uniformity is achieved at 250 mTorr for the chosen parameters applied here. At the comparatively high etch rates observed in discharges, result from gravimetry (full squares in Fig. 4.46-b) agree very well to those obtained from ellipsometry. According to the chemically driven etch process, the selectivity increases slightly when increasing the pressure, and hence providing more fluorine radicals for chemical etching.

4.4.4 Variation of gas flow rate

60 MHz single frequency discharges

In contrast to MFCs used for HBr and Ar which allow for very high gas flow rates, variation of the NF_3 gas flow rate was limited to 200 and 400 sccm, respectively, due to the size of the installed MFC. The influence of different NF_3 gas flows in 60 MHz frequency NF_3 discharges was investigated by applying mass resolved ion energy analysis without changing pressure and 60 MHz power. From Fig. 4.47-a, recorded ion distributions for $^{19}\text{F}^+$ plasma ions were not found to be subject to changes in ion energies, as was observed for $^{36}\text{Ar}^+$ ions in argon discharges and $^{79}\text{Br}^+$ ions in HBr discharges. The F^+ mean ion energy at the passive electrode remained constant at about 27 eV for the different NF_3 gas flow rates. From Fig. 4.47-b, the floating potential did not change either by applying different gas flow rates, however the ion flux increased considerably for high NF_3 gas flow rates. As discussed for Ar and HBr, this is attributed to an increasing plasma density due to a reduction of the gas temperature. From the ratio of the time constant for ionization and

residence time in the reactor, the F^+ ion uniformity distribution can be also subject to changes when increasing the NF_3 gas flow. From an unchanged mean ion energy, temperature deviations might be small compared to changes observed for Ar and HBr (since the maximum flow rate is only about half of the argon or HBr gas flow), and compensation by other discharge parameters might contribute as well.

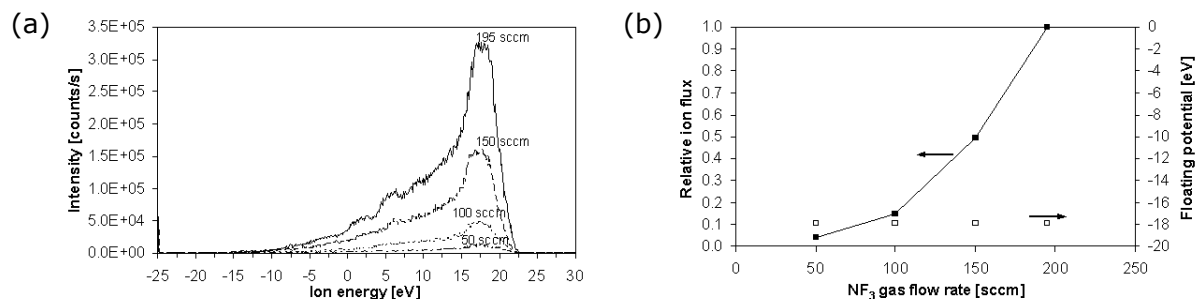


Figure 4.47: (a) $^{19}F^+$ ion distribution functions for variation of the NF_3 gas flow rate in 60 MHz frequency NF_3 discharges (1500 W, 150 mTorr, no magnetic field, silicon substrate); (b) corresponding relative ion flux (solid squares) and floating potentials at the extraction aperture (open squares) as determined from the position of the lowest energy peak. The IVDFs are plotted without applying corrections for the offset in the energy scale.

Influences of 60 MHz power and NF_3 gas flow rate on the silicon etch rate was studied as well (Fig. 4.48-a to Fig. 4.48-c). From these investigations, the following conclusions can be drawn: As described in the previous sections, the silicon etch rate is driven by the radical concentration in the gas phase. Increasing the 60 MHz source power yields a higher degree of the NF_3 dissociation and hence creation of higher amounts of free fluorine. A high NF_3 flow will probably result in a lower degree of dissociated NF_3 but also reduce the concentration of reaction products in the gas phase, as described before. A more efficient desorption and removal of etch products occurs due to a decreased residence time. The number of etch species adsorbed on the sidewall is efficiently reduced, offering a larger surface area for enhanced etching. At high 60 MHz power and NF_3 gas flow combinations, the silicon etch rate starts to saturate due to surface reaction processes becoming rate limiting.

Similar but less pronounced effects were found for SiO_2 (Fig. 4.48-d to Fig. 4.48-f). As observed for a variation of process pressure, the selectivity drops slightly for an increased residence time which is due to the silicon etch rate that changes drastically for a variation of the gas flow rate. Nonuniformities in the etch rate distribution pattern across the wafer yield high values for the standard deviation at high 60 MHz source power where a further increase is found for high gas flow rates. The hat-shaped etch rate pattern measured from 49 point ellipsometry is observed to flip when increasing the 60 MHz source power: At low source power, high etch rates occur in the center and at the wafer edge area (low etch rates inbetween both regions), whereas at high 60 MHz power low etch rates are measured in the center and at the wafer edge region (high etch rates inbetween both regions). The pattern is not noticeably influenced by the gas flow rate.

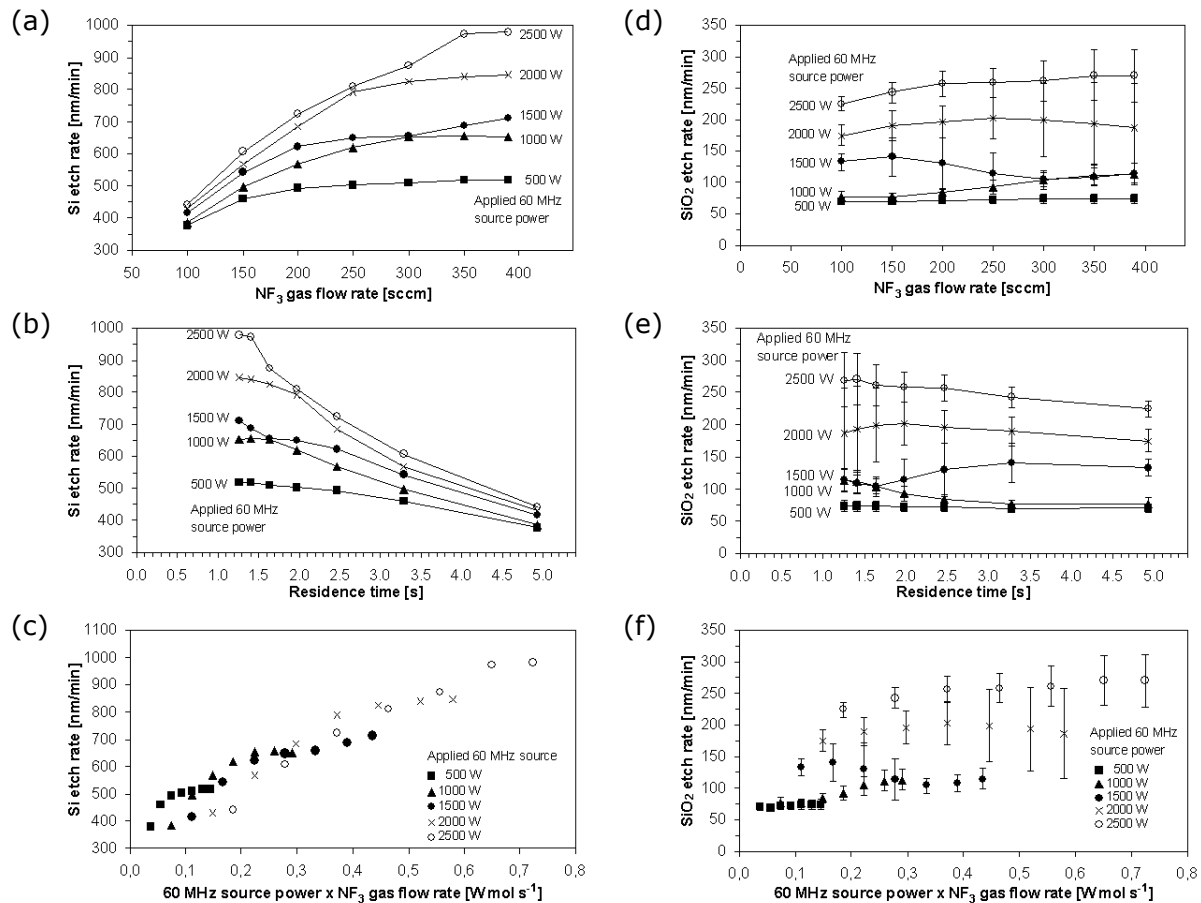


Figure 4.48: Silicon etch rates (as determined from gravimetry) for variation of the NF₃ gas flow rate and different 60 MHz powers displayed as a function of (a) gas flow rate, (b) corresponding residence time, and (c) the product of gas flow rate and source power; silicon dioxide etch rates (as determined from ellipsometry) for variation of the NF₃ gas flow rate and different 60 MHz powers displayed as a function of (d) gas flow rate, (e) corresponding residence time, and (f) the product of gas flow rate and source power (150 mTorr, no magnetic field).

60+2 MHz dual frequency discharges

The influence of different NF₃ gas flow rates in 60+2 MHz dual frequency NF₃ discharges was investigated from recorded ¹⁹F⁺ ion distributions. From Fig. 4.49-a and Fig. 4.49-b, IDF structures and ion energies are affected slightly for different NF₃ gas flow rates. The fluorine ion flux in Fig. 4.49-c was found to strongly increase for high gas flow rates, which is in agreement with findings for 60 MHz frequency NF₃ discharges. Again, this can be explained by a higher plasma density due to a reduced gas temperature and/or influences of an F⁺ ion uniformity distribution. As observed for Ar⁺ and Br⁺ ions in dual frequency Ar and HBr discharges, respectively, F⁺ ion energies rise with NF₃ gas flow rates which can not be explained by variations of the neutral gas temperature alone. As suggested for flow variations in argon and HBr, more detailed investigations should be addressed in future analysis.

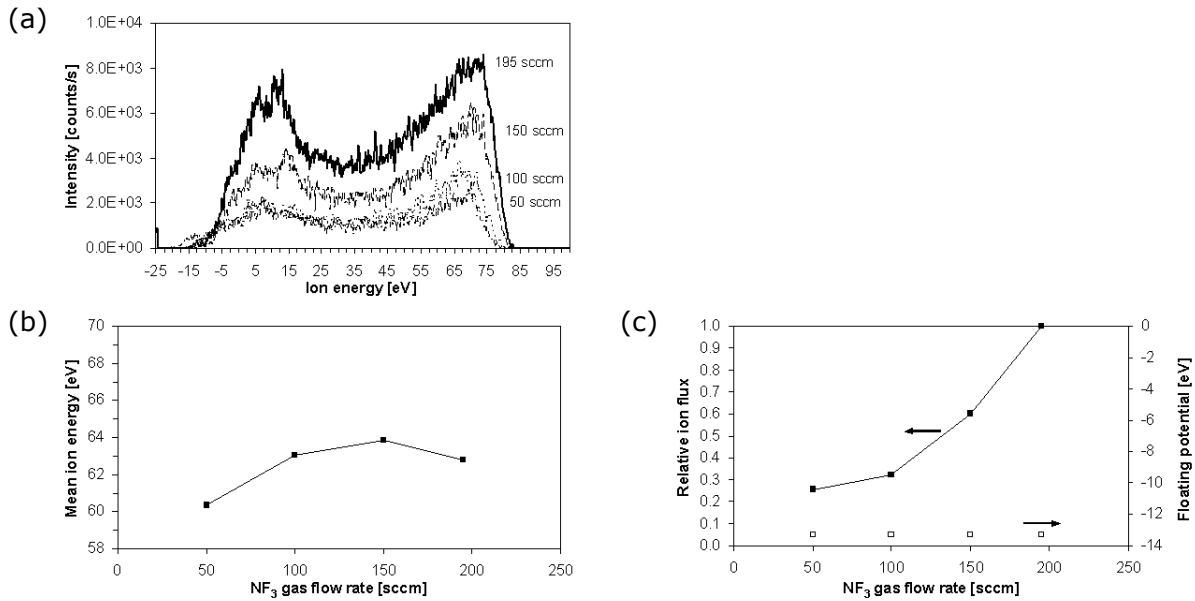


Figure 4.49: (a) $^{19}\text{F}^+$ ion distribution functions for variation of the NF_3 gas flow rate in 60+2 MHz dual frequency NF_3 discharges (1500+1500 W 60+2 MHz power, 150 mTorr, no magnetic field, silicon substrate); (b) corresponding mean ion energies; (c) relative ion flux (solid squares) and floating potentials at the extraction aperture (open squares) as determined from the position of the lowest energy peak. The IVDFs are plotted without applying corrections for the offset in the energy scale.

4.4.5 Variation of magnetic field

60 MHz single frequency discharges

IDF measurements for $^{19}\text{F}^+$ ions were conducted for stationary magnetic fields up to 140 G for constant 60 MHz power (1500 W) and discharge pressure (150 mTorr). Measured F^+ ion distributions look similar to those already discussed for typical discharge settings applied before (Fig. G.4-a to Fig. G.4-e in appendix G) where secondary peak structures from charge exchange collisions in the sheath can be even more pronounced under certain conditions (cf., Fig. G.4-d). For some situations, distributions are distorted further which can be due to a strongly nonuniform plasma density distribution causing a locally varying sheath thickness and/or influence sheath oscillations. Furthermore, distortions of the measured IDFs could also result from the magnetic field affecting trajectories of sampled ions. Corresponding mean ion energies (calculated by averaging over the four distributions for each of the different magnetic fields settings) decrease from about 31 eV without magnetic field to about 21 eV for 140 G (Fig. G.4-f). The corresponding F^+ ion flux illustrated in Fig. G.4-g is found to develop non-monotonically where maximum values are found for discharge conditions without magnetic field, and further at 110 G. As discussed earlier, experimental conditions may not be representative for discharge dynamics that occur during constant rotation of the applied magnetic field, although the applied rotation frequency of 0.25 Hz may still be considered quasistationary. Also, mass resolved ion energy analysis appears to require further modifications to the measurement setup to allow for more meaningful studies when magnetic fields are present.

60+2 MHz dual frequency discharges

The influence of magnetic fields on 60+2 MHz dual frequency NF_3 discharges was investigated for 150 mTorr constant pressure, and 1500+1500 W 60+2 MHz power.

Experiments include IDF measurements for F^+ plasma ions for stationary magnetic fields, as well as rf probe an etch rate measurement for slowly rotating magnetic fields. IDF analysis comprises variation of magnetic fields up to 80 G, since the discharge could not be stabilized for magnetic flux densities exceeding 80 G. In Fig. G.5-a to Fig. G.5-c, ion distribution functions for $^{19}F^+$ ions are plotted for the different magnetic fields configurations as indicated in Fig. G.5-a. Floating potentials at the surface of the MACOR orifice plate are found to vary between -5 eV and -18 eV, as is illustrated in Fig. G.5-e. Distortions of the typical saddle-shaped IDFs for F^+ ions appear at high magnetic fields. This again indicates local distortions of the sheath dynamics, and trajectories of sampled fluorine ions might be affected as well. Increasing the magnetic field leads also to an increased broadening of the double peak structure. Calculation of mean ion energies after transformation of corrected IDFs to the corresponding IEDFs results in an increase from about 55 eV without magnetic field to 88 eV for 80 G (cf., Fig. G.5-d). This increase in the ion energy is in contrast to the findings for NF_3 single frequency operation, but resembles to findings for application of magnetic fields in 60+2 MHz HBr discharges. Possible root causes were discussed before, the complex sheath dynamics for dual frequency operation can be severely distorted from the strongly nonuniform magnetic field distribution. The averaged F^+ ion flux plotted in Fig. G.5-e does not change much at low magnetic fields and is subject to a sudden increase at 80 G. This might be caused from an increasingly unstable discharge.

Experiments to investigate the influence of magnetic fields on silicon and SiO_2 etch rates were conducted by applying a 0.25 Hz sinusoidal voltage to the magnet coils. While increasing the magnetic flux density, rf probe voltages strongly decrease when using silicon substrate, whereas only slight changes are observed for substrates with a 2 μm thick SiO_2 surface layer (cf., Fig. G.3-a). However, changes of the measured voltage are observed to be smaller than those observed for the power variation conducted in 60+2 MHz NF_3 discharges. From rf voltage measurements, an onset of saturation is indicated at about 100 G when using bare silicon substrates, and around 40 G when silicon substrates with a thick SiO_2 top layer were used. For the latter case, scaling of the rf voltage is found to agree pretty well to the scaling of sheath parameters from HPSM calculations for 60 MHz HBr discharges (cf., Fig. D.5-a and Fig. D.5-e in appendix D). As discussed above, measured ion energies are not found to decrease according to the decline of measured rf voltages. Similar to results from variation of the magnetic field in 60+2 MHz HBr discharges, mean ion energies calculated from measured IDFs appear again roughly comparable to results from HPSM simulations for HBr (Fig. D.5-k) with regards to absolute values. Scaling of ion energies might change when applying rotating magnetic fields, and ion energies are expected to decrease according to the decline observed for the measured rf voltage. For an increasing magnetic field, the plasma density is expected to increase as well to some extent which is supported from increasing currents (Fig. G.3-b). From Fig. 4.50, silicon and SiO_2 etch rates are found to increase up to 50 G which could be explained by an enhanced dissociation from an enhanced interaction path of electrons with the background neutral gas. Further, an increasing ion flux will also contribute to some extent to the etch rates. Consequences for the influence of an additional magnetic field supports the role of chemical reactions during etching silicon and silicon dioxide in NF_3 discharges. At higher magnetic fields silicon and SiO_2 etch rates finally saturate, resulting in an essentially constant selectivity for the SiO_2 hard mask. High standard deviations of the oxide etch rate are caused by a highly nonuniform etch rate pattern, as determined from ellipsometry (open

squares in Fig. 4.50-b). Low etch rates are observed at the wafer extreme edge region where a high gradient occurs towards high etch rates measured in the wafer center. Further, the etch rate at the wafer edge region remains unchanged from the magnetic field, whereas the center etch rate increases when increasing the magnetic field.

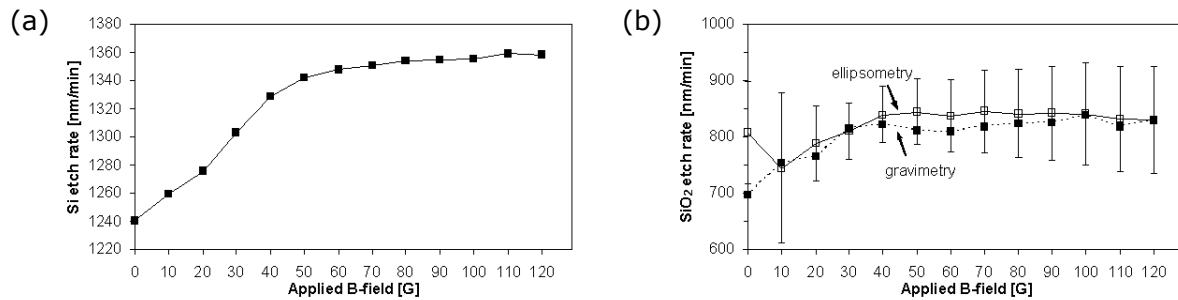


Figure 4.50: Etch rates for variation of the magnetic field (1500+1500 W 60+2 MHz, 150 mTorr, 300 sccm NF₃ gas flow rate) for (a) silicon from gravimetry, and (b) SiO₂ from gravimetry (full squares) and 49 point ellipsometry measurements (open squares).

4.4.6 Summary

As was discussed for argon and HBr, the concept of separate control of ion energy and ion flux by the dual frequency operation is generally valid also in NF₃ discharges. Besides ion fluxes, the 60 MHz frequency mainly determines formation of radicals from a very effective dissociation of the NF₃ molecular feed gas. Fluorine plasma ions were usually monitored since they are most relevant determining the etch process. From the IDFs of comparably low mass fluorine plasma ions, high frequency oscillations could not be resolved and ion distributions are mainly controlled by the dynamics of the low frequency component. F⁺ ions were generally found to exhibit highest energies from the influence of both 60 MHz and 2 MHz frequency, being comparable to or even exceeding those observed for species from corresponding HBr discharges. This is likely due to a wide sheath thickness as a result of a low electron density for the highly electronegative NF₃ discharges. Due to a generally high probability of elastic scattering for ions in the sheath caused by high radical densities, mean ion energies determined by the 2 MHz frequency are hardly reduced from additional 60 MHz application in 60+2 MHz discharges.

From studies of the NF₃ feed gas dissociation it was found that undissociated NF₃ molecules comprise less than half of the gas in the plasma reactor where NF₃ appears completely dissociated for 60 MHz power levels of 2.5 kW and above. For high 60 MHz power, deeper NF₃ dissociation can occur yielding higher concentrations of free fluorine. From mass spectra for NF₃ discharges, SiF_x species (SiF⁺, SiF₂⁺, SiF₃⁺, SiF₄⁺) indicate the main etch products which are created through chemical reactions at the substrate surface involving fluorine radicals. Application of APMS reveals that SiF_x⁺ (x=1...3) products are formed through dissociative ionization of SiF₄ molecules inside the ionizer of the EQP. Hence, the etch process can be characterized by the reaction



forming highly volatile SiF₄ etch products. Final SiF₄ etch products are very stable - from maximum dissociation of about 16% and 20% at the highest 60 MHz power level applied in this work, contribution to silicon and SiO₂ etch rates remains comparably low.

Both silicon and SiO₂ etch rates were found to substantially increase when rising 60 MHz and 2 MHz power, where a saturation is indicated at high 2 MHz power levels. Etch rates

can be increased further by 60 MHz power through an enhanced dissociation of NF_3 , hence creating higher fluorine radical densities and increasing ion fluxes. Ion-assisted chemical etch rates for both silicon and SiO_2 decreased when reducing the discharge pressure which indicates a limitation due to reduced radical densities. Obviously, increasing ion energies can not compensate for the reduced radical density at low pressures. In the high pressure regime, silicon and SiO_2 etch rates finally saturate due to surface reactions becoming rate-limiting. From the point of saturation, the etch rate could be increased further by increasing the NF_3 gas flow rate. Tuning the two parameters pressure and gas flow can yield a maximum etch rate for a given power level. This is achieved by increasing the fluorine radical density as well as reducing the residence time of etch products locally hindering the etch process to proceed. The number of etch species adsorbed on the sidewall is efficiently reduced, offering a larger surface area for enhanced etching. At high NF_3 feed gas flows, etch rates can start to saturate again due to surface reaction processes becoming rate limiting. Silicon and SiO_2 etch rates were found to increase slightly when medium magnetic fields were applied. This is again due to an enhanced dissociation from enhanced electron-neutral interactions with further support by an increased ion flux. The influence of additional magnetic fields supports the role of chemical reactions during etching silicon and silicon dioxide in NF_3 discharges. Investigations of NF_3 discharges confirm chemical etching of silicon and SiO_2 with fluorine occurs spontaneously [110], where etch rates can be strongly enhanced through the impact of ion bombardment energy and ion flux.

From a pronounced chemical etching of silicon and SiO_2 , changes in the Si-to- SiO_2 selectivity are primarily caused by a different scaling of the chemical etch component for both materials. The highest selectivity remains below 8:1 at minimum 60 MHz power from all discharge settings investigated here. From addition of 2 MHz power, the selectivity can drop even below 2:1. From investigated discharge parameters, the selectivity is generally decreased by (1) increasing 60 MHz power through a higher feed gas dissociation as well as higher ion fluxes to the substrate, (2) increasing 2 MHz power through a strong support by the ion energy, (3) increasing the discharge pressure through creating more fluorine radicals at higher NF_3 concentrations, and (4) reducing the NF_3 feed gas flow due to a more efficient dissociation for high residence times of the feedgas molecules. From predominantly low selectivities of 1:1-2:1 for most of the parameter settings investigated here, chemical etching of silicon and SiO_2 appears quite unselective (cf., Fig. 4.51). From high etch rates in NF_3 discharges (up to $1.5 \mu\text{m}/\text{min}$ for silicon and $1.0 \mu\text{m}/\text{min}$ for SiO_2), high etch product concentrations are typically created. Here, SiF_4 etch products comprise up to several ten percent of the total discharge pressure, and hence efficiently reduce the partial pressure of the feed gas components.

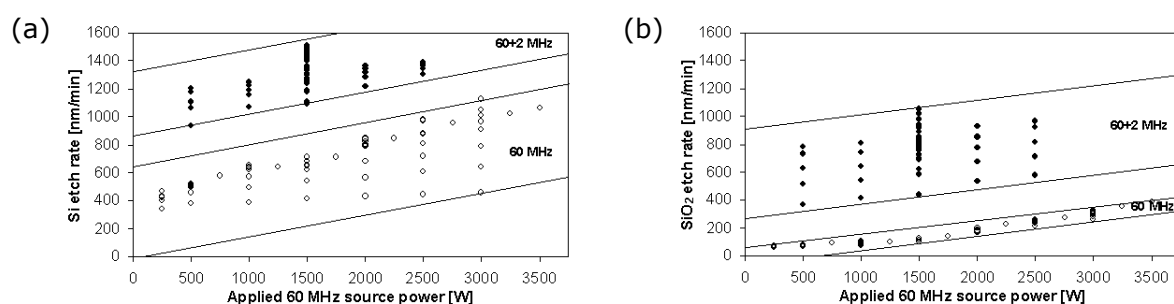


Figure 4.51: Etch rates collected from all nitrogen trifluoride discharge experiments discussed in this chapter and plotted as a function of 60 MHz source power (a) for silicon; (b) for silicon dioxide.

From a quantitative assessment of SiF_4 etch product concentrations, mean neutral gas temperatures arising during discharge operation could be approximated. For the range of 60 MHz power levels investigated here, the gas temperature was found to rise from 70°C reactor temperature to about 1000°C. This indicates that concentrations of discharge species will be further reduced due to the discharge pressure remaining constant. From comparison to HPSM simulations (Fig. C.3-j in appendix C and Fig. D.3-k in appendix D) this could further explain rising mean ion energies that are observed when increasing the 60 MHz power level (cf., Fig. 4.39-b).

IDFs for F^+ were strongly influenced by resonant charge exchange collisions which resulted in secondary peak structures in the low energy tail of measured ion distributions. The distinct occurrence of the secondary peak structures was explained by a dominating fraction of resonant collisions between fluorine ions and the high number of fluorine radicals created from the extensive dissociation of NF_3 . Since the number of peaks corresponds to the ratio of ion transit time and rf period, F^+ ions were observed to take about 6 rf cycles to cross the sheath in 60 MHz NF_3 discharges. From the number of charge exchange peaks, the average sheath thickness at the ground electrode exceeds about 600 μm for the 60 MHz modulated collisional sheath conditions investigated here.

After standard NF_3 plasma reactor cleans, quite significant amounts of adsorbed fluorine and stable SiF_4 product molecules still remain in the reactor since the yttria hard anodized surfaces of the reactor walls exhibit a relatively high porosity. Fluorine species remain adsorbed at the surfaces inside the reactor. During application of subsequent discharges, fluorine can become released from the reactor surfaces through ion bombardment and chemical activation during discharge operation. A highly efficient removal of fluorine was found during HBr discharge operation through formation of HF [258]. Since generally high F^+ ion energies were recorded at the reactor wall, this indicates that erosion of reactor surfaces through ion bombardment is also high in NF_3 discharges.

4.5 HBr/ NF_3 mixtures

Expanding the basic knowledge obtained from pure HBr and NF_3 chemistries, contribution of bromine and fluorine during reactive ion etching as well as interactions in HBr/ NF_3 mixed discharges are investigated in this section. Limitations of etch processes are analyzed in more detail and a simple etch model is discussed. The impact of fluorine additions to HBr on etch selectivities is studied further since a high degree of anisotropy has to be maintained and consumption of the SiO_2 hard mask must be minimized for etching HAR 3D structures, besides generally desired high silicon etch rates. For application of mass resolved ion energy analysis, $^{19}\text{F}^+$ and $^{79}\text{Br}^+$ ions were chosen to study the plasma and sheath behavior for HBr/ NF_3 mixed discharges examined in this work.

4.5.1 Neutral mass spectra

In Fig. 4.52-a, a typical mass spectrum is shown that is observed for 85.5% HBr/9.5% NF_3 /5.0% Ar mixed chemistries from the reactor when the discharge is off. As expected, the spectrum is found to be a superposition of the mass spectra observed for pure HBr (cf., Fig. 4.22-a) and NF_3 (cf., Fig. 4.37-a), also taking into account the HBr/ NF_3 ratio investigated here. The Ar^+ peak results from small additions of argon feed gas. The mass spectrum for the situation where the discharge is turned on is shown in Fig. 4.52-b.

The recorded spectrum exhibits a reduction in the relative intensities of ions derived from HBr, such as HBr^+ and Br^+ , and NF_3 , such as NF_3^+ , NF_2^+ , and NF^+ and the appearance of ions such as H_2^+ , N_2^+ , and Br_2^+ that are associated with discharge-generated decomposition and product species like HF, H_2 , N_2 , and Br_2 . The various peaks observed further are attributed to the formation of different silicon etch products containing bromine (SiBr^+ , SiBr_2^+ , SiBr_3^+ , SiBr_4^+), fluorine (SiF^+ , SiF_2^+ , SiHF_2^+ , SiF_3^+ , SiF_4^+), and both bromine and fluorine (SiBrF^+ , SiBrF_2^+ , SiBrF_3^+ , SiBr_2F^+ , $\text{SiBr}_2\text{F}_2^+$, SiBr_3F^+). These species are associated with etch products like SiBr_4 , SiBr_3F , SiBr_2F_2 , SiBrF_3 , and SiF_4 formed through chemical reactions during etching at the surface of silicon substrates. Etching of the quartz ring and silicon deposits inside the reactor yield minor contributions to SiF_4 products. The mass peak at $m/q = 28$ u is attributed to N_2^+ and further includes significant contributions of Si^+ , where N_2^+ molecules result from dissociation of the NF_3 feed gas, and Si^+ is formed through dissociative ionization of silicon etch products.

Fig. 4.52-c shows the difference mass spectrum as obtained after subtracting the mass spectra from Fig. 4.52-b and Fig. 4.52-a for the same mass-spectrometer settings. Basically, all HBr and NF_3 feed gas components are reduced due to a discharge-generated decomposition in the plasma, and etch product species yield considerable concentrations in the discharge.

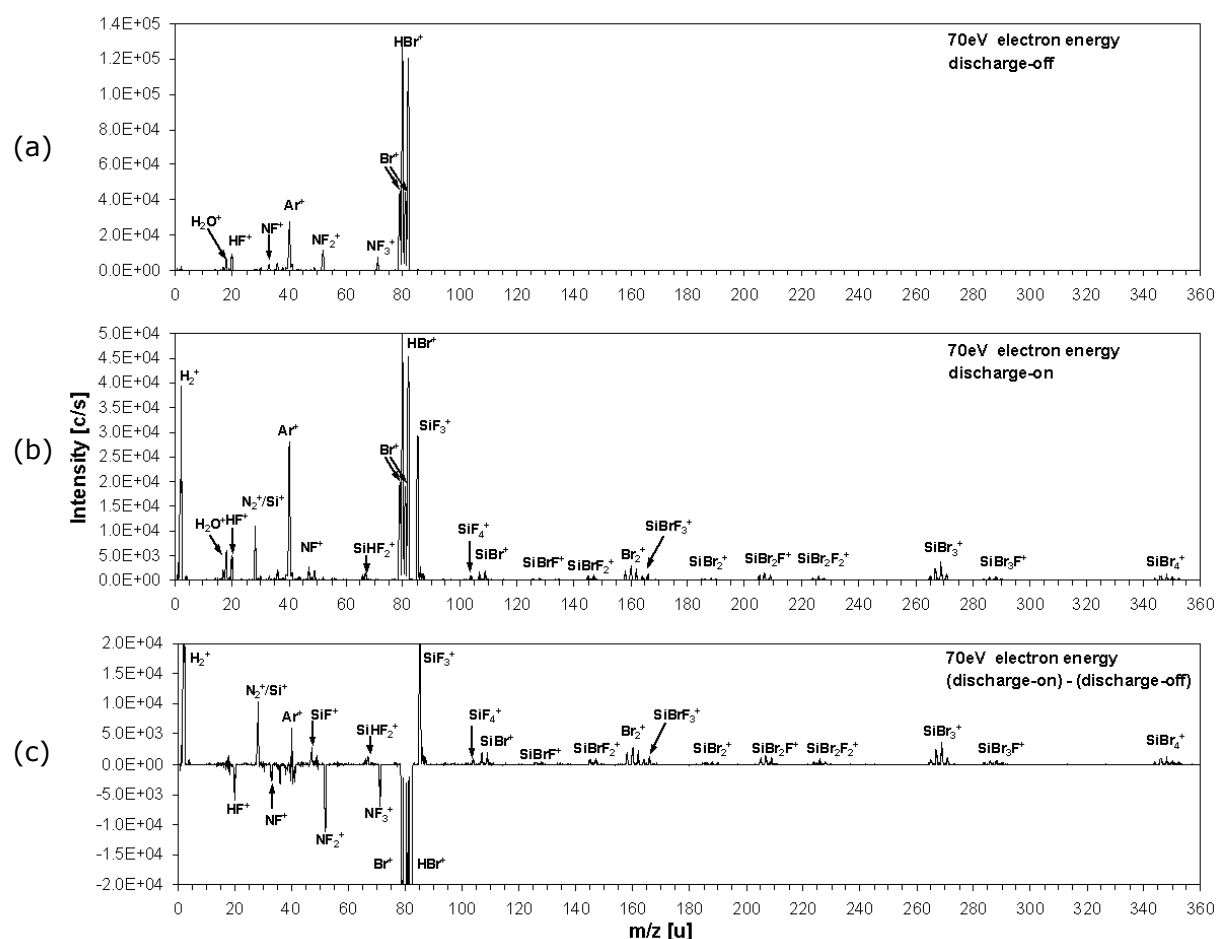


Figure 4.52: Mass spectrum of neutral species ionized by 70 eV electrons for (a) HBr/NF₃ (+Ar) gas mixture sampled from the reactor without discharge; (b) HBr/NF₃ (+Ar) gas mixture sampled from the reactor with rf discharge (150 mTorr, 1500+1500 W 60+2 MHz power, 270 sccm HBr + 30 sccm NF₃ + 16 sccm Ar gas flow rate, silicon substrate); (c) difference of mass spectra b-a (negative values indicate a loss when the discharge is on).

4.5.2 Variation of power

60 MHz single frequency discharges

Ion distribution functions were measured for $^{19}\text{F}^+$ and $^{79}\text{Br}^+$ plasma ions sampled from 60 MHz frequency discharges of HBr/NF₃ mixed chemistries at constant pressure, 60 MHz power and total gas flow rates, as depicted in Fig. 4.53-a and Fig. 4.53-b. Variation of the HBr/NF₃ feed gas mixture was performed by changing the NF₃ content as indicated by the labeling, where 0% NF₃ content indicates pure HBr discharges, and 100% NF₃ indicates pure NF₃ discharges. To allow for better illustration, IDFs for different halogen mixed chemistries are shown in two separate plots for ranges of 0-50% and 60-100% NF₃ content in HBr/NF₃. Ion distributions are plotted after applying corrections for the energy scale offset from the floating potential at the sampling aperture (cf., open circles in Fig. 4.53-c). F^+ and Br^+ mean ion energies are plotted in Fig. 4.53-c as well, F^+ and Br^+ ion fluxes are illustrated in Fig. 4.53-d. Surprisingly, $^{19}\text{F}^+$ ions are also observed in pure HBr discharges where no NF₃ was added, initially yielding the highest $^{19}\text{F}^+$ ion flux to the reactor wall for all mixtures investigated (indicated by full triangles in Fig. 4.53-d). The ion flux was found to even exceed that measured from pure NF₃ discharges. The measurement was found to be reproducible and can be explained by conditioning effects from previous NF₃ plasma cleaning: As was observed from application of standard mass spectrometry also, after standard NF₃ plasma reactor cleans quite significant amounts of fluorine still remain in the reactor. This can be visualized by the reactor walls acting like a sponge for the different molecule species, since the yttria hard anodized surfaces exhibit a relatively high porosity. Fluorine species remain adsorbed at the surfaces inside the reactor. During application of subsequent discharges, fluorine can be reactivated and desorb from the reactor walls. For the known reactor wall surface area, contribution of desorbed fluorine can be estimated as follows. Assuming a complete desorption of a one monolayer thick fluorine film from the wall surface within one minute yields a fluorine gas flow of about 1 sccm. Since it is known that typical Al₂O₃ and Y₂O₃ anodized reactor surfaces exhibit a quite high porosity, the assumption of an area enhancement factor for a fluorine coverage of about 100 to 1000 appears reasonable. Depending on the NF₃ cleaning regime and time, this would enable adsorption of a 100 to 1000 monolayer thick fluorine film on the porous yttria surface in the current setup. From this assumption, an average fluorine gas flow of about 20 to 200 sccm could occur during a typical outgassing process (for the reactor setup, the F signal decreases in a 5-8 min timeframe exponentially by about 3-4 orders of magnitude after a typical NF₃ reactor clean [258]). Due to the exponential decrease, the gas flow rate is expected to be even higher during the first minute (recording IDFs takes only few seconds which allows for investigation of several different HBr/NF₃ mixtures within only a few minutes). From further investigations it can be shown that the discussed artefact from a reactor wall conditioning is real: The experiment was extended by starting from a pure HBr discharge after a standard NF₃ plasma clean procedure and first ramping up the NF₃ content. After recording IDFs in a pure NF₃ discharge, the NF₃ content was finally ramped down again. Structures of recorded IDFs for F^+ and Br^+ plasma ions are generally reproducible during both the NF₃ ramp-up and ramp-down phase where changes in the recorded intensities become obvious for certain conditions. Ion fluxes extracted from the IDFs are plotted in Fig. 4.53-d, where the NF₃ ramp-up phase is indicated by full symbols connected with a full line, and the NF₃ ramp-down phase is plotted with open symbols and a broken line for F^+ plasma ions (triangles) and Br^+ ions (squares). As can be seen from

this plot, the F⁺ ion flux dominates in pure HBr discharges only during the ramp-up phase directly after the standard NF₃ clean, and becomes suppressed for the repeated experiment at the end of the NF₃ ramp-down. This observation leads to the following simple model: The reactor wall is completely loaded with fluorine right after the NF₃ reactor clean. During the HBr discharge operation, fluorine desorbs from the surrounding walls with a comparably high rate that decreases exponentially, as described above. Addition of low NF₃ contents initially results in a reduced fluorine desorption rate, until an equilibrium for adsorption and desorption is reached at about 40% NF₃. Increasing the NF₃ content further yields again to an effective loading of the reactor walls with fluorine since the adsorption rate now exceeds the desorption rate. For 100% NF₃, the fluorine loading at the reactor walls appears to saturate which yields a higher number of fluorine radicals in the plasma. During the subsequent NF₃ ramp-down, the fluorine ion flux is about comparable with results during the ramp-up down to 40% NF₃. When further reducing NF₃ admixtures, the F⁺ ion flux starts to rise again which could be explained by an increasing contribution of bromine to the etch process. The substrate surface starts to become passivated by less volatile SiBr₄ products, and hence less fluorine radicals are consumed (cf., section 4.5.6). Since bromine rich SiBr₃F and SiBr₂F₂ product molecules are easier to dissociate than SiF₄ molecules, the increasing contribution of such molecules could be another source of fluorine. Reducing the NF₃ content below 20% finally results in an expected strong suppression of F⁺ ions. This can be explained by an essentially lower loading of the reactor walls with fluorine during the experiment which appears reasonable for the duration (below 5 min) and conduction of the experimental investigations (compared to the experiment with 100% HBr during the ramp-up phase immediately after the NF₃ reactor clean, less than one order of magnitude lower fluorine concentration is assumed for the repeated experiment with 100% HBr during the NF₃ ramp-down phase). Besides the influence of a fluorine desorption from the reactor walls, hydrogen formed through dissociation of HBr may contribute to considerable extents to a loss channel of fluorine radicals through



by creating stable HF molecules that do not participate in etch processes further. Formation of HF is supported from earlier investigations applying mass spectrometry [258], and might support the strongly increased F⁺ ion flux when HBr feed gas is no longer supplied to the discharge (cf., Fig. 4.53-d).

With respect to the results for the Br⁺ ion flux, similar phenomena involving a loading of the reactor walls with bromine are expected to occur in parallel. As noticed for the presence of F⁺ in pure HBr discharges, Br⁺ ions are still present in subsequently run pure NF₃ discharges, although in comparably lower amounts as was observed for F⁺ ions in the vice versa case (due to a less pronounced reactor wall coverage with bromine during the experiment). From this discussion it became obvious, that suppression of conditioning artefacts in HBr/NF₃ mixed discharges can be achieved from choosing appropriate experimental conditions. To minimize the influence of outgassing from the reactor walls, IDFs for F⁺ (Br⁺) plasma ions plotted in Fig. 4.53-a (Fig. 4.53-b) where chosen from the NF₃ ramp-down (NF₃ ramp-up) experiments, respectively. At this point, a different contribution from elastic scattering in the F⁺ and Br⁺ IDFs for the different gas mixtures remains unexplained. A precise analysis about changes of the discharge parameters for the different HBr/NF₃ mixture would be required to finally enable detailed investigation about the impact on IDFs with the HPSM simulator. As can be seen from the evolvement of F⁺

IDFs in Fig. 4.53-a, collisions in the sheath start to significantly contribute to the distributions when the NF_3 content exceeds 50%. Since mean ion energies rise continuously for above 70% NF_3 admixtures, the sheath width in NF_3 dominated discharges appears to be thicker compared to HBr dominated HBr/NF_3 mixtures. This is consistent with results for pure HBr and NF_3 discharges discussed in previous sections. From Fig. 4.53-c, Br^+ ion energies appear typically lower than F^+ ion energies which might be attributed to bromine ions experiencing more collisions, and/or the higher mass for bromine (compared to fluorine) which due to a higher inertia will gain less kinetic energy while traversing the sheath.

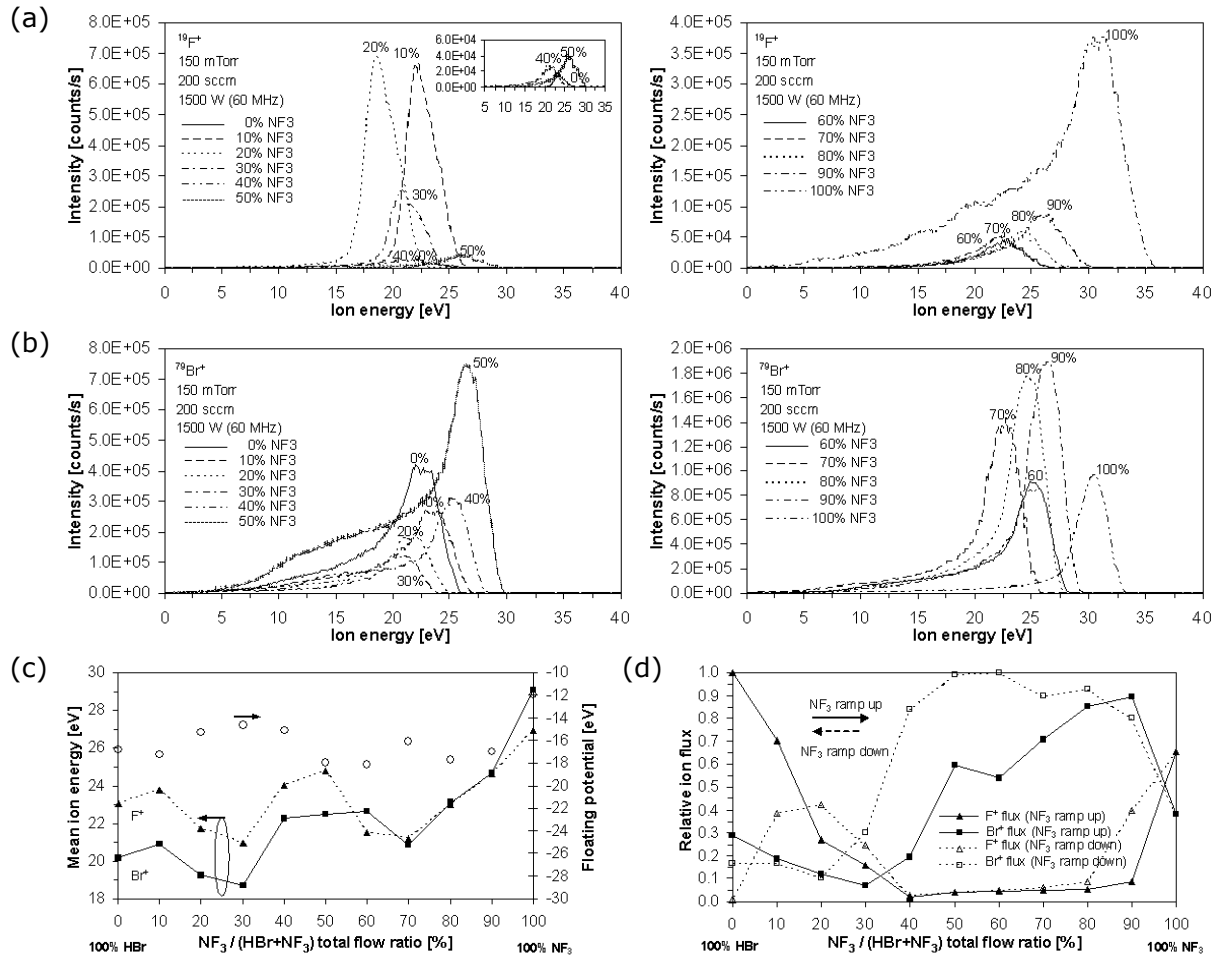


Figure 4.53: (a) $^{19}\text{F}^+$ and (b) $^{79}\text{Br}^+$ ion distribution functions measured in 60 MHz frequency HBr/NF_3 mixed discharges for different admixtures of NF_3 (1500 W, 150 mTorr, 200 sccm HBr/NF_3 total gas flow rate, no magnetic field, silicon substrate); (c) corresponding mean ion energies; (d) relative ion fluxes (solid symbols) and floating potentials at the extraction aperture (open symbols) as determined from the position of the lowest energy peak. The IVDFs have already been corrected for the offset in the energy scale.

In contrast to other experiments discussed in this work, the experiment conducted here was influenced much stronger by a fluorine desorption since recording of the IDFs takes only a few seconds which explains the high fluorine intensity immediately after an NF_3 plasma clean. As the effect of an outgassing can become severe and influence sensitive etch processes, reactor wall conditioning effects are generally subject of intense investigations and discussions in literature [284,285]. For other experiments conducted in this work it was however ensured that results were not influenced by such parasitic effects.

For investigations in HBr discharges, the silicon etch rate does not change much below 50% NF₃ admixtures - unlike the SiO₂ etch rate that is more sensitive above 20% NF₃ contents (for the worst case, one could therefore expect a slightly reduced selectivity from pronounced contribution of fluorine outgassing). From a comparison between the influence of NF₃ gas flow rates on the silicon etch rate in 60 MHz discharges (cf., Fig. 4.50), the silicon etch rate in HBr does not appear to be dominated by a fluorine contamination (Fig. 4.24). Finally, no major deviations were observed between etch rates in HBr from experiments conducted after NF₃ reactor clean and repeated experiments without additional cleaning (conditioning).

Etch rates for silicon and silicon dioxide obtained from 60 MHz frequency discharges for different HBr/NF₃ chemistries are included in Fig. 4.55-a and Fig. 4.56-a, as indicated by solid symbols. Silicon etch rates are found to rise according to a power law when increasing the NF₃ content. For NF₃ contents exceeding 30%, slopes of the increasing etch rates appear to be steepest and also become more linear for higher 60 MHz power levels. Interestingly, a maximum etch rate is not found for pure NF₃ discharges, as initially would be thought from the previous investigations. Instead, the etch rate for pure NF₃ drops clearly below the maximum which is found for 10%HBr/90%NF₃ mixed chemistries. From F⁺ and Br⁺ ion energies plotted in Fig. 4.53-c, the etch rate does not appear limited by the ion energy but rather influenced by the total ion flux and/or the chemical component. Compared to NF₃, HBr is considerably less electronegative which would allow for a higher electron density in 10%HBr/90%NF₃ chemistries as compared to pure NF₃ discharges. A higher electron density allows for higher dissociation of the feed gas chemistry, where a higher NF₃ dissociation in turn could lead to higher concentrations of fluorine radicals provided to the etch process. From previous discussions it has become clear that chemical etching is strongly supported by the (total) ion flux. From high Br⁺ ion fluxes recorded for low HBr contents in HBr/NF₃ gas mixtures (cf., Fig. 4.53-d), maximum silicon etch rates discussed here are believed to mainly result from an efficient contribution of a high Br⁺ ion flux to the fluorine dominated chemical etching.

SiO₂ etch rates plotted in Fig. 4.56-a (solid symbols) are found to increase more noticeably above 20% NF₃ admixtures in 60 MHz HBr discharges. Whereas etch rates appear to saturate in fluorine dominated chemistries for 1500 W applied 60 MHz power levels, SiO₂ etch rates are virtually rising linearly for 500 W and 2500 W 60 MHz power. This supports both chemical etching and physical contribution determined by the amount of halogen atoms (in particular fluorine) from the feed gas dissociation, as well as ion fluxes to the substrate surface. As discussed for NF₃ discharges, the delivery of radicals might change within certain ranges of 60 MHz power, where a deeper NF₃ dissociation can occur at higher input power yielding higher concentrations of free fluorine (cf., section 4.4.2). Moreover, chemical reactions at the substrate surface are influenced as well by the amount of dissociation products that can both support and also suppress the corresponding etch rate by surface passivation effects (discussed in more detail in section 4.5.6). From the influence of different discharge as well as substrate surface conditions it becomes clear, that scaling of the etch rate is usually nonlinear and can become quite complex. Selectivities from Si and SiO₂ etch rates are plotted in Fig. 4.57-a, as indicated by solid symbols. From what was observed for HBr and NF₃ discharges so far it is confirmed that pure HBr discharges exhibit highest selectivities (in the order of up to - or even exceeding - 50:1) when no significant ion energy is involved. Minimum selectivities ranging between

5:1 and 10:1 for the parameter set investigated here are found for 30-50% NF_3 content, as well as for pure NF_3 chemistries.

60+2 MHz dual frequency discharges

For 60+2 MHz frequency discharges of different HBr/NF_3 mixed chemistries, ion distribution functions were measured again for $^{19}\text{F}^+$ and $^{79}\text{Br}^+$ ions from the plasma while maintaining constant power levels, pressure and total gas flow rates. Distributions plotted in Fig. 4.54-a and Fig. 4.54-b have already been corrected for the offset energy axis from the floating potential at the sampling aperture. Corresponding mean ion energies are plotted in Fig. 4.54-c, measured ion fluxes and floating potentials are drawn in Fig. 4.54-d.

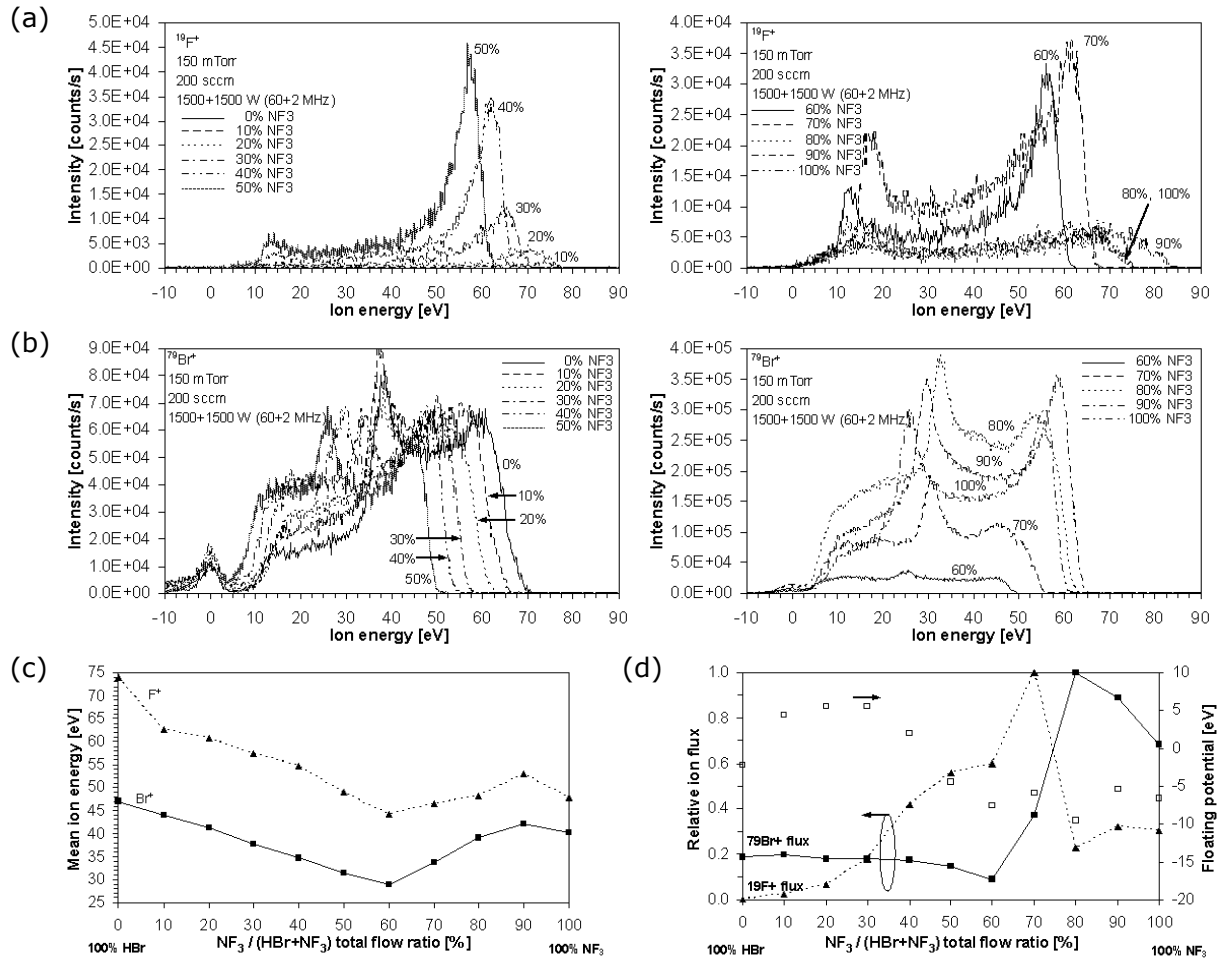


Figure 4.54: (a) $^{19}\text{F}^+$ and (b) $^{79}\text{Br}^+$ ion distribution functions measured in 60+2 MHz dual frequency HBr/NF_3 mixed discharges for different admixtures of NF_3 (1500+1500 W 60+2 MHz power, 150 mTorr, 200 sccm HBr/NF_3 total gas flow rate, no magnetic field, silicon substrate); (c) corresponding mean ion energies; (d) relative ion fluxes (solid symbols) and floating potentials at the extraction aperture (open symbols) as determined from the position of the lowest energy peak. The IVDFs have already been corrected for the offset in the energy scale.

From Fig. 4.54-c, mean ion energies for F^+ are considerably higher than those for Br^+ ions. Again, this appears to be mainly due to bromine ions experiencing more collisions in the sheath, as concluded from comparison of the low energy part of the distributions. According to the discussion for 60 MHz HBr/NF_3 discharges, care was taken to minimize the influence of contributions from chamber wall outgassing when recording the IDFs. However, IDFs were generally not subject of major changes as was observed for 60 MHz

single frequency discharges. Increasing the NF₃ content in HBr up to 60% causes a reduction of the F⁺ and Br⁺ mean ion energy (Fig. 4.54-c) which reflects the shift of IDFs for both ion species towards lower energies (cf., Fig. 4.54-a and Fig. 4.54-b). Further increasing the NF₃ content yields again an increase of ion energies as a result of IDFs shifting and/or extending again towards higher energies. Whereas from F⁺ ion distributions contribution of sheath collisions are low, sheath collisions highly contribute to the IDF structure for bromine ions which results in a pronounced low energy part in the Br⁺ IDFs. Both F⁺ and Br⁺ ion fluxes are at a maximum at high NF₃ contents. Whereas the F⁺ ion fluxes rises continuously, the Br⁺ ion flux is subject to a more sudden increase after remaining initially nearly constant. The considerable drop of the F⁺ ion flux for NF₃ admixtures exceeding 70% in HBr is in further contrast to results for 60 MHz single frequency discharges.

From rf probe measurements in Fig. H.1 (in appendix H), both rf voltages and currents measured at 2 MHz do not change much for different HBr/NF₃ ratios and for variation of the 60 MHz power. However, these parameters strongly increase when rising the 2 MHz bias power. Increasing the bias power by a factor of 5 (from 500 W to 2500 W) yields voltages and currents that have doubled for the investigated range of parameters. From the influence of the 2 MHz frequency, the average sheath thickness has increased substantially causing high ion energies, as was already observed from previous investigations for pure HBr and NF₃ discharges. The 2 MHz addition appears to dominate by far changes in the number of charge carriers (from variations of the 60 MHz power) which also confirms results obtained from pure HBr and NF₃ discharges. From about equal changes of rf current and voltage, the plasma impedance remains roughly constant for the different HBr/NF₃ mixed chemistries.

Etch rates from variations of the HBr/NF₃ ratio for different 60+2 MHz power combinations (cf., Fig. 4.55 and Fig. 4.56) yield again clear indications of a strong chemical etch component when adding NF₃ to HBr discharges. From Fig. 4.55-a, modification of the 60 MHz source power level for constant 2 MHz power does not drastically change the silicon etch rate. This corresponds to the small changes observed in the rf voltage and current which indicates that etch rates are subject to small changes from modifications of plasma density and hence mainly ion flux. It should be noted that higher 60 MHz power levels must not necessarily cause a higher number of charge carriers but could influence more significantly the neutral gas temperature and hence ion energies from changes in the sheath thickness (as discussed in previous sections). Increasing the 60 MHz power will also enhance chemical etching by creating higher fractions of radical species. This is supported from etch rates for dominating NF₃ contents which increase stronger when rising the 60 MHz power level (since chemical etching is more pronounced in NF₃ compared to HBr). Surprisingly, silicon etch rates are found to remain nearly constant for medium to low admixtures of NF₃, possible reasons are discussed in detail in section 4.5.6. As observed from 60 MHz single frequency HBr/NF₃ discharges, silicon etch rates are rising by a power law when increasing the NF₃/HBr ratio further from 40% NF₃ content. However, the incline is not as strong as observed for the etch rate enhancement in corresponding 60 MHz single frequency discharges. This appears to be due to stronger enhanced etch rates for HBr from the influence of 2 MHz power. The impact of ion bombardment through addition of 2 MHz power is lower for NF₃ dominated mixtures with HBr which indicates that etching is not limited as strongly by ion energy. For these NF₃ dominated HBr/NF₃ mixtures, the Br⁺ ion flux can however efficiently support chemical etching which is mainly driven by F radicals.

These investigation generally confirmed observations from pure HBr and NF_3 discharges where silicon etch rates are mainly determined by a higher (or more efficient) contribution of the physical etch component through the impact of ion flux and ion energy for bromine dominated chemistries, as compared to a more chemically driven etching for pure fluorine chemistries. Whereas in 60 MHz frequency discharges etch rates were found to drop substantially for the transition of 10% HBr/90% NF_3 mixed chemistries to pure NF_3 discharges, this phenomenon has vanished when additionally applying 2 MHz bias power.

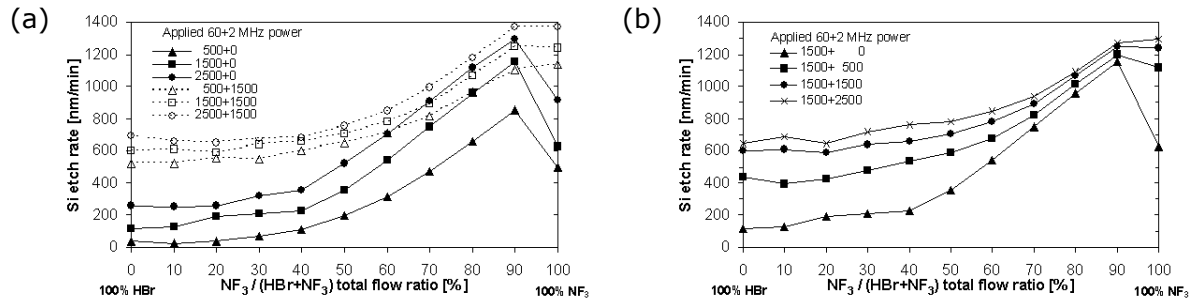


Figure 4.55: Silicon etch rates for variation of (a) 60 MHz source power and (b) 2 MHz bias power in single and dual frequency discharges (150 mTorr, 300 sccm HBr/ NF_3 total gas flow rate, no magnetic field), as determined from gravimetry.

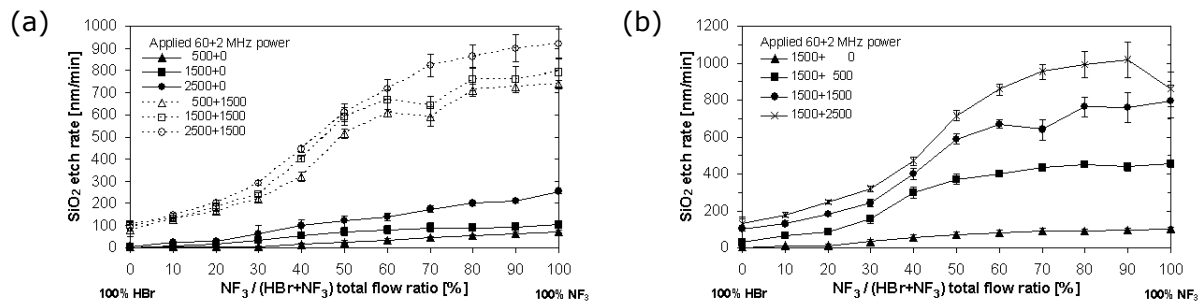


Figure 4.56: SiO_2 etch rates for variation of (a) 60 MHz source power and (b) 2 MHz bias power in single and dual frequency discharges (150 mTorr, 300 sccm HBr/ NF_3 total gas flow rate, no magnetic field), as determined from ellipsometry.

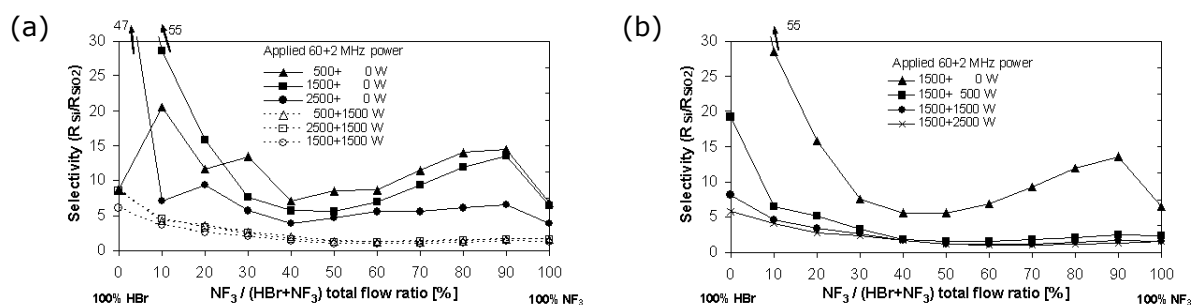


Figure 4.57: Etch selectivities for variation of (a) 60 MHz source power and (b) 2 MHz bias power in single and dual frequency discharges (150 mTorr, 300 sccm HBr/ NF_3 total gas flow rate, no magnetic field).

From Fig. 4.56-a, SiO_2 etch rates are found to rise stronger from contribution of the 60 MHz power when increasing the NF_3 content. This is attributed to chemical etching of SiO_2 in the presence of fluorine atoms, whereas SiO_2 is subject to predominantly physical

sputtering (at lower rates) in HBr discharges. SiO₂ etch rates start increasing from already 10-20% NF₃ admixtures in HBr, until they eventually start saturating for NF₃ dominated HBr/NF₃ chemistries. From investigations of pure NF₃ discharges, a more efficient dissociation of the NF₃ feed gas can be achieved at high 60 MHz powers where more fluorine radicals are provided for chemically etching at the substrate surface. Etching is additionally supported through the physical impact from an additionally increasing ion flux. Maximum SiO₂ etch rates do not exceed about two third of the corresponding silicon etch rates. The influence of modulated ion bombardment energies (from variation of the 2 MHz power) on etch rates in Fig. 4.56-b demonstrates a strong contribution from physical impact on reactive ion etching for >20-30% NF₃ content in HBr. In contrast, a gain in etch rates for heavily HBr dominated chemistries is limited due to predominantly physical sputtering of SiO₂. Scaling of SiO₂ etch rates are clearly in contrast to findings for silicon etch rates discussed above. This is mainly attributed to the differences in the etch mechanisms for etching silicon and SiO₂ in HBr discharges (discussed in section 4.3). From these results it becomes obvious that an efficient increase in silicon etch rates by addition of NF₃ can not be achieved before SiO₂ etching becomes effective. From a more detailed investigation of SiO₂ etch rate distributions obtained from ellipsometry, etch rate pattern on the substrates turn from more pronounced edge-fast (for pure HBr discharges) to more uniform or slightly edge-slow pattern (for pure NF₃ discharges). Etch rates calculated from weight loss measurements are not shown here since they yielded comparable results for the integral SiO₂ etch rate.

Etch selectivities are plotted as well for the chosen set of parameters discussed here, the influence of different 60 MHz as well as 2 MHz power levels for both single and dual frequency discharges are depicted in Fig. 4.57-a and Fig. 4.57-b, respectively. As expected from the discussion of etch rates, addition of even small amounts of NF₃ in HBr discharges dramatically reduce the Si-to-SiO₂ selectivity (compared to silicon, the SiO₂ etch rate starts to increase already at lower NF₃ contents). Whereas the 60 MHz frequency negligibly affect etch selectivities in dual frequency discharges investigated here, a severe reduction is noticed from the influence of the 2 MHz frequency. Due to physical sputtering of SiO₂ in pure HBr, the selectivity reduction from the 2 MHz frequency is most severe for highly HBr dominated chemistries. From strongly chemically driven etch rates for high NF₃ contents in HBr, etch selectivities are not much decreased further when increasing the 2 MHz power. Si-to-SiO₂ etch selectivities drop below 3:1 for NF₃ contents exceeding 20% in HBr/NF₃ mixed chemistries where minimum selectivities close to 1:1 are found in the range of 50-70% NF₃ content.

4.5.3 Variation of pressure

60+2 MHz dual frequency discharges

The influence of different process pressures between 50 and 600 mTorr was investigated for 60+2 MHz dual frequency HBr/NF₃ discharges, where 60 MHz and 2 MHz power levels and total gas flow rates remained fixed. Due to a strong suppression of ion intensities at higher pressures (as was also described in sections 4.3.3 and 4.4.3), investigations remain limited to 300 mTorr maximum pressure. Here, IDFs for F⁺ and Br⁺ ions from the plasma determined from 50 mTorr (Fig. 4.58) and 300 mTorr discharges (Fig. 4.59) for different HBr/NF₃ mixed chemistries are compared to results for 150 mTorr discussed in the previous section (cf., Fig. 4.54). To allow for a comparison of measured ion energies, corrections

were applied to the measured distributions after determination of respective floating potentials plotted in Fig. 4.58-d, Fig. 4.54-d, and Fig. 4.59-d.

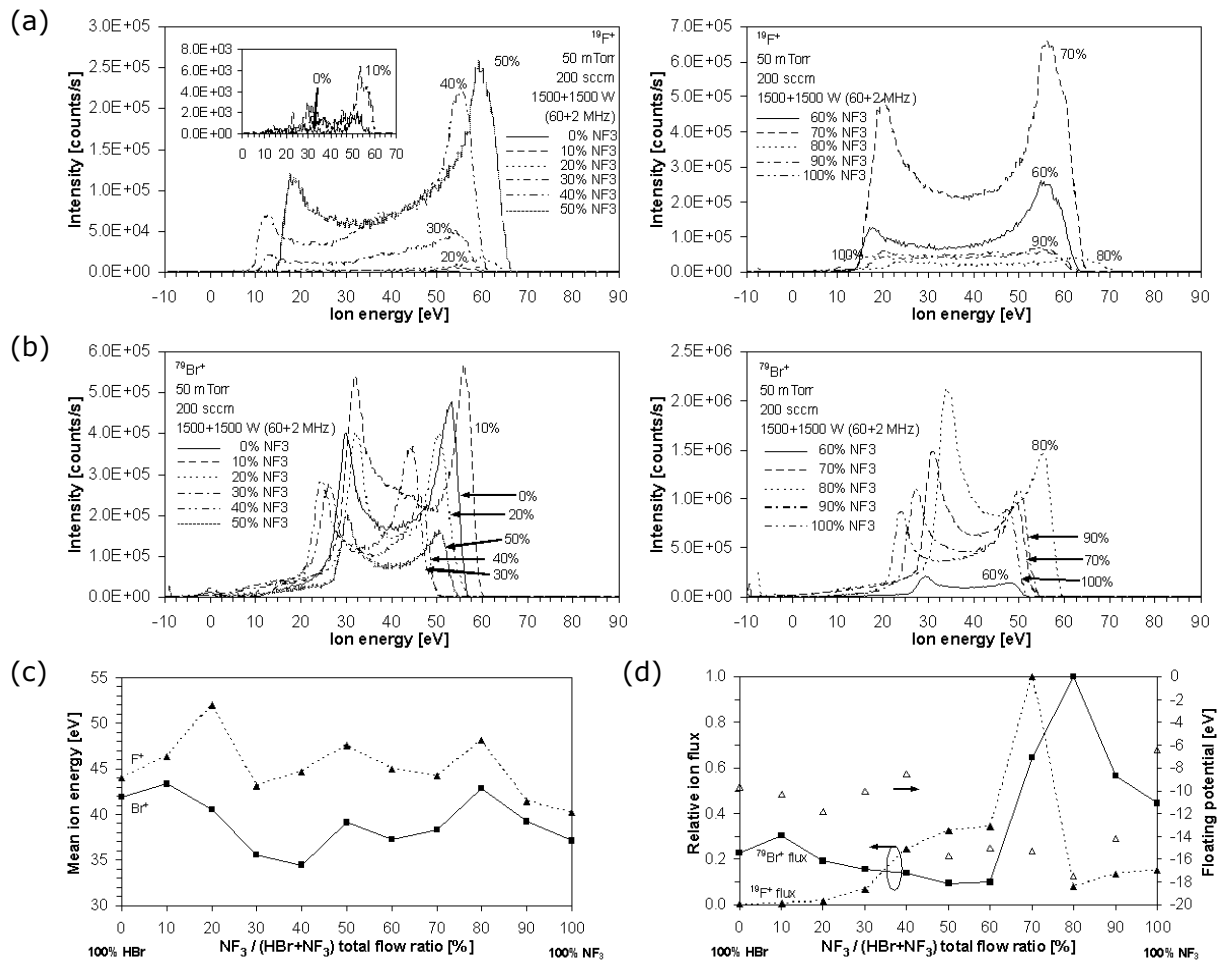


Figure 4.58: (a) $^{19}\text{F}^+$ and (b) $^{79}\text{Br}^+$ ion distribution functions measured in 60+2 MHz dual frequency HBr/NF₃ mixed discharges for different admixtures of NF₃ (1500+1500 W 60+2 MHz power, 50 mTorr, 200 sccm HBr/NF₃ total gas flow rate, no magnetic field, silicon substrate); (c) corresponding mean ion energies; (d) relative ion fluxes (solid symbols) and floating potentials at the extraction aperture (open symbols) as determined from the position of the lowest energy peak. The IVDFs have already been corrected for the offset in the energy scale.

Contribution of collisions to the low energy part of recorded IDFs is generally very low at 50 mTorr and becomes significant at 150 mTorr. At 300 mTorr, bromine ions are efficiently scattered into the low energy part of the IDF causing highly distorted IDF structures. From the dominating low energy part of IDFs for Br^+ ions at high pressures, the low and high energy peak of the bimodal structure have almost vanished. Reduced ion energies from elastic scattering and (mostly resonant) charge exchange collisions of F^+ ions at high pressures are not as severe as for Br^+ . This can be explained by a high consumption of fluorine during enhanced silicon etching in the presence of NF₃, and further by an efficient hydrogen capture to form stable HF species, thus reducing the number of resonant collisions. At 300 mTorr, F^+ IDFs plotted in Fig. 4.59-a are subject to noise due to low intensities measured, and fall below the detection limit for 0-30% and 90-100% NF₃ admixtures. Despite minor differences, F^+ and Br^+ mean ion energies appear to change similarly for different feed gas mixtures in 50 mTorr (Fig. 4.58-c), 150 mTorr (Fig. 4.54-c), and 300 mTorr (Fig. 4.59-c) dual frequency HBr/NF₃ discharges. Mean ion energies

measured at the reactor wall range between 22 eV and 47 eV for Br⁺, and 40 eV and 74 eV for F⁺ ions. Differences between generally higher F⁺ and lower Br⁺ ion energies from differences in the ion mass become somewhat smaller for NF₃ dominated chemistries which is attributed to variations for the probability of sheath collisions, as discussed above. Further contributions result from changes of the mean sheath thickness due to variations of discharge parameters for the different mixed chemistries. A clear scaling of calculated mean ion energies with pressure is not observed here.

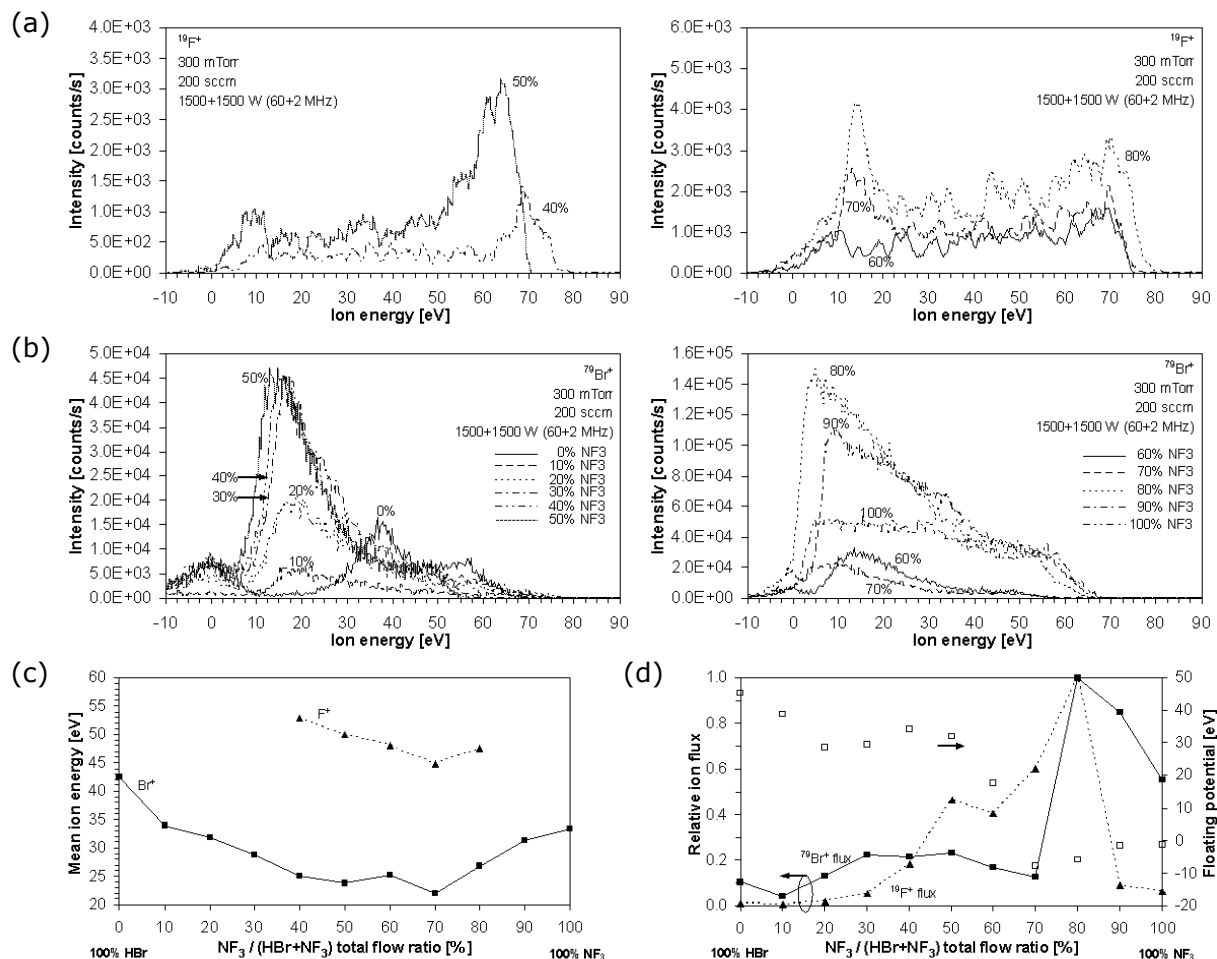


Figure 4.59: (a) $^{19}\text{F}^+$ and (b) $^{79}\text{Br}^+$ ion distribution functions measured in 60+2 MHz dual frequency HBr/NF₃ mixed discharges for different admixtures of NF₃ (1500+1500 W 60+2 MHz power, 300 mTorr, 200 sccm HBr/NF₃ total gas flow rate, no magnetic field, silicon substrate); (c) corresponding mean ion energies; (d) relative ion fluxes (solid symbols) and floating potentials at the extraction aperture (open symbols) as determined from the position of the lowest energy peak. The IVDs have already been corrected for the offset in the energy scale.

Ion fluxes for F⁺ and Br⁺ plotted in Fig. 4.58-d, Fig. 4.54-d, and Fig. 4.59-d are found to yield similar qualitative changes for different HBr/NF₃ ratios, without being influenced much by the pressure. Changes in both F⁺ and Br⁺ ion flux are influenced by the feed gas delivery and dissociation of feed gas and product molecules, a consumption of both species during etching, loss channels like formation of HF, and changing discharge parameters. Maximum F⁺ and Br⁺ ion fluxes are noted in the range of 70-80% NF₃ contents in HBr/NF₃ chemistries. Changes in the F⁺ ion flux observed at 300 mTorr agree within certain limits, deviations from the above discussions are due to the exponential drop in the count rates at high pressures, and consequently a higher contribution of noise.

From rf probe measurements plotted in Fig. H.2 (in appendix H), a rising pressure tends to generally reduce the rf voltage. This was already observed from pure HBr and NF_3 discharges and explained with a reduction of the sheath thickness and hence potential drop across the sheaths. At high pressures, rf voltages exhibit no significant changes when comparing results for the different HBr/ NF_3 mixed chemistries. In contrast, rf currents generally exhibit a non-monotonic decrease when increasing the NF_3 content in HBr within the pressure range investigated here. This can be explained by a reduction of the plasma density and hence reduction of the effective number of charge carriers when increasing the NF_3 content. Compared to weakly electronegative HBr discharges, the electron density is expected to be more efficiently reduced through electron attachment processes in gas mixtures containing more fluorine (the discharge becomes more electronegative).

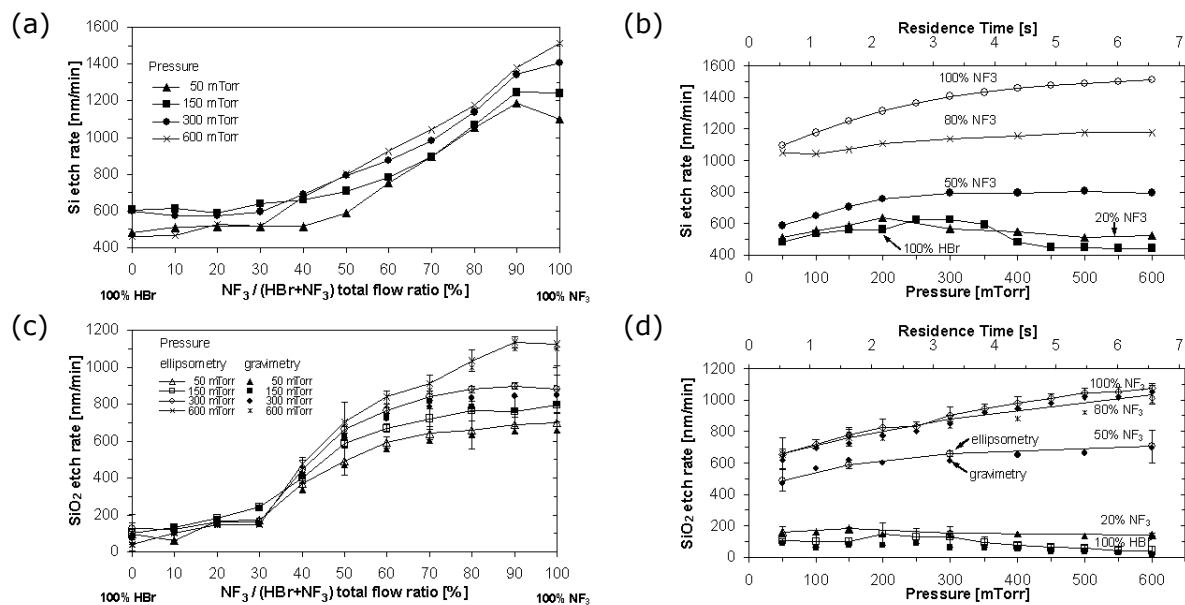


Figure 4.60: Silicon and silicon dioxide etch rates for variation of pressure in dual frequency discharges displayed as a function of (a+c) NF_3 admixture and (b+d) pressure and corresponding residence time (1500+1500 W 60+2 MHz power, 300 sccm total gas flow rate, no magnetic field), as determined from gravimetry (full symbols) and ellipsometry (open symbols), respectively.

The non-monotonic silicon etch rate dependency on the pressure observed for pure HBr discharges (cf., Fig. 4.31-a) is still visible at low admixtures of NF_3 (cf., Fig. 4.60-a and Fig. 4.60-b), but changes for NF_3 admixtures of equally and above 50%. For dominating NF_3 contents, scaling of the etch rates resembles to the known pressure dependency of a chemical driven etch process observed from pure NF_3 discharges (cf., Fig. 4.46-a). The same holds qualitatively true for the pressure dependency of SiO_2 etch rates (Fig. 4.60-c and Fig. 4.60-d), where physical sputtering occurs for HBr and chemical etching at the SiO_2 surface becomes important from addition of NF_3 feed gas and (supported by F^+ and, more importantly, by Br^+ ion energies and ion fluxes) strongly influences etch rate above 30% NF_3 contents in HBr. From more detailed investigations of SiO_2 etch rate distributions obtained from ellipsometry, etch rate pattern on the substrates turn from quite uniform to more pronounced edge-fast pattern when increasing the pressure for HBr dominated discharges. This appears somewhat comparable to results for pure 60+2 MHz HBr discharges (discussed in section 4.3.3). Medium to high NF_3 contents in HBr result in quite uniform etch rate distributions across the wafer. Silicon-to- SiO_2 selectivities calculated for

different HBr/NF₃ mixed chemistries were found to develop similarly to those observed from Fig. 4.57, and hence are not plotted here. An increased selectivity at high pressures in HBr was found to be efficiently reduced through addition of NF₃ feed gas.

4.5.4 Variation of gas flow rate 60+2 MHz dual frequency discharges

The influence of different HBr+NF₃ total gas flow rates from 150 to 600 sccm was investigated for 60+2 MHz frequency HBr/NF₃ discharges with fixed 60 MHz and 2 MHz power levels (1500 W) and constant pressure (150 mTorr). Due to limitations of the MFC for NF₃ allowing for maximum flow rates of 400 sccm (during the phase of these investigations), experiments with 600 sccm total gas flow rate could only be conducted up to a maximum of 60% NF₃ content in HBr. For investigations about the influence of different flow rates, only results of rf probe and etch rate measurements will be considered here.

RF voltages and currents plotted in Fig. H.3 (appendix H) tend to decrease when increasing the NF₃ content. RF measurements indicate stronger variations for different flow rates when the electrostatic chuck is covered by a silicon substrate, whereas they exhibit less changes for substrates with an SiO₂ hardmask. From rf probe measurements it might be concluded, that higher ion energies as well as higher ion fluxes will occur for HBr dominated discharges. From previous discussions this was however only partly supported by IDF measurements for ions incident at the reactor wall.

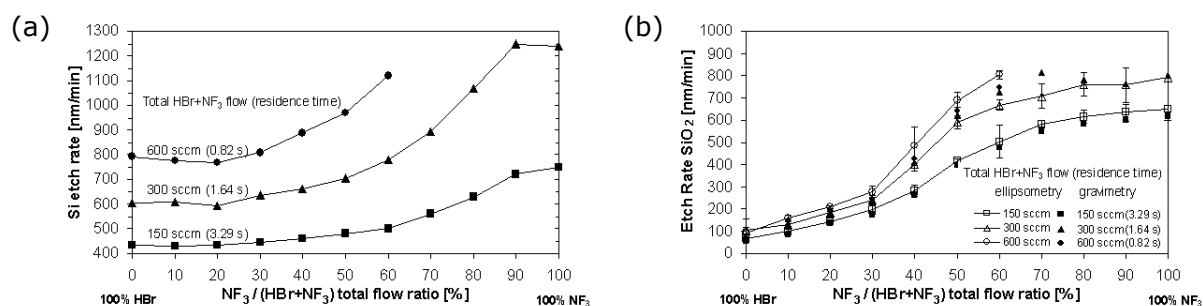


Figure 4.61: Etch rates for variation of the total gas flow rate in dual frequency discharges (1500+1500 W 60+2 MHz power, 150 mTorr, no magnetic field) for (a) silicon from gravimetry, and (b) SiO₂ from gravimetry (full symbols) and 49 point ellipsometry measurements (open symbols).

Increasing gas flow rates from 150 to 600 sccm total flow constantly increases silicon etch rates for HBr dominated chemistries with up to 30% NF₃ admixtures (Fig. 4.61-a). This confirms the trend observed from investigations of an HBr flow variation in pure HBr discharges (cf., Fig. 4.33). For higher NF₃ contents, the gain in etch rate becomes more pronounced from enhanced desorption of etch products and supply of fluorine for the high gas flow regime. This was about expected from previous investigations of NF₃ discharges where chemical etching dominates (cf., Fig. 4.48). An efficient desorption and removal of etch products causes the etch rate to increase by reducing the concentration of reaction products in the gas phase through enhanced flow rates and hence reduced residence times (as indicated in Fig. 4.61). The major contribution is due to transport limitation effects that determine the etch rate here. To some extent, the etch process is also limited by generation of radical species from a decomposition of the feed gas since high NF₃ gas flow rates will result in a lower degree of dissociated NF₃ (cf., Fig. 4.48-a).

From Fig. 4.61-b, the influence of total gas flow rates on SiO₂ etch rates yields similar results. Again, the gain in etch rates becomes higher for NF₃ admixtures exceeding 30% and starts to saturate for NF₃ dominated chemistries. Etch selectivities for different HBr/NF₃ mixtures remain comparable with those trends plotted in Fig. 4.57. Higher gas flow rates appear to generally result in slightly higher etch selectivities where differences remain below 10%. As indicated in Fig. 4.61-b, nonuniformities in etch rate distributions across the wafer remain quite low.

4.5.5 Variation of magnetic field

60+2 MHz dual frequency discharges

The influence of magnetic fields up to 120 G was investigated for 60+2 MHz frequency HBr/NF₃ discharges with fixed 60 MHz and 2 MHz power levels, as well as constant total gas flow rate and discharge pressure. Experiments were conducted while simulating slowly rotating magnetic fields from application of a 0.25 Hz sinusoidal voltage to the magnet coils. The following discussion comprises results of rf probe and etch rate measurements.

From Fig. H.4 in appendix H, measured rf voltages are found to decrease monotonically when increasing magnetic fields for all HBr/NF₃ mixed chemistries investigated. As discussed in previous sections for a variation of magnetic fields in HBr as well as NF₃ dual frequency discharges, scaling of the rf voltage (Fig. H.4-a) is found to agree very well to the scaling of sheath thickness and dc bias voltage from HPSM calculations for 60 MHz Ar discharges (cf., Fig. C.5-a and Fig. C.5-d in appendix C), when using bare silicon substrates. From rf voltage measurements, an onset of saturation is indicated around 100 G for NF₃ dominated feed gas mixtures, for HBr dominated chemistries a saturation appears to start at even higher magnetic fields. When silicon substrates with a thick SiO₂ top layer were used, scaling of the rf voltage (cf., Fig. H.4-d) is found inbetween results for a scaling of sheath thickness and dc bias voltage in 60 MHz Ar discharges (Fig. C.5-a and Fig. C.5-d) and in 60 MHz HBr discharges (Fig. D.5-a and Fig. D.5-e in appendix D). From rf voltage measurements, the onset of saturation starts around 40 G for NF₃ dominated chemistries, and around 70 G for HBr dominated mixtures. Comparing these results, a lower collisionality and/or smaller collision cross sections are expected for electron-neutral collisions in NF₃ discharges which results in a stronger confinement of electrons. Hence, the electron mobility is already reduced at weaker magnetic fields from initially higher mobilities as compared to HBr discharges. Interestingly, for the cases discussed here scaling of the sheath thickness appears to be predominantly determined by the 60 MHz frequency. From the decline of measured rf voltages, ion energies are expected to decrease according to results from HPSM simulations (cf., Fig. C.5-j and Fig. C.5-k in appendix C, as well as Fig. D.5-k and Fig. D.5-l in appendix D). For rising magnetic fields, ion densities are expected to increase at least to some extent which might be supported by increasing rf currents from Fig. H.4-b and Fig. H.4-e (appendix H). From these measurements, a saturation is indicated again at high magnetic fields, where for NF₃ dominated feed gas mixtures the saturation appears to start earlier compared to HBr dominated chemistries. These measurement results generally confirm trends from HPSM simulations for the influence of weak magnetic fields on the discharge behavior as well as differences in the discharge behavior when using different substrates, as discussed in previous sections.

From Fig. 4.62-a, silicon etch rates are observed to constantly increase for HBr dominated chemistries when rising the magnetic flux density, where a saturation occurs

around 100 G. For NF₃ dominated mixtures, silicon etch rates start saturating above 70 G. For 50%HBr/50%NF₃ mixtures, the etch rate saturates around 90 G. Increasing etch rates are attributed to an increase of ion fluxes and radicals, when assuming the feed gas dissociation is influenced through an enhanced interaction path of electrons with background neutrals. Saturation of the etch processes are likely due to saturating ion fluxes at high magnetic fields as well as limitations from decreasing ion energies. SiO₂ etch rates generally do not change much (Fig. 4.62-b) where it appears that increasing ion fluxes as well as radical formation are compensating somehow for decreasing ion energies. From the slight changes of the silicon etch rates up to 10%, etch selectivities remain essentially constant with respect to the magnetic flux density. For 80%HBr/20%NF₃, the Si-to-SiO₂ selectivity ranges between 3:1 and 4:1. For HBr/NF₃ feed gas mixtures with equal and dominating NF₃ content the selectivity finally drops below 2:1. From ellipsometry measurements, an enhanced etch rate nonuniformity is observed at higher magnetic fields which develops into a hat shaped distribution across the wafer, where low etch rates occur at the outer edge region and further a slight dip is observed at the center plateau region of the wafer.

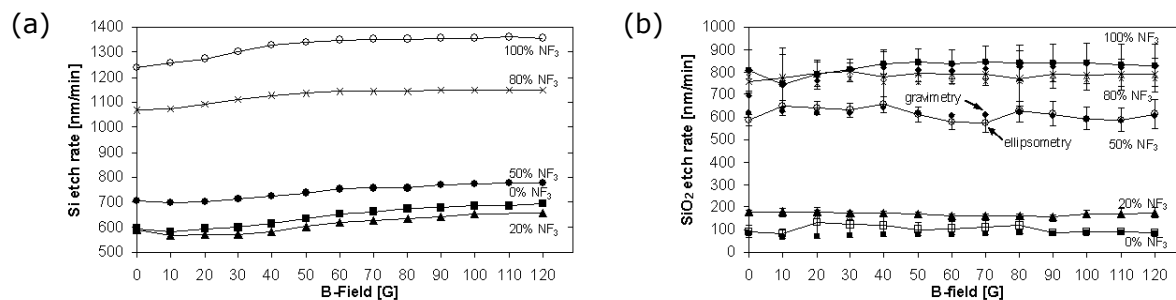


Figure 4.62: Etch rates for variation of the magnetic field in dual frequency discharges (1500+1500 W 60+2 MHz power, 150 mTorr, 300 sccm total gas flow rate) for (a) silicon from gravimetry, and (b) SiO₂ from gravimetry (full symbols) and 49 point ellipsometry measurements (open symbols).

4.5.6 Etch mechanisms in HBr/NF₃ discharges

From more detailed investigations, limitations of silicon etch processes in HBr/NF₃ mixed discharges are analyzed and a simplified etch model is discussed. The following investigations were motivated from results of a nearly unchanged silicon etch rate when increasing the NF₃ content up to about 50% in HBr/NF₃ discharges.

When changing the HBr/NF₃ feed gas mix, other discharge parameters like 60+2 MHz power (1500+1500 W), discharge pressure (150 mTorr) and total gas flow rate (300 sccm) remained unchanged. Standard mass spectrometry was applied to investigate intensities of the various etch species described in section 4.5.1. In Fig. 4.63-a, relative intensities are shown for ³⁴⁸SiBr₄⁺, ²⁸⁶SiBr₃F⁺, ²²⁶SiBr₂F₂⁺, ¹⁶⁶SiBrF₃⁺ and ¹⁰⁴SiF₄⁺ isotopes that exhibit the highest probability of occurrence. The species represent the five main etch products SiBr₄, SiBr₃F, SiBr₂F₂, SiBrF₃, and SiF₄ that can be observed from the mass spectrum after formation through direct ionization in the EQP ionizer. It was found that an introduction of even very few amounts of NF₃ to HBr strongly suppresses a formation of SiBr₄ product molecules where a reduction of about 70% is noted for 10% NF₃ admixtures. Moreover, introducing small amounts of NF₃ in HBr discharges yields an enhanced formation of mixed halogen etch products. For increasing NF₃ admixtures, the composition of those mixed halogen products shifts rapidly from bromine-dominated to fluorine-

dominated etch products where maximum intensities for SiBr_3F , SiBr_2F_2 and SiBrF_3 are recorded for 10%, 15% and 20% NF_3 content, respectively. Comparable to SiBr_4 , intensities for these mixed halogen products drop nearly exponentially when increasing the NF_3 content further. The SiF_4^+ intensity is subject to a monotonic increase, until it reaches its maximum for the transition from a 10% $\text{HBr}/90\%\text{NF}_3$ discharge to a pure NF_3 discharge.

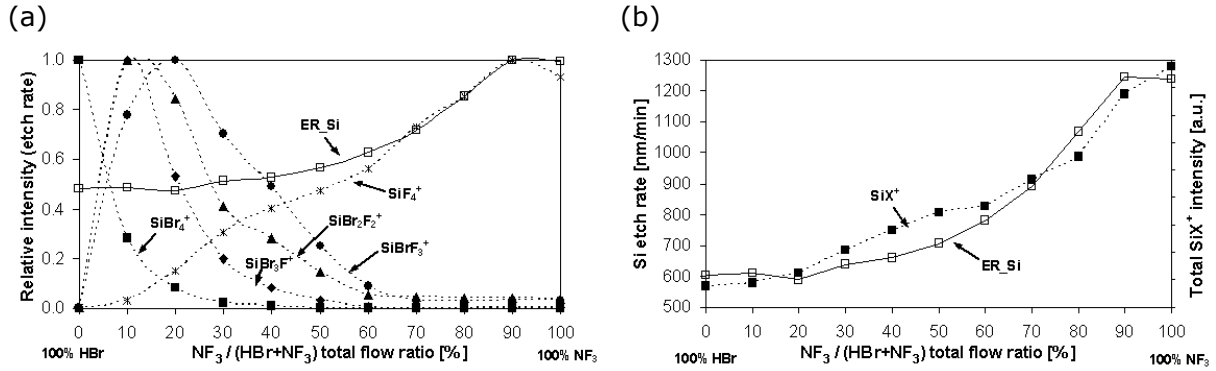


Figure 4.63: (a) Intensities of neutral SiX etch product species ionized by 70 eV electrons for HBr/NF_3 gas mixture sampled from the reactor with rf discharge (150 mTorr, 1500+1500 W 60+2 MHz power, 300 sccm total HBr/NF_3 gas flow rate, Si substrate). (b) SiX total integrated intensity agrees with the silicon etch rate within known uncertainties.

Table 4.2: Relative contributions of the different silicon etch product species in discharges with HBr/NF_3 mixed chemistries.

Species	m/q [u]	Species mole fractions [%]										
		100% HBr	10% NF_3	20% NF_3	30% NF_3	40% NF_3	50% NF_3	60% NF_3	70% NF_3	80% NF_3	90% NF_3	100% NF_3
SiF^+	47.11	0.92	3.41	3.13	3.20	2.43	2.64	2.08	2.05	2.20	2.87	2.92
SiF_2^+	66.11	-	1.03	1.21	0.96	0.74	0.69	0.54	0.41	0.38	0.49	0.46
SiHF_2^+	67.11	-	1.89	3.78	4.16	3.60	2.99	1.13	-	-	-	-
SiF_3^+	85.11	21.37	56.61	77.16	85.47	89.43	91.44	94.02	95.47	95.43	94.24	94.44
SiF_4^+	104.11	0.58	1.33	1.52	1.40	2.07	2.02	2.23	2.07	2.00	2.39	2.18
SiBr^+	108.10	13.64	4.24	1.06	0.22	-	-	-	-	-	-	-
SiBrF^+	127.10	-	0.72	0.35	0.15	-	-	-	-	-	-	-
SiBrF_2^+	146.10	-	2.87	2.60	1.14	0.40	-	-	-	-	-	-
SiBrF_3^+	165.10	-	2.35	2.62	1.10	0.40	0.21	-	-	-	-	-
SiBr_2^+	188.08	2.83	0.52	-	-	-	-	-	-	-	-	-
SiBr_2F^+	207.08	1.21	4.69	1.52	0.61	-	-	-	-	-	-	-
$\text{SiBr}_2\text{F}_2^+$	226.08	-	1.79	1.36	0.57	0.66	-	-	-	-	-	-
SiBr_3^+	268.07	42.48	11.71	1.90	0.51	-	-	-	-	-	-	-
SiBr_3F^+	287.07	0.96	2.38	1.06	0.32	0.28	-	-	-	-	-	-
SiBr_4^+	348.05	16.01	4.44	0.73	0.19	-	-	-	-	-	-	-
total SiBr_x^+		74.97	20.91	3.69	0.93	0.00	0.00	0.00	0.00	0.00	0.00	0.00
total $\text{SiBr}_x\text{F}_y^+$		2.17	14.81	9.51	3.88	1.74	0.21	0.00	0.00	0.00	0.00	0.00
total SiF_x^+		22.86	64.28	86.80	95.19	98.26	99.79	100.00	100.00	100.00	100.00	100.00

Following a similar procedure as described in section 4.4.2, a quantitative assessment of silicon etch product concentrations was performed through combined application of different diagnostic techniques. Experiments conducted for this approach were carefully performed in order to minimize secondary effects, like influences of background contribution and detector degradation while performing mass spectrometry. To receive more stable results for peaks with even very low intensities, integration was performed for the peaks at m/q ratios of interest as well as for the complete mass spectrum recorded in the 0-512 amu range. All isotopes relevant for each product species were added after applying corrections for the mass ratio dependent decrease of the intensity caused by the EQP analyzer (see section 2.4.4). A total SiX^+ integrated intensity can be finally obtained after adding all relevant silicon product intensities. From Fig. 4.63-b, it is found to closely correlate to the silicon etch rate for the different HBr/NF₃ mixed chemistries. Relative contributions of the different etch product species are shown in Table 4.2. Surprisingly for pure HBr discharges, SiF_x^+ ($x=1\dots4$) integrated intensities contribute to about 23% to the total SiX concentration. SiF_x^+ intensities are associated with stable SiF_4 reaction products resulting from previous NF₃ plasma cleans. Since SiF_4 is not observed in the background spectra recorded before these experiments, SiF_4 will more likely become released from the reactor surfaces through ion bombardment and chemical activation after the plasma is turned on. Due to the relatively high porosity, the yttria hard anodized surfaces provide a large surface area which can in general efficiently collect various product species (as discussed in section 4.5.2). For the lowest admixture of 10% NF₃ in HBr investigated here, SiF_4 related intensities are observed to already dominate the different etch products formed during chemical reactions at the substrate surface. Finally, SiF_4 species have become the only etch product in HBr/NF₃ chemistries exceeding 50% NF₃ content. SiBr_4 intensities exponentially decrease when introducing NF₃, contributing less than 1% for 70%HBr/30%NF₃ mixtures and becoming efficiently suppressed for even higher NF₃ contents. From these results it is assumed, that addition of even small amounts of fluorine are effective to strongly suppress an SiBr_4 product formation. Mixed SiBr_xF_y ($x=1\dots3, y=4-x$) products contribute for a 15% maximum in 90%HBr/10%NF₃ and dominate SiBr_4 products for 20% and higher NF₃ admixtures. Mixed halogen product species are practically vanished for equal and above 50% NF₃ contents in HBr.

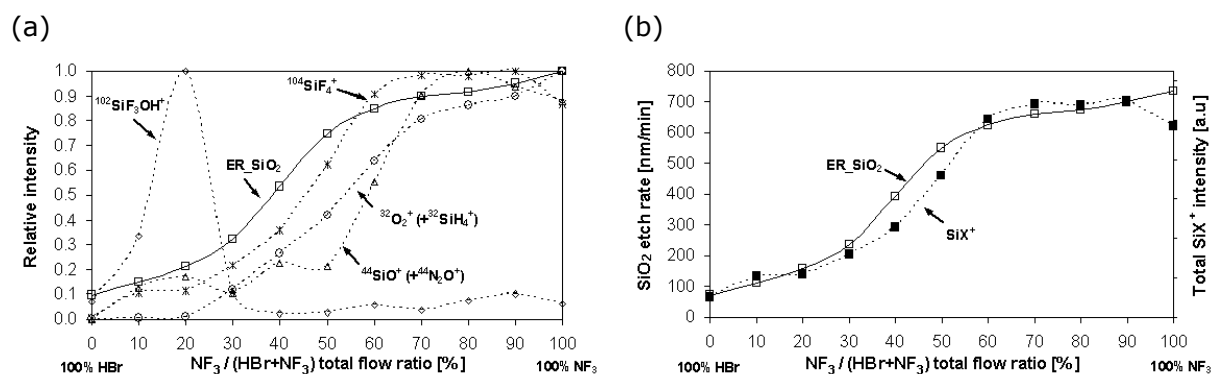


Figure 4.64: (a) Intensities of neutral etch product species ionized by 70 eV electrons for HBr/NF₃ gas mixtures sampled from the reactor with rf discharge (150 mTorr, 1500+1500 W 60+2 MHz power, 300 sccm total HBr/NF₃ gas flow rate, SiO₂ hard mask layer on silicon substrate). (b) SiX⁺ total integrated intensity agrees with the silicon dioxide etch rate within the known uncertainties.

From similar investigations using silicon substrates with a 2 μm thick SiO_2 hard mask layer in the presence of different HBr/NF_3 mixed chemistries, SiF_x^+ species were observed to be the main silicon etch products (that are associated with stable SiF_4 molecules), besides minor contribution from species like $^{44}\text{SiO}^+$ (with potential contribution from $^{44}\text{N}_2\text{O}^+$) and $^{102}\text{SiF}_3\text{OH}^+$. Further, oxygen molecules were detected which are released during chemically etching at the SiO_2 surface and/or dissociation of oxygen containing product molecules (e.g., SiO_2 , SiF_3OH) in the plasma. As can be seen from Fig. 4.64-a, $^{104}\text{SiF}_4^+$ and $^{32}\text{O}_2^+$ intensities correlate very well to measured SiO_2 etch rates. Calculation of the total amount of SiX^+ etch product species was again found to agree quite well to SiO_2 etch rates for the different HBr/NF_3 chemistries (Fig. 4.64-b).

From the results presented above, a basic etch model is developed for simplified assumptions in silicon trench structures with a top SiO_2 hard mask layer, as illustrated in Fig. 4.65: For pure HBr discharges, a thin bromosilyl (SiBr_x) layer will form at the surface of a silicon substrate [110,116]. Bromination of silicon surfaces is described in the literature to result from gasification and film growth which can be explained by thermodynamics. For highly exothermic Si/Br and Si/Br_2 reactions (bond energy about 3.2 eV [286]), bromine can spontaneously and strongly chemisorb forming a stable monolayer in the absence of ion bombardment [110,286]. Compared to chlorine or fluorine radicals, a gasification of silicon by atomic bromine is more effectively retarded by steric effects since bromine atoms have the largest radius. Ion bombardment is necessary for etching silicon by bromine atoms. For the dual frequency discharges considered here, additional ion bombardment involves ions with sufficient kinetic energies to initiate and further enhance silicon etching. SiBr_4 final etch products are formed and released from the surface allowing the etch process to proceed. When initially introducing few amounts of NF_3 feed gas to the HBr discharge, fluorine radicals will be formed as well from dissociation of the feed gas mix. Compared to bromine radicals, their number is lower and the surface layer consists to a major extent still of the thin bromosilyl (SiBr_x) layer described above. Chemisorbed bromine atoms form a protective film, thus inhibiting formation of silicon etch products through further impinging species and limiting the etch process at the substrate surface. Silicon can be gasified when a sufficient number of Si-F and/or Si-Br bonds has formed ($n=2\dots4$). If the surface is covered with a bromosilyl layer, fluorine atoms can only be physisorbed [286]. Hence, ion bombardment leads to release of SiBr_4 products formed through a first reaction. Due to their low volatility (e.g., compared to SiF_4), SiBr_4 species have a comparably high surface residence time and hence form a weak surface passivation. Since fluorine radicals can hardly reach the silicon interface directly they are instead predominantly consumed by oxidizing SiBr_x ($x=1\dots4$) in a second reaction. These reactions lead to more volatile SiBr_xF_y ($x=1\dots4$, $y=4-x$) halogen etch products. The SiBr_4 surface layer may locally be efficiently reduced through such secondary reactions. Since fluorine containing etch products exhibit a higher volatility compared to SiBr_4 [218] (referred to 101.325 kPa pressure)

$$T_v(\text{SiBr}_4) = 154^\circ\text{C} > T_v(\text{SiBr}_3\text{F}) > T_v(\text{SiBr}_2\text{F}_2) > T_v(\text{SiBrF}_3) > T_v(\text{SiF}_4) = -86^\circ\text{C}, \quad (4.21)$$

introduction of fluorine can therefore be considered equivalent to rising the substrate temperature for an improved volatility of SiBr_4 etch products. From these considerations, formation of SiBr_4 is the rate limiting step which determines the silicon etch rate in HBr dominated HBr/NF_3 chemistries. When increasing the fluorine content further, a fluorosilyl (SiF_x) layer will form [110] yielding final SiF_4 etch products. The SiF_4 etch product is highly

volatile and therefore efficiently released to allow subsequent etching to proceed. For HBr/NF₃ chemistries involving a dominating content of fluorine, the etch process can change from a surface reaction limited regime to a limitation by the supply of etch species. More complex mechanisms are expected when oxygen is present in non-negligible concentrations (mainly from addition of oxygen feed gas, as discussed in section 4.6), which in particular results in formation of a thin SiO₂ surface layer at the etch front inside silicon trench structures. SiBr₄ etch products may be efficiently dissociated in the plasma bulk and redeposit and/or recombine into bromine molecules when oxygen is present. Mixed SiBr_xF_yO_z layers of different stoichiometries may form at the substrate surfaces which can also yield volatile oxygen-containing etch products, such as SiO and SiF₃OH.

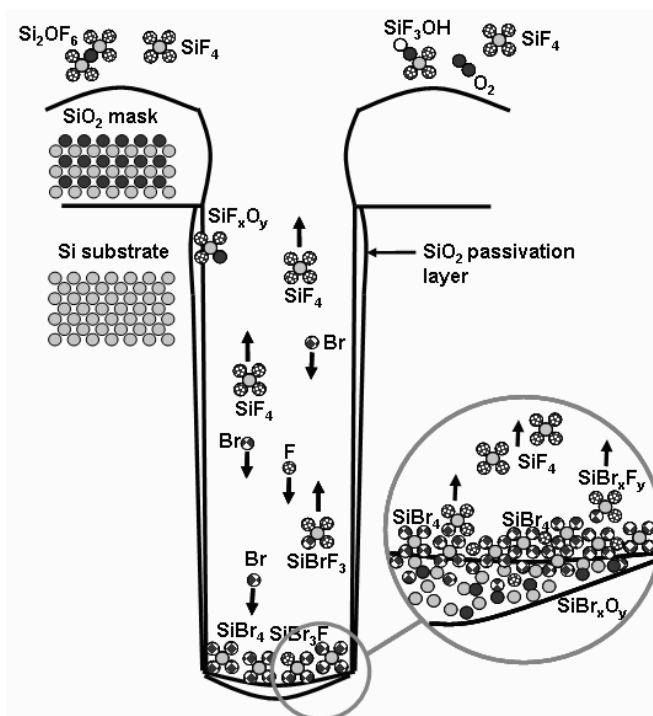


Figure 4.65: Illustration of etch mechanisms for etching silicon trench structures with a top SiO₂ hard mask layer in HBr/NF₃ mixed chemistries, as discussed in this section.

From the data presented above, a quantitative assessment of SiF₄ etch product concentrations is continued to allow again for calibration of the QCLAS technique and comparison to results obtained previously. Following the procedure described in section 4.4.2, partial pressures for SiF₄ products were calculated from mass spectrometry data by taking into account all relevant isotopes, and further correcting for the mass transmission function of the EQP. To assess on the accuracy of the applied method, similar calculations were performed for the feed gas components from mass spectra measured for different HBr/NF₃ chemistries when the discharge was turned off. From calculations of the total pressure (taking into account all relevant species), up to 10% maximum deviations were found from the experiments giving confidence to a quite high accuracy of the applied method. Besides processing mass spectrometry data, calculation of SiX partial pressures from weight loss measurements was performed as well by applying equations (4.15), (4.16) and (4.17). Results for the SiF₄ partial pressures calculated from weight loss measurements (solid triangles) and mass spectrometry (solid circles) are plotted in Fig. 4.66-a. SiF₄ concentrations measured with QCLAS are included in Fig. 4.66-a as well,

where a comparison of data is shown after applying corrections for an SiF_4 dissociation (solid squares) as well as uncompensated data (open squares) as a reference. Calculation of SiF_4 concentrations was performed after generally applying corrections for intensity losses caused by a degradation of the SrF_2 optical windows. Concentrations were determined from equation (3.9), by initially assuming gas temperatures of 343 K (corresponding to the constant reactor wall and lid temperature). Corrections accounting for a loss of SiF_4 due to dissociation in the HBr/NF_3 mixed discharges were applied by assuming an average 6% SiF_4 dissociation (cf., Fig. I.2 in appendix I). It should be noted that deviations from true values for the SiF_4 dissociation fraction in different HBr/NF_3 chemistries might occur which was not subject of further investigations here.

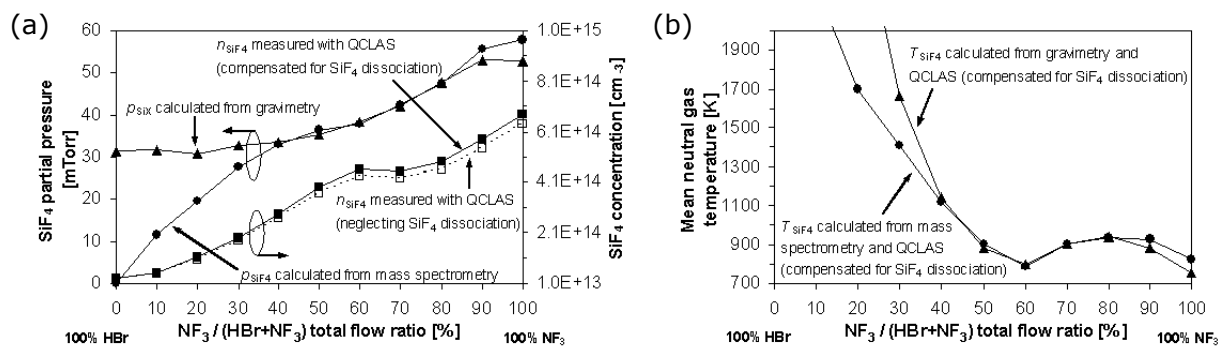


Figure 4.66: Combined application of mass spectrometry, gravimetry and QCLAS for NF_3 variation in HBr/NF_3 dual frequency discharges (150 mTorr process pressure, 1500+1500 W 60+2 MHz power, 300 sccm total HBr/NF_3 gas flow rate, no magnetic field, bare silicon substrate): (a) SiF_4 partial pressure calculated from gravimetry (solid triangles) and mass spectrometry (solid circles) where SiF_4 contributes about 100% above 40% NF_3 content, SiF_4 etch product concentrations measured with QCLAS when assuming a constant gas temperature of 343 K in the discharges (open squares: data obtained when neglecting an SiF_4 dissociation, solid squares: data after applying corrections for an SiF_4 dissociation); (b) SiF_4 neutral gas temperatures calculated from combined application of gravimetry and QCLAS (solid triangles) as well as mass spectrometry and QCLAS (solid circles). Knowledge of the gas temperature for the species to be monitored is necessary for calibration of QCLAS for determination of absolute SiF_4 concentrations here.

Note the good agreement of SiX and SiF_4 partial pressures determined from weight loss measurements (solid triangles) and mass spectrometry (solid circles), respectively, for NF_3 contents exceeding 40% from Fig. 4.66-a. This is easily understood from contribution of the different etch products, where differences for NF_3 admixtures below 40% are attributed to an additional formation of SiBr_xF_y ($x=1\dots4$, $y=4-x$) products. As expected, SiF_4 concentrations corrected for an SiF_4 dissociation (solid squares) as well as uncompensated data (open squares) are generally found to increase when rising the NF_3 content. However, deviations between results from the different techniques are observed once more when calculating corresponding partial pressures for SiF_4 from concentrations measured by QCLAS through application of the ideal gas law. Again, this is mainly attributed to considerably higher neutral gas temperatures during discharge operation compared to the 343 K temperature initially used here (that strictly applies only for cases when the discharge is off). Reasonable gas temperatures for the 60+2 MHz HBr/NF_3 discharges can be estimated from calculation of SiF_4 neutral gas temperatures by applying (4.18). Neutral gas temperatures calculated from combined application of weight loss measurements and QCLAS (solid triangles) as well as mass spectrometry and QCLAS (solid circles) are plotted in Fig. 4.66-b. SiF_4 neutral gas temperatures are found to drop from about 850°C for dual

frequency discharges with 60% HBr/40% NF₃ mixed chemistries to approximately 550°C for pure NF₃ chemistries. From these results, gas temperatures are found to quantitatively agree for NF₃ contents exceeding 40% with those observed from SiF₄ discharges (cf., Fig. I.4 in appendix I). Rather unrealistically high temperatures are calculated for low NF₃ admixtures in HBr where multiple SiBr_xF_y etch product species strongly contribute to the total etch rate. This might be attributed to SiBr_xF_y (x=1...3, y=4-x) etch products being more unstable compared to SiF₄, and hence can more easily be dissociated again in the plasma before getting sampled from the reactor. This is supported from comparison of the fractional degree of a dissociation for SiCl₄ and SiF₄ precursor gases plotted in Fig. J.2 in appendix J and Fig. I.2 in appendix I, respectively. As discussed in section 4.6, both SiCl₄ and SiF₄ are used as additional precursor gases in complex halogen discharges, and were hence subject of further studies. Whereas a 6% average SiF₄ dissociation was determined from 60 MHz frequency SiF₄ discharges (for 1500 W applied power), the average SiCl₄ dissociation was found to be 40%, as determined from corresponding 60 MHz frequency SiCl₄ discharges. From additional comparison of literature data [219,249-251], energies required to dissociate SiBr₄ are even lower than for SiCl₄ and SiF₄. For example, below 20 eV electron impact energy would be sufficient to completely dissociate SiBr₄, whereas dissociation of SiF₄ molecules would require energies around or even exceeding 30 eV. Comparably low dissociation energies as for SiBr₄ should also be sufficient to dissociate bromine rich SiBr_xF_y molecules. From this comparison it becomes clear, that an overestimation of more stable SiF₄ product molecules from EQP measurements is likely, and could hence explain deviations for low NF₃ admixtures in HBr. Furthermore, contribution of nonlinear degradation effects at the SrF₂ windows can also not be excluded here.

4.5.7 Summary

Although investigation of HBr/NF₃ mixed discharges can be interpreted to some extent from the knowledge obtained previously for pure HBr and NF₃ discharges, pronounced differences can occur due to more complex interactions of the various species in the plasma bulk and on the substrate surface. This generally complicates to draw simple conclusions about the detailed impact of the dual frequency concept. However, findings from previous detailed studies of the single gases highly enable or support ideas about possible mechanisms. From application of mass spectrometry in HBr/NF₃ mixed chemistries, the main etch product species are related to SiBr_xF_y (x=0...4, y=4-x) molecules when the electrostatic chuck is covered by bare silicon substrates. If the surface of the silicon substrates is covered by a 2 μm thick SiO₂ layer, SiF₄ is the main etch product with minor contribution of O₂, SiO and SiF₃OH product species. SiBr₄ etch products appear to be efficiently dissociated in the plasma bulk and redeposited and/or recombines into bromine molecules when oxygen is present.

Rising the 60 MHz power level generally increased etch rates stronger for NF₃ dominated HBr/NF₃ chemistries, whereas the etch rate enhancement from 2 MHz power was more pronounced for HBr dominated mixtures. This can be attributed to a higher (or more efficient) contribution of the physical etch component through the impact of ion flux and ion energy for bromine dominated HBr/NF₃ chemistries, as compared to a more chemically driven etching for fluorine dominated mixtures. Physical contribution of bromine ions was already encouraged from investigations of pure HBr and NF₃ discharges where silicon

etching could be increased by a maximum of about 50% in NF_3 and more than 70% in HBr through the impact of 2 MHz power. Scaling of SiO_2 etch rates in HBr/ NF_3 is in contrast to findings for silicon etch rates which is mainly attributed to differences in the etch mechanisms for etching silicon and SiO_2 in HBr discharges. Although maximum SiO_2 etch rates did not exceed about two third of the corresponding silicon etch rates, an efficient increase in silicon etch rates by addition of NF_3 could not be achieved before SiO_2 etching became effective. Compared to pure NF_3 discharges, etch rates can be higher for NF_3 dominated HBr/ NF_3 mixtures. This might result from general changes of the discharge behavior for even low admixtures of HBr to NF_3 discharges which could allow for higher plasma densities (since HBr is considerably less electronegative) and hence yield a higher dissociation and ionization rates in the plasma bulk compared to pure NF_3 . An enhanced chemical etching (from a higher fraction of fluorine radicals) is further supported by delivering high ion fluxes where maximum silicon etch rates are believed to mainly result from an efficient contribution of high Br^+ ion fluxes to the fluorine dominated chemical etching.

The non-monotonic etch rate dependency on discharge pressure observed for pure HBr discharges was still visible at low admixtures of NF_3 , but changed for NF_3 admixtures of equally and above 50% in HBr. For dominating NF_3 contents, scaling of the etch rates resembles to the known pressure dependency of a chemical driven etch process observed from pure NF_3 discharges. From IDF analysis for Br^+ and F^+ plasma ions incident on the reactor wall at different discharge pressures, contribution of collisions was very low at 50 mTorr and became significant at 150 mTorr. At 300 mTorr, bromine ions were efficiently scattered into the low energy part of the IDF causing highly distorted IDF structures. From the dominating low energy part of IDFs for Br^+ ions at high pressures, the low and high energy peak of the bimodal structure almost vanished. From less pronounced elastic scattering and (mostly resonant) charge exchange collisions at high pressures, F^+ ion energies were not as severely reduced as for Br^+ . From results for applying mass spectrometry, this was explained by a high consumption of fluorine during enhanced silicon etching in the presence of NF_3 (forming stable SiF_4 molecules), and further by an efficient hydrogen capture to form stable HF molecules that do not participate in etch processes further. Hydrogen from dissociated HBr thus contributes to considerable extents to a loss channel of fluorine radicals which reduces the F-atom concentration, and can hence shift the equilibrium of the etch process. Due to bromine ions experiencing more collisions, Br^+ mean ion energies were found to be typically lower than F^+ ion energies. However, differences between maximum ion energies for F^+ and Br^+ in HBr/ NF_3 mixed discharges remained generally small.

Increasing gas flow rates caused generally higher silicon and SiO_2 etch rates, where the gain in etch rate became more pronounced for NF_3 contents exceeding 30% in HBr. Again, this results from enhanced desorption of etch products and supply of fluorine for high gas flow regimes. This was about expected from previous investigations of pure NF_3 discharges where chemical etching dominates. Transport limitation effects as well as limitations by a generation of radical species from the feed gas decomposition both influence the etch rate here.

When applying magnetic fields, measured rf voltages were found to decrease for all HBr/ NF_3 mixed chemistries investigated. Scaling of the rf voltage was found to agree very well to scaling of sheath thickness and dc bias voltage from HPSM calculations. From differences for the onset of saturation for the rf voltage at higher magnetic fields, a lower collisionality

and/or smaller collision cross sections are expected for electron-neutral collisions in NF₃ discharges, as compared to corresponding HBr discharges. This results in a stronger confinement of electrons in NF₃ discharges when magnetic fields are present. Scaling of the sheath thickness appears to be predominantly determined by the 60 MHz frequency. Silicon etch rates were observed to increase up to 10% with additional magnetic field and saturated at higher magnetic flux densities. This was explained from the influence of saturating ion fluxes at high magnetic fields as well as limitations from decreasing ion energies. SiO₂ etch rates generally did not change much where it appeared that increasing ion fluxes as well as radical formation were compensating somehow for decreasing ion energies.

From what was observed for HBr and NF₃ discharges so far it is confirmed that pure HBr discharges exhibit highest selectivities (in the order of up to - or even exceeding - 50:1) when no significant ion energy is involved. Addition of even small amounts of NF₃ in HBr discharges dramatically reduce the Si-to-SiO₂ etch selectivity. Minimum selectivities ranging between 5:1 and 10:1 for the parameter set investigated here were found for 30-50% NF₃ content, as well as for pure NF₃ chemistries. Reduction in selectivity caused by the 2 MHz frequency drive was most severe for highly HBr dominated chemistries due to physical sputtering of SiO₂ in pure HBr. Si-to-SiO₂ etch selectivities dropped below 3:1 for NF₃ contents exceeding 20% in HBr/NF₃ mixtures where minimum selectivities close to 1:1 were found for 50-70% NF₃ content. Whereas the impact of magnetic fields on Si-to-SiO₂ etch selectivities remained negligibly low, higher gas flow rates (and hence, reduced residence times of the molecules in the reactor) appeared to generally result in slightly higher etch selectivities (where differences remained below 10%).

Corresponding to simplified assumptions for etching high aspect ratio features into silicon substrates with an SiO₂ hard mask layer, a simplified etch model was suggested to explain limitations of silicon etch processes in HBr/NF₃ mixed discharges. From introduction of even very few amounts of NF₃ to HBr, formation of SiBr₄ etch products become strongly suppressed by SiF₄ product formation. Mixed halogen etch products SiBr₃F, SiBr₂F₂, and SiBrF₃ can contribute to the major product SiF₄ but will drop exponentially for further increasing NF₃ admixtures to HBr. For equal HBr and NF₃ feeding as well as higher NF₃ contents in HBr, SiF₄ will finally constitute the only etch product species. Since silicon etch rates hardly change below equal HBr and NF₃ feeding, SiBr₄ is believed to form a weak surface passivation due to its low volatility (compared to SiF₄). Fluorine radicals can hardly reach the silicon interface directly but are instead consumed by oxidizing SiBr_x (x=1...4) at the substrate surface which leads to more volatile SiBr_xF_y (x=1...4, y=4-x) mixed halogen products. Since fluorine containing SiBr_xF_y product molecules exhibit a higher volatility compared to SiBr₄, introduction of fluorine can be considered equivalent to rising the substrate temperature for an improved volatility of the initial SiBr₄ etch product species. From these considerations, formation of SiBr₄ is the rate limiting step which determines the silicon etch rate in the HBr/NF₃ mixed chemistries with dominating HBr contents. When increasing the fluorine content further, a SiF_x (x=1...3) layer will mainly form at the substrate surface which then yields final SiF₄ etch products. SiF₄ molecules are highly volatile and therefore efficiently released for subsequent etching. For HBr/NF₃ chemistries involving a dominating content of fluorine, the etch process can finally change from a surface reaction limited regime to a limitation by the supply of etch species. It should be noted that an overestimation of more stable SiF₄ product molecules might occur since SiBr₄ and SiBr_xF_y molecules can be dissociated at already lower electron impact

energies. More complex mechanisms are expected when oxygen is present (e.g., from additional feed gas supply). This might result in formation of a thin SiO_2 surface layer at the etch front inside silicon trench structures. Mixed $\text{SiBr}_x\text{F}_y\text{O}_z$ layers of different stoichiometries may form at the substrate surfaces which can also yield volatile SiF_4 as major etch product species, and furthermore minor O_2 , SiO and SiF_3OH products.

Conditioning effects from previous NF_3 plasma cleaning became evident from F^+ and Br^+ ion flux measurements in HBr/NF_3 discharges which also confirmed earlier investigations about a reactor conditioning with fluorine and bromine [258]. After typical NF_3 plasma reactor cleans, quite significant amounts of fluorine can remain in the reactor since the yttria hard anodized surfaces exhibit a relatively high porosity. This considerably enhances the effective surface area for adsorption. During application of subsequent discharges, fluorine can be reactivated and desorb from the reactor walls. From a general balancing between adsorption and desorption processes during discharge operation, loading of the reactor walls by further species (like bromine) will occur in parallel. From these findings, conditioning artefacts in HBr/NF_3 mixed discharges can be minimized from choosing appropriate experimental conditions. From that knowledge, and further from comparison of results obtained after NF_3 reactor clean procedures and repeated experiments without additional cleaning (conditioning) it was ensured that such parasitic effects were generally minimized for the experiments conducted in this work.

4.6 Complex halogen mixtures

Complex $\text{HBr}/\text{NF}_3/\text{O}_2$ chemistries are typically used for high aspect ratio silicon etching [1,134,135,287]. In this section, $\text{HBr}/\text{NF}_3/\text{O}_2/\text{SiCl}_4$ mixtures are investigated for application in DRAM DT etch processes. To ensure precise profile control and uniform trench geometries, typical recipe settings comprise several steps where pressure, 60 MHz and 2 MHz power, gas flow rates, magnetic field, and gas flow ratios are adjusted. HBr should enable achieving highly anisotropic silicon etching by providing sufficiently high ion energies to remove passivation layers at the trench bottom etch front, and ensure minimized erosion of the SiO_2 mask and trench sidewalls from initially high Si-to- SiO_2 etch selectivities. Oxygen is added to form an SiO_2 passivation layer at the trench sidewalls for protection against attack by reactive species, and hence suppress an unwanted widening of trench geometries. NF_3 is added to control the trench width by reducing the thickness of the sidewall passivation layer at the top part of the trench, which in turn is necessary to avoid clogging through a reduced cross-section and maintain constant supply of etch species as well as efficient removal of etch products. SiCl_4 is added as a silicon source to somewhat reduce hard mask erosion through an enhanced deposition at the surface of the SiO_2 hard mask during etching. SiF_4 was initially used as precursor and substituted by SiCl_4 since the latter species allows for a considerably enhanced silicon deposition at the hard mask region. This was supported from differences from comparison of the fractional degree of a dissociation for SiF_4 and SiCl_4 plotted in Fig. I.2 (appendix I) and Fig. J.2 (appendix J), respectively. The discharge pressure needs to be optimized mainly from reasons for sufficient supply of etch radicals. As was discussed in previous sections, the process pressure further influences the physical etch component as well as formation of the trench geometry since it determines ion scattering in the powered electrode sheath and hence dictates both the angular distribution as well as ion energies. Highly forward-directed ions

are favored to deliver a sufficient ion energy and directional flux to the bottom of high aspect ratio structures. Whereas 60 MHz power is needed to achieve a high degree of decomposition of the feed gas components to provide high radical and ion fluxes, the 2 MHz power predominantly determines the ion energy. The wafer temperature (which usually remains unknown) can be changed by adjusting the temperature of the actively cooled powered electrode as well as the helium backside pressure for an efficient thermal coupling between wafer and electrostatic chuck. Adjusting the wafer temperature influences sticking of oxygen and fluorine at the trench sidewall, and hence can be efficient to control bottom CDs of the features on the substrate. The wafer temperature is also influenced by the energy of ion and neutral projectiles bombarding the surface, and hence by the 2 MHz power level. The geometry of HAR structures is further influenced by magnetic fields which can compensate high ion energies to a certain extent by reducing dc bias voltage and hence, sheath thickness. Furthermore, the magnetic field also allows for higher densities in the plasma, thus delivering high ion fluxes to the substrate.

Investigations performed here are limited to an analysis of typical DT etch process settings that have been found empirically. Basic knowledge obtained from interactions in pure HBr and NF_3 as well as HBr/ NF_3 mixed chemistries is used for interpretation of the main interactions in HBr/ $\text{NF}_3/\text{O}_2/\text{SiCl}_4$ mixed discharges, and limitations of the etch process during HAR etching. For application of mass resolved ion energy analysis, $^{19}\text{F}^+$ and $^{79}\text{Br}^+$ plasma ions were chosen again to study the plasma and sheath behavior for the complex halogen mixed discharges. Before conducting experiments on DRAM trench capacitor product wafers, the reactor was conditioned with standard HBr/ NF_3 processes on bare silicon wafers. Furthermore, the reactor is cleaned prior DT etch experiments using optimized NF_3 plasma cleans on bare silicon wafers.

4.6.1 Neutral mass spectra

In Fig. 4.67-a, a typical mass spectrum is shown that is observed for HBr/ $\text{NF}_3/\text{O}_2/\text{SiCl}_4$ mixed chemistries from the reactor when the discharge is off. The figure inset shows enlarged details of minor species contributions. Settings applied for discharge operation were taken from a typical 90 nm DRAM DT etch process. The spectrum is found to be a superposition of the mass spectra observed for pure HBr (cf., Fig. 4.22-a), NF_3 (cf., Fig. 4.37-a), and SiCl_4 (Fig. J.1-a in appendix J) comprising characteristic fragmentation pattern for the feedstock gas molecules (taking into account the feed gas ratio). Additionally, O^+ and O_2^+ are detected from addition of oxygen feed gas. The mass spectrum for the situation where the discharge is turned on is shown in Fig. 4.67-b. Fig. 4.67-c shows the difference mass spectrum as obtained after subtracting the mass spectra from Fig. 4.67-b and Fig. 4.67-a for the same mass-spectrometer settings, as well as using relevant DT patterned process substrates with a structured SiO_2 hard mask layer. The recorded spectrum exhibits a reduction in the relative intensities of ions derived from HBr, NF_3 and SiCl_4 feed gas components, such as HBr^+ , NF_x^+ ($x=1\dots3$) and SiCl_x^+ ($x=1\dots4$), and further the appearance of ions such as H_2^+ , HF^+ , N_2^+ , $\text{SiO}^+/\text{N}_2\text{O}^+$, Br_2^+ , SiF_x^+ ($x=1\dots4$) and SiF_3OH^+ that are associated with discharge-generated decomposition and reaction products like H_2 , HF , N_2 , SiO , N_2O , Br_2 , SiF_4 , and SiF_3OH . Besides minor contribution from SiO and SiF_3OH , SiF_4 is measured to be the only silicon etch product. Although from typical parameter settings the HBr/ NF_3 ratio is about 20%, SiBr_4 and SiBr_xF_y ($x=1\dots3$, $y=4-x$) etch product species observed from HBr/ NF_3 discharges when using

silicon substrates are not detected here (cf., Fig. 4.63-a). Peaks associated with Br_2 and HF exhibit the highest intensities which supports the following basic assumptions: Whereas fluorine is responsible for chemical etching of silicon, bromine contributes the physical etch component by assisting the etch process. Besides its physical contribution, bromine may form only very low volatile etch product concentrations that remain below the detection limit of the EQP probe. It is constantly removed from the plasma reactor as recombined molecular bromine. This is supported from investigations in the previous sections. Alternatively, SiBr_4 and SiBr_xF_y etch products might also be efficiently dissociated in the plasma bulk when oxygen is present from the feed gas mix. A high amount of fluorine radicals is obviously lost through formation of inert HF molecules since hydrogen is available in relatively high amounts from dissociation of HBr in the plasma. Compared to HF^+ intensities, H_2^+ appears to be present in comparably smaller concentrations which emphasizes a highly efficient loss channel for fluorine radicals. To investigate the absence of SiBr_4 and SiBr_xF_y etch products in more detail, further experiments were conducted as described in the following.

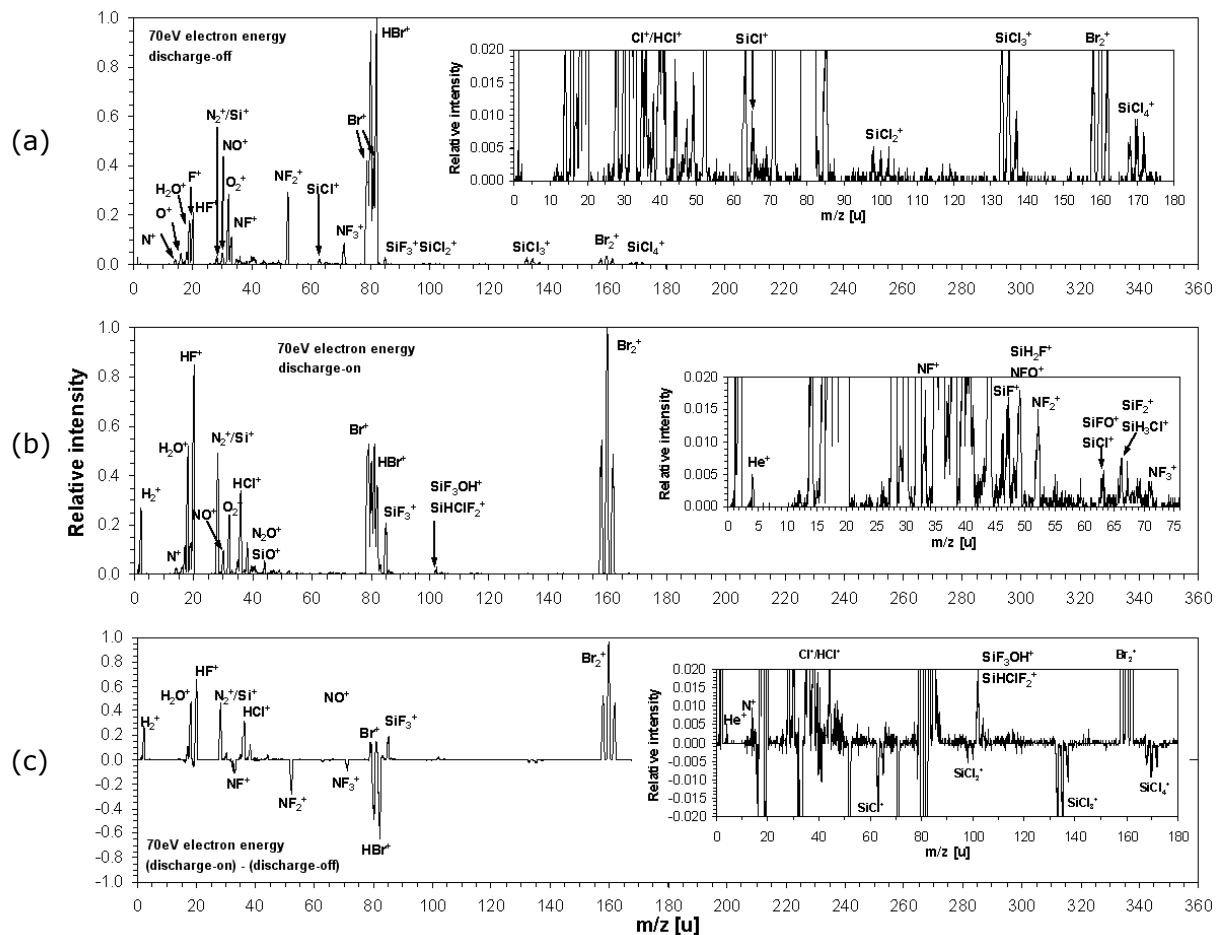


Figure 4.67: Mass spectrum of neutral species ionized by 70 eV electrons for (a) HBr/ NF_3 / O_2 / SiCl_4 complex chemistry sampled from the reactor without discharge; (b) HBr/ NF_3 / O_2 / SiCl_4 mixed chemistry sampled from the reactor with rf discharge (250 mTorr, 1900+2000 W 60+2 MHz power, 546 sccm total gas flow rate (20% NF_3 /HBr ratio), using DT patterned process substrates with a structured SiO_2 hard mask layer - 20% Si open area); (c) difference of mass spectra b-a (negative values indicate a loss when the discharge is on).

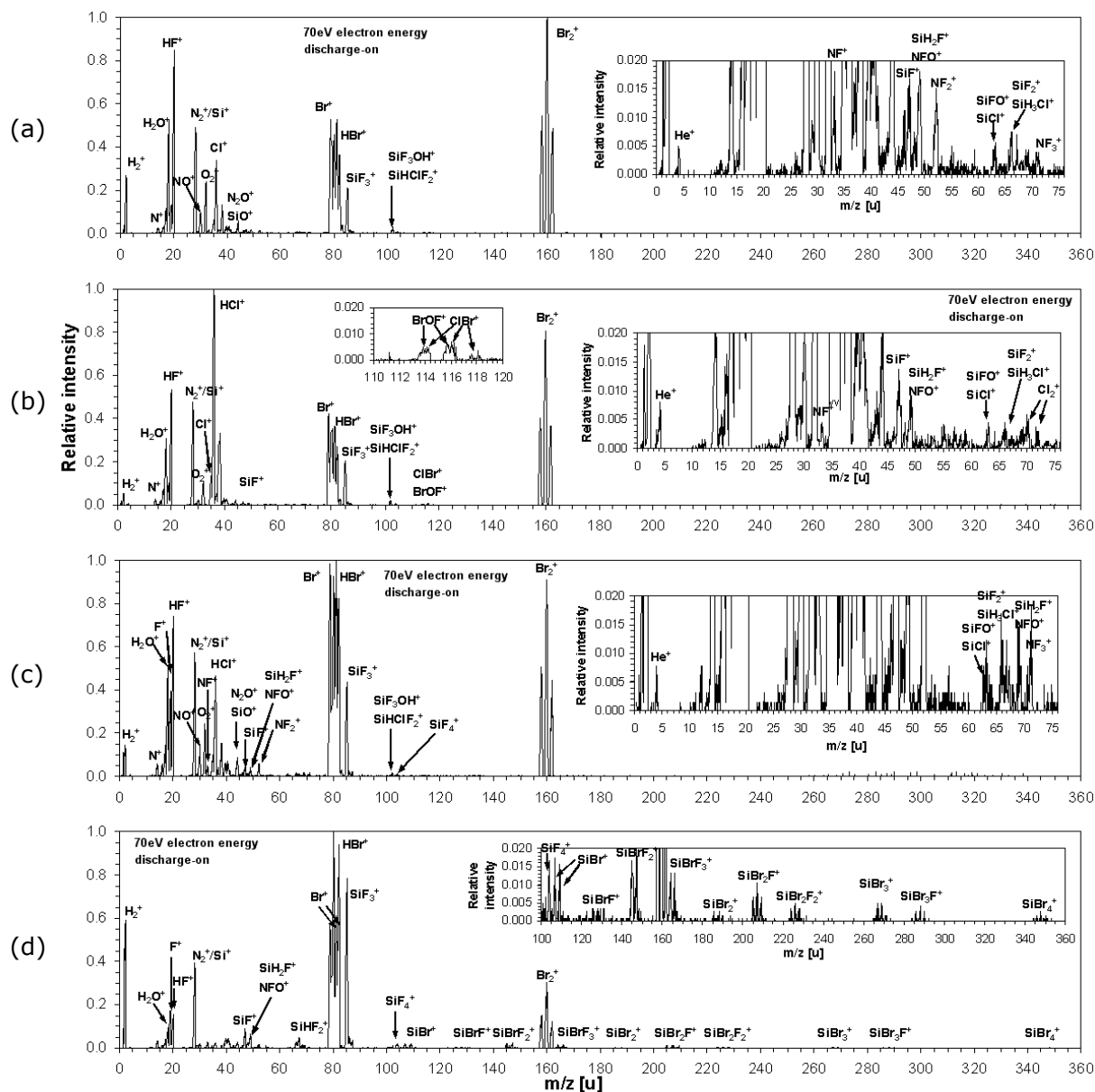


Figure 4.68: Mass spectrum of neutral species ionized by 70 eV electrons for (a) HBr/NF₃/O₂/SiCl₄ process gas mix sampled from the reactor with rf discharge (250 mTorr, 1900+2000 W 60+2 MHz power, 546 sccm total gas flow rate (20% NF₃/HBr ratio), using a DT patterned process substrate with a structured SiO₂ hard mask layer - 20% Si open area); (b) HBr/NF₃/O₂/SiCl₄ process chemistry reduced total flow (250 mTorr, 1900+2000 W 60+2 MHz power, 142 sccm total gas flow rate (20% NF₃/HBr ratio), using a DT patterned process substrate); (c) HBr/NF₃/O₂/SiCl₄ mixed chemistry sampled from the reactor with rf discharge (250 mTorr, 1900+2000 W 60+2 MHz power, 546 sccm total gas flow rate (20% NF₃/HBr ratio), using a bare silicon substrate); (d) HBr/NF₃ process gas mix (without addition of O₂+SiCl₄) sampled from the reactor with rf discharge (250 mTorr, 1900+2000 W 60+2 MHz power, 485 sccm total gas flow rate (20% NF₃/HBr ratio), using bare silicon).

(1) To minimize dilution effects from feed gas components and enhance the detection limit for low number density species, individual HBr, NF₃, O₂ gas flow rates were reduced to about one fourth of the initial flow rates. The initial SiCl₄ feed gas flow could not be reduced further which was due to limitations by the MFC to still maintain reliable flow rates. Comparing neutral mass spectra recorded for the initial process (Fig. 4.68-a) and for the modified process with reduced gas flow rates (Fig. 4.68-b) reveals no major differences for

the species recorded. From the latter spectrum, HCl^+ is found to dominate the spectrum which is attributed to an enhanced SiCl_4 contribution as compared to the initial feed gas ratio. Formation of HCl is associated with an efficient dissociation of the SiCl_4 feed gas and subsequent reactions of chlorine with hydrogen. Due to the enhanced detection limit, minor byproducts such as BrOF^+ and ClBr^+ are now observed that could not be detected with initial process discharge settings. SiF_x^+ and SiF_3OH^+ intensities were not found to have changed which corresponds to only negligible changes in the etch rate observed.

(2) To investigate the influence of the silicon open area on etch product formation, a bare silicon substrate was used during discharge operation with identical process chemistry and further process parameters. The initial silicon open area was estimated about 20% of the total surface area for DT patterned process substrates with a structured SiO_2 hard mask layer. From a five times higher silicon surface area, a considerably higher concentration of etch products should be created which in turn should again rise the detection limit. Comparing neutral mass spectra recorded for about 20% silicon open area (Fig. 4.68-a) and 100% silicon open area (Fig. 4.68-c) reveals indeed higher intensities for SiF_4 etch product species, whereas other intensities remain essentially constant.

(3) To investigate the influence of O_2 and SiCl_4 admixtures, the previous experiment was repeated without addition of oxygen and SiCl_4 when using again a bare silicon substrate. The intention was to exclude formation of (oxygen containing) passivation layers that potentially lead to black silicon formation at the silicon surface [135], and to further exclude a different dissociation behavior of silicon etch products when oxygen is added to the discharge. As can be seen from the neutral mass spectrum plotted in Fig. 4.68-d, various species are detected that are associated with SiBr_4 , SiBr_3F , SiBr_2F_2 , SiBrF_3 , and SiF_4 etch products. The mass spectrum appears comparable to mass spectra obtained from HBr/NF_3 mixed discharges for different process conditions described in the previous section. Bromine is actively involved in chemical reactions leading to formation of SiBr_xF_y ($x=1..4$, $y=4-x$) species, and furthermore reduced amounts of Br_2 byproducts. Higher intensities noted for SiF_x^+ species are attributed to higher silicon etch rates for an oxygen-free process chemistry.

From the above experiments it is concluded that detection of SiBr_4 etch products might be suppressed by comparably small silicon open areas, a more pronounced contribution of bromine through physical sputtering at a somehow oxidized silicon etch front, a low probability of less volatile SiBr_4 molecules to leave HAR structures prior to an effective substitution of Si-Br bonds by fluorine radicals (the initial aspect ratio from the SiO_2 hard mask is around 20 and at final trench depth aspect ratios of about 60 are achieved), dilution effects due to high feed gas flows from the DT etch process settings, and/or oxygen additions may lead to an enhanced or even complete dissociation of SiBr_4 product molecules in the plasma. From different investigations it was also found that addition of even small amounts of oxygen to bromine chemistries can efficiently decrease spectral intensities of SiBr_4 related species below the detection limit of the mass spectrometer [288]. It was speculated that SiBr_4 is dissociated in the plasma bulk when oxygen is present and partially redeposited after formation of SiBr_xO_y . Due to a very low volatility of such species, an increasing oxygen feeding could finally lead to a deposition rate exceeding the etch rate, hence causing a theoretically infinite etch selectivity. SiBr_xF_y ($x=1..3$, $y=4-x$) species are described as unstable intermediate etch products that can react either with oxygen (from the feed gas or from etching the SiO_2 hard mask) to redeposit as SiO_2 , or with fluorine to form volatile SiF_4 [287]. Volatile SiF_4 can further also react with oxygen to

redeposit as SiO_2 on the trench bottom or sidewall, or on the vertical SiO_2 hard mask. The trench profile is thus highly affected by the SiO_2 sidewall deposition and its uniformity. Measurement of ion fluxes from the investigated mixed halogen discharges hints that SiBr_xF_y product molecules are indeed created, although in very minor concentrations (cf., Fig. 4.69). From the recorded spectrum it is already hard to properly identify relevant peaks for $\text{SiBr}_x\text{F}_y^+$ plasma ions since corresponding intensities are at the edge of the detection limit. The plasma ion mass spectrum was recorded for EQP lens settings for $^{79}\text{Br}^+$ plasma ions (28 eV energy) that were obtained from tuning routines to optimize the signal-to-noise ratio [153].

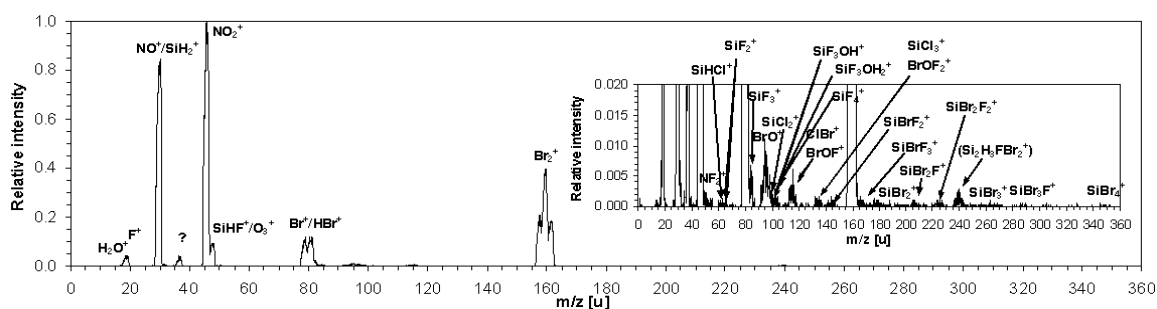


Figure 4.69: Mass spectrum of relative ion fluxes at the reactor wall recorded for EQP lens settings optimized from recommended tuning routines [153] for $^{79}\text{Br}^+$ plasma ions (energy = 28 V). Discharge conditions were 250 mTorr, 1900+2000 W 60+2 MHz power, 546 sccm total gas flow rate (20% NF_3/HBr ratio), and a DT patterned process substrate with a structured SiO_2 hard mask layer (20% Si open area) was used.

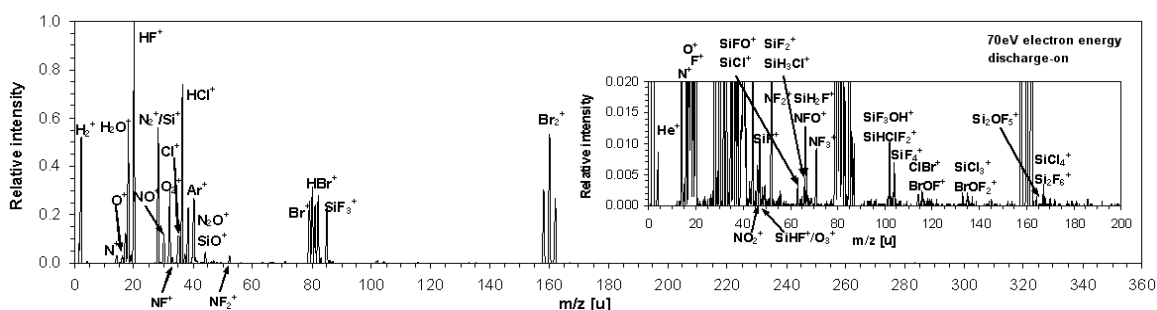


Figure 4.70: Mass spectrum of neutral species ionized by 70 eV electrons for $\text{HBr}/\text{NF}_3/\text{O}_2/\text{SiCl}_4$ gas mixture sampled from the reactor with rf plasma (250 mTorr, 750+3000 W 60+2 MHz power, 550 sccm total gas flow rate (20% NF_3/HBr ratio), using a DT patterned process substrate with a structured SiO_2 hard mask layer - 20% Si open area).

Finally, Fig. 4.70 shows a mass spectrum which is obtained for an etch process modified for a 60 nm DRAM DT etch process experiment. Again, SiF_x^+ ($x=1\dots4$) and SiF_3OH^+ are the only detected species that result from main SiF_4 and minor SiF_3OH product molecules. The peak observed at $m/q = 167$ u is attributed to Si_2OF_5^+ which is associated with further minor Si_2OF_6 etch product species formed through chemically etching the SiO_2 hard mask [288]. From comparison of the isotope distribution for SiCl_4 with measured peaks, the mass peaks around $m/q = 170$ u - which corresponds to the SiCl_4 main isotope - also indicates contributions from Si_2F_6^+ species. However, Si_2F_6^+ intensities remain just slightly above the EQP detection limit. In [110], Si_2F_6 was reported to be one of the major etch species formed during etching of silicon and silicon dioxide in fluorine chemistries.

From formation of bromine containing byproducts, like ClBr and BrOF_x , this experiment also hints how bromine is consumed and removed from the reactor (besides a major Br_2 formation). However, from the low intensities these products appear to be of minor concentrations or efficiently dissociated in the plasma.

4.6.2 Further discharge analysis

Investigations performed here are limited to a very basic analysis of typical settings for DT etch processing and might serve as an initial startpoint of more detailed future analysis. Recipes comprise several steps where discharge settings are defined and adjusted. During etching high aspect ratio features, the discharge pressure is raised from typically low (75 mTorr) to medium (250 mTorr) pressure. 60+2 MHz power levels are increased as well from medium (1400+1000 W) to high (1900+2000 W) powers. Besides minor changes, the HBr/NF_3 ratio remains about 80% $\text{HBr}/20\%\text{NF}_3$ which appeared to be an optimum with regards to a comparably high Si-to- SiO_2 selectivity in 60+2 MHz HBr/NF_3 discharges. Gas flow rates are slightly adjusted during the different recipe steps where the total gas flow rate can exceed 500 sccm. A magnetic field of 120 G parallel to the wafer surface is constantly applied and is typically set to rotate azimuthally with a period of four seconds. The magnetic field was switched off when performing mass spectrometry and IDF analysis.

IDFs recorded for F^+ and Br^+ ions from the plasma are plotted in Fig. 4.71-a and Fig. 4.71-b. Measured IDFs were already corrected for the offset in the energy scale. Whereas a broad peak splitting is observed for F^+ ion distributions, the peak separation remains low for Br^+ ions. Contribution from collisions to the low energy part of recorded IDFs increase as etching proceeds which is mainly a result of an increasing process pressure. At medium pressures, ions are efficiently scattered into the low energy part of the IDF where the low and high energy peak of the bimodal structure almost vanish. Again, reduced ion energies from elastic scattering and (mostly resonant) charge exchange collisions of F^+ ions at high pressures are not as severe as for Br^+ . Assuming a relatively low contribution of non-resonant collisions to scattering processes in NF_3 discharges, this appears to result from a high consumption of fluorine atoms during silicon etching through substitution of initial SiBr_4 products, and further from an efficient hydrogen capture to form stable HF species (cf., Fig. 4.68-a) which will reduce the number of resonant collisions for fluorine. Despite a less pronounced peak splitting in case of bromine, the IDFs resemble to those measured for HBr/NF_3 discharges under slightly different conditions (cf., Fig. 4.54). Mean ion energies measured at the reactor wall range between 25 eV and 35 eV for Br^+ , and 37 eV and 59 eV for F^+ ions (cf., Fig. 4.71-c). The results indicate slightly lower ion energies here as compared to similar settings in dual frequency HBr/NF_3 discharges. This might result from higher gas flows and/or slight differences in the discharge behavior due to additions of O_2 and SiCl_4 feed gas. The increase of ion energies with the different recipe steps is likely to result from increased 2 MHz power levels, until finally contribution from collisions starts to dominate and causes mean ion energies to slightly drop. Differences between generally higher F^+ and lower Br^+ ion energies from differences in the ion mass further increase with the different recipe steps which is mainly attributed to an increasing discharge pressure, and hence a rising sheath collisionality. Ion fluxes for F^+ and Br^+ plotted in Fig. 4.71-d are found to decrease as the etching process progresses. This is again attributed to a rising process pressure from the different recipe steps. A significant loss of ions due to an increasing number of collisions in the sheath and/or enhanced recombination effects in the

plasma bulk were discussed previously as potential root causes. From comparison to HBr as well as NF_3 discharges (cf., Fig. 4.30-e and Fig. 4.45-c for a setpoint of 1500 W 60 MHz power), ion fluxes appear less reduced here which could be explained by an increased ion generation at higher 60 MHz power levels (up to 2 kW setpoint for the experiments discussed here).

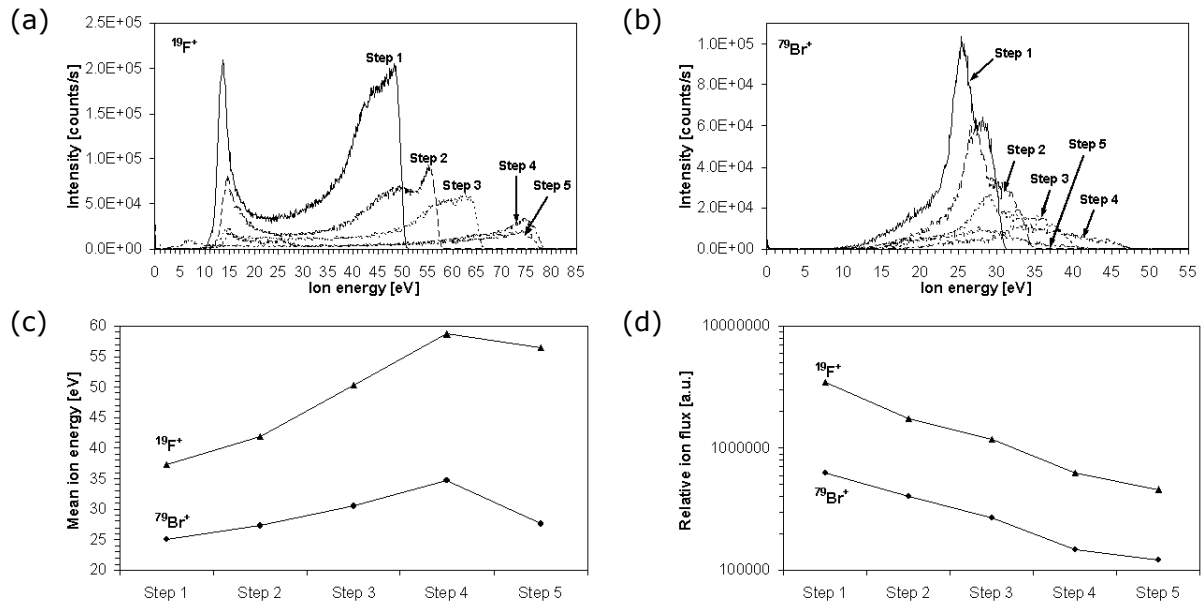


Figure 4.71: IVDFs for (a) F^+ and (b) Br^+ plasma ions measured during different recipe steps of typical DT etch discharge operation (60+2 MHz HBr/ NF_3 / O_2 / SiCl_4 discharges, no magnetic field, DT patterned process substrate with a structured SiO_2 hard mask layer - 20% Si open area); (c) corresponding mean ion energies; (d) relative ion fluxes. The IVDFs have already been corrected for the offset in the energy scale.

From rf probe measurements, the rf voltage is observed to constantly decrease with recipe steps (Fig. H.5-a in appendix H). This is in accordance with results from pressure variation in HBr, NF_3 and HBr/ NF_3 mixed discharges (cf., Fig. F.3-a, Fig. G.2-a and Fig. H.2-a in the appendix) where the general reduction appears slightly amplified by the additional magnetic field. Compensation by a rising 2 MHz power is not apparent from these results, as observed from investigations in the previous sections. The rf probe current plotted in Fig. H.5-b (appendix H) is found to rise after an initial decline. This is consistent with results from pressure variation in pure HBr and NF_3 discharges (cf., Fig. F.3-b and Fig. G.2-b in the appendix), amplified by the influence of the magnetic field (cf., Fig. F.4-b and Fig. G.3-b) as well as 2 MHz power (cf., Fig. F.2-b and Fig. G.1-b).

Evolution of the feature height (or depth, respectively) for the trench profile determined by both SiO_2 hard mask layer and silicon substrate during the total etch time, as well as corresponding aspect ratios for both materials are plotted in Fig. 4.72. As can be seen from Fig. 4.72, the silicon etch rate decreases with etch time and hence trench depth (i.e., the trench growth continues with a decreasing velocity). From rising 60+2 MHz power levels during the subsequent recipe steps, etch rates are expected to increase as well, as was found for HBr/ NF_3 mixed chemistries (cf., Fig. 4.55). However, a potential increase is compromised by the influence of a rising process pressure, as was observed again from HBr/ NF_3 mixed chemistries (cf., Fig. 4.60-a). As the etching proceeds, the oxygen gas flow rate has to be increased to account for the increased trench surface that needs to be

passivated to maintain a high degree of anisotropy. For a rising amount of oxygen, oxidation of the etch front at the trench bottom can become more severe which compromises the etch rate. When the concentration of the oxygen additive exceeds a critical value, sidewall deposition influences the profile evolution by shadowing parts of the trench bottom. Since all species enter the trench structure through the top opening, this region is most severely affected by an enhanced sidewall growth. To avoid clogging at the trench top opening, the NF_3 gas flow rate has to be increased accordingly. A higher NF_3 content could potentially reduce again the extent to which the silicon etch rate is reduced. Since the silicon etch rate clearly decreases as a function of the depth-to-width or aspect ratio, this indicates that the RIE lag effect (or ARDE) [136-138] has to be accounted for as well, besides influences from the changing process settings. Compared to the decreasing silicon etch rate, the SiO_2 etch rate from mask erosion decreases less strongly. Provided the etch selectivity is not subject to major changes, this might support the dominating influence of ARDE on the silicon etch rate as the aspect ratio increases. From the different scaling of the etch rates, the Si-to- SiO_2 selectivity is indeed only slightly reduced as the etching proceeds. The aspect ratio is reduced to a minor degree by the slightly (about 15%) increasing trench top CD. The obtained profile after etching is nearly ideally anisotropic with a negligibly tapered profile (not shown here), the taper angle remains below 0.2° . For such optimized trench profiles, no capacitance loss due to profile tapering will occur which means that the required storage capacitance can be obtained with the smallest trench depth. Furthermore, no etch profile distortions like undercutting, sidewall bowing, or microtrenching at the feature bottom due to ion scattering at the trench sidewalls were observed from the optimized process settings.

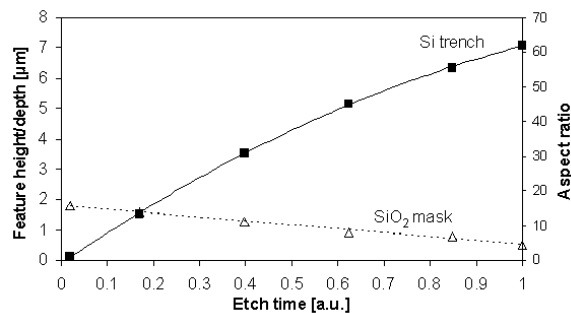


Figure 4.72: Profile evolution during DT etching.

4.6.3 Summary and discussion

From the various results obtained it was concluded that typical process settings used for high aspect ratio silicon etching appear well optimized with regards to the process chemistry. The variety of silicon etch product species measured from HBr/NF_3 and $\text{HBr}/\text{NF}_3/\text{O}_2/\text{SiCl}_4$ mixed discharges is reviewed again in Fig. 4.73 and Fig. 4.74.

For an efficient passivation removal at the etch front in high aspect ratio structures with small top CDs, generally high ion energies are required. Internal TRIM simulations have shown that ion energies of several hundred eV are required to remove a minimum SiO_2 passivation layer of about 1-3 nm thickness at the etch front. To obtain a dominating fraction of ions with high energy, high plasma density and high rf peak voltage are required which is supported by HPSM simulations. Practically, high plasma density and rf peak voltage can be provided by high 60+2 MHz power levels. An optimized etch process would

also require a highly efficient coupling at high power levels. This can be addressed by an efficient match box and power transmission line concept designed for the required power level. Enhanced etch rates at the trench bottom were observed from injection of high power levels, but also compromised by severely enhanced SiO_2 mask erosion.

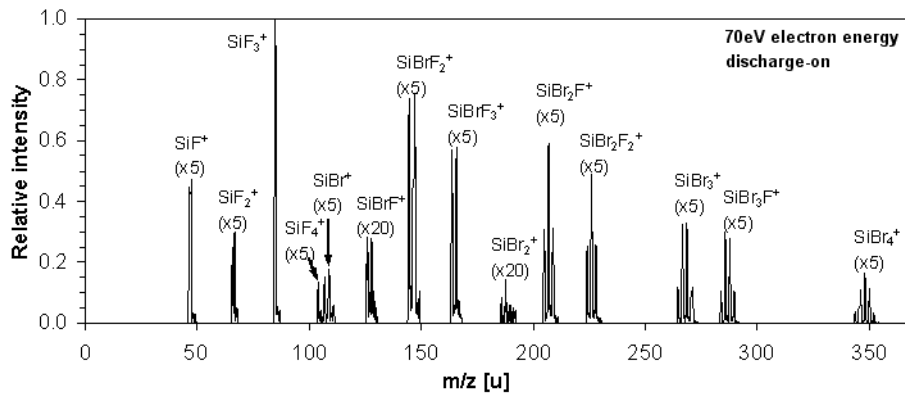


Figure 4.73: Mass spectrum of neutral SiX etch product species ionized by 70 eV electrons for HBr/ NF_3 gas mixture sampled from the reactor with rf discharge (250 mTorr, 1500+800 W 60+2 MHz power, 100 sccm HBr + 20 sccm NF_3 gas flow rate, using a bare silicon substrate)

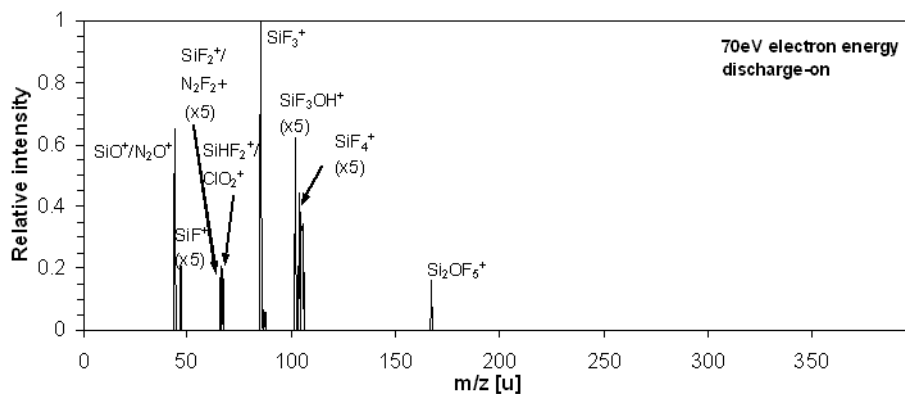


Figure 4.74: Mass spectrum of neutral SiX etch product species ionized by 70 eV electrons for HBr/ $\text{NF}_3/\text{O}_2/\text{SiCl}_4$ gas mixture sampled from the reactor with rf plasma (160 mTorr, 1400+1400 W 60+2 MHz power, 546 sccm total gas flow rate (20% NF_3/HBr ratio), using a DT patterned process substrate with a structured SiO_2 hard mask layer - 20% Si open area).

To minimize removal of the (SiO_2) hard mask and keep the (Si-to- SiO_2) selectivity high, it appears important to suppress the fraction of ions with low and medium energy. This expresses the need for an appropriately tuned IEDF that should predominantly consist of highly energetic ions. Generally, the 2 MHz frequency part is suitable to achieve the required high ion energies. However, the distribution typically extends also to low energies around the second (2 MHz) characteristic peak. A favored high-energy fraction could be acquired by further tuning the 60+2 MHz IEDF, e.g. by increasing the plasma density with 60 MHz power. Alternatively, multi-frequency rf source concepts beyond the already used 2 different frequencies might be required to achieve maximum etch rates in the HAR structures at optimized etch selectivity, by enabling better control of appropriately tuned IEDFs. Further options could include pulsing the plasma [289,290] to enhance both silicon etch rate and Si-to- SiO_2 selectivity and offer additional flexibility and control of the etch

process, or using alternative hard mask materials [290-292] with reduced erosion rates during bombardment with highly energetic projectiles.

Besides both high plasma density and rf peak voltage, a reduction of the discharge pressure appears suitable to efficiently increase the mean ion energy. According to HPSM calculations, decreasing the pressure reduces the number of collisions (ES, CX) and off-axis scattering in the sheath. Since the low energy part of the IEDF is mainly defined through the influence of collisions, decreasing the pressure can generally be an option to keep the fraction of low-energy ions small. A pressure reduction gives rise to an increased sheath width. As a result, the angular distribution becomes more anisotropic in forward direction, and ions will gain more energy on their way through the sheath region. This finally results in a higher fraction of ion projectiles that experience less collisions with the sidewalls in high aspect ratio structures. Practically, reduction of the discharge pressure from an intermediate pressure regime was found to be only slightly beneficial, mainly with regards to an improved profile control. At medium discharge pressures, ion distribution functions predominantly consist of low and medium ion energies where the high pressure tail is suppressed due to sheath collisions. Also, off-axis scattering in the sheath is more severe which expresses the need of an appropriate sidewall protection when etching high aspect ratio features. A beneficial enhancement of silicon etch rates at high power levels might compromise anisotropy through local erosion/consumption of the SiO_x sidewall passivation. This emphasizes the need of highly erosion resistant sidewall protection layers (like SiN, SiC, or TiN). The choice for these materials is of course limited from the requirements of subsequent removal leaving no residues inside the high aspect ratio features.

From HPSM simulations, the discharge asymmetry was found to increase with plasma density and rf peak voltage, and somewhat also for reduced pressures. This indicates that the net energy gain becomes higher for ions incident at the substrate. Due to the described need of highly energetic ions incident on the substrate, the discharge asymmetry should be as high as possible to minimize reactor wall erosion. Nevertheless, the energy for ions incident on the reactor walls will increase when tuning both parameters. This emphasizes the general need for appropriate hard anodization layers to minimize erosion of the reactor walls.

When increasing the 60 MHz power at constant reactor pressure, the neutral gas density is reduced due to gas heating effects. According to results from HPSM simulations, the increased gas temperature will result in an enhanced ion energy at the powered electrode by a factor of about 2, whereas the gain in ion energy at the ground electrode remains below 50% compared to initial values close to room temperature. The actual neutral gas density will always result from a superposition of the impact of gas heating and the adjusted reactor pressure which can complicate determination of the different discharge parameters.

Besides the positive impact of low pressures with regards to a reduced off-axis scattering and higher ion energies, the low pressure discharge still has to provide a required fraction of neutrals and radicals to maintain a sufficient chemical etch component. At optimum pressure, both required physical and chemical etch components should be balanced. Without compromising this balance, the pressure could be minimized by applying higher 60 MHz power levels to more efficiently dissociate the precursor molecules at reduced neutral gas densities. The increased 60 MHz power will however affect again the fraction of highly energetic ions which is due to a partial reduction of the increased sheath width at low pressures. This effect of a reduced pressure and high 60 MHz power will be intensified

further since the EEDF is expected to be influenced as well, causing a higher mean electron temperature. Increasing the electron temperature was found to yield a reduced sheath width in front of the powered electrode and hence reduced ion energies at this electrode. From the decreased discharge asymmetry, ion energies for projectiles incident on the ground reactor walls will increase, yielding an enhanced wall erosion. From the complex interactions, a pressure reduction and increase of the 60 MHz power could practically compensate for a favored gain in ion energy at the powered electrode. As a drawback of this approach, an enhanced wall erosion would result from the reasons discussed above. Besides rising 60 MHz power, application of weak magnetic fields is suited to provide an enhanced fraction of chemically active radicals (plus ions) at reduced pressure. During application of weak magnetic fields, the drawback of reduced ion energies should still be reasonable.

Besides contribution from ion energy as well as ion and radical fluxes, etch rates can become limited by an efficient removal of etch products from the substrate surface. This indicates requirements for optimized feed gas flow rates, as well as substrate temperatures. For HBr dominated chemistries, SiBr_4 etch species were found to apparently limit the etch rate at the trench bottom. From a proposed chemical etch model, enhancing etch rates is enabled by addition of higher NF_3 admixtures. Increasing NF_3 admixtures however compromises the required anisotropy and leads to an enhanced SiO_2 mask erosion. Alternatively, significantly raising the electrostatic chuck temperature was suggested to enable a higher volatility of etch species without compromising anisotropy again. Unfortunately, high temperatures will introduce additional severe difficulties for the CCP concept where high voltages require small leakage currents for the rf power coupling through the electrostatic chuck. Besides technical difficulties, a high substrate temperature could compromise maintaining a good feature profile control during HAR etching. An increased substrate temperature will for example decrease the sticking coefficient for oxygen at the sidewalls leading to less effective sidewall passivation and hence more isotropic etching (CD widening).

To somewhat enhance the etch selectivity, the initially used SiF_4 precursor was substituted by SiCl_4 as a result of the investigations performed during this work. The SiCl_4 species allows for a considerably enhanced silicon deposition at the hard mask region, hence reducing an SiO_2 mask erosion during etching. This was supported from differences for the decomposition measured for both precursors.

5 Summary and conclusions

In this study, physical and chemical interactions during dry etching of silicon in capacitively coupled asymmetric discharges were investigated in detail. This work was intended to gain better understanding of the complex interactions during high aspect ratio silicon etching with halogen chemistries for aspect ratios exceeding 70 and critical dimensions below 70 nm. Experiments were conducted in an industrial dual frequency MERIE CCP reactor at medium pressures typically used for etching high aspect ratio features for DRAM applications. Initial basic studies of the discharge behavior in this work comprised electropositive argon as well as electronegative HBr and NF_3 discharges. Further analysis was performed for mixed HBr/ NF_3 and complex HBr/ $\text{NF}_3/\text{O}_2/\text{SiCl}_4$ process chemistries to get a more detailed insight into the complex plasma chemistry and sheath behavior. Generally, the influence of applied power, discharge pressure, gas flow rates, as well as magnetic fields was investigated for 60 MHz single frequency as well as 60+2 MHz dual frequency operation. The final goal of this work was to investigate the utilization of the dual frequency concept as well as the impact on discharge properties and finally on etching at relevant substrate surfaces.

The complex nature of multi frequency rf sheaths was both analyzed experimentally and from simulations. The rf sheath behavior in front of the grounded electrode was investigated by applying mass resolved ion energy analysis from a Hiden EQP 500 analyzer installed at the reactor wall. To support an interpretation of results from plasma diagnostic measurements and to gain further insight into the discharge behavior at even difficult or impossible experimental conditions, the Hybrid Plasma Sheath Model [17,18] was used for calculation of angle-resolved ion energy distributions. The discharge chemistry was investigated in detail by applying mass spectrometry, APMS, QCLAS, as well as rf probe measurements. Gravimetry and ellipsometry were used additionally to characterize etch processes at different relevant substrates.

A comparison between IDF measurements and simulations to obtain more detailed information about the influence of discharge parameters is generally rather challenging due to inherent difficulties in the measurement of ion distribution functions. Orifice geometry and voltage settings on the electrostatic lenses of the analyzer are limiting factors that affect the ion transmission. Based on simulations of ion trajectories and experimental verification, chromatic aberration effects were minimized. Due to the fact that the EQP orifice plate as well as the reactor walls are insulating, the comparison of different discharge conditions and chemistries is quite challenging. An important but complicated task was therefore a rather precise determination of the floating potential that developed from surface charging around the aperture of the orifice plate. Low-energy peaks could be identified from measured distributions that were attributed to charge exchange collisions in the proximity of the sampling aperture. Peak positions were used for determination of the floating potential at the orifice plate, and hence calibration of the energy axis to enable for comparison of different plasma conditions. Finally, both the energy dependent acceptance angle and the resulting energy dependent transmission function of the adapted Hiden EQP analyzer design were taken into account to enable a comparison of results from experiment and simulation. For calculation of IDFs, the hybrid-fluid simulator was

additionally modified by implementation of differential cross sections resulting from ab-initio calculations for relevant ion-atom collisions in the sheath regions. This effort appeared necessary to achieve an accurate modeling of the scattering angle as a function of impact parameter and energy for the wide range of relevant scattering energies (about zero eV to keV range) occurring in the sheaths of typical medium pressure CCP discharges. The HPSM model initially suited to calculate single species Ar discharges was furthermore extended to enable simulations of HBr discharges consisting of multiple ion species as determined experimentally from typical CCRF hydrogen bromide discharges. Parameter studies were performed for both the modified Ar and the HBr model, including variations of the rf peak voltage, neutral gas pressure, neutral gas temperature, electron density, electron temperature, magnetic field, and the rf frequency mix. From the careful analysis it initially appeared feasible to gain access to information about IEADs of ions incident on the substrate by simply measuring IDFs of ions incident on the reactor wall. However, due to the highly complex discharge chemistry, the lack of precise knowledge for discharge parameters and required collision cross-sections, absolute calibration between experiment and simulation is impossible at this point. Nevertheless, relative trends for the results from simulation and measurement are generally well comparable. As an example, Langmuir probe measurements would be suited to extend the knowledge about discharge parameters and should therefore be applied in further studies. Besides the general disadvantage of disturbing the plasma, application of Langmuir probe measurements appears however not straightforward for investigation of electronegative gas discharges in an insulating discharge reactor.

A new diagnostic arrangement based on the infrared absorption spectroscopy technique QCLAS was designed and constructed during the time of the present work. For the first time, concentrations of the precursor gas NF_3 and of the etch product SiF_4 were measured on-line and in situ under clean room conditions [165]. Requirements regarding the infrared beam coupling into the plasma reactor were achieved by application of mid-infrared transparent fibres and internal reflections in the reactor chamber [266,267]. From application of QCLAS, changes from plasma species determined by mass spectrometry could be confirmed. Furthermore, the technique provides an attractive opportunity for calibration to quantify discharge parameters, like species concentrations and the neutral gas temperature. Besides application to expand the fundamental knowledge about process characteristics, QCLAS appears as a valuable nonintrusive and species-selective diagnostic technique to monitor and control etch processes.

Electropositive Ar discharges were investigated for an initial baseline characterization, to enable a comparison to literature data and allow for HPSM modeling calibrations. Experiments with ionized argon noble gas were also intended to obtain results for purely physical sputtering since the physical etch component can initiate and enhance reactive ion etching in molecular halogen discharges. Results obtained from measurements of argon ion distributions mostly confirm the trends obtained from different simulations. As expected, the Si-to- SiO_2 etch selectivity supports purely physical sputtering of both materials for the range of discharge settings investigated in this work. From detailed investigations, sputtering can be influenced by differences in the discharge parameters (from variations of ion-impact secondary electron emission coefficients, power coupling, plasma chemistry) as well as amorphization and recrystallization effects and subsequent native oxide growth at

the silicon surface (when the wafers are exposed to atmosphere again), and less importantly also by an argon incorporation.

Besides efficiently increasing sputter rates with 60 MHz and 2 MHz power, a further distinct gain in argon ion energy and sputter rates could be achieved through reducing the discharge pressure below 100 mTorr. This is likely due to changes in the EEDF and mean electron energy that accompany a discharge transition from stochastic (collisionless) to ohmic (collisional) electron heating and/or from the low-voltage (or α) to the high-voltage (or γ) mode through an increasing discharge current density. Strong changes of the argon feed gas flow appear to change the background gas temperature and hence the neutral gas density, which in turn will affect discharge properties (like plasma density, Ar^+ ion uniformity) to some extent.

From investigations of electronegative HBr discharges it is concluded that silicon is chemically etched where etch reactions are induced and strongly supported by ion energy. In contrast, SiO_2 appears to be predominantly physically sputtered. From these findings, changes in the Si-to- SiO_2 selectivity are primarily caused by changes of the chemical etch component during silicon etching. The contribution of chemical etching can become fairly low but always plays a non-negligible role in HBr discharges, as was concluded from comparison to purely physical sputtering in argon discharges. From mass spectrometry and APMS, SiBr_4 was confirmed as main etch product resulting from chemical reactions involved in the etch process.

From detailed IDF analysis and HPSM simulations, a higher sheath thickness can be obtained in molecular HBr discharges as compared to corresponding argon discharges. This can be explained by a higher mean electron temperature in HBr discharges [215] and results in a more distinct scattering of ions in the sheath region. Due to pronounced sheath collisions for the relatively high pressures applied, mean ion energies will be typically lower than the time averaged sheath potential. As expected, the measured IDF peak splitting increased with rf voltage and decreased with rf frequency and ion mass. Ion energies of low mass species (e.g., hydrogen molecules) usually appeared evenly distributed over a broad range which is due to the light ions being able to respond to temporal variations of the sheath potential caused by both the low and high frequency component. For other ion species, high frequency oscillations could generally not be resolved. Consequently, IDFs were mainly determined by the dynamics of the low frequency component. This reflects the fact that control over the energy of light ions in molecular discharges can not be achieved to a comparably high extent observed for heavy ion species. In practice, these light ions may however only play a minor role during etching.

From HPSM calculations, both qualitative differences in the IEDF structure as well as quantitative differences in the scaling of the investigated parameters appear for the different ion species in HBr. Those deviations can be explained by a currently insufficient description of the collisional processes for the different molecular species in HBr discharges. To gain more reasonable results, the HBr model implemented during this work should be subject of further improvements.

Investigations of strongly electronegative NF_3 discharges confirmed chemical etching of silicon and SiO_2 with fluorine occurs spontaneously, where etch rates can be strongly enhanced through the impact of ion bombardment energy and ion flux. Etching is generally influenced by transport limitation effects as well as limitations by a generation of radical

species from the feed gas decomposition. From mass spectrometry and APMS, SiF_4 was confirmed to be the main etch product. Generally, NF_3 molecules are effectively dissociated in the plasma where complete dissociation is achieved for high 60 MHz power levels. This results in a very effective conversion of the NF_3 feed gas into SiF_4 products (and N_2 byproducts). Due to a pronounced chemical etching of silicon and SiO_2 , changes in the Si-to- SiO_2 etch selectivity are primarily caused by a different scaling of the chemical etch component for both materials. From a quantitative assessment of SiF_4 etch product concentrations, mean neutral gas temperatures arising during discharge operation could be approximated. For the range of 60 MHz power levels investigated here, the gas temperature was found to rise from 70°C reactor temperature to about 1000°C. F^+ ions were generally found to exhibit highest energies, being comparable to or even exceeding those observed for species from corresponding HBr discharges. Since ion energies were recorded at the reactor wall this indicates that erosion of reactor surfaces through ion bombardment can become severe in NF_3 discharges.

Interpretation of interactions in HBr/ NF_3 mixed discharges was enabled from knowledge obtained from investigations of pure HBr and NF_3 discharges. However, differences from a simple superposition indicated that more complex interactions will occur during etching on the substrate surface as confirmed from the various species in the plasma bulk. The main etch product species in HBr/ NF_3 mixed chemistries are related to mainly fluorine-rich SiBr_xF_y ($x=0\dots4$, $y=4-x$) molecules when the electrostatic chuck is covered by bare silicon substrates. When etching SiO_2 , SiF_4 becomes the main etch product with minor contribution of O_2 , SiO and SiF_3OH product species. From simplified assumptions for etching high aspect ratio features into silicon substrates with an SiO_2 hard mask layer, a basic etch model is suggested to explain limitations of silicon etching in HBr/ NF_3 mixed discharges. According to the model, fluorine radicals are consumed by subsequently oxidizing an SiBr_x ($x=1\dots4$) passivation layer at the substrate surface which leads to more volatile fluorine-rich SiBr_xF_y ($x=1\dots4$, $y=4-x$) mixed halogen products (SiBr_4 formation becomes strongly suppressed). SiBr_4 etch products are finally completely suppressed through efficient dissociation in the plasma bulk and redeposition and/or recombination into bromine molecules when oxygen is present in the discharge. The model appears suitable to explain passivation properties of bromine and oxygen to achieve highly anisotropic etching.

Rising the 60 MHz power level generally increased etch rates stronger for NF_3 dominated HBr/ NF_3 chemistries, whereas the etch rate enhancement from 2 MHz power was more pronounced for HBr dominated mixtures. This can be attributed to a higher (or more efficient) contribution of the physical etch component through the impact of ion flux and ion energy for bromine dominated HBr/ NF_3 chemistries, as compared to a more chemically driven etching for fluorine dominated mixtures. Scaling of SiO_2 etch rates in HBr/ NF_3 differs in detail from silicon etch rates which is mainly attributed to differences in the etch mechanisms for etching silicon and SiO_2 in HBr discharges. Although maximum SiO_2 etch rates did not exceed about two third of the corresponding silicon etch rates, an efficient increase in silicon etch rates by addition of NF_3 could not be achieved before SiO_2 etching became effective. From what was observed for HBr and NF_3 discharges so far it is confirmed that pure HBr discharges exhibit highest selectivities (in the order of up to - or even exceeding - 50:1) when no significant ion energy is involved. Addition of even small amounts of NF_3 in HBr discharges dramatically reduce the Si-to- SiO_2 etch selectivity where

minimum selectivities range between 5:1 and 10:1. Etch selectivities are further reduced by application of 2 MHz frequency power where selectivities can even approach the 1:1 ratio.

Hydrogen radicals from dissociated HBr can be an effective loss channel of fluorine radicals which reduces the F-atom concentration and hence shifts the equilibrium for the etch process [258]. According to F^+ and Br^+ ion flux measurements in HBr/NF₃ discharges and earlier investigations comprising standard mass spectrometry [258], considerable amounts of adsorbed (fluorine, bromine) species can continuously desorb for several minutes. This was explained by the high porosity of the yttria hard anodized surfaces which significantly enhances the effective surface area for adsorption. The influence of conditioning artefacts (in particular from previous NF₃ plasma clean processes) on discharge parameters and etch processes can be minimized by taking into account high latency times for desorption and choosing appropriate experimental conditions. From that knowledge, and further from comparison of results obtained after NF₃ reactor clean procedures and repeated experiments without additional cleaning (conditioning) it was ensured that such parasitic effects were generally minimized for the experiments conducted in this work.

From investigation of complex HBr/NF₃/O₂/SiCl₄ discharges and results obtained from the previous pure and mixed halogen chemistries, empirical found process settings used for high aspect ratio silicon etching appear already well optimized with regards to the process chemistry. Enhancing silicon etch rates by addition of higher NF₃ admixtures, optimized discharge pressure, feed gas flow rates and magnetic fields, injection of high power levels, application of multi-frequency rf source concepts, plasma pulsing [289,290] and the impact on SiO₂ mask erosion was discussed in detail. From the knowledge obtained here, only minor improvements are expected from such approaches. To gain selectivity by reducing the SiO₂ mask erosion during etching, the initially used SiF₄ precursor was substituted by SiCl₄. From a considerably higher dissociation measured for SiCl₄, this precursor gas allows for a considerably enhanced silicon deposition at the hard mask region during etching [290]. From results of the investigations performed in this work, application of alternative hard mask materials to offer enhanced etch selectivities [290-292], highly erosion resistant sidewall protection layers to provide a reduced sidewall erosion, and novel high-temperature capable electrostatic chuck designs to enable an enhanced volatility of etch species were suggested.

Linear correlations between applied power levels and ion flux/energy can not be assumed since the efficiency of power coupling and dissipation in the plasma will decrease somehow for intermediate to high power levels [258]. Factors like rf matching limits and temperature drift effects were assumed as root cause. Although it has been subject of various discussions, the actual power dissipation for the different applied power levels remains generally unknown here. For example, non-ideal matching networks can absorb a considerable fraction of source power which (due to a lack of precise information from the supplier) remains unknown at this point. The same holds for the unknown power losses through the coaxial feedthrough at 60 MHz which is above the resonance frequency of the reactor geometry. Moreover, knowledge of the dc bias remains limited to a rough approximation from rf probe measurements obtained for 2 MHz frequency. More accurate data for the dc bias, matching network circuit elements and parasitics in the power

transmission circuit would allow for a reasonable estimation of the power utilization for the reactor setup. Regarding current limitations by the very specific discharge settings to estimate the dc bias, this would also require further wafer contact HV measurements for different discharge settings and chemistries.

As reported in literature [13], a significant fraction of fast neutrals can contribute to sputtering where the fast atom flux might even exceed the ion flux. This is believed to also apply here, where typical operating conditions typically involved medium to high pressures, and hence cause a high probability of charge exchange collisions in the sheath region. Since the role of fast neutrals during etching was not investigated in this work, a study of neutral energy distributions should be subject for future work.

From this work, the concept of separate control of ion energy and ion flux by the two frequencies appears to generally work well for the investigated reactor setup. The high frequency component mainly determines ion flux, whereas ion energies are strongly influenced by the low frequency component. In contrast to argon discharges, the 60 MHz frequency determines both ion flux and radical formation from dissociation of the HBr and NF_3 molecular feed gas. Deviations from an ideally separated control of ion flux and energy are caused by interactions between the two frequencies since the rf power sources are coupled to each other in the current setup [258]. By increasing the 60 MHz power, the distribution shifts to lower energies which is attributed to a decreased sheath voltage at higher plasma densities. Compared to argon, contribution of sheath collisions to the low energy part of ion distributions is generally higher in HBr and NF_3 discharges due to a higher mean electron temperature resulting in a higher sheath thickness in HBr and NF_3 [215]. A higher collisionality is further supported by a formation of radicals from an enhanced dissociation of the HBr and NF_3 feed gas that can yield more pronounced scattering in the sheath. Despite the fact that ion energies are mainly determined by the low frequency component, comparably low ion energies are obtained in the ground electrode sheath which is due to the asymmetric discharge geometry. This yields the high frequency component non-negligibly impacting ion energies as well, as was also concluded from measured high neutral gas temperatures and HPSM simulations. An effective gas heating will influence the neutral gas density and hence changes plasma density and sheath thickness.

Appendix A

Heavy particle collision parameters for Ar

Table A.1: Heavy particle collision parameters for argon discharges calculated in this work.

Reaction	Cross section, rate constant	Exponent	Probability
$\text{Ar}^+ + \text{Ar} \rightarrow \text{Ar}^+ + \text{Ar}$	$\sigma_{\text{ES}} = 6.408966 \times 10^{-19} \text{ m}^2$	0.195146	-
	$\sigma_{\text{CX}} = 1.200000 \times 10^{-18} \text{ m}^2$	0.195146	0.5
	$K_{\text{L}} = 6.711179 \times 10^{-16} \text{ m}^3 \text{ s}^{-1}$	-	-
$\text{Ar} + \text{Ar} \rightarrow \text{Ar} + \text{Ar}$	$\sigma_{\text{ES}} = 6.408966 \times 10^{-19} \text{ m}^2$	0.195146	-

Appendix B

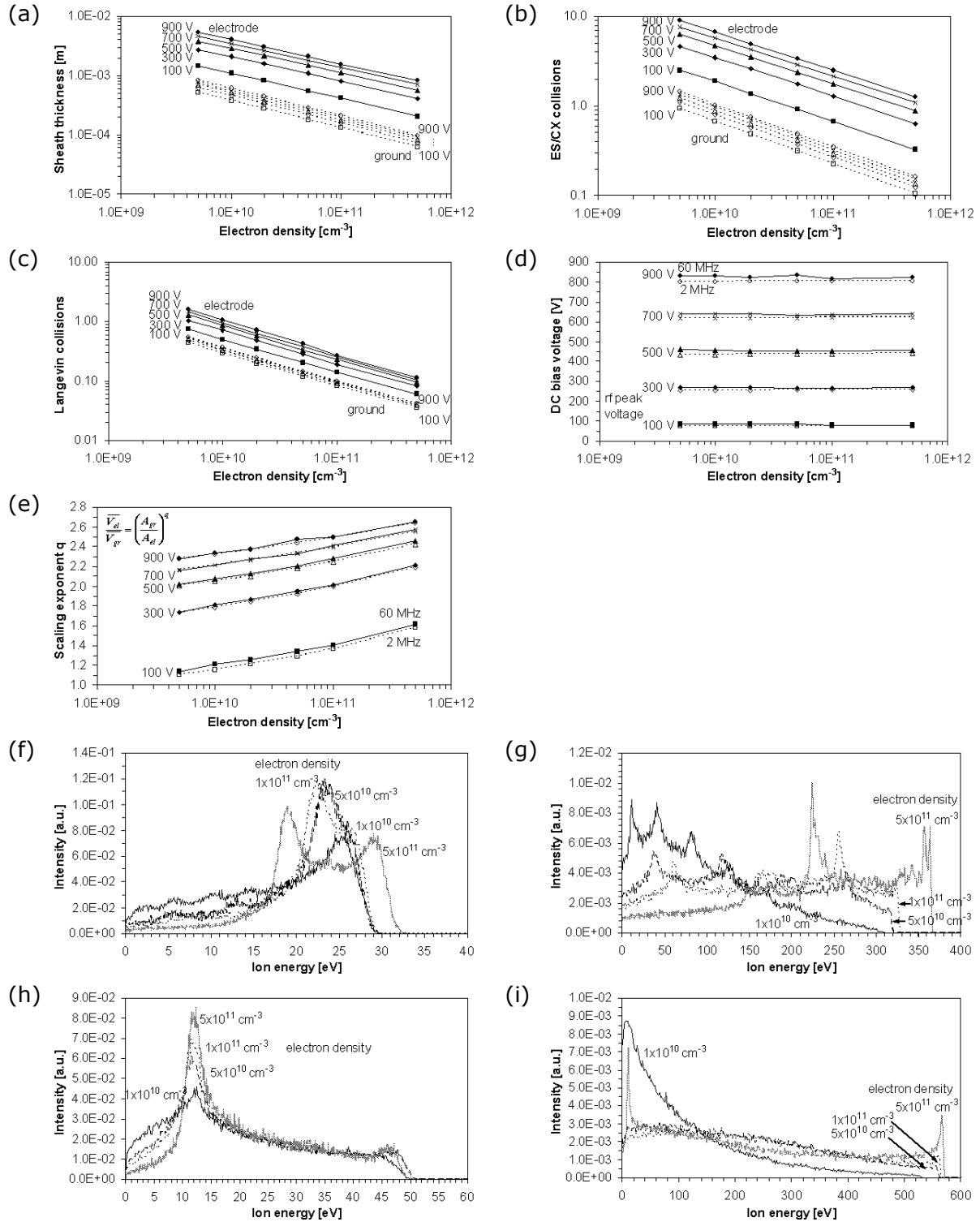
Heavy particle collision parameters for HBr

Table B.1: Heavy particle collision parameters for hydrogen bromide discharges calculated in this work.

Reaction	Cross section, rate constant	Exponent	Probability
$\text{Br}^+ + \text{Br} \rightarrow \text{Br}^+ + \text{Br}$	$\sigma_{\text{ES}} = 7.416564 \times 10^{-19} \text{ m}^2$	0.177043	-
	$\sigma_{\text{CX}} = 1.800000 \times 10^{-18} \text{ m}^2$	0.177043	0.5
	$K_{\text{L}} = 6.470907 \times 10^{-16} \text{ m}^3 \text{ s}^{-1}$	-	-
$\text{Br} + \text{Br} \rightarrow \text{Br} + \text{Br}$	$\sigma_{\text{ES}} = 7.416564 \times 10^{-19} \text{ m}^2$	0.177043	-
$\text{Br}^+ + \text{HBr} \rightarrow \text{Br}^+ + \text{HBr}$	$\sigma_{\text{ES}} = 7.416564 \times 10^{-19} \text{ m}^2$	0.177043	-
	$\sigma_{\text{CX}} = 7.416564 \times 10^{-19} \text{ m}^2$	0.177043	0.0
	$K_{\text{L}} = 7.016394 \times 10^{-16} \text{ m}^3 \text{ s}^{-1}$	-	-
$\text{HBr}^+ + \text{Br} \rightarrow \text{HBr}^+ + \text{Br}$	$\sigma_{\text{ES}} = 7.416564 \times 10^{-19} \text{ m}^2$	0.177043	-
	$\sigma_{\text{CX}} = 7.416564 \times 10^{-19} \text{ m}^2$	0.177043	0.0
	$K_{\text{L}} = 6.449268 \times 10^{-16} \text{ m}^3 \text{ s}^{-1}$	-	-
$\text{Br} + \text{HBr} \rightarrow \text{Br} + \text{HBr}$	$\sigma_{\text{ES}} = 7.416564 \times 10^{-19} \text{ m}^2$	0.177043	-
$\text{Br}^+ + \text{H}_2 \rightarrow \text{Br}^+ + \text{H}_2$	$\sigma_{\text{ES}} = 5.313507 \times 10^{-19} \text{ m}^2$	0.252413	-
	$\sigma_{\text{CX}} = 5.313507 \times 10^{-19} \text{ m}^2$	0.252413	0.0
	$K_{\text{L}} = 1.517218 \times 10^{-15} \text{ m}^3 \text{ s}^{-1}$	-	-
$\text{H}_2^+ + \text{Br} \rightarrow \text{H}_2^+ + \text{Br}$	$\sigma_{\text{ES}} = 5.313507 \times 10^{-19} \text{ m}^2$	0.252413	-
	$\sigma_{\text{CX}} = 5.313507 \times 10^{-19} \text{ m}^2$	0.252413	0.0
	$K_{\text{L}} = 2.927898 \times 10^{-15} \text{ m}^3 \text{ s}^{-1}$	-	-
$\text{Br} + \text{H}_2 \rightarrow \text{Br} + \text{H}_2$	$\sigma_{\text{ES}} = 5.313507 \times 10^{-19} \text{ m}^2$	0.252413	-
$\text{Br}^+ + \text{Br}_2 \rightarrow \text{Br}^+ + \text{Br}_2$	$\sigma_{\text{ES}} = 1.483313 \times 10^{-18} \text{ m}^2$	0.177043	-
	$\sigma_{\text{CX}} = 1.483313 \times 10^{-18} \text{ m}^2$	0.177043	0.0
	$K_{\text{L}} = 8.500413 \times 10^{-16} \text{ m}^3 \text{ s}^{-1}$	-	-
$\text{Br}_2^+ + \text{Br} \rightarrow \text{Br}_2^+ + \text{Br}$	$\sigma_{\text{ES}} = 1.483313 \times 10^{-18} \text{ m}^2$	0.177043	-
	$\sigma_{\text{CX}} = 1.483313 \times 10^{-18} \text{ m}^2$	0.177043	0.0
	$K_{\text{L}} = 5.603010 \times 10^{-16} \text{ m}^3 \text{ s}^{-1}$	-	-
$\text{Br} + \text{Br}_2 \rightarrow \text{Br} + \text{Br}_2$	$\sigma_{\text{ES}} = 1.483313 \times 10^{-18} \text{ m}^2$	0.177043	-

Appendix C

HPSM simulation results for Ar



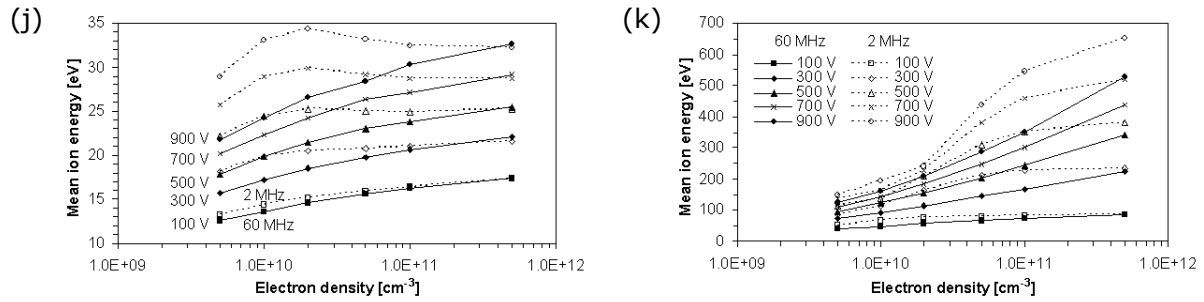
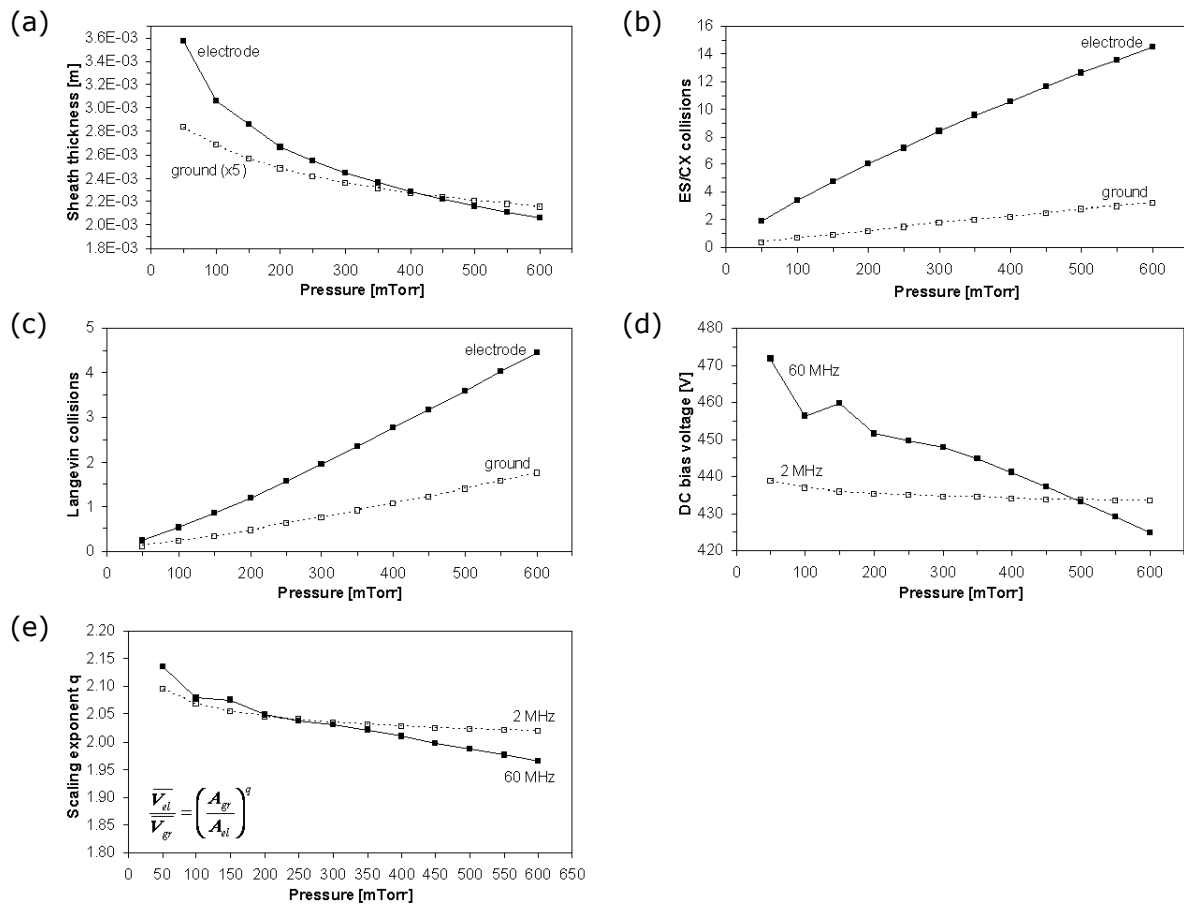


Figure C.1: HPSM simulation results for variation of electron density and rf peak voltage in Ar discharges (a) sheath thickness in front of ground (open symbols with dotted lines) and powered electrode (solid symbols with continuous lines); (b) number of elastic/charge exchange collisions for Ar⁺ ions in the sheath region; (c) number of Langevin collisions for Ar⁺ ions in the sheath region; (d) dc bias voltage for 60 MHz (solid symbols with continuous lines) and 2 MHz Ar discharges (open symbols with dotted lines); (e) scaling exponent q for equation (1.6) for 60 MHz (solid symbols with continuous lines) and 2 MHz Ar discharges (open symbols with dotted lines); Ar⁺ IEDFs at (f) ground electrode and (g) powered electrode for 60 MHz Ar discharges; Ar⁺ IEDFs at (h) ground electrode and (i) powered electrode for 2 MHz Ar discharges; Ar⁺ mean energies at (j) ground electrode and (k) powered electrode for 60 MHz and 2 MHz Ar discharges. Ar⁺ IEDFs in (f)-(i) are plotted for 150 mTorr, 300 V rf peak voltage, 2.58 eV electron temperature, 500 K neutral gas temperature, no magnetic field.



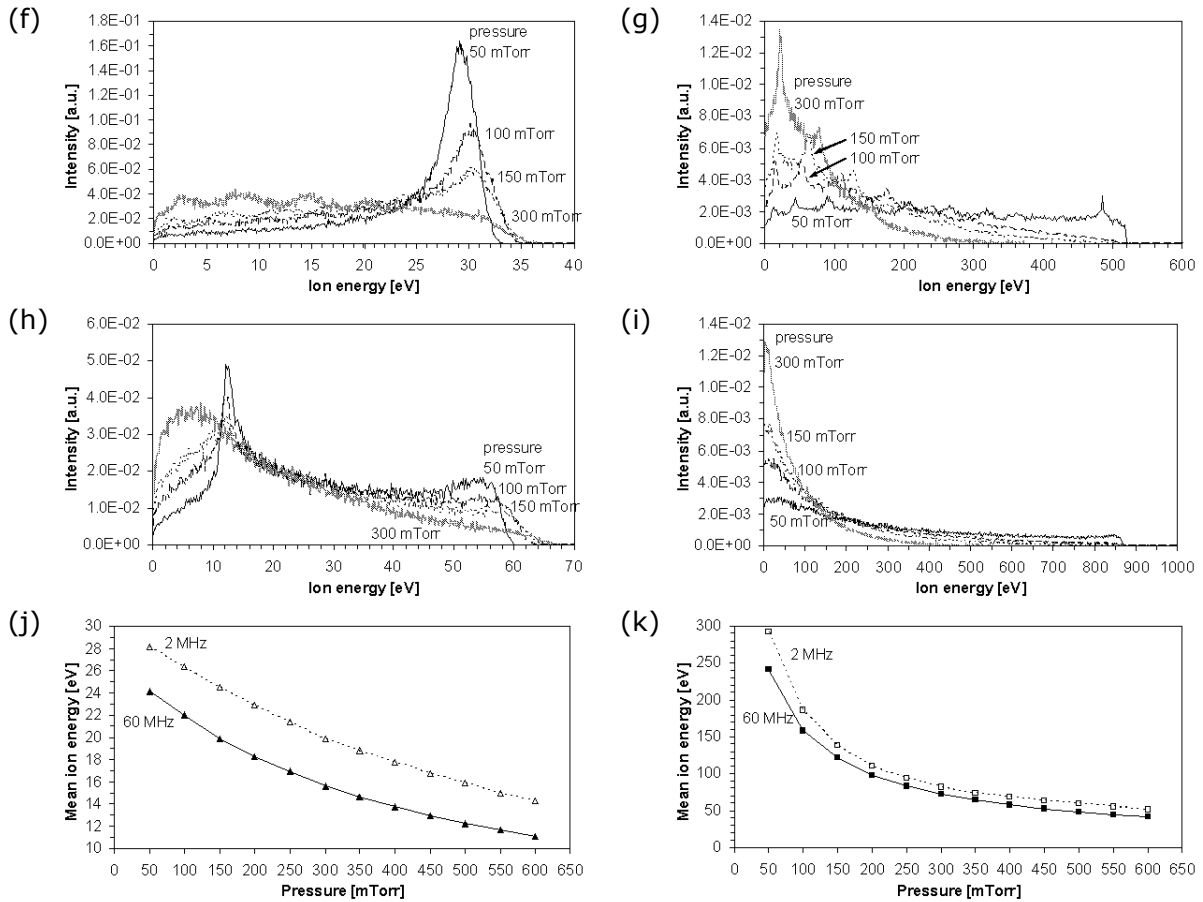
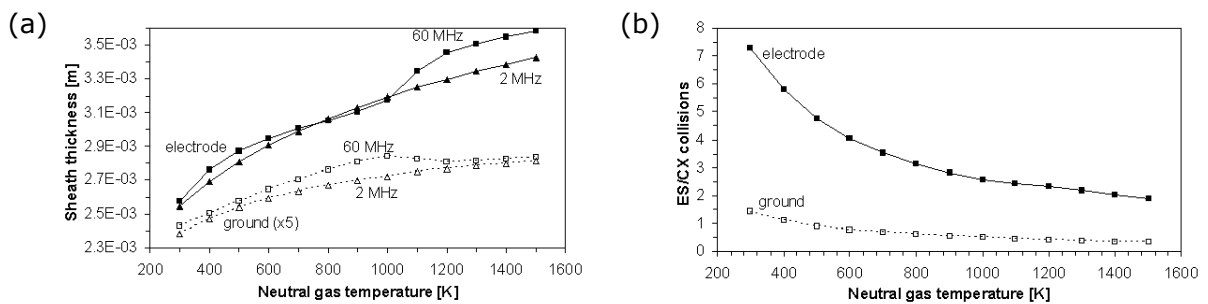


Figure C.2: HPSM simulation results for variation of pressure in Ar discharges (a) sheath thickness in front of ground (open squares with dotted lines, values have been multiplied by a factor of five) and powered electrode (solid squares with continuous lines); (b) number of elastic/charge exchange collisions for Ar^+ ions in the sheath region; (c) number of Langevin collisions for Ar^+ ions in the sheath region; (d) dc bias voltage for 60 MHz (solid squares with continuous lines) and 2 MHz Ar discharges (open squares with dotted lines); (e) scaling exponent q for equation (1.6) for 60 MHz (solid squares with continuous lines) and 2 MHz Ar discharges (open squares with dotted lines); Ar^+ IEDFs at (f) ground electrode and (g) powered electrode for 60 MHz Ar discharges; Ar^+ IEDFs at (h) ground electrode and (i) powered electrode for 2 MHz Ar discharges; Ar^+ mean energies at (j) ground electrode and (k) powered electrode for 60 MHz and 2 MHz Ar discharges. Ar^+ IEDFs in (f)-(i) are plotted for 500 V rf peak voltage, 2.58 eV electron temperature, $1 \times 10^{10} \text{ cm}^{-3}$ electron density, 500 K neutral gas temperature, no magnetic field.



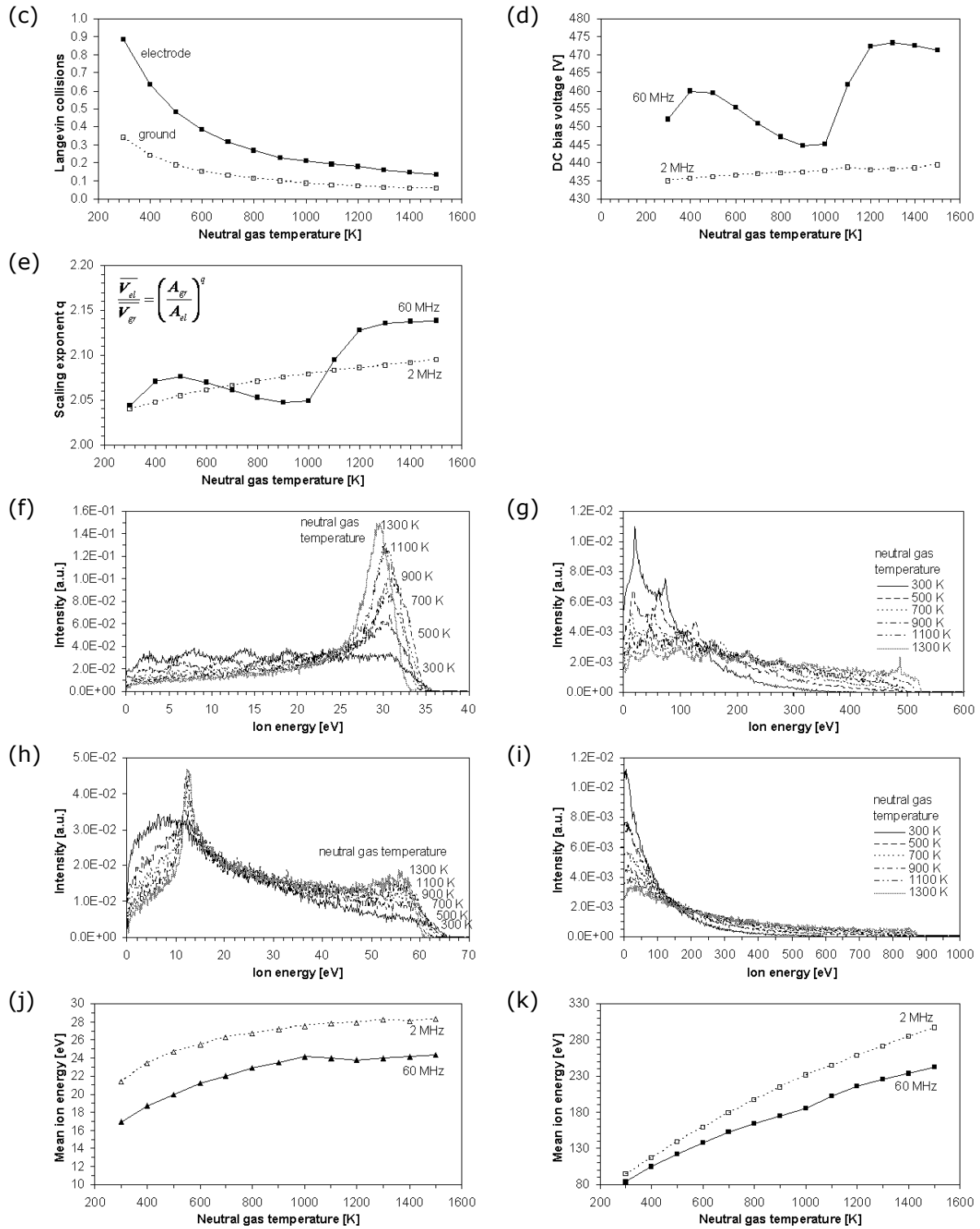
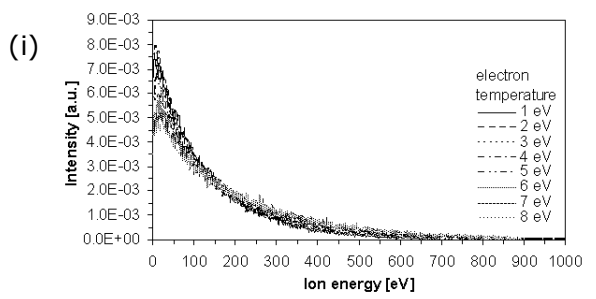
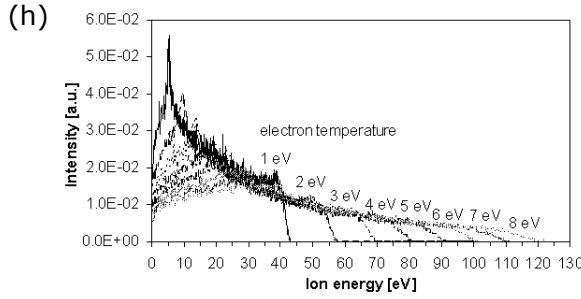
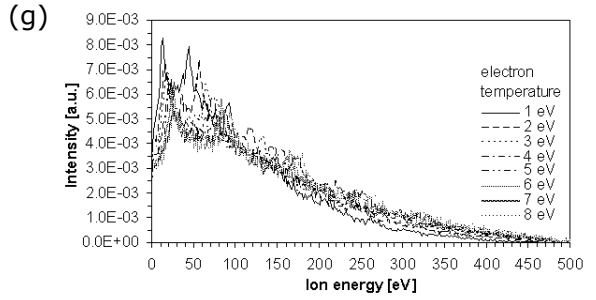
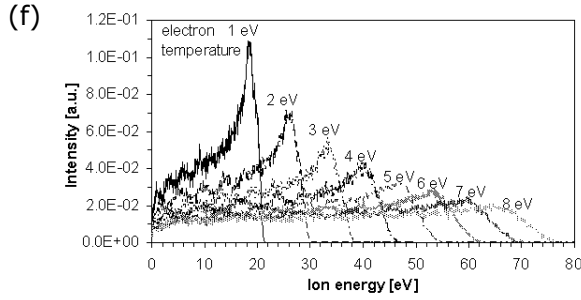
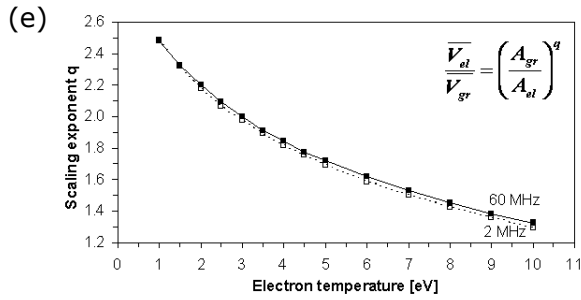
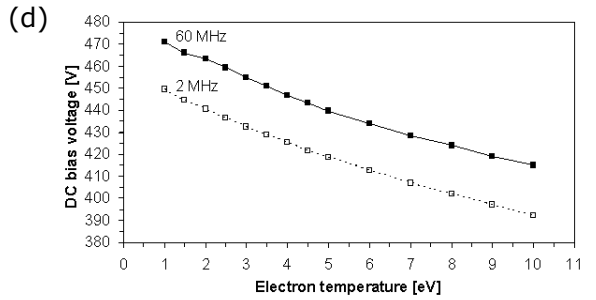
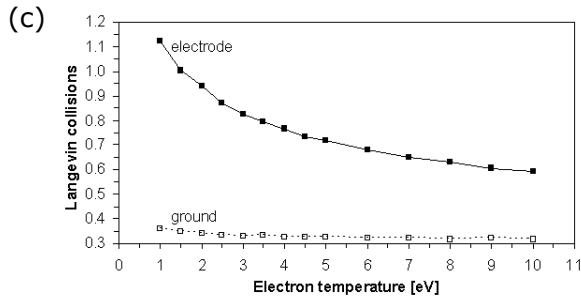
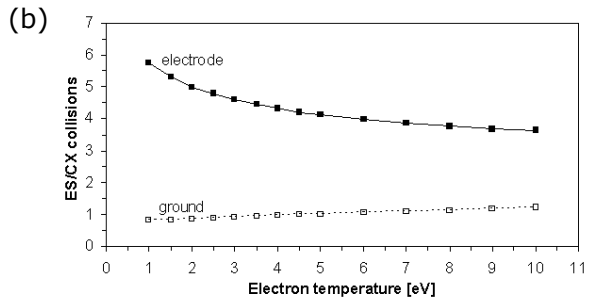
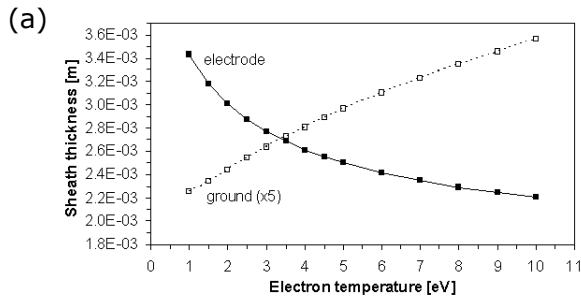


Figure C.3: HPSM simulation results for variation of neutral gas temperature in Ar discharges (a) sheath thickness in front of ground (open symbols with dotted lines, values have been multiplied by a factor of five) and powered electrode (solid symbols with continuous lines); (b) number of elastic/charge exchange collisions for Ar^+ ions in the sheath region; (c) number of Langevin collisions for Ar^+ ions in the sheath region; (d) dc bias voltage for 60 MHz (solid squares with continuous lines) and 2 MHz Ar discharges (open squares with dotted lines); (e) scaling exponent q for equation (1.6) for 60 MHz (solid squares with continuous lines) and 2 MHz Ar discharges (open squares with dotted lines); Ar^+ IEDFs at (f) ground electrode and (g) powered electrode for 60 MHz Ar discharges; Ar^+ IEDFs at (h) ground electrode and (i) powered electrode for 2 MHz Ar discharges; Ar^+ mean energies at (j)

ground electrode and (k) powered electrode for 60 MHz and 2 MHz Ar discharges. Ar⁺ IEDFs in (f)-(i) are plotted for 150 mTorr, 500 V rf peak voltage, 2.58 eV electron temperature, 1×10¹⁰ cm⁻³ electron density, no magnetic field.



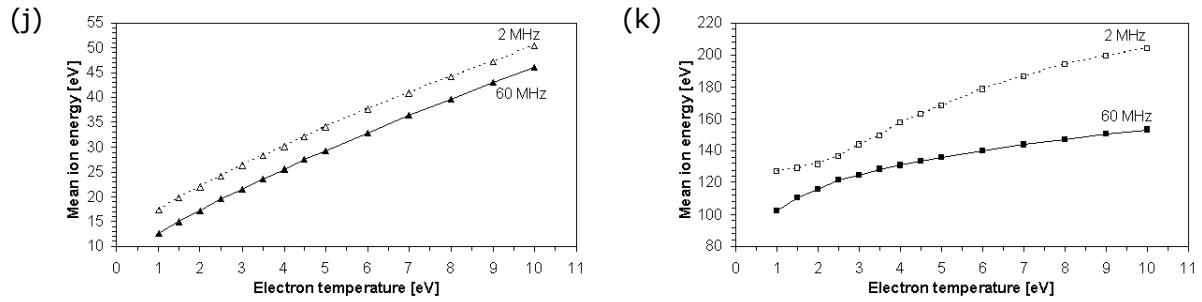
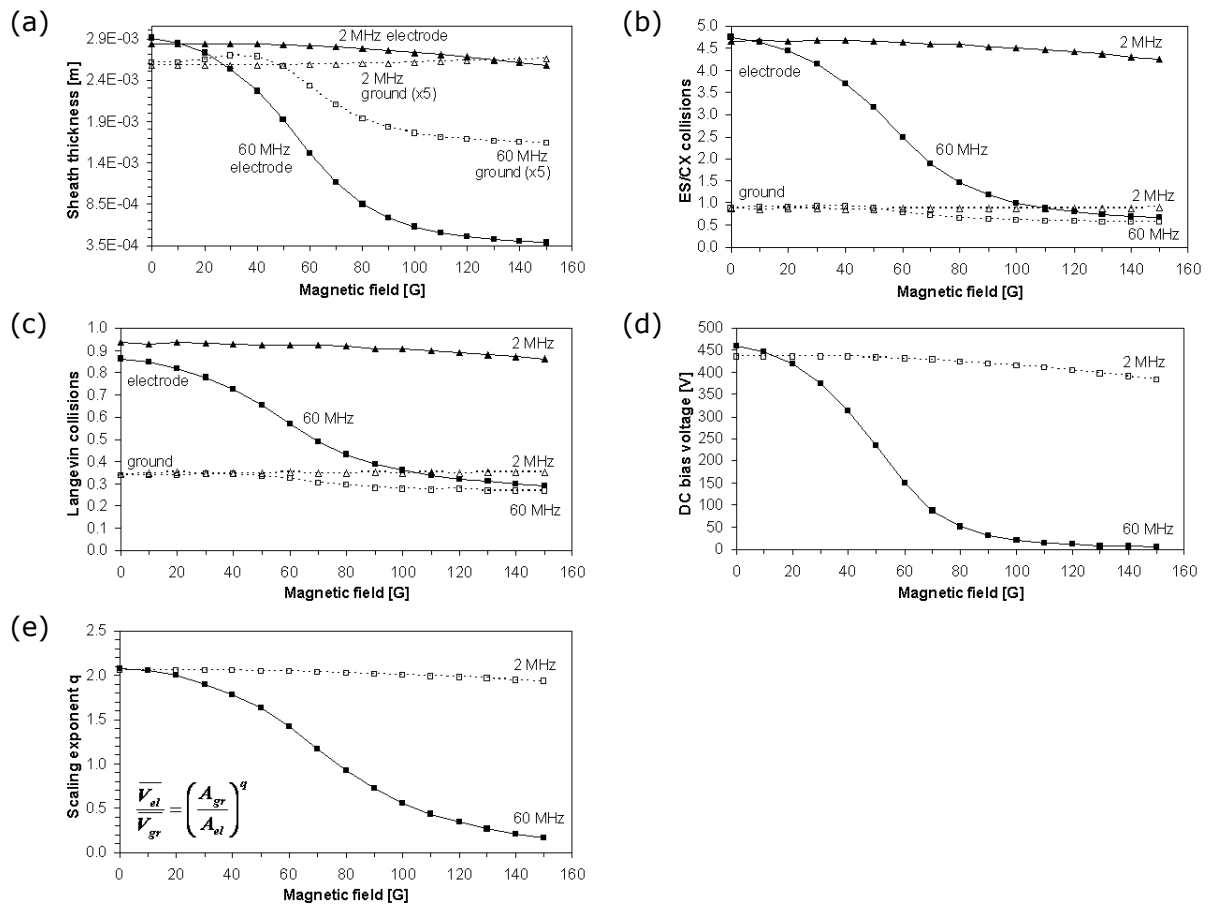


Figure C.4: HPSM simulation results for variation of electron temperature in Ar discharges (a) sheath thickness in front of ground (open squares with dotted lines, values have been multiplied by a factor of five) and powered electrode (solid squares with continuous lines); (b) number of elastic/charge exchange collisions for Ar^+ ions in the sheath region; (c) number of Langevin collisions for Ar^+ ions in the sheath region; (d) dc bias voltage for 60 MHz (solid squares with continuous lines) and 2 MHz Ar discharges (open squares with dotted lines); (e) scaling exponent q for equation (1.6) for 60 MHz (solid squares with continuous lines) and 2 MHz Ar discharges (open squares with dotted lines); Ar^+ IEDFs at (f) ground electrode and (g) powered electrode for 60 MHz Ar discharges; Ar^+ IEDFs at (h) ground electrode and (i) powered electrode for 2 MHz Ar discharges; Ar^+ mean energies at (j) ground electrode and (k) powered electrode for 60 MHz and 2 MHz Ar discharges. Ar^+ IEDFs in (f)-(i) are plotted for 150 mTorr, 500 V rf peak voltage, $1 \times 10^{10} \text{ cm}^{-3}$ electron density, 500 K neutral gas temperature, no magnetic field.



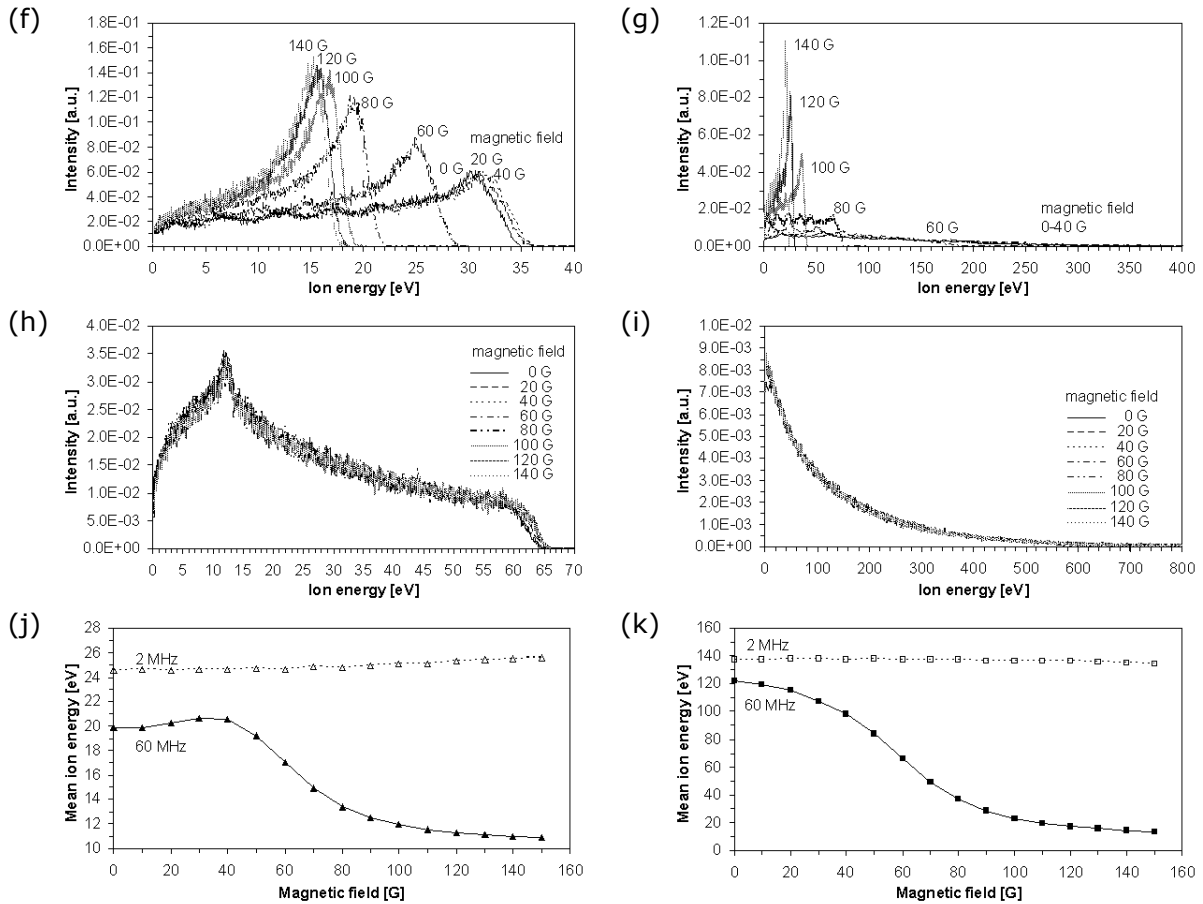
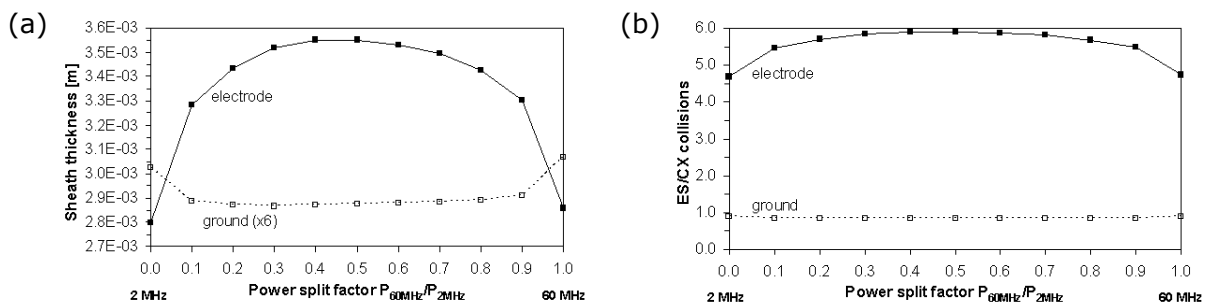


Figure C.5: HPSM simulation results for variation of magnetic field in Ar discharges (a) sheath thickness in front of ground (open symbols with dotted lines, values have been multiplied by a factor of five) and powered electrode (solid symbols with continuous lines); (b) number of elastic/charge exchange collisions for Ar^+ ions in the sheath region; (c) number of Langevin collisions for Ar^+ ions in the sheath region; (d) dc bias voltage for 60 MHz (solid squares with continuous lines) and 2 MHz Ar discharges (open squares with dotted lines); (e) scaling exponent q for equation (1.6) for 60 MHz (solid squares with continuous lines) and 2 MHz Ar discharges (open squares with dotted lines); Ar^+ IEDFs at (f) ground electrode and (g) powered electrode for 60 MHz Ar discharges; Ar^+ IEDFs at (h) ground electrode and (i) powered electrode for 2 MHz Ar discharges; Ar^+ mean energies at (j) ground electrode and (k) powered electrode for 60 MHz and 2 MHz Ar discharges. Ar^+ IEDFs in (f)-(i) are plotted for 150 mTorr, 500 V rf peak voltage, $1 \times 10^{10} \text{ cm}^{-3}$ electron density, 2.58 eV electron temperature, 500 K neutral gas temperature.



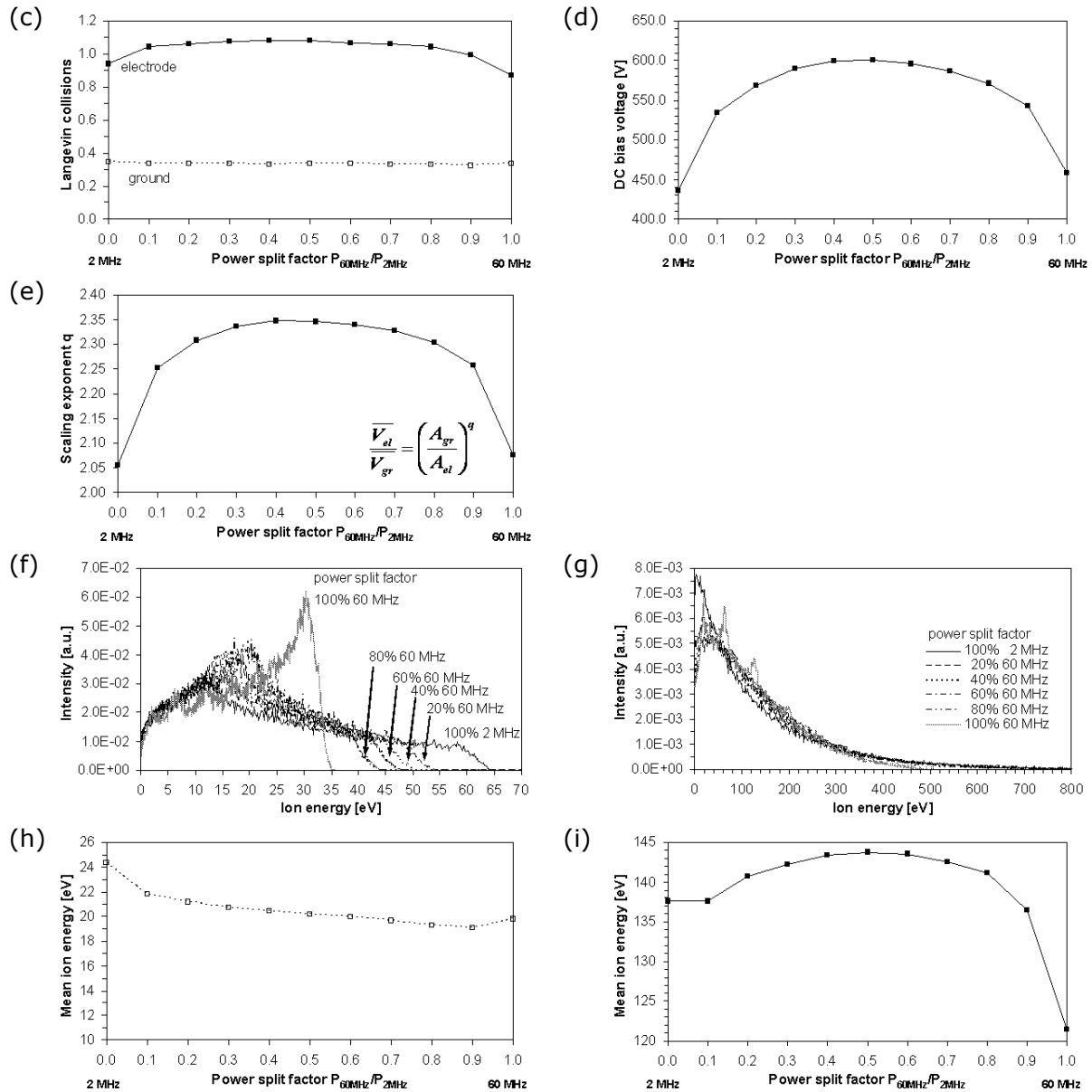
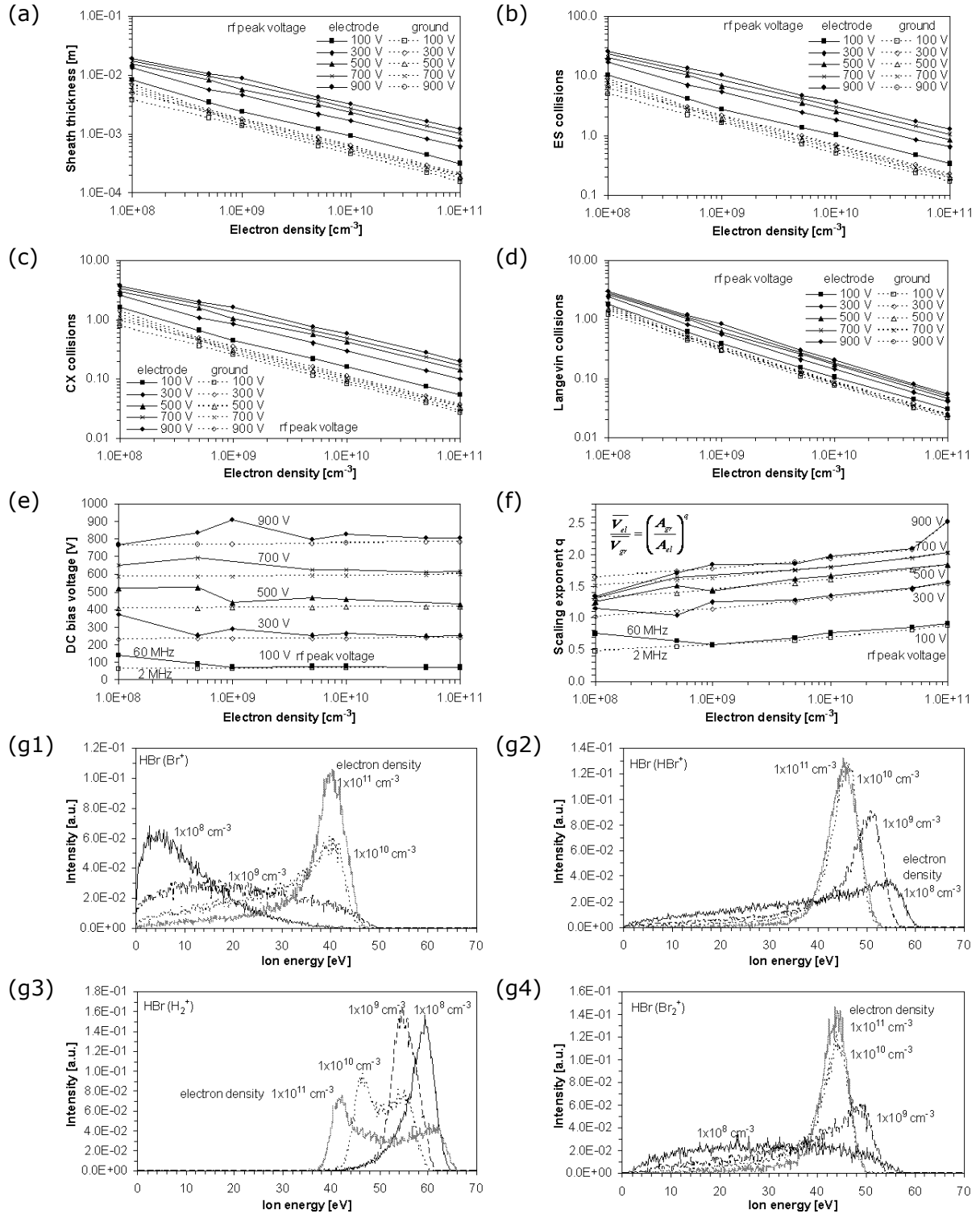
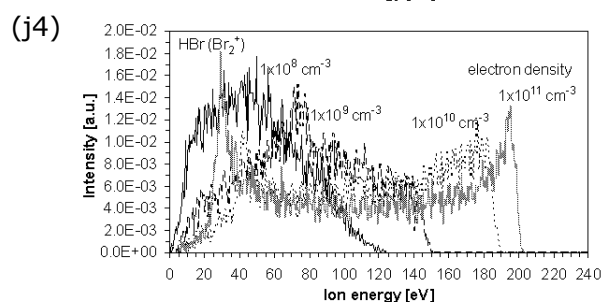
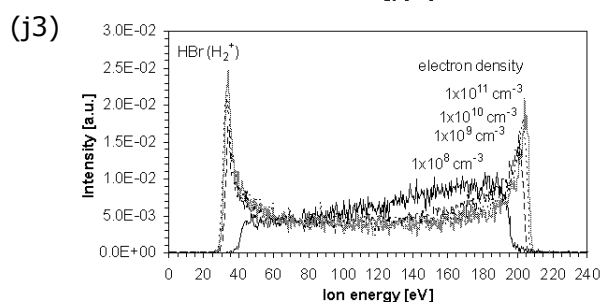
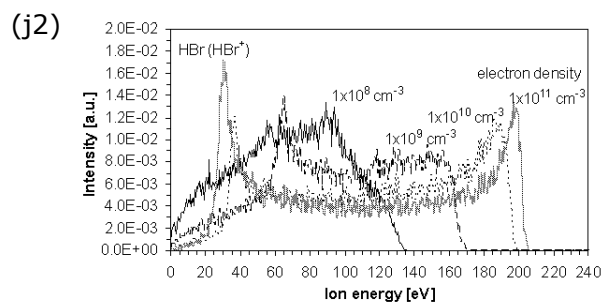
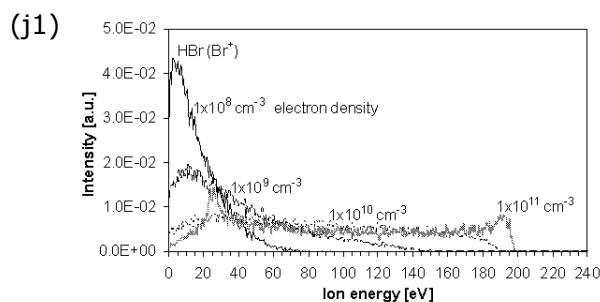
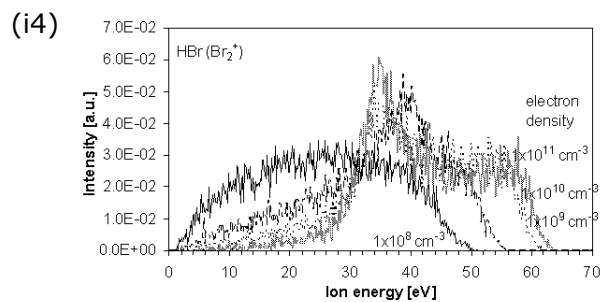
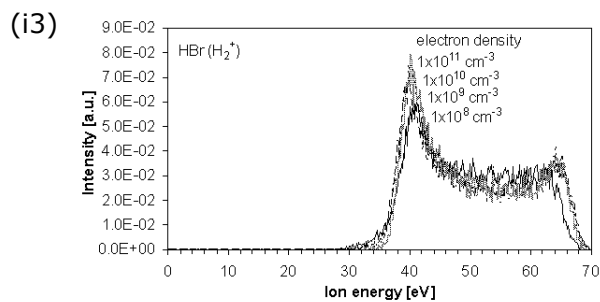
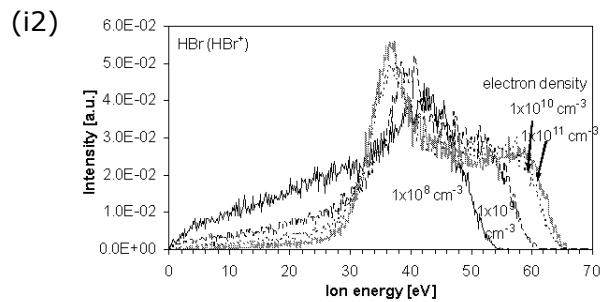
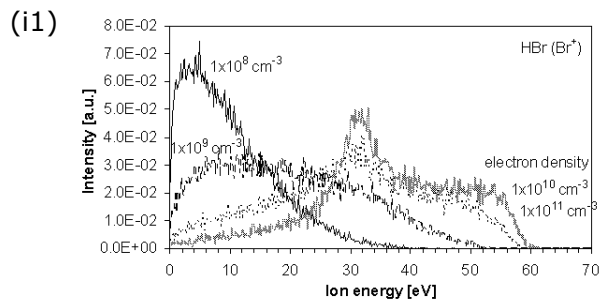
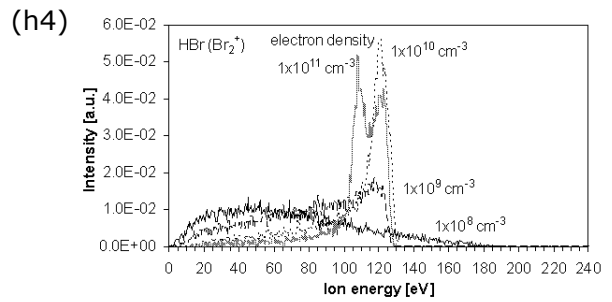
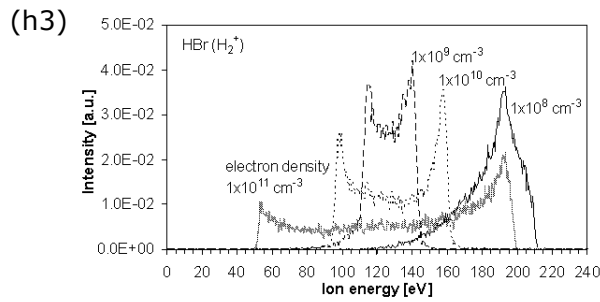
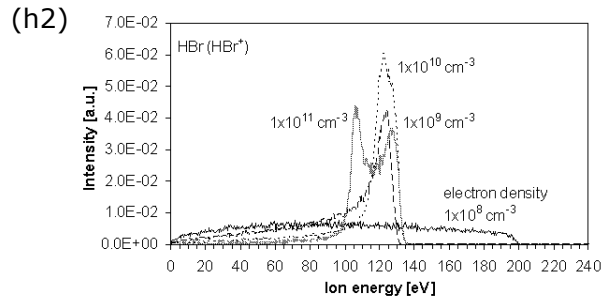
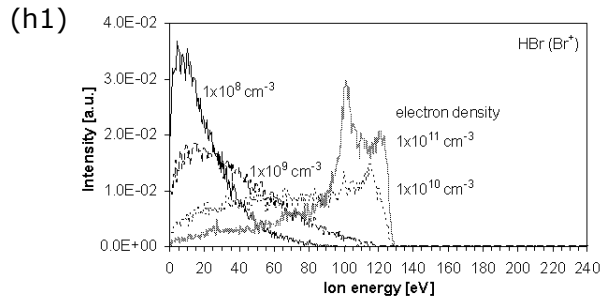


Figure C.6: HPSM simulation results for variation of 60+2 MHz frequency mix in Ar discharges (a) sheath thickness in front of ground (open squares with dotted lines, values have been multiplied by a factor of six) and powered electrode (solid squares with continuous lines); (b) number of elastic/charge exchange collisions for Ar⁺ ions in the sheath region; (c) number of Langevin collisions for Ar⁺ ions in the sheath region; (d) dc bias voltage; (e) scaling exponent q for equation (1.6); Ar⁺ IEDFs at (f) ground electrode and (g) powered electrode for 60+2 MHz dual frequency Ar discharges; Ar⁺ mean energies at (h) ground electrode and (i) powered electrode for 60 MHz and 2 MHz Ar discharges. Ar⁺ IEDFs in (f),(g) are plotted for 150 mTorr, 500 V rf peak voltage, $1 \times 10^{10} \text{ cm}^{-3}$ electron density, 2.58 eV electron temperature, 500 K neutral gas temperature, no magnetic field.

Appendix D

HPSM simulation results for HBr





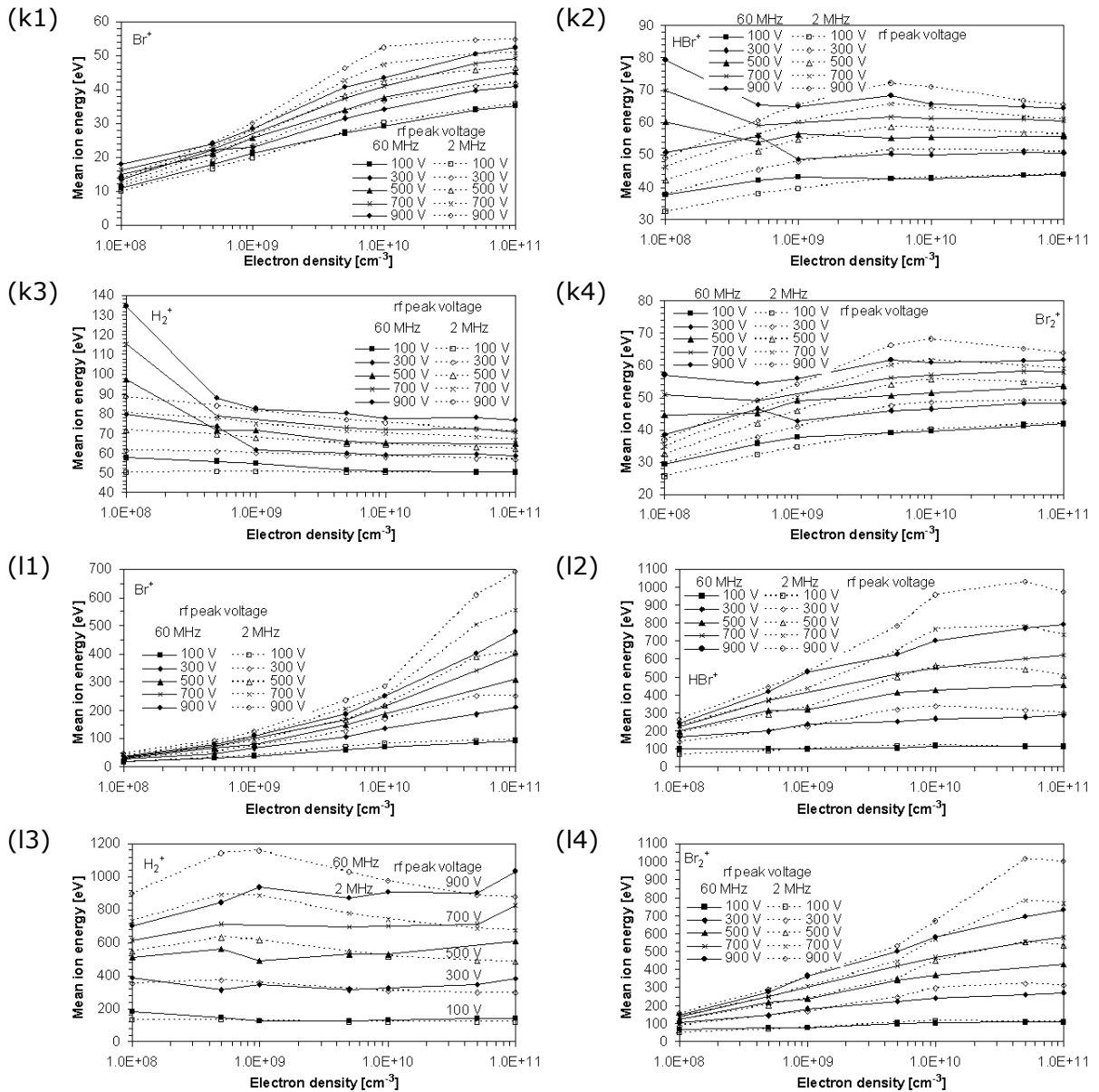
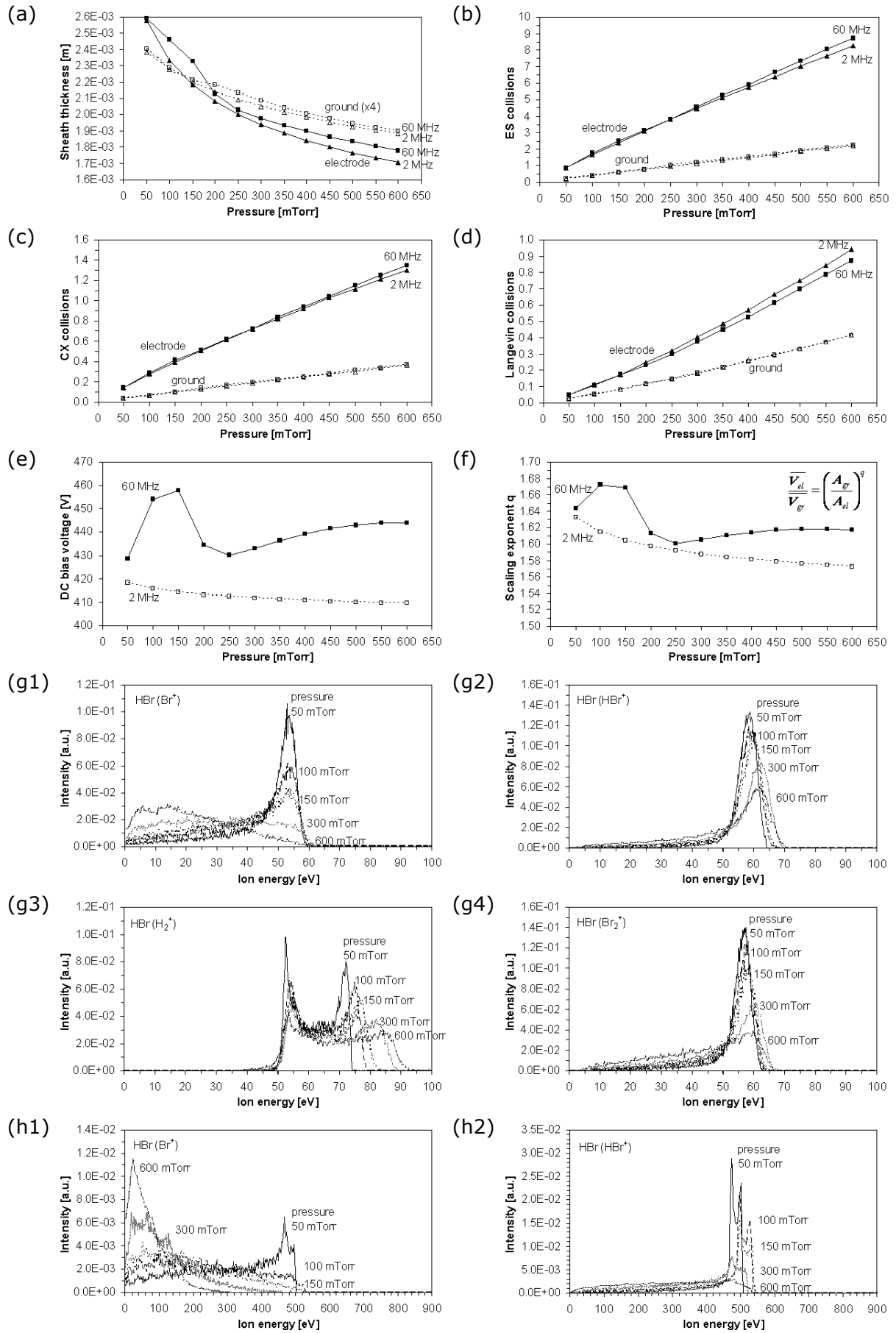
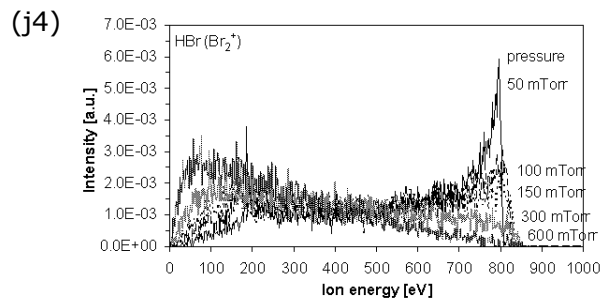
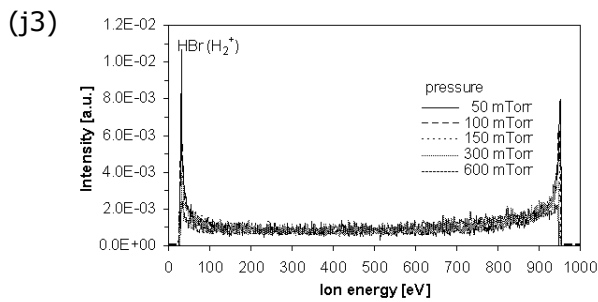
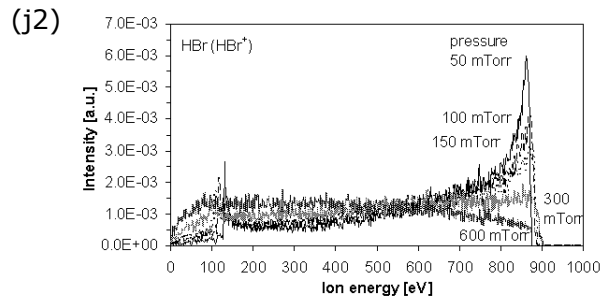
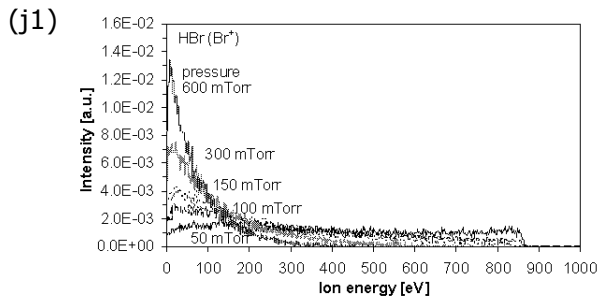
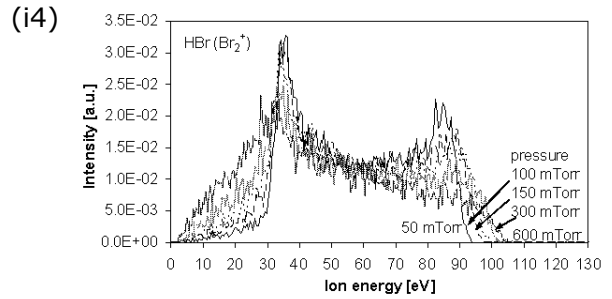
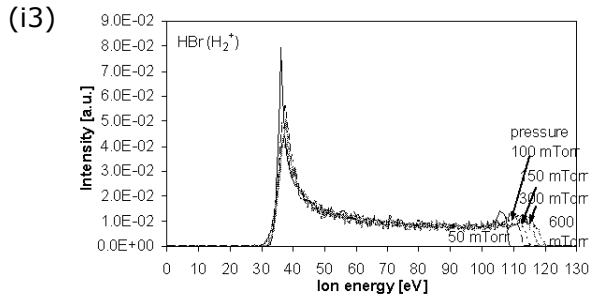
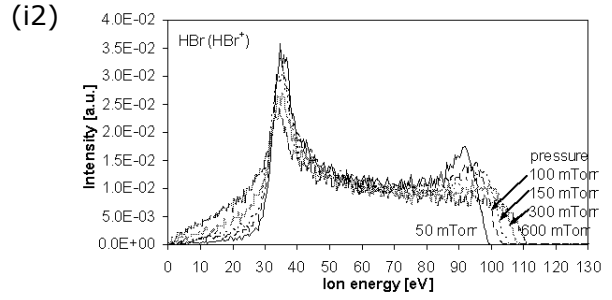
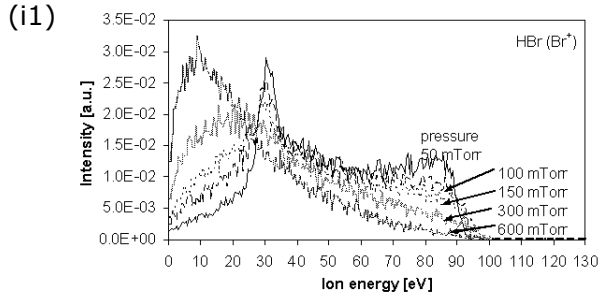
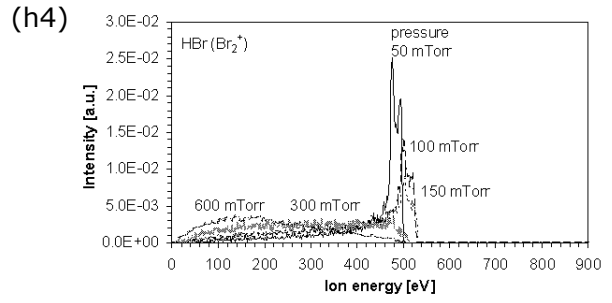
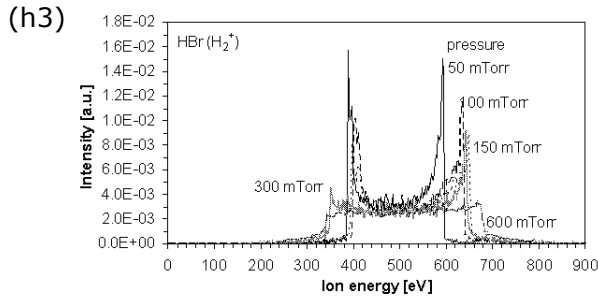


Figure D.1: HPSM simulation results for variation of electron density and rf peak voltage in HBr discharges (a) sheath thickness in front of ground (open symbols with dotted lines) and powered electrode (solid symbols with continuous lines); (b) number of elastic collisions, (c) charge exchange collisions, and (d) Langevin collisions for ions in the sheath region; (e) dc bias voltage for 60 MHz (solid symbols with continuous lines) and 2 MHz HBr discharges (open symbols with dotted lines); (f) scaling exponent q for equation (1.6) for 60 MHz (solid symbols with continuous lines) and 2 MHz HBr discharges (open symbols with dotted lines); IEDFs at the ground electrode for (g1) Br⁺, (g2) HBr⁺, (g3) H₂⁺, and (g4) Br₂⁺ for 60 MHz HBr discharges; IEDFs at the powered electrode for (h1) Br⁺, (h2) HBr⁺, (h3) H₂⁺, and (h4) Br₂⁺ for 60 MHz HBr discharges; IEDFs at the ground electrode for (i1) Br⁺, (i2) HBr⁺, (i3) H₂⁺, and (i4) Br₂⁺ for 2 MHz HBr discharges; IEDFs at the powered electrode for (j1) Br⁺, (j2) HBr⁺, (j3) H₂⁺, and (j4) Br₂⁺ for 2 MHz HBr discharges; mean energies for (k1) Br⁺, (k2) HBr⁺, (k3) H₂⁺, and (k4) Br₂⁺ ions at the ground electrode for 60 MHz and 2 MHz HBr discharges; mean energies for (l1) Br⁺, (l2) HBr⁺, (l3) H₂⁺, and (l4) Br₂⁺ ions at the powered electrode for 60 MHz and 2 MHz HBr discharges. IEDFs in (g1)-(j4) are plotted for 150 mTorr, 100 V rf peak voltage, 6.32 eV electron temperature, 500 K neutral gas temperature, no magnetic field.





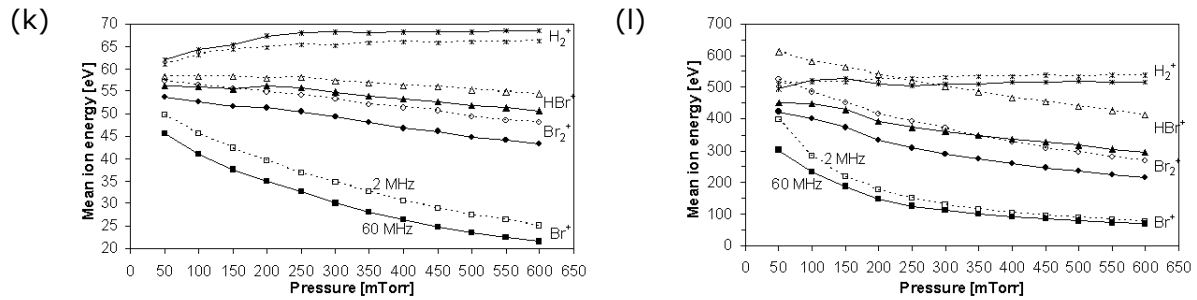
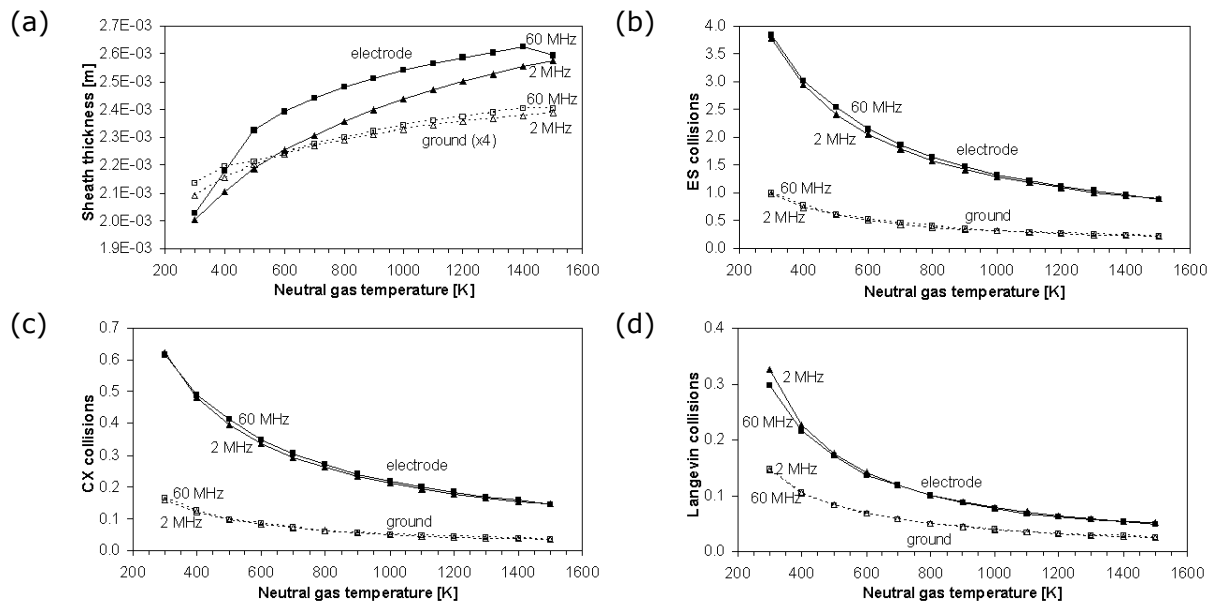
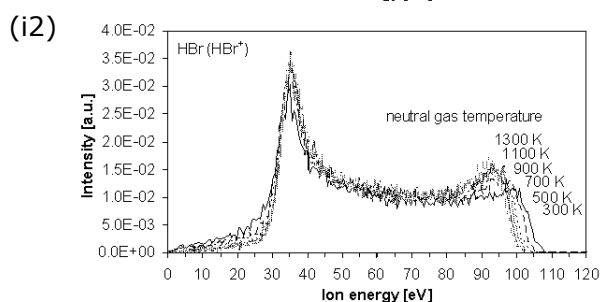
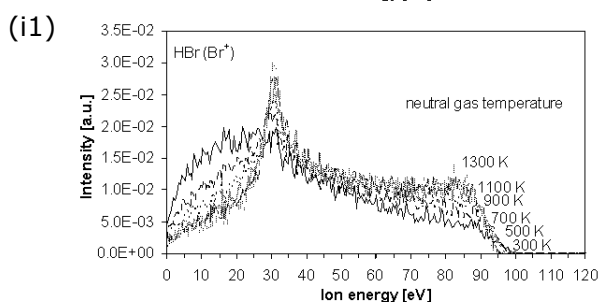
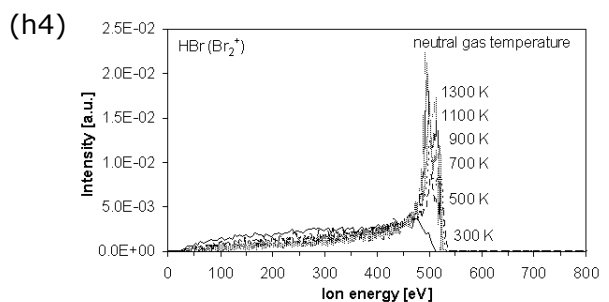
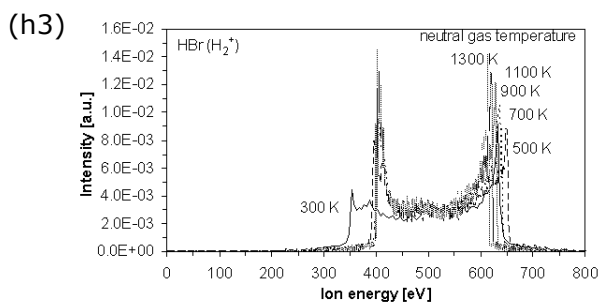
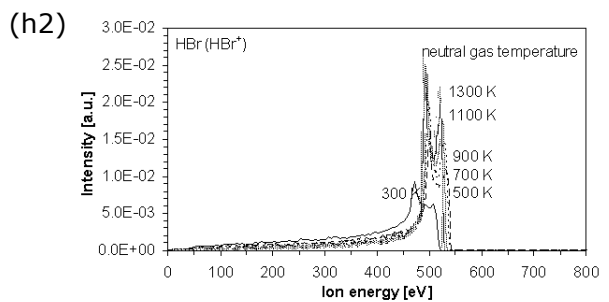
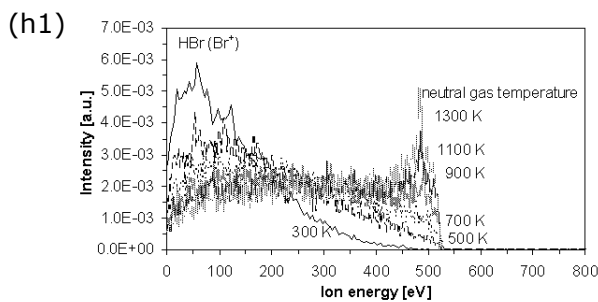
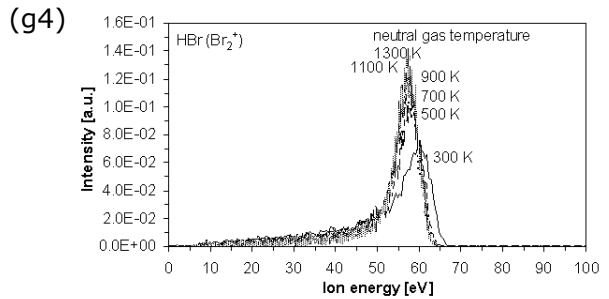
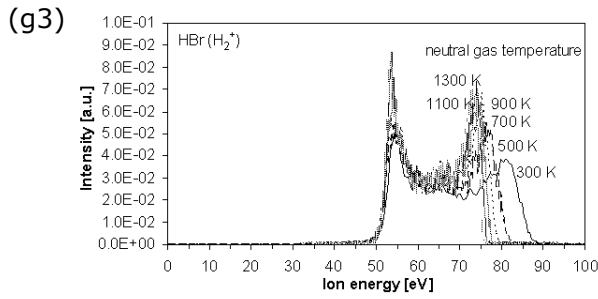
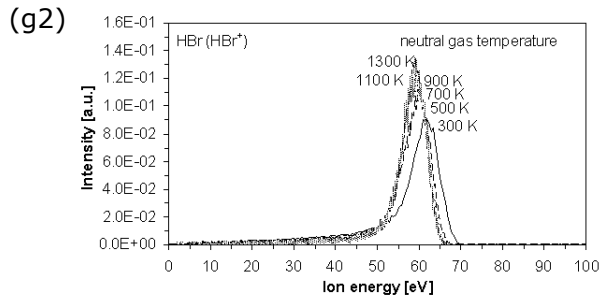
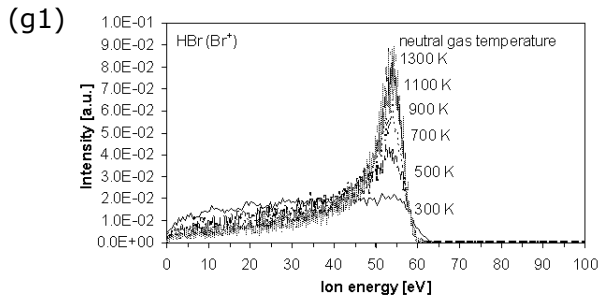
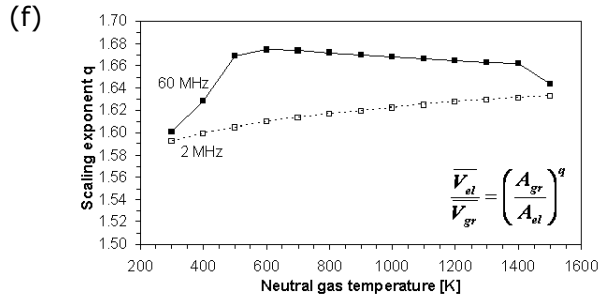
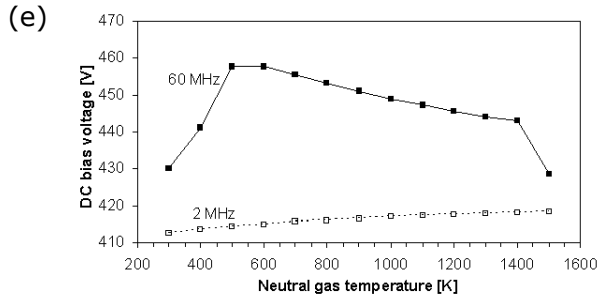


Figure D.2: HPSM simulation results for variation of pressure in HBr discharges (a) sheath thickness in front of ground (open symbols with dotted lines, values have been multiplied by a factor of four) and powered electrode (solid symbols with continuous lines); (b) number of elastic collisions, (c) charge exchange collisions, and (d) Langevin collisions for ions in the sheath region; (e) dc bias voltage for 60 MHz (solid symbols with continuous lines) and 2 MHz HBr discharges (open symbols with dotted lines); (f) scaling exponent q for equation (1.6) for 60 MHz (solid symbols with continuous lines) and 2 MHz HBr discharges (open symbols with dotted lines); IEDFs at the ground electrode for (g1) Br^+ , (g2) HBr^+ , (g3) H_2^+ , and (g4) Br_2^+ for 60 MHz HBr discharges; IEDFs at the powered electrode for (h1) Br^+ , (h2) HBr^+ , (h3) H_2^+ , and (h4) Br_2^+ for 60 MHz HBr discharges; IEDFs at the ground electrode for (i1) Br^+ , (i2) HBr^+ , (i3) H_2^+ , and (i4) Br_2^+ for 2 MHz HBr discharges; IEDFs at the powered electrode for (j1) Br^+ , (j2) HBr^+ , (j3) H_2^+ , and (j4) Br_2^+ for 2 MHz HBr discharges; (k) mean energies for Br^+ , HBr^+ , H_2^+ and Br_2^+ ions at the ground electrode for 60 MHz and 2 MHz HBr discharges; (l) mean energies for Br^+ , HBr^+ , H_2^+ and Br_2^+ ions at the powered electrode for 60 MHz and 2 MHz HBr discharges. IEDFs in (g1)-(j4) are plotted for 150 mTorr, 500 V rf peak voltage, 6.32 eV electron temperature, $1 \times 10^{10} \text{ cm}^{-3}$ electron density, 500 K neutral gas temperature, no magnetic field.





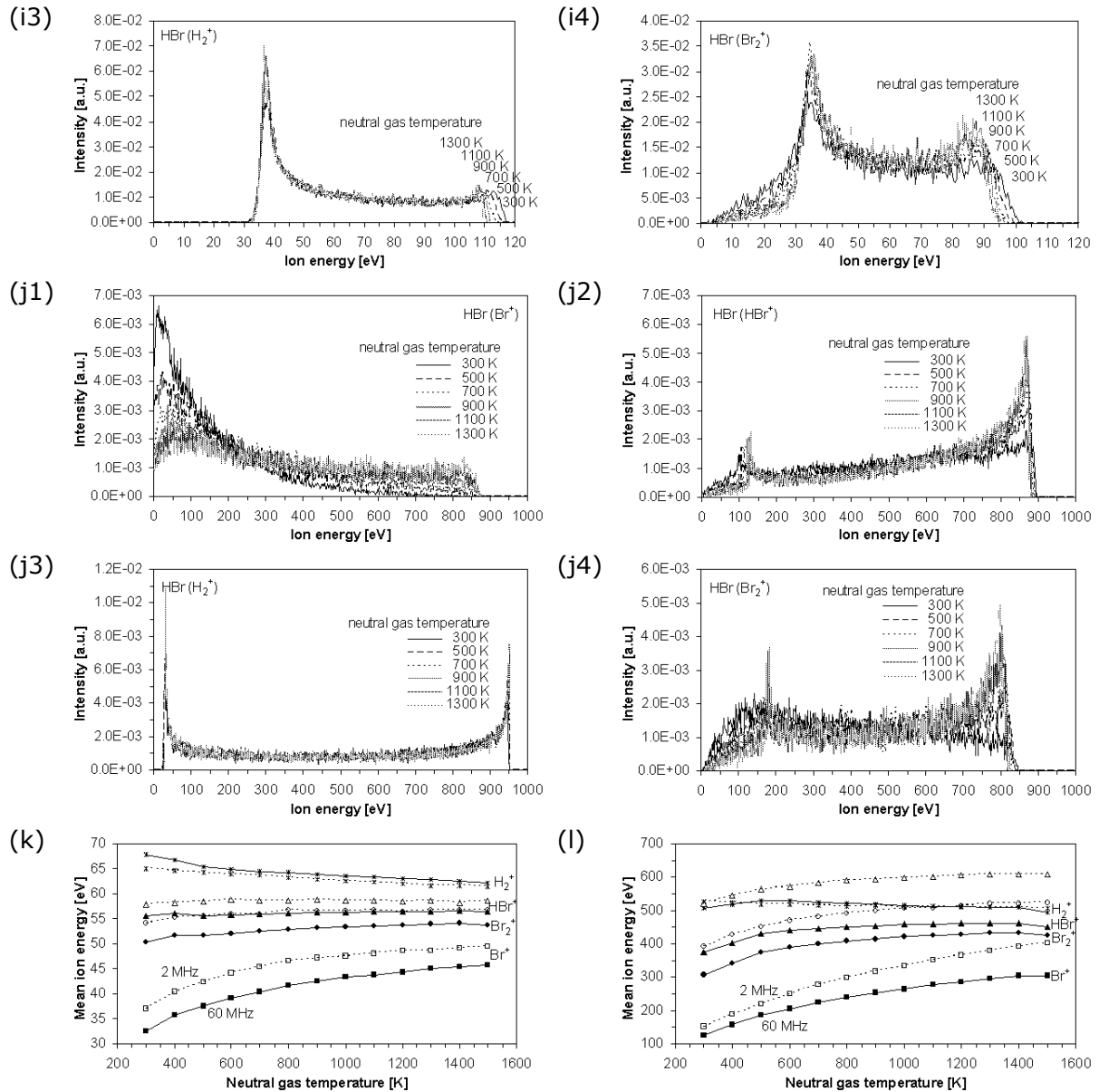
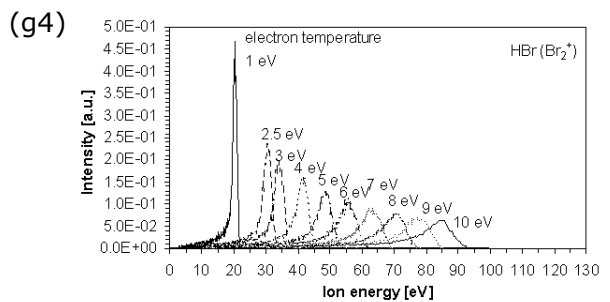
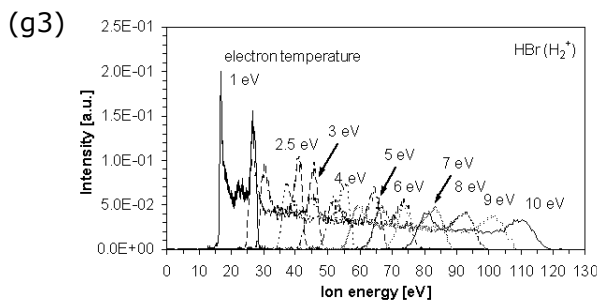
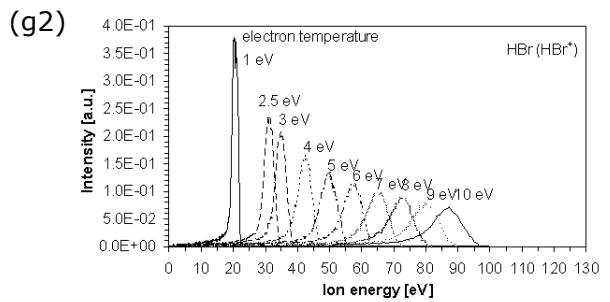
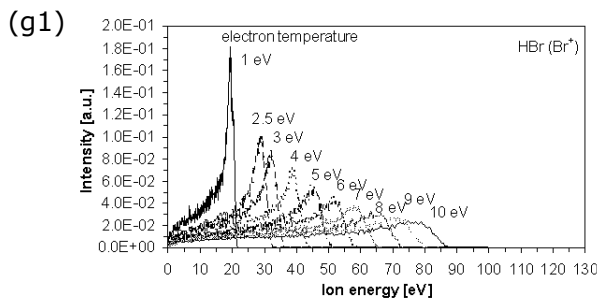
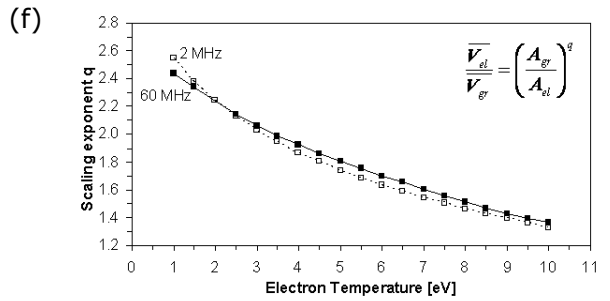
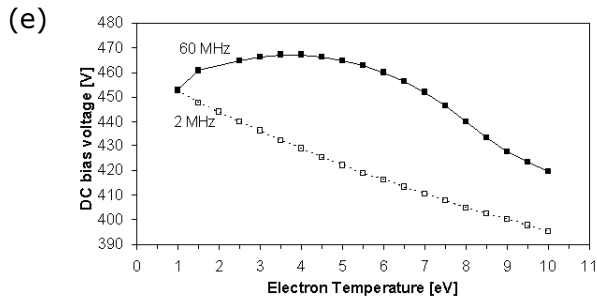
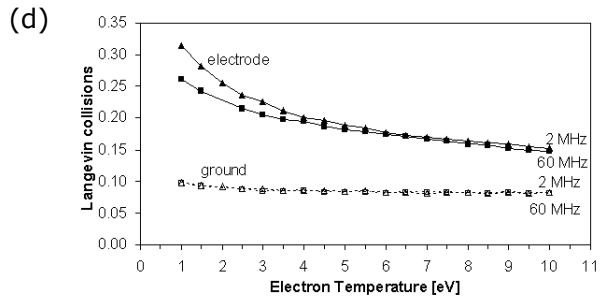
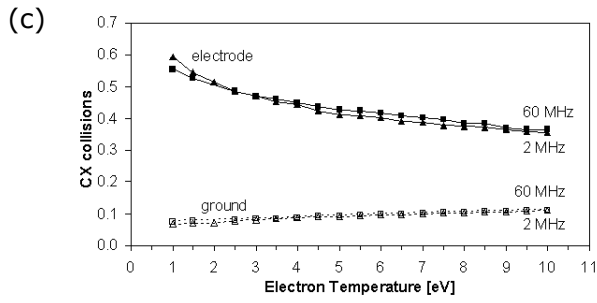
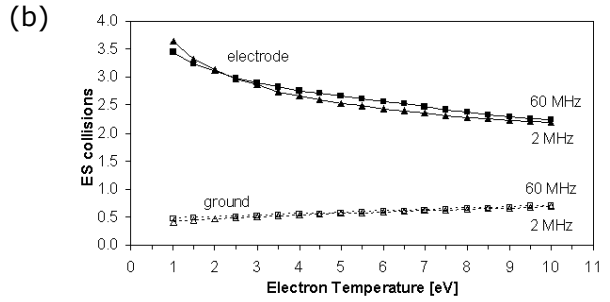
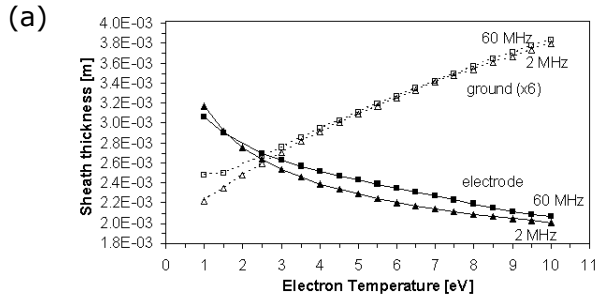
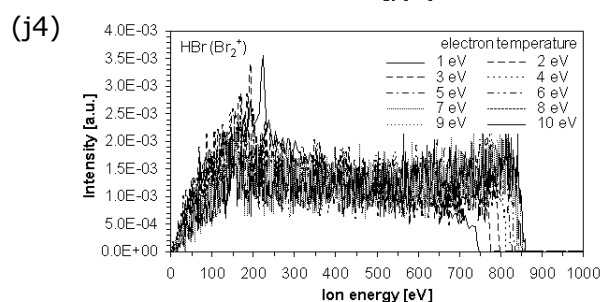
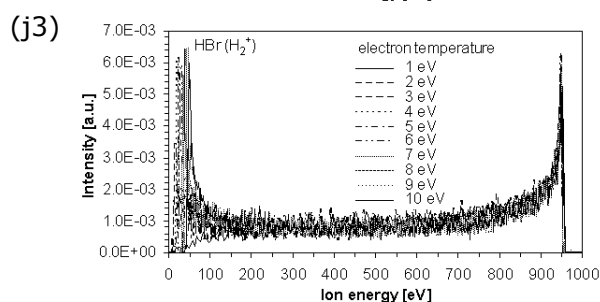
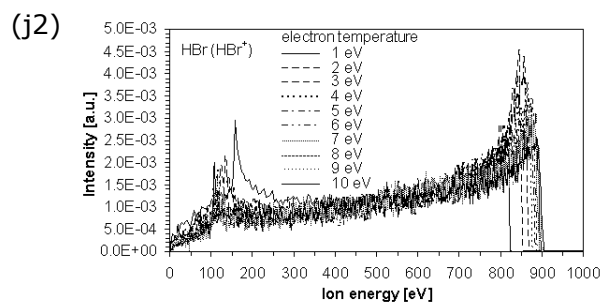
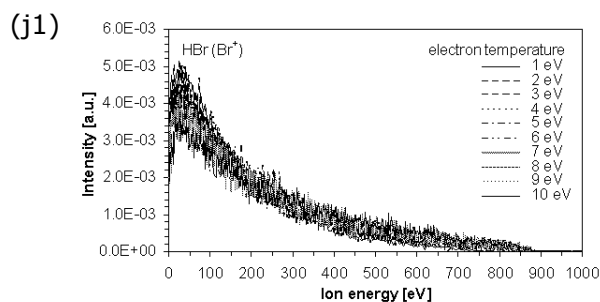
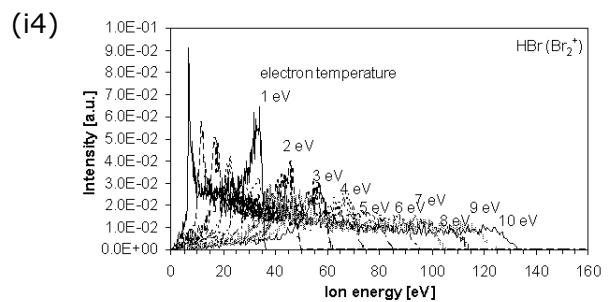
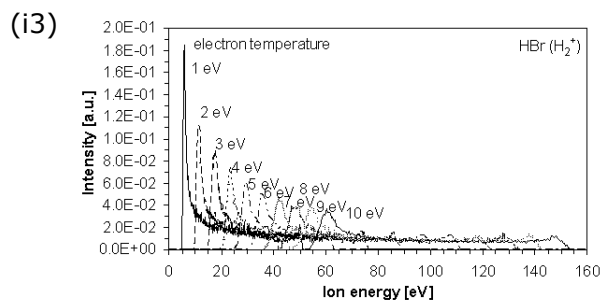
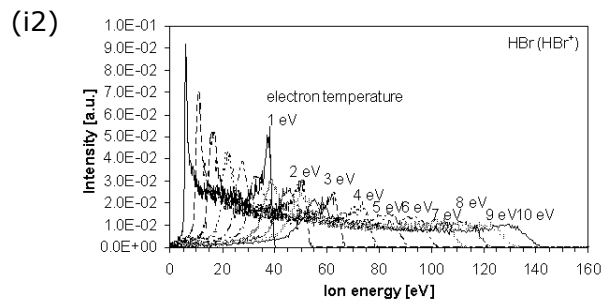
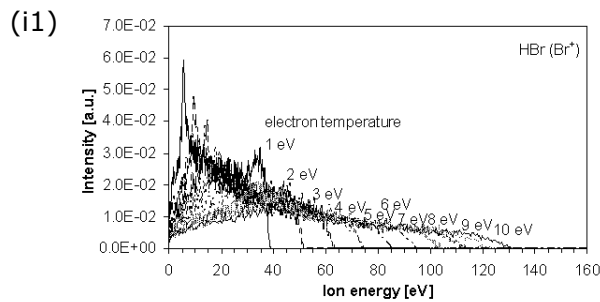
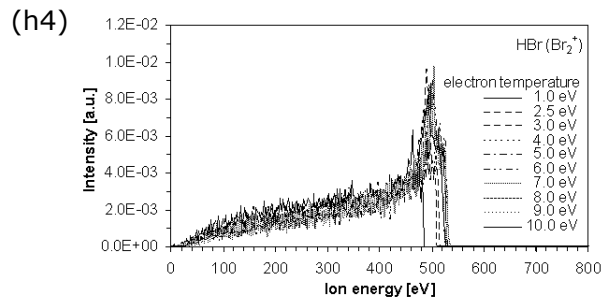
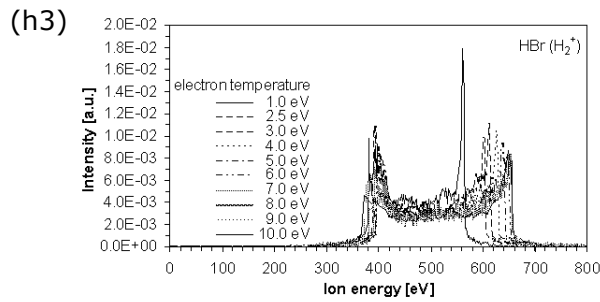
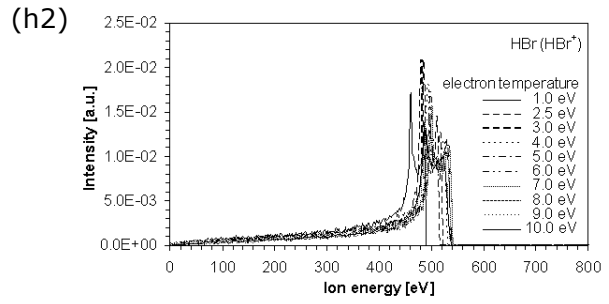
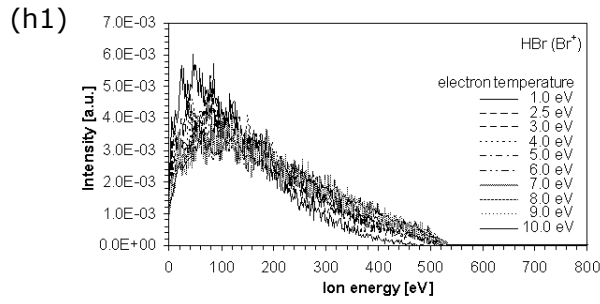


Figure D.3: HPSM simulation results for variation of neutral gas temperature in HBr discharges (a) sheath thickness in front of ground (open symbols with dotted lines, values have been multiplied by a factor of four) and powered electrode (solid symbols with continuous lines); (b) number of elastic collisions, (c) charge exchange collisions, and (d) Langevin collisions for ions in the sheath region; (e) dc bias voltage for 60 MHz (solid symbols with continuous lines) and 2 MHz HBr discharges (open symbols with dotted lines); (f) scaling exponent q for equation (1.6) for 60 MHz (solid symbols with continuous lines) and 2 MHz HBr discharges (open symbols with dotted lines); IEDFs at the ground electrode for (g1) Br^+ , (g2) HBr^+ , (g3) H_2^+ , and (g4) Br_2^+ for 60 MHz HBr discharges; IEDFs at the powered electrode for (h1) Br^+ , (h2) HBr^+ , (h3) H_2^+ , and (h4) Br_2^+ for 60 MHz HBr discharges; IEDFs at the ground electrode for (i1) Br^+ , (i2) HBr^+ , (i3) H_2^+ , and (i4) Br_2^+ for 2 MHz HBr discharges; IEDFs at the powered electrode for (j1) Br^+ , (j2) HBr^+ , (j3) H_2^+ , and (j4) Br_2^+ for 2 MHz HBr discharges; (k) mean energies for Br^+ , HBr^+ , H_2^+ and Br_2^+ ions at the ground electrode for 60 MHz and 2 MHz HBr discharges; (l) mean energies for Br^+ , HBr^+ , H_2^+ and Br_2^+ ions at the powered electrode for 60 MHz and 2 MHz HBr discharges. IEDFs in (g1)-(j4) are plotted for 150 mTorr, 500 V rf peak voltage, 6.32 eV electron temperature, $1 \times 10^{10} \text{ cm}^{-3}$ electron density, no magnetic field.





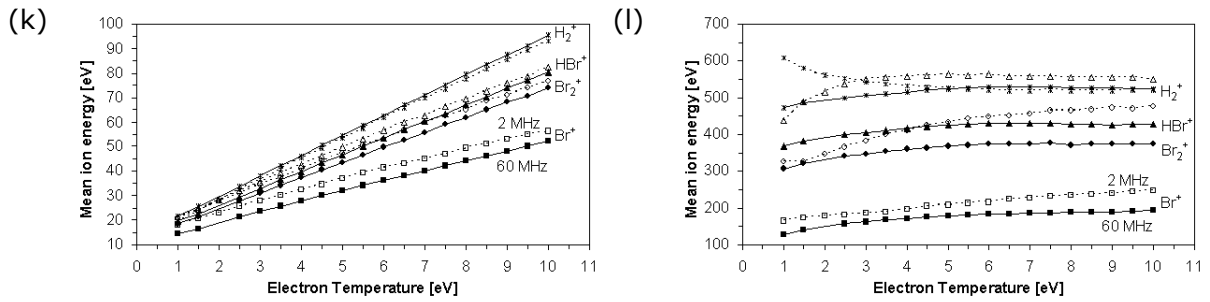
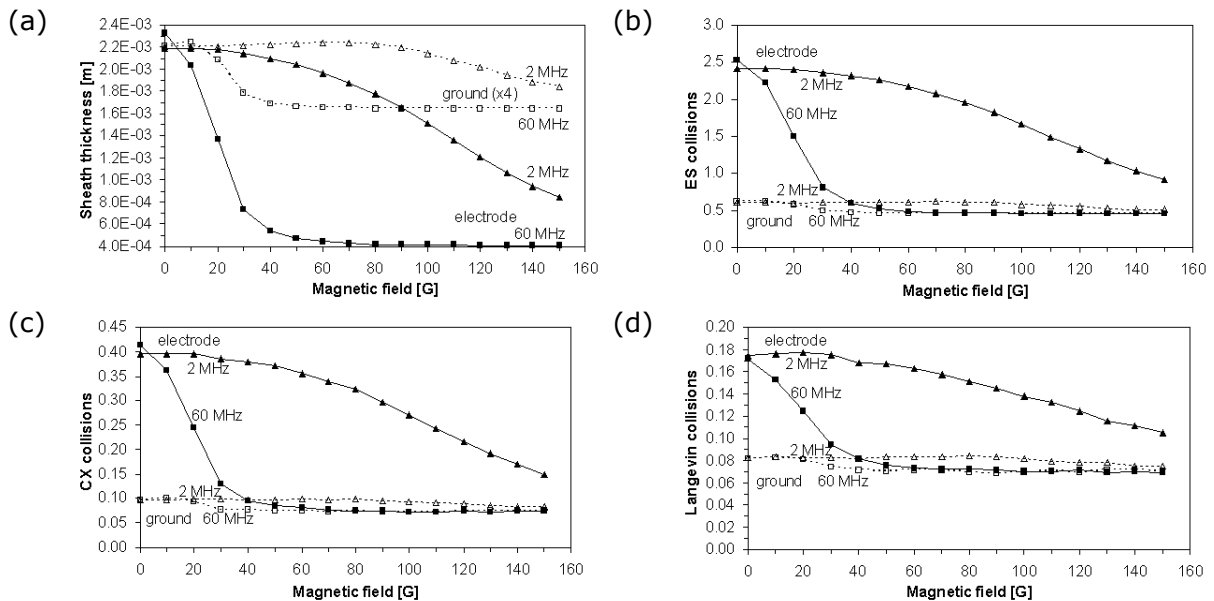
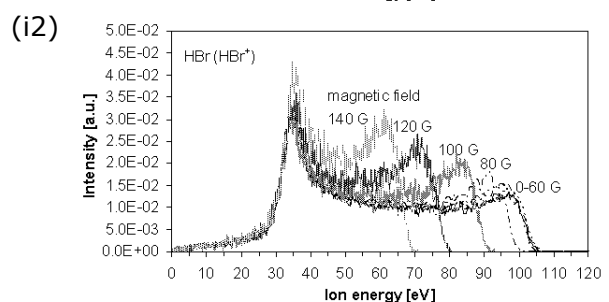
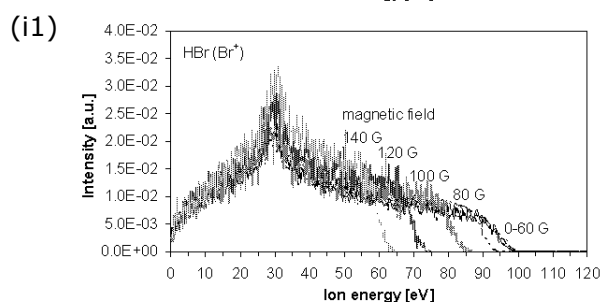
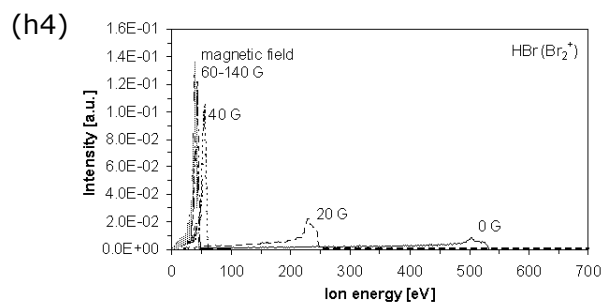
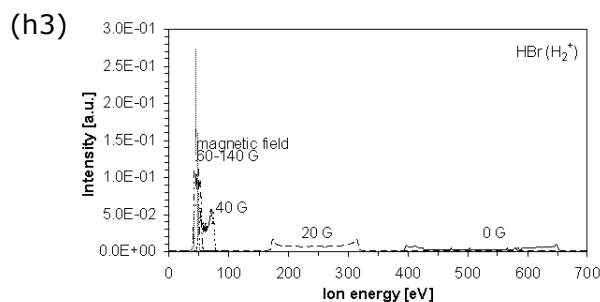
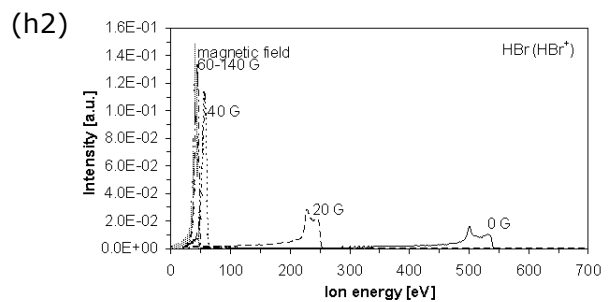
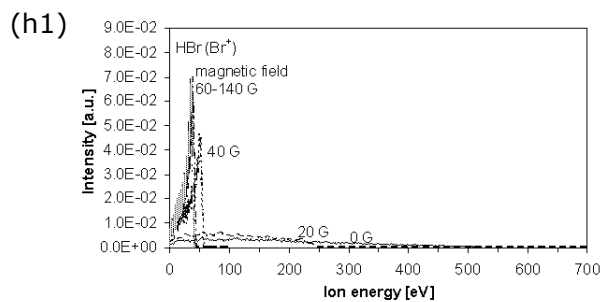
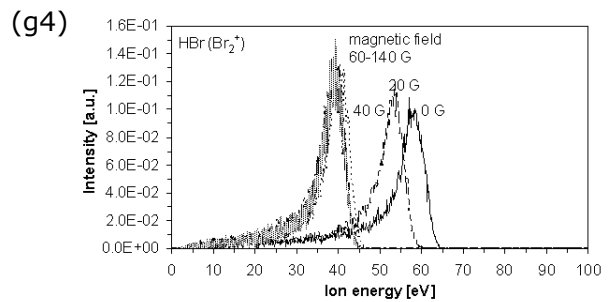
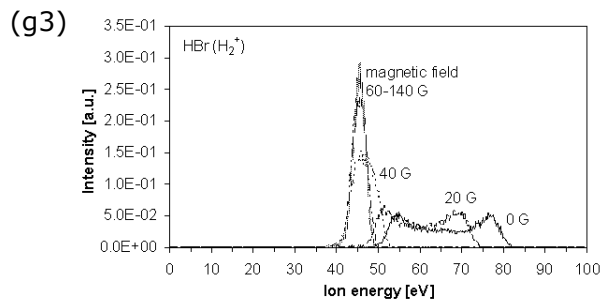
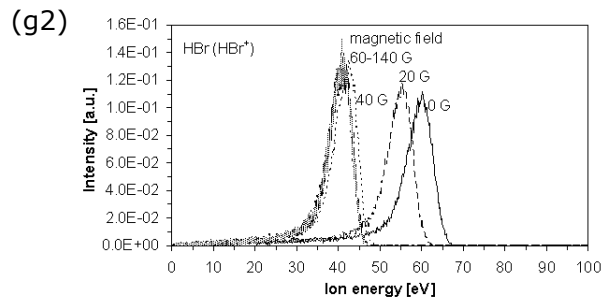
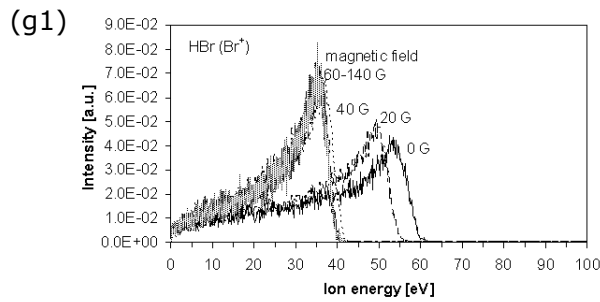
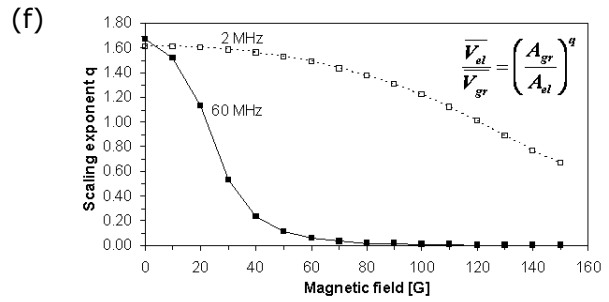
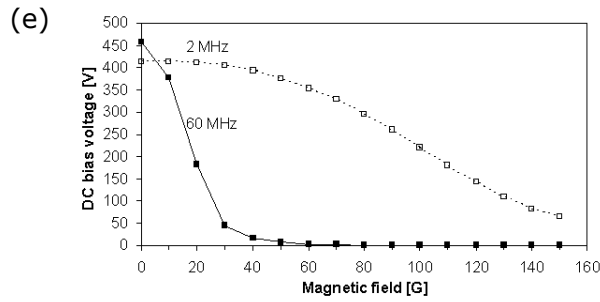


Figure D.4: HPSM simulation results for variation of electron temperature in HBr discharges (a) sheath thickness in front of ground (open symbols with dotted lines, values have been multiplied by a factor of six) and powered electrode (solid symbols with continuous lines); (b) number of elastic collisions, (c) charge exchange collisions, and (d) Langevin collisions for ions in the sheath region; (e) dc bias voltage for 60 MHz (solid symbols with continuous lines) and 2 MHz HBr discharges (open symbols with dotted lines); (f) scaling exponent q for equation (1.6) for 60 MHz (solid symbols with continuous lines) and 2 MHz HBr discharges (open symbols with dotted lines); IEDFs at the ground electrode for (g1) Br^+ , (g2) HBr^+ , (g3) H_2^+ , and (g4) Br_2^+ for 60 MHz HBr discharges; IEDFs at the powered electrode for (h1) Br^+ , (h2) HBr^+ , (h3) H_2^+ , and (h4) Br_2^+ for 60 MHz HBr discharges; IEDFs at the ground electrode for (i1) Br^+ , (i2) HBr^+ , (i3) H_2^+ , and (i4) Br_2^+ for 2 MHz HBr discharges; IEDFs at the powered electrode for (j1) Br^+ , (j2) HBr^+ , (j3) H_2^+ , and (j4) Br_2^+ for 2 MHz HBr discharges; (k) mean energies for Br^+ , HBr^+ , H_2^+ and Br_2^+ ions at the ground electrode for 60 MHz and 2 MHz HBr discharges; (l) mean energies for Br^+ , HBr^+ , H_2^+ and Br_2^+ ions at the powered electrode for 60 MHz and 2 MHz HBr discharges. IEDFs in (g1)-(j4) are plotted for 150 mTorr, 500 V rf peak voltage, $1 \times 10^{10} \text{ cm}^{-3}$ electron density, 500 K neutral gas temperature, no magnetic field.





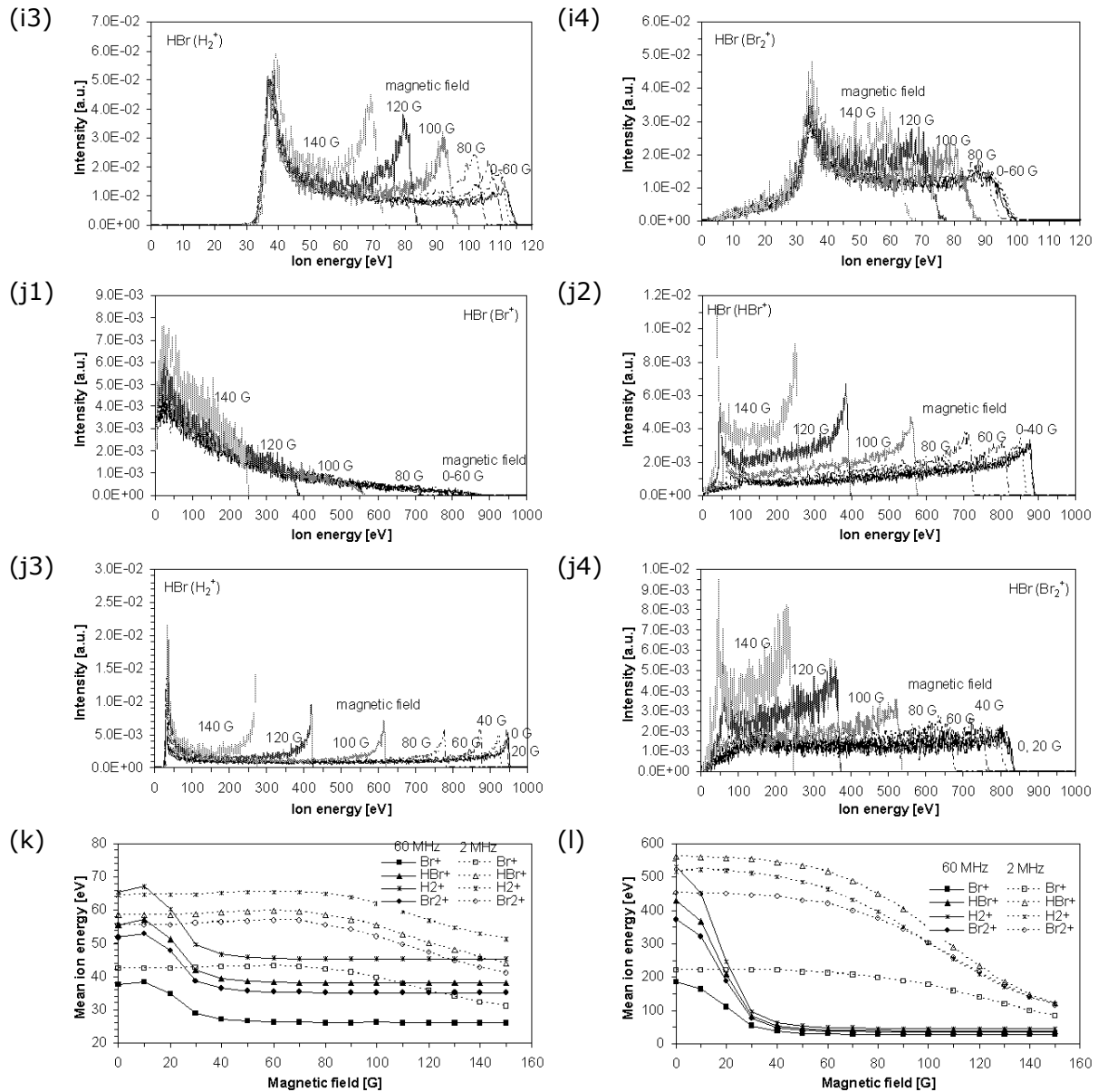
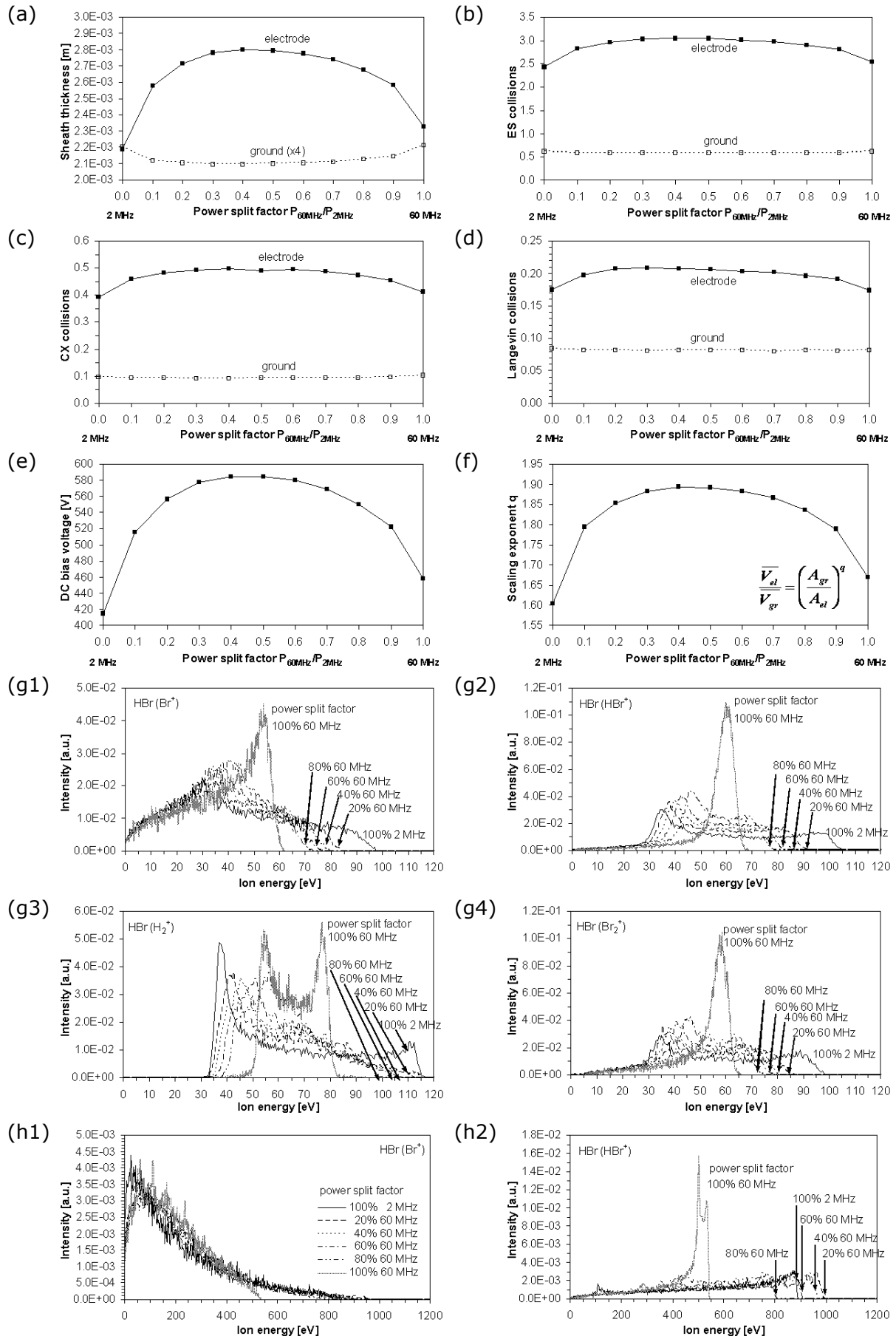


Figure D.5: HPSM simulation results for variation of magnetic field in HBr discharges (a) sheath thickness in front of ground (open symbols with dotted lines, values have been multiplied by a factor of four) and powered electrode (solid symbols with continuous lines); (b) number of elastic collisions, (c) charge exchange collisions, and (d) Langevin collisions for ions in the sheath region; (e) dc bias voltage for 60 MHz (solid symbols with continuous lines) and 2 MHz HBr discharges (open symbols with dotted lines); (f) scaling exponent q for equation (1.6) for 60 MHz (solid symbols with continuous lines) and 2 MHz HBr discharges (open symbols with dotted lines); IEDFs at the ground electrode for (g1) Br^+ , (g2) HBr^+ , (g3) H_2^+ , and (g4) Br_2^+ for 60 MHz HBr discharges; IEDFs at the powered electrode for (h1) Br^+ , (h2) HBr^+ , (h3) H_2^+ , and (h4) Br_2^+ for 60 MHz HBr discharges; IEDFs at the ground electrode for (i1) Br^+ , (i2) HBr^+ , (i3) H_2^+ , and (i4) Br_2^+ for 2 MHz HBr discharges; IEDFs at the powered electrode for (j1) Br^+ , (j2) HBr^+ , (j3) H_2^+ , and (j4) Br_2^+ for 2 MHz HBr discharges; (k) mean energies for Br^+ , HBr^+ , H_2^+ and Br_2^+ ions at the ground electrode for 60 MHz and 2 MHz HBr discharges; (l) mean energies for Br^+ , HBr^+ , H_2^+ and Br_2^+ ions at the powered electrode for 60 MHz and 2 MHz HBr discharges. IEDFs in (g1)-(j4) are plotted for 150 mTorr, 500 V rf peak voltage, 6.32 eV electron temperature, $1 \times 10^{10} \text{ cm}^{-3}$ electron density, 500 K neutral gas temperature.



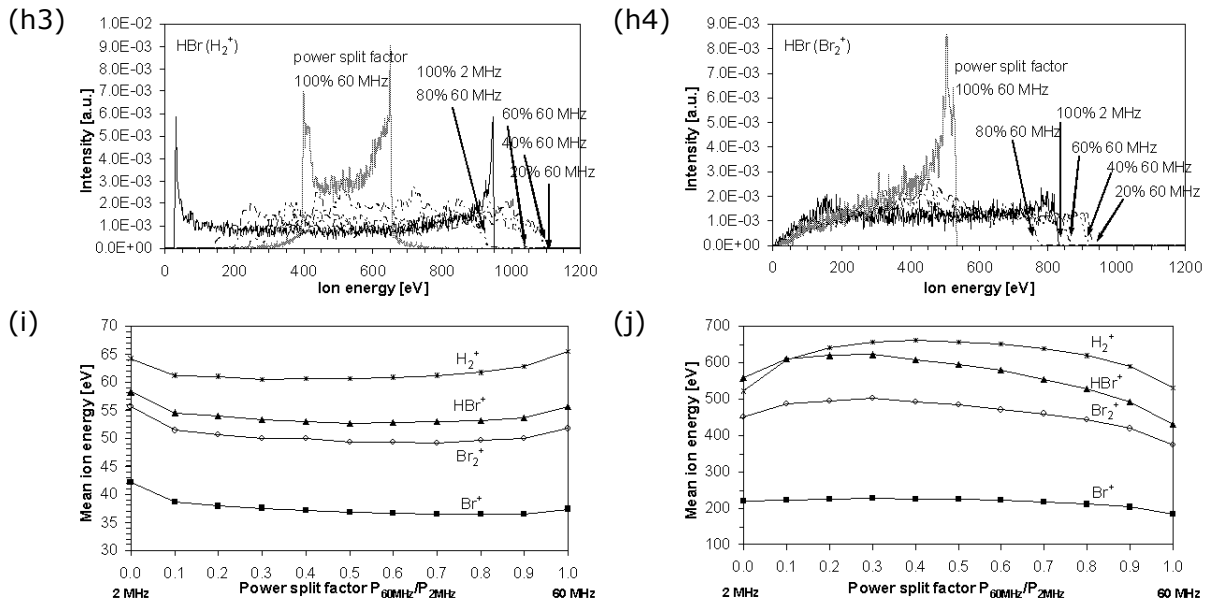


Figure D.6: HPSM simulation results for variation of 60+2 MHz frequency mix in HBr discharges (a) sheath thickness in front of ground (open symbols with dotted lines, values have been multiplied by a factor of four) and powered electrode (solid symbols with continuous lines); (b) number of elastic collisions, (c) charge exchange collisions, and (d) Langevin enhanced collisions for ions in the sheath region; (e) dc bias voltage; (f) scaling exponent q for equation (1.6); IEDFs at the ground electrode for (g1) Br^+ , (g2) HBr^+ , (g3) H_2^+ and (g4) Br_2^+ for 60+2 MHz dual frequency HBr discharges; IEDFs at the powered electrode for (h1) Br^+ , (h2) HBr^+ , (h3) H_2^+ and (h4) Br_2^+ for 60+2 MHz dual frequency HBr discharges; (i) mean energies for Br^+ , HBr^+ , H_2^+ and Br_2^+ ions at the ground electrode for 60+2 MHz dual frequency HBr discharges; (j) mean energies for Br^+ , HBr^+ , H_2^+ and Br_2^+ ions at the powered electrode for 60+2 MHz dual frequency HBr discharges. IEDFs in (g1)-(h4) are plotted for 150 mTorr, 500 V rf peak voltage, 6.32 eV electron temperature, $1 \times 10^{10} \text{ cm}^{-3}$ electron density, 500 K neutral gas temperature, no magnetic field.

Appendix E

Experimental results for Ar

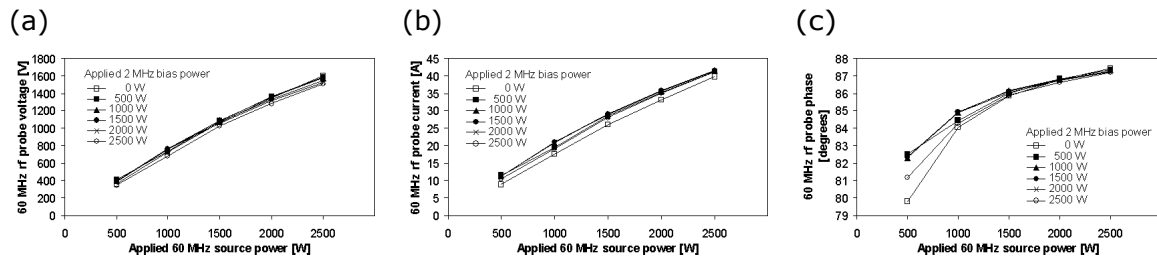


Figure E.1: 60 MHz rf probe data for 60+2 MHz power variation in Ar discharges: (a) mean voltage; (b) mean current; (c) phase angle. Experiments were conducted at 150 mTorr, 300 sccm Ar gas flow rate, no magnetic field, using silicon substrates.

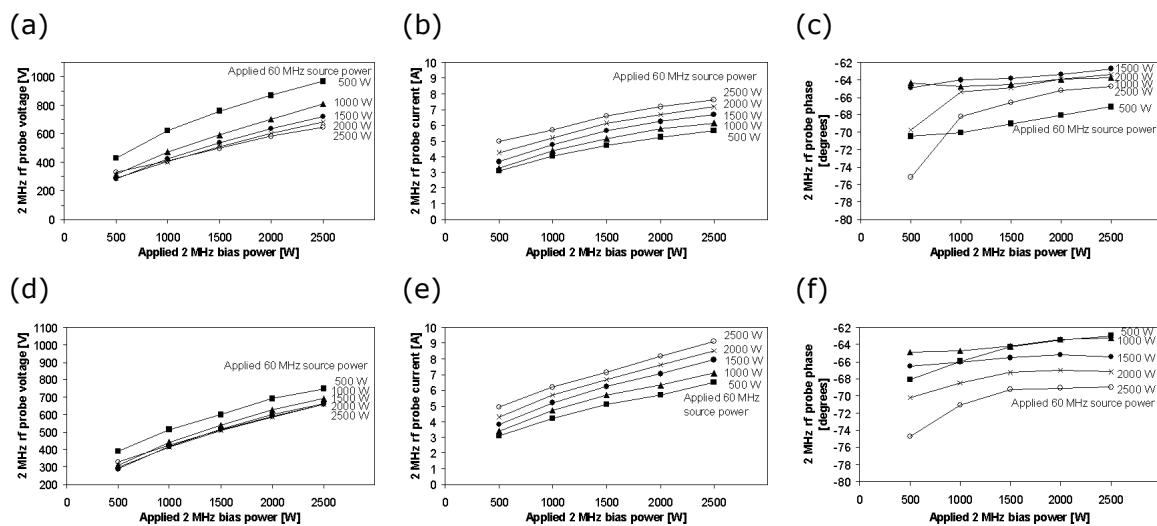


Figure E.2: 2 MHz rf probe data for 60+2 MHz power variation in Ar discharges: (a) mean voltage; (b) mean current; (c) phase angle when using silicon substrates. 2 MHz rf probe data for 60+2 MHz power variation in Ar discharges: (d) mean voltage; (e) mean current; (f) phase angle when using silicon substrates with an SiO₂ hard mask layer. Experiments were conducted at 150 mTorr, 300 sccm Ar gas flow rate, without magnetic field.

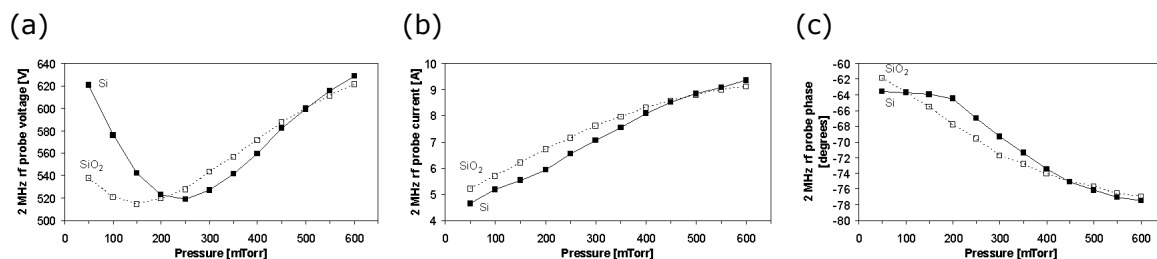


Figure E.3: 2 MHz rf probe data for variation of the pressure in Ar discharges: (a) mean voltage; (b) mean current; (c) phase angle. Experiments were conducted at 1500+1500 W 60+2 MHz power, 300 sccm Ar gas flow rate, no magnetic field, using silicon substrates with and without SiO₂ hard mask layer.

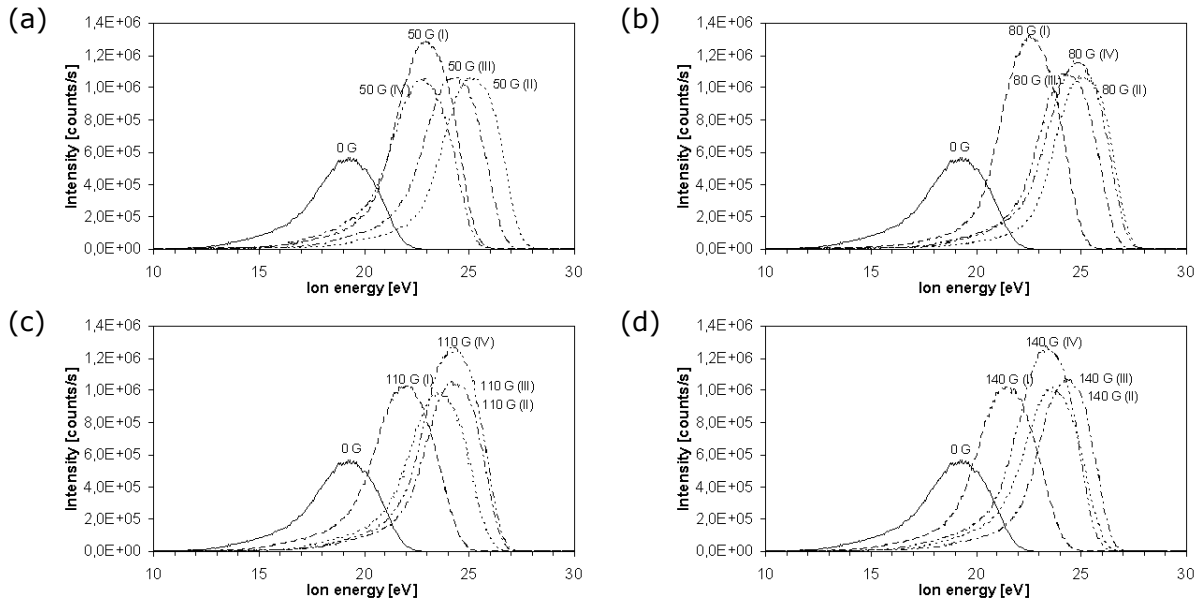


Figure E.4: $^{36}\text{Ar}^+$ IVDFs for variation of the magnetic field in 60 MHz single frequency argon discharges shown for different configurations of the stationary magnetic field from the four-coil configuration as indicated in Fig. 4.18-a for (a) 50 G, (b) 80 G, (c) 110 G, (d) 140 G with the reference curve measured without magnetic field as indicated by 0 G (1500 W, 150 mTorr, 300 sccm Ar gas flow rate, silicon substrate). The IVDFs are plotted without applying corrections for the offset in the energy scale.

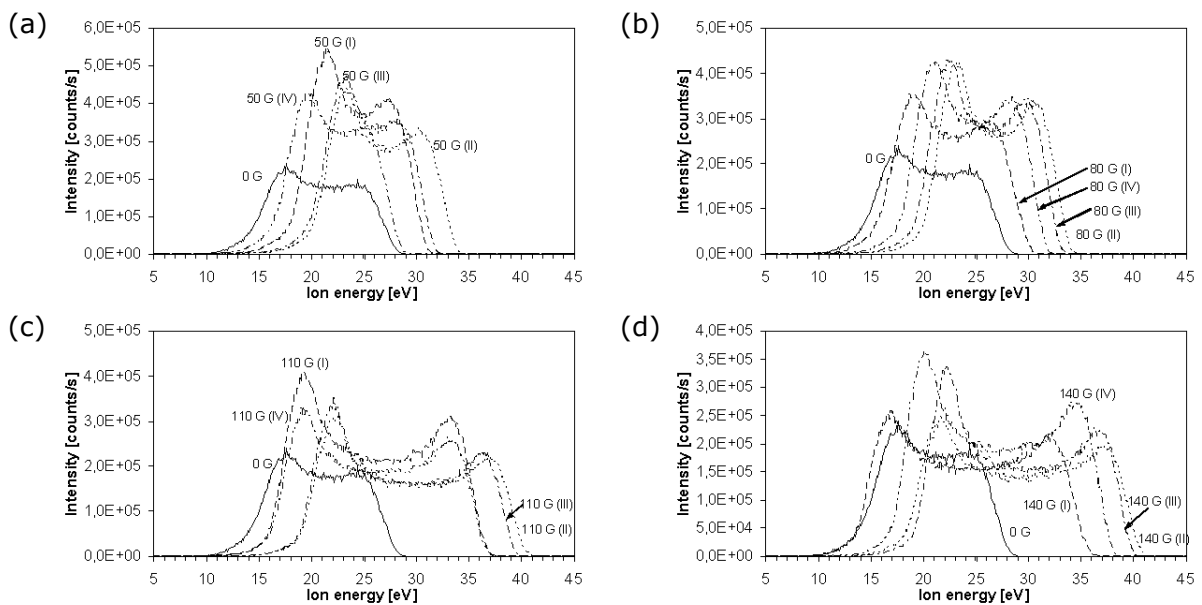


Figure E.5: $^{36}\text{Ar}^+$ IVDFs for variation of the magnetic field in 60+2 MHz dual frequency argon discharges shown for different configurations of the stationary magnetic field from the four-coil configuration as indicated in Fig. 4.19-a for (a) 50 G, (b) 80 G, (c) 110 G, (d) 140 G (1500+1500 W 60+2 MHz power, 150 mTorr, 300 sccm Ar gas flow rate, silicon substrate). The IVDFs are plotted without applying corrections for the offset in the energy scale.

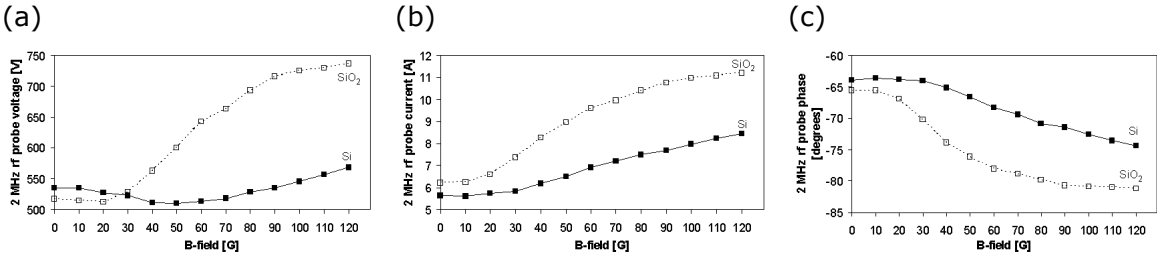


Figure E.6: 2 MHz rf probe data for variation of the magnetic field in Ar discharges: (a) mean voltage; (b) mean current; (c) phase angle. Experiments were conducted at 1500+1500 W 60+2 MHz power, 150 mTorr, 300 sccm Ar gas flow rate, using silicon substrates with and without SiO₂ hard mask layer.

Appendix F

Experimental results for HBr

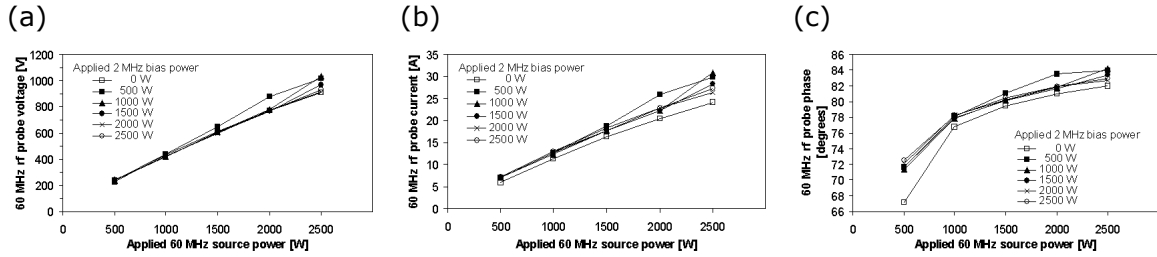


Figure F.1: 60 MHz rf probe data for 60+2 MHz power variation in HBr discharges: (a) mean voltage; (b) mean current; (c) phase angle. Experiments were conducted at 150 mTorr, 300 sccm HBr gas flow rate, no magnetic field, using silicon substrates.

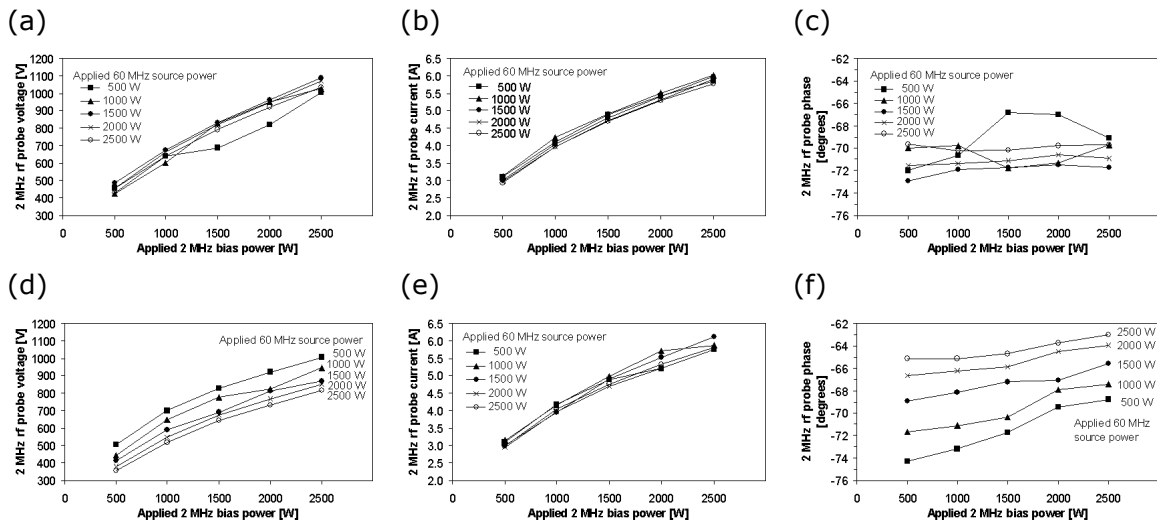


Figure F.2: 2 MHz rf probe data for 60+2 MHz power variation in HBr discharges: (a) mean voltage; (b) mean current; (c) phase angle when using silicon substrates. 2 MHz rf probe data for 60+2 MHz power variation in HBr discharges: (d) mean voltage; (e) mean current; (f) phase angle when using silicon substrates with an SiO₂ hard mask layer. Experiments were conducted at 150 mTorr, 300 sccm HBr gas flow rate, without magnetic field.

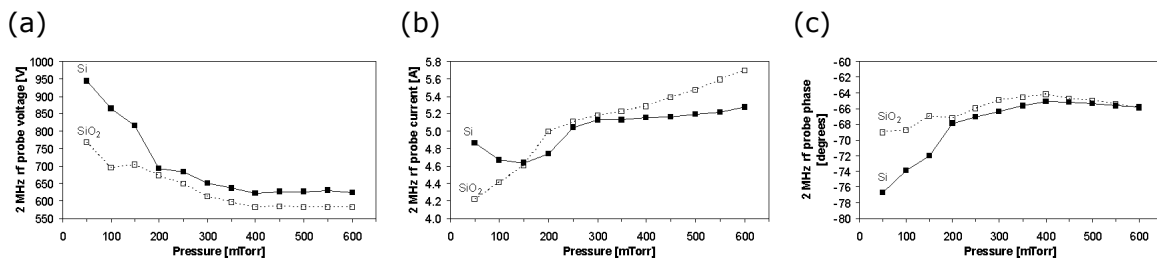


Figure F.3: 2 MHz rf probe data for variation of the pressure in HBr discharges: (a) mean voltage; (b) mean current; (c) phase angle. Experiments were conducted at 1500+1500 W 60+2 MHz power, 300 sccm HBr gas flow rate, no magnetic field, using silicon substrates with and without SiO₂ hard mask layer.

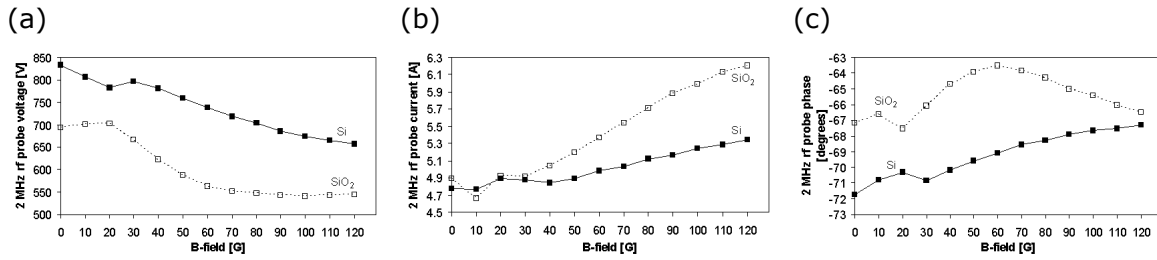


Figure F.4: 2 MHz rf probe data for variation of the magnetic field in HBr discharges: (a) mean voltage; (b) mean current; (c) phase angle. Experiments were conducted at 1500+1500 W 60+2 MHz power, 150 mTorr, 300 sccm HBr gas flow rate, using silicon substrates with and without SiO₂ hard mask layer.

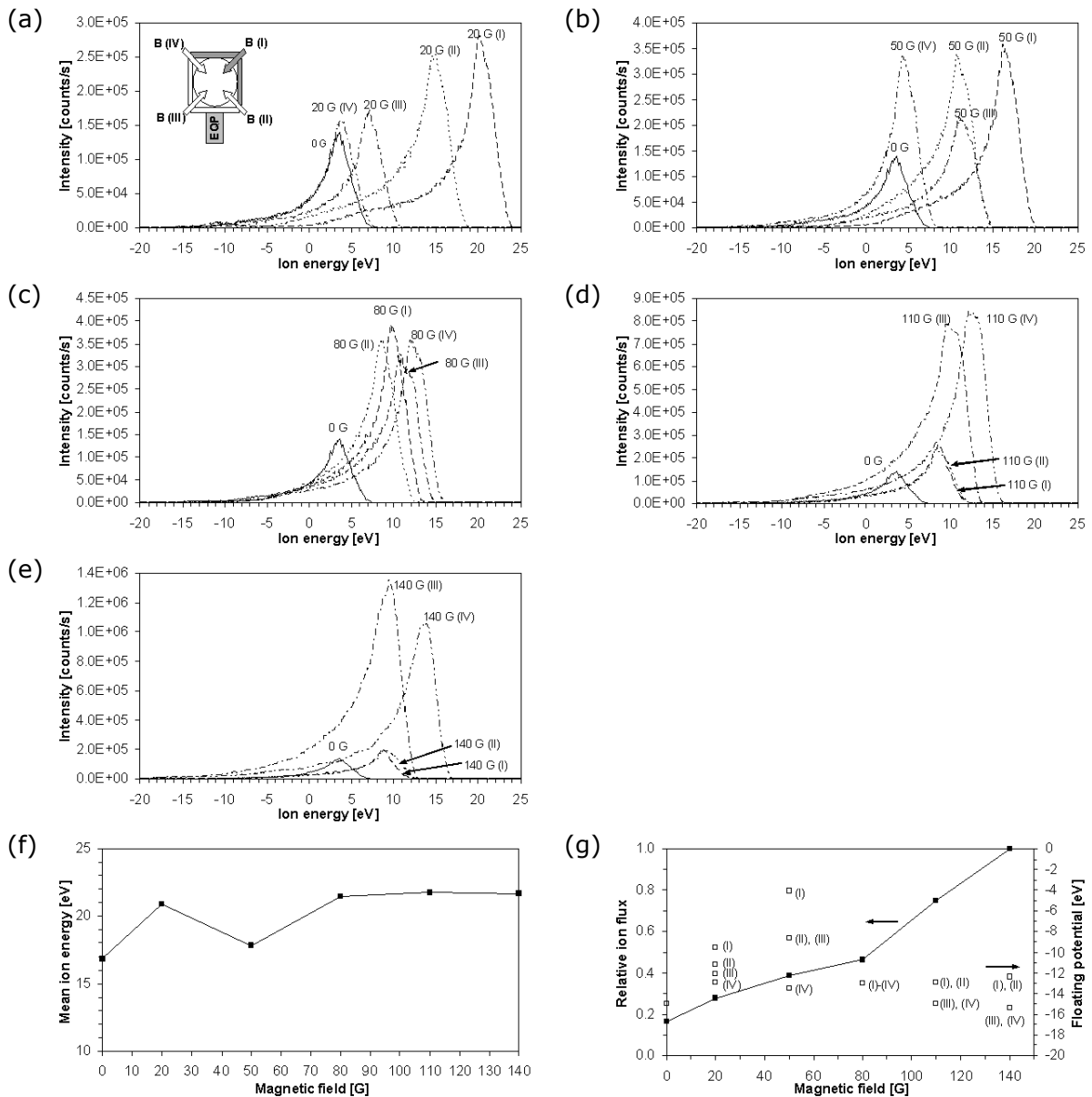


Figure F.5: ⁷⁹Br⁺ IVDFs for variation of the magnetic field in 60 MHz single frequency HBr discharges shown for different configurations of the stationary magnetic field from the four-coil configuration as indicated in (a) for (a) 20 G, (b) 50 G, (c) 80 G, (d) 110 G, (e) 140 G with the reference curve measured without magnetic field as indicated by 0 G (1500 W, 150 mTorr, 300 sccm HBr gas flow rate, silicon substrate); (f) corresponding mean ion energies; (g) relative ion flux (solid

squares) and floating potentials at the extraction aperture (open squares) as determined from the position of the lowest energy peak. The IVDFs are plotted without applying corrections for the offset in the energy scale.

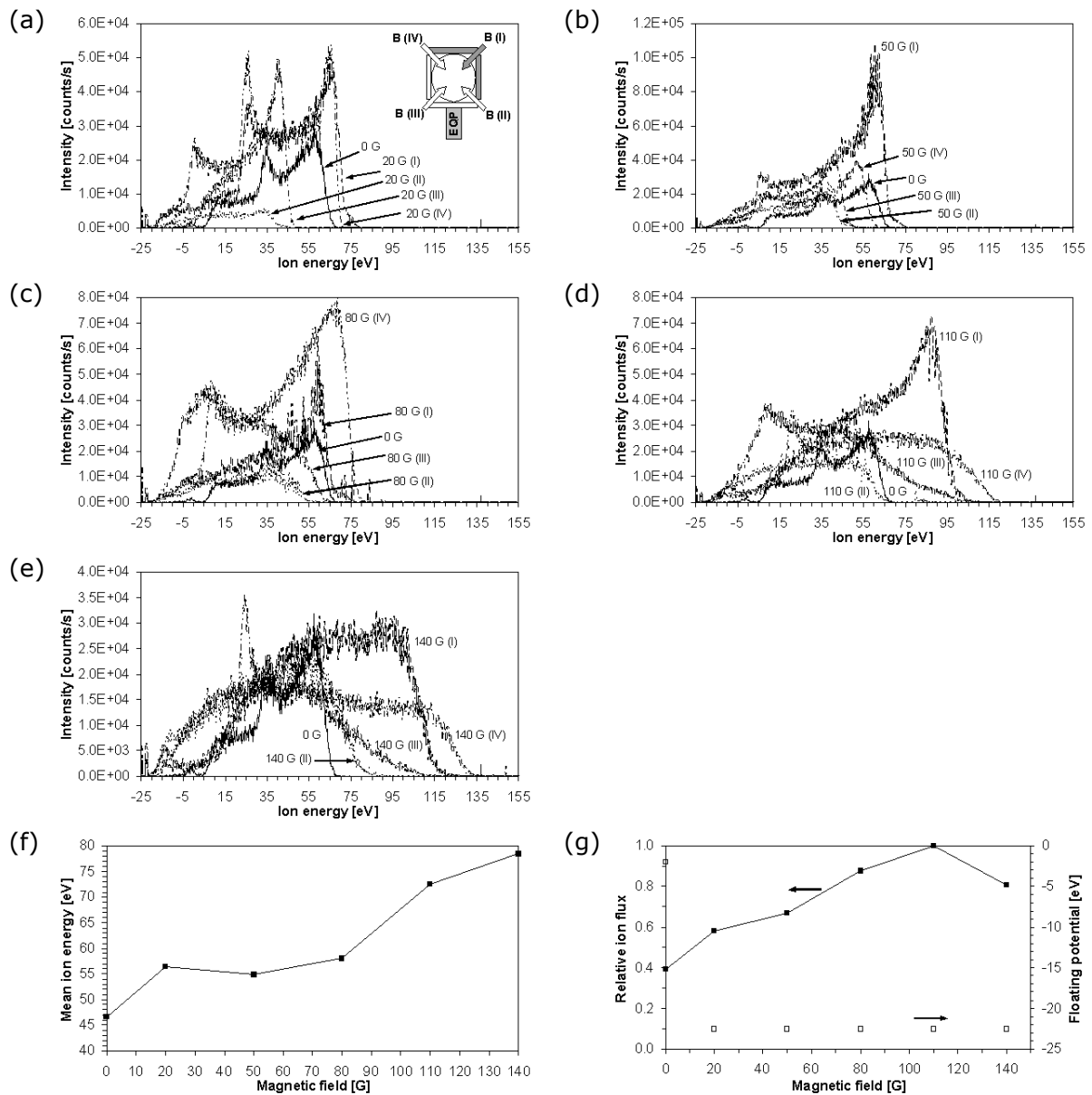


Figure F.6: $^{79}\text{Br}^+$ IVDFs for variation of the magnetic field in 60+2 MHz dual frequency HBr discharges shown for different configurations of the stationary magnetic field from the four-coil configuration as indicated in (a) for (a) 20 G, (b) 50 G, (c) 80 G, (d) 110 G, (e) 140 G (1500+1500 W 60+2 MHz power, 150 mTorr, 300 sccm HBr gas flow rate, silicon substrate); (f) corresponding mean ion energies; (g) relative ion flux (solid squares) and floating potentials at the extraction aperture (open squares) as determined from the position of the lowest energy peak. The IVDFs are plotted without applying corrections for the offset in the energy scale.

Experimental results for NF_3

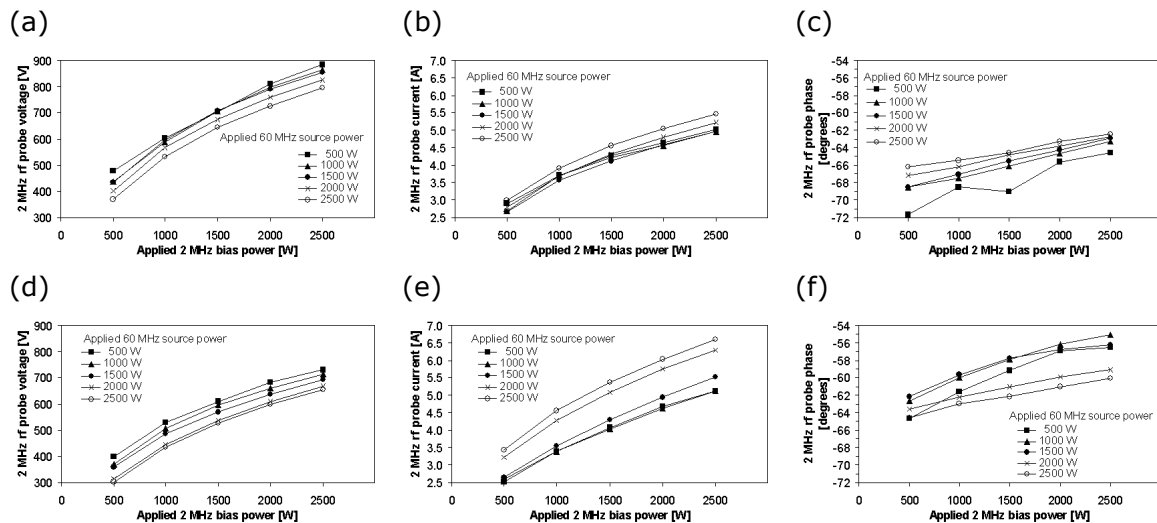


Figure G.1: 2 MHz rf probe data for 60+2 MHz power variation in NF_3 discharges: (a) mean voltage; (b) mean current; (c) phase angle when using silicon substrates. 2 MHz rf probe data for 60+2 MHz power variation in NF_3 discharges: (d) mean voltage; (e) mean current; (f) phase angle when using silicon substrates with an SiO_2 hard mask layer. Experiments were conducted at 150 mTorr, 300 sccm NF_3 gas flow rate, without magnetic field.

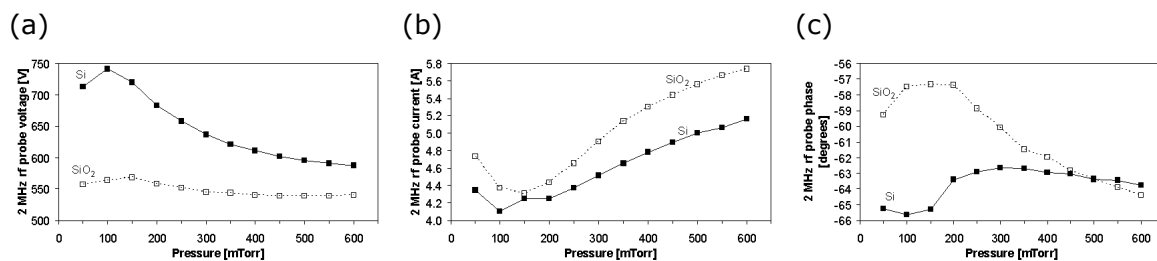


Figure G.2: 2 MHz rf probe data for variation of the pressure in NF_3 discharges: (a) mean voltage; (b) mean current; (c) phase angle. Experiments were conducted at 1500+1500 W 60+2 MHz power, 300 sccm NF_3 gas flow rate, no magnetic field, using silicon substrates with and without SiO_2 hard mask layer.

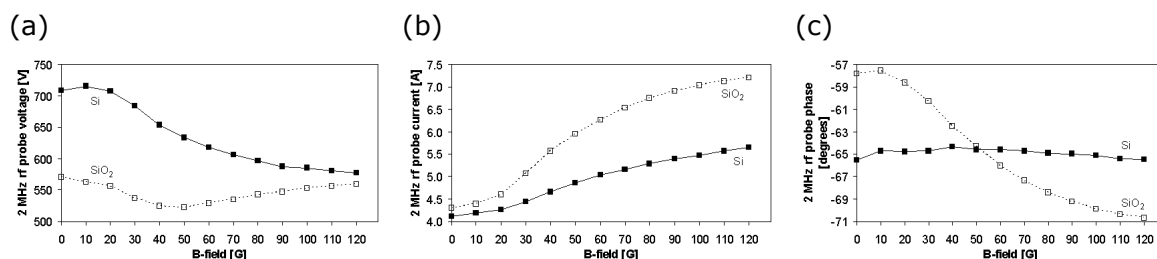


Figure G.3: 2 MHz rf probe data for variation of the magnetic field in NF_3 discharges: (a) mean voltage; (b) mean current; (c) phase angle. Experiments were conducted at 1500+1500 W 60+2 MHz power, 150 mTorr, 300 sccm NF_3 gas flow rate, using silicon substrates with and without SiO_2 hard mask layer.

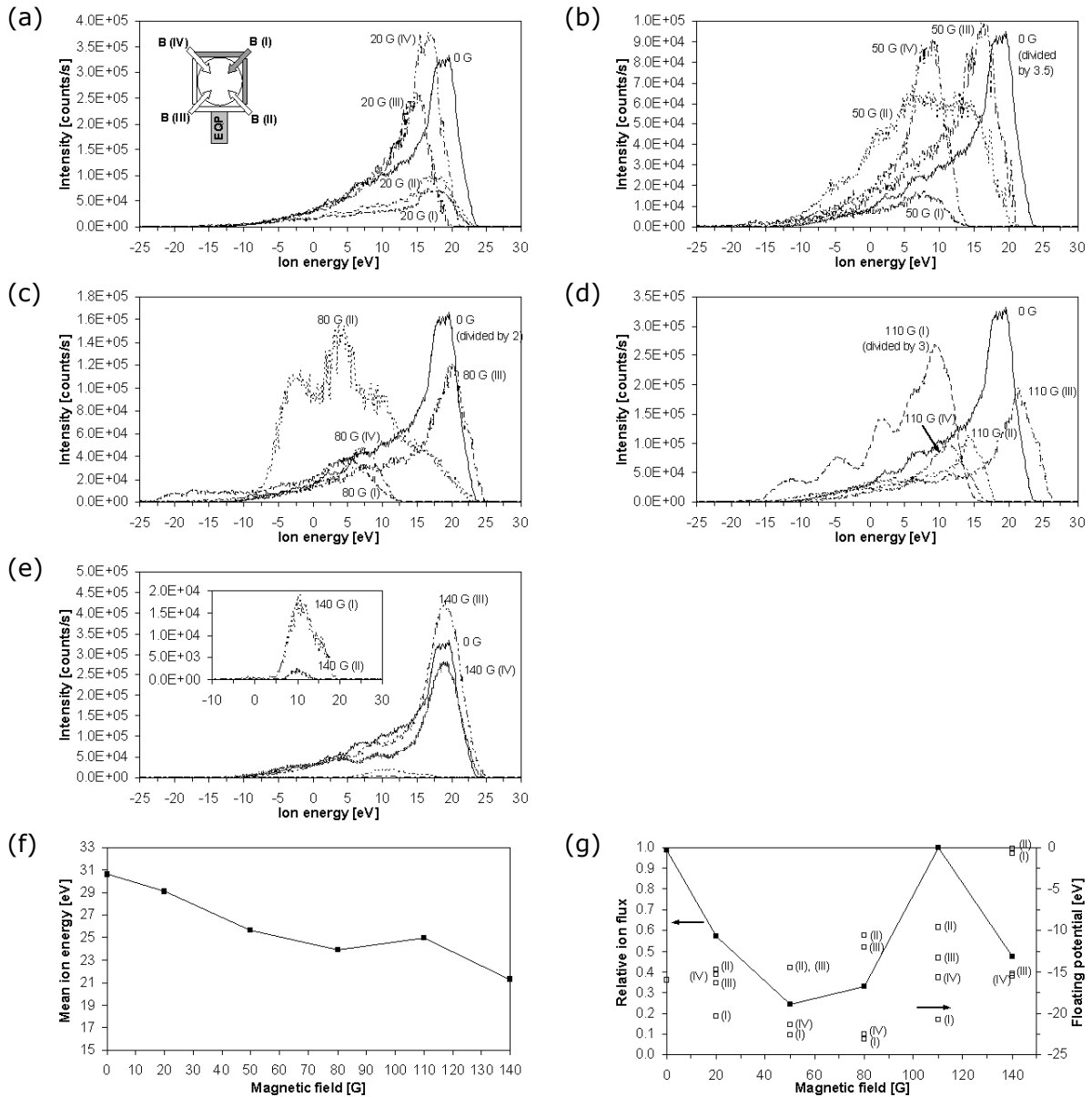


Figure G.4: $^{19}\text{F}^+$ IVDFs for variation of the magnetic field in 60 MHz single frequency NF_3 discharges shown for different positions of the stationary magnetic field from the four-coil configuration as indicated in (a) for (a) 20 G, (b) 50 G, (c) 80 G, (d) 110 G, (e) 140 G with the reference curve measured without magnetic field as indicated by 0 G (1500 W, 150 mTorr, 200 sccm NF_3 gas flow rate, silicon substrate); (f) corresponding mean ion energies; (g) relative ion flux (solid squares) and floating potentials at the extraction aperture (open squares) as determined from the position of the lowest energy peak. The IVDFs are plotted without applying corrections for the offset in the energy scale.

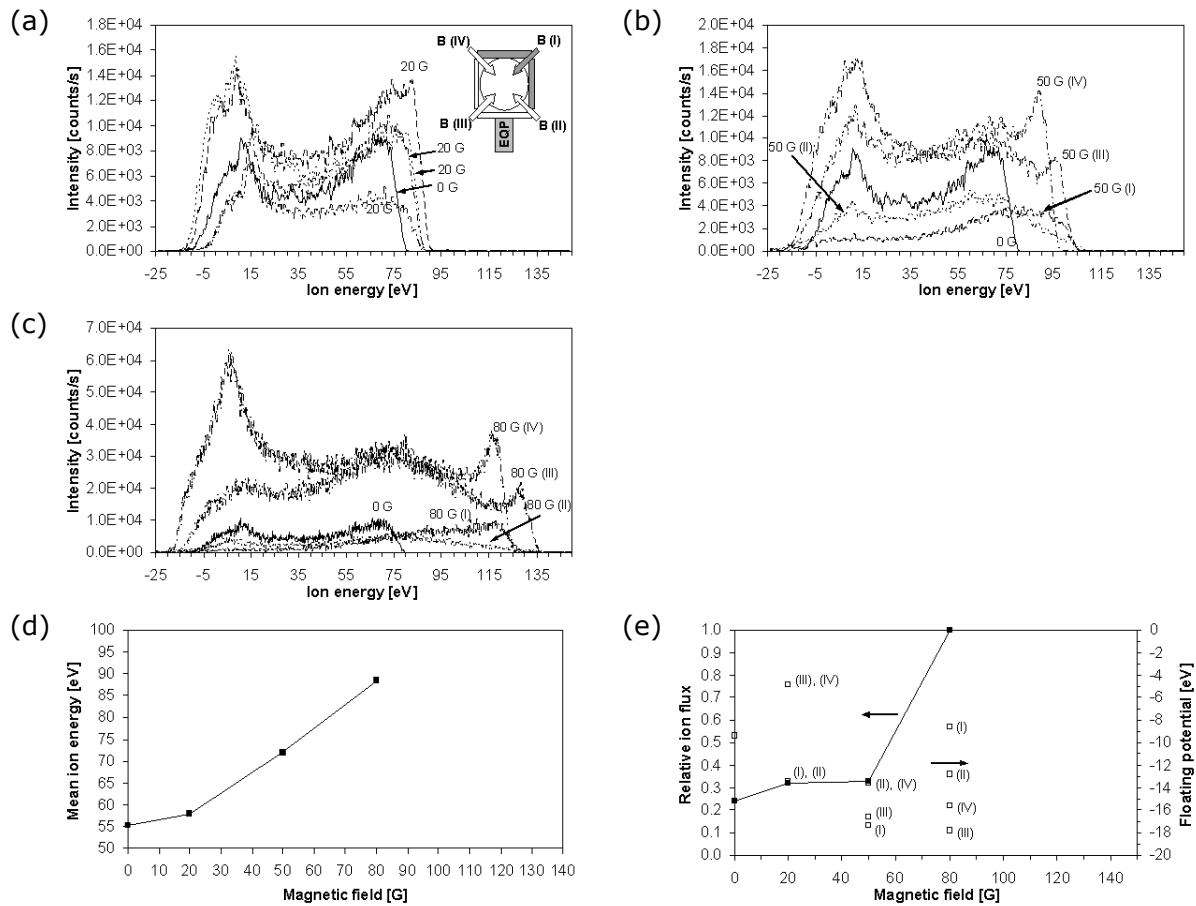


Figure G.5: ¹⁹F⁺ IVDFs for variation of the magnetic field in 60+2 MHz dual frequency NF₃ discharges for different configurations of the stationary magnetic field from the four-coil configuration as indicated in (a) for (a) 20 G, (b) 50 G, (c) 80 G with the reference curve measured without magnetic field as indicated by 0 G (1500+1500 W 60+2 MHz power, 150 mTorr, 200 sccm NF₃ gas flow rate, silicon substrate); (d) corresponding mean ion energies; (e) relative ion flux (solid squares) and floating potentials at the extraction aperture (open squares) as determined from the position of the lowest energy peak. The IVDFs are plotted without applying corrections for the offset in the energy scale.

Experimental results for HBr/NF₃

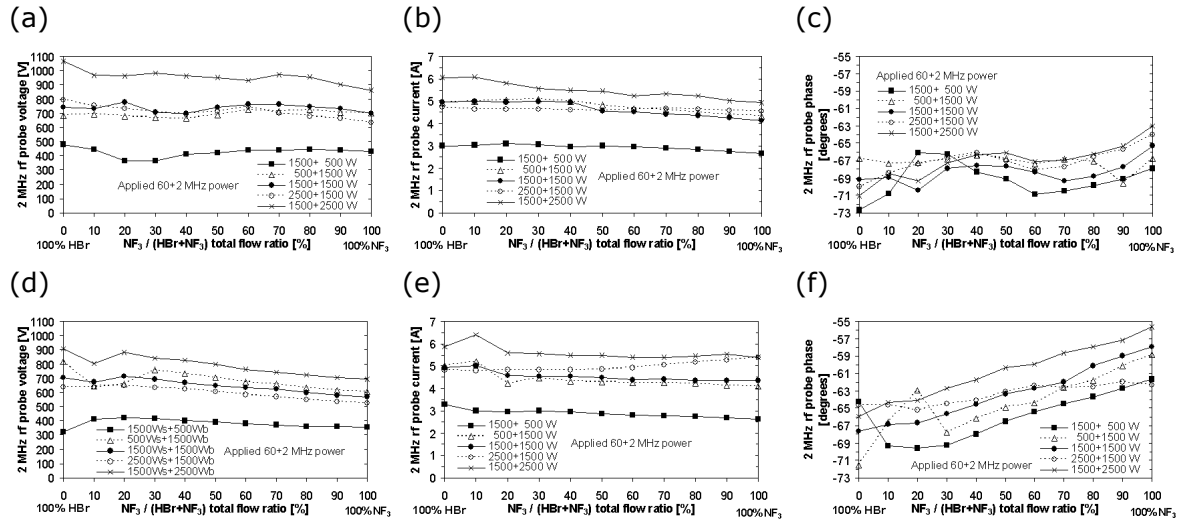


Figure H.1: 2 MHz rf probe data for 60+2 MHz power variation in HBr/NF₃ mixed discharges: (a) mean voltage; (b) mean current; (c) phase angle when using silicon substrates. 2 MHz rf probe data for 60+2 MHz power variation in HBr/NF₃ mixed discharges: (d) mean voltage; (e) mean current; (f) phase angle when using silicon substrates with an SiO₂ hard mask layer. Experiments were conducted at 150 mTorr, 300 sccm HBr/NF₃ total gas flow rate, without magnetic field.

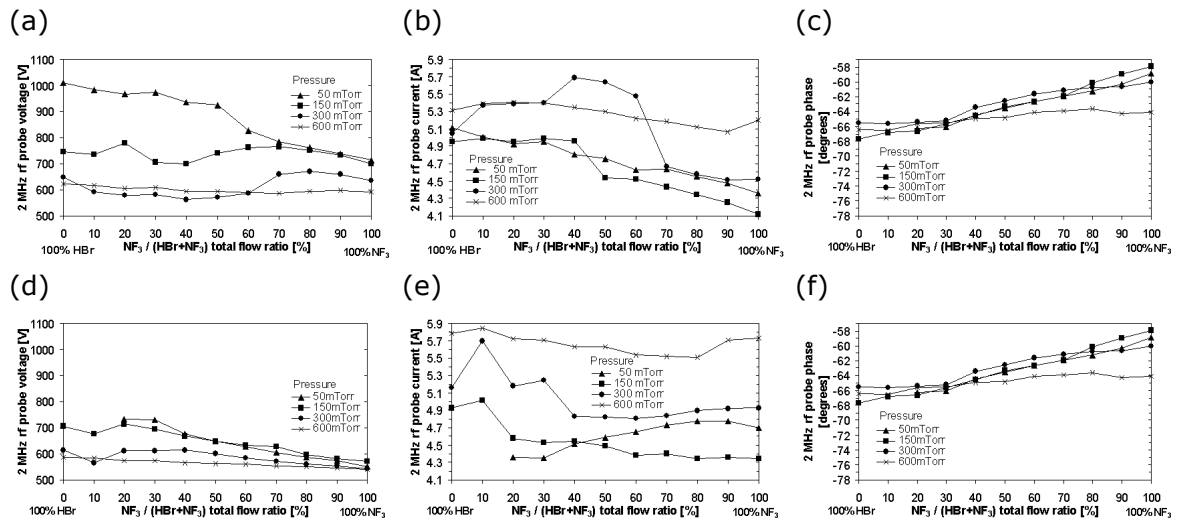


Figure H.2: 2 MHz rf probe data for variation of the pressure in HBr/NF₃ mixed discharges: (a) mean voltage; (b) mean current; (c) phase angle when using silicon substrates. 2 MHz rf probe data for variation of the pressure in HBr/NF₃ mixed discharges: (d) mean voltage; (e) mean current; (f) phase angle when using silicon substrates with an SiO₂ hard mask layer. Experiments were conducted at 1500+1500 W 60+2 MHz power, 300 sccm HBr/NF₃ total gas flow rate, without magnetic field.

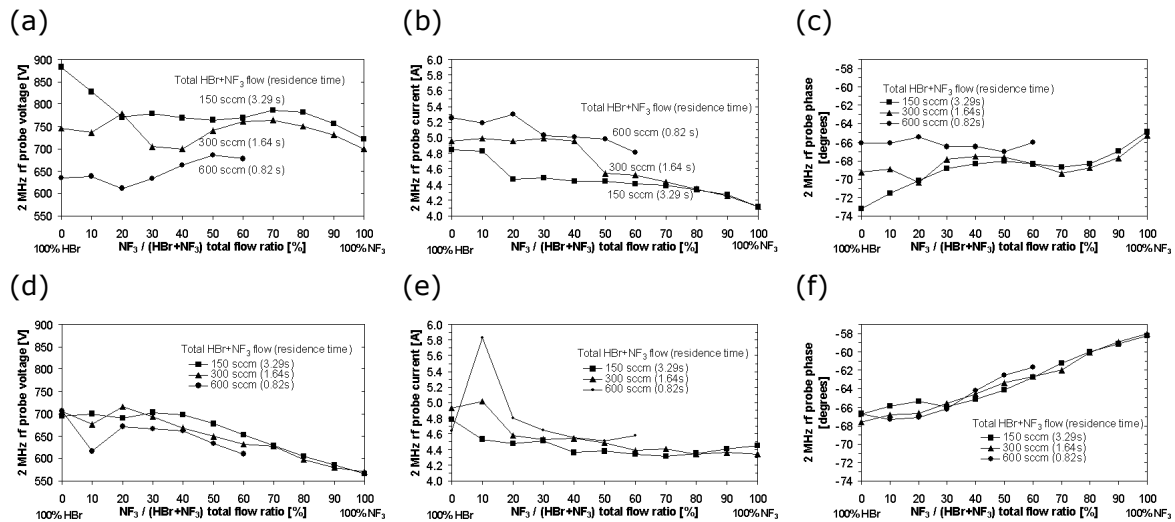


Figure H.3: 2 MHz rf probe data for variation of the total gas flow rate in HBr/NF₃ mixed discharges: (a) mean voltage; (b) mean current; (c) phase angle when using silicon substrates. 2 MHz rf probe data for variation of the total gas flow rate in HBr/NF₃ mixed discharges: (d) mean voltage; (e) mean current; (f) phase angle when using silicon substrates with an SiO₂ hard mask layer. Experiments were conducted at 1500+1500 W 60+2 MHz power, 150 mTorr, without magnetic field.

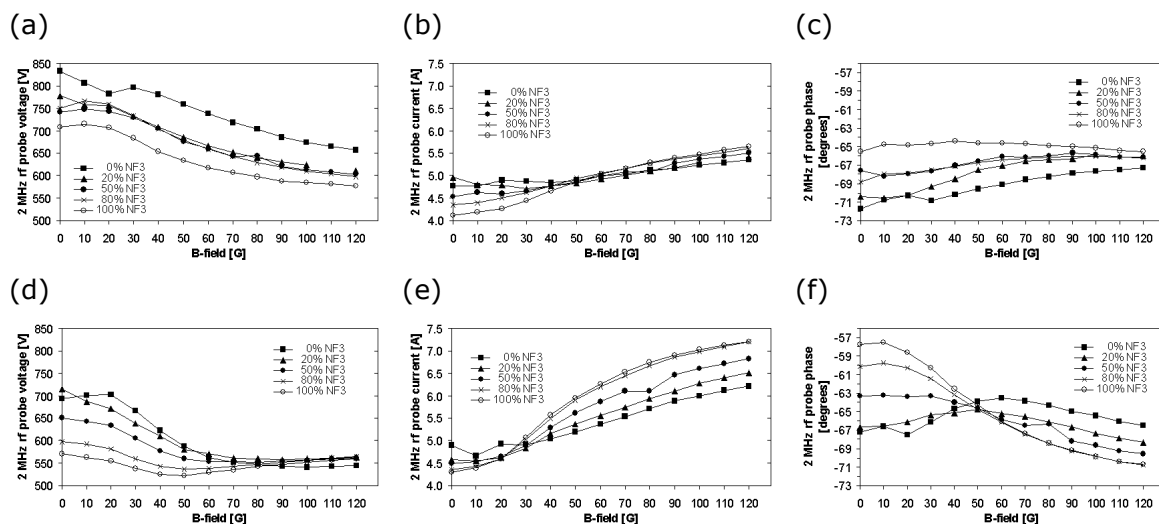


Figure H.4: 2 MHz rf probe data for variation of the magnetic field in HBr/NF₃ mixed discharges: (a) mean voltage; (b) mean current; (c) phase angle when using silicon substrates. 2 MHz rf probe data for variation of the magnetic field in HBr/NF₃ mixed discharges: (d) mean voltage; (e) mean current; (f) phase angle when using silicon substrates with an SiO₂ hard mask layer. Experiments were conducted at 1500+1500 W 60+2 MHz power, 150 mTorr, 300 sccm HBr/NF₃ total gas flow rate.

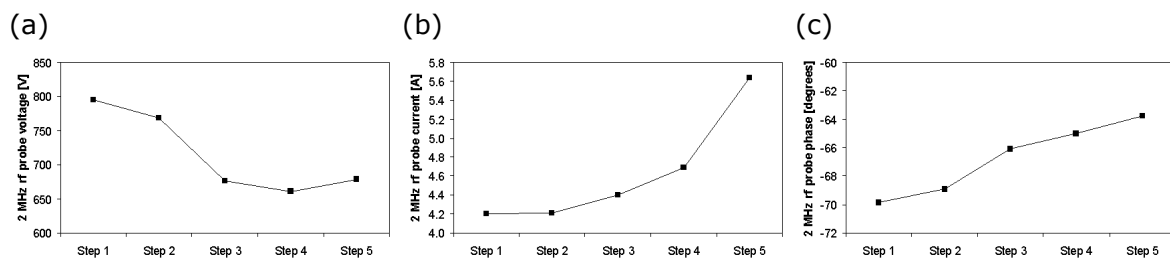


Figure H.5: 2 MHz rf probe data for different recipe steps of typical DT etch discharge operation (60+2 MHz HBr/NF₃/O₂/SiCl₄ discharges, DT patterned process substrate with a structured SiO₂ hard mask layer - 20% Si open area) : (a) mean voltage; (b) mean current; (c) phase angle.

Appendix I

Experimental results for SiF₄

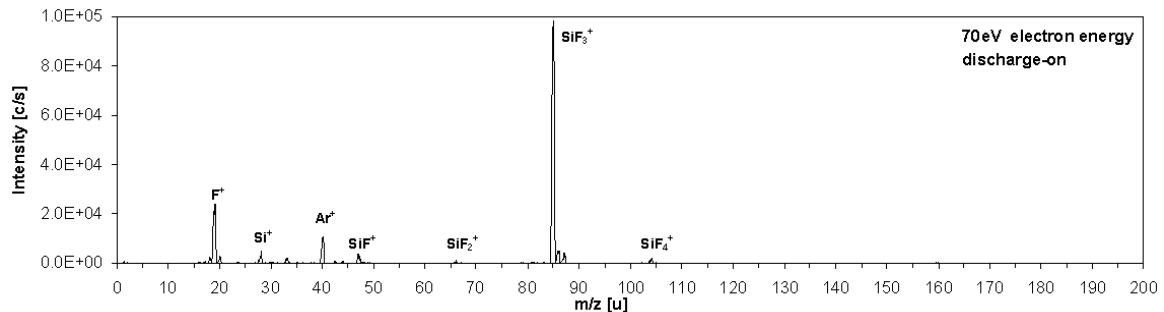


Figure I.1: Mass spectrum of neutral species ionized by 70 eV electrons for SiF₄ gas sampled from the reactor with rf discharge (150 mTorr, 1500 W 60 MHz power, 190 sccm SiF₄ + 16 sccm Ar gas flow rate, silicon substrate). The spectrum for SiF₄ gas without discharge was observed to be identical.

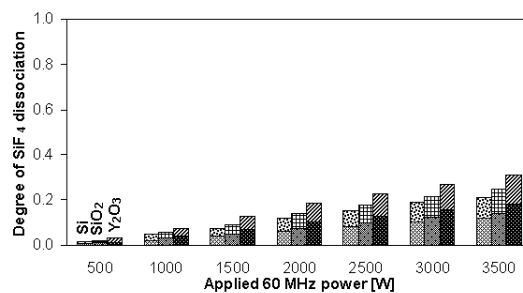


Figure I.2: Fractional degree of SiF₄ dissociation (dotted, crosshatched and striped area) with lower and upper limits determined from equations (4.7) and (4.8) applied to the mass spectral data for SiF₄ discharges at 150 mTorr with different 60 MHz power levels applied for silicon substrate (dotted area), silicon substrate with SiO₂ hardmask layer (crosshatched area), and yttria substrates (striped area) covering the surface of the electrostatic chuck. For all discharge conditions, a constant SiF₄ gas flow rate of 190 sccm (1.41×10^{-4} mol/s) was used.

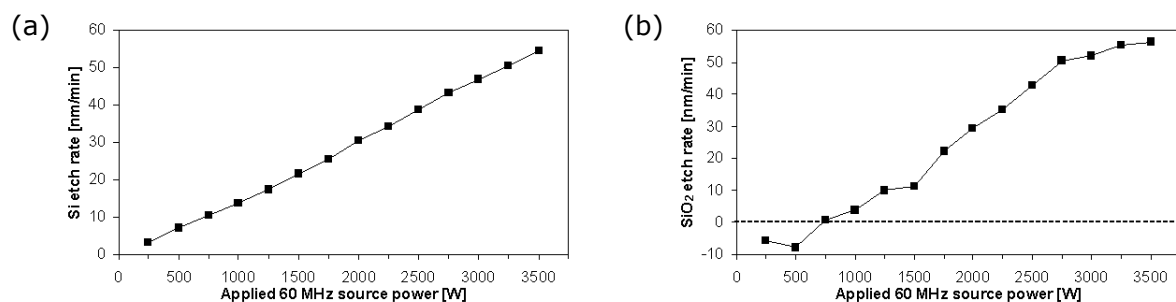


Figure I.3: Etch rates for 60 MHz power variation at (a) Si substrate, (b) SiO₂ layer on Si substrate (150 mTorr, 300 sccm SiF₄, no magnetic field).

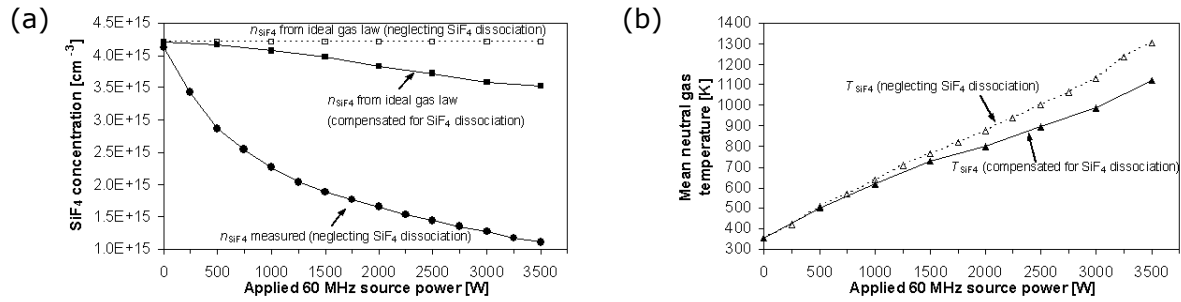


Figure I.4: (a) Measurements of SiF₄ concentrations and (b) calculation of neutral gas temperature

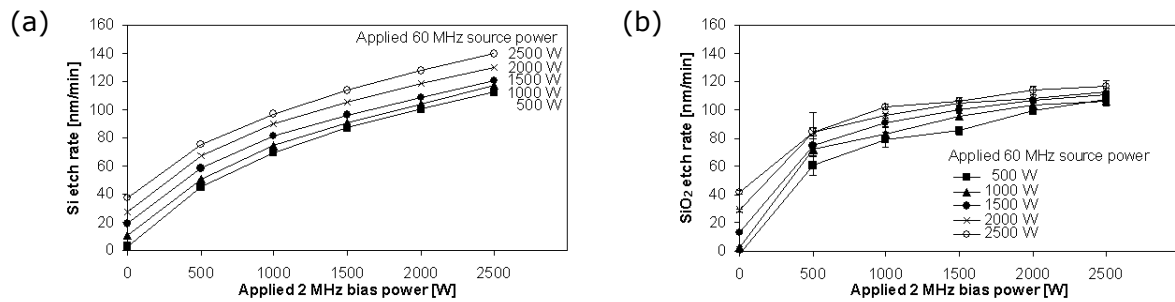


Figure I.5: Etch rates for 60+2 MHz power variation at (a) Si substrate, (b) SiO₂ layer on Si substrate (150 mTorr, 300 sccm SiF₄, no magnetic field).

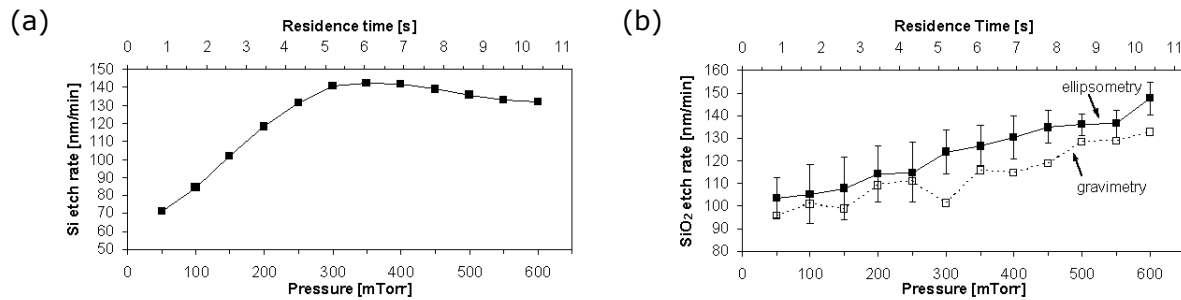


Figure I.6: Etch rates for pressure variation at (a) Si substrate, (b) SiO₂ layer on Si substrate (1500 W 60 MHz, 1500 W 2 MHz, 300 sccm SiF₄, no magnetic field).

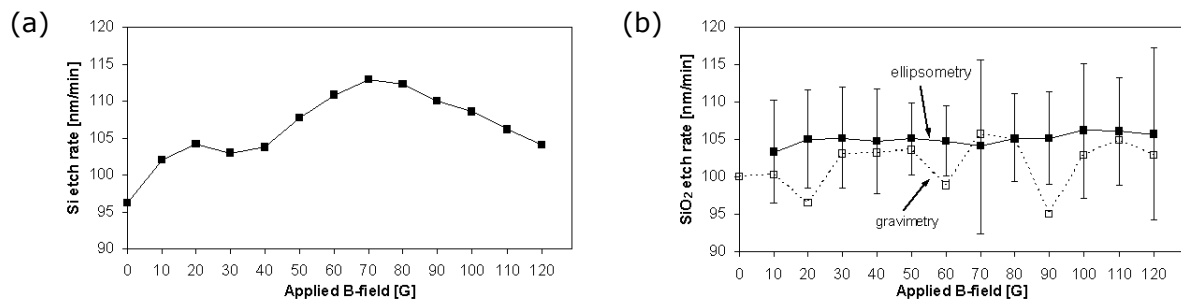


Figure I.7: Etch rates for variation of the magnetic field at (a) Si substrate, (b) SiO₂ layer on Si substrate (1500 W 60 MHz, 1500 W 2 MHz, 150 mTorr, 300 sccm SiF₄).

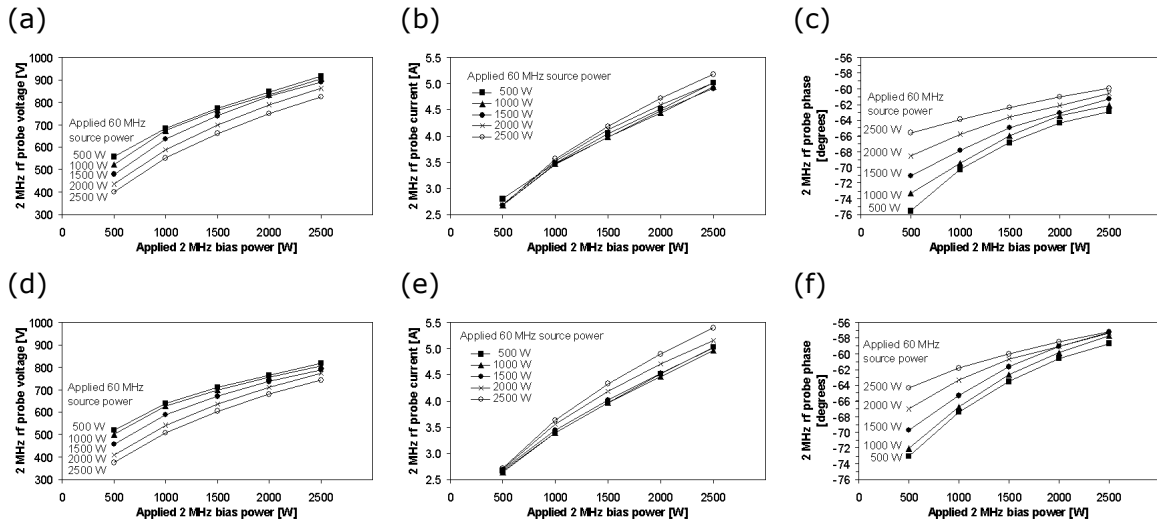


Figure I.8: 2 MHz rf probe data for 60+2 MHz power variation in SiF₄ discharges: (a) mean voltage; (b) mean current; (c) phase angle when using silicon substrates. 2 MHz rf probe data for 60+2 MHz power variation in SiF₄ discharges: (d) mean voltage; (e) mean current; (f) phase angle when using silicon substrates with a SiO₂ hard mask layer. Experiments were conducted at 150 mTorr, 190 sccm SiF₄ gas flow rate, without magnetic field.

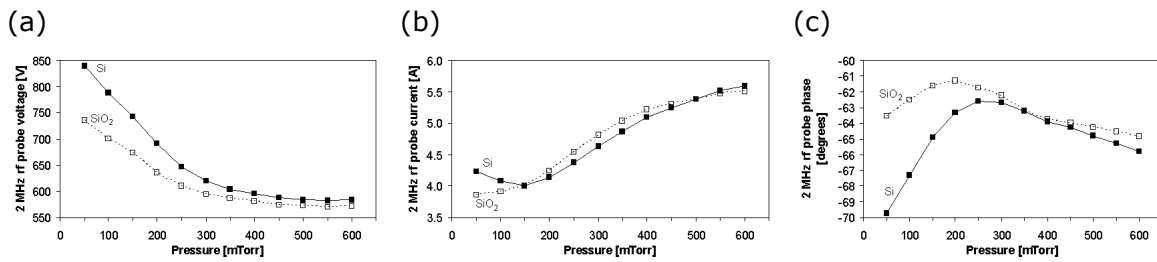


Figure I.9: 2 MHz rf probe data for variation of the pressure in SiF₄ discharges: (a) mean voltage; (b) mean current; (c) phase angle. Experiments were conducted at 1500+1500 W 60+2 MHz power, 190 sccm SiF₄ gas flow rate, no magnetic field, using silicon substrates with and without SiO₂ hard mask layer.

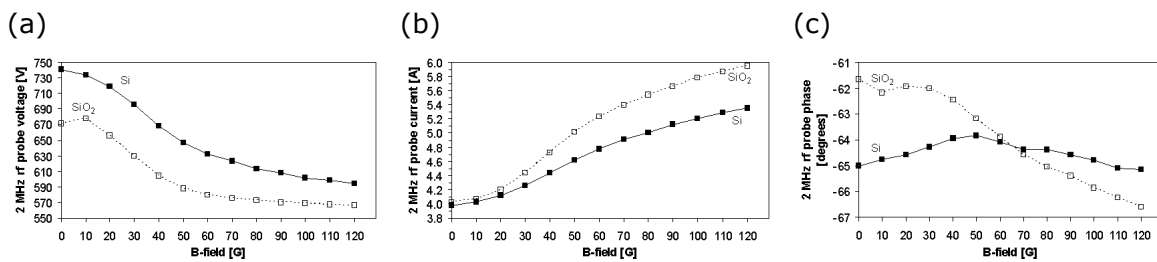


Figure I.10: 2 MHz rf probe data for variation of the magnetic field in SiF₄ discharges: (a) mean voltage; (b) mean current; (c) phase angle. Experiments were conducted at 1500+1500 W 60+2 MHz power, 150 mTorr, 190 sccm SiF₄ gas flow rate, using silicon substrates with and without SiO₂ hard mask layer.

Appendix J

Experimental results for SiCl₄

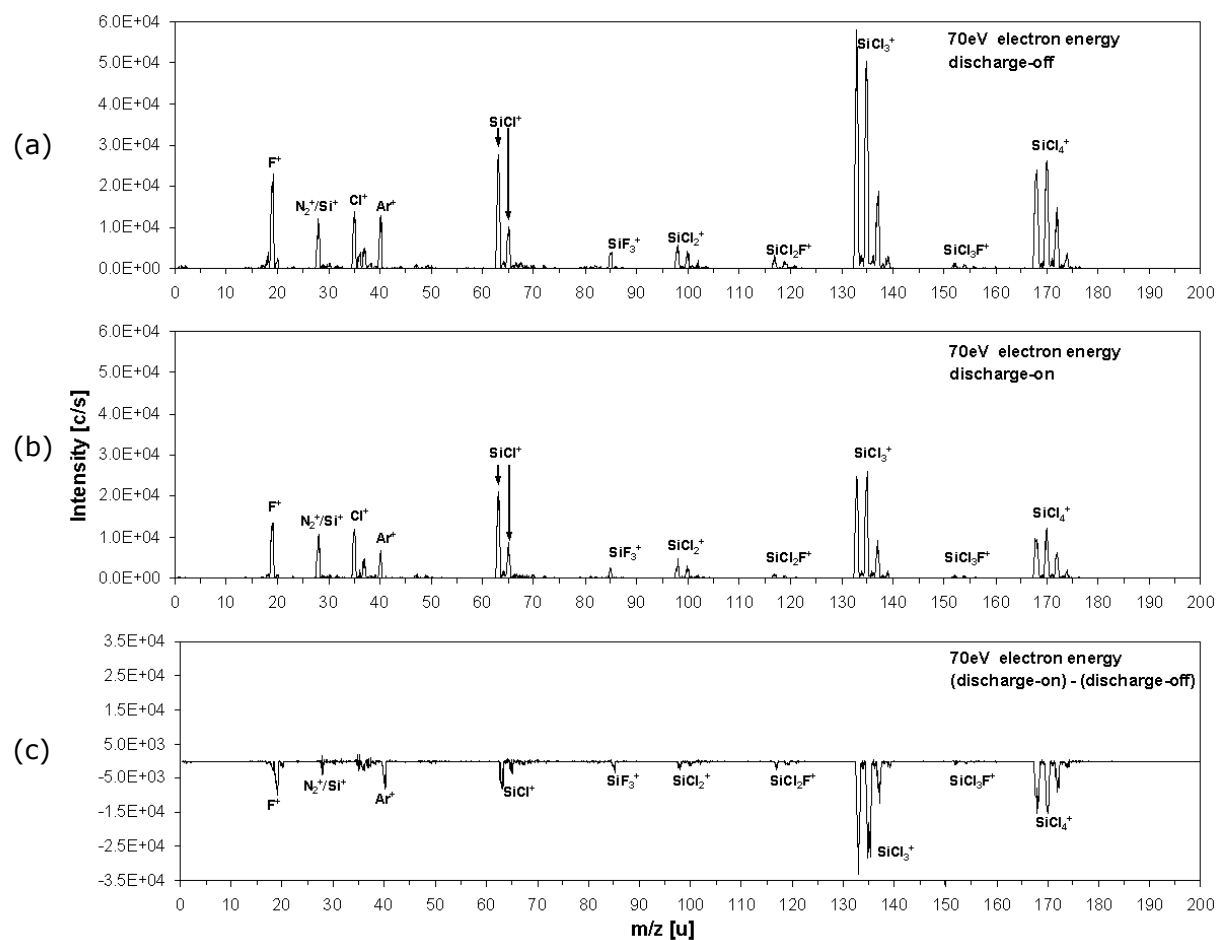


Figure J.1: Mass spectrum of neutral species ionized by 70 eV electrons for (a) SiCl₄ gas sampled from the reactor without discharge; (b) SiCl₄ gas sampled from the reactor with rf discharge (150 mTorr, 1500 W 60 MHz power, 190 sccm SiCl₄ + 16 sccm Ar gas flow rate, silicon substrate); (c) difference of mass spectra b-a (where negative values indicate a loss when the discharge is on).

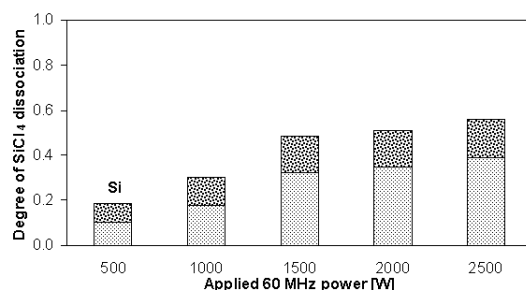


Figure J.2: Fractional degree of SiCl₄ dissociation (dotted, crosshatched and striped area) with lower and upper limits determined from equations (4.7) and (4.8) applied to the mass spectral data for SiCl₄ discharges at 150 mTorr with different 60 MHz power levels applied using a silicon substrate to cover the electrostatic chuck surface. For all discharge conditions, a constant SiCl₄ gas flow rate of 190 sccm (1.41×10^{-4} mol/s) was used.

References

- [1] M. ENGELHARDT: Single-crystal silicon trench etching for fabrication of highly integrated circuits, Proc. SPIE 1392 Advanced Techniques for Integrated Circuit Processing, 1990, 210
- [2] E. ADLER, J.K. DEBROSSE, S.F. GEISSLER, S.J. HOLMES, M.D. JAFFE, J.B. JOHNSON, C.W. KOBURGER III, J.B. LASKY, B. LLOYD, G.L. MILES, J.S. NAKOS, W.P. NOBLE JR., S.H. VOLDMAN, M. ARMACOST, R. FERGUSON: The evolution of IBM CMOS DRAM technology, IBM J. Res. Develop. Vol. 39 No. 1/2, 1995, 167
- [3] J.A. MANDELMAN, R.H. DENNARD, G.B. BRONNER, J.K. DEBROSSE, R. DIVAKARUNI, Y. LI, C.J. RADENS: Challenges and future directions for the scaling of dynamic random-access memory (DRAM), IBM J. Res. Develop. Vol. 46 No. 2/3, 2002, 187
- [4] Y.P. RAIZER: Gas discharge physics, 1991 Springer Verlag
- [5] V.A. GODYAK, R.B. PIEJAK, B.M. ALEXANDROVICH: Evolution of the electron-energy-distribution function during rf discharge transition to the high-voltage mode, Phys. Rev. Lett. 68(1), 1992, 40
- [6] H.C. KIM, J.K. LEE: Mode transition induced by low-frequency current in dual-frequency capacitive discharges, Phys. Rev. Lett. 93(8), 2004, 085003-1
- [7] C. WILD, P. KOIDL: Structured ion energy distribution in radio frequency glow-discharge systems, Appl. Phys. Lett. 54(6), 1989, 505
- [8] C. WILD, P. KOIDL: Ion and electron dynamics in the sheath of radio-frequency glow discharges, J. Appl. Phys. 69 (5), 1991, 2909
- [9] B. CHAPMAN: Glow discharge processes: Sputtering and plasma etching, 1980 John Wiley & Sons, Inc.
- [10] J.W. COBURN, H.F. WINTERS: Ion- and electron-assisted gas-surface chemistry - An important effect in plasma etching, J. Appl. Phys. 50(5), 1979, 3189
- [11] D. O'CONNELL: Investigations of high voltage plasma boundary sheaths in radio-frequency discharges operated with multiple frequencies, PhD thesis, Dublin City University, Ireland (2004)
- [12] D. O'CONNELL, R. ZORAT, A.R. ELLINGBOE, M.M. TURNER: Comparison of measurements and particle-in-cell simulations of ion energy distribution functions in a capacitively coupled radio-frequency discharge, Physics of Plasmas 14, 2007, 103510
- [13] A. BOGAERTS: Plasma diagnostics and numerical simulations - insight into the heart of analytical glow discharges, J. Anal. At. Spectrom. 22, 2007, 13
- [14] J.K. OLTHOFF, R.J. VAN BRUNT, S.B. RADOVANOV: Effect of electrode material on measured ion energy distributions in radio-frequency discharges, Appl. Phys. Lett. 67 (4), 1995, 473
- [15] D. ISRAEL: Die Ionenverteilungsfunktion an der Elektrode einer kapazitiv gekoppelten Hochfrequenz-Entladung, PhD thesis, Ruhr University Bochum, 2006
- [16] APPLIED MATERIALS, INC., 3050 Bowers Avenue, Santa Clara, CA 95054, USA, <http://>

- www.appliedmaterials.com
- [17] M. KRATZER, R.P. BRINKMANN, W. SABISCH, H. SCHMIDT: Hybrid model for the calculation of ion distribution functions behind a direct current or radio frequency driven plasma boundary sheath, *J. Appl. Phys.* 90 (5), 2001, 2169
- [18] W. SABISCH, M. KRATZER, R.P. BRINKMANN: Energetic neutral fluxes towards surfaces in a magnetically enhanced reactive ion etch-like reactor, *J. Vac. Sci. Technol. A* 21 (4), 2003, 1205
- [19] Y.P. RAIZER, M.N. SHNEIDER, N.A. YATSENKO: *Radio-Frequency Capacitive Discharges*, 1995 CRC Press, Inc.
- [20] M.A. LIEBERMAN, A.J. LICHTENBERG: *Principles of plasma discharges and materials processing*, 2005 John Wiley & Sons, Inc.
- [21] G.R. CORN, A.G. HEGEDUS: Variable duty cycle, Multiple frequency, Plasma reactor, US Patent 4,585,516, publication date 1986-04-29
- [22] M. SURENDRA, D. B. GRAVES: Capacitively coupled glow discharges at frequencies above 13.56 MHz, *Appl. Phys. Lett.* 59(17), 1991, 2091
- [23] T. KITAJIMA, Y. TAKEO, Z LJ. PETROVIC, T. MAKABE: Functional separation of biasing and sustaining voltages in two-frequency capacitively coupled plasma, *Appl. Phys. Lett.* 77(4), 2000, 489
- [24] V. GEORGIEVA, A. BOGAERTS, R. GIJBELS: Numerical study of Ar-CF₄-N₂ discharges in single- and dual-frequency capacitively coupled plasma reactors, *J. Appl. Phys.* 94(6), 2003, 3748
- [25] H.C. KIM, J.K. LEE, J.W. SHON: Analytic model for a dual frequency capacitive discharge, *Phys. Plasmas* 10(11), 2003, 4545
- [26] P.C. BOYLE, A.R. ELLINGBOE, M.M TURNER: Independent control of ion current and ion impact energy onto electrodes in dual frequency plasma devices, *J. Phys. D: Appl. Phys.* 37, 2004, 697
- [27] J.K. LEE, O.V. MANUILENKO, N.YU BABAEVA, H.C. KIM, J.W. SHON: Ion energy distribution control in single and dual frequency capacitive plasma sources, *Plasma Sources Sci. Technol.* 14, 2005, 89
- [28] S. SHANNON, D. HOFFMAN, J.-G. YANG, A. PATERSON, J. HOLLAND: The impact of frequency mixing on sheath properties: Ion energy distribution and V_{dc}/V_{rf} interaction, *J. Appl. Phys.* 97, 2005, 103304
- [29] Y. YANG, M. J. KUSHNER: Modeling of magnetically enhanced capacitively coupled plasma sources: two frequency discharges, *J. Vac. Sci. Technol. A* 25(5), 2007, 1420
- [30] M.A. LIEBERMAN, J.P. BOOTH, P.CHABERT, J.M. RAX, M.M. TURNER: Standing wave and skin effects in large-area, high-frequency capacitive discharges, *Plasma Sources Sci. Technol.* 11, 2002, 283
- [31] R.N. FRANKLIN: Electronegative plasmas - why are they so different?, *Plasma Sources Sci. Technol.* 11, 2002, A31
- [32] E. STOFFELS, W.W. STOFFELS, D. VENDER, M. KANDO, G.M.W. KROESEN, F.J. DE HOOG: Negative ions in a radio-frequency oxygen plasma, *Phys. Rev. E* 51(3), 1995, 2425

-
- [33] D. VENDER, W.W. STOFFELS, E. STOFFELS, G.M.W. KROESEN, F.J. DE HOOG: Charged-species profiles in electronegative radio-frequency plasmas, *Phys. Rev. E* 51(3), 1995, 2436
- [34] P. BRYANT, A. DYSON, J.E. ALLEN: Langmuir probe measurements of weakly collisional electronegative RF discharge plasmas, *J. Phys. D: Appl. Phys.* 34, 2001, 95
- [35] H.M. KATSCH, T. STURM, E. QUANDT, H.F. DOBELE: Negative ions and the role of metastable molecules in a capacitively coupled radiofrequency excited discharge in oxygen, *Plasma Sources Sci. Technol.* 9, 2000, 323
- [36] J.P.P. PASSCHIER, W.J. GOEDHEER: Relaxation phenomena after laser-induced photodetachment in electronegative rf discharges, *J. Appl Phys.* 73(3), 1993, 1073
- [37] A.J. LICHTENBERG, I.G. KOUZNETSOV, Y.T. LEE, M.A. LIEBERMAN, I.D. KAGANOVICH, L.D. TSENDIN: Modelling plasma discharges at high electronegativity, *Plasma Sources Sci. Technol.* 6, 1997, 437
- [38] V. A. GODYAK, N. STERNBERG: Dynamic model of the electrode sheaths in symmetrically driven rf discharges, *Phys. Rev. A* 42(4), 1990, 2299
- [39] K. U. RIEMANN: The Bohm criterion and sheath formation, *J. Phys. D: Appl. Phys.* 24, 1991, 493
- [40] T. PANAGOPOULOS, D.J. ECONOMOU: Plasma sheath model and ion energy distribution for all radio frequencies, *J. Appl. Phys.* 85(7) , 1999, 3435
- [41] J. ROBICHE, P.C. BOYLE, M.M. TURNER, A.R. ELLINGBOE: Analytical model of a dual frequency capacitive sheath, *J. Phys. D: Appl. Phys.* 36, 2003, 1810
- [42] R.N. FRANKLIN: The dual frequency radio-frequency sheath revisited, *J. Phys. D: Appl. Phys.* 36, 2003, 2660
- [43] P.C. BOYLE, J. ROBICHE, M.M. TURNER: Modelling of the dual frequency capacitive sheath in the intermediate pressure range, *J. Phys. D: Appl. Phys.* 37, 2004, 1451
- [44] U. FLENDER, K. WIESEMANN: Ion distribution functions behind an RF sheath, *J. Phys. D: Appl. Phys.* 27, 1994, 509
- [45] M. FIVAZ, S. BRUNNER, W. SCHWARZENBACH, A.A. HOWLING, C. HOLLENSTEIN: Reconstruction of the time-averaged sheath potential profile in an argon radiofrequency plasma using the ion energy distribution, *Plasma Sources Sci. Technol.* 4, 1995, 373
- [46] K. U. RIEMANN: The validity of Bohm's sheath criterion in rf discharges, *Phys. Fluids B* 4(9), 1992, 2693
- [47] C.D. CHILD: Discharge from hot CaO, *Phys. Rev.* 32 , 1911, 492
- [48] R. WARREN: Interpretation of field measurements in the cathode region of glow discharges, *Phys. Rev.* 98 (6), 1955, 1658
- [49] V.A. GODYAK: Soviet Radio Frequency Discharge Research, Delphic Associates, Inc., Falls Church, VA (1986)
- [50] R.N. FRANKLIN: Plasmas with more than one species of positive ion and the Bohm Criterion, *J. Phys. D: Appl. Phys.* 33, 2000, 3186

- [51] R.N. FRANKLIN: The transition from collisionless to collisional in active low-temperature plasmas with more than one species of positive ion generated by electron impact and the Bohm criterion, *J. Phys. D: Appl. Phys.* 34, 2001, 1959
- [52] M. BAYRAK: Die Plasmarandschicht als nichtlineares Bauelement - Untersuchung und Implementation von Newton Verfahren, Diplomarbeit Ruhr-Universität Bochum, Germany (2003)
- [53] R.P. BRINKMANN: Beyond the step model: Approximate expressions for the field in the plasma boundary sheath, *J. Appl. Phys.* 102, 2007, 093303
- [54] K. U. RIEMANN: Theoretical analysis of the electrode sheath in rf discharges, *J. Appl. Phys.* 65, 1989, 999
- [55] J. GIERLING, K. U. RIEMANN: Comparison of a consistent theory of radio frequency sheaths with step models, *J. Appl. Phys.* 83, 1998, 3521
- [56] I.G. KOUZNETSOV, A.J. LICHTENBERG, M.A. LIEBERMAN: Internal sheaths in electronegative discharges, *J. Appl. Phys.* 86(8), 1999, 4142
- [57] T.E. SHERIDAN: Double layers in a modestly collisional electronegative discharge, *J. Phys. D: Appl. Phys.* 32, 1999, 1761
- [58] R.N. FRANKLIN: The plasma-wall boundary region in negative-ion-dominated plasmas at low pressures, *Plasma Sources Sci. Technol.* 9, 2000, 191
- [59] R.J.M.M. SNIJKERS, M.J.M. VAN SAMBEEK, M.B. HOPPENBROUWERS, G.M.W. KROESEN, F.J. DE HOOG: Mass-resolved ion energy measurements at both electrodes of a 13.56 MHz plasma in CF₄, *J. Appl. Phys.* 79 (12), 1996, 8982
- [60] R.N. FRANKLIN: Basic relationships in electronegative plasmas with a multiplicity of negative and positive ion species, *J. Phys. D: Appl. Phys.* 36, 2003, 823
- [61] K. KÖHLER, J.W. COBURN, D.E. HORNE, E. KAY, J.H. KELLER: Plasma potentials of 13.56-MHz rf argon glow discharges in a planar system, *J. Appl. Phys.*, 57 (1), 1985, 59
- [62] E. KAWAMURA, V. VAHEDI, M.A. LIEBERMAN, C. K. BIRDSALL: Ion energy distributions in rf sheath; review, analysis and simulation, *Plasma Sources Sci. Technol.* 8, 1999, R45
- [63] F. BECKER, I.W. RANGELOW, R. KASSING: Ion energy distributions in SF₆ plasmas at a radio-frequency powered electrode, *J. Appl. Phys.* 80 (1), 1996, 56
- [64] J.K. OLTHOFF, R.J. VAN BRUNT, S.B. RADOVANOV: Ion kinetic-energy distributions in argon rf glow discharges, *J. Appl. Phys.* 72 (10), 1992, 4566
- [65] M. ZEUNER, H. NEUMANN, J. MEICHSNER: Ion energy distributions in a dc biased rf discharge, *J. Appl. Phys.* 81 (7), 1997, 2985
- [66] K. KÖHLER, D.E. HORNE, J.W. COBURN: Frequency dependence of ion bombardment of grounded surfaces in rf argon glow discharges in a planar system, *J. Appl. Phys.* 58 (9), 1985, 3350
- [67] J.W. COBURN, E. KAY: Positive-ion bombardment of substrates in rf diode glow discharge sputtering, *J. Appl. Phys.* 43(12), 1972, 4965
- [68] A.D. KUYPERS, H.J. HOPMAN: Ion energy measurement at the powered electrode in an

- rf discharge, *J. Appl. Phys.* 63(6), 1988, 1894
- [69] A.D. KUYPERS, H.J. HOPMAN: Measurement of ion energy distributions at the powered rf electrode in a variable magnetic field, *J. Appl. Phys.* 67(3), 1990, 1229
- [70] A. MANENSCHIJN, G.C.A.M. JANSSEN, E. VAN DER DRIFT, S. RADELAAR: Measurement of ion impact energy and ion flux at the rf electrode of a parallel plate reactive ion etcher, *J. Appl. Phys.* 69(3), 1991, 1253
- [71] W.M. GREENE, M.A. HARTNEY, W.G. OLDHAM, D.W. HESS: Ion transit through capacitively coupled Ar sheaths: Ion current and energy distribution, *J. Appl. Phys.* 63(5), 1988, 1367
- [72] J. JANES, C. HUTH: Energy resolved angular distribution of argon ions at the substrate plane of a radio frequency plasma reactor, *J. Vac. Sci. Technol. A* 10(6), 1992, 3522
- [73] J. JANES, C. HUTH: Energy resolved angular distribution of O⁺ ions at the radio-frequency-powered electrode in reactive ion etching, *J. Vac. Sci. Technol. A* 10(5), 1992, 3086
- [74] D. BARTON, D.J. HEASON, R.D. SHORT, J.W. BRADLEY: The measurement and control of the ion energy distribution function at a surface in an RF plasma, *Meas. Sci. Technol.* 11, 2000, 1726
- [75] H.-P. HSUEH, R.T. MCGRATH, B. JI, B.S. FELKER, J.G. LANGAN, E.J. KARWACKI: Ion energy distributions and optical emission spectra in NF₃-based process chamber cleaning plasmas, *J. Vac. Sci. Technol. B* 19(4), 2001, 1346
- [76] J. JANES: Mass-selected ion angular impact energy distributions at the powered electrode in CF₄ reactive-ion etching, *J. Appl. Phys.* 74(1), 1993, 659
- [77] R.J.M.M. SNIJKERS, M.J.M. VAN SAMBEEK, G.M.W. KROESEN, F.J. DE HOOG: Mass-resolved ion energy measurements at the grounded electrode of an Ar rf plasma, *Appl. Phys. Lett.* 63(3), 1993, 308
- [78] J.K. OLTHOFF, R.J. VAN BRUNT, S.B. RADOVANOV, J.A. REES, R. SUROWIEC: Kinetic-energy distributions of ions sampled from argon plasmas in a parallel-plate, radio-frequency reference cell, *J. Appl. Phys.* 75 (1), 1994, 115
- [79] V.A. DONNELLY, D.L. FLAMM, R.H. BRUCE: Effects of frequency on optical emission, electrical, ion, and etching characteristics of a radio frequency chlorine plasma, *J. Appl. Phys.* 58 (6), 1985, 2135
- [80] R. FOEST, J.K. OLTHOFF, R.J. VAN BRUNT, E.C. BENCK, J.R. ROBERTS: Optical and mass spectrometric investigations of ions and neutral species in SF₆ radio-frequency discharges, *Phys. Rev. E* 54 (2), 1996, 1876
- [81] K. SANDO, M. SUGAWARA: Measurements of the Time-Averaged Sheath Drop Using the Gridded Energy Analyzer, *Jpn. J. Appl. Phys. Vol. 35, Pt. 2, No. 2A*, 1996, L171
- [82] M. J. KUSHNER: Distribution of ion energies incident on electrodes in capacitively coupled rf discharges, *J. Appl. Phys.*, 58 (11), 1985, 4024
- [83] S.G. INGRAM, N.S.J. BRAITHWAITE: rf modulation of positive-ion energies in low-pressure discharges, *J. Appl. Phys.* 68 (11), 1990, 5519
- [84] P. BENOIT-CATTIN, L.C. BERNARD: Anomalies of the energy of positive ions extracted

- from high-frequency ion sources. A theoretical study, *J. Appl. Phys.* 39 (12), 1968, 5723
- [85] R.T. FAROUKI, S. HAMAGUCHI, M. DALVIE: Analysis of a kinematic model for ion transport in rf plasma sheaths, *Phys. Rev. A* 45, 1992, 5913
- [86] S. HAMAGUCHI, R.T. FAROUKI, M. DALVIE: Ponderomotive force and ion energy distributions in an rf sheath, *Phys. Rev. Lett.* 68(1), 1992, 44
- [87] K.-U. RIEMANN, U. EHLEMANN, K. WIESEMANN: The ion energy distribution in front of a negative wall, *J. Phys. D: Appl. Phys.* 25, 1992, 620
- [88] W.D. DAVIS, T.A. VANDERSLICE: Ion energies at the cathode of a glow discharge, *Phys. Rev.* 131 (1), 1963, 219
- [89] J. LIU, G.L. HUPPERT, H.H. SAWIN: Ion bombardment in rf plasmas, *J. Appl. Phys.* Vol. 68 No. 8, 1990, 3917
- [90] A. MANENSCHIJN, W.J. GOEDHEER: Angular ion and neutral energy distribution in a collisional rf sheath, *J. Appl. Phys.* 69(5), 1991, 2923
- [91] P.W. MAY, D. FIELD, D.F. KLEMPERER: Modeling radio-frequency discharges: Effects of collisions upon ion and neutral particle energy distributions, *J. Appl. Phys.* 71(8), 1992, 3721
- [92] B.E. THOMPSON, H.H. SAWIN, D.A. FISHER: Monte Carlo simulation of ion transport through rf glow-discharge sheaths, *J. Appl. Phys.* 63(7), 15 March 1988, 2241
- [93] G.A. HEBNER, M.J. KUSHNER: Phase and energy distribution of ions incident on electrodes in radio-frequency discharges, *J. Appl. Phys.* 62 (6), 1987, 2256
- [94] H. HWANG, M. J. KUSHNER: Ion energy distributions in radio frequency discharges sustained in gas mixtures obtained using a Monte Carlo-fluid hybrid model: endothermic processes and ion holes, *Plasma Sources Sci. Technol.* 3, 1994, 190
- [95] D. VENDER, R.W. BOSWELL: Numerical modeling of low-pressure RF plasmas, *IEEE Trans. Plasma Sci.* 18, 1990, 725
- [96] M. SURENDRA, D.B. GRAVES: Particle simulation of radio-frequency glow discharges, *IEEE Trans. Plasma Sci.* 19, 1991, 144
- [97] V. GEORGIEVA, A. BOGAERTS, R. GIJBELS: Particle-in-cell/Monte Carlo simulation of a capacitively coupled radio frequency Ar/CF₄ discharge: Effect of gas composition, *J. Appl. Phys.* 93(5), 2003, 2369
- [98] V. GEORGIEVA, A. BOGAERTS, R. GIJBELS: Numerical investigation of ion-energy-distribution functions in single and dual frequency capacitively coupled plasma reactors, *Phys. Rev. E* 69, 2004, 026406
- [99] A. METZE, D.W. ERNIE, H.J. OSKAM: Application of the physics of plasma sheaths to the modeling of rf plasma reactors, *J. Appl. Phys.* 60, 1986, 3081
- [100] P.M. VALLINGA, F.J. DE HOOG: Sheath properties of RF plasmas in a parallel-plate etch reactor; the low-frequency regime ($\omega < \omega_i$), *J. Phys. D: Appl. Phys.* 22, 1989, 925
- [101] F.L. WAELBROECK: Analytic solution for low-frequency rf sheaths in pulsed discharges, *Phys. Rev. E* 65, 2002, 066407

-
- [102] P.A. MILLER, M.E. RILEY: Dynamics of collisionless rf plasma sheaths, *J. Appl. Phys.* 82, 1997, 3689
- [103] D. BOSE, T.R. GOVINDAN, M. MEYYPAN: Ion dynamics model for collisionless radio frequency sheaths, *J. Appl. Phys.* 87, 2000, 7176
- [104] D. BOSE, T.R. GOVINDAN, M. MEYYPAN: Semianalytical ion current model for radio-frequency driven collisionless sheaths, *J. Appl. Phys.* 89, 2001, 5932
- [105] N. XIANG, F.L. WAELBROECK: Collisional sheath dynamics in the intermediate radio-frequency regime, *J. Appl. Phys.* 95(3), 2004, 860
- [106] P.C. ZALM: Some useful yield estimates for ion beam sputtering and ion plating at low bombarding energies, *J. Vac. Sci. Technol. B2*, 1984, 151
- [107] J. BOHDANSKY, J. ROTH, H.L. BAY: An analytical formula and important parameters for low-energy ion sputtering, *J. Appl. Phys.* 51(5), 1980, 2861
- [108] J. BOHDANSKY, J. ROTH, H.L. BAY: Erratum: An analytical formula and important parameters for low-energy ion sputtering, *J. Appl. Phys.* 52(3), 1981, 1610
- [109] D.M. MANOS, D.L. FLAMM: *Plasma etching: An introduction*, 1989 Academic Press, New York
- [110] H.F. WINTERS, J.W. COBURN: *Surface Science Aspects of Etching Reactions*, *Surface Science Reports* 14, 1992, 161
- [111] K. NINOMIYA, K. SUZUKI, S. NISHIMATSU, O. OKADA: Reaction of atomic fluorine with silicon, *J. Appl. Phys.* 58, 1985, 1177
- [112] A. HERRICK, A.J. PERRY, R.W. BOSWELL: Etching silicon by SF₆ in a continuous and pulsed power helicon reactor, *J. Vac. Sci. Technol. A21*, 2003, 955
- [113] M.E. BARONE, D.B. GRAVES: Chemical and physical sputtering of fluorinated silicon, *J. Appl. Phys.* 77(3), 1995, 1263
- [114] M.E. BARONE, D.B. GRAVES: Molecular-dynamics simulations of direct reactive ion etching of silicon by fluorine and chlorine, *J. Appl. Phys.* 78(11), 1995, 6604
- [115] I.W. RANGELOW, A. FICHELSCHER: Chlorine or bromine chemistry in RIE Si-Trench etching?, *Proc. SPIE 1392 Advanced Techniques for Integrated Circuit Processing*, 1990, 240
- [116] M. KRATZER, W. STEINHÖGL, A. KERSCH, T. SACHSE, V. HÖINK: Multi-Scale Simulations of Silicon Etching by Halides: Effects of Surface Reaction Rates, *Mat. Res. Soc. Symp. Proc. Vol. 677*, 2001, AA5.6.1
- [117] S.A. VITALE, H. CHAE, H.H. SAWIN: Silicon etching yields in F₂, Cl₂, Br₂, and HBr high density plasmas, *J. Vac. Sci. Technol. A* 19(5), 2001, 2197
- [118] H. NAGAYOSHI, M. YAMAGUCHI, K. KAMISAKO, T. HORIGOME, Y. TARUI: High-Rate Selective Etching of a-Si:H Using Hydrogen Radicals, *Jpn. J. Appl. Phys., Part 2* 33, 1994, L621
- [119] A. DINGER, C. LUTTERLOH, J. KÜPPERS: Stationary and non-stationary etching of Si(100) surfaces with gas phase and adsorbed hydrogen, *Chem. Phys. Lett.* 320, 2000, 405
- [120] R.C. VAN OORT, M.J. GEERTS, J.C. VAN DEN HEUVEL, J.W. METSELAAR: Hydrogen plasma etching of amorphous and microcrystalline silicon, *Electron. Lett.* 23, 1987, 967

- [121] S. QIN, J.D. BERNSTEIN, C. CHAN: Hydrogen etching for semiconductor materials in plasma doping experiments, *J. Electron. Mater.* 25, 1996, 507
- [122] S. VEPREK, F.-A. SAROTT: Electron-impact-induced anisotropic etching of silicon by hydrogen, *Plasma Chem. Plasma Process.* 2, 1982, 233
- [123] M.-C. CHUANG, J.W. COBURN: Molecular-beam study of gas-surface chemistry in the ion-assisted etching of silicon with atomic and molecular hydrogen and chlorine, *J. Vac. Sci. Technol. A* 8, 1990, 1969
- [124] G.P. KOTA, J.W. COBURN, D.B. GRAVES: The recombination of chlorine atoms at surfaces, *J. Vac. Sci. Technol. A* 16(1), 1998, 270
- [125] G.P. KOTA, J.W. COBURN, D.B. GRAVES: Heterogeneous recombination of atomic bromine and fluorine, *J. Vac. Sci. Technol. A* 17(1), 1999, 282
- [126] C.C. CHENG, K.V. GUINN, I.P. HERMAN, V.M. DONNELLY: Competitive halogenation of silicon surfaces in HBr/Cl₂ plasmas studied with x-ray photoelectron spectroscopy and in situ, real-time, pulsed laser-induced thermal desorption, *J. Vac. Sci. Technol. A* 13(4), 1995, 1970
- [127] A.M. EL-MASRY, F.-O. FONG, J.C. WOLFE, J.N. RANDALL: Magnetically enhanced reactive ion etching of silicon in bromine plasmas, *J. Vac. Sci. Technol. B* 6(1), 1988, 257
- [128] C.C. CHENG, K.V. GUINN, V.M. DONNELLY: Mechanism for anisotropic etching of photoresist-masked, polycrystalline silicon in HBr plasmas, *J. Vac. Sci. Technol. B* 14(1), 1996, 85
- [129] J.-H. LEE, G.-Y. YEOM, J.-W. LEE, J.-Y. LEE: Study of shallow silicon trench etch process using planar inductively coupled plasmas, *J. Vac. Sci. Technol. A* 15, 1997, 573
- [130] T.D. BESTWICK, G.S. OEHRLEIN: Reactive ion etching of silicon using bromine containing plasmas, *J. Vac. Sci. Technol. A* 8, 1990, 1696
- [131] D.X. MA, T.-A. LIN, C.-H. CHEN: High selectivity electron cyclotron resonance etching of submicron polysilicon gate structures, *J. Vac. Sci. Technol. A* 10, 1992, 1217
- [132] D.P. HAMBLIN, A. CHA-LIN: Angular Etching Correlations from RIE, *J. Electrochem. Soc.* 135, 1988, 1816
- [133] M. HAVERLAG, G.S. OEHRLEIN, D. VENDER: Sidewall passivation during the etching of poly-Si in an electron cyclotron resonance plasma of HBr, *J. Vac. Sci. Technol. B* 12, 1994, 96
- [134] S. OHKI, M. ODA, H. AKIYA, T. SHIBATA: Cavernous undercuts appearing in reactive ion etched submicron-wide deep trenches, *J. Vac. Sci. Technol. B* 5 (6), Nov/Dec 1987, 1611
- [135] K. COOPER, B.-Y. NGUYEN, J.-H. LIN, B.J. ROMAN, P.J. TOBIN, W. RAY: Magnetically enhanced reactive ion etching of submicron silicon trenches, *Proc. SPIE 1392 Advanced Techniques for Integrated Circuit Processing*, 1990, 253
- [136] D. CHIN, S. DHONG, G. LONG: Structural Effects on a Submicron Trench Process, *J. Electrochem. Soc.* 132(7), 1985, 1705
- [137] Y.H. LEE, Z.H. ZHOU: Feature-Size Dependence of Etch Rate in Reactive Ion Etching,

- J. Electrochem. Soc. 138, 1991, 2439
- [138] R.A. GOTTSCHO, C.W. JURGENSEN, D.J. VITKAVAGE: Microscopic uniformity in plasma etching, *J. Vac. Sci. Technol. B* 10(5), 1992, 2133
- [139] J.W. COBURN, H.F. WINTERS: Conductance considerations in the reactive ion etching of high aspect ratio features, *Appl. Phys. Lett.* 55(26), 1989, 2730
- [140] E.S.G. SHAQFEH, C.W. JURGENSEN: Simulation of reactive ion etching pattern transfer, *J. Appl. Phys.* 66(10), 1989, 4664
- [141] K.P. GIAPIS, G.R. SCHELLER, R.A. GOTTSCHO, W.S. HOBSON, Y.H. LEE: Microscopic and macroscopic uniformity control in plasma etching, *Appl. Phys. Lett.* 57(10), 1990, 983
- [142] S.G. INGRAM: The influence of substrate topography on ion bombardment in plasma etching, *J. Appl. Phys.* 68(2), 1990, 500
- [143] J.C. ARNOLD, H.H. SAWIN: Charging of pattern features during plasma etching, *J. Appl. Phys.* 70(10), 1991, 5314
- [144] H. SINGH, J.W. COBURN, D.B. GRAVES: Mass spectrometric detection of reactive neutral species: Beam-to-background ratio, *J. Vac. Sci. Technol. A* 17(5), Sep/Oct 1999, 2447
- [145] H. SINGH, J.W. COBURN, D.B. GRAVES: Appearance potential mass spectrometry - Discrimination of dissociative ionization products, *J. Vac. Sci. Technol. A* 18(2), 2000, 299
- [146] M.A. SOBOLEWSKI, J.K. OLTHOFF, Y. WANG: Ion energy distributions and sheath voltages in a radio-frequency-biased, inductively coupled, high-density plasma reactor, *J. Appl. Phys.* 85 (8), 1999, 3966
- [147] Y. WANG, J.K. OLTHOFF: Ion energy distributions in inductively coupled radio-frequency discharges in argon, nitrogen, oxygen, chlorine, and their mixtures, *J. Appl. Phys.* 85 (9), 1999, 6358
- [148] J.-P. KRUMME, R.A.A. HACK, I.J.M.M. RAAIJMAKERS: Energy distribution of negative O^- and OH^- ions emitted from YBaCuO and iron garnet targets by dc and rf magnetron sputtering, *J. Appl. Phys.* 70 (11), 1991, 6743
- [149] E. STOFFELS, W.W. STOFFELS, D. VENDER, M. HAVERLAG, G.M.W. KROESEN, F.J. DE HOOG: Negative Ions in Low Pressure Discharges, *Contrib. Plasma Phys.* Vol. 35, Iss. 4-5, 1995, 331
- [150] Corning Incorporated, One Riverfront Plaza, Corning, NY 14831, USA, <http://www.corning.com>
- [151] W.W. STOFFELS, E. STOFFELS, K. TACHIBANA: Electron Attachment Mass Spectrometry for the Detection of Electronegative Species in a Plasma, *Jpn. J. Appl. Phys.* 36 1 7B, 1997, 4638
- [152] H. WOLLNIK: Optics of charged particles, 1987 Academic Press, Inc.
- [153] HIDDEN ANALYTICAL LTD., 420 Europa Boulevard, Gemini business Park, Warrington WA5 5UN, England, <http://www.hidden.co.uk>

- [154] P.H. DAWSON: *Quadrupole Mass Spectrometry and its applications*, 1976 Elsevier Scientific Publishing
- [155] BURLE Industries, Inc., 1000 New Holland Avenue, Lancaster, PA 17601-5688, USA, <http://www.burle.com>
- [156] V.M. DONNELLY: *Optical diagnostic techniques for low pressure plasmas and plasma processing*, in O. AUCIELLO, D.L. FLAMM: *Plasma Diagnostics Volume 1: Discharge parameters and chemistry*, 1989 Academic Press, Inc.
- [157] W. GRÄHLERT, I. DANI, O. THROL, V. HOPFE, K. PIETSCH, T. WÜNSCHE, T. DREYER, VDI-Berichte Nr. 19, 2006, 45
- [158] M. STERNHEIM, W. VAN GELDER, A.W. HARTMAN: A laser interferometer system to monitor dry etching of patterned silicon, *J. Electrochem. Soc.: Solid-State Sci. Technol.* 130(3), 1983, 655
- [159] D.J. HEASON, A.G. SPENCER: Infrared interference patterns for new capabilities in laser end point detection, *J. Phys. D: Appl. Phys.* 36, 2003, 1543
- [160] H.C. SUN, V. PATEL, B. SINGH, C.K. NG, E.A. WHITTAKER: Sensitive plasma etching endpoint detection using tunable diode laser absorption spectroscopy, *Appl. Phys. Lett.* 64 (21), 1994, 2779
- [161] J. FAIST, F. CAPASSO, D.L. SIVCO, C. SIRTORI, A.L. HUTCHINSON, A. CHO: Quantum Cascade Laser, *Science*, 264, 1994, 553
- [162] S. BLASER, 4-th Workshop on QCL Technology and Application, Freiburg, Germany, 2003
- [163] M. BECK, 4-th Workshop on QCL Technology and Application, Freiburg, Germany, 2003
- [164] C. GMACHL, D.L. SIVCO, R. COLOMBELLI, F. CAPASSO, A.Y. CHO: Ultra-broadband semiconductor laser, *Nature*, 415 883, 2002
- [165] G.D. STANCU, N. LANG, J. RÖPCKE, M. REINICKE, A. STEINBACH, S. WEGE: In situ monitoring of silicon plasma etch using a quantum cascade laser arrangement, *Chem. Vap. Deposition* 13, 2007, 351
- [166] M. REINICKE, J.W. BARTHA, S. WEGE, A. STEINBACH, S. BARTH, G. WENIG, A. KERSCH: Application of insitu Plasma Analysis on Deep Trench Plasma Etch Hardware Design and Process Development, presented at the AVS 53rd International Symposium, 2006, San Francisco (USA)
- [167] G.D. STANCU, N. LANG, J. RÖPCKE, M. REINICKE, A. STEINBACH, S. WEGE: In situ monitoring of silicon plasma etch using a quantum cascade laser arrangement, plenary talk at FLAIR, 2007, Florence (Italy)
- [168] S.V. BEREZHNOI, I.D. KAGANOVICH, L.D. TSENDIN, V.A. SCHWEIGERT: Fast modeling of the low-pressure capacitively coupled radio-frequency discharge based on the nonlocal approach, *Appl. Phys. Lett.* Vol. 69 (16), 1996, 2341
- [169] J.P. BOEUF: Numerical model of rf glow discharges, *Phys. Rev. A* 36 (6), 1987, 2782
- [170] M.M. MEYYPAN, J.P. KRESKOVSKY: Glow discharge simulation through solutions to the moments of the Boltzmann transport equation, *J. Appl. Phys.* 68(4), 1990, 1506

-
- [171] J.P. BOEUF: A two-dimensional model of dc glow discharges, *J. Appl. Phys.* 63 (5), 1988, 1342
- [172] J.D.P. PASSCHIER, W.J. GOEDHEER: A two-dimensional fluid model for an argon rf discharge, *J. Appl. Phys.* 74 (6), 1993, 3744
- [173] R.A. STEWART, P. VITELLO, D.B. GRAVES: Two-dimensional fluid model of high density inductively coupled plasma sources, *J. Vac. Sci. Technol. B* 12(1), 1994, 478
- [174] D. HERREBOUT, A. BOGAERTS, M. YAN, W. GOEDHEER, E. DEKEMPENEER, R. GIJBELS: One-dimensional fluid model for an rf methane plasma of interest in deposition of diamond-like carbon layers, *J. Appl. Phys.* 90 (2), 2001, 570
- [175] D. LOFFHAGEN, R. WINKLER: A New Nonstationary Boltzmann Solver in Self-Consistent Modelling of Discharge Pumped Plasmas for Excimer Lasers, *J. Comput. Phys.* 112, 1994, 91
- [176] F. SIGENEGER, R. WINKLER: Study of the electron kinetics in cylindrical hollow cathodes by a multi-term approach, *Eur. Phys. J.: Appl. Phys.* 19, 2002, 211
- [177] J.P. BOEUF, E. MARODE: A Monte Carlo analysis of an electron swarm in a nonuniform field the cathode region of a glow discharge in helium, *J. Phys. D: Appl. Phys.* 15, 1982, 2169
- [178] Z. DONKO, K. ROZSA, R. C. TOBIN: Monte Carlo analysis of the electrons' motion in a segmented hollow cathode discharge, *J. Phys. D: Appl. Phys.* 29, 1996, 105
- [179] M. OHUCHI, T. KUBOTA: Monte Carlo simulation of electrons in the cathode region of the glow discharge in helium, *J. Phys. D: Appl. Phys.* 16, 1983, 1705
- [180] R. PAYLING, O. BONNOT, E. FRETTEL, O. ROGERIEUX, M. AEBERHARD, J. MICHLER, T. NELIS, U. HANSEN, A. HARTMANN, P. BELENGUER, P. GUILLOT: Modelling the RF source in GDOES, *J. Anal. At. Spectrom.* 18, 2003, 656
- [181] L. WILKEN, V. HOFFMANN, K. WETZIG: Analysis of new electrical signals in respect to quantification of radio frequency glow discharge emission spectrometry, *Appl. Surf. Sci.* 252, 2005, 261
- [182] C.K. BIRDSALL, A.B. LANGDON: Plasma physics via computer simulation, 2005 Taylor & Francis Group, LLC
- [183] E. NEYTS, M. YAN, A. BOGAERTS, R. GIJBELS: Particle-in-cell/Monte Carlo simulations of a low-pressure capacitively coupled radio-frequency discharge: Effect of adding H₂ to an Ar discharge, *J. Appl. Phys.* 93(9), 2003, 5025
- [184] I. KOLEV, A. BOGAERTS, R. GIJBELS: Influence of electron recapture by the cathode upon the discharge characteristics in dc planar magnetrons, *Phys. Rev. E* 72, 2005, 056402
- [185] R. ZORAT, J. GOSS, D. BOILSON, D. VENDER: Global model of a radiofrequency H₂ plasma in DENISE, *Plasma Sources Sci. Technol.* 9, 2000, 161
- [186] R. ZORAT, D. VENDER: Global model for an rf hydrogen inductive plasma discharge in the deuterium negative ion source experiment including negative ions, *J. Phys. D: Appl. Phys.* 33 (14), 2000, 1728
- [187] C. LEE, D.B. GRAVES, M.A. LIEBERMAN, D.W. HESS: Global Model of Plasma Chemistry

- in a High Density Oxygen Discharge, *J. Electrochem. Soc.* 141 (6), 1994, 1546
- [188] C. LEE, M.A. LIEBERMAN: Global model of Ar, O₂, Cl₂, and Ar-O₂ high-density plasma discharges, *J. Vac. Sci. Technol. A* 13(2), 1995, 368
- [189] Y.T. LEE, M.A. LIEBERMAN, A.J. LICHTENBERG, F. BOSE, H. BALTES, R. PATRICK: Global model for high pressure electronegative radio-frequency discharges, *J. Vac. Sci. Technol. A* 15 (1), 1997, 113
- [190] Z. DONKO, M. JANOSSY: Model of the cathode dark space in noble gas mixture discharges, *J. Phys. D: Appl. Phys.* 25, 1992, 1323
- [191] Z. DONKO: Heavy-particle hybrid modeling of transients in a direct-current argon discharge, *J. Appl. Phys.* 88(5), 2000, 2226
- [192] W. JACOBS, A. KERSCH, P. MOLL, W. SABISCH, G. SCHULZE ICKING-KONERT: A Feature Scale Model for Trench Capacitor Etch Rate and Profile, 2002 IEEE
- [193] J.W. COBURN: A system for determining the mass and energy of particles incident on a substrate in a planar diode sputtering system, *Rev. Sci. Instrum.* 41, 1970, 1219
- [194] K. TOMINAGA, S. IWAMURA, Y. SHINTANI, O. TADA: Energy analysis of high-energy neutral atoms in the sputtering of ZnO and BaTiO₃, *Jpn. J. Appl. Phys.* 21, 1982, 688
- [195] K. SCHÄFER, W.Y. BAEK, K. FÖRSTER, D. GASSEN, W. NEUWIRTH: Analysis of initial energies of fragments produced by 65-keV proton-molecule collisions using a time-of-flight mass spectrometer, *Z. Phys. D: Atoms, Molecules and Clusters* 21, 1991, 137
- [196] J.R. WOODWORTH, M.E. RILEY, D.C. MEISTER, B.P. ARAGON, M.S. LE, H.H. SAWIN: Ion energy and angular distributions in inductively coupled radio frequency discharges in argon, *J. Appl. Phys.* 80 (3), 1996, 1304
- [197] J.R. WOODWORTH, M.E. RILEY, P.A. MILLER, G.A. HEBNER, T.W. HAMILTON: Ion energy and angular distributions in inductively driven radio frequency discharges in chlorine, *J. Appl. Phys.* 81 (9), 1997, 5950
- [198] E.A.G. HAMERS, W.G.J.H.M. VAN SARK, J. BEZEMER, W.J. GOEDHEER, W.F. VAN DER WEG: On the transmission function of an ion-energy and mass spectrometer, *Int. J. Mass Spectrom. Ion Processes* 173 (1998) 91
- [199] D.A. DAHL, J.E. DELMORE, A.D. APPELHANS: SIMION PC/PS2 electrostatic lens design program, *Rev. Sci. Instrum.* 61, 1990, 607
- [200] <http://www.freefem.org>
- [201] G.A. EMMERT: Model for expanding sheaths and surface charging at dielectric surfaces during plasma source ion implantation, *J. Vac. Sci. Technol. B* 12(2), 1994, 880
- [202] A. KERSCH, G. WENIG: private communication
- [203] M. OSIAC, T. SCHWARZ-SELINGER, D. O'CONNELL, B. HEIL, Z.LJ PETROVIC, M.M. TURNER, T. GANS, U. CZARNETZKI: Plasma boundary sheath in the afterglow of a pulsed inductively coupled RF plasma, *Plasma Sources Sci. Technol.* 16, 2007, 355
- [204] V. VARTOLOMEI, T. SCHWARZ-SELINGER: private communication

-
- [205] D. HEIM, H. STÖRI: Ion energy distributions on surfaces exposed to plasmas: An experimental and theoretical investigation, *J. Appl. Phys.* 72(8), 1992, 3330
- [206] K. ELLMER, R. WENDT, K. WIESEMANN: Interpretation of ion distribution functions measured by a combined energy and mass analyzer, *Int. J. Mass Spectrom.* 223-224, 2003, 679
- [207] J.E. ALLEN: On the plotting of electron and ion distribution functions, *J. Phys. D: Appl. Phys.* 25, 1992, 1839
- [208] C. BÖHM, J. PERRIN: Retarding-field analyzer for measurements of ion energy distributions and secondary electron emission coefficients in low-pressure radio frequency discharges, *Rev. Sci. Instrum.* 64(1), 1993, 31
- [209] J.W. COBURN, E. KAY: Pressure considerations associated with ion sampling from glow discharges, *J. Vac. Sci. Technol.* 8(6), 1971, 738
- [210] A. V. PHELPS: Cross sections and swarm coefficients for nitrogen ions and neutrals in N₂ and argon ions and neutrals in Ar for energies from 0.1eV to 10keV, *J. Phys. Chem. Ref. Data* 20, 1991, 557
- [211] A. V. PHELPS, C.H. GREENE, J.P. BURKE JR.: Collision cross sections for argon atoms with argon atoms for energies from 0.01 eV to 10 keV, *J. Phys. B: At. Mol. Opt. Phys.* 33, 2000, 2965
- [212] B.E. THOMPSON, K.D. ALLEN, A.D. RICHARDS, H.H. SAWIN: Ion bombardment energy distributions in radio-frequency glow-discharge systems, *J. Appl. Phys.* 59(6), 15 March 1986, 1890
- [213] W.M.M. KESSELS, C.M. LEEWIS, M.C.M. VAN DE SANDEN, D.C. SCHRAM: Formation of cationic silicon clusters in a remote silane plasma and their contribution to hydrogenated amorphous silicon film growth, *J. Appl. Phys.* Vol. 86 No. 7, 1999, 4029
- [214] Applied Materials internal measurements
- [215] A.KERSCH, W. SABISCH, D. FISCHER, W.JACOBS, S. BARTH, A. HENKE, J. SOBE, A. STEINBACH, S. WEGE, M. REINICKE: Development of high aspect ratio, selective Si etch model in CCP halogen plasma, presented at the AVS 53rd International Symposium, 2006, San Francisco (USA)
- [216] S.W. NAGY, S.M. FERNANDEZ, E. POLLACK: Small-angle charge-exchange scattering of He⁺ by He, Ne, and Kr at energies between 1 and 3keV, *Physical Review A* 3(1), 1971, 280
- [217] B.M. SMIRNOV: Tables for cross sections of the resonant charge exchange process, *Physica Scripta*. Vol. 61, 2000, 595
- [218] D.R. LIDE: 85th CRC Handbook of Physics and Chemistry, 2005 CRC
- [219] <http://webbook.nist.gov/chemistry>
- [220] E.W. MCDANIEL: *Collisional Phenomena in Ionized Gases*, 1964 Wiley, New York
- [221] E.W. MCDANIEL: *Atomic collisions - Heavy particle projectiles*, 1993 John Wiley & Sons, Inc.

- [222] T. SU, M.T. BOWERS: Ion-polar molecule collisions: The effect of ion size on ion-polar molecule rate constants; The parameterization of the average-dipole-orientation theory, *Int. J. Mass Spectrom. Ion Phys.* 12, 1973, 347
- [223] P.W. ATKINS, J. DE PAULA: *Physikalische Chemie*, 2006 Wiley-VCH
- [224] M. HAYASHI: Bibliography of electron and photon cross sections with atoms and molecules - Argon, *National Institute of Fusion Science Data* 72, 2003
- [225] M.J. VASILE, H.F. DYLLA: Mass spectrometry of plasmas, in O. AUCIELLO, D.L. FLAMM: *Plasma Diagnostics Volume 1: Discharge parameters and chemistry*, 1989 Academic Press, Inc.
- [226] H. SINGH, J.W. COBURN, D.B. GRAVES: Recombination coefficients of O and N radicals on stainless steel, *J. Appl. Phys.* 88(6), 2000, 3748
- [227] E. MEEKS, J.W. SHON, Y. RA, P. JONES: Effects of atomic chlorine wall recombination - Comparison of a plasma chemistry model with experiment, *J. Vac. Sci. Technol. A* 13(6), 1995, 2884
- [228] P. KAE-NUNE, J. PERRIN, J. GUILLON, J. JOLLY: Mass spectrometry detection of radicals in SiH₄-CH₄-H₂ glow discharge plasmas, *Plasma Sources Sci. Technol.* 4, 1995, 250
- [229] H. SUGAI, H. TOYODA: Appearance mass spectrometry of neutral radicals in radio frequency plasmas, *J. Vac. Sci. Technol. A* 10, 1992, 1193
- [230] R. ROBERTSON, D. HILS, H. CHATHAM, A. GALLAGHER: Radical species in argon-silane discharges, *Appl. Phys. Lett.* 43(6), 1983, 544
- [231] R. ROBERTSON, A. GALLAGHER: Mono- and disilicon radicals in silane and silane-argon dc discharges, *J. Appl. Phys.* 59(10), 1986, 3402
- [232] S. AGARWAL, G.W.W. QUAX, M.C.M. VAN DE SANDEN, D. MAROUDAS, E.S. AYDIL: Measurement of absolute radical densities in a plasma using modulated-beam line-of-sight threshold ionization mass spectrometry, *J. Vac. Sci. Technol. A* 22(1), 2004, 71
- [233] G.H. WANNIER: The Threshold Law for Single Ionization of Atoms or Ions by Electrons, *Phys. Rev.* 90, 1953, 817
- [234] S. GELTMAN: Theory of ionization probability near threshold, *Phys. Rev.* 102(1), 1956, 171
- [235] M.R.H. RUDGE, M.J. SEATON: Ionization of Atomic Hydrogen by Electron Impact, *Proc. R. Soc. A* 283(1393), 1965, 262
- [236] T.D. MÄRK: Cross section for single and double ionization of N₂ and O₂ molecules by electron impact from threshold up to 170 eV, *J. Chem. Phys.* 63, 1975, 3731
- [237] F.A. BAIOCCHI, R.C. WETZEL, R.S. FREUND: Electron-impact ionization and dissociative ionization of the CD₃ and CD₂ free radicals, *Phys. Rev. Lett.* 53, 1984, 771
- [238] D. RAPP, P. ENGLANDER-GOLDEN, D.D. BRIGLIA: Cross sections for dissociative ionization of molecules by electron impact, *J. Chem. Phys.* 42, 1965, 4081
- [239] R.J. VAN BRUNT, G.M. LAWRENCE, L.J. KIEFFER, J.M. SLATER: Electron energy dependence of the kinetic energy and angular distributions of O⁺ from dissociative

- ionization of O_2^* , J. Chem. Phys. 61, 1974, 2032
- [240] H.U. POLL, C. WINKLER, D. MARGREITER, V. GRILL, T.D. MÄRK: Discrimination effects for ions with high initial kinetic energy in a Nier-type ion source and partial and total electron ionization cross-sections of CF_4 , Int. J. Mass Spectrom. Ion Processes 112, 1992, 1
- [241] E. KRISHNAKUMAR, S.K. SRIVASTAVA: Cross sections for the production of N_2^+ , $N^+ + N_2^{2+}$ and N^{2+} by electron impact on N_2 , J. Phys. B 23, 1990, 1893
- [242] E. KRISHNAKUMAR, S.K. SRIVASTAVA: Cross-sections for electron impact ionization of O_2 , Int. J. Mass Spectrom. Ion Processes 113, 1992, 1
- [243] M.F. HARRISON: The determination of atomic collision cross sections using crossed electron and ion beams (and some sources of error in such experiments), Br. J. Appl. Phys. 17, 1966, 371
- [244] A.P. WYNTER, J.B. HASTED: Molecular beam detection using electron impact ionization, J. Phys. E 7, 1974, 627
- [245] K. KIMURA, T. YAMAZAKI, Y. ACHIBA: He I (584 Å) photoelectron spectra and photoionization cross sections of atomic chlorine and bromine, Chem. Phys. Lett. 58(1), 1978, 104
- [246] D.M. DE LEEUW, R. MOOYMAN, C.A. DE LANGE: He(I) photoelectron spectroscopy of halogen atoms, Chem. Phys. Lett. 54(2), 1978, 231
- [247] K. WATANABE: Ionization Potentials of Some Molecules, J. Chem. Phys. 26(3), 1957, 542
- [248] J.D. MORRISON, H. HURZELER, M.G. INGRAM, H.E. STANTON: Threshold law for the probability of excitation of molecules by photon impact. A study of the photoionization efficiencies of Br_2 , I_2 , HI, and CH_3I , J. Chem. Phys. 33(3), 1960, 821
- [249] T. NAKANO, H. SUGAI: Cross section measurements for electron-impact dissociation of SiF_4 into neutral radicals, J. Phys. D: Appl. Phys. 26, 1993, 1909
- [250] SEMATECH: Data Compilation for Plasma Chemistries #4 (ETCH009)
- [251] J.C. CREASEY, I.R. LAMBERT, R.P. TUCKETT, K. CODLING, L.J. FRASINSKI, P.A. HATHERLY, M. STANKIEWICZ: Photoionisation mass-spectrometric study of fragmentation of $SiBr_4$ and $GeBr_4$ in the range 400-1220 Å, J. Chem. Soc. Faraday Trans. 87(23), 1991, 3717
- [252] S. CRADOCK, E.A.V. EBSWORTH, R.A. WHITEFORD: Photoelectron spectra of some simple fluorosilanes, J. Chem. Soc. Dalton Trans., 1973, 2401
- [253] F. HEMPEL, S. GLITSCH, J. RÖPCKE, S. SAß AND H. ZIMMERMANN: On the measurement of absolute plasma species densities using quantum cascade laser-absorption spectroscopy, Plasma Polymers and Related Materials, (M. Mutlu ed.) Hacettepe University Press 2005, 142
- [254] J. RÖPCKE, G. LOMBARDI, A. ROUSSEAU, P. B. DAVIES: Application of mid-infrared tuneable diode laser absorption spectroscopy to plasma diagnostics: a review, Plasma Sources Sci. Technol. 15 2006, S148
- [255] L.S. ROTHMAN, C.P. RINSLAND, A. GOLDMAN, S.T. MASSIE, D.P. EDWARDS, J.-M. FLAUD, A.

- PERRIN, C. CAMY-PEYRET, V. DANA, J.-Y. MANDIN, J. SCHROEDER, A. MCCANN, R.R. GAMACHE, R.B. WATTSON, K. YOSHINO, K.V. CHANCE, K.W. JUCCS, L.R. BROWN, V. NEMTCHINOV, P. VARANASI: The HITRAN molecular spectroscopic database and HAWKS (HITRAN Atmospheric Workstation): 1996 edition, *J. Quant. Spectrosc. Radiat. Transfer* Vol. 60 No. 5, 1998, 665
- [256] F. KÖNIGER, A. MÜLLER, W.J. ORVILLE-THOMAS: The use of isotopic substitution and matrix isolation techniques in determining molecular constants for group IVA tetrahalides, *J. Molecular Structure*. 37, 1977, 199
- [257] T. HEMKE: Measuring rf impedance characteristics of plasma chambers by use of a vector network analyzer, Internship Report, Infineon Technologies Dresden GmbH & Co. OHG, 2005
- [258] M. REINICKE, A. STEINBACH, S. BARTH: Application of insitu Plasma Measurement Techniques on Etch Hardware Design and Process Development for 60nm Structures, presented at the AEC/APC conference, 2005, Dublin (Ireland)
- [259] A. STEINBACH, S. BARTH: Application of insitu Plasma Measurement Techniques on Etch Hardware Design and Process Development for 60nm Structures, presented at the AEC/APC conference, 2004, Dresden (Germany)
- [260] Metryx Ltd., Manor Park, Nailsea Wall Lane, Nailsea, Bristol BS48 4DD, England, <http://www.metryx.net>
- [261] H. G. TOMPKINS, W. A. MCGAHAN: Spectroscopic Ellipsometry and Reflectometry, 1999 John Wiley & Sons, Inc.
- [262] R.W. CAHN FRS: Concise Encyclopedia of Materials Characterization, 2005 Elsevier Ltd.
- [263] G. GAUGLITZ, T. VO-DINH: Handbook of spectroscopy, 2003 Wiley-VCH Verlag GmbH & Co. KGaA
- [264] KLA-Tencor, One Technology Drive, Milpitas, California 95035, USA, <http://www.kla-tencor.com>
- [265] M.B. KUBLY, N.M.P. BENJAMIN, S.D. GERMAIN: Methods and apparatuses for clamping and declamping a semiconductor wafer in a wafer processing system, publication number WO/1998/000861, publication date 1998-01-08
- [266] S. WEGE, A. HENKE, J. SOBE, A. STEINBACH, M. REINICKE, S. BARTH: Verfahren und Messeinrichtung zum Messen der Temperatur eines Prozessgases, Patent DE102005063259A1, publication date 2007-07-12
- [267] M. REINICKE, A. HENKE, A. STEINBACH, J. SOBE, S. BARTH, S. WEGE: Prozessgerät und Verfahren zur Bestimmung der Temperatur eines Substrats in dem Prozessgerät, Patent DE102006009460A1, publication date 2007-09-06
- [268] G.A. HEBNER, E.V. BARNAT, P.A. MILLER, A.M. PATERSON, J.P. HOLLAND: Frequency dependent plasma characteristics in a capacitively coupled 300mm wafer plasma processing chamber, *Plasma Sources Sci. Technol.* 15, 2006, 879
- [269] P.A. MILLER, E.V. BARNAT, G.A. HEBNER, A.M. PATERSON, J.P. HOLLAND: Spatial and frequency dependence of plasma currents in a 300mm capacitively coupled plasma reactor, *Plasma Sources Sci. Technol.* 15, 2006, 889

-
- [270] N.Y. BABAEVA, M.J. KUSHNER: Penetration of Plasma into the Wafer-Focus Ring Gap in Capacitively Coupled Plasmas, *J. Appl. Phys.* 101, 2007, 113307
- [271] N.YU. BABAEVA, M.J. KUSHNER: Ion Energy and Angular Distributions into the Wafer Focus Ring Gap in Capacitively Coupled Discharges, *J. Phys. D* 41, 2008, 062004
- [272] D.C. GRAY: Beam simulation studies of plasma-surface interactions in fluorocarbon etching of Si and SiO₂, Ph.D. thesis, MT Department of Chemical Engineering, 1992
- [273] D.J. OOSTRA: Sputtering of SiO₂ in a XeF₂ and in a Cl₂ atmosphere, *J. Vac. Sci. Technol. B* 4(6), 1986, 1278
- [274] C. STEINBRÜCHEL: Universal energy dependence of physical and ion-enhanced chemical etch yields at low ion energy, *Appl. Phys. Lett.* 55(19), 1989, 1960
- [275] M. REINICKE, J.W. BARTHA, S. WEGE, A. STEINBACH, S. BARTH, G. WENIG, A. KERSCH: In situ Plasma Analysis and Sheath Modeling of Silicon Etching in Capacitively Coupled Plasmas, presented at the AVS 54th International Symposium, 2007, Seattle (USA)
- [276] D. HUMBIRD, D.B. GRAVES: Ion-induced damage and annealing of silicon. Molecular dynamics simulations, *Pure Appl. Chem.* Vol. 74 No. 3, 2002, 419
- [277] S. QIN, M.P. BRADLEY, P.L. KELLERMAN, K. SAADATMAND: Measurements of secondary electron emission and plasma density enhancement for plasma exposed surfaces using an optically isolated Faraday cup, *Rev. Sci. Instrum.* Vol. 73 No. 3, 2002, 1153
- [278] V.A. GODYAK, R.B. PIEJAK: Abnormally low electron energy and heating-mode transition in a low-pressure argon rf discharge at 13.56 MHz, *Phys. Rev. Lett.* 65(8), 1990, 996
- [279] S.-I CHOU, D.S. BAER, R.K. HANSON, W.Z. COLLISON, T.Q. NI: HBr concentration and temperature measurements in a plasma etch reactor using diode laser absorption spectroscopy, *J. Vac. Sci. Technol. A* 19(2), 2001, 477
- [280] J.J. LANDER, J. MORRISON: Low Voltage Electron Diffraction Study of the Oxidation and Reduction of Silicon, *J. Appl. Phys.* 33(6), 1962, 2089
- [281] F.W. SMITH, G. GHIDINI: Reaction of Oxygen with Si(111) and (100): Critical Conditions for the Growth of SiO₂, *J. Electrochem. Soc.: Solid-State Sci. Technol.* 129(6), 1982, 1300
- [282] S. BARTH: Bestimmung der Neutralgastemperatur im Plasma Bulk eines Plasmaätzreaktors, Diploma thesis, Westsächsische Hochschule Zwickau, Germany (2007)
- [283] G. FRANZ: Comprehensive analysis of chlorine-containing capacitively coupled plasmas, *J. Vac. Sci. Technol. A* 23(3), 2005, 369
- [284] G. CUNGE, B. PELISSIER, O. JOUBERT, R. RAMOS, C. MAURICE: New chamber walls conditioning and cleaning strategies to improve the stability of plasma processes, *Plasma Sources Sci. Technol.* 14 No 3, 2005, 599
- [285] R. RAMOS, G. CUNGE, B. PELISSIER, O. JOUBERT: Cleaning aluminum fluoride coatings from plasma reactor walls in SiCl₄/Cl₂ plasmas, *Plasma Sources Sci. Technol.* 16 No 4, 2007, 711

-
- [286] D.L. FLAMM, P.L. COWAN, J.A. GOLOVCHENKO: Etching and film formation in CF_3Br plasmas - some qualitative observations and their general implications, *J. Vac. Sci. Technol.* 17 (6), Nov/Dec 1980, 1341
- [287] J. SU, G.W. HILLS, M. BIRANG, J.A. BONDUR, T. FUKAMACHI, S. OHKI, S. KITAMURA: Deep trench process performance enhancements in an MERIE reactor, *Proc. SPIE* 1803, 1992, 55
- [288] W. FRANK: Untersuchungen zum Einfluss von Druck, Magnetfeld, Leistung und Temperatur auf die Plasmazusammensetzung und die Ätzergebnisse beim anisotropen Trockenätzen von Siliziumschichten mit HBr, Diploma thesis, Siemens AG / Munich University of Technology, Germany (1989)
- [289] G. WENIG, A.KERSCH, S. BARTH, A. HENKE, J. SOBE, A. STEINBACH, S. WEGE, M. REINICKE: Investigation of source and bias pulsing for high aspect ratio silicon etching, presented at the AVS 54th International Symposium, 2007, Seattle (USA)
- [290] S. WEGE, S. BARTH, A. KERSCH, M. REINICKE, G. WENIG, M. RUDOLPH, J. SOBE, A. STEINBACH: High aspect ratio Deep Trench chamber and process development for Silicon etch in DRAM applications below 50 nm, presented at the AVS 54th International Symposium, 2007, Seattle (USA)
- [291] C. KLEIN, T. MAYER-UHMA, J. TREPTE, G. GORETZKI: Spin-coated Zirconia Layers for 300 mm Wafer Technology, presented at the XIVth International Sol-Gel Conference, 2007, Montpellier (France)
- [292] T. MAYER-UHMA: Dense, Uniform and Thick Zirconia Layer for Memory Processing, presented at the International Conference on Chemical Solution Deposition, 2007, Berchtesgaden (Germany)

Acknowledgement

First of all, I would like to thank my thesis advisor Professor Johann Wolfgang Bartha from Dresden University of Technology for his support and granting scientific freedom throughout this project. I would also like to thank my referees Professor Alfred Kersch from University of Applied Sciences Munich, and Professor Eberhard Schultheiß from Fraunhofer Institute for Electron Beam and Plasma Technology for their assistance to perform this project.

Having been enabled through the PhD student program at Qimonda Dresden and the former Infineon Technologies Dresden, this thesis would have not been possible without a full support from manufacturing and metrology resources. I am especially grateful to Dr Andreas Steinbach, Stephan Wege, Dr Axel Henke, Sven Barth, Matthias Rudolph, Jürgen Völkel and Jörg Sobe for many fruitful discussions and helpful comments, and the highly motivating atmosphere in the Future DT development project. Anja Kleiner's support during several metrology tasks as well as extensive data processing was most valuable. A warm thank you to Professor Alfred Kersch and Dr Georg Wenig from the former Qimonda AG process simulation group for their continuing support when performing plasma simulations and modifications of the HPSM code. Once more I am indebted to Stephan Wege, Dr Andreas Steinbach and Dr Georg Wenig, the value of their advice throughout this work and while reviewing the manuscript is hard to express. I would like to also thank Dr Alexander Ruf for enabling my PhD student contract.

As the research done at the Centura HART etch reactor was part of the Future DT joint development project between Qimonda and Applied Materials, I want to express my sincere thanks to especially Manfred Oswald, Frank Schäftlein, Marcus Meye, Uwe Leucke, Jan Rupf, Thorsten Lehmann, Steffen Preiss, Thorsten Lill and Dr Alex Paterson from Applied Materials Dresden and Santa Clara for their kind cooperation throughout my PhD project.

The close cooperation with the Institute of Low-Temperature Plasma Physics, Greifswald, during testing and implementation of the novel QCLAS diagnostic technique for process monitoring and control should be emphasized as well. I enjoyed the warm hospitality and the intense discussions with Professor Jürgen Röpcke, Dr Gabi Stancu, and especially Dr Norbert Lang during several stays and workshops in Greifswald and Dresden.

Furthermore, the commitment and support from Hiden Analytical Ltd., especially from Terry Whitmore and Dr Claire Greenwood, during adaption and application of the EQP probe for insitu plasma diagnostics is gratefully acknowledged.

Also, I would like to thank Dr Vasile Vartolomei from Max-Planck Institute for Plasma Physics, Garching, for his dedication to several fruitful discussions regarding plasma diagnostics in an electrically floating environment.

Special thanks goes to my family and friends, whose encouragement and support has been crucial in making this work possible. Finally, I would like to express my deepest gratitude to Andrea and Willi for their continuing love and appreciation.

The work for this paper was partly supported by the EFRE fund of the European Community and by funding of the State of Saxony of the Federal Republic of Germany, projects IGEL (project number 10758/1659) and DRACHEN (project number 11587/1836). The author is responsible for the content of the thesis.

Erklärung

Hiermit versichere ich, daß ich die vorliegende Arbeit ohne unzulässige Hilfe Dritter und ohne Benutzung anderer als der angegebenen Hilfsmittel angefertigt habe; die aus fremden Quellen direkt oder indirekt übernommenen Gedanken sind als solche kenntlich gemacht.

Weitere Personen waren an der geistigen Herstellung der vorliegenden Arbeit nicht beteiligt. Insbesondere habe ich nicht die Hilfe eines Promotionsberaters in Anspruch genommen. Dritte haben von mir weder unmittelbar noch mittelbar geldwerte Leistungen für Arbeiten erhalten, die im Zusammenhang mit dem Inhalt der vorgelegten Dissertation stehen.

Die Arbeit wurde bisher weder im Inland noch im Ausland in gleicher oder ähnlicher Form einer anderen Prüfungsbehörde vorgelegt und ist auch noch nicht veröffentlicht worden.

Ich bestätige, daß ich die Promotionsordnung der Fakultät Elektrotechnik und Informationstechnik vom 08.08.1994 in der geänderten Fassung vom 18.12.2001 der TU Dresden anerkenne.

Dresden, den 27.02.2009

Marco Reinicke

Publications

D. ZHOU, U. SCHRÖDER, G. JEGERT, M. KERBER, S. UPPAL, R. AGAIBY, M. REINICKE, J. HEITMANN, L. OBERBECK: Time dependent dielectric breakdown of amorphous $ZrAl_xO_y$ high-k dielectric used in dynamic random access memory metal-insulator-metal capacitor, J. Appl. Phys. 106, 2009, 044104

J. MÜLLER, T.S. BÖSCKE, U. SCHRÖDER, M. REINICKE, L. OBERBECK, D. ZHOU, W. WEINREICH, P. KÜCHER, M. LEMBERGER, L. FREY: Improved manufacturability of ZrO_2 MIM capacitors by process stabilizing HfO_2 addition, Microelectron. Eng. 86 (7-9), 2009, 1818, doi:10.1016/j.mee.2009.03.076

M. REINICKE, J.W. BARTHA, S. WEGE, A. STEINBACH, S. BARTH, G. WENIG, A. KERSCH: Insitu Plasma Analysis and Sheath Modeling of Silicon Etching in Capacitively Coupled Plasmas, presented at the AVS 54th International Symposium, 2007, Seattle (USA)

G. WENIG, A.KERSCH, S. BARTH, A. HENKE, J. SOBE, A. STEINBACH, S. WEGE, M. REINICKE: Investigation of source and bias pulsing for high aspect ratio silicon etching, presented at the AVS 54th International Symposium, 2007, Seattle (USA)

S. WEGE, S. BARTH, A. KERSCH, M. REINICKE, G. WENIG, M. RUDOLPH, J. SOBE, A. STEINBACH: High aspect ratio Deep Trench chamber and process development for Silicon etch in DRAM applications below 50 nm, presented at the AVS 54th International Symposium, 2007, Seattle (USA)

G.D. STANCU, N. LANG, J. RÖPCKE, M. REINICKE, A. STEINBACH, S. WEGE: In situ monitoring of silicon plasma etchig using a quantum cascade laser arrangement, Chem. Vap. Deposition 13, 2007, 351

G.D. STANCU, N. LANG, J. RÖPCKE, M. REINICKE, A. STEINBACH, S. WEGE: In situ monitoring of silicon plasma etchig using a quantum cascade laser arrangement, plenary talk at FLAIR, 2007, Florence (Italy)

M. REINICKE, J.W. BARTHA, S. WEGE, A. STEINBACH, S. BARTH, G. WENIG, A. KERSCH: Application of insitu Plasma Analysis on Deep Trench Plasma Etch Hardware Design and Process Development, presented at the AVS 53rd International Symposium, 2006, San Francisco (USA)

S. WEGE, S. BARTH, A. HENKE, A. KERSCH, M. REINICKE, W. SABISCH, J. SOBE, A. STEINBACH: Chamber and process development of high aspect ratio Deep Trench Si etch for DRAM application below 60nm", presented at the AVS 53rd International Symposium, 2006, San Francisco (USA)

A.KERSCH, W. SABISCH, D. FISCHER, W.JACOBS, S. BARTH, A. HENKE, J. SOBE, A. STEINBACH, S. WEGE, M. REINICKE: Development of high aspect ratio, selective Si etch model in CCP halogen plasma, presented at the AVS 53rd International Symposium, 2006, San Francisco (USA)

G.D. STANCU, N. LANG, M. REINICKE, A. STEINBACH, S. WEGE, S. BARTH, P.B. DAVIS, J. RÖPCKE: MIR Spectroscopic Techniques: from Basic Research to Industrial Applications", plenary talk at the 1st workshop on Infrared Plasma Spectroscopy, June 2006, Greifswald (Germany)

M. TESAURO, R. FORRISTER, D. PURVIS, M. REINICKE, A. STEINBACH: Characterization of Plasma Etch Process Conditions by direct Measurement of Ion Current and Potential Distribution on Wafer Surface, presented at the 7th European Advanced Equipment Control/Advanced Process Control (AEC/APC) Conference, 2006, Aix-en-Provence (France)

M. REINICKE, A. STEINBACH, S. BARTH: Application of insitu Plasma Measurement Techniques on Etch Hardware Design and Process Development for 60nm Structures, presented at the 6th European Advanced Equipment Control/Advanced Process Control (AEC/APC) Conference, 2005, Dublin (Ireland)

S. WEGE, M. STEGEMANN, A. HENKE, A. STEINBACH, S. BARTH, M. REINICKE, J. SOBE, A. KERSCH, W. SABISCH, G. SCHULZE-ICKING: High Aspect Ratio Deep Trench Silicon Etching For Technologies Below 70nm, presented at the ECS conference, 2005, Shanghai (China)

M. REINICKE, C. WENGER, C. WENZEL, J.W. BARTHA, H.-J. ENGELMANN, E. ZSCHECH: Electrical characterization of MOS structures to study the performance of ultra-thin TaSiN diffusion barriers for copper interconnect systems, EUROMAT (The European Congress and Exhibition on Advanced Materials and Processes) poster, 2003, Lausanne (Switzerland)

C. WENGER, R. HUEBNER, C. WENZEL, M. REINICKE, M. HECKER, N. MATTERN, K. WETZIG, J. BAUMANN, S. SCHULZ, J.W. BARTHA, H.-J. ENGELMANN, E. ZSCHECH: Stability of Graded Ta-TaN-Ta and Single Layer TaSiN Diffusion Barriers for Copper Interconnect Systems, AMC conference poster and paper, 2002, San Diego (USA)

Patents

S. WEGE, A. HENKE, J. SOBE, A. STEINBACH, M. REINICKE, S. BARTH: Verfahren und Messeinrichtung zum Messen der Temperatur eines Prozessgases, Patent DE102005063259A1, publication date 2007-07-12

M. REINICKE, A. HENKE, A. STEINBACH, J. SOBE, S. BARTH, S. WEGE: Prozessgerät und Verfahren zur Bestimmung der Temperatur eines Substrats in dem Prozessgerät, Patent DE102006009460A1, publication date 2007-09-06

Lebenslauf

Persönliches

Name: Marco Reinicke
Geburtsdatum: 04. September 1977
Geburtsort: Merseburg/Saale
Familienstand: ledig, 1 Kind

Schulbildung

1984 - 1989 Erich-Weinert-OS, Merseburg
1989 - 1991 Albrecht-Dürer-Schule I, Merseburg
1991 - 1996 Domgymnasium Merseburg
22.06.1996 Abitur

Hochschulausbildung

1997 - 2003 Studium Mikroelektronik, Fakultät Elektrotechnik und Informationstechnik, Technische Universität Dresden
12.08.2003 Abschluss als Diplom-Ingenieur
Diplomarbeit bei Prof.Dr.rer.nat. J.W. Bartha, TU Dresden:
"Charakterisierung von MOS-Strukturen zur Beurteilung der Stabilität von ultra-dünnen TaSiN-Diffusionsbarrieren gegenüber der Diffusion von Kupfer"
21.07.2009 Promotionsverteidigung
Doktorarbeit bei Prof.Dr.rer.nat. J.W. Bartha, TU Dresden:
"Investigation of physical and chemical interactions during etching of silicon in dual frequency capacitively coupled HBr+NF₃ gas discharges"

Berufliche Tätigkeiten

1997 Grundpraktikum bei SONOTEC Ultraschallsensorik Halle GmbH
2001 - 2002 Fachpraktikum bei Applied Materials Inc. (USA)
1998 - 2003 Studentische Hilfskraft am Institut für Halbleiter- und Mikrosystemtechnik, TU Dresden
2003 Wissenschaftlicher Mitarbeiter am Institut für Halbleiter- und Mikrosystemtechnik, TU Dresden
2004 - 2007 Promotionsstudent bei Infineon Technologies Dresden GmbH & Co. OHG und Qimonda Dresden GmbH & Co. OHG
2007 - 2009 Entwicklungsingenieur bei Qimonda Dresden GmbH & Co. OHG
seit 2009 Entwicklungsingenieur bei Bosch Solar Energy AG

